Biophysical mechanisms subserving stable and dynamic attractors within local frontal recurrent neural networks

Matthieu Sarazin

Sorbonne Université

École doctorale ED3C Cerveau, Comportement, Cognition

Institut des Systèmes Intelligents et de Robotique

Biophysical mechanisms subserving stable and dynamic attractors within local frontal recurrent neural networks

Par Matthieu SARAZIN

Thèse de doctorat en Neurosciences Computationnelles

Dirigée par Bruno Delord et co-encadrée par Jérémie Naudé

Publiquement soutenue le 28 Octobre 2021

Devant un jury composé de :

Abigail MORRISON	Prof., FZJ, Rhineland-Westphalia Technical University, Aachen	Rapporteuse
Suliann BEN HAMED	PU, ISC-MJ, Université Lyon 1	Rapporteuse
Emmanuel PROCYK	DR, SBRI, Université Lyon 1	Examinateur
Eleonora RUSSO	Indep. Fellow, CSG, Johannes Gutenberg University, Mainz	Examinatrice
Dr. Jérémie NAUDE	CR, IGF, Université de Montpellier	Co-superviseur de thèse
Pr. Bruno DELORD	PU, ISIR, Sorbonne Université, Paris	Directeur de thèse

Acknowledgments

I would first like to thank my supervisor, Bruno Delord, for giving me the opportunity to deepen my understanding of neuroscience computational modeling. The logical rigor of your scientific reasoning, combined with a great amount of kind and caring goodwill, has allowed me to considerably mature as a scientist. Thank you very much for consistently and indefatigably supporting me all throughout the thesis in innumerable ways, be it scientific, financial and administrative or personal, resulting in a fruitful partnership with many published or soon-to-be published articles. Thank you for having offered me the opportunity to develop close and stimulating partnerships with experimental teams (notably Jérémie and Emmanuel). I would also like to thank Jérémie, which has served as a close adviser and role model for me, systematically redirecting me toward critical thinking concerning my results and clarifying my strategical positioning within the neuroscience literature.

Many thanks go to the experts on my jury – Abigail Morrison, Ben Hamed Suliann, Emmanuel Procyk, and Eleonora Russo – for dedicating the time and energy into evaluating and helping me improve my work. Thank you Emmanuel Procyk for your wisdom and calm, representing the voice of reason on many occasions. Thank you Frederic Chavane and Bruno Cessac for helping me putting my work into perspective and giving thoughtful and sometimes-hard-to-hear necessary advice.

I would also like to thank my many comrades currently or formerly within the lab. Thank you David Medernach, Maud de Tollenaere, Nicolas Fontbonne, Morgane Leroux, Eleonore Schultz, Rémi Dromnelle, Paul Ecoffet, Giuseppe Paolo, Elisa Massi, Astrid Merckling, Benoit Girard, Mehdi Khamassi, Léni LeGoff, Marwen Belkaid, Stéphane Gourichon, Pierre Luce-Vayrac, for all the good times and laughs, helping me recover my spirits with every error and negative result, and all the thought-provoking, interesting and sometimes outright wildly abstract and mind-bending conversations in which I thrive.

Many thanks to my close family for the systematic support, through the tough patches and the roughly prepared presentations, and for everything. And finally, thank you Marion for doing it all with me and more, words don't suffice.

Abstract

Recurrent neuronal networks exhibit diverse types of collective dynamics, from stable network states and long timescales subserved by bursting or persistent neuronal activity, to dynamic trajectories resulting from transient sequential neuronal activity. This dynamical diversity contributes to the array of complex and flexible cognitive functions of the frontal cortex. Describing these dynamics in the language of dynamical systems as static stable or dynamical attractors is relevant, since attractors have the desirable property of being robust to the synaptic noise and chaotic activity regime characteristic of awake cortex. Through biologically-detailed descriptions of neural networks – necessary to account for these real cortical conditions –, the present thesis aims at identifying the biophysical determinants allowing for the emergence of stable and dynamic attractors robust to these destabilizing influences.

Stable attractors, such as peregrination between quasi-stable network states during working memory within the monkey prefrontal cortex (PFC) or temporal information integration within the monkey midcingulate cortex (MCC), arises from bursting or persistent activity within neurons. Chapter 2 proposes intrinsic conditional bistability, in which neuronal bistable activity is conditional upon subthreshold input after the initial trigger, as an important underpinning of flexible PFC working memory. In a complementary fashion, Chapter 3 and 4 identify strong intrinsic hyperpolarizing and slow synaptic inhibitory currents as being responsible for longer MCC neuronal timescales (compared to PFC), i.e. long-lasting bursts of neuronal activity. These slow neuronal responses amplify into stable network states at the behavioral timescale, allowing for the temporal integration of information, e.g. building an action-reward outcome history for behavioral adaptation and exploration.

Further results in Chapter 4 indicate these MCC network states are actually sequentially organized within macroscopic meta-states, within which each state contains persistent activity or neural activity sequences subserving stable or dynamic representations. Indeed, recent evidence suggests that MCC and PFC show stable and dynamic network encoding during temporal integration and working memory respectively, with sequences of transient sparse neural activity typically observed during rat working memory ("relay race"). Such sequences are also often observed in rat PFC and hippocampus (HP) in navigational tasks, being replayed at various speeds during sleep and immobility. Such behavior-independent replays require the formation of synaptic chains (pathways), e.g. via STDP and homeostatic meta-plasticity. Chapter 5 models the replay of previously learned dynamic attractors within chaotic synaptic noise after an external triggering cue, and identifies biophysical mechanisms increasing the reliability and robustness of such sequence replays. Furthermore, the model and its mechanisms are generically applicable to many stable/dynamic and discrete/continuous attractor types. Chapter 6 builds on the previous model by studying in depth the "online" learning of such trajectories during noisy network dynamics (rather than trajectories being phenomenologically "previously learned" in Chapter 5). It also studies their replay at different speeds (as for navigation), and capacity for simultaneous dynamic and stable coding. Finally, Chapter 7 goes further, describing the dual effect of dopaminergic modulation on 1) online learning of navigational trajectories toward a rewarding goal by building dynamic and stable neuronal assemblies, and 2) intrinsically-generated motivation-driven behaviors (without an external triggering cue) by unveiling the learned attractor through synaptic reverberation.

Contents

List of publications

Sarazin, Matthieu XB, Julie Victor, David Medernach, Jérémie Naudé, and Bruno Delord. "Online Learning and Memory of Neural Trajectory Replays for Prefrontal Persistent and Dynamic Representations in the Irregular Asynchronous State." Frontiers in Neural Circuits (**2021**): 57.

Procyk, Emmanuel, Vincent Fontanier, Matthieu XB Sarazin, Bruno Delord, Clément Goussi, and Charles RE Wilson. "The midcingulate cortex and temporal integration." What Does Medial Frontal Cortex Signal During Behavior? Insights from Behavioral Neurophysiology 158 (**2021**): 395.

Rodriguez, Guillaume, Matthieu XB Sarazin, Alexandra Clemente, Stephanie Holden, Jeanne T. Paz, and Bruno Delord. "Conditional bistability, a generic cellular mnemonic mechanism for robust and flexible working memory computations." Journal of Neuroscience 38, no. 22 (**2018**): 5209-5219.

Fontanier, Vincent, Matthieu XB Sarazin, Frederic Stoll, Bruno Delord, and Emmanuel Procyk. "Inhibitory control of frontal metastability sets the temporal signature of cognition", BioRXiv (under revision at eLife, **2021**)

Sarazin, Matthieu XB, David Medernach, Jérémie Naudé, and Bruno Delord. "Biophysical mechanistic account of functional ordered trajectories in the disordered neural regime." *in writing*

Naudé, Jérémie, Matthieu XB Sarazin, Sarah Mondoloni, Bernadette Hanesse, Éléonore Vicq, Fabrice Amegandjin, Ludovic Tricoire, Alexandre Mourot, Philippe Faure, Bruno Delord, "Dopamine builds and unveils reward-associated attractors", *in writing*

Table of abbreviations

PFC: Prefrontal cortex
LPFC: Lateral prefrontal cortex
MCC: Midcingulate cortex
HP: Hippocampus
CA1: First region of the hippocampal circuit
NR: Nucleus reuniens
V1: Primary visual cortex
HMM: Hidden Markov Model
AMPA: α-amino-3-hydroxy-5-methyl-4-isoxazolepropionic acid
NMDA: N-methyl-D-aspartate acid
GABA-B: γ-aminobutyric acid B
CaL: high-threshold L-type calcium current
CAN: Calcium-activated nonspecific cationic current
PV+: Parvalbumin expressing
SST+/CB+: Somatostatin or calbindin expressing
VIP+/CR+: Vasoactive-intestinal peptide or calretinin expressing
SWS: Slow wave sleep
REM: Rapid eye movement
SWR: Sharp wave ripple
STDP: Spike timing-dependent plasticity
LTP: Long-term potentiation
LTD: Long-term depression
aKP: kinase and phosphatase
BCM: Bienenstock Cooper Munro
CV: Coefficient of Variation
ISI: Inter-spike interval

Chapter 1. Introduction

Recurrent neuronal networks exhibit an array of population and neuronal dynamics, from stable network states and long timescales subserved by persistent or bursts of neuronal activity, to dynamic trajectories of population activity through underlying heterogeneous or transient sequential neuronal activity. It is assumed that the dynamical diversity that population and neuronal activity exhibit is necessary for successful execution of the large assortment of complex and flexible cognitive operations performed within biological recurrent neuronal networks. One way to mathematically describe these dynamics is through the language of dynamical systems as attractors, where population or neuronal dynamics converge to – or reside at – stationary (e.g. point, line, ring or plane) attractors, follow regular time-varying dynamics (such as limit cycle or quasi-periodic attractors), or peregrinate along chaotic attractors (irregular dynamics). This description is relevant, since attractors have the desirable property of describing reproducible activity patterns which are robust to thermal intrinsic and synaptic noise, as observed in cortical neuronal networks. Actually, in behaving animals, complex electrophysiological, plastic and neuromodulatory interactions generate neural dynamics that follow complex and ever changing combinations of all of these attractor archetypes.

→ **That being the case, what biophysical determinants within biological recurrent neuronal networks allow the emergence of stable and dynamic attractors**?

The study of such determinants requires a biophysically-detailed model, in which the temporal properties of synaptic and intrinsic currents, whose neurons are embedded within synaptic architectures learned via plasticity, result in network and neuronal attractor dynamics.

1.1. Stable network dynamics in frontal circuits

1.1.1. Long frontal timescales and stable population states

Several lines of evidence indicate that cortical activity displays marked patterns of stability reminiscent of stable attractors. Indeed, cortical areas are organized within an anatomical (Felleman and Van Essen, 1991; Markov et al., 2013) and temporal (Murray et al., 2014) hierarchy, with increasingly longer population (Murray et al., 2014) and neuronal (Wasmuht et al., 2018) activity timescales from fast posterior sensory to slow anterior associative cortical areas. Longer frontal timescales allow integration of information over longer durations, subserving higher cognitive functions such as working memory and decision-making (Cavanagh et al., 2018; Wasmuht et al., 2018), as well as evaluation of behavioral strategies by monitoring the recent history of reward integration (Bernacchia et al., 2011).

In the same vein, Hidden Markov Models (HMM) analyses, which model time series data as probabilistic transitions between few static hidden states, suggest network activity switches between stable discrete states in frontal cortices. Such behavior has been observed during sustained attentional states (Engel et al., 2016), in relation to the encoding of animals' position (Maboudi et al., 2018), working memory (Gat and Tishby, 1992; Batuev, 1994; Abeles et al., 1995; Seidemann et al., 1996; Rainer and Miller, 2000; La Camera et al., 2019), the maintenance of

behavioral rules (Durstewitz et al., 2010) and during extended periods of deliberation preceding the formation of behavioral decisions (Rich and Wallis, 2016; Taghia et al., 2018).

Both of these long population timescales and discrete states emerge from neuronal activity with long timescales (i.e. stable attractors or slow dynamics), corresponding to persistent or long bursts of neuronal activity such as that underlying working memory in primate PFC, e.g. during delayed response tasks (Funahashi et al., 1989; Goldman-Rakic, 1995; Shafi et al., 2007; Constantinidis et al., 2018; Leavitt et al., 2018).

→ What biophysical mechanisms allow the emergence of persistent or bursting neuronal activity underlying stable states and long timescales, i.e. stable attractors?

1.1.2. Synaptic reverberation within Hebbian assemblies

A proposed mechanistic explanation for the timescale hierarchy is the existence of gradients of synaptic local and long-range excitation (Chaudhuri et al., 2015), corresponding to increasing numbers of dendritic spines on pyramidal neurons (Elston, 2007; Wang, 2020) as well as slower NMDA currents along the hierarchy (Wang, 2020). This is notable, since stronger and slower excitatory NMDA currents naturally lead to the maintenance of persistent activity when combined with synaptic learning of Hebbian neuronal assemblies (Wang, 1999). Indeed, NMDA channels induce depolarizing currents most strongly when both pre-synaptic and post-synaptic neurons are simultaneously active. In the Hebbian framework (Hebb, 1949), synapses between excitatory neurons with coincident activity are potentiated, leading to the emergence of strong bidirectional connections between neurons and thus an assembly of strongly interconnected excitatory neurons. As such, high spiking frequency in a subset of the assembly induces strong excitatory currents, and thus high frequency, within the rest of the assembly. This positive feedback loop or reverberation of synaptic excitation, a.k.a. "synaptic reverberation", thus results in persistent neuronal and assembly activity (Brunel and Wang, 2001; Wang, 2001; Compte, 2006). The effect is mostly mediated by the slow decay of NMDA currents, maintaining excitation through temporal summation of excitatory post-synaptic potentials (EPSPs) in the absence of inputs, and is reinforced when NMDA currents are stronger and slower (Compte et al., 2000; Tegnér et al., 2002; Ermentrout, 2003; Wang et al., 2013). Assembly activity is then defined as one of 2 possible states, quiescent or high frequency, i.e. with bistable dynamics. When inscribing the bistable dynamics of each cortical area within the cortical hierarchy, this results in a multi-stable system composed of many bistable sub-systems with multiple distinct stable attractors, i.e. distributed working memory (Mejias and Wang, 2020).

However, alongside the gradient of increasing pyramidal spine counts and slower NMDA, also exists a systematic gradient of changing PV+, SST+/CB+ and VIP+/CR+ interneuron proportions (Torres-Gomez et al., 2020; Wang, 2020) along the hierarchy, alluding to an important functional role for inhibition (Wang and Yang, 2018). Indeed, it has been observed that MCC is subject to stronger & slower inhibitory currents compared to LFPC (lower in the temporal hierarchy, Medalla et al., 2017). The potentially important role of inhibition is further supported by theoretical analyses, showing that strong excitatory currents need to be balanced with strong inhibitory currents in order to avoid excitatory activity saturation or silencing, which

in turns counterintuitively allows more robust bistability (Joglekar et al., 2018). Additionally, modulating inhibitory activity and connectivity leads to greater effects upon model networks compared to modulation of their excitatory equivalent (Mongillo et al., 2018), since inhibitory neurons and connections are less numerous.

→ This being the case, what role do inhibitory synaptic currents hold in establishing long population timescales and states through bursting and persistent activity?

Biophysical modeling at the level of currents, which the aforementioned inter-areal excitatory gradient models (Chaudhuri et al., 2015) lack, would allow to disambiguate contributions of faster or slower excitatory and inhibitory currents.

1.1.3. Bistability through intrinsic currents

In addition to synaptic reverberation, intrinsic currents can lead to the emergence of persistent or bursts of neuronal activity, notably in the context of working memory tasks (e.g. object (Compte, 2006), spatial (Camperi and Wang, 1998), and parametric (Koulakov et al., 2002; Goldman et al., 2003) working memory), within cortical structures (Krnjević et al., 1971; Schwindt et al., 1988; Silva et al., 1991; Tahvildari et al., 2007; Zhang and Séguéla, 2010) and PFC (Haj-Dahmane and Andrade, 1997; Dembrow et al., 2010; Gee et al., 2012; Thuault et al., 2013). Intrinsic bistability originates from calcium-dependent depolarizing currents, which open due to spike-mediated calcium intake, and in turn bring about more spikes. This positive feedback loop results in a bistable system with two fixed points, one at low frequency or quiescence and the other at high frequency, allowing to maintain past information but this time in individual neurons (Booth and Rinzel, 1995; Delord, 1996; Marder and Calabrese, 1996; Delord et al., 1997; Shouval and Gavornik, 2011).

However, such forms of strongly stereotyped "absolute" bistability in vitro require strong levels of pharmacological manipulations (e.g. neuromodulation) and display extremely long highly regular spike trains, which are not observed in behaving animals (Haj-Dahmane and Andrade, 1997; Egorov et al., 2002; Tahvildari et al., 2007; Zhang and Séguéla, 2010; Gee et al., 2012). Furthermore, the rigidity of such bistability does not allow to account for the relative lability of stable attractors, e.g. transitions between stable network states (Abeles et al., 1995; Seidemann et al., 1996; Rainer and Miller, 2000).

→ As a result, do less stereotyped and more biophysically plausible forms of intrinsic bistability exist, and if so, what intrinsic currents are responsible of their emergence ?

1.2. Sequences of transient sparse neural activity

As mentioned before, network activity peregrinates between distinct states (Mazzucato et al., 2015). Indeed, other than the previous examples, sequences of assembly activations are observed in adult rat somatosensory and visual cortex and HP during wake, SWS and REM sleep (Almeida-Filho et al., 2014). Furthermore, rapid series of state transitions are observed before network activity settles into a stable state in monkey PFC during working memory tasks after cue onset (Abeles et al., 1995; Seidemann et al., 1996; Stokes et al., 2013), and alternating states are observed during spontaneous activity (Kenet et al., 2003; Mazzucato et al., 2015), although

it is not clear to which extent these network states are organized into repeating sequences (Abeles et al., 1995; Seidemann et al., 1996; Mazzucato et al., 2015; La Camera et al., 2019). Conversely, states themselves can contain sequences of neuronal activity, since propagation of neuronal activity sequences depends upon current network state in rat dissociated cortical neurons (Yada et al., 2016).

→ Therefore, to what extent do stable network states actually exhibit neural sequences within them ? Are these states themselves organized into repeatable sequences? And what biophysical mechanisms allow the replicable propagation of sequences?

1.2.1. Working memory

1.2.1.1 Dynamic vs persistent coding in monkey PFC

More generally, there has been debate recently over the extent of persistent activity – and thus stable attractors – in monkey PFC during working memory delay (Stokes and Spaak, 2016; Lundqvist et al., 2018a), in favor of more transient activity – and thus dynamic attractors. Lundqvist and colleagues argue instead for sparse transient activations within single trials, persistent activity being artificially caused by averaging sparse activity across trials or single-trial persistent activity only shown in cherry-picked example neurons. Indeed, while certain neurons do indeed show sustained firing during the delay period, they can also exhibit complex heterogeneous activity during working memory (Rainer and Miller, 2002; Brody et al., 2003; Shafi et al., 2007; Meyers et al., 2008). This complex heterogeneous activity can even strongly resemble transient dynamics (Meyers et al., 2008).

When reinterpreted within the context of population dynamics, PFC networks encode task-relevant variables dynamically, be it *via* changing population activity or neural tuning (Barak et al., 2010; Stokes et al., 2013; Sreenivasan et al., 2014). Stable representations can then result from the combination of changing neural activity and selectivity, with alternation between dynamic and stable coding epochs (Spaak et al., 2017) or stable coding dynamically morphed by distractors (Parthasarathy et al., 2017). Dynamic and stable coding can also simultaneously coexist, where stable representations emerge from a subpopulation of neurons with slow timescales and dynamic representations from the fast timescale neural subpopulation, Cavanagh et al., 2018; Wasmuht et al., 2018). Even without considering distinct neuronal subpopulations, such coexistence has been described at the network activity level as orthogonal stable and dynamic low-dimensional subspaces, network activity being stable along certain subspace dimensions and dynamic along others (Machens et al., 2010; Murray et al., 2017).

The aforementioned mixtures of dynamic coding schemes show repeated trajectories of network activity in low-dimensional subspaces (within the larger N-dimensional space spanning the activity of every neuron). The underlying pattern of neuronal activity can take many different forms, being at least necessarily heterogeneous and time-varying for a subset of neurons. Of the numerous possibilities, network activity can take the shape of an underlying sequence of transient neural activity during the cue, delay and response periods of working memory tasks. Theoretically, sequences of transient sparse neural activity naturally offer a framework able to reconcile (i.e. account for both) stable and dynamic coding. Indeed, persistent population-averaged frequency allows a downstream neuron receiving synapses from all neurons in the

population to decode categorical sustained information (i.e. is the population active or not). Simultaneously, time-varying individual neural frequency may allow other downstream neurons, receiving synapses from well-chosen subsets of the population, to decode temporal information (i.e. how much time has elapsed, or at what part is the sequence currently at, Goldman, 2009).

Are such sequences truly observed? They can be indirectly observed via large repeatable neural latency distributions (Zaksas and Pasternak, 2006) and sequences of neural selectivity (measured as strong activity differences between two conditions), which last 0.5-4s in monkey LPFC (Cromer et al., 2010; Hussar and Pasternak, 2012; Lara and Wallis, 2014; Spaak et al., 2017; Cavanagh et al., 2018; Lundqvist et al., 2018b), or more directly via delay-selective neurons (Batuev, 1994). In areas with activity associated to the PFC during working memory, such as the parietal cortex, long (3 s) sequences of transient activity can be observed (Crowe et al., 2010), with dynamic task-relevant and persistent task-irrelevant neural coding. Observations of neuronal activity sequences take many different forms (with different recorded observables, at different temporal scales) due to the lack of a unifying descriptive framework, although the following experimental literatures have prominently observed them directly.

1.2.1.2 Tiling the working memory delay period in rat with transient sparse neural sequences

Compelling evidence of neuronal activity sequences comes from rodent PFC, in which sequences of repeatable transient neuronal activity, a.k.a. "relay races", can be observed during the working memory delay period. Repeated sequences of transient sparse neural activity have been observed during working memory delays in PFC (Bakhurin et al., 2017; Bolkan et al., 2017; Schmitt et al., 2017; Rikhye et al., 2018) and associated areas such as dorsomedial thalamus (Rikhye et al., 2018) and striatum (Mello et al., 2015; Akhlaghpour et al., 2016; Bakhurin et al., 2016, 2017), as well as posterior parietal cortex (Harvey et al., 2012; Runyan et al., 2017) and auditory cortex (Runyan et al., 2017). The sequences can be of arbitrary length, spanning tens of seconds (up to 60 s, Mello et al., 2015; Bolkan et al., 2017; 2.5-10 s, Akhlaghpour et al., 2016), seconds (~5 s, Harvey et al., 2012; Yang et al., 2014; Bakhurin et al., 2016; 2.5s, Bakhurin et al., 2017) or hundreds of milliseconds (900ms, Rikhye et al., 2018; 400ms Schmitt et al., 2017). They are functionally relevant, supporting retrospective working memory of spatial (Yang et al., 2014) and behavioral rules (Schmitt et al., 2017), as well as prospective working memory by transforming previously encoded information, such as the representation of elapsed time (Tiganj et al., 2017) or encoding of forthcoming behaviors (Nakajima et al., 2019; Passecker et al., 2019).

Of particular interest is the observation that these sequences are intrinsically generated, since they are not continuously driven by sensory inputs or motor outputs during the working memory delay period. This suggests the existence of underlying synaptic chains (pathways) within the respective cerebral structures, which allow for the propagation of neural activity packets in reliable temporal order after an initial trigger (e.g. the cue onset). Several lines of evidence further hint at this idea, such as the observation that increased thalamocortical input leads to stronger sequences in PFC and better working memory performance by increasing functional connectivity between PFC pyramidal cells (Schmitt et al., 2017). Furthermore, the fact

that working memory performance increases with repetition, combined with the fact that task-related sequences are specific to different task cues (Schmitt et al., 2017), and that PFC is implicated in learning arbitrary associations rapidly (Asaad et al., 1998), suggests cue-specific learning of synaptic chains in PFC. Finally, neurons active at different time delays during sequences in parietal cortex are anatomically intermixed at the ~200µm scale (Harvey et al., 2012), alluding to local network synaptic plasticity mechanisms.

→ In this context, what local synaptic plasticity rule could allow the emergence of synaptic chains and propagation of neuronal activity sequences?

1.2.2. Prefrontal cortex and hippocampal replay during navigation

Nonetheless, the most conclusive evidence concerning sequence learning and replay comes from replay of spatial trajectories during navigational tasks in rodent PFC and HP. During navigational behavior, sequences of activity emerge within neurons spatially selective to the animal's position due to the animal's displacement across time (O'Keefe and Dostrovsky, 1971; Fujisawa et al., 2008; Ito et al., 2015; Zielinski et al., 2019). These behaviorally-driven sequences are then replayed at faster timescales within theta cycles in HP during awake (Skaggs et al., 1996) quiet wakefulness, such as during immobility (Kudrimoti et al., 1999; Diba and Buzsáki, 2007; Davidson et al., 2009; Jadhav et al., 2016) or consummatory behavior (Nádasdy et al., 1999), as well as wheel running (Nádasdy et al., 1999). Compressed sequences recapitulating sequences encountered during awake behavior also occur during SWS (Skaggs and McNaughton, 1996; Kudrimoti et al., 1999; Nádasdy et al., 1999; Lee and Wilson, 2002; Ji and Wilson, 2007; Peyrache et al., 2009; Mizuseki et al., 2012). The very existence of fast replays of sequences, previously observed during behavior, requires the formation of synaptic chains. Furthermore, these fast replays are generally associated with HP SWR events during wake (Nádasdy et al., 1999; Diba and Buzsáki, 2007; Davidson et al., 2009; Jadhav et al., 2016) and sleep (Kudrimoti et al., 1999; Nádasdy et al., 1999; Lee and Wilson, 2002; Ji and Wilson, 2007; Peyrache et al., 2009). HP SWR events have been shown to be necessary for memory formation and subsequent behavioral performance (Girardeau et al., 2009), further reinforcing the notion that sequences are learned.

Other than fast sequences, intrinsically-generated sequences at slow behavioral timescales can also be learned and replayed without being driven by motor or sensory components, such as during awake wheel running delay (Pastalkova et al., 2008; Itskov et al., 2011) predicting future navigational trajectory (Pastalkova et al., 2008), as well as during REM sleep following behavior, replaying behavioral sequences at equivalent or slower speeds (Louie and Wilson, 2001; Mizuseki et al., 2012).

Sequence learning and replay occur not only in HP but also within other areas involved in spatial navigational tasks. PFC replays are generally linked to HP SWR events during awake immobility (Jadhav et al., 2016; Kaefer et al., 2020), with spontaneous reactivations during SWS of patterns learned during behavior (Euston et al., 2007; Peyrache et al., 2009; Johnson et al., 2010b) linked to DOWN-UP state transitions (Peyrache et al., 2009; Johnson et al., 2010b). PFC-HP interactions are mediated by thalamic NR (Ito et al., 2015; Angulo-Garcia et al., 2018) which

also shows fast sequences during anesthesia-induced slow oscillations (Angulo-Garcia et al., 2018). Similarly to the PFC, visual cortex sequences are coordinated with HP sequences during SWS (Ji and Wilson, 2007). Moreover, superficial layers of medial entorhinal cortex replay fast sequences but independently of HP SWR (O'Neill et al., 2017). More generally, temporal biases throughout neocortex (PFC, motor, posterior parietal, and somatosensory cortex) are linked together after learning (Hoffman and McNaughton, 2002).

Learning fast and regular timescale replays holds functional relevance. Indeed, fast replays during awake immobility span both forward and backward directions in PFC (Kaefer et al., 2020) and HP (Diba and Buzsáki, 2007), which has been interpreted as prospective and retrospective planning with forward anticipation at the run start and backward retrospection at the run end (Diba and Buzsáki, 2007). However, due to the fact that replay starting points are not systematically tied to the animal's current position (Davidson et al., 2009), other interpretations have been proposed, e.g. PFC theta sequences encode the upcoming behavioral choice while CA1 theta sequences encode actual & alternative paths (Tang et al., 2021). More generally, the functional coordination of HP metric and PFC task-related spatial (Yu et al., 2018) representations (Pfeiffer and Foster, 2013; Zielinski et al., 2019) results in navigational trajectory-dependent firing in HP CA1, thus allowing prediction of upcoming and recent behavioral trajectory choices from regular timescale trajectory replays (Frank et al., 2000; Ferbinteanu and Shapiro, 2003; Fujisawa et al., 2008; Ito et al., 2015; Kaefer et al., 2020).

In summary, the prominence of functionally relevant sequences of transient sparse neural activity, which are replayed after successful behavioral learning across cortices, notably during working memory and navigational contexts, suggests that sequence learning and replay is a generic phenomenon.

→ To what extent is sequence learning and replay generic, e.g. can sequences emerge in a self-organized manner? And what are their structural properties, e.g. the temporal scale at which they emerge ?

1.2.3. Temporally precise motifs *in vivo* and *in vitro*

Working memory and navigational sequence replays are characterized by transient (~100-5s) increase in firing within neurons, suggesting information within sequences is conveyed solely through average firing frequency rather than the precise temporality of spikes. However, repeating precisely timed (~1ms) spike patterns have been observed across cortices in awake animals, be it in monkey frontal cortex during a delayed-response task (Abeles et al., 1993; Prut et al., 1998) and motor and premotor cortex during drawing (Shmiel et al., 2006), in head-fixed or anesthetized mouse somatosensory (Luczak et al., 2007, 2009) and auditory (Luczak et al., 2009) cortex, or in anesthetized cat V1 (Ikegaya et al., 2004). These precisely timed patterns can be observed even within cultured slices of rodent visual (Mao et al., 2001; Cossart et al., 2003; Ikegaya et al., 2004), somatosensory (Beggs and Plenz, 2003; MacLean et al., 2005; Tang et al., 2008; Kruskal et al., 2013) and auditory cortex (Buonomano, 2003) and hippocampus (Tang et al., 2008), as well as human cortex (Tang et al., 2008).

Poly-synaptic responses up to 300ms can be observed (Buonomano, 2003), once again suggesting the existence of underlying synaptic chains involving multiple synapses. Of particular interest is the observation that neuronal avalanches (repeated spontaneous events of spreading

activity) emerge within dissociated cultures of rat cortex after three to four weeks of self-organization (Pasquale et al., 2008), leading to a repertoire of sequences replayed according to specific network states (Yada et al., 2016), indicating the spontaneous formation of synaptic chains. Accordingly, chronic stimulation leads to precisely timed spike patterns in thalamocortical slices (Kruskal et al., 2013), organotypic cortical slices (Johnson et al., 2010a) and dissociated cortical cultures (Rolston et al., 2007; Pasquale et al., 2017), confirming that synaptic chains are learned through synaptic plasticity and serve as the substrate of precisely timed sequence propagation.

Correspondingly, initial observations of precisely timed spike patterns were motivated by the theoretical proposal of the existence of "synfire chains" (Abeles et al., 1993), i.e. fully feedforward synaptic chains organized in layers with all-to-all unidirectional connections of neurons from a previous layer projecting onto neurons of the next layer. However, insistence upon the precise timing of such spike patterns, and the underlying synfire chain theoretical proposition – necessitating strongly synchronous activity –, has received much criticism (Gerstein, 2004; McLelland and Paulsen, 2007; Mokeichev et al., 2007; Roxin et al., 2008). Indeed, detecting repeating precisely timed spiking patterns above chance level requires the adequate description of such null chance statistics. Most notably, when calculating the null probability of repeating temporally precise patterns against which observations are compared, taking into account firing rate modulation altogether removes the statistical significance of short patterns beyond chance, or renders it anecdotal (Oram et al., 1999; Baker and Lemon, 2000; McLelland and Paulsen, 2007). Consequently, the temporal modulation of firing rate is important in predicting precisely timed spike patterns, which has led to their reinterpretation as sequences of UP-state onsets (Luczak et al., 2007), closely resembling the sequences of sparse transient activations mentioned above.

Taken together, these results suggest that the precisely timed spike patterns observed across intact or sliced cortices are actually sequences of transient activity, subserved by synaptic chains which emerge either spontaneously or following stimulation through synaptic plasticity.

→ In this context, what generic synaptic plasticity rules could allow the emergence of transient neuronal activity sequences across cortices, and even within dissociated cultures?

1.3. Learning and replay of sequences of transient neural activity

1.3.1. Spike-Timing Dependent Plasticity

As stated before, replay of sequences during awake working memory and navigation immobility, SWS SWR, REM sleep or in slices, as well as self-organization within dissociated cultures, strongly suggests sequences are learned via synaptic plasticity. The observation of sequences across cerebral structures, be it prefrontal, parietal, auditory, visual and entorhinal cortex, or hippocampus, thalamus, and striatum, or even dissociated cultures, indicates the learning rule must be generic. Furthermore, this learning rule must allow the formation of unidirectional synaptic chains in an activity-dependent manner. As such, Hebbian plasticity, promoting the emergence of bidirectional connections between neurons with coincident firing,

cannot result in unidirectional synaptic chains, as it does not impose a temporal order upon spiking (instead favoring simultaneous firing).

A natural candidate for such learning is spike-timing dependent plasticity (STDP) (Bi and Poo, 1998) observed across structures (Abbott and Nelson, 2000). With STDP, synaptic strength is adjusted based upon the relative timing of pre- and post-synaptic action potentials, where pre-synaptic spike followed by post-synaptic spike arrival induces Long-Term Potentiation (LTP), and the reverse (post- before pre-) induces Long-Term Depression (LTD) (although other associative schemes are possible, c.f. Abbott and Nelson, 2000). The calcium hypothesis postulates that LTP is triggered by strong calcium entry mostly due to the detection of coincident pre-synaptic spike-induced glutamate release and post-synaptic spike-induced backpropagating dendritic depolarization by NMDA receptors, whereas LTD is caused by weak calcium entry on account of asynchrony and NMDA receptors staying closed, although recent evidence suggests otherwise (Sjöström et al., 2003). In particular, STDP is a strong candidate for learning navigational hippocampal sequences, since fast replay of trajectories at theta- or SWR-scale allows pre-post association within the optimal STDP learning temporal window of hundreds of milliseconds (Diba and Buzsáki, 2008). Furthermore, modeling studies have shown that STDP does induce synaptic chains after temporally-structured stimuli (Liu and Buonomano, 2009; Clopath et al., 2010; Fiete et al., 2010)

Additionally, STDP is neuromodulated by dopamine (He et al., 2015), with strong plasticity during reward delivery or anticipation. Since working memory and navigational sequences are reinforced by reward delivery, dopaminergic signaling allows the learning of sequences towards the rewarded objective. The temporal linkage of spikes and dopamine signaling, a.k.a. the distal reward problem, would arise from synaptic eligibility traces (Izhikevich, 2007), e.g. activation of an enzyme important for plasticity.

1.3.2. Homeostatic meta-plasticity

Yet, as with Hebbian learning, STDP models suffer from synaptic runaway, where synapse potentiation results in more pre-post spike association and thus synapse potentiation. A homeostatic form of meta-plasticity is necessary to keep neuronal parameters within reasonable physiological boundaries (Zenke et al., 2013). Synaptic scaling, i.e. the scaling of synaptic strengths according to network frequency, is one of different theoretical propositions of meta-plasticity (e.g. BCM, Bienenstock et al., 1982), which is ubiquitously observed across cortices (Turrigiano et al., 1998; Keck et al., 2017). However, synaptic scaling needs to act at an equal or faster pace than plasticity in order to ensure synaptic stability (Zenke et al., 2017), suggesting the existence of as yet unidentified rapid compensatory processes (e.g. heterosynaptic plasticity, implication of astrocytes, etc.).

1.3.3. Sequence learning and replay within synaptic noise

Learning synaptic chains via STDP requires relatively precise timing between spikes. However, it is well known that network activity is globally disorganized in the awake cortex of

active attentive animals. The irregularity of neural activity is measured via the coefficient of variation (CV) of inter-spike intervals (ISI). Purely random neural activity, where each spike occurs with a small random probability at each instant independently of past spikes, a.k.a. a Poisson point process, defines an ISI distribution with a CV of 1. Accordingly, ISI distributions within awake cortex also have a CV of 1 or above (Compte, 2003), suggesting they are as or more irregular than a random process (Shinomoto et al., 2005). This is thought to be caused by neurons being in a high conductance state (Destexhe et al., 2003), in which strong and tightly balanced excitatory and inhibitory currents lead to a sustained depolarized membrane potential. As such, small (relative to the total sum) current fluctuations are sufficient to induce spiking, allowing faster temporal integration of faint pre-synaptic spiking correlation signals and resulting in irregular activity. Cortical activity during wake is furthermore typically asynchronous (Brunel, 2000) during active behavioral states, showing desynchronized local field potentials (Poulet and Petersen, 2008) and only synchronizing with external or internal events (Riehle et al., 1997), which has been interpreted as a desirably energy-efficient neural code (only a single neuron's spike being required vs. many neurons simultaneously spiking, Denève and Machens, 2016). Finally, activity *in vivo* is sensitive to slight perturbations, i.e. cortical activity is chaotic (London et al., 2010).

It is unclear how synaptic chains can be learned and replayed within the globally disorganized chaotic activity of cortical networks during awake behavior. Indeed, the noisy activity regime can disrupt spike-induced sequence learning within individual synapses, since spike temporal jitter perturbs precise temporal spike differences and thus can cause accidental switches between LTP and LTD. At the network level, erratic spikes can recruit irrelevant synapses while randomly absent spikes fragilize the resulting dynamic engram. After learning, accumulation of non-specific plasticity resulting from noisy spike activity, counterbalanced by homeostatic meta-plasticity, can lead to engram forgetting. Furthermore, noisy excitatory activity can destabilize evoked replay by recruiting inhibitory interneurons, while also inducing spontaneous replays at pathological levels of repetition (i.e. incessantly). When considering the network as a chaotic dynamical system, noisy perturbations lead to exponential divergence in network activity which can lead to replay failure. Finally, sequence replay can further reinforce the synaptic engram via STDP, resulting in synaptic runaway starting with spontaneous replays and ending in paroxysmal epileptic activity.

→ In summary, can plastic synaptic and homeostatic meta-plastic processes, in combination with intrinsic bistability properties and slow synaptic currents, guarantee robust sequence learning and replay within the noisy dynamics characterizing of awake cortex?

A potential solution to the problems induced by synapse-activity interactions addressed above is to consider STDP learning within the context of dopaminergic neuromodulation. Indeed, learning is restricted to the time window immediately following a phasic dopaminergic signal caused by reward acquisition, prohibiting slow forgetting due to non-specific spiking outside of reward collection. However, dopamine-mediated STDP learning similarly suffers from the other aforementioned undesirable interactions between erratic activity and sequence learning.

→ This being the case, what mechanistic description of dopaminergic neuromodulation of STDP allows the learning of neuronal sequences towards an objective within noisy networks?

1.4. Theoretical background for attractor dynamics

1.4.1. Hebbian Assembly

A well-studied framework describing the learning of stable network activity attractors within noisy activity is the emergence of Hebbian assemblies encoding auto-associative memories via Hebbian synaptic plasticity, as mentioned above. While this framework allows for stable attractors within noisy networks, the resulting attractor is static rather than dynamic. Furthermore, the dynamic nature of sequential attractors leads to different challenges. Indeed, the propagation of neural sequences depends upon the unidirectional nature of synaptic weights, such that their stability cannot be mainly based upon the positive feedback loop of NMDA-mediated synaptic reverberation within bidirectional weights (Hebb, 1949; Brunel and Wang, 2001). Similarly, mechanisms which help stabilize bistable frequency in assemblies (e.g. strong intrinsic or dendritic bistability, Camperi and Wang, 1998; Koulakov et al., 2002; Goldman et al., 2003; Compte, 2006) may not apply to sequences of transient sparse neuronal activity.

1.4.2. Synfire chain

On the other end of the spectrum, synfire chains (Abeles et al., 1993) lead to unidirectional propagation of synchronous activity across neural layers, corresponding to dynamic engrams underlying dynamic attractors. While the existence of temporally precise sequences is debatable, synfire chains can result in unstable or uncontrolled sequential propagation (Mehring et al., 2003). Furthermore, synfire chains describe feedforward synaptic chains, whereas the aforementioned sequence-prone cortices have strongly recurrent synaptic architectures. Finally, they are organized into distinct layers, whereas unidirectional connections could overlap across neurons, forming more complex structures such as synfire braids (Izhikevich et al., 2004; Izhikevich, 2006). In summary, the stability issue, lack of recurrence and layer organization of synfire chains make them unlikely candidates for the emergence of stable repeatable sequences within local networks on many different timescales (0.5-60s).

1.4.3. Hebbian phase sequences

In between Hebbian assemblies and synfire chain, the hybrid model of Hebbian phase sequences offers the advantages of both, allowing stable propagation of dynamic attractors within recurrent synaptic structures (Kumar et al., 2008; Duarte and Morrison, 2014; Chenkov et al., 2017). However, the neural sequence is composed of discrete assemblies rather than continuous overlapping connections across neurons, which is difficult to verify experimentally and thus up to interpretation. Furthermore, it is unclear whether and how Hebbian phase

sequences are formed through uni- and bi-directional STDP, whereas the formation of unidirectional synaptic chains is more straightforward. Finally, the existence of neural activity sequences at the micro-column ~200µm scale (Harvey et al., 2012), combined with the fact that subnetworks in V1 layer 2/3 share interneurons (Yoshimura et al., 2005; Itskov et al., 2011), suggests propagation is not induced by inhibition local to each assembly, as shown in (Chenkov et al., 2017). Putting continuous sequences aside, the sequential activation of neuronal assemblies might account for the previously mentioned sequential transitions between discrete network states modeled as HMMs.

1.4.4. Continuous dynamic engrams

Models learning sequences through unidirectional STDP exist, although none satisfyingly answer all aspects of the problem introduced by learning and replay of sequences within noisy networks as mentioned above (namely noise-perturbed learning, non-specific plasticity-induced forgetting, synaptic runaway-induced paroxysmal epileptic activity, as well as incessant or unstable replay and chaotic divergence after initial triggering stimuli). Indeed, some studies do not study trajectory replay after learning (Clopath et al., 2010) or the trajectory cannot be replayed from an initial trigger (Klampfl and Maass, 2013). In others, trajectory learning is either absent (Chenkov et al., 2017), based on artificial learning rules (Sussillo and Abbott, 2009; Laje and Buonomano, 2013; Xue et al., 2021) or biologically unrealistic neuronal activity and synaptic plasticity (Liu and Buonomano, 2009; Fiete et al., 2010; Klampfl and Maass, 2013), or unrelated to external stimuli (Fiete et al., 2010). Additionally, certain models lack the asynchronous irregular regime of neuronal activity altogether (Liu and Buonomano, 2009; Fiete et al., 2010), removing the necessity for attractors robust to synaptic noise. Finally, none dissect how biophysical mechanisms can support the reliability and stability of neural sequence replay, nor study its maintenance in long-term memory.

1.5. Thesis outline

This thesis consists in trying to understand which biophysical determinants, such as intrinsic and synaptic currents, network architecture or plasticity rules, are essential to emergence of stable and dynamic attractors, which are repeatable across trials and robust to synaptic noise.

What intrinsic currents allow the emergence of stable yet labile network states and robust neuronal activity sequences? Chapter 2 studies a conditional form of robust and generic spike-mediated bistability subserved by high-threshold L-type calcium (CaL) and calcium-activated non-specific (CAN) ionic currents within a model of layer 5 PFC pyramidal neuron. In this context, intermediate CAN conductance levels result in the maintenance of activity induced by a supraliminal phasic depolarizing current input, but conditional to the presence of a tonic subliminal depolarizing current input. This tonic input could originate from other excitatory neurons within an excitatory assembly, thus facilitating transitions between labile network states defined by neuronal assemblies. Such conditional bistability could also help stabilize neural activity sequences, where the subliminal input originates from previous neurons of the sequence.

While persistent activity within monkey PFC allows stable network states during working memory, the MCC is at the pinnacle of the cortical hierarchy with the longest neuronal activity timescales (twice those of lateral PFC; LPFC). **Do the same intrinsic mechanisms subserve these long timescales, and to what end?** Starting from a biophysical neural network model closely replicating monkey LPFC working memory data, **Chapter 3** shows that plausible strong inhibitory after-hyperpolarization (AHP) ionic and slow GABA-B synaptic currents account for the longer neuronal timescales within MCC compared to LPFC. These neuronal timescales escalate at the network level into the metastable peregrination of network activity across much longer quasi-stable discrete network states, whose maintenance and transitions are controlled by synaptic inhibition. **Chapter 4** replaces these findings within the MCC's proposed central function, i.e. temporal integration of diverse multimodal inputs, allowing to construct an action-reward outcome history for behavioral adaptation and exploration. Additional results in **Chapter 4** then revealed the sequential organization of MCC network state peregrination within two larger pseudo-attractor spaces, where each network state could be defined by persistent activity or neural activity sequences.

While GABA-B conductance can be neuromodulated to generate the timescales necessary for task demands, these network states and sequences originate from the random architecture of the synaptic matrix, and are thus not learned nor related to external stimuli and task variables. **How can intrinsic and inhibitory synaptic currents stabilize and allow controlled replay of learned sequences within synaptic noise? Chapter 5** shows that strong tonic or slower inhibitory currents coupled with increased excitatory functional connectivity, as well as intrinsic CAN and AHP currents mediating transient bistability, increases the stability and controllability of learned sequence replay when faced with synaptic noise. Furthermore, the model is robust to variability in the biophysical parameters, and represents a common framework for many types of static or dynamic and discrete or continuous attractors (e.g. Hebbian assemblies, phase sequence, synfire chain, ring attractor, and bidirectional sequences).

Whereas the previous chapter studies mechanisms allowing robust replay within synaptic noise, STDP learning occurs before the network simulation, outside of the asynchronous irregular regime. **As such, what mechanisms allow the learning and maintenance in memory of the synaptic engram within noisy network activity, and can the resulting engrams be replayed?** Building upon the previous chapter's knowledge by instantiating a model network capable of stable and controllable replays, **Chapter 6** shows that STDP modeled as calcium-based activation of kinase and phosphatase couples (aKP) allows minimal interference between trajectory learning or replay and the asynchronous irregular regime. This results from the very slow aKP kinetics at low frequency, coupled with the network's low frequency during resting state activity. This model further describes how sequences can be learned through the presentation of discrete fragments, how they can be replayed at fast or regular timescales (such as for navigational trajectories) according to neuromodulated NMDA channel opening dynamics, and confirms that such sequences can reconcile simultaneous stable and dynamic coding. However, runaway synapse-activity interactions due to repeated sequence replays lead to paroxysmal network activity and engram forgetting, requiring slower plasticity and multiple stimulus presentations.

The previous two chapters describe learning of presented stimulus sequences within synaptic noise which are replayed after an external triggering cue. However, they do not describe how

sequences can be learned toward a rewarding goal (instead of replicating an external stimulus), nor do they not explain intrinsically-generated and motivated decisions in the absence of triggering cues, both effects which have been attributed to dopaminergic neuromodulation. **How can dopaminergic neuromodulation account for both the learning of, and motivation to retrieve, rewarded goals? Chapter 7** shows that multiplicative gating of online synaptic plasticity eligibility traces and synaptic excitability by phasic dopamine (DA) signals allows 1) the learning of rewarded locations as static neuronal assemblies dynamically oriented toward the reward location, as well as 2) their successful recall after an internally-generated motivational DA impulse, inducing slow excitatory NMDA-mediated synaptic reverberation within the assemblies learned through DA and subsequent mouse behavioral convergence toward them.

Chapter 2. PFC working memory persistent activity via intrinsic conditional bistability

2.1. Summary

Working memory is commonly believed to be supported by persistent neural activity within monkey PFC. Two non-mutually exclusive mechanistic origins of persistent neural activity have been proposed: synaptic network reverberation, and intrinsic cellular bistability. Network reverberation models have been criticized, notably since they lack the spiking irregularity and quasi-stationary state transitions observed experimentally. On the other hand, intrinsic cellular absolute bistability (AB) models require long onset and offset stimuli and strong levels of pharmacological neuromodulation, which result in long (~10s) high frequency regular discharges lacking the spiking irregularity and flexibility necessary for adaptive working memory cognitive processes. An intermediate proposal exists, a.k.a. conditional bistability (CB), in which persistent activity after an initial stimulus is conditional on subthreshold input current during the delay period. CB is notably found within layer 5 PFC pyramidal neurons, and has been overlooked in classical bistability protocols, as they test neuronal responses to an initial stimulus only (event), without the additional subthreshold input or depolarized membrane potential required during the delay period (event/delay).

As such, we present a mechanistic account of spike-induced CB in a Hodgkin-Huxley neuronal model of iso-potential PFC layer 5 pyramidal neuron. In this model, CB is implemented by spike-mediated high-threshold L-type calcium (CaL) and calcium-activated non-specific cationic (CAN) currents. The voltage-dependent CaL current induces after-depolarization potentials (ADP) and calcium entry during action potentials. This calcium then opens CAN channels, inducing further ADP and thus potentially action potentials. High CaL and CAN maximal conductances result in this positive feedback loop being sufficiently strong to sustain itself after the initial event stimulus without delay input (AB), while weaker conductance levels require a delay input current for the loop to sustain itself (CB).

However, the weak positive feedback of CB precisely leads to a richer diversity of behaviors, with varying moderate frequency and a repertoire of responses depending on the amplitude of the delay input current (from memoryless discharge to stable memory via various transient memory durations). The parametric region of maximal conductances characterizing CB is wide and within physiological neuromodulatory levels, and only the CaL asymmetric opening and closing dynamics are necessary and sufficient for CB, both elements suggesting this mechanism's genericity within PFC (and other) networks.

Considering *in vivo* asynchronous synaptic inputs, CB neurons alternate between bursting and non-bursting episodes, inducing higher CV and CV2 during the delay compared to without CB (though an after-hyperpolarization potential (AHP) current was necessary). As such, within a network, CB may underpin transitions between stable collective states of quasi-stationary firing at the second timescale, such as mental states during exploration of computational solutions promoting adaptive cognitive processes. Furthermore, the weak positive CB spike feedback loops could help stabilize sequences of neural activity, with stable firing being conditional on subliminal input from vanishing activities of previous neurons in the sequence.

2.1.1. Contributions

I helped develop the bistability assessment protocol code and analyze corresponding data, and reviewed the article during writing.

2.2. Article

Cellular/Molecular

Conditional Bistability, a Generic Cellular Mnemonic Mechanism for Robust and Flexible Working Memory Computations

Guillaume Rodriguez,[1] Matthieu Sarazin,[1] Alexandra Clemente,[2,3] Stephanie Holden,[2,3] Jeanne T. Paz,[2,3,4,5] and Bruno Delord[1]

[1]Institut des Systèmes Intelligents et de Robotique, Sorbonne Université, Centre National de la Recherche Scientifique, UMR 7222, 75005 Paris, France, [2]Gladstone Institutes, San Francisco, California 94158, [3]Neurosciences Graduate Program, [4]Department of Neurology, University of California, San Francisco, California, 94158, [5]Kavli Institute for Fundamental Neuroscience, University of California San Francisco

Persistent neural activity, the substrate of working memory, is thought to emerge from synaptic reverberation within recurrent networks. However, reverberation models do not robustly explain the fundamental dynamics of persistent activity, including high-spiking irregularity, large intertrial variability, and state transitions. While cellular bistability may contribute to persistent activity, its rigidity appears incompatible with persistent activity labile characteristics. Here, we unravel in a cellular model a form of spike-mediated conditional bistability that is robust and generic. and provides a rich repertoire of mnemonic computations. Under asynchronous synaptic inputs of the awakened state, conditional bistability generates spiking/bursting episodes, accounting for the irregularity, variability, and state transitions characterizing persistent activity. This mechanism has likely been overlooked because of the subthreshold input it requires, and we predict how to assess it experimentally. Our results suggest a reexamination of the role of intrinsic properties in the collective network dynamics responsible for flexible working memory.

Key words: **conditional bistability; flexible; generic; memory; robust; working memory**

Significance Statement

This study unravels a novel form of intrinsic neuronal property: conditional bistability. We show that, thanks to its conditional character, conditional bistability favors the emergence of flexible and robust forms of persistent activity in PFC neural networks, in opposition to previously studied classical forms of absolute bistability. Specifically, we demonstrate for the first time that conditional bistability (1) is a generic biophysical spike-dependent mechanism of layer V pyramidal neurons in the PFC and that (2) it accounts for essential neurodynamical features for the organization and flexibility of PFC persistent activity (the large irregularity and intertrial variability of the discharge and its organization under discrete stable states), which remain unexplained in a robust fashion by current models.

Introduction

Working memory (WM), the ability to maintain and manipulate information within seconds, is essential to cardinal brain functions. Persistent neural activity represents a major neural correlate of WM, especially in the prefrontal cortex (PFC). The theory postulates that once triggered, persistent activity self-sustains through spiking reverberation in recurrent networks (Wang, 2001; Compte, 2006). Cortical architectures may provide sufficiently positive and nonlinear feedback for network dynamics to converge toward persistent activity (attractor dynamics; Cossart et al., 2003; MacLean et al., 2005). However, network reverberation as a unique causal origin remains controversial because it fails to robustly account for fundamental aspects of persistent activity such as the higher irregularity of spiking during the delay period of WM tasks, the large intertrial variability of

Received July 13, 2017; revised Dec. 10, 2017; accepted Dec. 27, 2017.

Author contributions: A.C., S.H., J.T.P., and B.D. designed research; G.R., M.S., and B.D. performed research; G.R., M.S., and B.D. contributed unpublished reagents/analytic tools; G.R., M.S., and B.D. analyzed data; G.R., M.S., A.C., S.H., J.T.P., and B.D. wrote the paper.

This work was supported by the SMART Labex of the Agence Nationale de la Recherche (ANR; to G.R.), the Neuc 2016 program (Grant #ANR-16-NEUC-0006-01) of the ANR and the Collaborative Research in Computational Neuroscience, and the National Science Foundation Graduate Research Fellowship (Grant #1650113 to A.C.). We thank Jérémie Naudé for helpful discussions and comments on the manuscript.

The authors declare no competing financial interests.

Correspondence should be addressed to Bruno Delord, Institut des Systèmes Intelligents et de Robotique, Sorbonne Université, Centre National de la Recherche Scientifique, UMR 7222, 75005 Paris, France. E-mail: bruno.delord@upmc.fr.

DOI:10.1523/JNEUROSCI.1992-17.2017
 0270-6474/18/385209-11$15.00/0

the discharge and its temporal structure under quasi-stationary states, and the ability to encode parametric information (Seidemann et al., 1996; Koulakov et al., 2002; Compte et al., 2003; Goldman et al., 2003; Shafi et al., 2007; Barbieri and Brunel, 2008).

As a non-mutually exclusive alternative, intrinsic properties of neurons may underlie persistent activity, in interaction with synaptic mechanisms, for object (Compte, 2006), spatial (Camperi and Wang, 1998), and parametric (Koulakov et al., 2002; Goldman et al., 2003) WM, and the interaction of WM with long-term memory (Egorov et al., 2002; Larimer and Strowbridge, 2010). The intrinsic bistability of neurons (i.e., the coexistence of stable states of quiescence and self-sustained spiking) is central to this proposal because it allows memorizing transient inputs in individual neurons (Booth and Rinzel, 1995; Delord et al., 1996, 1997; Marder and Calabrese, 1996; Shouval and Gavornik, 2011). Bistability is ubiquitous in peripheral (Lee and Heckman, 1998; Perrier and Tresch, 2005), subcortical (Rekling and Feldman, 1997; Kawasaki et al., 1999), and cortical (Krnjević et al., 1971; Schwindt et al., 1988; Silva et al., 1991; Tahvildari et al., 2007; Zhang and Séguéla, 2010) structures, and in the PFC (Haj-Dahmane and Andrade, 1997; Dembrow et al., 2010; Gee et al., 2012; Thuault et al., 2013).

This hypothesis has been criticized because intrinsic bistability is generally strongly stereotyped *in vitro*: it does not depend on the level of background depolarization [absolute bistability (AB)], requires long on- and off-stimuli (seconds), strong levels of pharmacological manipulations (e.g., neuromodulation), and displays extremely long (tens of seconds), high-frequency, highly regular discharges with partially inactivated spikes (Haj-Dahmane and Andrade, 1997; Egorov et al., 2002; Tahvildari et al., 2007; Zhang and Séguéla, 2010; Gee et al., 2012). These rigid features contrast with the flexibility of WM-related computational processes and persistent activity [e.g., high intertrial variability (Shafi et al., 2007) and irregular spiking (Compte et al., 2003)].

However, nonstereotype, conditional forms of bistability, where self-sustained spiking depends on background depolarization, have been found in the cortex (Silva et al., 1991; Tahvildari et al., 2007) and other structures (Bourque, 1986; Rekling and Feldman, 1997; Lee and Heckman, 1998; Kawasaki et al., 1999; Perrier and Tresch, 2005). Conditional bistability (CB) has been observed in layer V (L5) PFC pyramidal neurons (Thuault et al., 2013), which is not surprising, since bistability is underlain in these neurons by two spike-mediated (i.e., suprathreshold) currents—the high-threshold L-type calcium (CaL) and the calcium-activated nonspecific cationic (CAN) current (Haj-Dahmane and Andrade, 1997; Gee et al., 2012; Thuault et al., 2013)—that correlate with CB in many other neuronal types (Bourque, 1986; Silva et al., 1991; Rekling and Feldman, 1997; Lee and Heckman, 1998; Kawasaki et al., 1999; Perrier and Tresch, 2005; Tahvildari et al., 2007). A spike-mediated form of AB was previously studied (Shouval and Gavornik, 2011), but spike-mediated CB remains unexplored hitherto. Yet, its mechanism may depart from more classical spiking-independent forms of bistability relying on dendritic calcium (Hounsgaard and Kiehn, 1993; Booth and Rinzel, 1995), NMDA (Milojkovic et al., 2005; Major et al., 2008; Larimer and Strowbridge, 2010), or subthreshold currents (Delord et al., 1996, 1997; Washburn et al., 2000; Genet and Delord, 2002; Loewenstein et al., 2005; Carrillo-Reid et al., 2009; Genet et al., 2010).

Here, we explore the computational and mnemonic consequences of spike-dependent CB in a model of a L5 PFC pyramidal neurons.

Materials and Methods

Design of the standard model. We consider an isopotential L5 PFC pyramidal neuron model that follows the Hodgkin–Huxley formalism. The neuron model is endowed with the leak (I_L) and action potential (AP) currents (I_{Na}, I_K) and a synaptic (I_{Syn}, "*in vivo* condition") or an injected (I_{Inj}, "*in vitro* condition") input current. Depending on the hypothesis tested, the model also comprises one or more calcium- and/or voltage-dependent suprathreshold currents, generically denoted I_{ion}. These currents can be depolarizing (I_{CaL}, I_{CAN}) or hyperpolarizing [afterhyperpolarization potential potassium current (I_{AHP})]. The standard version of the model comprises the following three currents: $I_{ion} = I_{CaL} + I_{CAN} + I_{AHP}$, with parameters described in the Parameter section (see below). The membrane potential evolves according to the following:

$$C\frac{dV}{dt} = -(I_L + I_{Na} + I_K + I_{ion} + I_{Syn}) + I_{Inj}. \quad (1)$$

Leak current I_L and action potential currents I_{Na} and I_K. The leak current is written as follows:

$$I_L = g_L(V - V_L), \quad (2)$$

and AP currents are taken from a previous model we devised to reproduce spike currents of excitatory regular-spiking neocortical neurons (Naudé et al., 2012).

High-threshold calcium current (I_{AHP}). The CaL current is derived from Delord et al. (1997) and follows as:

$$I_{CaL} = \bar{g}_{CaL}x_{CaL}^2(V - V_{CaL}), \quad (3)$$

where the activation x_{CaL} follows first-order kinetics:

$$\frac{dx_{CaL}}{dt} = \frac{x_{CaL}^{\infty}(V) - x_{CaL}}{\tau_{CaL}(V)}, \quad (4)$$

with a voltage-dependent time constant:

$$\tau_{CaL}(V) = 10^{\alpha_{CaL}+\beta_{CaL}V}, \quad (5)$$

with α_{Cal} and β_{Cal} adapted to fit the time constant observed *in vitro* (Helton et al., 2005).

The activation follows:

$$x_{CaL}^{\infty}(V) = \left(1 + \exp\frac{-(V - V_{1/2,CaL})}{K_{CaL}}\right)^{-1}, \quad (6)$$

where $V_{1/2,CaL}$ and K_{CaL}, respectively, denote the half-activation potential and the e-fold slope of Boltzmann activation voltage dependence, and were estimated from the *I–V* curve obtained *in vitro* (Helton et al., 2005).

Calcium-activated nonspecific cation current (I_{CAN}). The CAN current obeys the following:

$$I_{CAN} = \bar{g}_{CAN}\, x_{CAN}(V - V_{CAN}), \quad (7)$$

where the activation x_{CAN} follows first-order kinetics depending on the intracellular calcium concentration, as follows:

$$\frac{dx_{CAN}}{dt} = \frac{x_{CAN}^{\infty}(Ca) - x_{CAN}}{\tau_{CAN}(Ca)}, \quad (8)$$

with

$$\tau_{CAN}(Ca) = \frac{1}{\alpha_{CAN}Ca + \beta_{CAN}}, \quad (9)$$

and

$$x_{CAN}^{\infty}(Ca) = \frac{\alpha_{CAN}Ca}{\alpha_{CAN}Ca + \beta_{CAN}}, \quad (10)$$

where α_{CAN} and β_{CAN}, respectively, denote activation and deactivation kinetic constants chosen to get significant activation in the micromolar range with time constants fitting those observed *in vitro* after large cal-

cium influx in L5 PFC pyramidal neurons (i.e., ~35 ms in the range 5–10 μM in the model and up to ~100 ms at lower [Ca^{2+}] during interspike intervals (ISIs; Haj-Dahmane and Andrade, 1997)).

I_{AHP}. The AHP current modeled here corresponds to the SK potassium channel type and obeys the following:

$$I_{\mathrm{AHP}} = \bar{g}_{\mathrm{AHP}}\, x_{\mathrm{AHP}}^2 (V - V_{\mathrm{AHP}}), \tag{11}$$

where the activation x_{AHP} follows calcium-dependent first-order kinetics as follows:

$$\frac{dx_{\mathrm{AHP}}}{dt} = \frac{x_{\mathrm{AHP}}^{\infty}(Ca) - x_{\mathrm{AHP}}}{\tau_{\mathrm{AHP}}(Ca)}, \tag{12}$$

with

$$\tau_{\mathrm{AHP}}(Ca) = \frac{1}{\alpha_{\mathrm{AHP}} Ca + \beta_{\mathrm{AHP}}}, \tag{13}$$

and

$$x_{\mathrm{AHP}}^{\infty}(Ca) = \frac{\alpha_{\mathrm{AHP}} Ca}{\alpha_{\mathrm{AHP}} Ca + \beta_{\mathrm{AHP}}}, \tag{14}$$

where α_{AHP} and β_{AHP}, respectively, denote the activation and deactivation kinetic constants, fitted to account for the time constants of medium AHPs observed *in vitro* in L5 PFC pyramidal neurons (Villalobos et al., 2004; Faber and Sah, 2007).

Calcium concentration dynamics. In the model, calcium concentration dynamics results from the inward influx due to I_{CaL} and from first-order buffering /extrusion (Haj-Dahmane and Andrade, 1997) as follows:

$$\frac{dCa}{dt} = -\frac{1}{2F}\frac{\mathrm{Surf}}{\mathrm{Vol}} I_{\mathrm{CaL}} + \frac{Ca_0 - Ca}{\tau_{Ca}}, \tag{15}$$

where F is the Faraday constant, Ca_0 is the basal intracellular calcium concentration, τ_{Ca} is the buffering time constant, and the following:

$$\frac{\mathrm{Surf}}{\mathrm{Vol}} = r_1^{-1}\left(1 - \frac{r_1}{r_0} + \frac{r_1^2}{3r_0^2}\right)^{-1}, \tag{16}$$

is the surface area-to-volume ratio of an idealized intracellular shell compartment of thickness r_1 situated beneath the surface of a spherical neuron soma of radius r_0. Calcium dynamics possesses an intrinsic asymmetry resulting from the inward influx due to rapid increases of I_{CaL} and the slower first-order buffering process.

Synaptic currents. In *in vivo* conditions (see Protocols), synaptic activity is simulated with fluctuating excitatory AMPA and inhibitory $GABA_A$ conductances as studied in L5 PFC pyramidal neurons (Destexhe and Paré, 1999), and the synaptic current is modeled as follows:

$$I_{\mathrm{Syn}} = g_E(V - V_E) + g_I(V - V_I), \tag{17}$$

where V_E and V_I are the reversal potentials, and the fluctuating conductances g_E and g_I are given by two Uhlenbeck–Ornstein processes, as follows:

$$\frac{dg_E}{dt} = (g_E - g_{E_0})/\tau_E + \sigma_E x_E(t), \tag{18}$$

$$\frac{dg_I}{dt} = (g_I - g_{I_0})/\tau_I + \sigma_I x_I(t), \tag{19}$$

where τ_E and τ_I are the respective time constants of the temporal evolution of conductances, g_{E0} and g_{I0} are the mean conductances (that depend on the considered protocol), σ_E and σ_I are the SDs, and $x_E(t)$ and $x_I(t)$ are Gaussian stochastic processes with zero mean and unit SDs.

Determination of afterdepolarization potential amplitudes. The amplitude of afterdepolarization potentials (ADPs) is determined using a specific stimulation protocol composed of a 15 ms phasic current of fixed amplitude set to elicit a single action potential. The ADP amplitude is calculated as the maximal membrane potential difference between conditions in the presence and the absence of the tested supraliminar current (I_{CaL}, I_{CAN}, or both). This difference was calculated in a window starting 10 ms after the action potential peak (to avoid the influence of different action potential lengths due to the presence/absence of suprathreshold currents) and ending 1 s later, far after complete relaxation to resting potential.

Standard model parameters. Unless indicated in figure legends, standard parameter values are as follows: for the leak current, $g_L = 0.05$ mS · cm^{-2}, $V_L = -70$ mV; AP current parameters are as in a previous model that we developed of excitatory regular-spiking neocortical neurons (Naudé et al., 2012), with $\bar{g}_{\mathrm{Na}} = 24$ mS · cm^{-2}, $V_{\mathrm{Na}} = 50$ mV, $\bar{g}_K = 3$ mS · cm^{-2}, and $V_K = -90$ mV. For supraliminar ionic currents, parameters are $\bar{g}_{\mathrm{CaL}} = 0.0045$ mS · cm^{-2}, $V_{\mathrm{CaL}} = 150$ mV, $V_{1/2,\mathrm{CaL}} = -12$ mV, $K_{\mathrm{CaL}} = 7$ mV, $\alpha_{\mathrm{CaL}} = 0.6$, $\beta_{\mathrm{CaL}} = -0.02$ mV^{-1}, $\bar{g}_{\mathrm{CAN}} = 0.025$ mS · cm^{-2}, $V_{\mathrm{CAN}} = 30$ mV, $\alpha_{\mathrm{CAN}} = 0.0056$ $\mu M^{-1} \cdot ms^{-1}$ and $\beta_{\mathrm{CAN}} = 0.0125$ ms^{-1}, $\bar{g}_{\mathrm{AHP}} = 0.2$ mS · cm^{-2}, $V_{\mathrm{AHP}} = -90$ mV, $\alpha_{\mathrm{AHP}} = 0.05$ $\mu M^{-1} \cdot ms^{-1}$, and $\beta_{\mathrm{AHP}} = 0.2$ ms^{-1}. Geometrical and intracellular calcium dynamics parameters are as follows: $F = 96{,}500$ mol · $s^{-1} \cdot A^{-1}$, $r_0 = 4$ μm, $r_1 = 0.25$ μm, $Ca_0 = 0.1$ μM, $\tau_{\mathrm{Ca}} = 100$ ms. Synaptic parameters are $g_{E_0,\mathrm{BACKGROUND}} = 0.0325$ mS · cm^{-2}, $g_{E_0,\mathrm{EVENT}} = 0.065$ mS · cm^{-2}, $g_{E_0,\mathrm{DELAY}} = 0.040$ mS · cm^{-2}, and independently of the period considered, $\sigma_E = 0.0125$ mS · cm^{-2}, $g_{I_0} = 0.1$ mS · cm^{-2}, $\sigma_I = 0.0075$ mS · cm^{-2}, $\tau_E = 2.5$ ms, $\tau_I = 10$ ms, $V_E = 0$ mV, and $V_I = -75$ mV.

Numerical procedures. The models were numerically integrated using the forward Euler method with a $1e^{-2}$ ms time step. Bifurcation diagrams were obtained using the XPP software for qualitative analysis of dynamical systems (http://www.math.pitt.edu/~bard/xpp/xpp.html). Spikes were detected as a maximum of the membrane potential above −20 mV.

In *in vitro* protocols, the behavior maps (see Figs. 2, 3) were built as follows: the discharge during a 10 s delay period was classified as (1) memoryless, when no spike occurred during the delay period or when one spike occurred at <25 ms after the onset of the delay period; (2) transient memory, when an unstable discharge occurred during the delay period and lasted at least 25 ms after the delay period onset (to exclude cases where an ultimate spike is blown just after the phasic current pulse due to the activation of a fast sodium current in the last milliseconds of the phasic current pulse); and (3) stable memory, when the last spike of the discharge occurred after 9.5 s and the mean relative absolute difference between successive ISIs was <5% during the last 2 s of the delay period.

In *in vivo* protocols, spikes were defined as belonging to a burst when they were part of a succession of at least three spikes with all ISIs <100 ms (instantaneous frequencies >10 Hz). Other spikes were defined as not belonging to a burst [i.e., isolated spikes or doublet of spikes (with an intradoublet ISI inferior to 100 ms) that were separated from the rest of the spike train by ISIs >100 ms]. Bursting episodes were defined as contiguous periods of time within which all spikes belonged to a burst. Nonbursting episodes were defined as the periods outside the bursting epidsodes. The choice of 100 ms as a cutoff ISI value was arbitrarily set to separate periods with frequency inferior to 10 Hz, which are typical of the spontaneous state of activity in the awake cortex from periods of activity taking part in coding (Destexhe et al., 2001). This exact value is not important to the conclusions drawn in the present study.

Statistical methods. We used a two-tailed Wilcoxon rank-sum test to compare the medians of the CV distributions in the event and delay periods of the event/delay protocol, because the CV distributions were not normal, according to Kolmogorov–Smirnov goodness-of-fit hypothesis tests. A similar procedure was used to compare the medians of the CV_2 distributions in the event and delay periods of the event/delay protocol.

Results

Mimicking synaptic inputs during WM

Our main goal was to determine whether depolarizing spike-mediated currents can maintain the memory of an event at the level of the discharge of an individual neuron, while producing realistic spiking patterns, as observed during WM. To that end, we designed a realistic isopotential model of a L5 pyramidal PFC neuron endowed with high-threshold CaL (I_{CaL}), calcium-activated nonspecific cationic (I_{CAN}), afterhyperpolarization potassium (I_{AHP}),

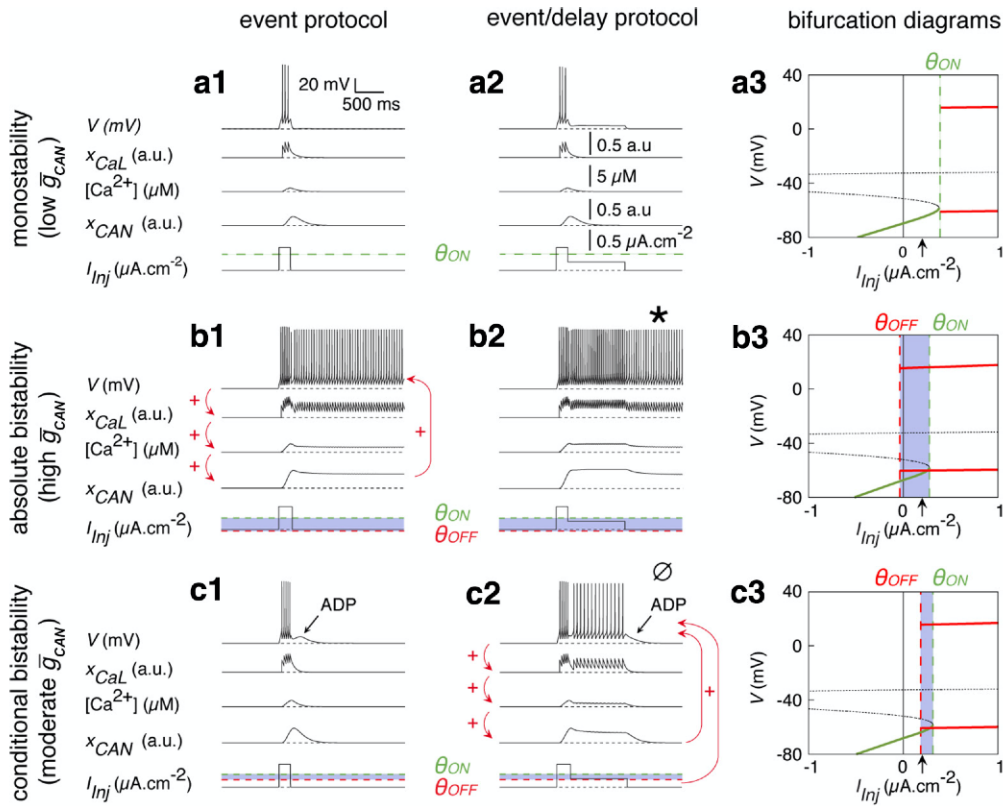

Figure 1. Conditional bistability is a hidden property in neurons endowed with a suprathreshold conductance in response to standard protocols applied *in vitro*. ***a1–c3***, The response of monostable (***a1–a3***; $g_{CAN} = 0.003$ mS · cm^{-2}), absolute bistable (***b1–b3***; $g_{CAN} = 0.03$ mS · cm^{-2}), and conditional bistable (***c1–c3***; $g_{CAN} = 0.02$ mS · cm^{-2}) neurons (standard model) to an event protocol with a 0.2 s suprathreshold current step (***a1***, ***b1***, ***c1***) and to the event-delay protocol, in which the event is followed by a 1 s subthreshold depolarizing current mimicking background activity in PFC networks during the delay of a working memory task (***a2***, ***b2***, ***c2***). Note that the discharge is continuing after the delay stimulus in the absolute bistable neuron (***b2***, star symbol). Note the ADP (***c2***, void symbol) following spiking in the conditional bistable neuron. The thresholds for initiating (θ_{ON}) and terminating (θ_{OFF}) spiking are represented as green and red dotted lines, respectively, and the bistability domains are shown in lavender. Red arrows denote the positive feedback loop among spiking, CaL activation (x_{CaL}), increased $[Ca^{2+}]$, and CAN activation (x_{CAN}). ***a3***, ***b3***, ***c3***, Right panels, Bifurcation diagrams illustrating the stable fixed point (resting potential, green solid curve) and the minimal/maximal potentials of action potentials during the limit cycle (rhythmic spiking, red solid curves), the thresholds for initiating (θ_{ON}, green doted lines) and terminating spiking (θ_{OFF}, red doted lines), and the $I_{Inj\text{-}delay}$ during the delay (black arrows). Bistability domains are shown in lavender. Black dotted lines indicate unstable fixed points of the models.

action potential and leak currents, and intracellular calcium ($[Ca^{2+}]$) linear dynamics (see Materials and Methods). In the model, I_{CaL} and I_{CAN} are spike mediated because I_{CaL} activates at membrane potentials above the spike threshold and is the unique source of intracellular calcium activating I_{CAN}, as found in PFC neurons exhibiting spike-mediated bistability (Haj-Dahmane and Andrade, 1997). Parameters were set such that I_{CAN} was the sole spike-mediated charge carrier between these two currents (Haj-Dahmane and Andrade, 1997).

To test whether spike-mediated currents contribute to persistent activity in the model, we used two stimulation protocols. The event protocol, classically used to assess bistability, consisted of a single, short (0.2 s) suprathreshold current pulse mimicking the arrival of an input (e.g., perceptive or motor) event. In the event/delay protocol, the event was followed by a longer (1 s) subthreshold depolarizing current mimicking background activity from the PFC network to the neuron during the delay of a WM task. This input may correspond to persistent activity reverberating within local PFC recurrent connections to maintain information about the event or to ongoing inputs related to motivational, attentional, anticipatory, or executive aspects of WM processes.

Conditional bistability is invisible with classical protocols

At low levels of the maximal CAN conductance (g_{CAN}), the neuron discharged only during the event (Fig. 1*a1*, event protocol), even when the event was followed by a background subthreshold delay current (Fig. 1*a2*, event/delay protocol). A bifurcation analysis as a function of the I_{Inj} indicated that the neuron was monostable (M): it admitted either a stable fixed point corresponding to the resting potential (Fig. 1*a3*, green solid curve) or, above the spiking threshold θ_{ON}, to a stable limit cycle corresponding to rhythmic spiking (Fig. 1*a3*, red solid curves).

At large g_{CAN} values, the event induced a self-sustained discharge that outlasted the triggering event, providing a cellular form of memory, with both protocols (Fig. 1*b1*,*b2*). Mechanistically, self-sustained spiking arose from the positive feedback among spiking, CaL activation, increased $[Ca^{2+}]$, and CAN activation (Fig. 1*b1*, red arrows), which did not operate at low g_{CAN} levels (compare with Fig. 1*a1*). Here, the neuron was bistable: the resting potential coexisted with rhythmic spiking in a bistability domain situated between θ_{ON}, the threshold for initiating spiking, and θ_{OFF}, the threshold for terminating spiking (Fig. 1*b3*, lavender domain). The bistability domain included $I_{Inj} = 0$ μA · cm^{-2} ($\theta_{OFF} < 0 < \theta_{ON}$), so that cellular memory did not require any background subthreshold input. Hence, the spike-mediated bistability was absolute, as observed in a previous model (Shouval and Gavornik, 2011) and in PFC neurons under pharmacological manipulations (Dembrow et al., 2010; Gee et al., 2012). Therefore, persistent activity outlasted the delay period (Fig. 1*b2*, star;

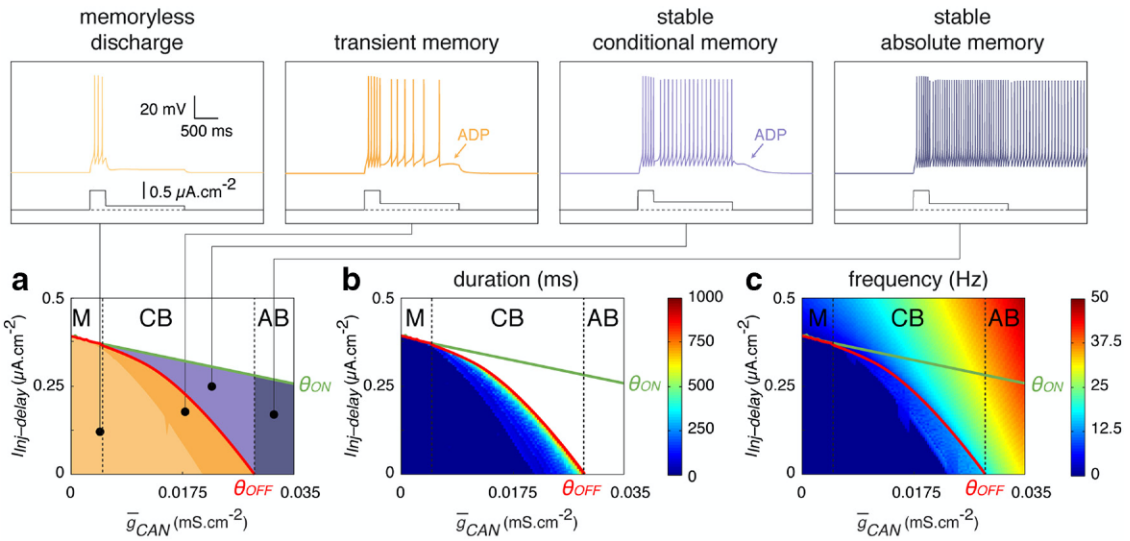

Figure 2. Existence and expression of conditional bistability *in vitro*. ***a***, Discharge behaviors of the standard neuron model in response to the event/delay protocol ($I_{Inj\text{-}event} = 0.6\ \mu A \cdot cm^{-2}$) as a function of the g_{CAN} and the $I_{Inj\text{-}delay}$. ***M***, CB, and AB indicate the monostability, conditional bistability, and absolute bistability domains, respectively. The memoryless and transient memory, stable conditional memory and stable absolute memory behaviors are indicated, respectively, as yellow, orange, lavender, and purple domains (bottom) and discharges (top panels). ***b***, ***c***, Heat maps of the duration of memoryless and transient memory behaviors (***b***) and of the mean firing frequency of stable memory behaviors (***c***) during the delay period, as a function of the g_{CAN} and the $I_{Inj\text{-}delay}$. Note that above θ_{ON}, the tonic current is suprathreshold and the neuron fires even when no event precedes the delay period. Sawteeth at the border between memoryless and transient regions correspond to the discharge of one spike occurring at >25 ms after the onset of the delay period, while the main part of the transient memory region corresponds to the discharge of several spikes during the delay period (see definition of transient memory behavior in Materials and Methods).

i.e., memory was infinite), unless a specific inhibitory input terminated it.

At intermediate g_{CAN} levels, we observed that bistability was conditional: spiking during the delay depended on the level of subthreshold depolarization, as found in several neural structures and in the PFC (Bourque, 1986; Silva et al., 1991; Rekling and Feldman, 1997; Lee and Heckman, 1998; Kawasaki et al., 1999; Perrier and Tresch, 2005; Tahvildari et al., 2007; Thuault et al., 2013). After the event, spiking stopped in the event protocol (Fig. 1*c1*) but persisted during the entire delay in the event/delay protocol (Fig. 1*c2*) even though the background delay current ($I_{Inj\text{-}delay}$) was subthreshold (i.e., below θ_{ON}; Fig. 1*c3*, black arrow). This was possible because $I_{Inj\text{-}delay}$ was above θ_{OFF} (i.e., in the bistability domain; $0 < \theta_{OFF} < \theta_{ON}$; Fig. 1*c3*). The background current was needed under CB, by contrast to AB, because the spike-mediated positive feedback was not sufficient to support autonomous self-sustained spiking at moderate g_{CAN} levels. This explains why persistent activity terminated at the end of the delay when I_{Inj} values returned to zero, below θ_{OFF} and the bistability domain (Fig. 1*c2*, void symbol), being followed by an ADP (Fig. 1*c2*, black arrow), as found in PFC neurons expressing spike-mediated currents and/or bistability (Haj-Dahmane and Andrade, 1997; Dembrow et al., 2010; Gee et al., 2012). Thus, under CB, the duration of cellular memory adapted to the duration of network memory (i.e., reverberation), alleviating the requirement for a dedicated inhibitory stimulus to terminate persistent activity. Note also that triggering spiking-dependent bistability did not require long stimulations, because of the moderate time constant of I_{CAN} (~100 ms; see Materials and Methods), as found in PFC neurons (Haj-Dahmane and Andrade, 1997).

CB is robust using the event/delay protocol

To assess the robustness of CB mnemonic properties, we parametrically explored the model in response to the event/delay protocol (Fig. 2*a*), as a function of $I_{Inj\text{-}delay}$ and g_{CAN}, which is important because it reflects the regulation history of spike-mediated excitability and dictates the possible existence of CB (Fig. 1). We found that CB existed in a large range of g_{CAN} values (Fig. 2*a*, CB domain). Moreover, the ranges of CB and AB domains were much wider than M domains, indicating the prevalence of mnemonic properties with spike-mediated excitability in the model. We also found that cellular memory expressed differentially, depending on delay stimulation conditions. In the g_{CAN} range of CB, there was no firing during the delay at the lowest $I_{Inj\text{-}delay}$ values (i.e., discharge was memoryless; Fig. 2*a*, yellow domain and trace). In contrast, delay firing was slowly decaying in a significant $I_{Inj\text{-}delay}$ range below θ_{OFF}, underlying a transient memory (Fig. 2*a*, orange), whereas above θ_{OFF} a stable conditional memory was observed (compare Figs. 2*a*, lavender, 1*c*). In addition, we observed a stable absolute memory (i.e., sustained activity without self-termination) in the range of AB (compare Figs. 2*a*, purple, 1*b*). Under CB, memory typically lasted hundreds of milliseconds when transient (Fig. 2*b*) and firing frequency was generally moderate (<50 Hz), in contrast to AB (Fig. 2*c*). These results indicated that spike-mediated CB is robust, multiform, with long durations and low frequencies, which is consistent with persistent activity in the PFC during WM tasks (Compte, 2006). Moreover, parametrically, CB lies between M and AB, which have both largely been observed (Haj-Dahmane and Andrade, 1997; Dembrow et al., 2010; Gee et al., 2012). This suggests that CB, although rarely observed in the PFC (Thuault et al., 2013), may have been previously overlooked, because the event/delay protocol, which is mandatory to reveal it, is almost never used in intracellular recordings.

CB generically emerges from spike-mediated excitability

We wondered whether CB mnemonic properties were generic in essence, or specific to the model considered. Spike-mediated biophysical determinants—CaL and CAN current gating variables and the intracellular calcium $[Ca^{2+}]$—share a common dynamical trait. Their spike-triggered activation operates faster, compared with

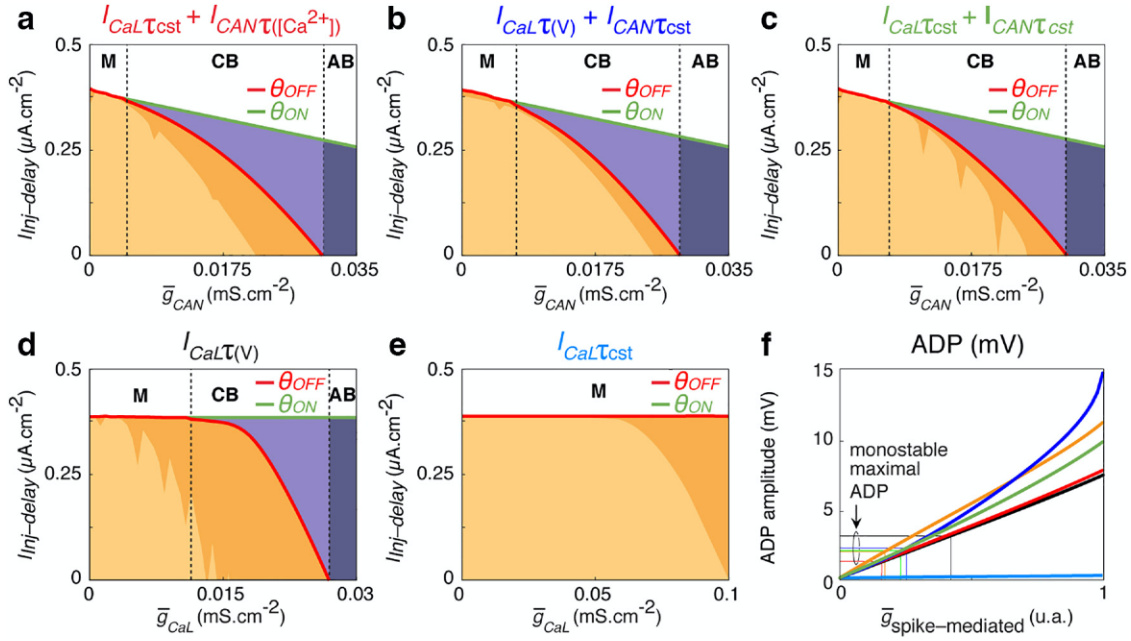

Figure 3. Conditional bistability is a generic mnemonic property of neurons endowed with depolarizing spike-mediated mechanisms. ***a–e***, Thresholds for initiating (θ_{ON}, green lines) and terminating spiking (θ_{OFF}, red lines) for models with fixed (i.e., voltage- or calcium-independent) time constants suppressing the dynamic asymmetry of the CaL current (***a***), the CAN current (***b***), or both (***c***), or for models endowed with the sole CaL current with a voltage-dependent (***d***) or a fixed (***e***) time constant as a function of the suprathreshold maximal conductance and background delay current. ***f***, ADP amplitudes of the five alternative models presented in ***a–e***. Line colors match the respective panel titles, and the orange line applies to the standard model. Note that for ADP amplitudes (***f***) suprathreshold maximal conductances were normalized by the boundary value defining the transition between conditional and absolute bistability for each model. M, CB, and AB indicate the monostability, conditional bistability, and absolute bistability domains, respectively. Sawteeth at the border between memoryless and transient regions correspond to the discharge of one spike occurring at >25 ms after the onset of the delay period, while the main part of the transient memory region corresponds to the discharge of several spikes during the delay period (see definition of transient memory behavior in Materials and Methods).

their relaxation timescale during the ISI. This asymmetry produces interspike traces that form a memory after each spike, favoring the firing of the following spike and, in turn, self-sustained spiking. We tested whether the dynamic asymmetry of these determinants was essential to cellular memory. We found that considering fixed (i.e., voltage- or calcium-independent) time constants to suppress the dynamic asymmetry of the CaL, the CAN, or both currents had no effect on cellular memory (compare Figs. 3*a–c*, 2*a*), indicating that [Ca^{2+}] dynamic asymmetry was sufficient to support cellular memory. We also found that, in the absence of both calcium dynamics and the CAN current, CaL asymmetry alone was both sufficient (Fig. 3*d*) and necessary (Fig. 3*e*). Therefore, while cellular memory required the asymmetry between activation/relaxation time constants of a least one determinant, it was independent of its exact nature. This demonstrated that dynamic asymmetry was generic in underlying the positive feedback of spike-mediated CB. Remarkably, we found that CB coexisted with marked ADP amplitudes (~2.5 to 15 mV) after spiking (Fig. 3*f*, above horizontal lines), contrasting with the smaller ADP of monostable neurons (<2.5 mV).

CB mnemonic properties under *in vivo* conditions

In vivo, PFC neurons continuously receive asynchronous synaptic inputs inducing strong membrane-potential fluctuations. These fluctuations may disrupt conditional memory, which relies on a minimal subthreshold depolarization. Thus, we assessed cellular memory with stochastic synaptic excitatory (AMPA) and inhibitory ($GABA_A$) inputs driving fluctuations as found *in vivo* in the PFC (i.e., several millivolts; Fellous et al., 2003). Here, we tested the response of the neuron to the protocols considered *in vitro* and to a delay protocol (i.e., devoid of event). The latter was used as a control, since stochasticity may induce spiking during the subthreshold delay input. We found that at g_{CAN} levels providing CB *in vitro*, the neuron responded *in vivo* to the event/delay protocol with a persistent activity (Fig. 4*a*, right) that was absent after the event protocol (left) and initially weaker during the delay protocol (middle). As a general rule, activity included episodes during which spikes clustered in bursts and spike-mediated currents were significantly activated (Fig. 4*a*, lavender). During bursting episodes, the positive feedback characterizing CB ensured self-sustained spiking, which was irregular and terminated because of synaptic fluctuations. Bursting episodes alternated with nonbursting episodes essentially characterized by single spiking at lower frequency and smaller spike-mediated current activation (Fig. 4*a*, yellow; i.e., during which the positive feedback was disengaged). A raster plot across trials (Fig. 4*b*) illustrates stronger activity, a larger bursting propensity, and important variability in the temporal structure of the discharge during the event/delay protocol.

While firing slowly increased during the delay protocol (Fig. 4*c*, fuschia) and rapidly decayed after the event protocol (Fig. 4*c*, light blue), it persisted longer during the delay in the event/delay protocol (Fig. 4*c*, lavender; τ_{memory} ~900 ms), with a frequency exceeding the sum of firing frequencies triggered by event or delay inputs alone (Fig. 4*c*, salmon). Thus, persistent activity is an emergent property arising from nonlinear interactions between spike-mediated currents and the delay background input. Persistent activity with τ_{memory} in the range of hundreds of milliseconds to seconds (i.e., consistent with WM) was robustly evoked for a large domain of event input parameters (Fig. 4*d*) and a thinner domain of the delay input parameters (Fig. 4*e*). Large τ_{memory} values were observed when the event was stronger than the delay

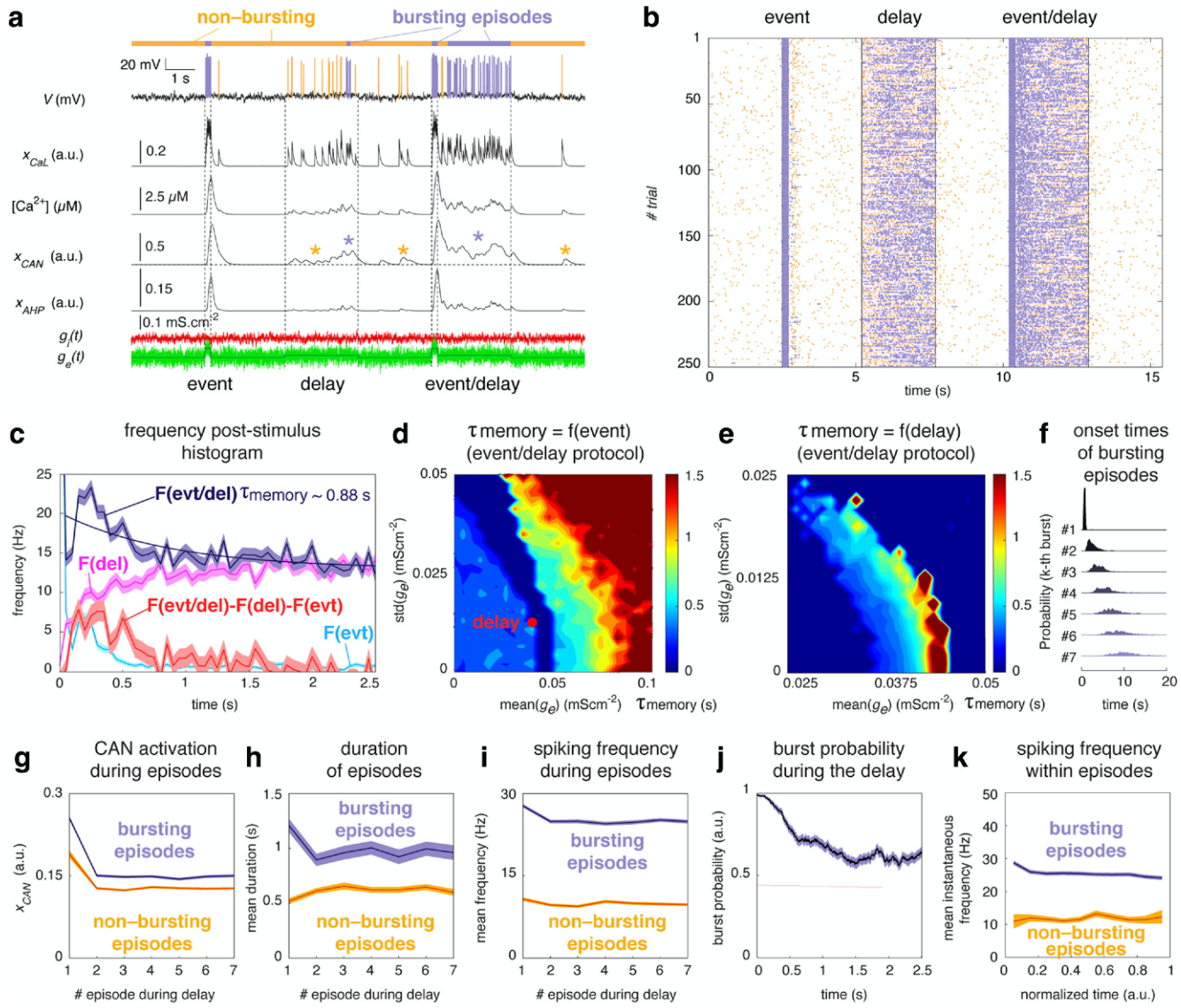

Figure 4. Conditional bistability confers robust event memory under strongly fluctuating synaptic inputs *in vivo*. ***a***, Membrane potential, CaL and CAN activation, calcium dynamics, and AHP activation traces of the standard neuron model in response to the event, delay, and event/delay protocols for a realization of the excitatory (green) and inhibitory (red) synaptic fluctuating conductances. Spikes belonging to bursting and nonbursting episodes are indicated in lavender and yellow, respectively. Small activation buildups of spike-mediated currents during nonbursting episodes and larger buildups during bursting episodes are signaled by yellow and lavender stars, respectively. See Materials and Methods for criteria that define bursting episodes. ***b***, Spike raster plot for 250 trials of the protocol depicted in ***a***, with different realizations of synaptic fluctuations. Color code as in ***a***. ***c***, Frequency poststimulus time histogram (PSTH) of the discharge (250 trials) after the onset of event (light blue), delay (fuschia), and event/delay (lavender) protocols; difference between the PSTH during the event/delay protocol, and the sum of PSTHs during the event and delay protocols (salmon). The mean ± SEM frequency values are displayed. The memory time constant is defined as the time constant of firing frequency relaxation to its steady-state value in the event/delay protocol. ***d***, Memory time constant map of persistent activity, as a function of the mean and SD of the excitatory fluctuating conductance of the event input during the event/delay protocol. The red dot indicates conductance parameters of the delay background input. When the event mean conductance is smaller than that of the delay input (left part of the map), the activity builds up to the steady state during the delay from the lower event trigger initial frequency (e.g., pink curve in ***c***, for a null event mean conductance) and the time constant is smaller. ***e***, Memory time constant map of persistent activity, as a function of the mean and SD of the excitatory fluctuating conductance of the delay input during the event/delay protocol. ***d–e***, Means across 100 trials; other synaptic parameters as in the standard model (see Materials and Methods). ***f***, Probability distribution of onset times of bursting episode as a function of their order of occurrence during the delay period (20 s) of the event/delay protocol, across 250 trials. ***g–i***, CAN conductance activation (***g***), mean duration (***h***), and mean spiking frequency (***i***) during bursting (lavender) and nonbursting (yellow) episodes, as a function of their order of occurrence during a delay period (20 s) in the event/delay protocol. Mean ± SEM values across 250 trials. ***j***, Probability of being in a burst episode during the delay period (2.5 s) in the event/delay protocol. ***k***, Mean instantaneous spiking frequency as a function of the normalized time within bursting and nonbursting episodes (normalized time equals 0 at the beginning of episodes, 1 at their end). Mean ± SEM values across 100 trials.

(Fig. 4*d*, right part of the map), with persistent activity decaying during the delay (Fig. 4*c*, lavender).

Mechanistically, the excitation provoked by the event favored the rapid engagement of the positive feedback during the delay, as reflected by the strong synchronization of the onset of the first bursting episode across trials (Fig. 4*f*). This first episode displayed a larger recruitment of spike-mediated currents (Fig. 4*g*) and an increased duration (Fig. 4*h*) and frequency (Fig. 4*i*), compared with the following bursting episodes. As a result, the probability of being in a bursting episode (i.e., at a higher firing frequency) remained high at the beginning of the delay and progressively decreased toward its steady state (Fig. 4*j*), accounting for the decreasing pattern of firing frequency (Fig. 4*c*, lavender). Note that the instantaneous firing frequency remained globally

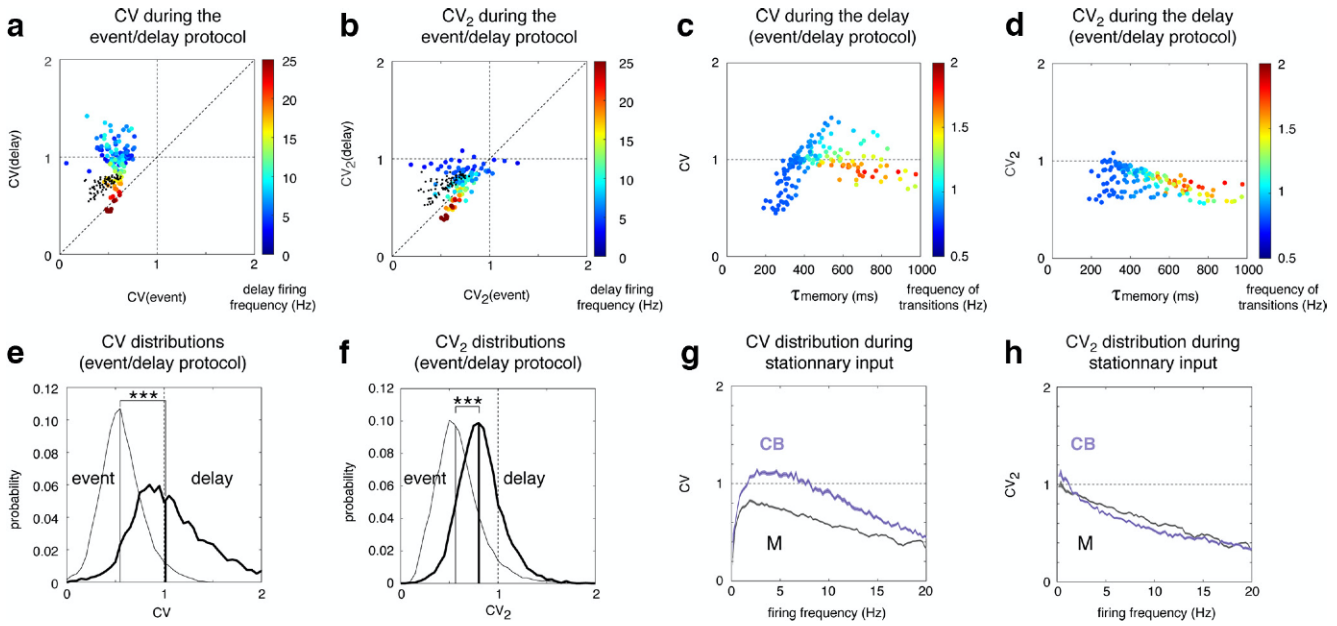

Figure 5. Conditional bistability promotes irregular discharge under *in vivo* conditions. ***a***, ***b***, CV (***a***) and CV_2 (***b***) measures of the ISI distribution of the discharge in monostable (black dots; $g_{CAN} = 0$ mS · cm $^{-2}$) and conditionally bistable (colored dots; $g_{CAN} = 0.025$ mS · cm $^{-2}$) neurons, in response to the input of an event protocol (*x*-axis) and to the 2.5 s delay input of an event/delay protocol (*y*-axis). The color code for conditionally bistable neurons indicates the firing frequency during the delay. Both inputs have the same excitatory input parameter taken in the ranges 0 – 0.05 mS · cm $^{-2}$ for the mean and 0 – 0.025 mS · cm $^{-2}$ for the SD, to limit the effect of firing frequency, which affects CV/CV_2 measures in a nontrivial fashion (Compte et al., 2003). In both protocols, the event input lasts 0.5 s, as in the study by Compte et al. (2003). In the event/delay protocol, the event input has a 0.065 mS · cm $^{-2}$ mean and a 0.0125 mS · cm $^{-2}$ SD. ***c***, ***d***, In the conditionally bistable neuron, the highest discharge irregularity during the delay, measured by the CV (***c***; *y*-axis) and the CV_2 (***d***; *y*-axis) is observed at intermediate memory time constants (~300 – 600 ms; *x*-axes) and frequencies of transitions between bursting and nonbursting episodes (color code). ***e***, ***f***, At moderate memory time constants (400 – 600 ms), the means of CV (***e***) and CV_2 (***f***) probability density functions during the delay are significantly higher in the CB neuron during the delay (thick black curve), compared with those during the event (thin black curve); $p < 1e^{-9}$ (***) on two-tailed Wilcoxon rank-sum tests for both the CV and CV_2 distributions (distributions were not normal, according to Kolmogorov–Smirnov goodness-of-fit hypothesis tests; for the CV distribution: $n_{event} = 29{,}092$, $n_{delay} = 5448$, median (CV_{event}) = 0.5478, and median (CV_{delay}) = 1.0142; for the CV_2 distribution: $n_{event} = 26{,}755$, $n_{delay} = 5345$, median ($CV_{2,event}$) = 0.5634, and median ($CV_{2,delay}$) = 0.8043). ***g***, ***h***, Irregularity of the discharge plotted as a function of firing frequency for the conditionally bistable (lavender) and monostable neurons (black) in response to stationary synaptic inputs, as measured by the CV (***g***) and the CV_2 (***h***).

constant within episodes (i.e., the discharge was quasi-stationary; Fig. 4*k*).

CB promotes irregular discharge under *in vivo* conditions

In WM tasks, spiking irregularity is larger during the delay than during stimulus presentation (i.e., event; Compte et al., 2003), with a higher coefficient of variation (CV) of ISIs over 1 and a CV_2 (a version of CV based on successive ISIs) of ~1, which has been difficult to reproduce robustly in theoretical models (Barbieri and Brunel, 2008). In our model, irregularity was generally higher during the delay, compared with the event (Fig. 5*a*,*b*, dots above first bisector), independently of whether neurons were M (Fig. 5*a*,*b*, no I_{CAN}, black dots) or CB (Fig. 5*a*,*b*, colored dots). Indeed, at a given similar firing mean frequency, the longer delay (2.5 s) allowed longer ISIs that could not occur during the shorter event (0.5 s). Thus, during the event, the sampling of the ISI distribution was truncated at low frequencies, and the apparent ISI variance was therefore decreased, compared with the delay. This effect was moderate for M neurons (Fig. 5*a*,*b*, black dots), but it dramatically increased for CB neurons firing at low frequency (<15 Hz; Fig. 5*a*,*b*, colored dots), since, in the latter neurons, alternations of bursting episodes (with smaller ISIs) and nonbursting episodes (with larger ISIs) strongly increased the variance of the ISI distribution during the delay. At such low-frequency firing, the CV was largely >1 and the CV_2 was ~1, as found during WM delays (Compte et al., 2003). Moreover, CV/CV_2 culminated for inputs leading to intermediate memory time constants in the range of ~400 – 600 ms (Fig. 5*c*,*d*) and transition frequencies between episodes at ~1 Hz (color code). In these conditions, both the CV and CV_2 were significantly larger during the delay (Fig. 5*e*,*f*, thick black trace), compared with the event (Fig. 5*e*,*f*, thin black trace). Remarkably, consistent with data (Compte et al., 2003), the CV distribution during the delay was broadened, compared with that during the event, which did not occur for the CV_2.

To fully confirm the genuine effect of depolarizing spike-mediated currents on spiking irregularity, we compared CV/CV_2 with and without CB (1) upon stationary stimuli to avoid the interference of frequency time variations due to the protocol and (2) at identical mean firing frequencies to avoid the nontrivial effects of frequency on these measures (Compte et al., 2003). In these conditions, where computing these observables admits its plain significance, we found that, compared with M neurons (Fig. 5*g*, black), the CV was systematically superior in CB neurons (Fig. 5*g*, lavender) < 20 Hz and was >1 below 10 Hz. In CB neurons, the CV_2 was also superior below 2 Hz, situated at ~1, whereas it was essentially similar to M neurons >2 Hz (Fig. 5*h*). Thus, although the mean local irregularity measured by the CV_2 was the same on average (because local increases of frequency regularity within bursting episodes compensated for the local frequency irregularities at transitions between bursting and nonbursting episodes), we found that the global irregularity of the discharge (measured by the CV; i.e., the normalized ISI SD) was increased in CB neurons due to the presence of spike-mediated currents.

Discussion

Here, we show that spike-mediated CaL and CAN currents of L5 pyramidal PFC neurons (Haj-Dahmane and Andrade, 1997; Gee

et al., 2012; Thuault et al., 2013) support CB. Moreover, our study suggests that CB is prevalent for several reasons. First, CB relies on suprathreshold mechanisms that are ubiquitous in pyramidal PFC neurons and operate robustly, independent of biophysical details, which are generic. Second, CB parametrically situates between M and AB regimes, both extensively observed in the PFC and other areas (Krnjević et al., 1971; Schwindt et al., 1988; Yang et al., 1996; Haj-Dahmane and Andrade, 1997; Dembrow et al., 2010; Zhang and Séguéla, 2010; Gee et al., 2012). AB is often observed under strong neuromodulatory manipulation that upregulates depolarizing spike-triggered conductances, yielding unrealistic stereotyped discharges inconsistent with WM firing patterns (Compte et al., 2003; Shafi et al., 2007). This suggests that neuromodulation regulates conductances below the range for AB in behaving animals. Below AB, the probability of being in CB is largely predominant (a much wider range than M; Fig. 2*a*). Moreover, minimal neuromodulation is crucial for optimal PFC computations (Wang et al., 2007), whereas M lies at the lowest neuromodulation (conductance) levels. Thus, CB is likely encountered in PFC pyramidal neurons under physiological neuromodulatory levels. Third, we show that ADP represents a generic marker distinguishing CB from M neurons. ADPs are ubiquitous across L5 PFC pyramidal types (Yang et al., 1996; Haj-Dahmane and Andrade, 1997) and share specific common features with CB neurons (>5 mV; durations up to ~100 ms, occurrence even at low frequencies, CAN/calcium dependence; Yang et al., 1996; Haj-Dahmane and Andrade, 1997; Boudewijns et al., 2013), suggesting that PFC neurons displaying ADP are conditionally bistable. Hence, CB was observed without artificial pharmacological activation in L5 PFC pyramidal neurons with prominent ADPs (Thuault et al., 2013). Altogether, these lines of evidence indicates that CB likely constitutes a prevalent property in PFC L5 pyramidal neurons in physiological conditions during WM tasks.

So, why has CB remained scarce in the PFC? CB requires a triggering suprathreshold input followed by a subthreshold input (or applied upon a depolarized subthreshold holding potential). Therefore, CB neurons are undetectable using the classic protocol ubiquitously used, which consists of a single suprathreshold input applied from the resting potential. Consequently, neurons can be categorized as M (Fig. 1*c1*), while actually displaying genuine CB (Fig. 1*c2*). Such misclassification should be frequent given the much larger CB domain (compared with M), and systematically applying event/delay protocols should unravel CB in a significant fraction of neurons. Remarkably, event/delay protocols are meaningful physiologically, mimicking the temporal profile of inputs during WM: a strong behaviorally relevant (e.g., perceptive) signal followed by a lower background input during the delay (e.g., reverberating persistent activity or WM-related feedforward inputs).

Information maintenance in CB neurons relies on the asymmetry between fast buildup/activation and slower relaxation/deactivation dynamics of spike-activated mechanisms. This asymmetry maintains spike-to-spike excitability through the positive feedback between depolarization and suprathreshold activation. Noticeably, the slow CAN deactivation time constant of ~100 ms (Haj-Dahmane and Andrade, 1997) allows the maintenance of self-sustained activity down to ~10 Hz. Slower CAN in the PFC (Sidiropoulou et al., 2009) may support lower frequencies, at some expense (see below). Under asynchronous inputs, CB generates bursting/nonbursting episodes. Bursting episodes can be triggered by—and form a memory of—incoming events, when a background input follows the event. Statistically, this persistent activity fades at the second timescale across trials, consistent with WM, reflecting the stochastic disruption of bursting episodes due to synaptic fluctuations. By contrast, firing frequency is steady within bursting episodes, so that information maintenance is constant within individual trials for the duration of the first bursting episode.

Overall, the spike-mediated mechanism we unravel is robust to the exact nature and parameter values of the model and displays a much higher resistance to transient episodes of inhibition, compared with subthreshold-based bistabilities (Washburn et al., 2000; Loewenstein et al., 2005; Carrillo-Reid et al., 2009). Sensitivity to inhibitory interference was used to discard the possible role of intrinsic bistability in maintaining persistent activity (Sanchez-Vives and McCormick, 2000; McCormick et al., 2003). Our results indicate that this reasoning does not apply to spike-mediated mechanisms, because they preserve resistance to inhibition, as does synaptic reverberation.

Previously described bistabilities are rigid, requiring strong/long stimuli to be turned on/off and producing long, high-frequency discharges primarily independent of the background input (Haj-Dahmane and Andrade, 1997; Egorov et al., 2002; Tahvildari et al., 2007; Zhang and Séguéla, 2010; Gee et al., 2012) By contrast, CB exhibits a rich repertoire of computational operations. It expresses as a memoryless discharge or subserve transient or stable conditional memory, depending on input parameters. Moreover, mnemonic activities can be initiated by short events because of the moderate CAN activation time constant (Haj-Dahmane and Andrade, 1997). Furthermore, the duration and frequency of mnemonic discharges are controlled by the delay input at low frequencies. Finally, under *in vivo*-like inputs, this diversity expresses as bursting/nonbursting episodes with variable frequencies and durations, resulting in a large variability of the discharge structure across trials, as found during WM (Shafi et al., 2007).

In response to asynchronous inputs, CB increases discharge irregularity, because smaller ISIs during bursting episodes and larger ISIs during nonbursting episodes increase the ISI distribution variance. The CV/CV_2 are highest at low firing frequencies i.e., under excitation/inhibition balance, two factors increasing irregularity; Compte et al., 2003. In such conditions, the CV is >1 and CV_2 ~1 in CB neurons during the delay, being higher than during the event, as in WM (Compte et al., 2003), properties previous models are unable to account for robustly (Barbieri and Brunel, 2008). This effect happens in CB neurons, because bursting/nonbursting episodes can alternate during delays of several seconds, but not during shorter events (0.2 s).

Besides, while CB clearly increases the CV, its effect on the CV_2 is mild. This results because whereas frequency changes at the transitions of episodes increase CV_2, the more regular discharge within bursting episodes decreases it. Synaptic inputs are not stationary *in vivo* (Shafi et al., 2007; Ostojic, 2014), which could explain the slightly higher CV/CV_2 observed experimentally (Compte et al., 2003), compared with the situation reported here. This could also explain the larger difference in CV_2 values between the delay and the event (Compte et al., 2003), as changes in the synaptic input rates have more time during the delay to exert their effect on successive ISIs and thus on the CV_2.

Interestingly, the overall increase in irregularity in CB neurons required an AHP current, which balanced the CAN current in the model (CAN alone decreased irregularity; data not shown). Finally, our conclusion that busting/nonbursting alternations underlie irregularity is additionally supported by the finding that very slow CAN currents—driving very long

bursts without alternations—decrease the CV (Sidiropoulou et al., 2009).

What roles may CB play at the network scale during maintenance? Here, CB requires a subthreshold constant background input from the network to memorize a transient event. However, inputs are not stationary in PFC networks and cellular CB should affect, in turn, network dynamics. Therefore, interactions between local cellular CB and global network recurrence may provide a rich repertoire of dynamics.

Hence, following an event, bursting in CB neurons may be sustained by the prolonged synaptic feedback due to bursting in other CB neurons. Such synergistic CB bursting recruitment may determine the extent to which activity is amplified and prolonged, possibly resulting in decaying, stable, or ramping temporal firing patterns of WM (Shafi et al., 2007). Synergy between CB neurons may also provide a realistic biophysical basis for WM of parametric information, which requires bistable elements to emerge robustly (Koulakov et al., 2002; Goldman et al., 2003). Such collective dynamics are plausible because CB is gradual in essence, by contrast to AB. WM-related drives during the delay and the regulation state of synaptic strengths and spike-mediated excitability should be fundamental in setting the gradual synergetic recruitment of CB neurons.

Within a recurrent network, CB neurons can discharge during the delay even when they have not received the event input, because of the subthreshold recurrent input provided by other neurons of the network actively maintaining the memory of that event (Fig. 4*c*, fuschia curve). This could be problematic if presynaptic and postsynaptic neurons belong to different populations encoding distinct memories (i.e., Hebbian assemblies), as memory would "bleed over" across populations (i.e., memory interference). This problem may arise even with monostable postsynaptic neurons, although CB neurons would discharge at higher rates for a similar recurrent delay input, enhancing interference. However, different mechanisms have been imagined that may circumscribe interference between memory representations [e.g., mutual (Miller and Wang, 2006) or global (Brunel and Wang, 2001) inhibition between assemblies]. Besides, enhanced "bleeding" due to CB could also improve pattern completion within Hebbian assemblies, because the easier recruitment of CB neurons not activated by the event (because of incomplete input pattern presentation) would facilitate complete memory retrieval through associative synaptic reverberation.

Besides, during WM delays, PFC networks encounter transitions between stable collective states of quasi-stationary firing at the second timescale, reflecting mental states during the exploration of computational solutions, as cognitive processes wander from stimulus encoding to decision-making and action (Seidemann et al., 1996; Cossart et al., 2003). Bursting/nonbursting episodes in CB neurons share similar quasi-stationary firing and generate maximal irregularity at this timescale. We suggest that CB may promote the emergence of stable collective states and the complexity of PFC neuronal operations, providing a basis for exploring computational solutions during WM. Intrinsic plasticity and neuromodulation would represent strategic processes to regulate spike-mediated mechanisms for the emergence of adapted WM-related cognitive processes.

While CB relies on a weak spike-mediated positive feedback, it is precisely this "weakness" that underpins the computational richness and flexibility it brings, compared with what was previously thought. We suggest that the traditional view should be overcome in favor of a reconciling perspective whereby synaptic reverberation and conditional bistability concur with the emergence of the highly flexible persistent activity required for elaborating adaptive WM-related cognitive processes and intelligent behavior.

References

Barbieri F, Brunel N (2008) Can attractor network models account for the statistics of firing during persistent activity in prefrontal cortex? Front Neurosci 2:114–122. CrossRef Medline

Booth V, Rinzel J (1995) A minimal, compartmental model for a dendritic origin of bistability of motoneuron firing patterns. J Comput Neurosci 2:299–312. CrossRef Medline

Boudewijns ZS, Groen MR, Lodder B, McMaster MT, Kalogreades L, de Haan R, Narayanan RT, Meredith RM, Mansvelder HD, de Kock CP (2013) Layer-specific high-frequency action potential spiking in the prefrontal cortex of awake rats. Front Cell Neurosci 7:99. CrossRef Medline

Bourque CW (1986) Calcium-dependent spike after-current induces burst firing in magnocellular neurosecretory cells. Neurosci Lett 70:204–209. CrossRef Medline

Brunel N, Wang XJ (2001) Effects of neuromodulation in a cortical network model of object working memory dominated by recurrent inhibition. J Comput Neurosci 11:63–85. CrossRef Medline

Camperi M, Wang XJ (1998) A model of visuospatial working memory in prefrontal cortex: recurrent network and cellular bistability. J Comput Neurosci 5:383–405. CrossRef Medline

Carrillo-Reid L, Tecuapetla F, Vautrelle N, Hernández A, Vergara R, Galarraga E, Bargas J (2009) Muscarinic enhancement of persistent sodium current synchronizes striatal medium spiny neurons. J Neurophysiol 102: 682–690. CrossRef Medline

Compte A, Constantinidis C, Tegner J, Raghavachari S, Chafee MV, Goldman-Rakic PS, Wang XJ (2003) Temporally irregular mnemonic persistent activity in prefrontal neurons of monkeys during a delayed response task. J Neurophysiol 90:3441–3454. CrossRef Medline

Compte A (2006) Computational and in vitro studies of persistent activity: edging towards cellular and synaptic mechanisms of working memory. Neuroscience 139:135–151. CrossRef Medline

Cossart R, Aronov D, Yuste R (2003) Attractor dynamics of network UP states in the neocortexs. Nature 423:283–288. CrossRef Medline

Delord B, Klaassen A, Burnod Y, Guigon E (1996) An intrinsic bistable mechanism in neocortical pyramidal neurons might be involved in the generation of sustained discharge patterns related to working memory. Neural Network World 4:525–533.

Delord B, Klaassen AJ, Burnod Y, Costalat R, Guigon E (1997) Bistable behaviour in a neocortical neurone model. Neuroreport 8:1019–1023. CrossRef Medline

Dembrow NC, Chitwood RA, Johnston D (2010) Projection-specific neuromodulation of medial prefrontal cortex neurons. J Neurosci 30:16922–16937. CrossRef Medline

Destexhe A, Paré D (1999) Impact of network activity on the integrative properties of neocortical pyramidal neurons in vivo. J Neurophysiol 81: 1531–1547. CrossRef Medline

Destexhe A, Rudolph M, Fellous JM, Sejnowski TJ (2001) Fluctuating synaptic conductances recreate in vivo-like activity in neocortical neurons. Neuroscience 107:13–24. CrossRef Medline

Egorov AV, Hamam BN, Fransén E, Hasselmo ME, Alonso AA (2002) Graded persistent activity in entorhinal cortex neurons. Nature 420:173–178. CrossRef Medline

Faber ES, Sah P (2007) Functions of SK channels in central neurons. Clin Exp Pharmacol Physiol 34:1077–1083. CrossRef Medline

Fellous JM, Rudolph M, Destexhe A, Sejnowski TJ (2003) Synaptic background noise controls the input/output characteristics of single cells in an in vitro model of in vivo activity. Neuroscience 122:811–829. CrossRef Medline

Gee S, Ellwood I, Patel T, Luongo F, Deisseroth K, Sohal VS (2012) Synaptic activity unmasks dopamine D_2 receptor modulation of a specific class of layer V pyramidal neurons in prefrontal cortex. J Neurosci 32:4959–4971. CrossRef Medline

Genet S, Delord B (2002) A biophysical model of nonlinear dynamics underlying plateau potentials and calcium spikes in Purkinje cell dendrites. J Neurophysiol 88:2430–2444. CrossRef Medline

Genet S, Sabarly L, Guigon E, Berry H, Delord B (2010) Dendritic signals command firing dynamics in a mathematical model of cerebellar Purkinje cells. Biophys J 99:427–436. CrossRef Medline

Goldman MS, Levine JH, Major G, Tank DW, Seung HS (2003) Robust persistent neural activity in a model integrator with multiple hysteretic dendrites per neuron. Cereb Cortex 13:1185–1195. CrossRef Medline

Haj-Dahmane S, Andrade R (1997) Calcium-activated cation nonselective current contributes to the fast afterdepolarization in rat prefrontal cortex neurons. J Neurophysiol 78:1983–1989. CrossRef Medline

Helton TD, Xu W, Lipscombe D (2005) Neuronal L-type calcium channels open quickly and are inhibited slowly. J Neurosci 25:10247–10251. CrossRef Medline

Hounsgaard J, Kiehn O (1993) Calcium spikes and calcium plateaux evoked by differential polarization in dendrites of turtle motoneurones in vitro. J Physiol 468:245–259. CrossRef Medline

Kawasaki H, Palmieri C, Avoli M (1999) Muscarinic receptor activation induces depolarizing plateau potentials in bursting neurons of the rat subiculum. J Neurophysiol 82:2590–2601. CrossRef Medline

Koulakov AA, Raghavachari S, Kepecs A, Lisman JE (2002) Model for a robust neural integrator. Nat Neurosci 5:775–782. CrossRef Medline

Krnjević K, Pumain R, Renaud L (1971) The mechanism of excitation by acetylcholine in the cerebral cortex. J Physiol 215:247–268. CrossRef Medline

Larimer P, Strowbridge BW (2010) Representing information in cell assemblies: persistent activity mediated by semilunar granule cells. Nat Neurosci 13:213–222. CrossRef Medline

Lee RH, Heckman CJ (1998) Bistability in spinal motoneurons in vivo: systematic variations in persistent inward currents. J Neurophysiol 80:583–593. CrossRef Medline

Loewenstein Y, Mahon S, Chadderton P, Kitamura K, Sompolinsky H, Yarom Y, Häusser M (2005) Bistability of cerebellar Purkinje cells modulated by sensory stimulation. Nat Neurosci 8:202–211. CrossRef Medline

MacLean JN, Watson BO, Aaron GB, Yuste R (2005) Internal dynamics determine the cortical response to thalamic stimulation. Neuron 48:811–823. CrossRef Medline

Major G, Polsky A, Denk W, Schiller J, Tank DW (2008) Spatiotemporally graded NMDA spike/plateau potentials in basal dendrites of neocortical pyramidal neurons. J Neurophysiol 99:2584–2601. CrossRef Medline

Marder E, Calabrese RL (1996) Principles of rhythmic motor pattern generation. Physiol Rev 76:687–717. CrossRef Medline

McCormick DA, Shu Y, Hasenstaub A, Sanchez-Vives M, Badoual M, Bal T (2003) Persistent cortical activity: mechanisms of generation and effects on neuronal excitability. Cereb Cortex 13:1219–1231. CrossRef Medline

Miller P, Wang XJ (2006) Power-law neuronal fluctuations in a recurrent network model of parametric working memory. J Neurophysiol 95:1099–1114. CrossRef Medline

Milojkovic BA, Radojicic MS, Antic SD (2005) A strict correlation between dendritic and somatic plateau depolarizations in the rat prefrontal cortex pyramidal neurons. J Neurosci 25:3940–3951. CrossRef Medline

Naudé J, Paz JT, Berry H, Delord B (2012) A theory of rate coding control by intrinsic plasticity effects. PLoS Comput Biol 8:e1002349. CrossRef Medline

Ostojic S (2014) Two types of asynchronous activity in networks of excitatory and inhibitory spiking neurons. Nat Neurosci 17:594–600. CrossRef Medline

Perrier JF, Tresch MC (2005) Recruitment of motor neuronal persistent inward currents shapes withdrawal reflexes in the frog. J Physiol 562:507–520. CrossRef Medline

Rekling JC, Feldman JL (1997) Calcium-dependent plateau potentials in rostral ambiguus neurons in the newborn mouse brain stem in vitro. J Neurophysiol 78:2483–2492. CrossRef Medline

Sanchez-Vives MV, McCormick DA (2000) Cellular and network mechanisms of rhythmic recurrent activity in neocortex. Nat Neurosci 3:1027–1034. CrossRef Medline

Schwindt PC, Spain WJ, Foehring RC, Chubb MC, Crill WE (1988) Slow conductances in neurons from cat sensorimotor cortex in vitro and their role in slow excitability changes slow conductances in neurons from cat sensorimotor cortex in vitro and their role in slow excitability changes. J Neurophysiol 59:450–467. CrossRef Medline

Seidemann E, Meilijson I, Abeles M, Bergman H, Vaadia E (1996) Simultaneously recorded single units in the frontal cortex go through sequences of discrete and stable states in monkeys performing a delayed localization task. J Neurosci 16:752–768. CrossRef Medline

Shafi M, Zhou Y, Quintana J, Chow C, Fuster J, Bodner M (2007) Variability in neuronal activity in primate cortex during working memory tasks. Neuroscience 146:1082–1108. CrossRef Medline

Shouval HZ, Gavornik JP (2011) A single spiking neuron that can represent interval timing: analysis, plasticity and multi-stability. J Comput Neurosci 30:489–499. CrossRef Medline

Sidiropoulou K, Lu FM, Fowler MA, Xiao R, Phillips C, Ozkan ED, Zhu MX, White FJ, Cooper DC (2009) Dopamine modulates an mGluR5-mediated depolarization underlying prefrontal persistent activity. Nat Neurosci 12:190–199. CrossRef Medline

Silva LR, Amitai Y, Connors BW (1991) Intrinsic oscillations of neocortex generated by layer 5 pyramidal neurons. Science 251:432–435. CrossRef Medline

Tahvildari B, Fransén E, Alonso AA, Hasselmo ME (2007) Switching between "On" and "Off" states of persistent activity in lateral entorhinal layer III neurons. Hippocampus 17:257–263. CrossRef Medline

Thuault SJ, Malleret G, Constantinople CM, Nicholls R, Chen I, Zhu J, Panteleyev A, Vronskaya S, Nolan MF, Bruno R, Siegelbaum SA, Kandel ER (2013) Prefrontal cortex HCN1 channels enable intrinsic persistent neural firing and executive memory function. J Neurosci 33:13583–13599. CrossRef Medline

Villalobos C, Shakkottai VG, Chandy KG, Michelhaugh SK, Andrade R (2004) SKCa channels mediate the medium but not the slow calcium-activated afterhyperpolarization in cortical neurons. J Neurosci 24:3537–3542. CrossRef Medline

Wang M, Ramos BP, Paspalas CD, Shu Y, Simen A, Duque A, Vijayraghavan S, Brennan A, Dudley A, Nou E, Mazer JA, McCormick DA, Arnsten AF (2007) 2A-adrenoceptors strengthen working memory networks by inhibiting cAMP-HCN channel signaling in prefrontal cortex. Cell 129:397–410. CrossRef Medline

Wang XJ (2001) Synaptic reverberations underlying mnemonic persistent activity. Trends Neurosci 24:455–463. CrossRef Medline

Washburn DL, Anderson JW, Ferguson AV (2000) A subthreshold persistent sodium current mediates bursting in rat subfornical organ neurones. J Physiol 529:359–371. Medline

Yang CR, Seamans JK, Gorelova N (1996) Electrophysiological and morphological properties of layers V-VI principal pyramidal cells in rat prefrontal cortex *in vitro*. J Neurosci 16:1904–1921. CrossRef Medline

Zhang Z, Séguéla P (2010) Metabotropic induction of persistent activity in layers II / III of anterior cingulate cortex. Cereb Cortex 20:2948–2957. CrossRef Medline

Chapter 3. Temporal signatures of cognition from LPFC to MCC controlled by inhibition

3.1. Summary

The previous chapter has showed that persistent activity within monkey PFC, subserved by CaL- and CAN-mediated intrinsic conditional bistability, allows stable yet labile network states during working memory. However, among frontal areas, the MCC presents activity timescales twice those of the LPFC. Moreover, MCC has stronger and slower synaptic inhibition impinging upon pyramidal neurons, suggesting a link between spiking timescales and synaptic inhibition. What are the exact nature of differences in timescales between LPFC and MCC? And are these timescales underpinned by the aforementioned intrinsic currents or by other mechanisms? Finally, how do these mechanisms result in temporally-extended MCC behaviors?

To answer these questions, Vincent Fontanier and Emmanuel Procyk (SBRI, Lyon) recorded within monkey LPFC and MCC, capturing the finer temporal dynamics of neuronal activity timescales by developing individual unit spike autocorrelograms. When extracting the peak latency (LAT) and time constant (TAU) from the autocorrelograms, we confirmed that MCC TAU was higher than LPFC TAU across cell-types (regular spiking RS and fast spiking FS, putatively pyramidal cells and interneurons respectively). Furthermore, LAT was similar across cell-types and areas except for longer LAT in MCC RS neurons.

TAU was modulated by cognitive involvement, with MCC RS TAU increasing during task engagement. Furthermore, neuronal activity timescales were correlated with task variable timescales, as generalized mixed linear model showed LPFC RS and MCC RS short TAU encoded short-term feedback within the inter-trial period, while MCC RS long TAU encoded long-term gauge size information throughout trials. These TAU differences were anatomically organized within an antero-posterior gradient in MCC, with higher TAU in posterior neurons encoding long-term gauge size information. Behavioral switching was potentially induced by MCC FS units, as they were most engaged in encoding negative feedback in the first second after feedback onset.

Starting from a detailed biophysical recurrent network model of LPFC, we identified AHP and GABA-B conductances as crucial determinants for varying neuronal activity timescales from LPFC to MCC, with AHP increasing excitatory (RS) LAT and GABA-B increasing TAU. These elements were consistent with experimental observations of lower MCC frequency-current gain in RS cells (consistent with stronger AHP), as well as stronger and slower inhibition in MCC (consistent with stronger GABA-B). Furthermore, increase in GABA-B conductance led to collective transitions between quasi-stationary metastable states, where spiking timescales were amplified into functionally-relevant network states of several seconds in MCC and hundreds of milliseconds in LPFC, while increase of gAHP decreased probabilities of short states. Finally, maintenance of and transitions between states was controlled by inhibitory neurons, predicting MCC state transitions when MCC FS neurons encoded negative feedback. Importantly, these states emerged without learning, inhibitory subnetworks naturally emerging from the synaptic weight's variability being increasingly contrasted by stronger slow synaptic GABA-B currents.

3.1.1. Contributions

I developed the biophysical neural network model, the autocorrelogram analysis and all analyses on model data (HMM, PCA, etc.), created the figures 5-7, wrote the first draft of the corresponding results text, figure legends, and methods, and reviewed all parts of the text.

3.2. Article

Inhibitory control of frontal metastability sets the temporal signature of cognition

Vincent Fontanier[1*], Matthieu Sarazin[2*], Frederic M. Stoll[3], Bruno Delord[2x], and Emmanuel Procyk[1x]

[1] Univ Lyon, Université Lyon 1, Inserm, Stem Cell and Brain Research Institute U1208, 69500 Bron, France.

[2] Institute of Intelligent Systems and Robotics (ISIR), Sorbonne Université, Centre National de la Recherche Scientifique, UMR 7222, 75005 Paris, France,

[3] Nash Family Department of Neuroscience and Friedman Brain Institute, Icahn School of Medicine at Mount Sinai, New York, NY, USA

[*x] Equal contributions

Correspondence and requests for materials should be addressed to V.F. (email: Vincent.fontanier@gmail.com) or to M.S. (email: Matthieu.Sarazin@live.fr).

Abstract

Cortical neural dynamics organizes over multiple anatomical and temporal scales. The mechanistic origin of the temporal organization and its contribution to cognition remain unknown. Here we demonstrate the cause of this organization by studying a specific temporal signature (autocorrelogram time constant and latency) of neural activity. In monkey frontal areas, recorded during flexible cognitive decisions, temporal signatures display highly specific area-dependent ranges, as well as anatomical and cell-type distributions. Moreover, temporal signatures are functionally adapted to behaviorally relevant timescales. Fine-grained biophysical network models, constrained to account for temporal signatures, reveal that after-hyperpolarization potassium and inhibitory GABA-B conductances critically determine areas' specificity. They mechanistically account for temporal signatures by organizing activity into metastable states, with inhibition controlling state stability and transitions. As predicted by models, state durations non-linearly scale with temporal signatures in monkey, matching behavioral timescales. Thus, local inhibitory-controlled metastability constitutes the dynamical core specifying the temporal organization of cognitive functions in frontal areas.

Keywords:

cingulate, prefrontal cortex, AHP, GABA(B), timescale, primate, recurrent networks, inhibition, attractor, metastable states

Introduction

Large scale cortical networks are anatomically organized in hierarchies of inter-connected areas, following a core-periphery structure (Markov et al., 2013). Within this large scale organization, the dynamical intrinsic properties of cortical areas seem to also form a hierarchy in the temporal domain (Chaudhuri et al., 2014; Murray et al., 2014). The temporal hierarchy arises from increasing timescales of spiking activity from posterior sensory areas to more integrative areas including notably the lateral prefrontal and midcingulate cortex. Intrinsic areal spiking timescales are defined from single unit activity autocorrelation (Murray et al., 2014). Long spiking timescales potentially allow integration over longer durations, which seems crucial in the context of higher cognitive functions, learning and reward-based decision-making (Bernacchia et al., 2011). Recent studies uncovered links between single unit working memory and decision-related activity and spiking timescales in the lateral prefrontal cortex (Cavanagh et al., 2018; Wasmuht et al., 2018). However, the mechanisms that causally determine the timescale of cortical neuron firings and their role in the functional specificity of areas remain to be described.

To address this question, we recorded in the midcingulate cortex (MCC) and lateral prefrontal cortex (LPFC), because these two frontal areas both display particularly long spiking timescales and are functionally implicated in cognitive processes operating over extended timescales. These interconnected regions collaborate in monitoring performance and in integrating the history of outcomes for flexible decisions (Kennerley et al., 2006; Khamassi et al., 2015; Kolling et al., 2018;

Medalla and Barbas, 2009; Rothe et al., 2011; Seo and Lee, 2007; Womelsdorf et al., 2014a). Recent anatomical and physiological investigations revealed that the cingulate region has relatively higher levels of synaptic inhibition on pyramidal neurons than LPFC, with higher frequency and longer duration of inhibitory synaptic currents (Medalla et al., 2017), suggesting that excitatory and inhibitory cell types differentially contribute to the specific dynamics of distinct frontal areas. Moreover, MCC also seems to have a longer spiking timescale than the LPFC (Cavanagh et al., 2018; Murray et al., 2014).

In this context, we sought to understand the relationship between temporal features of spiking activity, local neural network dynamics and the computations implemented by frontal neural networks. We focused on whether and how different temporal features play distinct roles in different frontal areas. To this aim, we addressed the following questions: what are the exact differences in the temporal organization of spiking in the LPFC and MCC? How do they relate to the distinct roles of excitation and inhibition? Do they reflect cognitive operations, and can they be adjusted to current task demands? Can they be accounted for by local biophysical circuit specificities? If so, do distinct collective network neurodynamics emerge from such areal biophysical characteristics and what are their functional implications?

We examined the contribution of single unit temporal signatures to dynamical differences between LPFC and MCC in monkeys. After clustering units based on spike shape (putative fast spiking and regular spiking units) we computed spike autocorrelograms and their temporal signatures (time constant and latency). We discovered that LPFC and MCC differed not only in average time constant, but also specifically in the autocorrelogram latency of their regular spiking units.

Regular and fast spiking MCC neurons showed different temporal signatures. Remarkably, through these signatures, neurons contributed to encoding information at different timescales, i.e. information relevant between trials or across multiple trials. Exploring constrained biophysical recurrent network models, we identified the ionic after-hyperpolarization potassium (AHP) and inhibitory GABA-B receptor conductances as critical determinants mechanistically accounting for the difference in spiking temporal signatures between LPFC and MCC. The models predicted how differences in temporal signature amounts to the ability of networks to undergo metastable states with different properties. Indeed, we found, in monkey data, long-lasting states in primate MCC activity but not in the LPFC.

Critically, we show that by controlling states stability and transitions, local inhibition – rather than synaptic excitation (Chaudhuri et al., 2015) – is the major factor setting temporal signatures. Moreover, inhibitory-mediated temporal signatures did not require specific disinhibition between molecularly identified subnetworks of interneurons but naturally emerged from inhibitory weight variability (Wang, 2020).

Results

We analyzed population spiking timescales for units recorded in MCC and LPFC (140 and 159 units, respectively), using the autocorrelogram of spike counts (see Online Methods), and observed population autocorrelograms similar to those obtained with other datasets (Cavanagh et al., 2018; Murray et al., 2014; Wasmuht et al., 2018) (**Fig. 1a**). At the population level, the characteristic timescale of spiking fluctuation over time, TAU (the time constant from the exponential fit), was longer for MCC than for LPFC (MCC= 519±168 ms, LPFC= 195±17 ms). In addition, MCC single units exhibited longer individual TAUs than LPFC units (medians, MCC=553 ms, LPFC=293 ms; Two-sided Wilcoxon signed rank test on log(TAU), W=15192, $p<10^{-8}$), as in previous datasets (Fig. 1c in Cavanagh

et al. (Cavanagh et al., 2018)). Aside from being characterized by a slow decay (long TAU), the MCC population autocorrelation displayed a distinctive feature: a positive slope at the shortest time lags equivalent to a latency in the autocorrelogram, that can be observed in previous publications (see Figure 1c in Murray et al. (Murray et al., 2014), Figure 1d in Cavanagh et al. (Cavanagh et al., 2018)). However, the method we employ above (derived from Murray et al.) cannot resolve the fine dynamics of neuronal activity at short time lags. To improve upon this approach, we instead developed a method based on the autocorrelogram of individual units from all spike times, that provides high temporal precision in parameter estimation (see Online Methods).

One basic assumption to explain local dynamical properties is that interactions between cell types (e.g. pyramidal cells and interneurons) might induce specific dynamics in different areas (Medalla et al., 2017; Wang, 2020; Womelsdorf et al., 2014b). To separate putative cell populations in extracellular recordings we clustered them using single unit waveform characteristics (Nowak et al., 2003). Clustering discriminated 3 populations, with short, large and very large spikes (**Fig. 1c**). The results below were obtained using 2 clusters (small, and large + very large), as detailed analyses showed no clear difference between large and very large spike populations (see **supplementary fig. S1**). We classified units as fast spiking (FS, short spikes; n_{MCC}=37, n_{LPFC}=61 units) or regular spiking (RS, long spikes; n_{MCC}=257, n_{LPFC}=215 units) which, in previous studies, were associated to putative interneurons and pyramidal cells respectively.

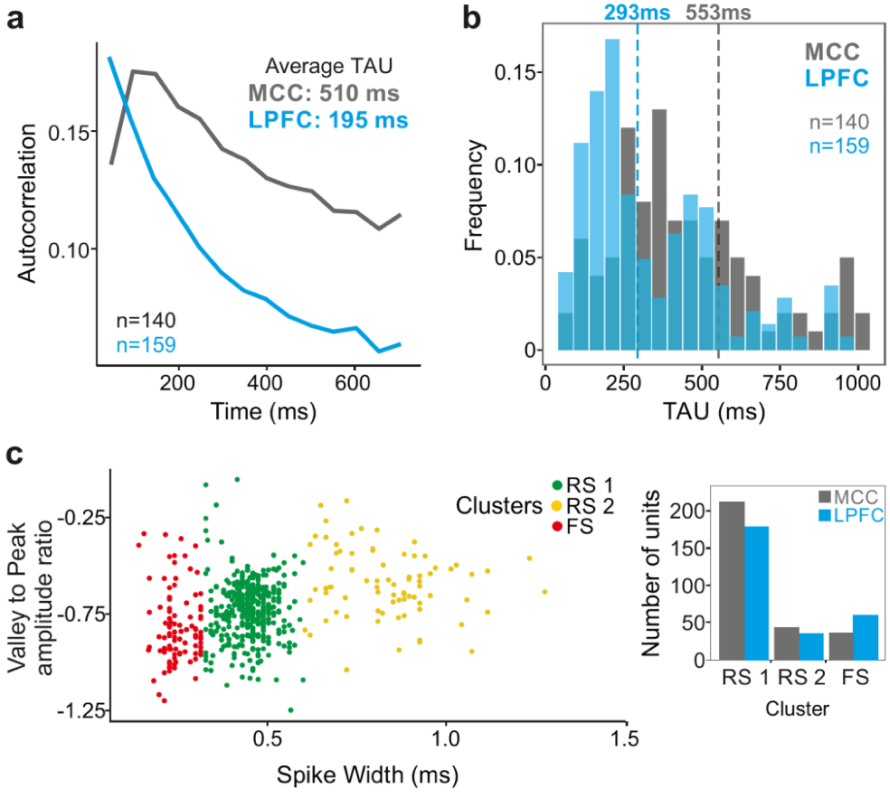

Figure 1. Midcingulate cortex (MCC) and lateral prefrontal cortex (LPFC) spike count autocorrelograms. (**a**) Population exponential fit: autocorrelograms were computed for each unit and the fit was performed on all the units of each area (as in Murray et al. 2014). (**b**) Single unit fits were used to capture individual spiking timescales and produce the distribution of TAU values for each region. Dotted lines represent the median of TAU. (**c**) Clustering of spike shape. We extracted spike width and valley to peak ratio (V2P) from each unit average waveform. A hierarchical clustering led to 3 groups of units (colored groups RS1, RS2, FS). In the paper, units with narrow

spike width were termed as fast spiking (FS), whereas units with broader waveform were marked as regular spiking (RS: RS1 + RS2). The histogram indicates the number of MCC and LPFC units belonging to each of the 3 clusters.

MCC temporal signatures differ for regular spiking units.

From spike autocorrelograms we extracted multiple metrics: the peak latency (LAT) and time constant (TAU) (see Online Methods). Together, TAU and LAT constituted the temporal signature of single neurons spiking dynamic. The success rate of fitting an exponential on spike autocorrelograms was 91.9% and largely outperformed the alternative method (see Online Methods). **Fig. 2a** shows comparative examples. Note that in the pool of neurons where TAU was successfully extracted using both methods (see method for criteria), we found the two measures (Murray methods vs. spike autocorrelograms) of TAU were correlated (Spearman correlation: rho(282) = 0.46,$p<10^{-15}$). Importantly, TAU was not correlated with firing rate across units (**supplementary fig. S2a**).

TAU was higher on average in MCC than in LPFC for both regular and fast spiking cells (medians ± sd: MCC FS= 284.7±132 ms , RS= 319.5±199 ms , LPFC FS= 175.1±67 ms , RS= 191.6±116 ms; linear model fit on Blom transformed TAU for normality, TAU = Area * Unit type, Area : F(1,520)=18.36, $p<10^{-4}$, Unit type: F(1,520)=2.72, p=0.12, interaction: F(1,520)=0.19, p=0.79) (**Fig. 2c**).

In addition, LAT became a precise measure obtained for most autocorrelograms. Importantly, it differed significantly between MCC and LPFC for RS but not for FS units, with MCC RS units having particularly long latencies (median ± sd: MCC FS = 48.5±30 ms, RS = 108.7±64 ms , LPFC FS = 48.5±35 ms , RS= 51.9±46 ms ; linear model fit on Blom transformed LAT for normality, LAT = Area * Unit type, interaction: F(1,520) = 11.81, p<0.005) (**Fig. 2c**).

TAU and LAT both reflect temporal dynamics, but those measures were significantly correlated only in LPFC RS units (Spearman correlations with Bonferroni correction, only significant in LPFC RS: rho(203) = 0.29, $p<10^{-3}$)). The absence of correlation suggested TAU and LAT likely reflect different properties of cortical dynamics. Moreover, the data suggested that and the different temporal signatures of RS units could reflect differences in the physiology and/or local circuitry determining the intrinsic dynamical properties of MCC and LPFC.

MCC temporal signatures are modulated by current behavioral state

A wide range of temporal signatures might reflect a basic feature of distributed neural processing (Bernacchia et al., 2011). But do different temporal signatures play distinct roles in terms of neural processing in different areas? And, are these signatures implicated differentially, depending on task demands? As single units were recorded while monkeys performed a decision-making task (described in Stoll et al., 2016; **Fig. 3a**), we extracted each unit's temporal signature separately for periods in which monkeys were either engaged in the cognitive task or were pausing from performing the task. TAU extracted during engage and pause periods were significantly correlated across neural populations (Pearson correlation: r(267)=0.24, $p<10^{-4}$), indicating that TAU reflects stable temporal properties across conditions. The MCC RS population exhibited a significant modulation of TAU, expressing longer TAU during engage periods compared to pause periods, suggesting that engagement in cognitive performance was accompanied by a lengthening of temporal dynamics for RS neurons in MCC (**Fig. 3b left**)(Wilcoxon signed-ranks test (Median=1) with Bonferroni correction, only significant for MCC RS: Median=1.08 , V=4265, $p<10^{-7}$). We observed no significant variation of LAT with task demands.

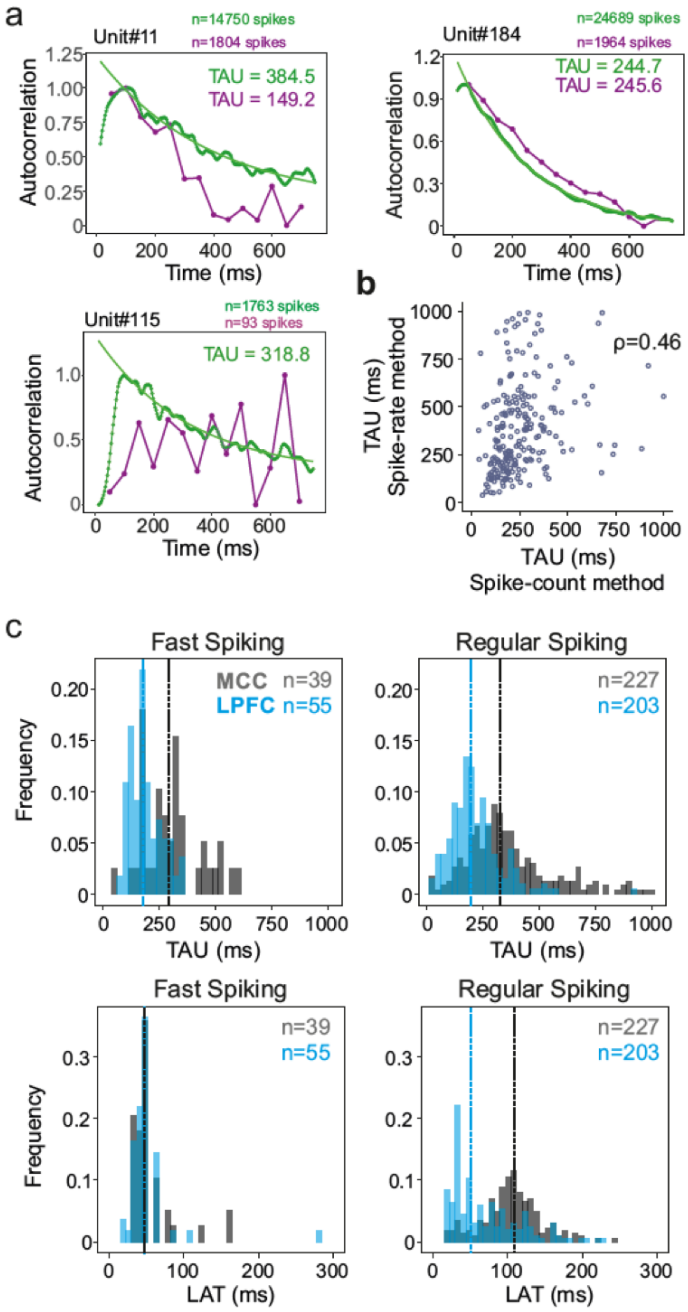

Figure 2. Spike autocorrelogram and temporal signatures in MCC and LPFC. (**a**) 3 single examples of spike count (purple) versus normalized spike autocorrelograms (green) contrasting the outcome of the 2 methods. The measured time constant (TAU) is indicated for both when possible. Numbers of spikes used for each method is also indicated. (**b**) TAU values extracted from each methods are significantly correlated (spearman rho(282) = 0.46,p<10-15). (**c**) Distributions of TAUs (upper histograms) and peak latencies (LAT - lower histogram) for FS (left) and RS (right) units. 'n' indicates the number of units. TAU values were longer in MCC than in LPFC for both FS and RS (linear model fit on BLOM transformed TAU for normality, TAU = Region * Unit type, Region: t=-4.68, p<10-6, Unit type: ns, interaction: ns). Peak latencies significantly differed between MCC and LPFC for RS but not for FS units (medians: MCC FS= 48.5 ms, RS= 102.0 ms , LPFC FS= 48.5 ms , RS= 51.8 ms ; linear model fit on BLOM transformed Latency for normality, Latency = Region * Unit type, interaction: t-value=-3.57, p< 10-3).

Temporal signatures are linked to cognitive processing

Contrary to MCC, LPFC temporal signatures were not modulated by engagement in the task. Multiple cognitive models propose a functional dissociation between MCC and LPFC and indeed empirical data reveal their relative contribution to feedback processing, shifting, and decision making (Khamassi et al., 2015; Kolling et al., 2018; Stoll et al., 2016). One important question is thus whether temporal signatures observed for a given area and/or cell type contribute to selected aspects of cognitive processing. For example, temporal signatures might be adjusted to the current functional context and time scale required to perform a task. In our experiment monkeys gained rewards by performing trials correctly in a categorization task while each success (reward) also brought them closer to obtaining a bonus reward (**Fig. 3a**, right panel, see Online Methods for task description). By

touching a specific lever at trial start, animals could either enter a categorization trial or check the status of a visual gauge indicating the proximity of the bonus reward availability. The number of rewards (i.e. correct categorization trials) needed to get the bonus, and thus the speed of the gauge increase, varied across blocks (i.e. either fast or slow). Previous analyses revealed that feedback influenced the likelihood of checking in the following trial (Stoll et al., 2016). Thus, feedback can be considered as information used on a short timescale (within the inter trial period). The animals also built an estimation of the gauge size that was updated upon checking in order to regulate the frequency of checks during blocks, allowing animals to seek and collect the bonus in a cost-efficient manner (Stoll et al., 2016). Gauge size can thus be considered as information used and carried over long timescales.

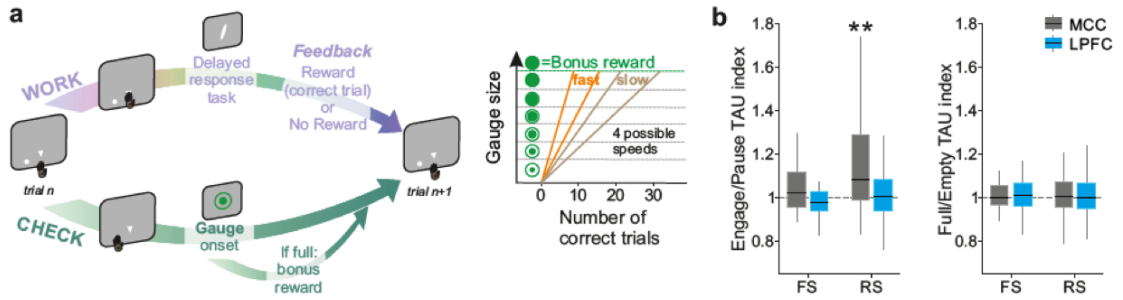

Figure 3. Behavioral engagement in task and spiking timescale changes. (**a**) Schematic representation of the task. At the start of each trial, animals can either initiate a delayed response task (WORK option) which can lead to 1 reward delivery, or use the CHECK option to check the current size of the gauge (or collect the bonus reward). Each reward in the task contributes to increase the gauge size and bring the bonus availability closer. The graph (right) schematized the speed of increase of the gauge size which varies between blocks (fast or slow blocks). (**b**) Boxplots of indices for each unit type and region calculated to estimate potential changes in TAU between Engage and Pause (left), and between empty and full gauge (right). TAUs increased in Engage vs. Pause only for MCC RS units.

We first hypothesized that blocks of different speeds and/or gauge encoding could engage neurons and modulate their spiking timescale. This was not the case. TAU values were not significantly modulated depending on the state of the gauge (less vs. more than half full, **fig. 3b right**), nor related to different speeds (Wilcoxon signed-ranks test (Median=1) with Bonferroni correction, for gauge state and gauge speed, all $p>0.6$).

Conversely, we assessed whether temporal signatures observed for certain cell types contributed to code specific aspects of the task. We used mixed effect models on groups of single units to test the contribution of population activity to encoding task relevant information: feedback in categorization trials (i.e. reward vs. no-reward), and gauge size. The rationale was that feedback information was relevant within the intertrial period, whereas Gauge information was relevant across trials between two successive checks. Previous analyses had revealed that both MCC and LPFC units encode such information, although MCC units showed greater contributions(Stoll et al., 2016). We classed both FS and RS units as either short *or* long TAU units using a median split. A time-resolved generalized mixed linear models (*glmm*) revealed notable dissociations between these populations. During the intertrial period, the population of MCC RS units with short TAU was mostly involved in encoding feedback information, which was relevant only for the current trial (**Fig. 4a**). By contrast, RS units with long TAU were mostly involved in encoding gauge information, which contributed to regulate decisions across trials (Stoll et al., 2016) (**Fig. 4a**, lower right). Long and short

TAU RS populations in LPFC contributed mostly to encode feedback during the intertrial period (Fig. 4a, right).

Interestingly FS units in the MCC were mostly engaged in the first second after feedback onset, with a strong bias toward encoding negative feedback (Fig. 4a, upper left, positive estimates). Effects were more transient and involved short TAU units in the LPFC (**Fig. 4a**).

Spiking timescales are anatomically organized in MCC

Spiking timescales measured in MCC and LPFC covered several orders of magnitudes (10-1000 ms; **Fig. 2c**). Because single unit recordings spanned large regions, such wide range could reflect anatomical organization of segregated populations with distinct homogeneous intrinsic properties. Such organization has been observed in MCC with human fMRI (Meder et al., 2017). We indeed found that average TAU values in MCC were higher in more posterior parts, in particular for RS units (ANOVA on Blom transformed TAU: MCC, monkey A: $F(5,112)=2.8$, $p=0.041$, monkey H: $F(5,54)=3.09$, $p=0.033$, LPFC, monkey A: $F(6,110)=0.34$, $p=1$, monkey H: $F(6,64)=2.49$, $p=0.066$; linear regression on Blom transformed TAU: MCC, monkey A: $t(1,112)=8.99$, $p=0.0067$, monkey H: $t(1,54)=2.22$, $p=0.28$, LPFC, monkey A: $t(1,110)=1.09$, $p=0.60$, monkey H: $t(1,64)=0.25$, $p=1$; all p-values are FDR corrected for n=2 comparison per monkey) (**Fig 4b**). This suggests an antero-posterior gradient of spiking timescales. No such effect was observed in LPFC. Similar analyses for LAT revealed no consistent inhomogeneity within MCC or LPFC (**Fig. S2b**).

The consequence of such an organization, knowing the respective functional involvement of units with long and short TAU (**Fig 4a**), should be an antero-posterior functional gradient. We tested this by separating MCC cells in posterior versus anterior subgroups and tested their contribution to feedback and gauge encoding (**Fig. 4b**). Indeed, posterior RS units' activity contributed to positive encoding of gauge size, preceded in time by encoding of positive feedback (negative estimates) (**Fig. 4c lower and upper right**), while anterior RS units showed primarily a contribution to feedback encoding (**Fig. 4c upper right**). Finally, anterior FS units were primarily (in time and in strength) contributing to encoding negative feedback. This remarkable contribution of FS to feedback encoding is studied and discussed further below.

In summary, MCC regular spiking units with relatively short or long TAU contributed to the encoding of task elements relevant over short and long terms, respectively. The spiking timescales seemed to be organized along the rostro caudal axis in MCC. This suggests a correspondence between cell type, temporal signatures and their functional involvement in processing specific aspects of cognitive information in different functional subdivisions of cortical regions. The crucial questions thus remain of the mechanistic origin of temporal signatures and of how they relate to cognitive functions.

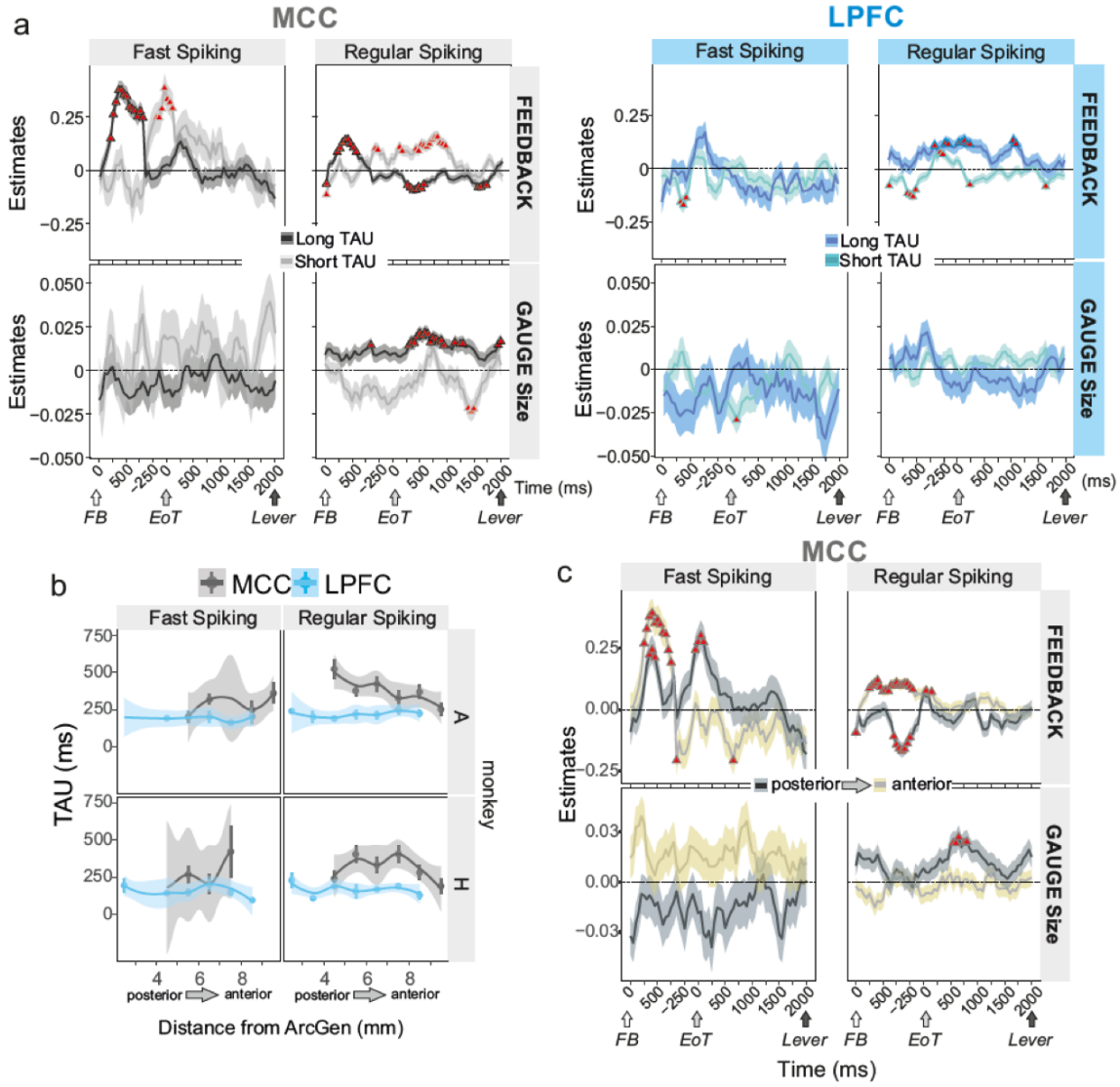

Figure 4. Encoding of feedback and gauge size for different unit types and spiking timescales and rostro-caudal distribution. (**a**) Estimates (β-coefficients) obtained from the MCC (grey) and LPFC (blue) unit populations obtained from time-resolved *glmm* for Feedback (reward vs no reward; top graphs) and Gauge size (bottom) (see 'Group analyses using *glmm*' in Methods). Estimates are obtained at successive time points covering the entire inter-trial period between feedback onset and the lever onset in the following trial. Significant effects are indicated by a red triangle ($p<0.05$ corrected), shadings indicate standard deviations. Positive values depict a population activity bias towards negative feedback (top) and positive slope of linear coding for gauge size (bottom). Data is presented for FS and RS units (left and right respectively for each panel) and have been performed on subpopulation with short or long TAU values (determined by a median split). Short and long TAU populations are represented by light and dark color intensity. Note in particular the dissociation for RS MCC units with short and long TAU respectively coding for feedback and gauge size. (**b**) Averaged TAU values along the postero-anterior axis in the MCC and LPFC, for both monkeys. (**c**). Estimates reflecting coding strength of Feedback and Gauge size for MCC unit populations separated by their rostro-caudal location.

Biophysical determinants of temporal signatures in frontal network models

To uncover the source and consequences of distinct temporal spiking signatures in the LPFC and MCC, we designed a fine-grained model of local recurrent frontal networks. This model is unique in combining 1) highly-detailed biophysical constraints on multiple ionic channels, synaptic receptors and architectural frontal specificities, and 2) the cardinal realistic features of mammals cortical

neurodynamics including the excitation/inhibition balance, high-conductance state of neuronal activity and asynchronous irregular regime characterizing the awake state (Brunel, 2000; Destexhe et al., 2003; Hennequin et al., 2017). Our specific goal was to evaluate whether biophysical circuit specificities could mechanistically account for differences in LPFC and MCC temporal signatures. We also assessed whether these specificities induce distinct collective network neurodynamics and functional implications, possibly explaining the empirical relationships between temporal signatures, cell type, and information processing.

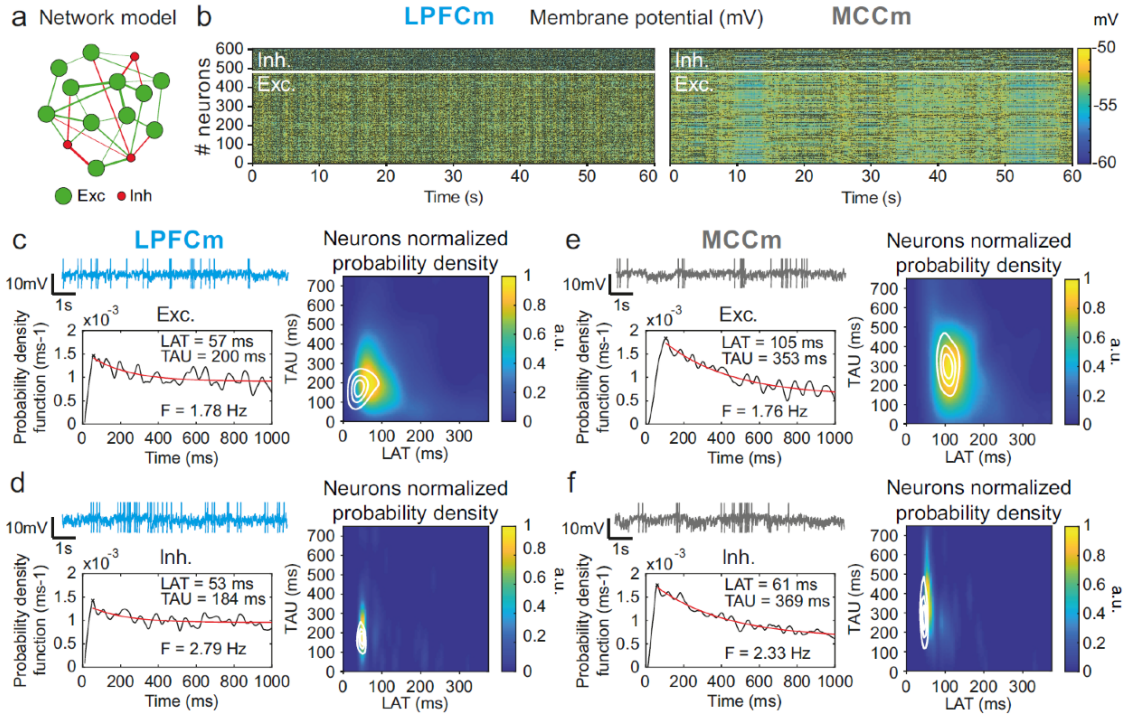

Figure 5. Temporal signature of LPFCm and MCCm recurrent network biophysical models. (**a**) Scheme of the frontal recurrent networks modelled, with 80% excitatory (green) and 20% inhibitory (red) neurons and sparsity of synaptic connections. (**b**) Membrane potential in the 484 excitatory (lower part) and 121 inhibitory (upper part) neurons of example network models with parameter set to approximate LPFC dynamics (g_{CAN}=0.025mS.cm^{-2}, g_{AHP}=0.022mS.cm^{-2}, $g_{GABA\text{-}B}$=0.0035mS.cm^{-2} ; see text and legend of Fig. 6b for the choice of LPFC and MCC standard g_{AHP} and $g_{GABA\text{-}B}$ maximal conductances) and MCC dynamics (g_{CAN}=0.025mS.cm^{-2}, g_{AHP}=0.087mS.cm^{-2}, $g_{GABA\text{-}B}$=0.0143mS.cm^{-2}). (**c**) (upper left) Membrane potential of an example excitatory neuron in the LPFC model (LPFCm). Scaling bars 1s and 10mV (spikes truncated). (lower left) Autocorrelogram of this LPFCm example excitatory neuron (black) and its exponential fit (red, see *Online Methods*). (right) Bivariate probability density distribution of autocorrelogram parameters in LPFCm excitatory neurons. Contour lines at 50, 75 and 90% of the maximum of the bivariate probability density distribution in LPFC monkey RS units. (**d**) Same as **(c)** for LPFCm inhibitory neurons, with contour lines from the bivariate probability density distribution in LPFC monkey FS units. **(e,f)** Same as **(c,d)**, for the MCCm and MCC.

We first explored, using Hodgkin-Huxley cellular models (see *Online Methods*), whether specific frontal temporal signatures may arise from ionic or synaptic properties of individual neurons. Extensive explorations of these models identified, among many ionic and synaptic conductances tested, the maximal cationic non-specific (g_{CAN}) and potassium after-hyperpolarization (g_{AHP}) conductances as the sole couple affecting both LAT and TAU. However, their regulation could not fully reproduce the monkey data set (see Supplementary **Fig. S4** and **S5**). Thus, we then assessed

whether collective dynamics at the level of recurrent networks models could better account for frontal temporal signatures (**Fig. 5a**, see *Online Methods*). One-dimensional explorations of the large parameter space failed to identify single biophysical determinants accounting, alone, for differences between LPFC and MCC (RS and FS) temporal signatures (Supplementary **Fig. S6 and Table S1**). However, these explorations targeted four parameters of interest regulating either LAT or TAU confirming those already revealed in cellular models (g_{CAN} and g_{AHP}) and uncovering, in addition, NMDA and GABA-B maximal conductance (g_{NMDA} and $g_{GABA\text{-}B}$) whose slow time constants strongly affected network dynamics.

Two-dimensional explorations using these key parameters (**Fig. 5** and supplementary **Fig. S7**) identified a single specific setup which demonstrated network dynamics that reproduced the shift from the LPFC-like temporal signature to that resembling the MCC with striking precision. An increase of both g_{AHP} and $g_{GABA\text{-}B}$, in the presence of g_{CAN}, drove the model from an LPFC-like temporal signature (LPFCm model) (**Fig. 5c & d**; map and contours: bivariate probability density model and monkeys' distributions, respectively) towards that of the MCC (MCCm model, **Fig. 5e-f**). Specifically, g_{AHP} increased LAT and decreased TAU in excitatory (likely equivalent to RS) neurons (**Fig. 6a** left) and had no effect in inhibitory (likely FS) neurons (**Fig. 6a** right). Besides, $g_{GABA\text{-}B}$ decreased LAT in both excitatory and inhibitory neurons (**Fig. 6a** top) and increased TAU in an intermediate range (**Fig. 6a** bottom). A bivariate probability density-based similarity measure (see *Online Methods*) revealed that monkey temporal signatures were robustly reproduced by the model in two large contiguous regions in the (g_{AHP}, $g_{GABA\text{-}B}$) plane, with both conductances increased in the MCC (**Fig. 6b**).

Several lines of evidence further indicated the model's relevance. First, the model properly accounted for the larger LAT variability in monkey RS vs FS units (**Fig. 5**). Moreover, it reproduced the complex relations between LAT and first-order latency (ISI distribution latency) remarkably well, in all populations (**Fig. 7c** and **Supplementary Fig. 7**). Furthermore, both the firing frequency and input-output gain were lower in MCCm excitatory neurons (**Fig. 6d**), because of its higher g_{AHP} (Naudé et al., 2012), as found experimentally(Medalla et al., 2017).

Metastable states underlie LPFC and MCC temporal signatures

The asynchronous irregular (presumably chaotic) dynamics of network models was highly structured in time (**Fig. 5b**). Hidden Markov models (HMM) revealed that it organized through collective transitions between so-called metastable (quasi-stationary) states in the models LPFCm and MCCm (**Fig. 7a**), as found in frontal areas (Abeles et al., 1995; Seidemann et al., 1996; Xydas et al., 2011). Moreover, while LPFCm states maximally lasted a few hundred milliseconds (**Fig. 7b, left, blue**), MCCm states persisted up to several seconds (**Fig. 7b, grey**). This suggested that such a difference in metastability may also parallel the difference of temporal signature in monkey LPFC and MCC areas. Applying HMM to experimental data revealed that, as predicted by the model, neural activity was organized as metastable states at slower timescales in the MCC (vs the LPFC, **Fig. 7b, right**). State durations were globally shorter in models (compared to monkeys), as they contained neither temporal task structure nor learning (see discussion) and were not optimized to fit data.

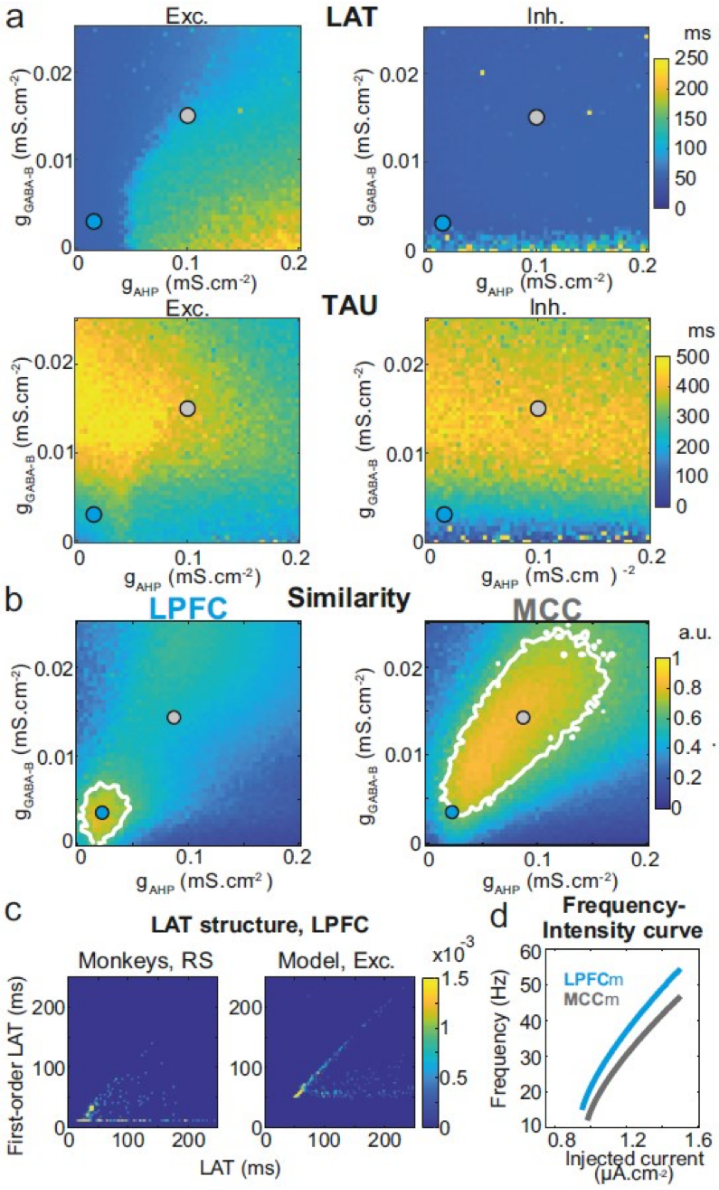

Figure 6. Similarity to monkey LPFC and MCC temporal signatures critically depends on AHP and $GABA_B$ conductance in the network model. (**a**) Mean population LAT (top) and TAU (bottom) in Exc (left) and Inh (right) neurons, as a function of AHP and GABA-B maximal conductances. Blue and grey disks indicate the (g_{AHP}, $g_{GABA\text{-}B}$) parameter values of the LPFCm and MCCm models, respectively. (**b**) Similarity of the temporal signature between the network model and monkey data in the LPFC (left) and MCC (right), as a function of AHP and GABA-B maximal conductances (see Online Methods). In (a) and (b), the value for each (g_{AHP}, $g_{GABA\text{-}B}$) is averaged over 5 simulations. Contour line at 80% of maximum similarity. LPFCm and MCCm (g_{AHP}, $g_{GABA\text{-}B}$) parameter values calculated as coordinates of the contour delimited area's weighted average. (**c**) Bivariate probability density distribution of the autocorrelogram LAT and first- order latency (the latency of the ISI distribution) in RS units in monkey LPFC (left) and excitatory neurons in the example LPFCm model (right). The model accounts for two distinct neuronal subsets in RS neurons, where LAT is determined by first-order latency solely (due to gAHP-mediated refractoriness; diagonal band), or in conjunction with other factors ($g_{GABA\text{-}B}$ slow dynamics-mediated burstiness and recurrent synaptic weight variability; horizontal band). (d) Single excitatory neuron frequency/intensity relationship in the LPFCm (blue) and MCCm (grey) models in response to a constant injected current.

Long states essentially required high $g_{GABA\text{-}B}$ in the MCCm, as they disappeared when $g_{GABA\text{-}B}$ was lowered to its LPFCm value ($MCCm_{LPFC\ GABA\text{-}B}$ model, **Fig. 7b** left, orange curve). In contrast, they only marginally depended on g_{AHP}. MCCm and an MCCm model with the g_{AHP} derived from that of LPFCm ($MCCm_{LPFC\ AHP}$) showed state duration distributions that were essentially similar, although there was a small increase in the probability of short states at lower g_{AHP} (pink vs gray curves). In the (g_{AHP}, $g_{GABA\text{-}B}$) space, $g_{GABA\text{-}B}$ systematically proved to be essential in increasing the duration of states, with a border region that clearly separated short states (<0.1s) from longer states (>1s) (**Fig. 7c**) At this intermediate border, lower g_{AHP} increased the probability of short states (grey vs pink dots; distributions were even bimodal at lowest g_{AHP} values, not shown), as witnessed by departure from log-normality (**Fig. 7c**). As such, the temporal structure of states in the LPFCm was dominated by short and unimodal state duration distributions (**Fig. 7c** and **7d**, blue dots), as in monkeys (**Fig. 7b**, right) and previous studies(Abeles et al., 1995; Seidemann et al., 1996). In the MCCm, by contrast, the distribution displayed large durations and a slight departure from log-normality (**Fig. 7c** and **7d**, grey dots), resulting in a majority of long states (>1s) coexisting with short states, as found in data (**Fig. 7b**).

State duration, i.e. stability, scaled with spatial separation in the neural space of activity (**Fig. 7e,** see Online Methods). Indeed, the shorter states of network models with lower $g_{GABA\text{-}B}$ (LPFCm and $MCCm_{LPFC\ GABAB}$, blue and orange dots) were less distant, compared to those of networks models with higher $g_{GABA\text{-}B}$ (MCCm and $MCCm_{LPFC\ AHP}$, grey and pink dots). While states were largely intermingled in the LPFCm and $MCCm_{LPFC\ GABAB}$ (**Fig. 7f**, upper & middle left), they clearly segregated in the MCC and $MCCm_{LPFC\ AHP}$ (**Fig. 7f**, upper & middle right). As predicted by the model, segregation between states was indeed higher in the monkey MCC (**Fig. 7e**, large grey triangle, and **Fig. 7f**, lower right), compared to the LPFC (**Fig. 7e**, large blue triangle, and **Fig. 7f**, lower left). This suggests that the higher stability of states in monkey MCC arose from a larger segregation of representations in the space of neural activity.

Altogether, these results suggested that itinerancy between metastable states constitutes a core neurodynamical principle underlying the diversity of computational processes and functions operated in primate frontal areas (**Fig. 7g**, see Discussion). From this perspective, the conditions governing transitions between states is critical. We thus evaluated how perturbations of selective neuronal populations would escape ongoing states and reach specified target states (**Fig. 7h**). In the MCCm, we substituted the membrane potentials and synaptic opening probabilities of a fraction of excitatory (vs inhibitory) neurons of the ongoing HMM state by those of a target state. This could mimic the effect of internal chaotic fluctuations or external inputs aimed at reaching that target state. Surprisingly, escaping the ongoing state or reaching the target state remained quite unlikely when substituting excitatory neurons, whatever the fraction (**Fig. 7h**, left). By contrast, both probabilities of escaping and reaching scaled with the fraction of substituted inhibitory neurons, with high maximal probabilities (mean: 0.89 and 0.59 for escaping and reaching, respectively – **Fig. 7h**, right panel). Interestingly, the probability of escaping a state could attained 0.24 even with as few as 2% of substituted inhibitory neurons, indicating the significant impact of single inhibitory neurons on state itineracy.

Thus, inhibition is a major factor controlling targeted transitions between metastable states in the MCC network model and is also crucial in determining their stability. Excitation had no such role. This result is remarkable, especially considering that MCC FS neurons encoded negative

outcomes immediately after feedback onset that triggered behavioral adaptive responses (**Fig. 4**). This could reflect the involvement of MCC FS neurons in inducing state changes on feedback associated to behavioral flexibility.

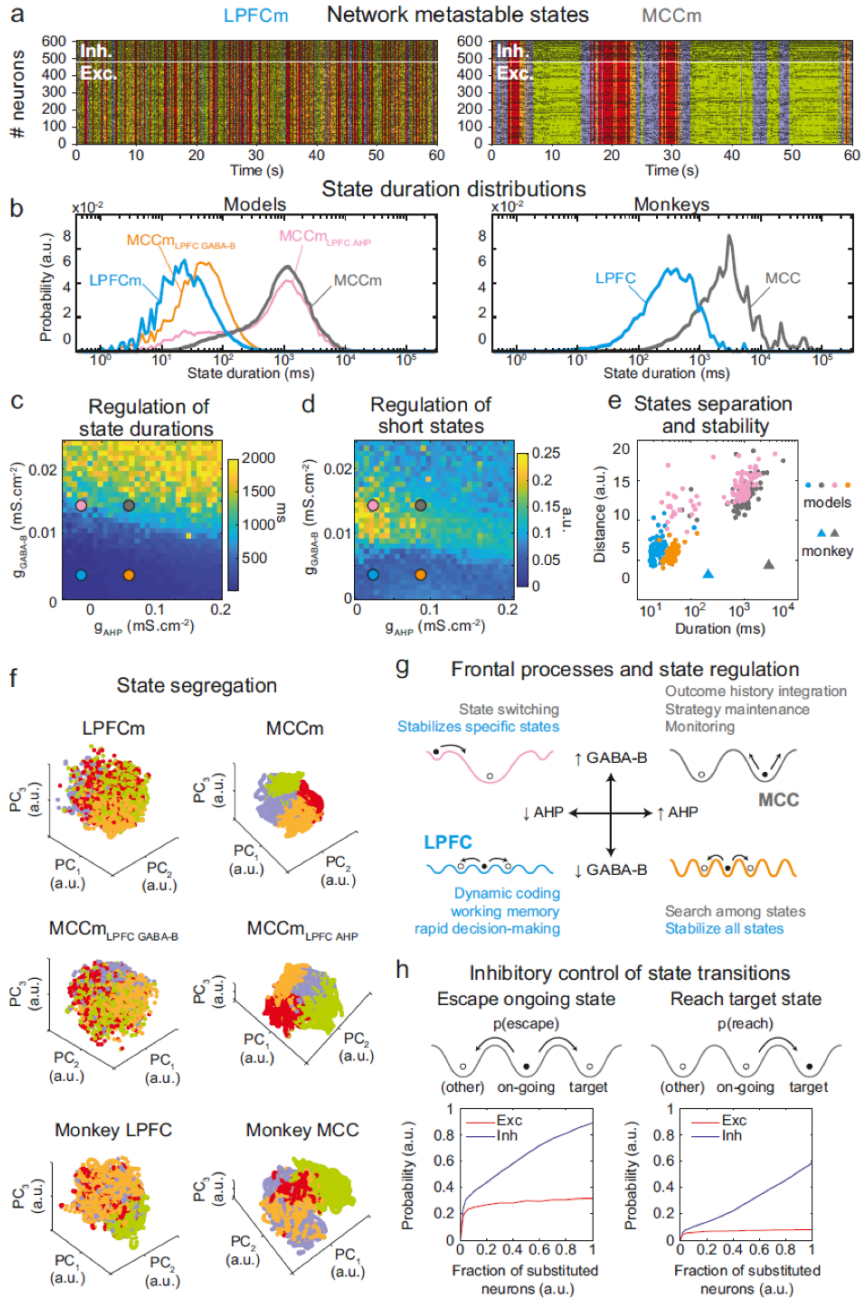

Figure 7. **Properties of metastable states in the LPFC and MCC** (**a**) LPFCm and MCCm models spiking raster plots (black dots), with Hidden Markov model states (HMM, colored bands) (**b**) State duration distributions: probability distributions of being in states of given durations in LPFCm (blue), MCCm (grey), MCCm with LPFCm g_{AHP} ($MCCm_{LPFC\ AHP}$ pink) and MCCm with LPFCm $g_{GABA\text{-}B}$ ($MCCm_{LPFC\ GABA\text{-}B}$, orange) models (left) and monkey LPFC (blue) and MCC (grey) areas (right). Each model was simulated 100 times and analyzed via HMM, while monkey data was analyzed via HMM with 100 different initiation parameter states. Periods above 300s were excluded. (**c, d**) Regulation of state duration and short states: median state duration (c) and Kolmogorov-Smirnov one-sample test statistic or maximal distance of state duration probability distributions to log-normality, as a measure of the over-representation of short states (d), as a function of g_{AHP}

and $g_{GABA\text{-}B}$ maximal conductances. Colored disks indicate parameter values of LPFCm, MCCm, $MCCm_{LPFC\ AHP}$ and $MCCm_{LPFC\ GABA\text{-}B}$ models, respectively. Each point is the average of 5 simulations. (**e**) Separation between states: average distances between HMM states (averaged pairwise distance between neural centered standardized frequency centroids (temporal averages) of HMM states), as a function of median state durations. Distances calculated over 100 simulations in models and once for monkey LPFC and MCC data. (**f**) State segregation: projection of neural activity on the principal components of the PCA space of example model simulations and of monkey data. State colors as in (a). (**g**) Frontal processes and state regulation: schematic attractor landscapes in the LPFC and MCC. Horizontal and vertical arrows indicate possible regulations of AHP and $GABA_B$ conductance levels respectively by intrinsic/synaptic plastic processes or neuromodulation in the LPFC and MCC. Likely functional processes operating in these landscapes are indicated in blue for the LPFC and grey for the MCC. (**h**) Inhibitory control of state transitions: probability to escape an ongoing state (left) and to reach a target state (right), when the ongoing state is perturbed by substituting a given proportion of its excitatory (vs inhibitory) neurons' activity by that of the same neurons in the (perturbing) target state (see Online Methods). Average (full line), +/- s.e.m. (shaded areas, almost imperceptible).

Discussion

We showed LPFC and MCC displayed long population spiking timescales (TAU), with larger values in MCC (TAU~500 vs 200 ms), consistent with previous observations (Chaudhuri et al., 2015; Murray et al., 2014). In fact, LPFC and MCC express distinctive and complex temporal organizations of their activity, which cannot be solely captured by the population spiking timescale. The spiking timescale has been used as a measure characterizing intrinsic areal properties and an inter-area temporal hierarchy. However, the spiking timescale of single units varied over two orders of magnitude within each area (Cavanagh et al., 2018; Murray et al., 2014; Wasmuht et al., 2018). The latency of autocorrelogram also demonstrate informative variability, which suggest important underlying functional richness. Our study demonstrates that the temporal signature (TAU and LAT) of single units, measured through spike autocorrelogram metrics and cell type segregation, can highlight specific local ionic and synaptic mechanisms. Differences in temporal signatures, for instance between LAT of FS and RS in MCC, and within regions, provide important information on the functional properties of the underlying neural network.

Unravelling the multidimensional nature of LPFC and MCC temporal signatures at the level of individual neurons enabled us to constrain refined biophysical recurrent network models and reveal the local biophysical determinants mechanistically accounting for their specific temporal organization. Moreover, we showed that these determinants control neurodynamical features that constitute core computational foundations for the executive cognitive processes operated by these frontal areas.

Functional spatio-temporal organization of temporal signatures in frontal areas

The correlation between temporal signatures and behavior suggests how such biophysical properties could contribute to functional specificities. Spiking timescales distributions have been related to persistent activity, choice value and reward history in the LPFC and MCC (Bernacchia et al., 2011; Cavanagh et al., 2018; Meder et al., 2017; Wasmuht et al., 2018). Here, the spiking timescales of MCC RS units increased on average during periods of engagement in cognitive performance, likely reflecting the global implication of neural processes in task performance at long timescales. MCC units with different temporal signatures differentially contributed to cognitive processes known to engage MCC, namely feedback/outcome processing and outcome history representations (Kennerley et al., 2009; Quilodran et al., 2008; Seo and Lee, 2007). Outcome processing generally enables rapid – trial by trial – adaptation of control and decisions, while outcome history representations contribute to the long-term – across trials – establishment of values guiding strategy adaptation (Behrens et al., 2007; Karlsson et al., 2012).

In our experiment, short spiking timescale units contributed to feedback processing, whereas long spiking timescale units and especially RS units, contributed to encode gauge size, which linearly increase with the accumulation of rewards across trials. In MCC, this temporal dissociation coincided with a spatial organization along the antero-posterior axis: anterior units mainly encoded feedback valence, more strongly and earlier than posterior units, whilst posterior units mostly encoded the long-term information related to gauge size. This antero-posterior gradient strikingly resembles that observed in humans (Meder et al., 2017).

Local molecular basis of frontal temporal signatures

Through extensive parameter exploration of constrained biophysical frontal network models, we identified 2 conductances that precisely reproduced all monkey temporal signatures. In the model, higher TAU (i.e. MCC vs LPFC, posterior vs anterior MCC) was accounted for by stronger synaptic GABA-B levels, consistent with reported higher GABA-B receptor densities (Zilles and Palomero-Gallagher, 2017), stronger and slower inhibitory currents in the MCC (vs LPFC) (Medalla et al., 2017), and stronger GABA-B receptor densities in the posterior (vs anterior) MCC (Palomero-Gallagher et al., 2009). Excitatory synaptic transmission has been proposed to be a crucial determinant of longer spiking timescales in the temporal cortical hierarchy (Chaudhuri et al., 2015). We found that while stronger excitatory transmission increases TAU (possibly accounting for longer MCC TAUs), it also decreases LAT. LAT, however, was longer in the monkey MCC. This suggests that GABA-B inhibitory – rather than excitatory – transmission is the causal determinant of longer spiking timescales, at least in the LPFC and MCC. Noticeably, long timescales do not require specific disinhibition between molecularly identified subnetworks of interneurons (Wang, 2020) but naturally emerge from inhibitory weights variability (see below). The model also predicts that higher LAT in the MCC originate from increased refractoriness through higher after-hyperpolarization potassium (AHP) conductances in RS units. Higher AHP implies lower input-output gains in MCC RS units, compared to the LPFC (Naudé et al., 2012), as found empirically (Medalla et al., 2017). Finally, reproducing appropriate temporal signatures required the cationic non-specific (CAN) conductance in the areas' RS units. This was observed in RS of rodent medial frontal areas (Haj-Dahmane and Andrade, 1997; Ratté et al., 2018), where it regulates, together with AHP, cellular bistability and memory, network persistent activity and computational flexibility (Compte, et al., 2003; Papoutsi et al., 2013; Rodriguez et al., 2018; Thuault et al., 2013). Our conclusions do not preclude the contribution of other factors to temporal signatures such as large-scale hierarchical gradients (Chaudhuri et al., 2015), distinct neuromodulations (see below), or inputs with different spectral contents to LPFC and MCC.

Frontal temporal signatures uncover metastable dynamics

The LPFC and MCC activity, both in models and in monkeys', was metastable, i.e. organized in sequences of discrete, quasi-stationary states in which activity fluctuates around fixed-point attractors (Abeles et al., 1995; La Camera et al., 2019; Rich and Wallis, 2016; Seidemann et al., 1996). As a general rule, the duration of states increases with the stability of their attractor (i.e. the depth/width of their basin of attraction) and decreases with spiking fluctuations. Fluctuations originate from stochastic inputs or chaotic noise (as in our model), and they trigger state transitions.

States were longer in monkeys, likely because extensive training induced attractors that were more stable, whereas models displayed less stable attractors that simply resulted from just random connectivity without learning. Thus metastability genuinely emerged from synaptic heterogeneity and did not require strong network clustering (La Camera et al., 2019). We showed that high GABA-B levels are crucial to stabilize states because they amplify the heterogeneity of inhibition and widens

attractors, as reflected by higher state separation in the MCC. In addition, GABA-B's long time constant naturally promotes burstiness, i.e. stable discharge episodes. Finally, higher AHP levels, required for higher LAT in MCC RS units, limited the occurrence of the shortest states, limiting frequent transitions between states.

In monkeys and biophysical models, temporal signatures, which correlate with state stability, actually reflect the underlying temporal organization of neurodynamics into metastable states. Interestingly, state durations (up to >10s) were longer than spiking timescales (<0.5s), reconciling the apparent discrepancy between typical spiking timescales in frontal areas (<1s) and the functional timescales at which those areas operate (up to tens of seconds, Bernacchia et al., 2011).

Functional significance of controlled metastable states in frontal areas

Metastable states can be linked to specific representations in the brain at a variety of levels of abstraction, from stimuli to mental states (Engel et al., 2016; La Camera et al., 2019; Mazzucato et al., 2015, 2019; Rich and Wallis, 2016; Taghia et al., 2018). In general, state transitions contain appreciable randomness, with high transition rates signing internal deliberation, whilst more stable states predicting forthcoming decisions (La Camera et al., 2019). We suggest that controlling itinerancy among metastable states constitutes a core neurodynamical process supporting executive functions in frontal areas, which allows to scan choices and strategies, generate deliberation and solve on-going tasks.

Specifically, in the MCC (**Fig. 7g**, gray landscape) GABA-B-mediated long metastable states underlying long spiking timescales may contribute to the maintenance of ongoing strategies (Durstewitz et al., 2010; Enel et al., 2016; Stoll et al., 2016) and to the integration of outcome history (Kennerley et al., 2006; Meder et al., 2017; Seo and Lee, 2007; Tervo et al., 2014). At shorter timescales, short states might instantiate dynamic coding, flexible computations and rapid decision-making in the LPFC (Fig. 7g, blue landscape) (Rich and Wallis, 2016; Rigotti et al., 2013; Stokes, 2015). Short states may be lengthened in the LPFC when AHP is increased (Fig. 7g, orange landscape), favoring longer timescales and a global stabilization of, for instance, working memory processes (Cavanagh et al., 2018; Durstewitz and Seamans, 2008). Conversely, decreasing GABA-B destabilizes all long states in the MCC model, globally favoring fast transitions (Fig. 7g, orange landscape). This mechanism might contribute to abandon prior beliefs and to rapid search for adapted representations, e.g. in uncertain environments (Karlsson et al., 2012; Quilodran et al., 2008; Stoll et al., 2016). In the LPFC model with increased GABA-B or in the MCC model with decreased AHP, activity destabilizes certain long states, favoring transitions to remaining long states (Fig. 7g, pink landscape). Such a configuration might be relevant for flexible behaviors, directed exploration and switching (Durstewitz et al., 2010; Pasupathy and Miller, 2005; Russo et al., 2020; Stoll et al., 2016). Regulating GABA-B and AHP to dynamically adapt computations and temporal signatures could be achieved through neuromodulatory or fast plastic processes (Froemke, 2015; Satake et al., 2008).

Macroscopic gradients of inhibitions and excitations appear as important determinants of the large scale organization of cortical dynamics (Wang, 2020; Womelsdorf et al., 2014b). Our results indicate a complementary fundamental dual role of local inhibition in regulating state durations and stability on one hand, and setting the timing and direction of state transitions, on the other. Moreover, transitions can be easily triggered using very few inhibitory neurons. Our study suggests that interneurons and inhibition might be causal in error-driven state transitions in the MCC. Such transitions, initiated by FS neurons immediately after feedback onset, would allow escaping currently unsuccessful states, reaching alternatives or exploring new states.

In conclusion, we showed that local ionic and synaptic determinants specify the scale of temporal organization of activity in frontal cortical areas. These determinants might produce the particularly long states observed in monkey MCC dynamics and could explain its contribution to functions operating over extended behavioral periods. More generally, our results suggest that the diversity of spiking timescales observed across the cortical hierarchy reflects the local excitability- and synaptic inhibition-mediated regulation of metastability, which sets the temporal organization of computational processes.

FIGURE LEGENDS

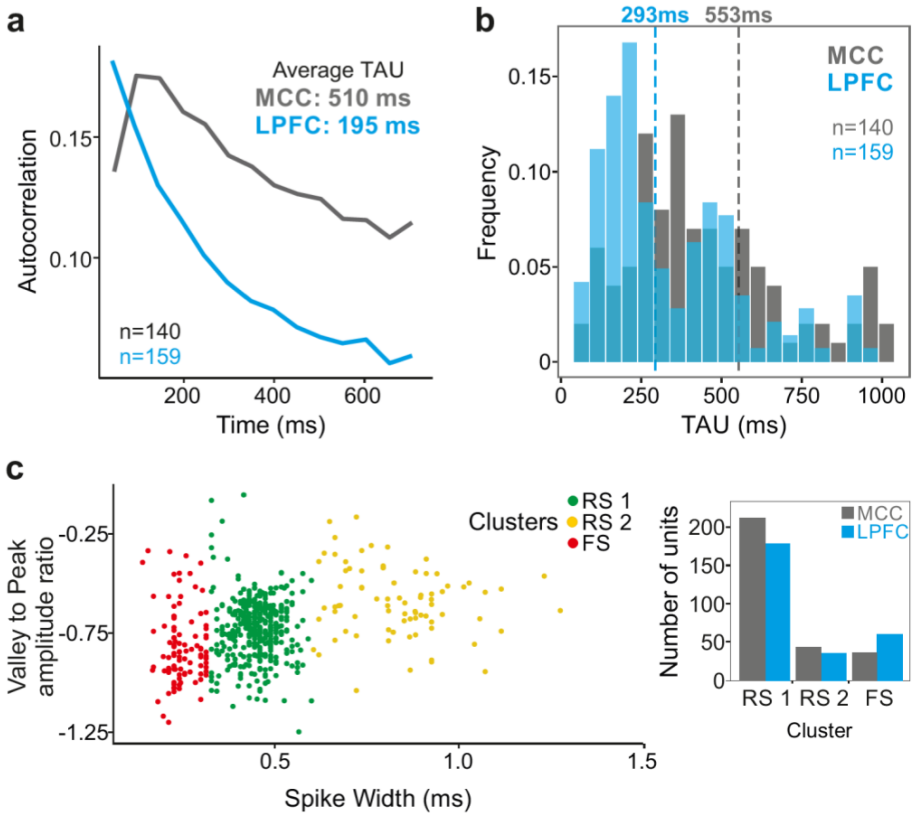

Figure 1. Midcingulate cortex (MCC) and lateral prefrontal cortex (LPFC) spike count autocorrelograms. (**a**) Population exponential fit: autocorrelograms were computed for each unit and the fit was performed on all the units of each area (as in Murray et al. 2014). (**b**) Single unit fits were used to capture individual spiking timescales and produce the distribution of TAU values for each region. Dotted lines represent the median of TAU. (**c**) Clustering of spike shape. We extracted spike width and valley to peak ratio (V2P) from each unit average waveform. A hierarchical clustering led to 3 groups of units (colored groups RS1, RS2, FS). In the paper, units with narrow spike width were termed as fast spiking (FS), whereas units with broader waveform were marked as regular spiking (RS: RS1 + RS2). The histogram indicates the number of MCC and LPFC units belonging to each of the 3 clusters.

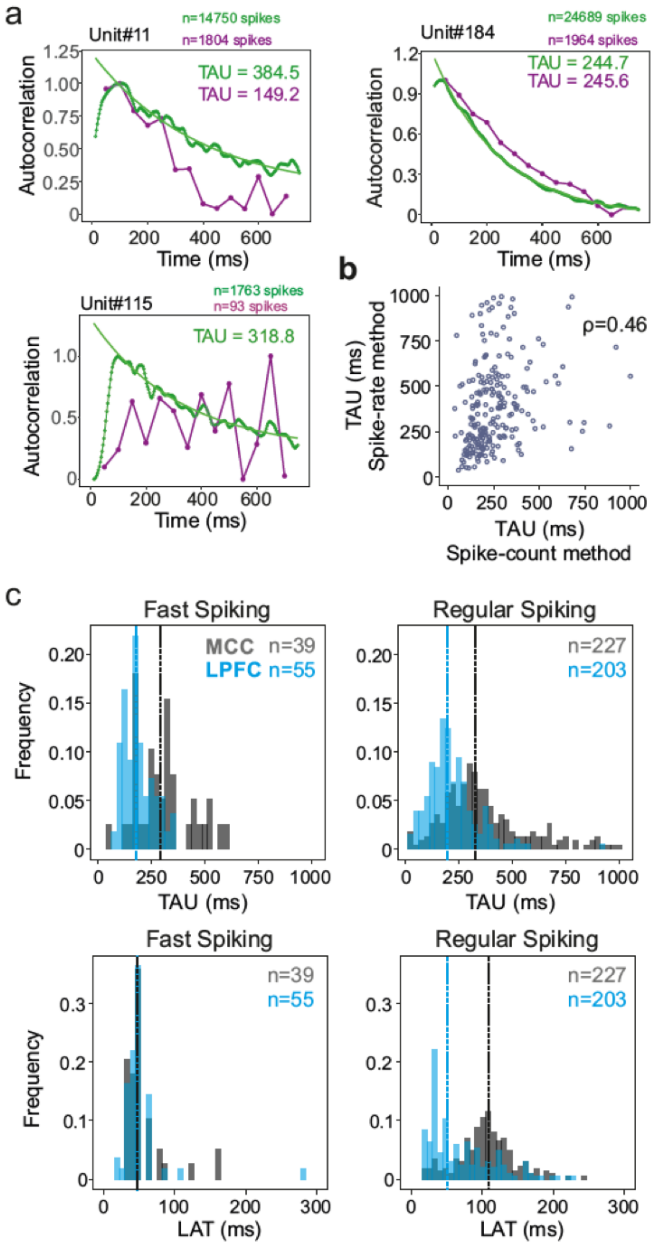

Figure 2. Spike autocorrelogram and temporal signatures in MCC and LPFC. (**a**) 3 single examples of spike count (purple) versus normalized spike autocorrelograms (green) contrasting the outcome of the 2 methods. The measured time constant (TAU) is indicated for both when possible. Numbers of spikes used for each method is also indicated. (**b**) TAU values extracted from each methods are significantly correlated (spearman rho(282) = 0.46,p<10-15). (**c**) Distributions of TAUs (upper histograms) and peak latencies (LAT - lower histogram) for FS (left) and RS (right) units. 'n' indicates the number of units. TAU values were longer in MCC than in LPFC for both FS and RS (linear model fit on BLOM transformed TAU for normality, TAU = Region * Unit type, Region: t=-4.68, p<10-6, Unit type: ns, interaction: ns). Peak latencies significantly differed between MCC and LPFC for RS but not for FS units (medians: MCC FS= 48.5 ms, RS= 102.0 ms , LPFC FS= 48.5 ms , RS= 51.8 ms ; linear model fit on BLOM transformed Latency for normality, Latency = Region * Unit type, interaction: t-value=-3.57, p< 10-3).

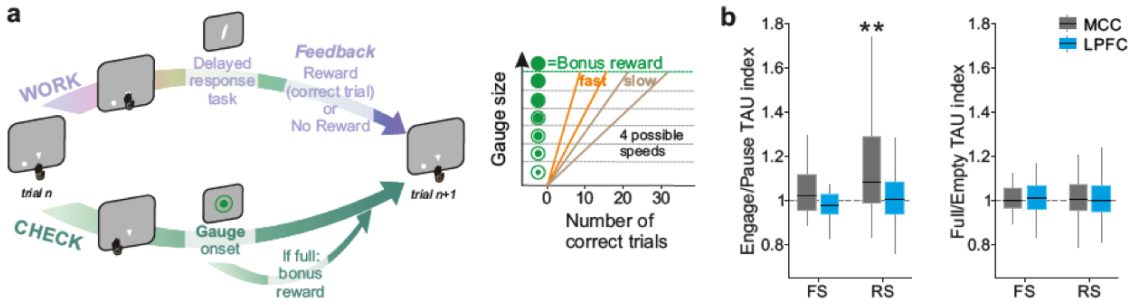

Figure 3. Behavioral engagement in task and spiking timescale changes. (**a**) Schematic representation of the task. At the start of each trial, animals can either initiate a delayed response task (WORK option) which can lead to 1 reward delivery, or use the CHECK option to check the current size of the gauge (or collect the bonus reward). Each reward in the task contributes to increase the gauge size and bring the bonus availability closer. The graph (right) schematized the speed of increase of the gauge size which varies between blocks (fast or slow blocks). (**b**) Boxplots of indices for each unit type and region calculated to estimate potential changes in TAU between Engage and Pause (left), and between empty and full gauge (right). TAUs increased in Engage vs. Pause only for MCC RS units.

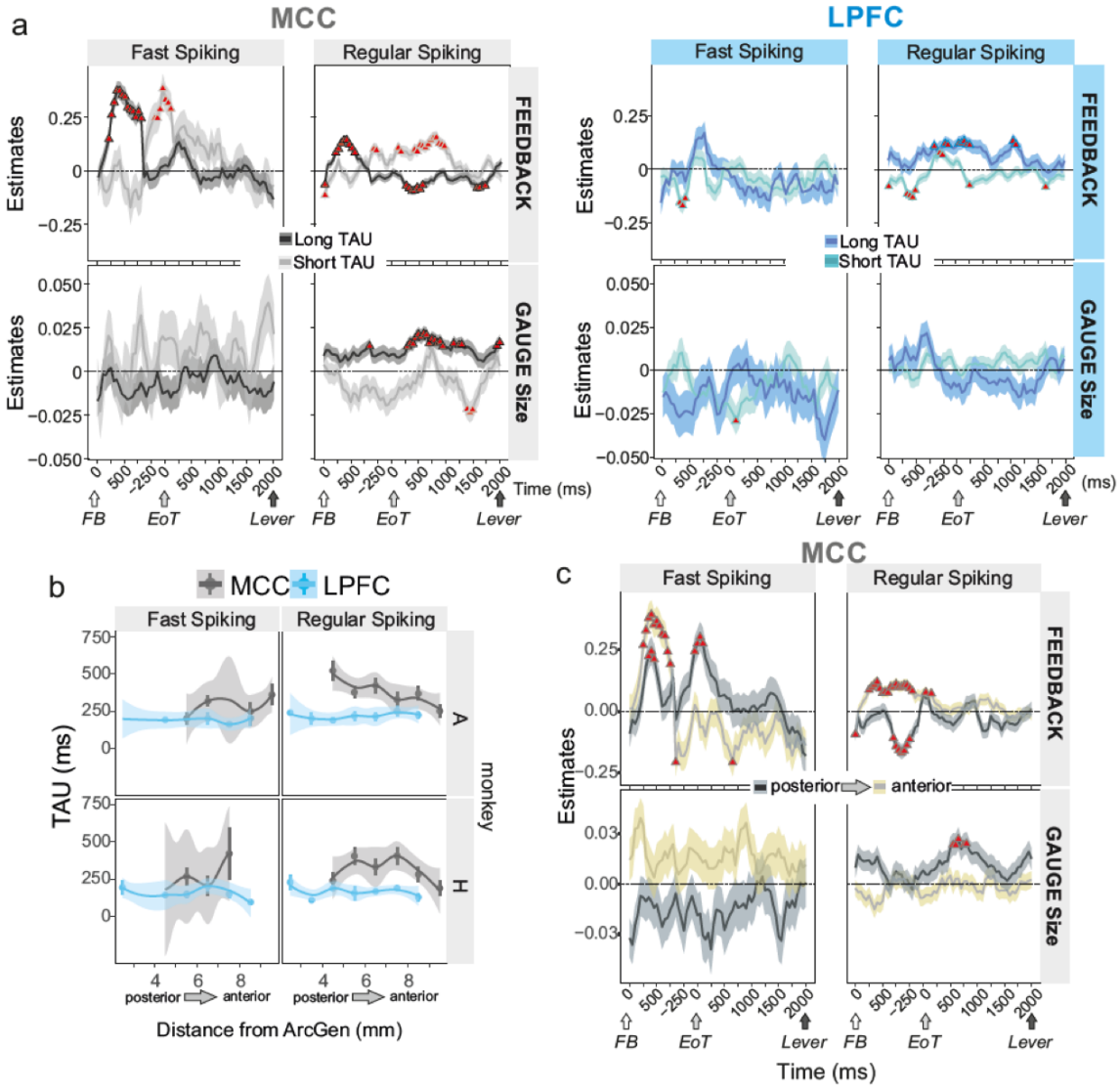

Figure 4. Encoding of feedback and gauge size for different unit types and spiking timescales and rostro-caudal distribution. (**a**) Estimates (β-coefficients) obtained from the MCC (grey) and LPFC (blue) unit populations obtained from time-resolved *glmm* for Feedback (reward vs no reward; top graphs) and Gauge size (bottom) (see 'Group analyses using *glmm*' in Methods). Estimates are obtained at successive time points covering the entire inter-trial period between feedback onset and the lever onset in the following trial. Significant effects are indicated by a red triangle ($p<0.05$ corrected), shadings indicate standard deviations. Positive values depict a population activity bias towards negative feedback (top) and positive slope of linear coding for gauge size (bottom). Data is presented for FS and RS units (left and right respectively for each panel) and have been performed on subpopulation with short or long TAU values (determined by a median split). Short and long TAU populations are represented by light and dark color intensity. Note in particular the dissociation for RS MCC units with short and long TAU respectively coding for feedback and gauge size. (**b**) Averaged TAU values along the postero-anterior axis in the MCC and LPFC, for both monkeys. (**c**). Estimates reflecting coding strength of Feedback and Gauge size for MCC unit populations separated by their rostro-caudal location.

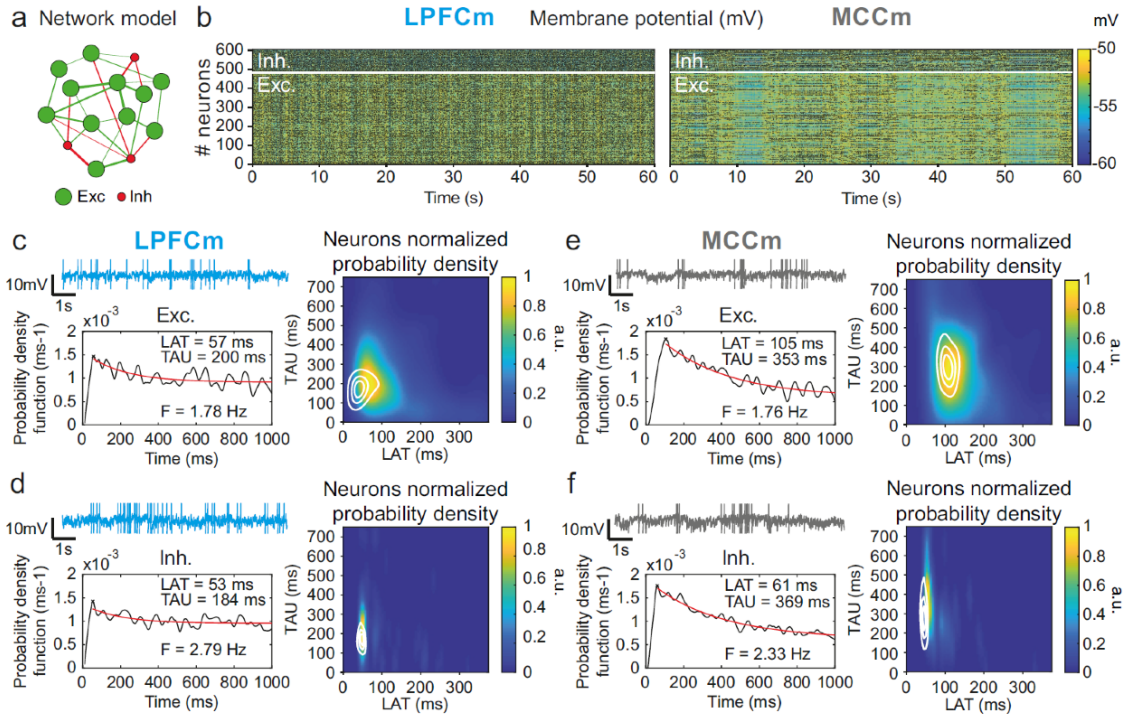

Figure 5. Temporal signature of LPFCm and MCCm recurrent network biophysical models. (**a**) Scheme of the frontal recurrent networks modelled, with 80% excitatory (green) and 20% inhibitory (red) neurons and sparsity of synaptic connections. (**b**) Membrane potential in the 484 excitatory (lower part) and 121 inhibitory (upper part) neurons of example network models with parameter set to approximate LPFC dynamics (g_{CAN}=0.025mS.cm^{-2}, g_{AHP}=0.022mS.cm^{-2}, $g_{GABA\text{-}B}$=0.0035mS.cm^{-2}; see text and legend of Fig. 6b for the choice of LPFC and MCC standard g_{AHP} and $g_{GABA\text{-}B}$ maximal conductances) and MCC dynamics (g_{CAN}=0.025mS.cm^{-2}, g_{AHP}=0.087mS.cm^{-2}, $g_{GABA\text{-}B}$=0.0143mS.cm^{-2}). (**c**) (upper left) Membrane potential of an example excitatory neuron in the LPFC model (LPFCm). Scaling bars 1s and 10mV (spikes truncated). (lower left) Autocorrelogram of this LPFCm example excitatory neuron (black) and its exponential fit (red, see *Online Methods*). (right) Bivariate probability density distribution of autocorrelogram parameters in LPFCm excitatory neurons. Contour lines at 50, 75 and 90% of the maximum of the bivariate probability density distribution in LPFC monkey RS units. (**d**) Same as **(c)** for LPFCm inhibitory neurons, with contour lines from the bivariate probability density distribution in LPFC monkey FS units. **(e,f)** Same as **(c,d)**, for the MCCm and MCC.

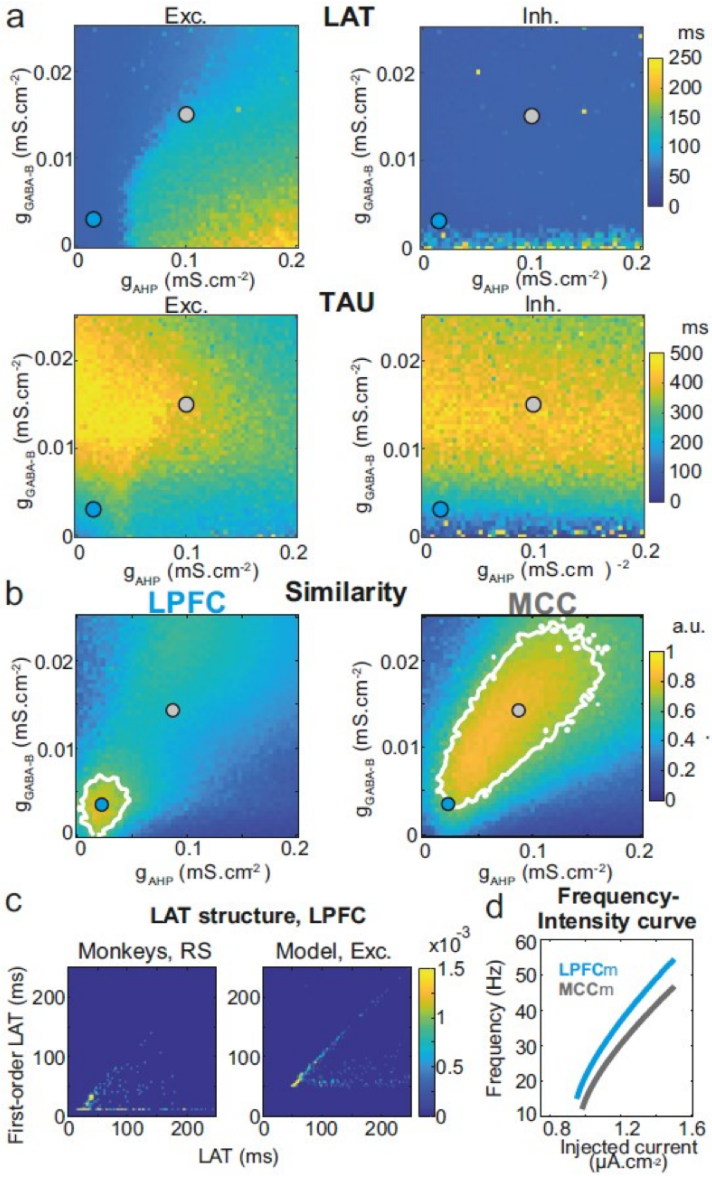

Figure 6. Similarity to monkey LPFC and MCC temporal signatures critically depends on AHP and $GABA_B$ conductance in the network model. (**a**) Mean population LAT (top) and TAU (bottom) in Exc (left) and Inh (right) neurons, as a function of AHP and GABA-B maximal conductances. Blue and grey disks indicate the (g_{AHP}, g_{GABA-B}) parameter values of the LPFCm and MCCm models, respectively. (**b**) Similarity of the temporal signature between the network model and monkey data in the LPFC (left) and MCC (right), as a function of AHP and GABA-B maximal conductances (see Online Methods). In (a) and (b), the value for each (g_{AHP}, g_{GABA-B}) is averaged over 5 simulations. Contour line at 80% of maximum similarity. LPFCm and MCCm (g_{AHP}, g_{GABA-B}) parameter values calculated as coordinates of the contour delimited area's weighted average. (**c**) Bivariate probability density distribution of the autocorrelogram LAT and first- order latency (the latency of the ISI distribution) in RS units in monkey LPFC (left) and excitatory neurons in the example LPFCm model (right). The model accounts for two distinct neuronal subsets in RS neurons, where LAT is determined by first-order latency solely (due to gAHP-mediated refractoriness; diagonal band), or in conjunction with other factors (gGABA-B slow dynamics-mediated burstiness and recurrent synaptic weight variability; horizontal band). (d) Single excitatory neuron frequency/intensity relationship in the LPFCm (blue) and MCCm (grey) models in response to a constant injected current.

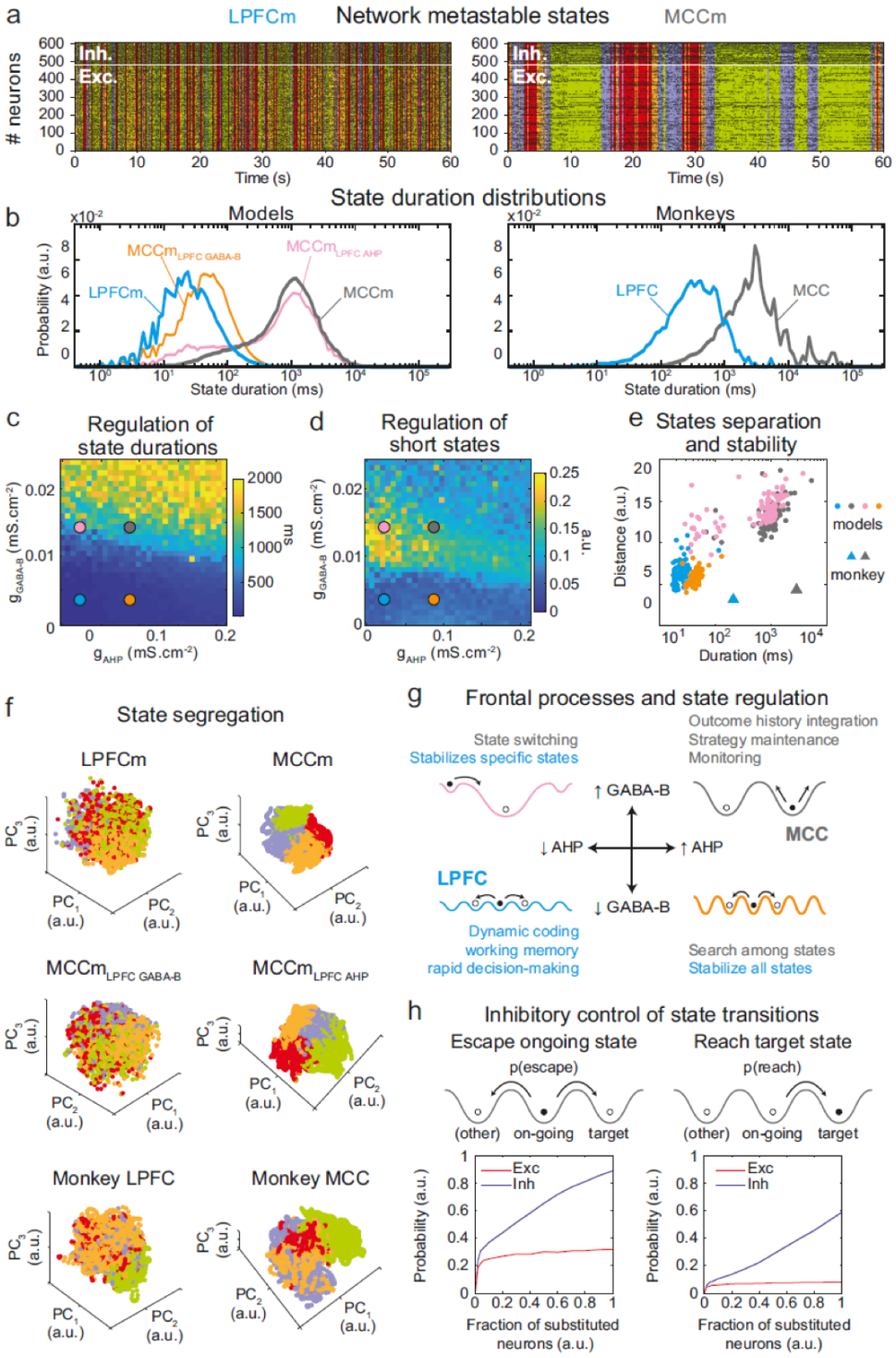

Figure 7. **Properties of metastable states in the LPFC and MCC** (**a**) LPFCm and MCCm models spiking raster plots (black dots), with Hidden Markov model states (HMM, colored bands) (**b**) State duration distributions: probability distributions of being in states of given durations in LPFCm (blue), MCCm (grey), MCCm with LPFCm g_{AHP} ($MCCm_{LPFC\ AHP}$ pink) and MCCm with LPFCm gGABAB ($MCCm_{LPFC\ GABA\text{-}B}$, orange) models (left) and monkey LPFC (blue) and MCC (grey) areas (right). Each model was simulated 100 times and analyzed via HMM, while monkey data was analyzed via HMM with 100 different initiation parameter states. Periods above 300s were excluded. (**c, d**) Regulation of state duration and short states: median state duration (c) and

Kolmogorov-Smirnov one-sample test statistic or maximal distance of state duration probability distributions to log-normality, as a measure of the over-representation of short states (d), as a function of g_{AHP} and $g_{GABA\text{-}B}$ maximal conductances. Colored disks indicate parameter values of LPFCm, MCCm, $MCCm_{LPFC\ AHP}$ and $MCCm_{LPFC\ GABA\text{-}B}$ models, respectively. Each point is the average of 5 simulations. (**e**) Separation between states: average distances between HMM states (averaged pairwise distance between neural centered standardized frequency centroids (temporal averages) of HMM states), as a function of median state durations. Distances calculated over 100 simulations in models and once for monkey LPFC and MCC data. (**f**) State segregation: projection of neural activity on the principal components of the PCA space of example model simulations and of monkey data. State colors as in (a). (**g**) Frontal processes and state regulation: schematic attractor landscapes in the LPFC and MCC. Horizontal and vertical arrows indicate possible regulations of AHP and $GABA_B$ conductance levels respectively by intrinsic/synaptic plastic processes or neuromodulation in the LPFC and MCC. Likely functional processes operating in these landscapes are indicated in blue for the LPFC and grey for the MCC. (**h**) Inhibitory control of state transitions: probability to escape an ongoing state (left) and to reach a target state (right), when the ongoing state is perturbed by substituting a given proportion of its excitatory (vs inhibitory) neurons' activity by that of the same neurons in the (perturbing) target state (see Online Methods). Average (full line), +/- s.e.m. (shaded areas, almost imperceptible).

Materials and methods

Subjects and materials

This project was conducted with two male rhesus monkeys (Macaca mulatta), monkey A and H. All procedures followed the European Community Council Directive (2010) (*Ministère de l'Agriculture et de la Forêt, Commission nationale de l'expérimentation animale*) and were approved by the local ethical committee (*Comité d'Ethique Lyonnais pour les Neurosciences Expérimentales*, CELYNE, C2EA #42). Electrophysiological data were recorded using an Alpha-Omega multichannel system (AlphaOmega Engineering, Israel).

Recording sites

Recording chambers (Gray Matter research, MT, USA) were centered on antero-posterior coordinates of +34.4 and +33.6 relative to ear bars (for monkey A and H, respectively)(Stoll et al., 2016). MCC recording sites covered an area extending over 10mm (anterior to posterior), and at depths superior to 4mm from cortical surface (corresponding to the anatomically defined aMCC or functionally defined dACC). Recording sites in LPFC were located between the principalis and arcuate sulcus (areas 6DR, 8B, 8A and 9/46) and at depths inferior to 2mm from cortical surface. Reconstructions of cortical surface, of MRI sections perpendicular to recording grids and of microelectrode tracks were performed using neuronavigation. Locations were confirmed with MRI reconstructions and stereotaxic measurements by keeping track of electrophysiological activity during lowering of electrodes.

Single unit activity and spike shapes

Electrophysiological activity was recorded using epoxy-coated tungsten electrodes (1–2MOhm at 1 kHz; FHC Inc., USA) independently lowered using Microdrive guidance (AlphaOmega Engineering). Neuronal activity was sampled at 22 kHz resolution. Single units were sorted offline using a specific toolbox (UltraMegaSort2000, Matlab toolbox, Kleinfeld Lab(Hill et al., 2011), University of California, San Diego, USA). Metrics served to verify the completeness and purity of single unit activity. Each single unit activity was selected, recorded and included in analyses on the basis of the quality of isolation only. We obtained 298 MCC units and 272 LPFC units while monkeys performed a checking task(Stoll et al., 2016). A subset of these data has been used in a previous publication(Stoll et al., 2016).

Spike shape clustering. Spike shapes can be clustered in different groups that might correspond to different putative cell populations. For each single unit, we computed the average spike shape on which we measured:

(1) Pre-valley (V1): the minimum value of the waveform prior to the peak

(2) Post-valley (V2): the minimum value of the waveform following the peak

(3) Spike width: the time between the occurrence of the peak and V2

(4) The ratio of V1 to V2 (V1/V2)

(5) The ratio of V2 to the spike peak (V2/PiK)

We clustered average units according to their spike width and V2/PiK. We first computed the spike width *vs.* V2/PiK Euclidean distance matrix (*dist* function in R). Then we performed hierarchical clustering using Ward's method (*hclust* function in R). The number of retained clusters was determined with the combination of data viewing, dendrogram examination and objective measures of clustering quality (Elbow method, Average silhouette method and Gap statistic method). The partitioning led to 3 clusters, one with narrow spike shapes, one with wide spikes and one with very wide spikes. Narrow and wide spikes were considered FS and RS, respectively. Although clustering

revealed 3 clusters, no differences were found between the 2 wide ones, both considered RS neurons (see supplements).

Spiking timescales.

The primary analysis of timescales was based on Murray et al(Murray et al., 2014). Spike counts were measured in 14 successive bins of 50ms from the pre-cue period (700ms) of each trial, when the monkey is in a controlled, attentive state awaiting stimulus onset. We first calculated the cross-trial bin cross-correlations. Each vector of spike counts from the 50ms bin t was correlated with vectors of spike counts at subsequent bins (t+1, t+2, etc) generating an autocorrelation matrix. The positive side of the autocorrelation was used to compute timescales. The autocorrelogram data was then fitted using non-linear least square (*nls* function in R) to a function of the form:

$$R \sim A * e^{\frac{-t}{TAU}} + B$$

where R is the correlation coefficient and t the bin time. TAU, representing the decay of the exponential function and thus the intrinsic timescale, and A, a scaling constant, were obtained from the fit. We computed TAU both at the population level, by using a global fit on all recorded units from a given area (as in Murray et al(Murray et al., 2014)), and at the single unit level.

However, the above method cannot resolve the fine dynamics of neuronal activity at short time lags because it is based on counts pooled across trials and from coarse-grained time bins (50ms). Moreover, the large variability of unit discharge resulted in a high variability of autocorrelograms, which could not be fitted in many cases (47.5% failures), as in other studies (52.1% and 48.4% failures in Wasmuht et al. 2018 and Cavanagh et al. 2018(Cavanagh et al., 2018; Wasmuht et al., 2018), respectively). Finally, tracking the causal determinants of LPFC and MCC temporal signatures in terms of local cellular and/or network dynamics requires a high temporal precision, because they rely on intrinsic and synaptic time constants, which often lie below the coarse time bin of the spike count method. To prevent these shortcomings, we directly computed the autocorrelogram of individual neurons from spike times, allowing for high temporal precision in parameter estimation. For this we leveraged all the data recorded for each neuron to reduce the large noise present at the level of individual neurons.

Autocorrelogram analysis

To capture the dynamics of neuronal activity, we computed autocorrelograms from individual unit spike timeseries and extracted their latencies (LAT) and time constants (TAU). The same method was applied to units from *in vivo* recordings and neurons from network models. To do so, we computed the lagged differences between spike times up to the 100th order, i.e. the time differences between any spike and its n successors (up to $n = 100$) at the unit level. The lagged differences were then sorted in 3.33ms bins from 0 to 1000ms. The resulting counts, once normalized, allowed to build the probability density function of the autocorrelogram, AC, which was smoothed by local non-linear regression (*loess* method, with span 0.1; to filter high frequency noise and correctly detect the peaks, see below) after removing its first 10ms, to eliminate source data contaminations, such as inter-spike intervals (ISIs) shorter than the absolute refractory period. We defined the peak of the autocorrelogram as its maximum, except when the maximum was the very first bin, in which case the peak was defined as the first local maximum after the first bin. The latency of the peak, LAT, was considered, for further analysis, as a structural parameter of the autocorrelogram characterizing the

temporal signature of the neuron/unit spiking set. For each autocorrelogram, a global mono-exponential fit (GLOBAL fit) was then performed on the part of the autocorrelogram situated after the peak using the Levenberg-Marquardt algorithm (*nlsLM function in R*) for monkey data or von-Neumann–Karmarkar interior-point algorithm (*fmincon in Matlab*) for network models (we checked that either algorithm on the same spiking sets gave similar results), as following:

$$AC \sim Ae^{-t/TAU} + B$$

TAU, the time constant of the autocorrelogram fit characterized the temporal signature of the neuron. A, the amplitude of the exponential, and B, the offset, are positive constants. Note that this mono-exponential fitting equation is strictly equivalent to that of Murray et al.(Murray et al., 2014), B here corresponding to AB in the Murray method. Choosing one or the other did not affect the resulting fit and we kept the present form as it is easier to interpret. Fits on each autocorrelogram were performed 50 times, with random initial guesses in the range $\left[0, 2\left(max(AC) - min(AC)\right)\right]$ for A, $[0, 2min(AC)]$ for B, and $[0, 1000]$ms for TAU, from which the best fit was kept.

In a minority of cases (less than 3% of neurons), the autocorrelogram following the peak (as defined above and denoted below the 1st peak) could present a shape that diverged from a simple exponential decay, because of a fast and large dip, followed by a second local maximum, which preceded the slower, final exponential decay. In this case, we developed a pipeline aiming at consistently choosing the peak from which the fit started. To do so, we defined the autocorrelogram as having a dip if the first local minimum in the 100ms after the 1st peak was below 75% of the global range of the autocorrelogram, $max(AC) - min(AC)$. In such cases, the second peak was defined as the maximum of the autocorrelogram after the dip and two additional mono-exponential fits of the autocorrelogram were performed, one from the first peak to the dip (FAST fit) and a second one from the second peak to the end of the autocorrelogram (SLOW fit). To be valid, any individual fit had to display positive A, B and TAU values. When neurons had a valid GLOBAL fit, two possibilities were considered. First, the valid GLOBAL fit was kept when at least one of the FAST and SLOW fits were not valid. Second, the valid GLOBAL fit was also kept when it was the best (i.e. its root-mean-square error was inferior to that of the sum of the valid FAST and SLOW fits) and excluded otherwise. Neurons that did not have a valid GLOBAL fit were also excluded from further analysis. Thus, while FAST and SLOW fits were *de facto* systematically excluded from further analysis, they were only used to ensure the quality of GLOBAL exponential fits. Note again that excluding less than 3% of neurons, this complex procedure was very conservative and designed for the sake of fitting performance.

Hidden Markov Model (HMM) analysis

We used HMM to map the spiking set of neural network models and unit populations in monkeys onto discrete states of collective activity, based on previously established methods(Abeles et al., 1995; Seidemann et al., 1996). HMM methods allow to determine the probability $p(S_k(t))$ of the network to be in state $S_k, k \in \{1 \ldots n_S\}$ at time t. Typically, we found that, as previously shown in frontal areas, population activity organized into periods that lasted in the range $\sim 10ms - 10s$, i.e. transition probabilities were small and states were quasi-stationary. When all probabilities of being in a state $p(S_k) < 0.8$, the network was considered to be in the null state S_0, signifying that the network was not in any of the states. Periods in the S_0 state were typically short (mean: LPFCm=16ms, MCCm=36ms, not shown). Thus, when immediately preceded and followed by two periods in the same state S_k, periods in S_0 were attributed the state S_k. For each network spiking set

assessed, we pooled the durations of all periods in all the states of the HMM model, to build the overall probability distribution of period durations $p(d)$. We then used this probability distribution to compute

$$p_t(d) = \frac{p(d)d}{\int_{u=0}^{+\infty} p(u)u\,du}$$

i.e. the proportion of time spent in state periods of duration d, that is, the probability, at any given instant in time, of being in state periods of duration d. We could not find any suitable method of stably determining the number of states n_S. However, as a low number of states is more parsimonious in terms of data interpretation(Pohle et al., 2017) in general and because the task structure contains a low number of possible states in terms of actions (four), reward on the last trial (incorrect trial, first correct trial, correct trial after previous correct trials) and behavioral states (exploration, exploitation), we arbitrarily fixed $n_S = 4$. Each HMM model analysis was conducted on a spiking set lasting 600 s, both in neural network models and unit populations in monkeys. For each monkey area, the activity of all neurons was pooled, regardless of their recording session. This was mandatory because the number of neurons simultaneously recorded in each session was typically inferior to 5, so that HMM models were inefficient in detecting states. Pooling all neurons allowed the detection of global states that corresponded to the combination of collective dynamics recorded during distinct sessions, i.e. that were not time-locked together (phase information lost across sessions) and causally independent. Although chimeric, these HMM states were nevertheless able to indirectly capture the underlying temporal structure of collective spiking discharges in frontal areas in a similar way and thus allowed comparing LPFC and MCC collective temporal structure. In control HMM models, both the timing and neuron assignment of all spikes were randomly shuffled. The initial estimation of the average state duration across all periods in a given state was taken at a high value (300ms), which was suggested to give better log-likelihood scores and converge to similar states across repetitions of the HMM (Seidemann et al., 1996). The time bin was $\Delta t = 0.5ms$.

Principal component analysis.

The principal component analysis (PCA) of LPFC and MCC of monkeys' units and neural network models' neurons spiking activity was computed from firing frequencies, in order to better visualize and characterize collective dynamics. PCA was achieved on the set of the spiking frequency vectors of all units/neurons in each case. Spiking frequency was estimated through convolution of spiking activity with a normalized Gaussian kernel with standard deviation $\sigma = 100ms$, as average frequencies were typically $< 10Hz$ in both areas. For each neuron, frequencies were then centered and standardized for optimal PCA. Cells with average frequencies less than 0.5 Hz were removed for the experimental data and for the model data, to avoid abnormal standardized frequencies when the neuron's average frequency was too low (at most 6 cells per area).

Perturbation protocol for state transitions

We assessed the contribution of excitatory and inhibitory neural populations to the stability of HMM states. To do so, we estimated the probability to stay in a given ongoing (or perturbed, see below) HMM state or to switch toward a distinct target (or perturbing) state in response to specified perturbations. The perturbation was achieved by substituting the value of neural variables

(membrane potential, spiking state, calcium concentration, downstream channel opening probabilities) of a random subset of excitatory (respectively inhibitory) neurons of the ongoing state by those of the same neurons taken from the (distinct) target state. Specifically, starting from an initial (unperturbed) 600 s simulation, perturbations were achieved by substituting state variables 50ms after the onset of a randomly chosen period of a specified perturbed state by those taken 50ms after the onset of a randomly chosen period of a distinct perturbing state and the resulting network states used as initial conditions for further "perturbation simulations". For each perturbation simulation, the network was simulated from the perturbation time to the end of the period when the network was not perturbed and the HMM state was determined as the posterior state probability based on HMM transition and emission matrices obtained from the entire initial unperturbed simulation. The probability to escape the ongoing state (Fig. 8.h, left) and to reach the target state (Fig. 8.h, right) were then computed as the proportion of time spent, during the ongoing period, in a HMM state different from the ongoing perturbed state (escape ongoing state probability), and in the target perturbing state (reach target state probability), respectively. The effects of perturbations were tested by replacing either excitatory or inhibitory populations, where proportions of replaced neurons systematically varied in the range 0-1. For each neuron type and proportion tested, the perturbation protocol was applied and results averaged for 50 random combinations of periods (with period durations > 100ms), for each of the 12 possible pairs of the 4 HMM states (excluding pairs of repeated states), over 20 different randomly initialized MCCs. Probabilities were offset and normalized to remove the basal probability of escaping the ongoing (0.09) and reaching the target (0.01) states when no perturbation was applied (such transitions were due to random selection of simultaneous spikes when initiating the HMM analysis).

Behaviour and context-dependent modulations

Behavioural Task. Monkeys were trained to perform a dual task involving rule-based and internally driven decisions(Stoll et al., 2016). Monkeys performed the task using a touch screen. In each trial they could freely choose whether to perform a rewarded categorization task or to check their progress toward a large bonus juice reward (**Fig. 3a**). Upon checking (selection of a disk-shaped lever) progress was indicated by the onset of a visual 'gauge' (an evolving disk inside a fixed circle). Choosing the categorization task (selection of an inverted triangle lever) started a delayed response task in which an oriented white bar (cue) was briefly presented, followed by a delay at the end of which 2 bars oriented 45° leftward and rightward where presented. Selecting the bar matching the cue orientation led to a juice reward. An incorrect response led to no reward delivery. The gauge increased based on correct performance in the categorization task following 7 steps to reach the maximum size. If the animal checked while the gauge was full, the bonus reward was delivered, and the gauge reset to step 1. The full gauge was reached after either 14, 21, 28 or 35 correct trials (= number of trials to complete the 7 steps, pseudo-randomly chosen in each block). Thus, the gauge could increase at one of 4 different speeds.

Pause vs. engage periods. As each trial was self-initiated by the animal, monkeys could decide to take a break in their work. We defined pauses as periods of at least 60 seconds without trial initialization. Monkeys made on average 3.4±2.57 pauses per session (mean±sd, monkey A: 3.44±2.55, monkey H: 3.34±2.63; see **Fig. 3b**). We extracted spike times during the defined pause and engage time segments for each unit, and then extracted TAU using the method described above. We

only kept units with successful TAU extraction for both periods ($n_{MCC\text{-}FS}$=19, $n_{MCC\text{-}RS}$=86, $n_{LPFC\text{-}FS}$=29, $n_{LPFC\text{-}RS}$ =95).

Fast vs. slow-paced blocks. We defined 14 and 21 correct trials blocks to be fast blocks and 28 and 35 correct trials blocks as slow blocks. We considered neuronal activity from the first-time monkeys checked in a block until the end of the block. We excluded pause periods from this analysis. We extracted spike timing from the segments and computed timescales as previously, keeping only units with successful timescale extraction for both periods ($n_{MCC\text{-}FS}$=33, $n_{MCC\text{-}RS}$=165, $n_{LPFC\text{-}FS}$=46, $n_{LPFC\text{-}RS}$ =165).

Emptier vs. fuller gauge size seen. In each block, monkeys used the gauge size observed upon checking to regulate their future decisions to check. The checking frequency increased with gauge size with a marked increase at steps > 4. We thus compared neuronal activity in periods in which monkeys saw gauges of size < 4, with periods in which they saw gauges > 4, excluding the very beginning of blocks when monkeys have not seen the gauge yet, and pauses periods. We perform this analysis on 430 units ($n_{MCC\text{-}FS}$=30, $n_{MCC\text{-}RS}$=178, $n_{LPFC\text{-}FS}$=47, $n_{LPFC\text{-}RS}$ =175).

To test whether current block speed had an influence on TAU at the unit level, we computed a modulation index for each unit: $\log(TAU_{slow})/\log(TAU_{fast})$. Similarly, to test whether gauge filling state had an influence on TAU at the unit level, we computed a modulation index for each unit: $\log(TAU_{empty})/\log(TAU_{full})$ where TAU_{full} corresponds to TAU calculated on the spike data recorded during the time in blocks where the gauge was superior of equal to the 4th level.

Statistical analyses

All analyses were performed using R (version 3.6.1) with the RStudio environment(R_core_team, 2014).

BLOM transformation. As some timescale measures are non-normally distributed, analyses required a robust non-parametric test. We opted for the BLOM transformation which is a subcase of Rank-Based Inverse Normal Transformations(Beasley et al., 2009). Basically, the data is ranked and then back transformed to approximate the expected normal scores of the normal distribution according to the formula:

$$Y_i = \Phi^{-1}\,\frac{r_i - c}{N - 2c + 1}$$

where r_i is the ordinary rank and Y_i the BLOM transformed value of the *i*th case among the N observations. Φ−1 is the standard normal quantile (or probit) function and c a constant set to 3/8 according to Blom(Blom, 1958). Regular parametric analyses can then be performed on the transformed data. Since z-scores of the transformed data are normally distributed and differences are expressed in standard errors, main effects and interactions can easily and robustly be interpreted. As sanity checks we also ran more classical non-parametric tests (Wilcoxon test) on non-normally distributed data leading to the same conclusions.

Task-related analyses

Single unit activity. Each unit's spikes were counted in sliding bins of 200ms overlapping by 50ms from feedback onset to 800ms post-feedback and during the intertrial interval from 400ms before the end of trial signal onset to 2000ms after its onset.

Group analyses using a glmm. We used a *glmm* using a Poisson family. p-values were corrected for multi-comparison with the false discovery rate algorithm with the number of comparisons being the number of timebins (p.adjust function in R).

The mixed models used were of the form:

$$y = \beta_0 + \beta_1.\text{CheckWork} + \beta_2.\text{Gauge} + \beta_3.\text{Previousfeedback} + \gamma .Z + \varepsilon$$

where $\gamma.Z$ is the random term, and CheckWork, Gauge and PreviousFeedback are the fixed effects describing the Check versus Work decision (0/1), the gauge size (1–7) and the feedback in the previous trial (0/1) with their respective parameters (β). In the *glmm*, the Single unit identity was used as a random factor.

A persistent problem with Poisson models in biology is that they often exhibit overdispersion. Not accounting for overdispersion can lead to biased parameter estimates. To deal with overdispersion we used observation-level random effects (OLRE), which model the extra variation in the response variable using a random effect with a unique level for every data point.

Median splits. To test the hypothesis that units with different timescales may encode feedback differently we divided the units into two groups based on the median of the timescale metric. We computed the median of the metric (e.g. peak latency or TAU) in all the units of a given cell type. Then we put units with a metric value below the median into the 'short' group and units with a metric value above the median into the 'long' group.

Timescale and coding variations along the antero-posterior axis

We considered the genu of the arcuate sulcus as an anatomical landmark from which we computed distances of recording location along the anterior-posterior axis from MRI reconstructions.

We questioned TAU antero-posterior variability keeping recording locations covering the same range in both monkeys. We ordered locations from the most posterior site for each area. We excluded FS units from statistical analysis due to their disparateness (RS units, monkey A: n_{MCC}=112, n_{LPFC}=110; monkey H: n_{MCC}=54, n_{LPFC}=64). This analysis was conducted separately between monkeys to account for inter-subject anatomical variability.

To test variation in population coding along the antero-posterior axis we divided single-units into a posterior and anterior group based on the range of locations of each area (MCCpost from 4.5 to 7mm, $n_{MCCRSpost}$=84, $n_{MCCFSpost}$=14 ; MCCant from 7 to 9.5mm, $n_{MCCRSant}$=82, $n_{MCCFSpost}$=16 ; LPFCpost from 2.5 to 6mm, $n_{LPFCRSpost}$=77, $n_{LPFCFSpost}$=19 ; LPFCant from 6 to 8.5mm, $n_{LPFCRSant}$=97, $n_{LPFCFSant}$=19). Population coding analysis is described in **Task-related analyses**.

Cellular model of pyramidal neurons in frontal areas

We built a generic biophysical Hodgkin-Huxley model of the detailed dynamics of membrane potential and of ionic and synaptic currents of individual pyramidal neurons in frontal areas. The model was generic, being endowed with a large set of ionic voltage- and calcium-dependent conductances, to encompass the wide possible repertoire of spiking discharge patterning encountered *in vivo*. In the model, the membrane potential followed

$$C\frac{dV}{dt} = -(I_{Ionic} + I_{Syn})$$

where C is the specific membrane capacity and the membrane ionic current writes

$$I_{Ionic} = I_L + I_{Na} + I_K + I_{CaL} + I_{CAN} + I_{AHP} + I_{CaT} + I_H$$

in which the leak current is

$$I_L = \bar{g}_L\,(V - V_L)$$

and action potential (AP) currents (I_{Na}, I_K) are taken from a previous model we devised to reproduce spike currents of frontal pyramidal regular-spiking neurons(Naudé et al., 2012). The high-threshold calcium current was

$$I_{CaL} = \bar{g}_{CaL}\,p_{CaL}^2(V - V_{CaL})$$

where the activation followed first-order kinetics

$$\frac{dp_{CaL}}{dt} = (p_{CaL}^{\infty}(V) - p_{CaL})/\tau_{CaL}(V)$$

with a voltage-dependent time constant

$$\tau_{CaL}(V) = 10^{\alpha_{CaL}+\beta_{CaL}V}$$

where α_{CaL} and β_{CaL} were fitted from *in vitro* data(Helton et al., 2005). The infinite activation followed

$$p_{CaL}^{\infty}(V) = 1/\left(1 + exp\left(-\left(V - V_{1/2,CaL}\right)/k_{CaL}\right)\right)$$

where $V_{1/2,CaL}$ and k_{CaL} respectively denote the half-activation potential and e-fold slope of the Boltzmann activation voltage-dependence, estimated from *in vitro* data(Helton et al., 2005). The cationic non-selective (I_{CAN}) current and the medium after-hyperpolarization (I_{AHP}) current, responsible for frequency adaptation in pyramidal neurons were taken as in Rodriguez et al., 2018, with

$$I_{CAN} = \bar{g}_{CAN}\,p_{CAN}(V - V_{CAN})$$

and

$$I_{AHP} = \bar{g}_{AHP}\,p_{AHP}^2(V - V_{AHP})$$

The activation of both currents, p_x ($x \in \{CAN,\ AHP\}$) followed

$$\frac{dp_x}{dt} = (p_x^{\infty}(Ca) - p_x)/\tau_x(Ca)$$

with

$$\tau_x(Ca) = 1/(\alpha_x Ca + \beta_x)$$

and

$$p_x^{\infty}(Ca) = \alpha_x/(\alpha_x Ca + \beta_x)$$

where α_x and β_x respectively denote activation and deactivation kinetic constants consistent with experimental data in layer 5 PFC pyramidal neurons(Faber and Sah, 2007; Haj-Dahmane and Andrade, 1997; Villalobos et al., 2004). The low-threshold calcium (I_{CaT}) and hyperpolarization-activated (I_H) currents were from reference(Ritter-Makinson et al., 2019). To account for autocorrelogram parameters, we employed different versions of the model that contained distinct subsets of ionic currents, which have been implicated in adaptation and bursting (I_{CaL}, I_{AHP}), rebound (I_{CaT}, I_H), and regenerative and bistable discharge (I_{CaL}, I_{CAN}, I_{AHP}) in cortical pyramidal neurons (see *Results* and *Supplementary Material*). Calcium concentration dynamics resulted from the inward influx due to $I_{CaL}$and I_{CaT} and first-order buffering or extrusion(Rodriguez et al., 2018) through:

$$\frac{dCa}{dt} = -(1/2F)(S/V)(I_{CaL} + I_{CaT}) + (Ca_0 - Ca)/\tau_{Ca}$$

where F is the Faraday constant, Ca_0 is the basal intracellular calcium concentration, τ_{Ca} is the buffering time constant, and

$$S/V = r_1^{-1}(1 - r_1/r_0 + r_1^2/(3r_0^2))^{-1}$$

is the surface area to volume ratio of an idealized intracellular shell compartment of thickness r_1 situated beneath the surface of a spherical neuron soma of radius r_0.

The synaptic current (I_{Syn}) mimicked *in vivo* conditions encountered by neurons in the asynchronous irregular regime, summing random synaptic excitatory inputs, through AMPA and NMDA receptors, and inhibitory inputs, through $GABA_A$ and $GABA_B$ receptors. Thus,

$$I_{Syn} = I_{AMPA} + I_{NMDA} + I_{GABA_A} + I_{GABA_B}$$

For AMPA, $GABA_A$ and $GABA_B$,

$$I_x = \bar{g}_x \, p_x (V - V_x)$$

where p_x is the opening probability of channel-receptors and V_x the reversal potential of the current. The NMDA current followed

$$I_{NMDA} = \bar{g}_{NMDA} \, p_{NMDA} \, x_{NMDA}(V)(V - V_{NMDA})$$

incorporating the magnesium block voltage-dependence modeled(Jahr and Stevens, 1990) as

$$x_{NMDA}(V) = (1 + [Mg^{2+}] e^{-0.062\,V}/3.57)^{-1}$$

To simulate fluctuations encountered *in vivo*, all opening probabilities followed Ornstein-Uhlenbeck processes(Destexhe and Paré, 1999)

$$\frac{dp_x}{dt} = \frac{(m_x - p_x)}{\tau_x^{decay}} + \sigma_x \varepsilon(t)$$

where $\varepsilon(t)$ is a Gaussian stochastic process with zero mean and unit standard deviation and m_x and σ_x are the mean and standard deviation of the opening probabilities. For AMPA and $GABA_A$, the mean was taken as the steady-state value of first-order synaptic dynamics described in the network model (see below):

$$m_x = \left(1 + {\tau_x^{decay}}^{-1} {\Delta p_x}^{-1} {f_{Syn}}^{-1} {n_{Syn}}^{-1}\right)^{-1}$$

with n_{Syn} pre-synaptic neurons firing at a frequency f_{Syn} (with $Syn \in \{Exc,\ Inh\}$, depending on the type of current considered), an instantaneous increase Δp_x of opening probability upon each pre-synaptic spike and first-order decay dynamics with time constant τ_x^{decay} between spikes. For NMDA and $GABA_B$, the mean was taken as the steady-state value of second-order synaptic dynamics described in the network model (see below):

$$m_x = \left(1 + {\tau_x^{decay}}^{-1} \alpha^{-1} \left(1 + {\tau_x^{rise}}^{-1} {\Delta p_x}^{-1} {f_{Syn}}^{-1} {n_{Syn}}^{-1}\right)\right)^{-1}$$

For all currents, standard deviations were taken as $\sigma_x = 0.5 m_x$. Feed-forward excitatory and inhibitory currents were balanced (Xue et al., 2014), according to the driving forces and the excitation/inhibition ratio, through

$$\begin{cases} \bar{g}_{GABA_A} = g_{GABA_A} \dfrac{-(V_{mean} - V_{Exc})}{(V_{mean} - V_{GABA_A})} \dfrac{n_{Exc}}{n_{Inh}} \\ \bar{g}_{GABA_B} = g_{GABA_B} \dfrac{-(V_{mean} - V_{Exc})}{(V_{mean} - V_{GABA_B})} \dfrac{n_{Exc}}{n_{Inh}} \end{cases}$$

Model of local recurrent neural networks in frontal areas

We built a biophysical model of a generic local frontal recurrent neural network, endowed with detailed biological properties of its neurons and connections. The network model contained N neurons that were either excitatory (E) or inhibitory (I) (neurons projecting only glutamate or GABA, respectively(Dale, 1935)), with probabilities p_E and $p_I = 1 - p_E$ respectively, and $p_E/p_I = 4$ (Beaulieu et al., 1992). Connectivity was sparse (i.e. only a fraction of all possible connections existstho(Thomson, 2002)) with no autapses (self-connections) and EE connections (from E to E neurons) drawn to insure the over-representation of bidirectional connections in cortical networks

(four times more than randomly drawn according to a Bernoulli scheme(Song et al., 2005)). The synaptic weights $w_{(i,j)}$ of existent connections were drawn identically and independently from a log-normal distribution of parameters μ_w and σ_w (Song et al., 2005). To cope with simulation times required for the massive explorations ran in the parameter space, neurons were modeled as leaky integrate-and-fire (LIF) neurons, i.e. the AP mechanism was simplified, compared to the cellular model (see above). Moreover, leveraging simulations at the cellular level, we only considered the I_{CAN} and I_{AHP} amongst the ionic currents of the cellular model (see above). Thus, the membrane potential followed

$$\begin{cases} \frac{dV_{(j)}}{dt} = -(I_{Ionic(j)} + I_{Syn.Rec(j)} + I_{Syn.FF(j)}) \\ V_{(j)} > \theta \rightarrow V_{(j)} = V_{rest} \end{cases}$$

where repolarization occurred after a refractory period Δt_{AP}. The ionic current followed

$$I_{Ionic(j)} = I_{L(j)} + I_{CAN(j)} + I_{AHP(j)}$$

with parameters and gating dynamics of ionic currents identical to the cellular model. The intra-somatic calcium concentration Ca evolved according to discrete spike-induced increments and first-order exponential decay:

$$\frac{dCa_{(j)}}{dt} = \frac{Ca_0 - Ca_{(j)}}{\tau_{Ca}} + \Delta Ca\ \delta\left(t - t_{(j)}^k\right)$$

where $t_{(j)}^k$ is the time of the k_{th} spike in the spike train of neuron j, δ the Dirac delta function, τ_{Ca} the time constant of calcium extrusion, Ca_0 the basal calcium and ΔCa a spike-induced increment of calcium concentration. The recurrent synaptic current on post-synaptic neuron j, from – either excitatory or inhibitory – pre-synaptic neurons (indexed by i), was

$$I_{Syn.Rec(j)} = \sum_i \left(I_{AMPA(i,j)} + I_{NMDA(i,j)} + I_{GABA_A(i,j)} + I_{GABA_B(i,j)}\right)$$

The delay for synaptic conduction and transmission, Δt_{syn}, was considered uniform across the network(Brunel and Wang, 2001). Synaptic recurrent currents followed

$$I_{x(i,j)} = \bar{g}_x\ w_{(i,j)}\ p_{x(i)}\left(V_{(j)} - V_x\right)$$

where $w_{(i,j)}$ is the synaptic weight, $p_{x(i)}$ the opening probability of channel-receptors and V_x the reversal potential of the current. The NMDA current followed

$$I_{NMDA(i,j)} = \bar{g}_{NMDA}\ w_{(i,j)}\ p_{NMDA(i)}\ x_{NMDA}\left(V_{(j)}\right)\left(V_{(j)} - V_{NMDA}\right)$$

with $x_{NMDA}(V)$ the magnesium block voltage-dependence (see cellular model). AMPA and $GABA_A$ rise times were approximated as instantaneous (Brunel and Wang, 2001) and bounded, with first-order decay

$$\frac{dp_{x(i)}}{dt} = -\frac{p_{x(i)}}{\tau_x^{decay}} + \Delta p_x\left(1 - p_{x(i)}\right)\delta\left(t - t_{(i)}^k\right)$$

To take into account the longer NMDA (Wang et al., 2008) and GABA-B (Destexhe et al., 1998) rise times, opening probabilities followed second-order dynamics (Brunel and Wang, 2001)

$$\begin{cases} \frac{dq_{x(i)}}{dt} = -\frac{q_{x(i)}}{\tau_x^{rise}} + \Delta q_x\left(1 - q_{x(i)}\right)\delta\left(t - t_{(i)}^k\right) \\ \frac{dp_{x(i)}}{dt} = -\frac{p_{x(i)}}{\tau_x^{decay}} + \alpha_x\ q_{x(i)}\left(1 - p_{x(i)}\right) \end{cases}$$

Recurrent excitatory and inhibitory currents were balanced in each post-synaptic neuron (Xue et al., 2014), according to driving forces and excitation/inhibition weight ratio, through

$$\begin{cases} \bar{g}_{GABA_A} = g_{GABA_A} \dfrac{-(V_{mean} - V_{Exc})}{(V_{mean} - V_{GABA_A})} \dfrac{\sum_{i \in Exc} w_{(i,j)}}{\sum_{i \in Inh} w_{(i,j)}} \\ \bar{g}_{GABA_B} = g_{GABA_B} \dfrac{-(V_{mean} - V_{Exc})}{(V_{mean} - V_{GABA_B})} \dfrac{\sum_{i \in Exc} w_{(i,j)}}{\sum_{i \in Inh} w_{(i,j)}} \end{cases}$$

with $V_{mean} = (\theta + V_{rest})/2$ approximating the average membrane potential.

The feed-forward synaptic current $I_{Syn.FF(j)}$ (putatively arising from cortical and sub-cortical inputs) consisted of an AMPA component

$$I_{Syn.FF(j)} = \bar{g}_{AMPA_{FF}} p_{AMPA_{FF}} \left(V_{(j)} - V_{AMPA}\right)$$

with a constant opening probability $p_{AMPA_{FF}}$.

Numerical integration and parameters of the models

Models were simulated and explored using custom developed code under MATLAB and were numerically integrated using the forward Euler method with time-steps $\Delta t = 0.1ms$ in cellular models and $\Delta t = 0.5ms$ in network models.

Unless indicated in figure legends, standard cellular parameter values were as following. Concerning ionic currents, $C = 1\mu F.cm^{-2}$, $\bar{g}_L = 0.05mS.cm^{-2}$, $V_L = -70mV$, $\bar{g}_{Na} = 30mS.cm^{-2}$, $V_{Na} = 50mV$, $\bar{g}_K = 2mS.cm^{-2}$, $V_K = -90mV$, $\bar{g}_{CaL} = 0.01mS.cm^{-2}$, $V_{CaL} = 150mV$, $\bar{g}_{CAN} = 0.05mS.cm^{-2}$, $V_{CAN} = 30mV$, $\alpha_{CAN} = 0.0015\mu M^{-1}.ms^{-1}$, $\beta_{CAN} = 0.005ms^{-1}$, $\bar{g}_{AHP} = 0.1mS.cm^{-2}$, $V_{AHP} = -90mV$, $\alpha_{AHP} = 0.025\mu M^{-1}.ms^{-1}$, $\beta_{AHP} = 0.025ms^{-1}$, $\bar{g}_{CaT} = 0mS.cm^{-2}$, $V_{CaT} = 120mV$, $\bar{g}_H = 0mS.cm^{-2}$, $V_H = -40mV$, $V_{\tau H1/2} = -105mV$, $k_{\tau H} = 10mV$, $\tau_{H,min} = 1000ms$, $\tau_{H,max} = 6000ms$, $Ca_0 = 0.1\mu M$, $\tau_{Ca} = 25ms$, $F = 96500\ mol.s^{-1}.A^{-1}$, $r_0 = 4 \cdot 10^{-4}cm$, $r_1 = 0.25 \cdot 10^{-4}cm$. Concerning synaptic currents, $\bar{g}_{AMPA} = 0.02mS.cm^{-2}$, $\tau_{AMPA}^{decay} = 2.5ms$, $\bar{g}_{NMDA} = 0.03mS.cm^{-2}$, $\alpha_{NMDA} = 0.275ms^{-1}$, $\tau_{NMDA}^{rise} = 4.65ms$, $\tau_{NMDA}^{decay} = 75ms$, $V_{AMPA} = V_{NMDA} = 0mV$, $g_{GABA_A} = 0.0063mS.cm^{-2}$, $\tau_{GABA_A}^{decay} = 10ms$, $V_{GABA_A} = -70mV$, $g_{GABA_B} = 3.125 \cdot 10^{-4}mS.cm^{-2}$, $\alpha_{GABA_B} = 0.015ms^{-1}$, $\tau_{GABA_B}^{rise} = 90ms$, $\tau_{GABA_B}^{decay} = 160ms$, $V_{GABA_B} = -90mV$, $\Delta x_{AMPA} = \Delta x_{NMDA} = \Delta x_{GABA_A} = \Delta x_{GABA_B} = 0.1$, $V_{mean} = -57.5mV$, $n_{Exc} = 484$, $n_{Inh} = n_{Exc}/4 = 121$, $f_{Exc} = 7Hz$, $f_{Inh} = 7Hz$, $[Mg^{2+}] = 1.5mM$.

Unless indicated in figure legends, standard parameter values in network models were identical to cellular model parameters, except for the following. Concerning the network, $N = n_{Exc} + n_{Inh} = 605$ neurons, $p_{Exc} = 0.8$, so that $n_{Exc} = Np_{Exc} = 484$ and $n_{Inh} = Np_{Inh} = 121$. Concerning the weight matrix, $\mu_w = 0.03$, $\sigma_w = 0.02$, $p_{EE} = p_{EI} = p_{II} = 0.3$, $p_{IE} = 0.55$. Concerning Integrate-and-Fire neuron properties and intrinsic currents, $V_{rest} = -65mV$, $\theta = -50mV$, $V_{mean} = (V_{rest} + \theta)/2 = -57.5mV$, $\Delta t_{AP} = 3ms$, $\Delta Ca = 0.2\mu M$, $\bar{g}_{CAN} = 0.025mS.cm^{-2}$. Concerning synaptic currents, $\Delta t_{syn} = 0.5ms$, $\tau_{AMPA_{FF}} = 2.5ms$, $\Delta x_{AMPA_{FF}} = 0.1$, $\bar{g}_{AMPA} = \bar{g}_{AMPA_{FF}} = 0.23mS.cm^{-2}$, $\bar{g}_{NMDA} = 0.35mS.cm^{-2}$, $g_{GABA_A} = 0.4mS.cm^{-2}$, $p_{AMPA_{FF}} = 0.101$ a.u.

Model similarity to monkey data

The bivariate probability density distribution of neuronal TAU and LAT autocorrelogram parameters was estimated in RS and FS units in monkey in both the LPFC and MCC, using bivariate normal kernel density functions. For cellular models, similarity maps to monkey data was determined as following: for each model parameter couple of the map, the similarity to the considered cortex (PFC or MCC) was defined as the probability density of that cortex to display the TAU and LAT parameters produced by the model. Cellular models with mean firing frequency superior to 20 Hz were considered to discharge in an unrealistic fashion, compared to data, and were discarded. In network models, for each parameter value (one-dimensional explorations) or model parameter couples of the map (two-dimensional explorations), the similarity (S) was defined as the normalized Frobenius inner product between the bivariate probability density distributions of units in monkeys (U) and that of neurons in the network model (N), following

$$S_{U,N} = \frac{< U, N >_F}{\|U\|_F \|N\|_F}$$

In order to account for the TAU and LAT autocorrelogram parameters for both RS and FS populations, the similarity was calculated separately as RS with Exc and FS with Inh. Seeing as excitatory neurons represent $p_{Exc} = 0.8$ of the neurons in cortex (Beaulieu et al., 1992), the overall similarity was then calculated as

$$S = p_{Exc}\, S_{RS,Exc} + p_{Inh}\, S_{FS,Inh}$$

Additional information

Acknowledgement

This work was supported by the Medical Research Foundation (FRM) (*Equipe* DEQ20160334905, and VF: FDT201904008187), the French National Research Agency (DECCA ANR-10-SVSE4-1441 and PARABIST ANR-16-NEUC-0006-01), and was performed within the framework of the labex CORTEX ANR-11-LABX-0042 of Université de Lyon. EP is employed by the Centre National de la Recherche Scientifique. We thank C. Nay for administrative support and C. Wilson and J. Naudé for helpful discussions and proofreading the manuscript.

Author contributions

VF, FS and EP acquired and analyzed experimental data; VF, MS, BD and EP designed the analysis procedures; MS and BD designed, constrained, simulated models and analyzed modelling results; VF, FS, MS, BD and EP wrote the article.

Declaration of interests

The authors declare no conflict of interest.

Data availability

All spike time series from monkey recordings and scripts for temporal signatures extraction are freely accessible on the zenodo repository (https://doi.org/10.5281/zenodo.3947745). Scripts of computational models are available upon request.

References

Abeles, M., Bergman, H., Gat, I., Meilijson, I., Seidemann, E., Tishby, N., and Vaadia, E. (1995). Cortical activity flips among quasi-stationary states. Proceedings of the National Academy of Sciences *92*, 8616–8620.

Beasley, T.M., Erickson, S., and Allison, D.B. (2009). Rank-based inverse normal transformations are increasingly used, but are they merited? Behav. Genet. *39*, 580–595.

Beaulieu, C., Kisvarday, Z., Somogyi, P., Cynader, M., and Cowey, A. (1992). Quantitative distribution of gaba-immunopositive and -immunonegative neurons and synapses in the monkey striate cortex (area 17). Cerebral Cortex *2*, 295–309.

Behrens, T.E.J., Woolrich, M.W., Walton, M.E., and Rushworth, M.F.S. (2007). Learning the value of information in an uncertain world. Nature Neuroscience *10*, 1214–1221.

Bernacchia, A., Seo, H., Lee, D., and Wang, X.-J. (2011). A reservoir of time constants for memory traces in cortical neurons. Nature Neuroscience *14*, 366–372.

Blom, G. (1958). Statistical Estimates and Transformed Beta-Variables (Wiley).

Brunel, N. (2000). Dynamics of sparsely connected networks of excitatory and inhibitory spiking neurons. J Comput Neurosci *8*, 183–208.

Brunel, N., and Wang, X.J. (2001). Effects of neuromodulation in a cortical network model of object working memory dominated by recurrent inhibition. Journal of Computational Neuroscience *11*, 63–85.

Cavanagh, S.E., Towers, J.P., Wallis, J.D., Hunt, L.T., and Kennerley, S.W. (2018). Reconciling persistent and dynamic hypotheses of working memory coding in prefrontal cortex. Nature Communications *9*.

Chaudhuri, R., Bernacchia, A., and Wang, X.-J. (2014). A diversity of localized timescales in network activity. ELife *3*, e01239.

Chaudhuri, R., Knoblauch, K., Gariel, M.-A., Kennedy, H., and Wang, X.-J. (2015). A Large-Scale Circuit Mechanism for Hierarchical Dynamical Processing in the Primate Cortex. Neuron *88*, 419–431.

Compte, A., Constantinidis, C., Tegnér, J., Raghavachari, S., Chafee, M.V., Goldman-Rakic, P.S., and Wang, X.-J. (2003). Temporally Irregular Mnemonic Persistent Activity in Prefrontal Neurons of Monkeys During a Delayed Response Task. Journal of Neurophysiology *90*, 3441–3454.

Dale, H. (1935). Pharmacology and Nerve-endings (Walter Ernest Dixon Memorial Lecture): (Section of Therapeutics and Pharmacology). Proc. R. Soc. Med. *28*, 319–332.

Destexhe, A., and Paré, D. (1999). Impact of network activity on the integrative properties of neocortical pyramidal neurons in vivo. J. Neurophysiol. *81*, 1531–1547.

Destexhe, A., Mainen, Z.F., and Sejnowski, T.J. (1998). Kinetic models of synaptic transmission. Methods in Neuronal Modeling *2*, 1–25.

Destexhe, A., Rudolph, M., and Paré, D. (2003). The high-conductance state of neocortical neurons in vivo. Nat. Rev. Neurosci. *4*, 739–751.

Durstewitz, D., and Seamans, J.K. (2008). The Dual-State Theory of Prefrontal Cortex Dopamine Function with Relevance to Catechol-O-Methyltransferase Genotypes and Schizophrenia. Biological Psychiatry *64*, 739–749.

Durstewitz, D., Vittoz, N.M., Floresco, S.B., and Seamans, J.K. (2010). Abrupt Transitions between Prefrontal Neural Ensemble States Accompany Behavioral Transitions during Rule Learning. Neuron *66*, 438–448.

Enel, P., Procyk, E., Quilodran, R., and Dominey, P.F. (2016). Reservoir Computing Properties of Neural Dynamics in Prefrontal Cortex. PLOS Computational Biology *12*, e1004967.

Engel, T.A., Steinmetz, N.A., Gieselmann, M.A., Thiele, A., Moore, T., and Boahen, K. (2016). Selective modulation of cortical state during spatial attention. Science *354*, 1140–1144.

Faber, E.S.L., and Sah, P. (2007). Functions of SK channels in central neurons. Clin. Exp. Pharmacol. Physiol. *34*, 1077–1083.

Froemke, R.C. (2015). Plasticity of cortical excitatory-inhibitory balance. Annu. Rev. Neurosci. *38*, 195–219.

Haj-Dahmane, S., and Andrade, R. (1997). Calcium-Activated Cation Nonselective Current Contributes to the Fast Afterdepolarization in Rat Prefrontal Cortex Neurons. Journal of Neurophysiology *78*, 1983–1989.

Helton, T.D., Xu, W., and Lipscombe, D. (2005). Neuronal L-type calcium channels open quickly and are inhibited slowly. J. Neurosci. *25*, 10247–10251.

Hennequin, G., Agnes, E.J., and Vogels, T.P. (2017). Inhibitory Plasticity: Balance, Control, and Codependence. Annu. Rev. Neurosci. *40*, 557–579.

Hill, D.N., Mehta, S.B., and Kleinfeld, D. (2011). Quality metrics to accompany spike sorting of extracellular signals. J. Neurosci. *31*, 8699–8705.

Jahr, C.E., and Stevens, C.F. (1990). Voltage dependence of NMDA-activated macroscopic conductances predicted by single-channel kinetics. The Journal of Neuroscience : The Official Journal of the Society for Neuroscience *10*, 3178–3182.

Karlsson, M.P., Tervo, D.G.R., and Karpova, A.Y. (2012). Network Resets in Medial Prefrontal Cortex Mark the Onset of Behavioral Uncertainty. Science *338*, 135–139.

Kennerley, S.W., Walton, M.E., Behrens, T.E.J., Buckley, M.J., and Rushworth, M.F.S. (2006). Optimal decision making and the anterior cingulate cortex. Nature Neuroscience *9*, 940–947.

Kennerley, S.W., Dahmubed, A.F., Lara, A.H., and Wallis, J.D. (2009). Neurons in the Frontal Lobe Encode the Value of Multiple Decision Variables. Journal of Cognitive Neuroscience *21*, 1162–1178.

Khamassi, M., Quilodran, R., Enel, P., Dominey, P.F., and Procyk, E. (2015). Behavioral Regulation and the Modulation of Information Coding in the Lateral Prefrontal and Cingulate Cortex. Cerebral Cortex *25*, 3197–3218.

Kolling, N., Scholl, J., Chekroud, A., Trier, H.A., and Rushworth, M.F.S. (2018). Prospection, Perseverance, and Insight in Sequential Behavior. Neuron *99*, 1069-1082.e7.

La Camera, G., Fontanini, A., and Mazzucato, L. (2019). Cortical computations via metastable activity. Curr. Opin. Neurobiol. *58*, 37–45.

Markov, N.T., Ercsey-Ravasz, M., Van Essen, D.C., Knoblauch, K., Toroczkai, Z., and Kennedy, H. (2013). Cortical High-Density Counterstream Architectures. Science *342*, 1238406–1238406.

Mazzucato, L., Fontanini, A., and La Camera, G. (2015). Dynamics of multistable states during ongoing and evoked cortical activity. J. Neurosci. *35*, 8214–8231.

Mazzucato, L., La Camera, G., and Fontanini, A. (2019). Expectation-induced modulation of metastable activity underlies faster coding of sensory stimuli. Nat. Neurosci. *22*, 787–796.

Medalla, M., and Barbas, H. (2009). Synapses with Inhibitory Neurons Differentiate Anterior Cingulate from Dorsolateral Prefrontal Pathways Associated with Cognitive Control. Neuron *61*, 609–620.

Medalla, M., Gilman, J.P., Wang, J.-Y., and Luebke, J.I. (2017). Strength and Diversity of Inhibitory Signaling Differentiates Primate Anterior Cingulate from Lateral Prefrontal Cortex. The Journal of Neuroscience *37*, 4717–4734.

Meder, D., Kolling, N., Verhagen, L., Wittmann, M.K., Scholl, J., Madsen, K.H., Hulme, O.J., Behrens, T.E.J., and Rushworth, M.F.S. (2017). Simultaneous representation of a spectrum of dynamically changing value estimates during decision making. Nature Communications *8*.

Murray, J.D., Bernacchia, A., Freedman, D.J., Romo, R., Wallis, J.D., Cai, X., Padoa-Schioppa, C., Pasternak, T., Seo, H., Lee, D., et al. (2014). A hierarchy of intrinsic timescales across primate cortex. Nature Neuroscience *17*, 1661–1663.

Naudé, J., Paz, J.T., Berry, H., and Delord, B. (2012). A Theory of Rate Coding Control by Intrinsic Plasticity Effects. PLoS Comput Biol *8*, e1002349.

Nowak, L.G., Azouz, R., Sanchez-Vives, M.V., Gray, C.M., and McCormick, D.A. (2003). Electrophysiological Classes of Cat Primary Visual Cortical Neurons In Vivo as Revealed by Quantitative Analyses. Journal of Neurophysiology *89*, 1541–1566.

Palomero-Gallagher, N., Vogt, B.A., Schleicher, A., Mayberg, H.S., and Zilles, K. (2009). Receptor architecture of human cingulate cortex: Evaluation of the four-region neurobiological model. Human Brain Mapping *30*, 2336–2355.

Papoutsi, A., Sidiropoulou, K., Cutsuridis, V., and Poirazi, P. (2013). Induction and modulation of persistent activity in a layer V PFC microcircuit model. Front Neural Circuits *7*, 161.

Pasupathy, A., and Miller, E.K. (2005). Different time courses of learning-related activity in the prefrontal cortex and striatum. Nature *433*, 873–876.

Pohle, J., Langrock, R., van Beest, F., and Schmidt, N.M. (2017). Selecting the Number of States in Hidden Markov Models - Pitfalls, Practical Challenges and Pragmatic Solutions. ArXiv:1701.08673 [q-Bio, Stat].

Quilodran, R., Rothé, M., and Procyk, E. (2008). Behavioral Shifts and Action Valuation in the Anterior Cingulate Cortex. Neuron *57*, 314–325.

Ratté, S., Karnup, S., and Prescott, S.A. (2018). Nonlinear Relationship Between Spike-Dependent Calcium Influx and TRPC Channel Activation Enables Robust Persistent Spiking in Neurons of the Anterior Cingulate Cortex. J. Neurosci. *38*, 1788–1801.

R_core_team (2014). R: A language and environment for statistical computing. R Foundation for Statistical Computing, Vienna, Austria. URL http://www.R-project.org/.

Rich, E.L., and Wallis, J.D. (2016). Decoding subjective decisions from orbitofrontal cortex. Nat. Neurosci. *19*, 973–980.

Rigotti, M., Barak, O., Warden, M.R., Wang, X.J., Daw, N.D., Miller, E.K., and Fusi, S. (2013). The importance of mixed selectivity in complex cognitive tasks. Nature *497*, 585–590.

Ritter-Makinson, S., Clemente-Perez, A., Higashikubo, B., Cho, F.S., Holden, S.S., Bennett, E., Chkhaidze, A., Eelkman Rooda, O.H.J., Cornet, M.-C., Hoebeek, F.E., et al. (2019). Augmented Reticular Thalamic Bursting and Seizures in Scn1a-Dravet Syndrome. Cell Rep *26*, 1071.

Rodriguez, G., Sarazin, M., Clemente, A., Holden, S., Paz, J.T., and Delord, B. (2018). Conditional Bistability, a Generic Cellular Mnemonic Mechanism for Robust and Flexible Working Memory Computations. J. Neurosci. *38*, 5209–5219.

Rothe, M., Quilodran, R., Sallet, J., and Procyk, E. (2011). Coordination of High Gamma Activity in Anterior Cingulate and Lateral Prefrontal Cortical Areas during Adaptation. Journal of Neuroscience *31*, 11110–11117.

Russo, E., Ma, T., Spanagel, R., Durstewitz, D., Toutounji, H., and Köhr, G. (2020). Coordinated prefrontal state transition leads extinction of reward-seeking behaviors. BioRxiv 2020.02.26.964510.

Satake, T., Mitani, H., Nakagome, K., and Kaneko, K. (2008). Individual and additive effects of neuromodulators on the slow components of afterhyperpolarization currents in layer V pyramidal cells of the rat medial prefrontal cortex. Brain Res. *1229*, 47–60.

Seidemann, E., Meilijson, I., Abeles, M., Bergman, H., and Vaadia, E. (1996). Simultaneously recorded single units in the frontal cortex go through sequences of discrete and stable states in monkeys performing a delayed localization task. J. Neurosci. *16*, 752–768.

Seo, H., and Lee, D. (2007). Temporal filtering of reward signals in the dorsal anterior cingulate cortex during a mixed-strategy game. The Journal of Neuroscience : The Official Journal of the Society for Neuroscience *27*, 8366–8377.

Song, S., Sjöström, P.J., Reigl, M., Nelson, S., and Chklovskii, D.B. (2005). Highly Nonrandom Features of Synaptic Connectivity in Local Cortical Circuits. PLOS Biology *3*, e68.

Stokes, M.G. (2015). "Activity-silent" working memory in prefrontal cortex: a dynamic coding framework. Trends Cogn. Sci. (Regul. Ed.) *19*, 394–405.

Stoll, F.M., Fontanier, V., and Procyk, E. (2016). Specific frontal neural dynamics contribute to decisions to check. Nature Communications *7*, 11990.

Taghia, J., Cai, W., Ryali, S., Kochalka, J., Nicholas, J., Chen, T., and Menon, V. (2018). Uncovering hidden brain state dynamics that regulate performance and decision-making during cognition. Nat Commun *9*, 2505.

Tervo, D.G.R., Proskurin, M., Manakov, M., Kabra, M., Vollmer, A., Branson, K., and Karpova, A.Y. (2014). Behavioral Variability through Stochastic Choice and Its Gating by Anterior Cingulate Cortex. Cell *159*, 21–32.

Thomson, A.M. (2002). Synaptic Connections and Small Circuits Involving Excitatory and Inhibitory Neurons in Layers 2-5 of Adult Rat and Cat Neocortex: Triple Intracellular Recordings and Biocytin Labelling In Vitro. Cerebral Cortex *12*, 936–953.

Thuault, S.J., Malleret, G., Constantinople, C.M., Nicholls, R., Chen, I., Zhu, J., Panteleyev, A., Vronskaya, S., Nolan, M.F., Bruno, R., et al. (2013). Prefrontal cortex HCN1 channels enable intrinsic persistent neural firing and executive memory function. J. Neurosci. *33*, 13583–13599.

Villalobos, C., Shakkottai, V.G., Chandy, K.G., Michelhaugh, S.K., and Andrade, R. (2004). SKCa channels mediate the medium but not the slow calcium-activated afterhyperpolarization in cortical neurons. J. Neurosci. *24*, 3537–3542.

Wang, X.-J. (2020). Macroscopic gradients of synaptic excitation and inhibition in the neocortex. Nat. Rev. Neurosci. *21*, 169–178.

Wang, H., Stradtman, G.G., Wang, X.-J., and Gao, W.-J. (2008). A specialized NMDA receptor function in layer 5 recurrent microcircuitry of the adult rat prefrontal cortex. PNAS.

Wasmuht, D.F., Spaak, E., Buschman, T.J., Miller, E.K., and Stokes, M.G. (2018). Intrinsic neuronal dynamics predict distinct functional roles during working memory. Nat Commun *9*, 3499.

Womelsdorf, T., Ardid, S., Everling, S., and Valiante, T.A. (2014a). Burst firing synchronizes prefrontal and anterior cingulate cortex during attentional control. Current Biology : CB *24*, 2613–2621.

Womelsdorf, T., Valiante, T.A., Sahin, N.T., Miller, K.J., and Tiesinga, P. (2014b). Dynamic circuit motifs underlying rhythmic gain control, gating and integration. Nature Neuroscience *17*, 1031–1039.

Xue, M., Atallah, B.V., and Scanziani, M. (2014). Equalizing excitation–inhibition ratios across visual cortical neurons. Nature *511*, 596–600.

Xydas, D., Downes, J.H., Spencer, M.C., Hammond, M.W., Nasuto, S.J., Whalley, B.J., Becerra, V.M., and Warwick, K. (2011). Revealing ensemble state transition patterns in multi-electrode neuronal recordings using hidden Markov models. IEEE Trans Neural Syst Rehabil Eng *19*, 345–355.

Zilles, K., and Palomero-Gallagher, N. (2017). Multiple Transmitter Receptors in Regions and Layers of the Human Cerebral Cortex. Front Neuroanat *11*, 78.

8o

Chapter 4. Temporal integration within the MCC

4.1. Summary

The previous chapter has identified strong and slow synaptic inhibition as being responsible for the long neuronal activity timescales and quasi-stable network states within the MCC. What are the functions subserved by MCC, and how do these mechanisms contribute to them? We proposed that the MCC's central function is temporal integration of diverse information at multiple timescales required for adaptive behavior, such as integrating outcome history for behavioral planning, due to converging evidence from its anatomical, intrinsic network, neurophysiological, and behavioral properties.

The MCC was defined here as the region of the medial wall dorsal to the corpus callosum (also referred as dACC). The MCC lies at the core of a densely connected network, receiving a rich diversity of cognitive cortical feedback, domain-specific posterior to anterior somato-motor inputs and para- and ortho-sympathetic autonomic information. This convergence of multimodal excitatory inputs was proposed to be gated by frequent, strong and slow local network inhibition, with an increasing GABA-B anteroposterior gradient in MCC. Inhibition is indeed important to temporal information integration, as evidenced by the latter's link with MCC GABA/glutamate concentrations, and the previous chapter's model findings that strong and slow inhibition resulted in long neuronal timescales and network states peregrinating within discrete quasi-stationary states (i.e. metastability).

These timescales and network states were proposed to form the basis of the MCC's capacity to encode the history of expected and actual outcomes and feedback values in terms of behavioral adaptation and future strategy shifts, regulating decisions according to the action-reward feedback history and providing the motivation for temporally-extended behaviors. Indeed, individual neurons encode the history of reward magnitude through intrinsic activity timescales of varying lengths (particularly inhibitory neurons). Accordingly, MCC deactivation and lesion leads to loss of adaptation when facing diminishing reward through shorter reward history, loss of exploratory behavior, and of motivation for time-extended behaviors. Conversely, MCC stimulation induces the incentive for – and realization of – behaviors directed toward information search, as well as faster learning rates. Furthermore, MCC network state switches are shown to be concomitant with switches between exploration and exploitative strategies, where network activity is proposed to alternate between two pseudo-attractor spaces of exploration and exploitation composed of dynamic and stable subspaces.

Continuing research on the MCC model of the last chapter, additional results showed the complementary roles of fast GABA-A and slow GABA-B in defining these transitions, with GABA-A predicting the timing and GABA-B the nature of transitions. Investigating the synaptic matrix more closely revealed depressed inhibitory assemblies (inhibitory neurons least connected to each other fire together) underpinning persistent activity associated with certain network states, as well as depressed synaptic chains (or pathways; inhibitory neurons least inhibited next neurons in the sequence) underpinning neural activity sequences associated with other states. At the network level, these led to alternation between dynamic and stable coding, as well as sequential peregrination of network activity between states within two larger pseudo-attractor spaces (putatively exploration and exploitation).

4.1.1. Contributions

I reviewed the Procyk et al., 2021 article's text; and performed the research for the additional results, and wrote the corresponding text.

4.2. Article

CHAPTER FOURTEEN

The midcingulate cortex and temporal integration

Emmanuel Procyk[a,*], Vincent Fontanier[a], Matthieu Sarazin[b], Bruno Delord[b], Clément Goussi[a], and Charles R.E. Wilson[a,*]

[a]Univ Lyon, Université Claude Bernard Lyon 1, Inserm, Stem Cell and Brain Research Institute U1208, Bron, France

[b]Institute of Intelligent Systems and Robotics (ISIR), Sorbonne Université, Centre National de la Recherche Scientifique, UMR 7222, Paris, France

*Corresponding authors: e-mail address: emmanuel.procyk@inserm.fr; charles.wilson@inserm.fr

Contents

Abstract

The ability to integrate information across time at multiple timescales is a vital element of adaptive behavior, because it provides the capacity to link events separated in time, extract useful information from previous events and actions, and to construct plans for behavior over time. Here we make the argument that this information integration capacity is a central function of the midcingulate cortex (MCC), by reviewing the anatomical, intrinsic network, neurophysiological, and behavioral properties of MCC. The MCC is the region of the medial wall situated dorsal to the corpus callosum and sometimes referred to as dACC. It is positioned within the densely connected core network of the primate brain, with a rich diversity of cognitive, somatomotor and autonomic connections. Furthermore, the MCC shows strong local network inhibition which appears to control the metastability of the region—an established feature of many cortical networks in which the neural dynamics move through a series of quasi-stationary states. We propose that the strong local inhibition in MCC leads to particularly long dynamic state durations, and so less frequent transitions. Apparently as a result of these anatomical features and synaptic and ionic determinants, the MCC cells display the longest

International Review of Neurobiology, Volume 158
ISSN 0074-7742
https://doi.org/10.1016/bs.irn.2020.12.004

neuronal timescales among a range of recorded cortical areas. We conclude that the anatomical position, intrinsic properties, and local network interactions of MCC make it a uniquely positioned cortical area to perform the integration of diverse information over time that is necessary for behavioral adaptation.

1. On time and behavior

Integrating information across time at multiple timescales is a key feature of higher order cognition. Information integration across time permits us to link events and actions separated in time; to draw out useful evidence from a history of behavioral and environmental reactions; and to construct serial, time-extended plans that provide both retrospective and prospective contexts to behavior. This capacity is thus linked to the fact that the environment itself is structured along multiple timescales. This capacity appears phenomenologically in the structure of behaviors of animal species that have advanced adaptive abilities and problem-solving skills. Primates, for instance, can plan extended routes to seek resources; and they can decide, reorganize, and use detours in the face of intervening events and knowledge acquired from past events (Janmaat, Byrne, & Zuberbühler, 2006; Noser & Byrne, 2007). Certain primates and birds also use the history of interactions with objects to build tools (Gruber, Zuberbühler, & Neumann, 2016). In laboratory settings the ability of monkey species to extract adaptive performance rules over a long task history is well established (Harlow, 1949). These capacities can be considered together as capacities of behavioral adaptation. In its essence, the adaptation of behavior requires integration of multiple information sources over multiple time scales, to integrate action, outcomes, and episodic information. Adapting to real life situations is mostly non-Markovian because the history of behavioral interaction is crucial.

In a highly dynamical system like the brain, performing functions and calculations at multiple concurrent timescales requires specialized algorithms and machinery. This is therefore a difficult task requiring a complex neurobiological implementation, but in highly adaptive species the development of such capacities is clearly worthwhile (Pearson, Watson, & Platt, 2014). Several lines of research suggest that certain frontal areas have specific roles in the elaboration of behaviors over long timescales (Passingham & Wise, 2012). In this chapter we collect evidence from multiple domains suggesting that the midcingulate cortex (MCC) of primates contributes to the integration of information over long timescales. We propose that the physiological properties of the MCC network provide the dynamical properties necessary

for this temporal integration, and that in turn these properties permit the multiple functions that have been ascribed to MCC, i.e., learning, feedback adaptation, and regulation of exploratory behavior.

The first lines of evidence for a role of frontal medial cortex regions in temporal integration come from studies focused on adaptive behavior. Indeed, efficient adaptation relies on extracting knowledge, structures as well as changes, from a series of interactions with the environment. In experimental setups this corresponds to learning from outcomes and feedback after a series of choices. In human and non-human primates a large-scale network encompassing frontal and posterior associative cortical areas contributes to adaptive behaviors (Duncan, 2010; Mitchell et al., 2016; Premereur, Janssen, & Vanduffel, 2018). Moreover, fMRI consistently reveals activations in one region in the medial wall in relation to outcome monitoring and the apparent regulation of cognitive control (Amiez, Sallet, Procyk, & Petrides, 2012; Bush et al., 2002; Jueptner et al., 1997; Kouneiher, Charron, & Koechlin, 2009; Passingham, 1996). The region, often named dACC in the primate literature, corresponds to the anatomically defined midcingulate cortex (MCC, see Fig. 1). Studies sometimes show extensions of activation into preSMA or SMA and in more or less anterior parts of the MCC, and the dissociation of these activations remains an important task for the field (Amiez et al., 2013). MCC activation is observed when subjects actively seek information and/or rewards, for example, when they are exploring or foraging. The MCC seems sensitive to the volatility of the environment, for example, to the temporal stability of outcomes, as well

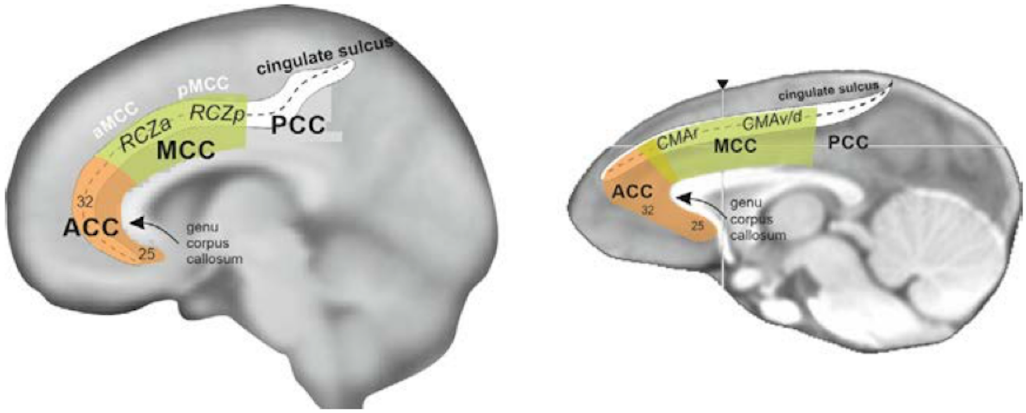

Fig. 1 Schematic representation of the cingulate regions MCC and ACC in human (left) and monkey (right). In both species the MCC contains cingulate motor areas, CMAr, CMAd and CMV in monkeys, and RCZa and RCZp in humans.

as to the propensity of subjects to make choices based on information integrated over multiple trials (Behrens, Woolrich, Walton, & Rushworth, 2007; Meder et al., 2017). The activation of this region in particular during exploratory decisions reveals its particular role in encoding values and prospective information relevant to adaptation (Kolling et al., 2016; Kolling, Behrens, Mars, & Rushworth, 2012). Studies suggest, then, that evaluation and temporal integration of information in or through the MCC might serve to guide and sustain selected behaviors in the face of current and changing features of the environment (Kolling, Wittmann, et al., 2016).

Testing in patients for clinical investigations has provided compelling data on the behavioral effect but also on the subjective feeling induced by electrical microstimulation of the MCC (Caruana et al., 2018; Parvizi, Rangarajan, Shirer, Desai, & Greicius, 2013; Talairach et al., 1973). This stimulation regularly leads to localized effects on natural goal-directed behaviors like exploratory scanning of the environment with the eyes or the head, tactile search, kneading or palpation directed toward the body or toward nearby objects (Caruana et al., 2018; Talairach et al., 1973). Patients also report general feelings of an urge to act. These results could be interpreted as reflecting MCC's contribution to generate the incentive for behaviors directed toward information search. The effects of microstimulation on search-oriented behaviors concern mostly the anterior part of the MCC, the equivalent of CMAr in monkeys.

Studies in human subjects reveal a wide array of correlative roles for the MCC, but there is among these a clear case for a role for the MCC in the temporal integration of diverse signals necessary for adaptive behavior. Our proposition here is that the best way to understand this role, and the way in which seemingly diverse responses emerge from the same region, is to consider in detail the mechanisms within MCC and its position within the anatomical hierarchy. The rest of this chapter therefore considers the evidence, largely from animal studies, for mechanisms of temporal integration in MCC.

2. The neurobiological source of temporal integration in MCC

Multiple neuroanatomical and physiological features suggest that the MCC holds a special position within the executive and more global networks, and that it is well placed and constructed to integrate diverse information in the temporal domain.

2.1 Anatomical specificities of the MCC

In most monkey recording studies referred to in this chapter, the regions of interest have been the cortex lying within the cingulate sulcus, most often the dorsal bank, and at rostro-caudal levels anterior to the genu of the arcuate sulcus (Procyk et al., 2016). We refer to this region as MCC. The entire MCC region is subject to debate in part because of the multiple versions of labeling used to describe its subdivisions. Regions' names as well as cytoarchitectonic labels are used in different ways across multiple papers, reviews, and even brain atlases. Major labeling issues are the definitions of "ACC" or "24c," which have evolved. Here we provide a definition of the term MCC we use.

The MCC is an anatomical entity defined by Vogt and colleagues, based on connectivity, cytoarchitectonics, and receptor mappings. It is evidenced in humans and monkeys, with putative equivalents in rodents, and it appears to have a separate functional identity (Vogt, 2016; Vogt, Nimchinsky, Vogt, & Hof, 1995; Vogt & Paxinos, 2012).

2.1.1 Cytoarchitecture

In humans, the MCC includes the functional subdivision frequently referred to as dACC. It is positioned dorsal to the corpus callosum and, in humans, posterior to the level of the genu of the corpus callosum. MCC cyto-architecture can be contrasted to the cytoarchitecture of the ACC (anterior cingulate cortex) which is rostral to MCC, and to the cytoarchitecture of the PCC (posterior cingulate cortex). MCC is composed of agranular cortex, which like ACC lacks a granular layer IV (Palomero-Gallagher, Vogt, Schleicher, Mayberg, & Zilles, 2009). In Vogt's nomenclature, MCC includes cytoarchitectonic areas a24c', b', and a', areas p24c', b' and a' as well as area 24d. The posterior part of MCC, containing area 24d, has the largest pyramidal cells which contribute to cingulate spinal projections and form the caudal cingulate motor areas in monkeys. Debates regarding comparative assessments in monkeys and humans relate to the dorsal and anterior parts of the MCC. Anteriorly, the limit with ACC is not clearly identified and could contain an intermediate (rACC) region. The dorsal limit of the sulcus, in terms of architecture and function is also debated (Sallet et al., 2011). Histological work from multiple groups show that indeed the dorsal limit position might vary along the rostral-caudal axis and potentially vary with species and individuals. More precise work is required to solve these issues. In this chapter we include the dorsal bank of the cingulate sulcus because the

cytoarchitecture, the connectivity patterns and the extension of cingulate motor areas (see below) suggest an anatomo-functional link to the rest of MCC (Petrides & Pandya, 1994; Procyk et al., 2016; Sallet et al., 2011).

2.1.2 Receptor mapping

In humans and non-human primates, the MCC region and its subdivisions are also characterized by specific patterns of receptor distributions. We cite here two remarkable features. The anterior MCC contains higher levels of dopamine receptor D1 binding in the superficial layers, whereas area 24d has virtually none in superficial and deep layers. Also of note is the relative level of GABAergic receptor mappings: anterior MCC contains relatively lower levels of GABA-B receptors and slightly higher levels of GABA-A, compared to posterior MCC. The distribution of GABA receptors differs also clearly between anterior MCC and ACC (Bozkurt et al., 2005; Palomero-Gallagher, Mohlberg, Zilles, & Vogt, 2008; Palomero-Gallagher et al., 2009).

2.2 MCC in the anatomical hierarchy

The MCC also sits at a remarkable anatomical position, first within the large-scale network formed by cortical areas, second within the somato-motor systems, and third in relation to the autonomic system. The large-scale cortical network is, in primates, a system with heterogeneous densities of inter-area connectivity (Markov et al., 2013). It forms a so-called bow-tie organization including a core network with high density (>90%) of connections between areas, linked to side systems by low density connectivity patterns (Markov et al., 2013). The structure has some similarities with the early model of global workspace architecture that contained a central general workspace network connected to hierarchically distant modules processing specific information (Dehaene, Kerszberg, & Changeux, 1998). Within the core network lies the MCC and its interconnections with the lateral prefrontal cortex, as well as other cortical regions that were shown to form the Multiple-demand network (Duncan, 2013). As we shall see, MCC's position within this architecture, combined with more local intrinsic properties, appears crucial for its functional identity.

The MCC displays other anatomical features that, we think, must be considered to comprehend its functional specificity and contributions to cognition. First the MCC has anatomical links with the sensorimotor system, and contains, in monkeys and humans, two sensorimotor maps named CMAr and CMAc in monkeys (M3 and M4 in Morecraft, Schroeder, & Keifer, 1996)

and RCZa and RCZp in humans (Amiez & Petrides, 2014; Picard & Strick, 1996). These maps are somatotopically organized and are connected to corresponding fields in supplementary premotor, lateral premotor, motor and spinal regions, with a rostro-caudal gradient displaying more primary and spinal connections posteriorly and more premotor and prefrontal connections anteriorly (Dum & Strick, 1991, 2002; He, Dum, & Strick, 1995; Loh, Hadj-Bouziane, Petrides, Procyk, & Amiez, 2018). Face, eye, upper and lower limbs seem to be represented, with one face representation positioned at the most anterior limit of the MCC. The most rostral and dorsal MCC region has been shown active in multiple studies involving behavioral adaptation in one way or another. The region mentioned in the human brain imaging literature is often referred to as dACC or dmPFC, with terms associated to significantly variable locations of activation within the human brain. In fact, the anterior and posterior subdivisions of the MCC (aMCC and pMCC) seem to be activated differently during cognitive tasks and more precise descriptions of brain activations, potentially on a subject by subject basis, are required to really grasp the functional specificity within this region (Amiez et al., 2013). We have suggested recently that the somatotopic organization of MCC reflects fields devoted to the detection and evaluation of domain-specific feedback relevant for adaptations (Loh et al., 2020; Procyk et al., 2016). Because of the specificity of connectivity patterns of MCC maps it is possible that they contribute to different functional uses of feedback, i.e., contributing to trigger different adaptive cognitive or behavioral reactions.

Finally, the MCC is, within the medial frontal cortex of primates, one main source and target of connections with the autonomic system. Recent investigations have shown that, contrary to rodents, the primate medial frontal cortex is 3–4 synapses away from an organ like the adrenal medulla (Dum, Levinthal, & Strick, 2016, 2019). Neurons trans-synaptically labeled after injection in the adrenal medulla are notably located within the somato-motor fields of the CMAr and CMAc. A review of human brain activations testing covariations of brain activity with autonomic measures showed that the MCC might have subdivisions related to the sympathetic and parasympathetic systems respectively (Amiez & Procyk, 2019).

In sum, the most rostral subdivisions of MCC that contain somatomotor fields also have connections with the lateral prefrontal cortex and with the sympathetic system. Such overlap of cognitive, somatomotor and autonomic connectivity is, we propose, a crucial property of the MCC. This connectivity and position within the cortical core bring rich and diverse inputs to the MCC, permitting it to perform functions that extend beyond

any specific modality of information type, in particular favoring an integrative function. Our argument here is that a particularly important part of this role is the integration across time that can be carried out with this diversity of information. Central to this claim is the idea that the intrinsic properties of the cortical cells themselves, the construction of the local circuits, and in particular the nature of local inhibition, allow MCC to perform temporal integration over longer timescales than other cortical regions, and to do so with diverse information provided by its position in the cortical hierarchy.

2.3 Intrinsic cortical features of MCC

The cell physiological properties of MCC can provide clues to its dynamical specificities and position in the temporal hierarchy. Specific physiological data in monkeys for a region at the border between ACC and MCC show that the nature of local inhibition might be an important feature in MCC (Medalla, Gilman, Wang, & Luebke, 2017). Spontaneous inhibitory postsynaptic currents are more frequent, long and large in cingulate layer III neurons compared to other prefrontal regions (Medalla et al., 2017). Data from human MCC shows that GABA-B receptors are dense, especially in its posterior part, pMCC (Zilles & Palomero-Gallagher, 2017). Robust inhibition and long inhibitory time constants should contribute to the extension of the time window for signal summation and thus extend local temporal receptive fields. In artificial hierarchical networks, environmental uncertainty can be dynamically captured by variations of the E/I tone (Pettine, Louie, Murray, & Wang, 2020). In humans, dynamical integration of environmental uncertainty is circumscribed to the MCC (Behrens et al., 2007). A recent study also linked subjects' ability to integrate information in time and their glutamate and GABA concentrations in the MCC (Scholl, Kolling, Nelissen, Stagg, & Harmer, 2017). In general terms, inhibition is a strong determinant of network activity (Mongillo, Rumpel, & Loewenstein, 2018). The diversity of synaptic inhibition can flexibly structure network dynamics by gating pyramidal inputs depending on the current task demand (Tremblay, Lee, & Rudy, 2016; Wang, 2020; Womelsdorf, Valiante, Sahin, Miller, & Tiesinga, 2014). For example, MCC inhibitory activity has been proposed as a mechanism for transient network disengagement in response to errors (Rothé, Quilodran, Sallet, & Procyk, 2011; Shen et al., 2015). Inhibitory controlled circuits are more robust to excitatory volatility (Mongillo et al., 2018). This robustness might be particularly important for areas receiving converging multimodal inputs, and that need to integrate

that information across time. Indeed, there is a macroscopic gradient of synaptic inhibition from sensory cortices to associative areas (Wang, 2020). MCC slow inhibitory decay times generate low frequency rhythmic oscillatory activity (Kopell, Kramer, Malerba, & Whittington, 2010; Medalla et al., 2017) supporting communication between distant cortical areas (Hahn, Bujan, Frégnac, Aertsen, & Kumar, 2014). MCC excitatory and inhibitory spike trains synchronize to different frequency bands (Voloh & Womelsdorf, 2018). Such cell type specific oscillations could be a means for flexible long-range tuning of coherent network activities according to the current demand. A recent study reported that MCC stimulation elicits recurrent activity in the LPFC (Nácher, Hassani, & Womelsdorf, 2019), an activity pattern that has been associated with working memory temporal maintenance (Mongillo et al., 2018; Wasmuht, Spaak, Buschman, Miller, & Stokes, 2018). In this framework, MCC activity and in particular inhibition would contribute to network synchronization and structuration of local and distant cortical areas.

We propose therefore that MCC inhibitory tone determines the activity of local units and leads to more stable or slowly evolving network dynamics favoring multimodal associations in the temporal domain. And these properties appear to be particularly exaggerated within MCC relative to other areas of association cortex, placing MCC not just at the heart of the dense core of associative cortical areas (Markov et al., 2013), but also as new analyses and modeling suggest, at the pinnacle of a hierarchy of cortical timescales.

Based on anatomical data and large-scale network modeling, Wang and colleagues have recently shown that the anatomical organization and hierarchies within the large-scale cortical network was accompanied by temporal hierarchies (Chaudhuri, Knoblauch, Gariel, Kennedy, & Wang, 2015; Murray et al., 2014). Individual neuron spiking shows some level of autocorrelation that reflects its propensity to keep a firing mode. The autocorrelation decay, referred to as spiking timescale (Murray et al., 2014), measured at the population level in different areas increases from posterior (sensory) areas to anterior frontal regions, forming a temporal hierarchy. Within the set of areas investigated in this study MCC displayed the longest timescale (about 300 ms), compared to LPFC (190 ms) or area MT (65 ms) (Cavanagh, Towers, Wallis, Hunt, & Kennerley, 2018; Murray et al., 2014). Medial frontal regions also show longer timescales in rats (Murakami, Shteingart, Loewenstein, & Mainen, 2017). Such differences in timescale might provide areas with different information processing capability, and in particular

the capacity to integrate information over long temporal scales, like rewards or feedback encountered across trials of a cognitive task (Bernacchia, Seo, Lee, & Wang, 2011). Indeed very recent work proposes that cortical dynamics are modulated by a range of timescales, potentially generated by independent mechanisms, some of which directly link to relevant task parameters, while others like the general intrinsic timescale remain independent (Spitmaan, Seo, Lee, & Soltani, 2020). Large scale modeling leads to the proposition that the specific timescale of cortical areas emerges both from the large-scale pattern of inter-areal connectivity and from intrinsic properties of areas, including local recurrent excitatory connectivity which was found to increase in density in parallel to the temporal hierarchy (Chaudhuri et al., 2015). Other important features that appear to change across the cortical hierarchy and may relate to these changes in timescale include the ratio T1w/T2w in structural MRI scans, and the level of tonic inhibition (Wang, 2020). We explore the interplay between the macroscopic gradient of synaptic inhibition and timescale hierarchy (possibly via disinhibition; Wang, 2020) in the final section.

The outcome of this work is that the MCC is situated at the core of a cortical network, with the longest neuronal timescale of recorded cortical areas, relatively strong local network inhibition, and a rich diversity of cognitive, somatomotor and autonomic connections. We argue that these are the building blocks for a system whose neurophysiological role will be to integrate diverse signals over time, a role particularly relevant in the context of behavioral adaptation. In the following sections we discuss the neurophysiological correlates of behavior in MCC and relate them to the properties described above. We propose that the diversity of neural responses in MCC makes particular sense in the light of this overarching function of temporal integration for adaptation.

3. Neurophysiological and causal correlates of temporal integration in MCC

Neurophysiological studies in rodent and non-human primate models provide details of the neural processes implemented by MCC and reveal neural correlates of the history of outcomes and values in a task, as well as the switching between behavioral states. These point to a role for MCC neurons in functions dedicated to gathering information over time for subsequent regulation of behavior, a role that a limited number of intervention studies appear to confirm. Similar properties have been observed in the rat

medial frontal cortex and while the anatomical correspondence in the rat brain is still in discussion, we will refer here to relevant data from medial frontal cortex (MFC) areas IL, PL and AC (Mars et al., 2018; Schaeffer et al., 2020; Vogt & Paxinos, 2012).

3.1 History of outcomes and values

MCC and MFC single unit activity encodes for reward-based action selection in simple tasks in rats, monkeys and humans (Shima & Tanji, 1998; Sul, Kim, Huh, Lee, & Jung, 2010; Williams, Bush, Rauch, Cosgrove, & Eskandar, 2004), but also for the enactment of serial actions where each action is coded relative to future outcomes (Procyk & Joseph, 2001; Procyk, Tanaka, & Joseph, 2000; Shidara & Richmond, 2002). Intervention studies in the MCC are rare, but those that exist confirm that MCC is directly contributing to the regulation of decisions based on rewards (Amiez, Joseph, & Procyk, 2006; Kennerley, Walton, Behrens, Buckley, & Rushworth, 2006; Shima & Tanji, 1998). Shima and Tanji (1998), for example, showed that neurons in the cingulate motor areas within MCC signaled a reduction of reward that indicated that a change in action should be subsequently chosen, but only when the action was indeed successfully changed. Such activity is necessarily a response to a recent reward history over several trials, rather than a single outcome. The alteration of this MCC activity by local muscimol injection leads to a deterioration in the adaptation of action selection based on the diminishing reward size (Shima & Tanji, 1998). These responses in MCC are therefore driven by more information than the immediate action to be committed—they include information about the temporal context of that action. This temporal context is of course mostly of use to ensure that the action is well adapted, and importantly MCC activity also encodes feedback of actions or choices that is relevant to adaptation, i.e., in situations where action and feedback are the focus of attention and where it can reduce uncertainty.

It is long established that cells in MCC respond to both rewards and errors (Amiez, Joseph, & Procyk, 2005), and that responses to these events are modulated by their predictability and potentially their behavioral relevance (Quilodran, Rothé, & Procyk, 2008). In addition, MCC neurons represent the expected magnitude or the probability of an upcoming reward on trial-and-error learning tasks (Kennerley, Behrens, & Wallis, 2011). While initial reports made a straight link between immediate reward and cell activity, it is now clear that the recent history of reward alters the firing of these

cells (Kawai, Yamada, Sato, Takada, & Matsumoto, 2015; Seo & Lee, 2007), and that this effect will occur with varying timescales across neurons (Bernacchia et al., 2011). For example, Kawai et al. (2015) showed that MCC cells, and in particular putative inhibitory neurons (Kawai, Yamada, Sato, Takada, & Matsumoto, 2019), not only maintained the information about the last outcome but also stored outcome experiences from several past trials. MCC cells in this protocol also signaled a subsequent shift in strategy, activity that is discussed in more detail below.

The ability of MCC activity to reflect outcome history has an impact on behavior. Monkeys with bilateral MCC sulcus lesions have difficulties in integrating and building reward-action history in an uncertain context and in adapting choice behavior (Kennerley et al., 2006). Effectively the lesion appears to reduce the span over which recent outcomes are used to adjust decisions. MCC appears to have a central role in updating action values based on the outcome history, helping to improve behavioral performance toward a specific goal (Kennerley et al., 2006; Seo, Barraclough, & Lee, 2007). In general therefore these deficits seem to involve a loss of exploratory behaviors—the observed effects appear to combine altered valuation of outcomes and a reduced capacity to integrate the implications of those outcomes over time, the consequence on adaptive behavior being quite consistent.

Rodent pharmacological inactivation and chemogenetic perturbation also show that medial frontal regions in rats have a causal role in integrating outcome history and in regulating explore/exploit behaviors (Tervo et al., 2020). Indeed, the distributed ensemble dynamics might be tuned by monoaminergic afferents. Noradrenergic (NA) inputs are proposed to contribute to abrupt network reconfiguration and to promote transitions between exploitation and exploration (Bouret & Sara, 2005), and we discuss these state transitions in more detail below. NA inputs to the MCC would allow the dynamical modulation of learning rates (Silvetti, Vassena, Abrahamse, & Verguts, 2018). Consistent with those views, selective NA input enhancement in the rat MCC artificially increases behavioral stochasticity and leads to an increase in response variability. In turn, NA input suppression restores the ability to weight previously received feedback for choice regulation (Tervo et al., 2014).

In addition rare studies can provide information on the effect of cingulotomy in human patients, supporting a role for ongoing behavioral adaptation based on context from prior trials, both in the context of decisions

to act (Williams et al., 2004) and in more cognitive contexts where previous trials might provide interfering information (Sheth et al., 2012). Wider lesions to the cingulate region have been reported to lead to global reductions of action and speech, often characterized as akinetic mutism (Devinsky, Morrell, & Vogt, 1995; Németh, Hegedüs, & Molnár, 1988). Such deficits have been proposed consistent with much of the above evidence if we consider the role of the MCC as acting to motivate time-extended behaviors, rather than driving trial-by-trial adaptations (Holroyd & Yeung, 2012).

Recent work proposes how the MCC goes about using outcome history to drive upcoming behavior: it is proposed that MCC neurons encode expected outcomes as a latent state representation of actual outcomes (Hyman, Holroyd, & Seamans, 2017). The interaction between expected and actual outcome representations on trials where they do not match may drive a dynamical shift that we often record as an error signal. MCC cells certainly do show error signals—they respond to errors in the form of absent rewards (Niki & Watanabe, 1979). Again this error activity is modulated in a manner that reflects the temporal context, for example, how much or how close a reward was before the error (Amiez et al., 2005). Cells in MCC also encode both the overall task value in terms of reward, as well as the actual reward obtained (Amiez et al., 2006; Sallet et al., 2007). This activity has a causal impact on behavior as alteration of local MCC activity by local muscimol injection leads to a loss of efficiency in exploration for more rewarded stimuli in a choice task (Amiez et al., 2006).

These comparative feedback responses translate to the population level, where error- and feedback-related potentials (such as the error-related negativity [ERN] and feedback potentials [FRPs]) have been widely shown to differentiate outcome valences when recorded over the medial part of the frontal lobe in electroencephalography (EEG) (Falkenstein et al., 2001; Gehring, Goss, Coles, & Meyer, 1993; Miltner, Braun, & Coles, 2001), electrocorticography (EcoG; Wilson et al., 2016), and the local field potential (LFP) (Gemba, Sasaki, & Brooks, 1986). Of course these are not standalone signals, rather they appear to provide information about the value of the feedback in terms of behavioral adaptation, be it for directly driving adaptation on subsequent trials (Khamassi, Quilodran, Enel, Dominey, & Procyk, 2015; Monosov, 2017; Quilodran et al., 2008; Shima & Tanji, 1998), or for motivating more extended behaviors beyond simple trial-to-trial adaptation (Holroyd & Yeung, 2012; Walsh & Anderson, 2011). It is this concept of time-extended behaviors that is of particular relevance here,

therefore, and it is this time-extended information that is necessary to signal the necessity to change state or strategy in a task.

3.2 Neural and behavioral state switches

Monkey MCC and rat MFC show phasic neural changes at behaviorally relevant events together with global neural state changes between different behavioral states or strategies separated by switches, like exploratory behavior and repetitive behavior (Enel, Procyk, Quilodran, & Dominey, 2016; Karlsson, Tervo, & Karpova, 2012). For example MCC neurons signal behavioral shifts on subsequent trials (Kawai et al., 2015), while neural signals anticipating and signaling patch leaving or strategy switching in sequential foraging tasks are observed in phasic unitary and high-gamma activities in both primates and rodents (Karlsson et al., 2012; Quilodran et al., 2008; Rothé et al., 2011). Powell and Redish (2016) showed that on tasks where a reward criterion change was imposed, rats showed state transitions of MFC activity after they had learned about that contingency change, but before their behavior changed. In contrast, when rats were permitted to change strategies themselves (i.e., without imposed criterion changes), similar state transitions occurred before changes in behavior, therefore in a manner predictive of this un-imposed strategy switch (Powell & Redish, 2016). This implies that the MFC is signaling the need for a change in strategy, rather than passively reflecting such a change.

Across a range of studies, a picture emerges where the neural dynamics of MCC correlate with the state of uncertainty inherent to exploratory situations and the control or monitoring of information seeking behavior (Stoll, Fontanier, & Procyk, 2016; White et al., 2019). In addition, MCC activity has strong correlation with valuation processes—a multiplicity of signals reflect dynamical information accumulation in the MCC (Hunt et al., 2018; Kennerley et al., 2011). These signals are absent from OFC and LPFC activities. This integrated information is therefore used to make the decision to maintain or change the current course of action (Khamassi et al., 2015; Mansouri, Tanaka, & Buckley, 2009; Quilodran et al., 2008; Stoll et al., 2016).

Hayden, Pearson, and Platt (2011) found that neural activity during foraging scaled with the value of leaving the current exploited option and reflected an integrate-to-threshold process built across trials and leading to patch leaving (Hayden et al., 2011). Accumulation processes are observed in other frontal areas such as the FEF but they are continuous and ramp

within trials, i.e., over a short timescale (Hanes & Schall, 1996). It is tempting to think that the specific neural dynamics observed during exploration or foraging provide the MCC with neural state properties that favor integration of information across time, i.e., over long timescales.

The way these correlated activity states are expressed over time is an important feature of encoding in MCC and across the frontal cortex. It may be that the capacity to shift neural state is an intrinsic feature of these cortical architectures, perhaps independent of external stimuli or constraints, which is then tuned to the needs of any ongoing task. An interesting and open question in the field is therefore how these properties are harnessed for the functional uses we ascribe to them, and a starting point is to consider how general this dynamic shifting of neural state is in MCC.

For example, we described above that information about feedback is encoded in the MCC, but this encoding occurs dynamically within the time course of a trial, starting just before outcome delivery until the next decision is made (Hunt et al., 2018; Stoll et al., 2016). The term dynamic here refers to the idea that information encoding changes over time, such that a decoder that can decode some behavioral variable from neural data at one period in time is no longer able to decode the same information later in time, while the variable is still encoded by the neural activity. In this sense the encoding is dynamic. The question of whether representations in MCC are dynamic or stable over time depends on the timescale in question, but it is increasingly clear that frontal cortical regions inherently combine elements of stable and dynamic coding. For example values in MCC are represented by mixed activity regimes composed of a stable subspace and a dynamic ensemble (Enel, Wallis, & Rich, 2020). This configuration grants the system a level of flexibility, i.e., a substrate of sustained information which can be combined with time-sensitive representations. The combination of both representations is likely crucial for the organization of behaviors in time and resembles the properties of delay activity much discussed regarding lateral prefrontal cortex (Cavanagh et al., 2018; Miller, Lundqvist, & Bastos, 2018).

It is becoming increasingly clear that there is a distinct organization in this combination of stable and dynamic coding regimes. For example, Stoll et al. (2016) used cross-temporal decoding of MCC activity to show semi-stable codes of feedback and decisions that carry over inter-trial periods during foraging tasks. This appears to be particularly the case when, as in this study, decisions rely on the history of previous choices. MCC activity in this case can be considered as a set of trajectories organized in a sequence of discrete quasi-stationary states. This organization of activities in time is referred

to as metastability (Durstewitz, Vittoz, Floresco, & Seamans, 2010; La Camera, Fontanini, & Mazzucato, 2019). States can be organized around key perceptual and motor events or structured by ensemble activity regimes independently from external cues.

Metastability has been observed in other cortical areas and is proposed to form a neuronal substrate for specific internal representations of the environment (La Camera et al., 2019; Rich & Wallis, 2016). State stability is believed to reflect internal representations and the deployment of selective attention required for the current task demand (Engel et al., 2016). Transitions are more frequent when representations of internal rules are susceptible to change and are marked by an abrupt shift of dynamics in distributed neuronal ensemble (Durstewitz et al., 2010).

How might these metastable states be used to promote the functions of MCC? There are likely to be several answers to this question, again depending on the temporal scale of investigation. Value signaling in the MCC reflects temporal integration of experienced rewards (Amiez et al., 2006; Hunt et al., 2018) while also monitoring counterfactual options (Hayden, Pearson, & Platt, 2009; Kolling, Behrens, Wittmann, & Rushworth, 2016), and network transitions occur in periods when internal states are being updated and actively monitored. So, state transitions may well represent shifts in belief based on the same weighting of prior evidence and current outcomes. For example such state transitions would be signaling a shift to a more exploratory strategy of choice (Karlsson et al., 2012). Indeed, in foraging tasks, MCC trajectories describe two pseudo attractor spaces reflecting the structure of the task that alternates between phases of behavioral exploration and exploitation. Here state-space transitions are triggered by the monitoring of specific events such as feedback that reflect the need to adapt the current strategy (Enel et al., 2016; Quilodran et al., 2008).

3.3 Inhibitory control of MCC metastable states

Our most recent work provides direct evidence on how local intrinsic properties and timescales of MCC cells cause metastability, suggesting how such dynamical properties contribute to the role of MCC in adaptive behavior (Fontanier, Sarazin, Stoll, Delord, & Procyk, 2020). We studied the temporal signatures, specifically the spike auto-correlogram time constant and latency, of single neurons in monkey MCC and lateral prefrontal cortex (LPFC), recorded during a decision-making task. As suggested by Murray et al. (2014), cells demonstrated a longer intrinsic timescale in the MCC than

LPFC. We then showed that the temporal signatures were highly structured, showing anatomical organization within the MCC, and specific cell-type differences in the spike auto-correlogram features between fast and regular spiking neurons.

Importantly the timescales of certain neurons showed functional adaptation to the timescale of behaviorally relevant information in the task at hand. In MCC and for regular spiking neurons only, we observed that on average neuronal timescales lengthened when the monkeys were engaged in the task compared to when they were pausing from the task. In addition, we showed that both the neuron-type and the timescale of that neuron were determinant of the contribution of that neuron to encoding important behavioral features of the task, like reward feedback provided after choices (particularly putative interneurons for negative feedback), or value-related information used across multiple trials (Fontanier et al., 2020).

We then used these data to inform research using biophysically constrained network models to link back to the inhibitory properties discussed above. This work revealed that specific cellular conductances in the modeled cells (specifically intrinsic after-hyperpolarization (AHP) potassium and synaptic inhibitory GABA-B conductances) were critical determinants of the specificity of MCC and LPFC dynamics. These features were sufficient to provide a causal account for temporal signatures. Intriguingly, these conductances drove the cells to the recorded timescales by organizing activity into metastable states, with inhibition controlling state stability and transitions. Our model predicted therefore that the state duration in this metastable system would scale non-linearly with the timescales of different cortical regions, and we provided strong evidence to support this prediction from the monkey neurophysiological data, even reaching behavioral timescales. Our proposition on the basis of this work, therefore, is that inhibitory-controlled metastability constitutes the central dynamical process of MCC network function, locally specifying the temporal organization underlying cognitive processes operated by frontal areas.

4. Conclusion

The MCC, the region of the medial wall situated dorsal to the corpus callosum and sometimes referred to as dACC, is positioned within the densely connected core network of the primate brain, and has a rich diversity of cognitive, somatomotor and autonomic connections. The MCC shows strong local network inhibition in particular driven by GABA-B activity.

This inhibition appears to control the metastability of the region—an established feature of many cortical networks in which the neural dynamics move through a series of quasi-stationary states with jump-like modulations between them. In particular it is proposed that the strong local inhibition in MCC leads to particularly long dynamic state durations, and so less frequent transitions, with the duration of these states even approaching the timescale of behavioral phenomena. Apparently as a result of these anatomical features and synaptic and ionic determinants, the MCC cells display the longest neuronal timescales among a range of recorded cortical areas.

We have argued that the anatomical position, intrinsic properties, and local network interactions of MCC make it a uniquely positioned cortical area to perform the integration of diverse information over time that is necessary for behavioral adaptation. The functional role of the MCC is therefore defined by these properties and we consider it a single central function. The MCC will perform this integrative function on different information types that arrive, given its rich connectivity. Performing the same integrative function on different incoming types of information will lead to a diversity of behavioral correlates. While one reading of the literature might be that these diverse behavioral correlates mean that MCC has many different cognitive functions, we underline that the evidence presented above suggests that the operation performed by MCC itself is a single underlying function common to different cognitive labels.

This proposal leaves of course many important questions to be addressed. The neurobiological source of these temporal features, and the contribution of the place within the cortical hierarchy remain to be further examined. We also need to better understand the extent to which the variations in metastability and timescale are causal of the functions of MCC and other regions, or whether in fact those features result from adaptation to the context. Are these intrinsic properties that are applied to different functional uses, or are these properties tuned to fit the task in hand? Studies during task acquisition will be crucial here. Regions like the MCC do not, of course, act independently but as part of a densely connected network, for example, showing interaction with LPFC. As such there remain questions to be answered about how regions with differing timescales and differing dynamic regimes can interact in a manner that permits computations that are relevant for cognition.

The purpose of this chapter was to elaborate a synthesis of data from multiple levels of investigation, in order to seek a coherent multi-scale view of the function of the midcingulate cortex. While many pieces of information

are still required from anatomical, biophysical, neurophysiological and behavioral experiments, the recent data suggest that the synaptic and cellular properties, the local network configuration as well as the embedding of MCC in specific large scale functional networks provide this region with capabilities relevant to the regulation and adaptation of behavior over long time scales.

References

Amiez, C., Joseph, J.-P., & Procyk, E. (2005). Anterior cingulate error-related activity is modulated by predicted reward. *The European Journal of Neuroscience*, *21*, 3447–3452.

Amiez, C., Joseph, J.-P., & Procyk, E. (2006). Reward encoding in the monkey anterior cingulate cortex. *Cerebral Cortex*, *16*, 1040–1055.

Amiez, C., Neveu, R., Warrot, D., Petrides, M., Knoblauch, K., & Procyk, E. (2013). The location of feedback-related activity in the midcingulate cortex is predicted by local morphology. *Journal of Neuroscience*, *33*, 2217–2228.

Amiez, C., & Petrides, M. (2014). Neuroimaging evidence of the anatomo-functional organization of the human cingulate motor areas. *Cerebral Cortex*, *24*, 563–578.

Amiez, C., & Procyk, E. (2019). Midcingulate somatomotor and autonomic functions. In B. A. Vogt (Ed.), *Handbook of clinical neurology* (1st ed., pp. 53–71). Elsevier B.V.

Amiez, C., Sallet, J., Procyk, E., & Petrides, M. (2012). Modulation of feedback related activity in the rostral anterior cingulate cortex during trial and error exploration. *NeuroImage*, *63*, 1078–1090.

Behrens, T. E. J., Woolrich, M. W., Walton, M. E., & Rushworth, M. F. S. (2007). Learning the value of information in an uncertain world. *Nature Neuroscience*, *10*, 1214–1221.

Bernacchia, A., Seo, H., Lee, D., & Wang, X.-J. (2011). A reservoir of time constants for memory traces in cortical neurons. *Nature Neuroscience*, *14*, 366–372.

Bouret, S., & Sara, S. J. (2005). Network reset: A simplified overarching theory of locus coeruleus noradrenaline function. *Trends in Neurosciences*, *28*, 574–582.

Bozkurt, A., Zilles, K., Schleicher, A., Kamper, L., Arigita, E. S., Uylings, H. B. M., et al. (2005). Distributions of transmitter receptors in the macaque cingulate cortex. *NeuroImage*, *25*, 219–229.

Bush, G., Vogt, B. A., Holmes, J., Dale, A. M., Greve, D., Jenike, M. A., et al. (2002). Dorsal anterior cingulate cortex: A role in reward-based decision making. *Proceedings of the National Academy of Sciences of the United States of America*, *99*, 523–528.

Caruana, F., Gerbella, M., Avanzini, P., Gozzo, F., Pelliccia, V., Mai, R., et al. (2018). Motor and emotional behaviours elicited by electrical stimulation of the human cingulate cortex. *Brain*, *24*. 563–17.

Cavanagh, S. E., Towers, J. P., Wallis, J. D., Hunt, L. T., & Kennerley, S. W. (2018). Reconciling persistent and dynamic hypotheses of working memory coding in prefrontal cortex. *Nature Communications*, *9*, 1–16.

Chaudhuri, R., Knoblauch, K., Gariel, M.-A., Kennedy, H., & Wang, X.-J. (2015). A large-scale circuit mechanism for hierarchical dynamical processing in the primate cortex. *Neuron*, *88*, 419–431.

Dehaene, S., Kerszberg, M., & Changeux, J. P. (1998). A neuronal model of a global workspace in effortful cognitive tasks. *Proceedings of the National Academy of Sciences of the United States of America*, *95*, 14529–14534.

Devinsky, O., Morrell, M. J., & Vogt, B. A. (1995). Contributions of anterior cingulate cortex to behaviour. *Brain*, *118*(Pt. 1), 279–306.

Dum, R. P., Levinthal, D. J., & Strick, P. L. (2016). Motor, cognitive, and affective areas of the cerebral cortex influence the adrenal medulla. *Proceedings of the National Academy of Sciences*, 201605044.
Dum, R. P., Levinthal, D. J., & Strick, P. L. (2019). The mind-body problem: Circuits that link the cerebral cortex to the adrenal medulla. *Proceedings of the National Academy of Sciences of the United States of America*, *116*, 26321–26328.
Dum, R. P., & Strick, P. L. (1991). The origin of corticospinal projections from the premotor areas in the frontal lobe. *The Journal of Neuroscience*, *11*, 667–689.
Dum, R. P., & Strick, P. L. (2002). Motor areas in the frontal lobe of the primate. *Physiology & Behavior*, *77*, 677–682.
Duncan, J. (2010). The multiple-demand (MD) system of the primate brain: Mental programs for intelligent behaviour. *Trends in Cognitive Sciences*, *14*, 172–179.
Duncan, J. (2013). The structure of cognition: Attentional episodes in mind and brain. *Neuron*, *80*, 35–50.
Durstewitz, D., Vittoz, N. M., Floresco, S. B., & Seamans, J. K. (2010). Abrupt transitions between prefrontal neural ensemble states accompany behavioral transitions during rule learning. *Neuron*, *66*, 438–448.
Enel, P., Procyk, E., Quilodran, R., & Dominey, P. F. (2016). Reservoir computing properties of neural dynamics in prefrontal cortex. O'Reilly JX, ed *PLoS Computational Biology*, *12*, e1004967.
Enel, P., Wallis, J. D., & Rich, E. L. (2020). Stable and dynamic representations of value in the prefrontal cortex. *eLife*, *9*, 1040.
Engel, T. A., Steinmetz, N. A., Gieselmann, M. A., Thiele, A., Moore, T., & Boahen, K. (2016). Selective modulation of cortical state during spatial attention. *Science*, *354*, 1140–1144.
Falkenstein, M., Hielscher, H., Dziobek, I., Schwarzenau, P., Hoormann, J., Sunderman, B., et al. (2001). Action monitoring, error detection, and the basal ganglia: An ERP study. *Neuroreport*, *12*, 157–161.
Fontanier, V., Sarazin, M., Stoll, F. M., Delord, B., & Procyk, E. (2020). Local inhibitory control of frontal network metastability underlies the temporal signature of cognitive states. *bioRxiv*, *28*, 319.
Gehring, W. J., Goss, B., Coles, M., & Meyer, D. E. (1993). A neural system for error detection and compensation. *Psychological Science*, *4*, 385–390.
Gemba, H., Sasaki, K., & Brooks, V. B. (1986). "Error" potentials in limbic cortex (anterior cingulate area 24) of monkeys during motor learning. *Neuroscience Letters*, *70*, 223–227.
Gruber, T., Zuberbühler, K., & Neumann, C. (2016). Travel fosters tool use in wild chimpanzees. *eLife*, *5*, 93.
Hahn, G., Bujan, A. F., Frégnac, Y., Aertsen, A., & Kumar, A. (2014). Communication through resonance in spiking neuronal networks. Brunel N, ed. *PLoS Computational Biology*, *10*, e1003811–e1003816.
Hanes, D. P., & Schall, J. D. (1996). Neural control of voluntary movement initiation. *Science*, *274*, 427–430.
Harlow, H. F. (1949). The formation of learning sets. *Psychological Review*, *56*, 51–65.
Hayden, B. Y., Pearson, J. M., & Platt, M. L. (2009). Fictive reward signals in the anterior cingulate cortex. *Science*, *324*, 948–950.
Hayden, B. Y., Pearson, J. M., & Platt, M. L. (2011). Neuronal basis of sequential foraging decisions in a patchy environment. *Nature Neuroscience*, *14*, 933–939.
He, S. Q., Dum, R. P., & Strick, P. L. (1995). Topographic organization of corticospinal projections from the frontal lobe: Motor areas on the medial surface of the hemisphere. *The Journal of Neuroscience*, *15*, 3284–3306.
Holroyd, C. B., & Yeung, N. (2012). Motivation of extended behaviors by anterior cingulate cortex. *Trends in Cognitive Sciences*, *16*, 122–128.

Hunt, L. T., Malalasekera, W. M. N., Berker, A. O., Miranda, B., Farmer, S. F., Behrens, T. E. J., et al. (2018). Triple dissociation of attention and decision computations across prefrontal cortex. *Nature Neuroscience*, *21*, 1–17.

Hyman, J. M., Holroyd, C. B., & Seamans, J. K. (2017). A novel neural prediction error found in anterior cingulate cortex ensembles. *Neuron*, *95*, 447–456.e3.

Janmaat, K. R. L., Byrne, R. W., & Zuberbühler, K. (2006). Primates take weather into account when searching for fruits. *Current Biology*, *16*, 1232–1237.

Jueptner, M., Stephan, K. M., Frith, C. D., Brooks, D. J., Frackowiak, R. S., & Passingham, R. E. (1997). Anatomy of motor learning. I. Frontal cortex and attention to action. *Journal of Neurophysiology*, *77*, 1313–1324.

Karlsson, M. P., Tervo, D. G. R., & Karpova, A. Y. (2012). Network resets in medial prefrontal cortex mark the onset of behavioral uncertainty. *Science*, *338*, 135–139.

Kawai, T., Yamada, H., Sato, N., Takada, M., & Matsumoto, M. (2015). Roles of the lateral Habenula and anterior cingulate cortex in negative outcome monitoring and behavioral adjustment in nonhuman primates. *Neuron*, 1–16.

Kawai, T., Yamada, H., Sato, N., Takada, M., & Matsumoto, M. (2019). Preferential representation of past outcome information and future choice behavior by putative inhibitory interneurons rather than putative pyramidal neurons in the primate dorsal anterior cingulate cortex. *Cerebral Cortex*, *29*, 2339–2352.

Kennerley, S. W., Behrens, T. E. J., & Wallis, J. D. (2011). Double dissociation of value computations in orbitofrontal and anterior cingulate neurons. *Nature Neuroscience*, *14*(12), 1581–1589.

Kennerley, S. W., Walton, M. E., Behrens, T. E. J., Buckley, M. J., & Rushworth, M. F. S. (2006). Optimal decision making and the anterior cingulate cortex. *Nature Neuroscience*, *9*, 940–947.

Khamassi, M., Quilodran, R., Enel, P., Dominey, P. F., & Procyk, E. (2015). Behavioral regulation and the modulation of information coding in the lateral prefrontal and cingulate cortex. *Cerebral Cortex*, *25*, 3197–3218.

Kolling, N., Behrens, T. E. J., Mars, R. B., & Rushworth, M. F. S. (2012). Neural mechanisms of foraging. *Science*, *336*, 95–98.

Kolling, N., Behrens, T., Wittmann, M. K., & Rushworth, M. (2016). Science direct multiple signals in anterior cingulate cortex. *Current Opinion in Neurobiology*, *37*, 36–43.

Kolling, N., Wittmann, M. K., Behrens, T. E. J., Boorman, E. D., Mars, R. B., & Rushworth, M. F. S. (2016). Value, search, persistence and model updating in anterior cingulate cortex. *Nature Neuroscience*, *19*, 1280–1285.

Kopell, N., Kramer, M. A., Malerba, P., & Whittington, M. A. (2010). Are different rhythms good for different functions? *Frontiers in Human Neuroscience*, *4*, 1–9.

Kouneiher, F., Charron, S., & Koechlin, E. (2009). Motivation and cognitive control in the human prefrontal cortex. *Nature Neuroscience*, *12*, 939–945.

La Camera, G., Fontanini, A., & Mazzucato, L. (2019). Cortical computations via metastable activity. *Current Opinion in Neurobiology*, *58*, 37–45.

Loh, K. K., Hadj-Bouziane, F., Petrides, M., Procyk, E., & Amiez, C. (2018). Rostro-caudal organization of connectivity between cingulate motor areas and lateral frontal regions. *Frontiers in Neuroscience*, *11*. 13786–17.

Loh, K. K., Procyk, E., Neveu, R., Lamberton, F., Hopkins, W. D., Petrides, M., et al. (2020). Cognitive control of orofacial motor and vocal responses in the ventrolateral and dorsomedial human frontal cortex. *Proceedings of the National Academy of Sciences of the United States of America.*, *117*, 4994–5005.

Mansouri, F. A., Tanaka, K., & Buckley, M. J. (2009). Conflict-induced behavioural adjustment: A clue to the executive functions of the prefrontal cortex. *Nature Reviews. Neuroscience*, *10*, 141–152.

Markov, N. T., Ercsey-Ravasz, M., Van Essen, D. C., Knoblauch, K., Toroczkai, Z., & Kennedy, H. (2013). Cortical high-density counterstream architectures. *Science*, *342*, 1238406.

Mars, R. B., Sotiropoulos, S. N., Passingham, R. E., Sallet, J., Verhagen, L., Khrapitchev, A. A., et al. (2018). Whole brain comparative anatomy using connectivity blueprints. *eLife*, *7*, 870.

Medalla, M., Gilman, J. P., Wang, J.-Y., & Luebke, J. I. (2017). Strength and diversity of inhibitory signaling differentiates primate anterior cingulate from lateral prefrontal cortex. *The Journal of Neuroscience*, *37*, 4717–4734.

Meder, D., Kolling, N., Verhagen, L., Wittmann, M. K., Scholl, J., Madsen, K. H., et al. (2017). Simultaneous representation of a spectrum of dynamically changing value estimates during decision making. *Nature Communications*, *8*, 1–11.

Miller, E. K., Lundqvist, M., & Bastos, A. M. (2018). Working memory 2.0. *Neuron*, *100*, 463–475.

Miltner, W. H. R., Braun, C. H., & Coles, M. G. H. (2001). Event-related brain potentials following incorrect feedback in a time-estimation task: Evidence for a "generic" neural system for error detection. *Journal of Cognitive Neuroscience*, *9*, 788–798. Available at: http://eutils.ncbi.nlm.nih.gov/entrez/eutils/elink.fcgi?dbfrom=pubmed&id=23964600&retmode=ref&cmd=prlinks.

Mitchell, D. J., Bell, A. H., Buckley, M. J., Mitchell, A. S., Sallet, J., & Duncan, J. (2016). A putative multiple-demand system in the macaque brain. *Journal of Neuroscience*, *36*, 8574–8585.

Mongillo, G., Rumpel, S., & Loewenstein, Y. (2018). Inhibitory connectivity defines the realm of excitatory plasticity. *Nature Neuroscience*, *21*(10), 1463–1470.

Monosov, I. E. (2017). Anterior cingulate is a source of valence-specific information about value and uncertainty. *Nature Communications*, *8*(134), 1–12.

Morecraft, R. J., Schroeder, C. M., & Keifer, J. (1996). Organization of face representation in the cingulate cortex of the rhesus monkey. *Neuroreport*, *7*, 1343–1348.

Murakami, M., Shteingart, H., Loewenstein, Y., & Mainen, Z. F. (2017). Distinct sources of deterministic and stochastic components of action timing decisions in rodent frontal cortex. *Neuron*, *94*. 908–919.e7.

Murray, J. D., Bernacchia, A., Freedman, D. J., Romo, R., Wallis, J. D., Cai, X., et al. (2014). A hierarchy of intrinsic timescales across primate cortex. *Nature Neuroscience*, *17*, 1661–1663.

Nácher, V., Hassani, S. A., & Womelsdorf, T. (2019). Asymmetric effective connectivity between primate anterior cingulate and lateral prefrontal cortex revealed by electrical microstimulation. *Brain Structure & Function*, *224*, 779–793.

Németh, G., Hegedüs, K., & Molnár, L. (1988). Akinetic mutism associated with bicingular lesions: Clinicopathological and functional anatomical correlates. *European Archives of Psychiatry and Neurological Sciences*, *237*, 218–222.

Niki, H., & Watanabe, M. (1979). Prefrontal and cingulate unit activity during timing behavior in the monkey. *Brain Research*, *171*, 213–224.

Noser, R., & Byrne, R. W. (2007). Mental maps in chacma baboons (Papio ursinus): Using inter-group encounters as a natural experiment. *Animal Cognition*, *10*, 331–340.

Palomero-Gallagher, N., Mohlberg, H., Zilles, K., & Vogt, B. (2008). Cytology and receptor architecture of human anterior cingulate cortex. *The Journal of Comparative Neurology*, *508*, 906–926.

Palomero-Gallagher, N., Vogt, B. A., Schleicher, A., Mayberg, H. S., & Zilles, K. (2009). Receptor architecture of human cingulate cortex: Evaluation of the four-region neurobiological model. *Human Brain Mapping*, *30*, 2336–2355.

Parvizi, J., Rangarajan, V., Shirer, W. R., Desai, N., & Greicius, M. D. (2013). The will to persevere induced by electrical stimulation of the human cingulate gyrus. *Neuron*, *80*, 1359–1367.

Passingham, R. E. (1996). Attention to action. *Philosophical Transactions of the Royal Society of London. Series B, Biological Sciences*, *351*, 1473–1479.
Passingham, R. E., & Wise, S. P. (2012). *The neurobiology of the prefrontal cortex: Anatomy, evolution, and the origin of insight*. OUP Oxford.
Pearson, J. M., Watson, K. K., & Platt, M. L. (2014). Decision making: The neuroethological turn. *Neuron*, *82*, 950–965.
Petrides, M., & Pandya, D. N. (1994). Comparative architectonic analysis of the human and the macaque frontal cortex. In F. Boller, & J. Grafman (Eds.), *Handbook of neuropsychology* (pp. 17–58). Amsterdam.
Pettine, W. W., Louie, K., Murray, J. D., & Wang, X.-J. (2020). Hierarchical network model excitatory-inhibitory tone shapes alternative strategies for different degrees of uncertainty in multi-attribute decisions. *bioRxiv*. https://doi.org/10.1101/2020.01.28.923649.
Picard, N., & Strick, P. L. (1996). Motor areas of the medial wall: A review of their location and functional activation. *Cerebral Cortex*, *6*, 342–353.
Powell, N. J., & Redish, A. D. (2016). Representational changes of latent strategies in rat medial prefrontal cortex precede changes in behaviour. *Nature Communications*, *7*, 12830.
Premereur, E., Janssen, P., & Vanduffel, W. (2018). Functional MRI in macaque monkeys during task switching. *Journal of Neuroscience*, *38*, 10619–10630.
Procyk, E., & Joseph, J.-P. (2001). Characterization of serial order encoding in the monkey anterior cingulate sulcus. *The European Journal of Neuroscience*, *14*, 1041–1046.
Procyk, E., Tanaka, Y. L., & Joseph, J.-P. (2000). Anterior cingulate activity during routine and non-routine sequential behaviors in macaques. *Nature Neuroscience*, *3*, 502–508.
Procyk, E., Wilson, C. R. E., Stoll, F. M., Faraut, M. C. M., Petrides, M., & Amiez, C. (2016). Midcingulate motor map and feedback detection: Converging data from humans and monkeys. *Cerebral Cortex*, *26*, 467–476.
Quilodran, R., Rothé, M., & Procyk, E. (2008). Behavioral shifts and action valuation in the anterior cingulate cortex. *Neuron*, *57*, 314–325.
Rich, E. L., & Wallis, J. D. (2016). Decoding subjective decisions from orbitofrontal cortex. *Nature Neuroscience*, *19*, 973–980.
Rothé, M., Quilodran, R., Sallet, J., & Procyk, E. (2011). Coordination of high gamma activity in anterior cingulate and lateral prefrontal cortical areas during adaptation. *Journal of Neuroscience*, *31*, 11110–11117.
Sallet, J., Mars, R. B., Quilodran, R., Procyk, E., Petrides, M., & Rushworth, M. F. (2011). Neuroanatomical basis of motivational and cognitive control: A focus on the medial and lateral prefrontal cortex. In R. B. Mars, J. Sallet, M. F. S. Rushworth, & N. Yeung (Eds.), *Neural basis of motivational and cognitive control* The MIT Press.
Sallet, J., Quilodran, R., Rothé, M., Vezoli, J., Joseph, J.-P., & Procyk, E. (2007). Expectations, gains, and losses in the anterior cingulate cortex. *Cognitive, Affective, & Behavioral Neuroscience*, *7*, 327–336.
Schaeffer, D. J., Hori, Y., Gilbert, K. M., Gati, J. S., Menon, R. S., & Everling, S. (2020). Divergence of rodent and primate medial frontal cortex functional connectivity. *Proceedings of the National Academy of Sciences of the United States of America*, *5*, 202003181–202021689.
Scholl, J., Kolling, N., Nelissen, N., Stagg, C. J., & Harmer, C. J. (2017). Excitation and inhibition in anterior cingulate predict use of past experiences. *Elife*, *6*, e20365. https://doi.org/10.7554/eLife.20365.
Seo, H., Barraclough, D. J., & Lee, D. (2007). Dynamic signals related to choices and outcomes in the dorsolateral prefrontal cortex. *Cerebral Cortex*, *17*(Suppl. 1), i110–i117.
Seo, H., & Lee, D. (2007). Temporal filtering of reward signals in the dorsal anterior cingulate cortex during a mixed-strategy game. *Journal of Neuroscience*, *27*, 8366–8377.

Shen, C., Ardid, S., Kaping, D., Westendorff, S., Everling, S., & Womelsdorf, T. (2015). Anterior cingulate cortex cells identify process-specific errors of attentional control prior to transient prefrontal-cingulate inhibition. *Cerebral Cortex*, *25*, 2213–2228.

Sheth, S. A., Mian, M. K., Patel, S. R., Asaad, W. F., Williams, Z. M., Dougherty, D. D., et al. (2012). Human dorsal anterior cingulate cortex neurons mediate ongoing behavioural adaptation. *Nature*, *488*, 218–221.

Shidara, M., & Richmond, B. J. (2002). Anterior cingulate: Single neuronal signals related to degree of reward expectancy. *Science*, *296*, 1709–1711.

Shima, K., & Tanji, J. (1998). Role for cingulate motor area cells in voluntary movement selection based on reward. *Science*, *282*, 1335–1338.

Silvetti, M., Vassena, E., Abrahamse, E., & Verguts, T. (2018). Dorsal anterior cingulate-brainstem ensemble as a reinforcement meta-learner. O'Reilly J, ed. *PLoS Computational Biology*, *14*. e1006370–32.

Spitmaan, M., Seo, H., Lee, D., & Soltani, A. (2020). Multiple timescales of neural dynamics and integration of task-relevant signals across cortex. *Proceedings of the National Academy of Sciences of the United States of America*, *21*. 202005993–10.

Stoll, F. M., Fontanier, V., & Procyk, E. (2016). Specific frontal neural dynamics contribute to decisions to check. *Nature Communications*, 7, 11990.

Sul, J. H., Kim, H., Huh, N., Lee, D., & Jung, M. W. (2010). Distinct roles of rodent orbitofrontal and medial prefrontal cortex in decision making. *Neuron*, *66*, 449–460.

Talairach, J., Bancaud, J., Geier, S., Bordas-Ferrer, M., Bonis, A., Szikla, G., et al. (1973). The cingulate gyrus and human behaviour. *Electroencephalography and Clinical Neurophysiology*, *34*, 45–52.

Tervo, D., Kuleshova, E., Manakov, M., Proskurin, M., Karlsson, M., Lustig, A., et al. (2020). Anterior cingulate cortex directs exploration of alternative strategies. *bioRxiv*. https://doi.org/10.1101/2020.05.23.098822.

Tervo, D. G. R., Proskurin, M., Manakov, M., Kabra, M., Vollmer, A., Branson, K., et al. (2014). Behavioral Variabilitythrough stochastic choice and its gating by anterior cingulate cortex. *Cell*, *159*, 21–32.

Tremblay, R., Lee, S., & Rudy, B. (2016). GABAergic interneurons in the neocortex: From cellular properties to circuits. *Neuron*, *91*, 260–292.

Vogt, B. A. (2016). Midcingulate cortex: Structure, connections, homologies, functions and diseases. *Journal of Chemical Neuroanatomy*, *74*, 28–46.

Vogt, B. A., Nimchinsky, E. A., Vogt, L. J., & Hof, P. R. (1995). Human cingulate cortex: Surface features, flat maps, and cytoarchitecture. *The Journal of Comparative Neurology*, *359*, 490–506.

Vogt, B. A., & Paxinos, G. (2012). Cytoarchitecture of mouse and rat cingulate cortex with human homologies. *Brain Structure & Function*, *219*, 185–192.

Voloh, B., & Womelsdorf, T. (2018). Cell-type specific burst firing interacts with theta and beta activity in prefrontal cortex during attention states. *Cerebral Cortex*, *28*, 4348–4364.

Walsh, M. M., & Anderson, J. R. (2011). Modulation of the feedback-related negativity by instruction and experience. *Proceedings of the National Academy of Sciences of the United States of America*, *108*, 19048–19053.

Wang, X.-J. (2020). Macroscopic gradients of synaptic excitation and inhibition in the neocortex. *Nature Reviews. Neuroscience*, 1–10.

Wasmuht, D. F., Spaak, E., Buschman, T. J., Miller, E. K., & Stokes, M. G. (2018). Intrinsic neuronal dynamics predict distinct functional roles during working memory. *Nature Communications*, *9*, 1–13.

White, J. K., Bromberg-Martin, E. S., Heilbronner, S. R., Zhang, K., Pai, J., Haber, S. N., et al. (2019). A neural network for information seeking. *Nature Communications*, *10*, 1–19.

Williams, Z. M., Bush, G., Rauch, S. L., Cosgrove, G. R., & Eskandar, E. N. (2004). Human anterior cingulate neurons and the integration of monetary reward with motor responses. *Nature Neuroscience*, *7*, 1370–1375.

Wilson, C. R. E., Vezoli, J., Stoll, F. M., Faraut, M. C. M., Leviel, V., Knoblauch, K., et al. (2016). Prefrontal markers and cognitive performance are dissociated during progressive dopamine lesion. *PLoS Biology*, *14*, e1002576.

Womelsdorf, T., Valiante, T. A., Sahin, N. T., Miller, K. J., & Tiesinga, P. (2014). Dynamic circuit motifs underlying rhythmic gain control, gating and integration. *Nature Neuroscience*, *17*, 1031–1039.

Zilles, K., & Palomero-Gallagher, N. (2017). Multiple transmitter receptors in regions and layers of the human cerebral cortex. *Frontiers in Neuroanatomy*, *11*, e1000489–26.

4.3. Linking states and sequences

The last chapter proposed that transitioning network states subserve peregrination of network activity between and within two pseudo-attractor domains of exploration and exploitation, with respectively dynamic and stable behaviors (Enel et al., 2016; Stoll et al., 2016).

In Chapter 3 **Fig. 8**, we have shown that states are maintained, and transitions induced, by inhibitory currents and neurons in the MCC model. But how exactly do these inhibitory currents maintain network states and induce transitions? More precisely, what is the role of both GABA-A and GABA-B currents in inducing transitions, and how are network states maintained through GABA-B currents? Furthermore, does MCC collective activity show network dynamic and stable coding, as well as two pseudo-attractor spaces (putatively for exploration and exploitation), as observed experimentally?

Dual contribution of inhibitory currents to transitions

To understand network dynamics more clearly, we grouped neurons according to the HMM state in which they fire the most, defined as the state s for which the emission of neuron n is maximal in the HMM emission matrix $E(s,n)$, i.e. $\underset{s}{\operatorname{argmax}} E(s,n)$. This allowed us to define 4 mixed (excitatory and inhibitory) subpopulations, one for each state, where each neuron belonged to one state only. In the following, we defined excitatory and inhibitory subpopulations as the excitatory and inhibitory neurons of each subpopulation. As such, when referring to an excitatory or inhibitory subpopulation, there is a corresponding inhibitory or excitatory subpopulation, respectively.

We found that major variations of averaged inhibitory currents received by each inhibitory subpopulation (inhibitory neurons underlying a given state, i.e. having their largest mean firing frequency in that state) actually correlate with transition times between two states (**Fig. 1**), and that GABA-A and B showed complementary roles of the 2 inhibitory currents.

On the one hand, we found that the GABA-B current impinging on the subpopulation underlying the next state (**Fig. 1a**) decreases long before the transition (~500ms). Because no other synaptic current showed such anticipatory variation (not shown), this GABA-B decrease most likely caused the transition to the next state. Actually, the higher frequency defining the current (e.g. previous or following) inhibitory subpopulation was causally accounted for by the lower amount of received GABA-B currents (**Fig. 1a**, see below).

On the other hand, the GABA-A current (**Fig. 1b**) decreased just before the transition (~10ms), with a larger decrease in the subpopulation underlying the next state, defining the precise moment when the transition, gated by GABA-B dynamics, took place.

Altogether, these data indicated that collective network dynamics were essentially determined by competitive cross-inhibition between inhibitory subpopulations, which was central in setting state maintenance and transitions. Specifically, 1) the least inhibited (most disinhibited) inhibitory subpopulation induced the current network state, 2) transition to a new state occurred through the conjunction of a slow and progressive GABA-B disinhibition terminated by an additional fast GABA-A disinhibition triggering of the next subpopulation.

A rich repertoire of static and dynamic attractors in synaptic engrams underlying stable and dynamic coding

The question arises: how do inhibitory neurons associated with the current state receive less inhibitory currents? We reasoned that inhibitory subpopulations should project weaker inhibitory synapses onto themselves, and stronger synapses onto other subpopulations. To assess this hypothesis, we measured the average synaptic weights between and within each subpopulation (**Fig. 2a**) and found that weights were indeed weaker within each inhibitory subpopulation, compared to between them (**Fig. 2a**, Inh→Inh., blue within vs. orange between subpopulations), resulting in "anti-" or "negative" assemblies of inhibitory neurons, with strong synaptic cross-inhibition between them. This synaptic structure accounted for the dynamical properties (states, transitions) observed in these assemblies (see above). Contrary to the classical notion of (e.g. Hebbian) neural assemblies (defined by excitatory neurons being more connected with each other among the assembly than with neurons outside of the assembly), "anti-assemblies" are defined here by how weakly neurons connect to other neurons in the assembly, compared to the rest of the network (i.e. other assemblies).

Furthermore, inhibitory subpopulations projected weaker weights onto their corresponding excitatory subpopulations (**Fig. 2a**, Inh.→Exc., blue vs. orange). Combined with the fact that excitatory subpopulations projected similar weights to all excitatory and inhibitory subpopulations (**Fig. 2a**, Exc.→Exc. and Exc.→Inh., blue vs. orange), this confirmed that excitatory subpopulations are defined by inhibitory projections, i.e. namely, weaker inhibitory connections to inhibitory neurons and stronger inhibitory connections to excitatory neurons within each subpopulation.

In summary, the network dynamics analyzed through HMM allowed us to define neuronal subpopulations, from which we were able to backtrack organized structure in the form of inhibitory anti-assemblies, within the randomly initialized synaptic weight matrix. Note here that no form of learning was present in defining assemblies and that they purely emerged from structural and synaptic heterogeneity, i.e. randomness of connection sparsity and weights. The principal factor at play here was that strong and slow synaptic GABA-B currents amplified the effect of the synaptic weight matrix's random structure on network dynamics.

In principle, HMMs assume stationary data, thus the synaptic structure we could unveil through them is limited to stationary activity, and not dynamic sequences of neural activity. These sequences might nevertheless exist, emerging through GABA-B slow currents propagating along synaptic chains (pathways) within the unveiled assemblies of the synaptic weight matrix.

To address this possibility, we reordered neurons within each subpopulation according to their average median activation times (**Fig. 2b** top). Within the time period when the network is in a given state, the median activation time of a neuron of the corresponding state's subpopulation was taken as the timing of the neuron's median spike (for a neuron firing 5 spikes, the timing of the 3rd spike). Median activation times were then averaged across all time periods when the network was in the associated state (i.e. all green time periods for a neuron within the green state's subpopulation, **Fig. 2b** bottom). When doing so, we could observe a rich repertoire of dynamic and static attractors in MCC simulations, with repeating sequences of activity of neurons activating successively within states/subpopulations (**Fig. 2b** bottom, green, orange, and red bottom states) and systematic persistent activities in others (**Fig. 2b** bottom, purple top

state). The slopes of correlations between neural index and timing of spikes within HMM state subpopulations confirmed this analysis, with horizontal slopes for static attractor states and diagonal slopes for dynamic attractor states (**Fig. 2b** bottom, essentially horizontal slopes for purple top state, and diagonal slopes for green, orange and red bottom states).

Sequences of neural activity should be accompanied by a directed synaptic chain in the synaptic weight matrix. Within the synaptic matrix connecting pre- and post-synaptic excitatory neurons ordered according to their activation times, a synaptic chain would correspond to 1) stronger synapses in the forward direction, i.e. on diagonals below the main diagonal (**Fig. 2c**, yellow band below the red main diagonal), from pre-synaptic to post-synaptic neurons situated further along the sequence, and 2) weaker synapses in the backward direction, i.e. on diagonals above the main diagonal (**Fig. 2c**, dark blue band above the red main diagonal). We studied the average difference between forward and backward weight diagonals (i.e. below and above the main diagonal) for each synaptic type within subpopulations. We found significantly weaker forward (stronger backward) synapses for Inh.→Inh. and Inh.→Exc. connections only (**Fig. 2d**, blue and purple curves and shaded areas below zero, respectively), by opposition to Exc.→Exc. and Exc.→Inh. connections, which displayed no specific trend (**Fig. 2d**, red and green curves and shaded areas centered on zero). Thus, within each subpopulation, inhibitory neurons were connected through forward weaker synapses, with each inhibitory neuron inhibiting the following neurons less, forming an "anti-synaptic chain". Such disinhibition would result in higher frequency in subsequent neurons, propagating the sequence of neural activity. This effect was found when averaging across all states (even those resulting in persistent neural activity), suggesting that the synaptic chains of states resulting in sequences were more pronounced than the shown average (across states displaying static activity and sequences) shown in Fig. 2d.

At the network level, these sequential or persistent activities in subpopulations impacted network activity, resulting in alternation between dynamic (**Fig.2e**, yellow diagonals) and stable (**Fig.2e**, yellow squares) network activity.

Sequential peregrination of network state within two meta-states

The presence of a temporal structure of network activity at the 100ms-1s HMM state temporal scale suggests that there might be a structure at larger temporal scales, i.e. the peregrination between network states itself could be structured. This structure could be static, e.g. correspond to a random alternation between two-macroscopic static attractors, each of which including one or several similar states with underlying persistent activity. Such a possibility could for example putatively correspond to a dichotomy between exploratory and exploitative strategies. Alternatively, this structure could be sequential, i.e. displaying reoccurring specific sequences of states, as during the successive evaluation of network states, putatively encoding different behavioral strategies. Both possibilities may even co-exist in the same network.

Simple visual inspection seemed to suggest that network states were indeed organized in sequences of N-states (**Fig. 2b**, green-orange-red 3-state sequences). We assessed whether network state transitions solely depended upon the previous state (i.e. were Markovian), or organized into longer sequences, with certain sequences of N states (N > 2) more probable than others. To answer this question, we calculated the Shannon entropy of the probability of N-state sequences in the simulation data (**Fig. 3a**, red curve), and compared this number to a control condition where N-state sequences were solely derived from information about 2-state

sequences (a.k.a. the HMM transition matrix), i.e. purely Markovian sequences of 2 states (where the probability of the next state depended exclusively upon the current state, **Fig. 3a**, black line). We observed that the longer sequences were, the more the Shannon entropy of N-state sequence probabilities decreased compared to those of Markovian sequences. This indicated that there was temporal dependence of states to the history of states beyond simply the previous state, with certain sequences of N-states more probable than others, i.e. states were sequentially organized at a longer timescale.

In the example considered, visual inspection of the cross-temporal similarity of network activity vectors at each time step (**Fig. 2e** and **Fig. 3b**) also suggested that the network alternated between two macroscopic meta-states, one being stable (large yellow squares, e.g. 26-33 seconds) and the other dynamic (yellow diagonals grouped together, e.g. 10-17 seconds). Coloring the similarity matrix according to previously established HMM network states (**Fig. 3b** left, bottom right triangle, cyan rectangles corresponding to green and orange HMM states, orange rectangles corresponding to the red and purple HMM states) matched this macroscopic structure well, suggesting two macroscopic meta-states existed and each corresponded to two combined HMM states. Visualizing network activity in a reduced dimensionality (PCA) space (colored as above, **Fig. 3b** right) also revealed two separated macroscopic meta-states, with orbits peregrinating between meta-states, as well as within them between their constitutive states.

In conclusion, peregrination of network states was organized according to alternations between two macroscopic meta-states. These two meta-states could putatively subserve exploratory and exploitative regions, i.e. with respectively dynamic (cyan meta-state) vs static (orange meta-state) global behavior, as unraveled experimentally (Enel et al., 2016; Stoll et al., 2016). Network trajectory orbits sequentially visited underlying HMM states within these meta-states (putatively encoding different exploratory and exploitative strategies). At a lower temporal scale, each network state itself contained neural sequences or persistent activity, subserving dynamic and stable coding. Together, this opened the possibility to encode information at different timescales in the network (states with sequences for short information and persistent activity for intermediate durations, as well as dynamic and stable macroscopic meta-states for longer and longest information timescales respectively).

Such a dynamical richness could form the neural substrate allowing the temporal integration of information at multiple timescales and behavioral switches necessary to MCC function. Furthermore, it shows the promising potential of GABA-B neuromodulation in actual monkeys learning behavioral tasks which induce synaptic plasticity within MCC networks. Indeed, such a large dynamical repertoire was obtained simply through GABA-B-mediated amplification of the effects of the synaptic matrix's randomized heterogeneity on network dynamics. As GABA-B temporally amplifies even minute differences in synaptic structure, it should increase the impact of synaptic plasticity and resulting synaptic structures on behaviors, thus making learning more effective. This hypothesis deserves future exploration.

References

Enel, P., Procyk, E., Quilodran, R., and Dominey, P. F. (2016). Reservoir Computing Properties of Neural Dynamics in Prefrontal Cortex. *PLOS Comput. Biol.* 12, e1004967. doi:10.1371/journal.pcbi.1004967.

Stoll, F. M., Fontanier, V., and Procyk, E. (2016). Specific frontal neural dynamics contribute to decisions to check. *Nat. Commun.* 7, 1–14. doi:10.1038/ncomms11990.

Figure legends

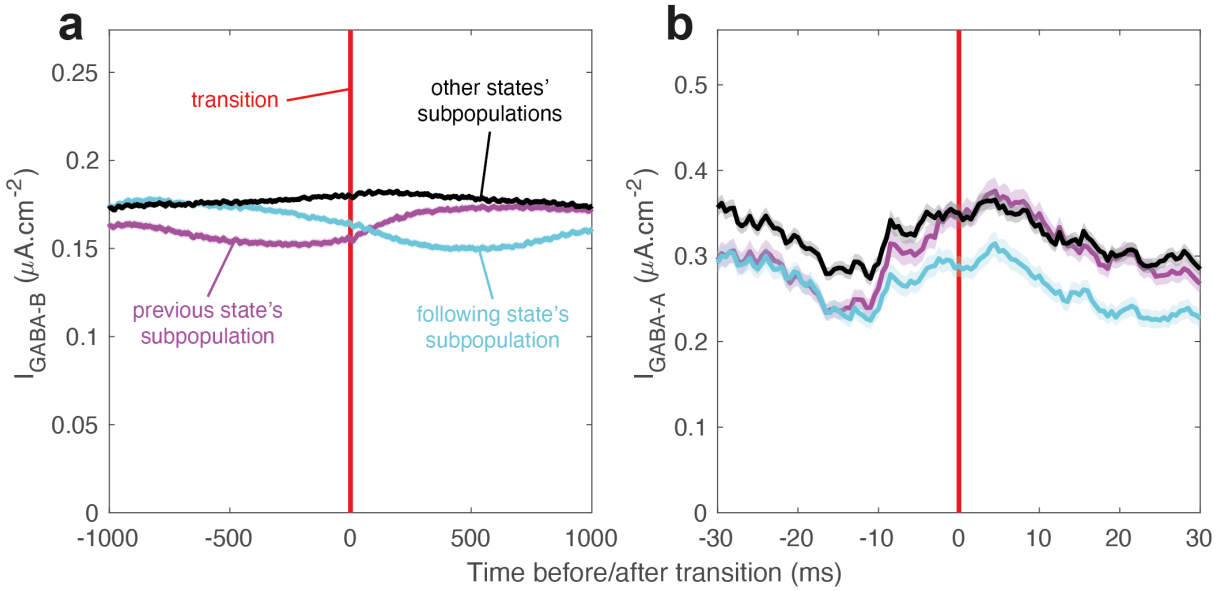

Figure 1. Dual contribution of inhibitory currents to transitions. GABA-B (**a**) and GABA-A (**b**) currents received by each inhibitory subpopulation (i.e. neurons of each state), around transitions between two states. Only transitions between 2 states that last more than 100ms are included.

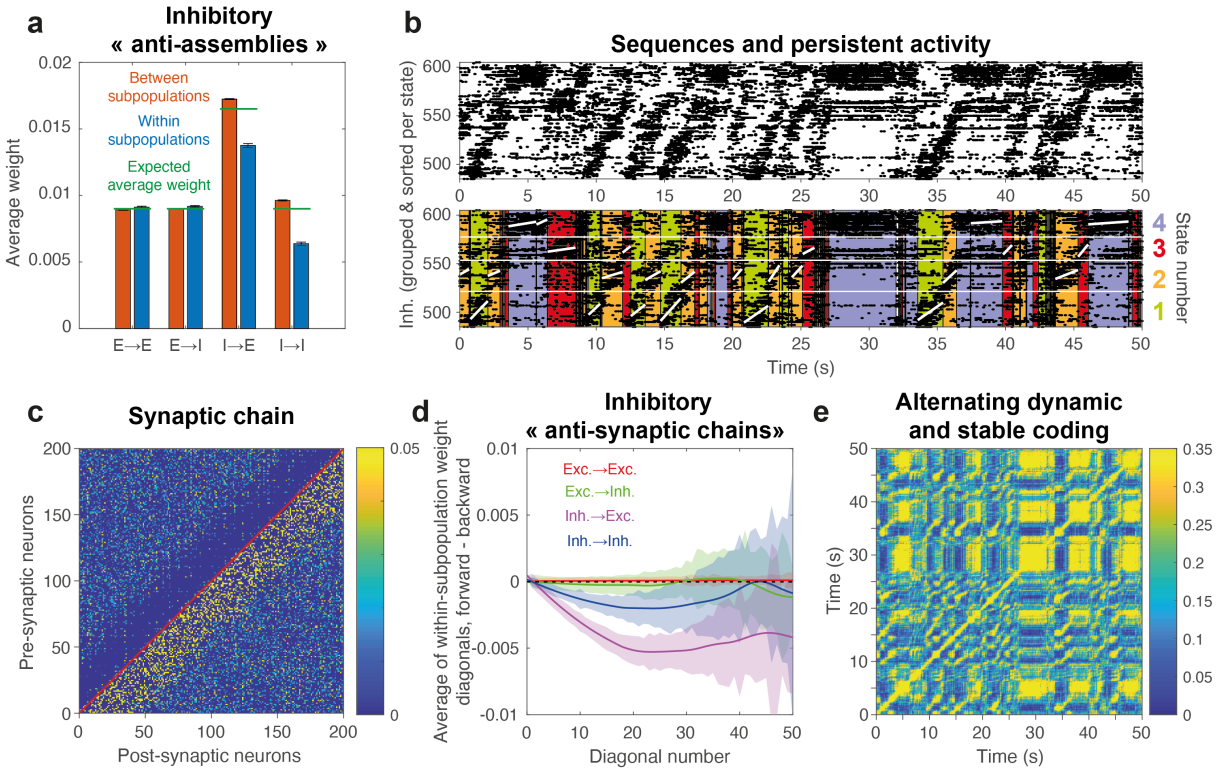

Figure 2. Rich repertoire of static and dynamic attractors and synaptic engrams underlying stable and dynamic coding. (**a**) Average weights between and within neurons associated with a state, averaged over all couples of states for 100 MCC network simulations. Green lines indicated expected average weights, taking into account synapse sparsity (Inh.→Exc. weights are more probable, since $p_{E\to E} = p_{E\to I} = p_{I\to I} = 0.3$ and $p_{I\to E} = 0.55$, see Chapter 3 Methods). (**b**) Raster plot (top), and identical raster plot with colored HMM state periods (bottom) of a MCC simulation lasting 50s. Thin white horizontal lines delimit subpopulations of each HMM state (from bottom to top, states 1 to 4 are the green, orange, red, and purple states respectively). Black horizontal lines separate state periods. Large white diagonal lines within state periods indicate strong correlations between neural identity and timing of spikes within the subpopulation of the current HMM state period (only $p < 0.05$ are shown). (**c**) Synaptic weight matrix describing how the synaptic weights of a synaptic chain would connect excitatory pre-synaptic and post-synaptic neurons, when neurons are ordered according to their activation time in the resulting sequence. Red diagonal line is drawn across synapses of neurons onto themselves (i.e. autapses). Synaptic matrix taken from an example network simulation in the Chapter 5 article. (**d**) Average value of synaptic matrix diagonals, for diagonals progressively further away from the middle diagonal. Shown are mean +/- 95% confidence intervals of the standard error of the mean over 100 MCC network simulations. Purple curve (Inh.→Exc.) is farther from 0 than the blue curve (Inh.→Inh.) for the same reasons as in (**a**). (**e**) Cosine similarity between network activity vectors at different timepoints. Neural frequency was estimated through 100ms bins of spike data.

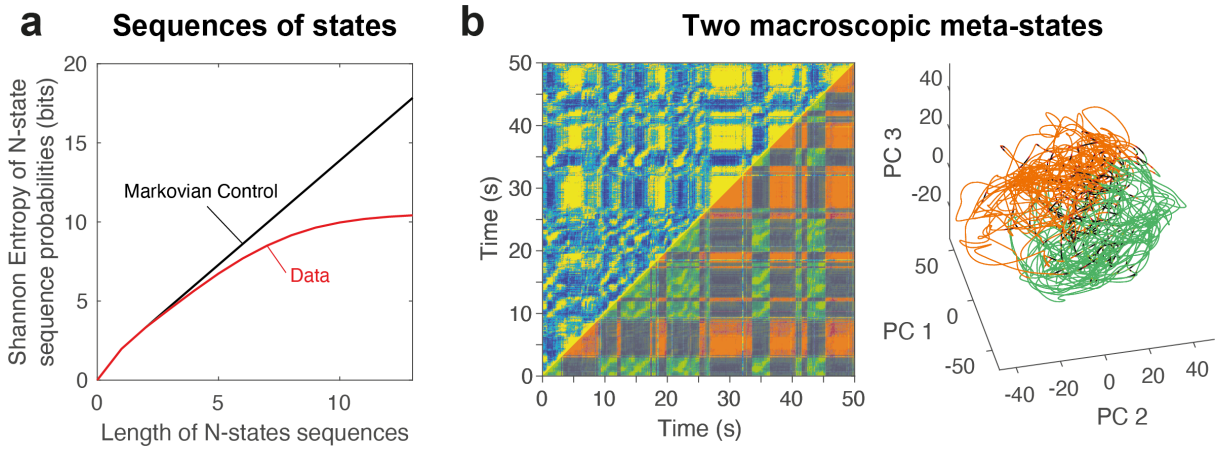

Figure 3. Sequential peregrination of network states within two macroscopic meta-states. (**a**) Shannon entropy of the probability of N-state sequences (during the 60os of the MCC simulation shown in **Fig. 2b,d** and **Fig. 3b**), compared to that of purely Markovian sequences of N-states (where N-state sequences are derived from 2-state sequences, a.k.a. the HMM transition matrix). Other MCC simulations exhibited similar results (not shown). (**b**) (Left) Same as **Fig. 2d**, but with a superposed coloring scheme in the bottom right triangle reflecting macroscopic attractors. In this second coloring scheme, the 1st macroscopic (orange) meta-state is constituted of the green and orange HMM states (from **Fig. 2b** bottom), and the 2nd macroscopic meta-state (cyan) of the red and purple HMM states (from **Fig. 2b** bottom). The intersections between meta-states is colored in black. (Right) Network activity during 20os colored as above within a reduced dimensionality space estimated via PCA (principal component analysis) of neural frequency (estimated as the convolution of spikes with a Gaussian temporal window where $\sigma = 100\ ms$) across 60os.

Chapter 5. Mechanistic origin of robust neural trajectory replay within synaptic noise

5.1. Summary

In the previous chapters, strong and slow inhibitory GABA-B currents induced long-lasting labile network states with neural activity sequences within them. However, these network states and sequences originate from the synaptic matrix's random structure amplified by slow GABA-B synaptic currents, and are thus not learned nor related to external stimuli in the models. In contrast, neural trajectories, i.e. sequences of transient sparse neural activity, prominently observed for working memory and navigation in rodent PFC and hippocampus (HP) respectively, propagate during behavior and are intrinsically generated during subsequent sleep and awake immobility without external stimuli. This hints at the existence of underlying synaptic chains (pathways) learned through spike-timing dependent plasticity (STDP), being subsequently triggered through an internal or external trigger. However, the asynchronous irregular (AI) and even chaotic activity regime of awake cortex can result in incessant spontaneous replays and destabilized sequence propagation when triggering synaptic chains, hindering behavioral performance. Conversely, pack propagation may perturb global AI network activity, e.g. prohibiting other concurrent network computations and trajectory replays, hindering other behaviors. What biophysical mechanisms allow sequences to be reliably evoked when necessary (*controllability*), and steadily propagate (*stability*), without significantly altering network activity (*independence*), within potentially jeopardizing chaotic synaptic noise?

We modeled a biophysically constrained recurrent network of conductance-based Integrate-and-Fire neurons, whose balanced excitatory and inhibitory currents led to AI chaotic dynamics. Presentation of a trajectory stimulus led to the learning of synaptic chains through STDP and synaptic scaling, inducing replays after a triggering stimulus or spontaneously (due to AI dynamics) with varying degrees of propagation stability, as mentioned above. Spiking was driven by inhibitory GABA-A current fluctuations outside of trajectory replay, and strong excitatory NMDA current average within trajectory replay. This allowed us to predict that an excitatory frequency threshold separated both activity regimes in a reduced model, and model transitions between them as bistable excitatory frequency dynamics with added random noise.

Armed with this knowledge, we identified three biophysical mechanisms which can increase trajectory replay controllability and stability: 1) slow inhibitory currents, 2) combining tonic frequency-independent inhibition with stronger recurrent excitatory functional connectivity, and 3) spike-mediated CAN and AHP ionic currents promoting intrinsic, transient (i.e. weaker than conditional) bistability. We found that, while increased controllability and stability generally decreased independence, CAN and AHP preserved trajectory independence, intrinsic transient bistability alleviating constraints on synapse-mediated pack propagation. Reliable replay with the aforementioned mechanisms was robust to variation of model parameters, and modulating the STDP temporal window and trajectory stimulus allowed reliable replay of many different attractor types (i.e. Hebbian assemblies, synfire chains, Hebbian phase sequences, ring attractors, as well as possible uni-/bi-directional propagation), reinforcing the genericity of the model and its mechanisms across cerebral structures and species.

5.1.1. Contributions

I developed the biophysical neural network model and all analyses, participated to the elaboration of reduced models, wrote the first draft of the article and subsequently reviewed it entirely, and produced all figures.

5.2. Article

Biophysical emergence of reliable neural trajectories for cognitive functions under disordered brain dynamics

Matthieu Sarazin[1], David Medernach[1], Jérémie Naudé[2*], and Bruno Delord[1*]

[1] Institut des Systèmes Intelligents et de Robotique, Sorbonne Université, Centre National de la Recherche Scientifique, UMR 7222, 75005 Paris, France,

[2] Institut de Biologie Paris Seine, Sorbonne Université, Centre National de la Recherche Scientifique, Institut national de la santé et de la recherche médicale, UMR 8246 Neuroscience, 7 quai Saint Bernard, 75005 Paris, France

[*] Equal contributions

Abstract

Neural trajectories propagate as activity packs on connective pathways embedded within recurrent networks, subserving cognitive representations across structures and species. In awake animals, asynchronous irregular network dynamics exert a profoundly disorganizing influence that could either spuriously and incessantly induce neural trajectories, or jeopardize ongoing ones. In biophysical recurrent network models endowed with plasticity, we assessed which specific intrinsic and synaptic processes are required for functional trajectories under neural noise. Theoretical analysis and simulations of the model unraveled that trajectory replays organize around a frequency threshold. This threshold separates inhibitory fluctuation-driven spontaneous spiking and a deterministic excitatory-driven active regime of propagation along the learned connective pathway. More precisely, we identify three specific processes – lowered inhibitory fluctuations, strong tonic inhibition and functional excitatory connectivity, and increased CAN/AHP conductance – that increase regimes separation and qualitative replays (i.e. reliably evoked and stably propagated). The latter one further provides independence between replay and network activity, alleviating constraints on synaptic-mediated propagation. Dual regime-based reliable replays proved robust in the parameter space, suggesting its genericity across neural structures. Moreover, we find that they generalize to a wide spectrum of known discrete and continuous attractors (Hebbian assemblies, synfire chains, Hebbian phase sequence, ring attractors), with steady-state dynamics or uni-/bi-directional propagation. The dual regime mechanism underlying reliable neural trajectory replays therefore both constitutes an unprecedented generic biophysical principle and provides a unified framework accounting for the generation of complex dynamics robust to neural noise in the awake state required for cognition.

Introduction

Neural trajectories, i.e. sequences of transient neural activity, subserve many brain functions across species and cerebral structures. Neural trajectories are prevalent during working memory, indirectly observed as sequences of neural selectivity (Cromer et al., 2010; Hussar and Pasternak, 2012; Lara and Wallis, 2014; Lundqvist et al., 2018) or delay-selective neurons (Batuev, 1994) in monkey prefrontal cortex (PFC), and directly observed as neural activity sequences in rodent medial PFC (mPFC; Yang et al., 2014; Bakhurin et al., 2017; Bolkan et al., 2017; Schmitt et al., 2017; Rikhye et al., 2018). These neural sequences are not exclusive to PFC, also being observed in many other cortical and sub-cortical structures (Hoffman and McNaughton, 2002; Crowe et al., 2010; Harvey et al., 2012; Mello et al., 2015; Akhlaghpour et al., 2016; Bakhurin et al., 2016, 2017; Runyan et al., 2017; Rikhye et al., 2018). Notably, navigational trajectories prevalently activate sequences of spatially selective neurons within rodent hippocampus (HP; O'Keefe and Dostrovsky, 1971). Such neural trajectories are subsequently replayed offline (e.g. during awake quiet immobility, consummatory behavior, wheel running, and slow-wave or rapid eye-movement sleep) at fast (Skaggs and McNaughton, 1996; Skaggs et al., 1996; Kudrimoti et al., 1999; Nádasdy et al., 1999; Lee and Wilson, 2002; Diba and Buzsáki, 2007; Ji and Wilson, 2007; Davidson et al., 2009; Peyrache et al., 2009; Mizuseki et al., 2012; Jadhav et al., 2016) or slower (behavioral) timescales (Louie and Wilson, 2001; Pastalkova et al., 2008; Itskov et al., 2011; Mizuseki et al., 2012). Similar navigational trajectory sequences experienced during behavior (Fujisawa et al., 2008; Ito et al., 2015; Zielinski et al., 2019) and replayed offline during awake immobility (Jadhav et al., 2016; Kaefer et al., 2020) and slow-wave sleep (Euston et al., 2007; Peyrache et al., 2009; Johnson et al., 2010) have been observed in the mPFC, as well as other structures (Ji and Wilson, 2007; O'Neill et al., 2017; Angulo-Garcia et al., 2018). Altogether, the existence of sequences in different functional contexts and many cerebral structures hints at generic mechanisms underlying their emergence and propagation.

Neural trajectories are intrinsically generated since they can occur offline, when sensory inputs and motor outputs are absent, suggesting the existence of underlying learned synaptic structures within these recurrent networks. A natural candidate for the biophysical learning rule leading to the emergence of neural trajectories is the ubiquitous Spike-Timing Dependent Plasticity (STDP) (Bi and Poo, 1998), in which pre- and post-synaptic potentials lead to synaptic potentiation or depression according to the temporal difference between them, potentially inducing the formation of synaptic chains (Clopath et al., 2010). STDP is observed across structures (Abbott and Nelson, 2000), and can thus account for the ubiquity of intrinsically-generated synaptic chain-induced trajectories.

However, a major issue concerns the ability to learn and express functional neural trajectories within noisy brain dynamics during the awake state. It remains unclear how neural trajectories can be learned, emerge and propagate within globally disorganized neuronal activity in the awake state in e.g. cortical networks, which present asynchronous (Riehle et al., 1997; Brunel, 2000; Poulet and Petersen, 2008) and irregular (CV~1, Compte, 2003; Shinomoto et al., 2005) activity characteristic of the high conductance state (Destexhe et al., 2003). Their dynamics is furthermore chaotic (London et al., 2010), i.e. repeated presentations of the same external stimulus lead to very different high-dimensional responses due to internal cortical activity and the sensitivity to initial conditions. These questions are particularly challenging for neural trajectories compared to standard, static neural assemblies. Neural trajectories are dynamical representations likely based on

unidirectional weights, being thus more fragile than static synaptic reverberation within neuronal Hebbian assemblies with bidirectional weights (Hebb, 1949; Brunel and Wang, 2001). Moreover, stabilizing mechanisms of neuronal assemblies (e.g. intrinsic properties; Camperi and Wang, 1998; Koulakov et al., 2002; Goldman et al., 2003; Compte, 2006) may not identically apply to sequences, since activity is not maintained within a static – but rather a continuously changing – pool of neurons.

Here we operationalize the constraints posed to sequence learning by chaotic dynamics. First, chaotic and noisy synaptic transmission can hinder sequence replay by a trigger or induce spontaneous replays, questioning the issue of *controllability* of learned replays (i.e. the ability to trigger replays solely when required). Second, chaotic noise alter the *stability* of sequence propagation once triggered. Third, trajectory replay could strongly modulate network activity of neurons outside the trajectory, perturbing the *independence* of any other concurrent computations within the local network considered (e.g. independent replay of multiple sequences simultaneously). Most importantly, while neural trajectories are usually learned with artificial learning rules (Sussillo and Abbott, 2009; Fiete et al., 2010; Laje and Buonomano, 2013; Xue et al., 2021) or replayed in the absence of chaotic noisy dynamics (Liu and Buonomano, 2009; Fiete et al., 2010), none dissect in detail how biophysical mechanisms could allow these constraints (controllable triggering, stable propagation and network independence) to be met. Here, we propose a detailed realistic biophysical model in which continuous synaptic structures and reliable neural trajectories emerge from STDP in the asynchronous irregular (AI) regime. The model presents most physiological properties of local cortical recurrent networks, be it the synaptic architecture, conductance-based neural model, or AI activity regime.

Using simulations and theoretical analyses, we discovered the intrinsic and synaptic determinants of functionally reliable, robust and generic attractor dynamics, including neural trajectories, despite the permanent disorganizing effects of chaotic asynchronous irregular (AI) dynamics. We show that synaptic plasticity (STDP and synaptic scaling) can lead to a diversity of replay types, from unstable to stable replays and from spontaneous incessant to triggered-only replays. Neural trajectories consisted in the propagation of an activity pack along the connective pathway through deterministic associative NMDA local transmission at high frequencies, contrasting with spontaneous AI activity, which was based on GABA-A-fluctuation at low frequencies. Our theoretical analyzes characterized a frequency threshold separating spontaneous and pack propagation regimes, and point at mechanisms increasing the separation between regimes as key to trajectory stability and controllability. We then identify three classes of biophysical processes increasing such separation, being lowered inhibitory fluctuations, strong tonic inhibition and excitatory connectivity, as well as intrinsic (afterhyperpolarization/afterdepolarization) currents. The later intrinsic properties also grant a relative independence between trajectory replay and network activity outside the trajectory, alleviating constraints on synaptic pathways. Finally, we show that these results are robust to model parameters and generalize to a spectrum of static, dynamic, discrete or continuous attractor subserving cognitive representations. We thus unveil a generic principle (dual dynamical regime) and biophysical solutions (inhibition or intrinsic properties) for learning and replay of complex trajectories robust to neural noise.

Results

Robust STDP-induced neural trajectories in the asynchronous irregular (AI) regime

We designed a detailed physiologically-constrained biophysical model of a recurrent neural network with random connectivity (**Fig. 1.a**, see *Methods*). Neuronal activity displayed low frequencies typical of behaving mammals (**Fig. 1.b**, $\nu < 10Hz$; **Fig. S1.a**; Boudewijns et al. 2013; Shafi et al. 2007). Moreover, collective spiking showed levels of irregularity (coefficient of variation of inter-spike intervals (ISIs) $CV \sim 1$, $CV_2 \sim 0.8$, **Fig. S1.b-d**; Compte, 2003; Shinomoto et al., 2005) and asynchrony (pairwise correlation coefficient averaged over all neurons $< \rho > \sim 0.01$, **Fig. S1.e-g**; Tchumatchenko et al., 2010) characteristic of the AI regime (Brunel, 2000) observed in the cortex (Riehle et al., 1997; Poulet and Petersen, 2008), and reflecting underlying low–order chaotic dynamics ($\lambda \sim 0.01$; **Fig. S1.h-j**; London et al. 2010). This global disordered regime emerged from fluctuation-based spiking (**Fig. 1.c** top) due to the balanced, strong total current generated by excitatory and inhibitory input currents (**Fig. 1.c** bottom, and **Fig. S1.k**; Renart et al., 2010; Xue et al., 2014), i.e. neurons were in a high-conductance state (Destexhe et al., 2003).

The network was trained with an external circular trajectory stimulus (**Fig. 1.d** left**)** inducing synaptic learning through biophysically plausible STDP and synaptic scaling rules that are ubiquitous in the neocortex (see *Methods*, Turrigiano et al., 1998; Abbott and Nelson, 2000). Synapses were potentiated by STDP when post-synaptic followed pre-synaptic spikes (**Fig. 1.d** center**)**. Thus, neurons sequentially activated by the stimulus potentiated synapses connecting neurons in the forward direction along the trajectory, forming an oriented connective pathway that constituted the engram of the trajectory stimulus (arrows, **Fig. 1.d** right). Instantaneous synaptic scaling homeostatically compensated for run-away effects of Hebbian plasticity by regulating the sum of incoming synaptic weights onto neurons (Turrigiano et al., 1998; Zenke et al., 2017; Sarazin et al., 2021). The sums of incoming weights were thus similar for neurons inside and outside the oriented connective pathway (homogeneous background map, **Fig. 1.d** right), the latter structure arising exclusively from the direction in which outgoing synaptic weights were the most potentiated. In principle, such a synaptic structure – a "*connective pathway"* – can propagate an activity packet of co-active spiking neurons – hereafter denoted as a "*pack"* – downstream the trajectory because of oriented synaptic weights, subserving trajectory *"replays"*, whether spontaneously or when triggered by initiating stimuli.

In awake animals, connective pathways and propagating packs could respectively constitute a likely biological basis for the learning and replay of neural trajectories. However, this possibility may not be trivial in reality. The permanent disorganizing influence of chaotic synaptic fluctuations in the AI state (London et al., 2010) and high conductance state (Destexhe et al., 2003) may jeopardize and disrupt packs at any moment, forbidding faithful propagation. To escape noise disorganization, a sufficient number of co-active neurons and sufficiently strong connective pathway would be required for propagation. By contrast, weights too strong may ignite packs in an uncontrolled fashion from a few spikes – or even a single one – in neurons along the trajectory (i.e. in a similar fashion to the very low triggering conditions of intrinsic- or synaptic-mediated persistent activity; Ratté et al., 2018; Carrillo-Reid et al., 2019). Furthermore, packs may possibly propagate and perturb neural activity outside the trajectory. We evaluated trajectory replay offline (with plasticity disabled) by simulating the network after the learning procedure and found that replays emerged within the disorganizing fluctuations of the AI regime, without necessarily affecting activity outside the trajectory (**Fig. 1.e-h**). Replays could emerge spontaneously (**Fig. 1.e**, **1.g**) or when

triggered by an initiating stimulus on the trajectory (red rectangle, **Fig. 1.f**, **1.h**). In all cases, synchronized excitatory spiking rapidly amplified along the connective pathway, recruiting more neurons and converging to a state of propagation implying around a hundred neurons.

However, different simulations of the same network yielded very diverse types of replays, depending on the exact realization of random connectivity (prior to learning) or initial conditions of activity (chaotic dynamics). In some cases, propagation appeared pathological (**Fig. 1.e-f**). For instance, the trajectory could spontaneously, stably and permanently be replayed, possibly overwhelming network dynamics, dampening the replay of other trajectories and, *in fine*, of downstream decoding (**Fig. 1.e**). On the other hand, replays triggered at the beginning of the trajectory could fail to propagate stably up to its end, rapidly vanishing after a few hundred ms, due to AI fluctuations (**Fig. 1.f**). Nevertheless, trajectory replays could also account for observations in physiological conditions **(Fig. 1.g-h**), leading to sparse spontaneous replays (e.g. free recall, **Fig. 1.g**) or stable evoked-only replays (e.g. correct task performance, **Fig. 1.h**). Thus, physiological replays, although possible, were not systematically granted in our recurrent network model. To understand how physiological replays emerge, we assessed the processes underlying the activity regimes where pack propagates or not.

Pack propagation relies on a transition from inhibitory fluctuation- to excitatory mean current-driven spiking

In order to unravel the mechanisms distinguishing regimes of pack propagation or non-propagation, we first identified the causes of spiking in excitatory neurons situated within a propagating pack (*Pack* neurons) or outside the pack (*non-Pack* neurons).

In *non-Pack* neurons, the membrane potential reached an average sub-threshold steady-state plateau (~54mV, **Fig. 2.a**, top left), as the total current was essentially near-balanced on average (**Fig. 2.b**, top left, star). Spiking arose from fast voltage transients (**Fig. 2.a**, top left, star) caused by strong current fluctuations (**Fig. 2.b**, bottom left, star). More specifically, $GABA_A$ fluctuations contributed the most among all individual currents (**Fig. 2.b**, bottom middle, star) such that spiking was mostly caused by sudden $GABA_A$ transient decrease (**Fig. 2.a**, bottom left, star). Spiking in neurons outside the pack was thus mostly driven by disinhibitory current fluctuations.

For *pack* neurons, the membrane potential rose to the spiking threshold without an intermediate steady-state plateau (**Fig. 2.a**, top right), because of a strongly imbalanced depolarizing total current (**Fig. 2.b**, top left, triangle). Rather than from a sudden GABA-A decrease, spiking was principally caused by a strong tonic drive of the NMDA current (**Fig. 2.b**, top right, triangle, and **Fig. 3.a**, right). This drive was particularly massive because of 1) the strong spiking frequency within the pack (f_{Pack}~$14.5\mathrm{Hz}$), 2) the large strength of potentiated synaptic weights within the connective pathway, 3) pre-/post- coincident spiking within the pack relieving Mg^{2+}-mediated NMDA blockade and inducing associative NMDA activation, and 4) the slow time constant of NMDA channel opening dynamics favoring temporal extended NMDA currents. Moreover, the pack was local (i.e. concerning only a small group of high frequency excitatory neurons), while inhibition was global (synapses to and from inhibitory neurons are non-specific in the network). As such, inhibitory population frequency increased only slightly during local excitatory pack propagation (**Fig. 1.h**), which further guaranteed strongly imbalanced depolarizing total current within local pack neurons. Altogether, pack spiking was mostly driven by high pack frequency inducing strong hetero-associative slow NMDA currents within potentiated synaptic weights, and allowed by the insufficient increase in global inhibition in order to dampen local pack propagation.

Thus, while spontaneous activity was fundamentally GABA-A-fluctuation-based at low frequencies characterizing the AI regime, pack propagation along the connective pathway revealed essentially deterministic associative NMDA local transmission at higher frequencies. We wondered how this activity regime dichotomy constrained the physiological characteristics of replays, by defining measures of plausibility and functionality.

We therefore assessed the biophysical mechanisms setting the *controllability* of replays, i.e. the ability to reliably evoke replays with an input while limiting spontaneous replays. We also assessed the biophysical parameters causally controlling the s*tability* of replays, i.e. the ability for trajectory representations to last in recurrent neural networks.

Theoretical predictions of transitions between spontaneous activity and pack propagation

Answering these questions first required understanding the dynamical rules setting the emergence and extinction of packs, i.e. transitions between spontaneous activity and pack propagation regimes. Characterizing these transitions required to identify the frontier separating regimes. Both regimes principally differed by their firing frequency (f), which determined the magnitude and fluctuations of synaptic currents responsible for spiking regimes (see above). Thus, we sought the frequency threshold separating regimes (**Fig. 3.a**) in a reduced (one-dimensional) analytical model assessing conditions for propagation of activity between preceding and succeeding neurons along the trajectory pathway, as a function of f (see *Methods*). This *propagation threshold* theory predicted that a frequency threshold f_θ separated both regimes in excitatory neurons (**Fig. 3.a**, left), as an unstable fixed-point, with self-amplifying activity above f_θ and extinction below. The model was validated by its ability to closely replicate current averages in spontaneous vs propagation regimes in the network model (**Fig. 3.a**, right) and its prediction was qualitatively close – using standard network model parameters $f_\theta \sim 10.8\text{Hz}$ – to an empirical estimation of $f_\theta \sim 9.2\text{Hz}$ in network model simulations (see *Methods*).

Based on this threshold, we next designed a *regime transition* theory (see *Methods*) to predict noise-driven transitions between spontaneous and propagation regimes across their common frontier. This model phenomenologically described firing frequency dynamics through a deterministic differential equation accounting for the two stable fixed-points characterizing spontaneous and propagation regimes ($f_{non-Pack}$ and f_{Pack}) as well as the unstable fixed-point threshold f_θ separating them (**Fig. 3.b**, left). It also incorporated a stochastic component to account for frequency fluctuations due to the global AI regime and regime transitions (example simulations in **Fig. 3.b**, right), with standard deviations $\sigma_{non-Pack}$ and σ_{Pack} estimated from network simulations.

We quantified the behavior of this theoretical reduced model by computing the probabilities for spontaneous $p(Spont.)$ and triggered $p(Evoked)$ transitions toward pack propagation, giving the controllability measure $p(Evoked) - (Spont.)$, as well as the stability (duration) of evoked packs (see *Methods*). We found that low levels of firing frequency or variability in the spontaneous regime ($f_{non-Pack}$ or $\sigma_{non-Pack}$) decreased $p(Spont.)$ but had no influence on $p(Evoked)$, increasing pack controllability (**Fig. 3.c**, far left and middle left, blue and red dashed and orange solid curves respectively). Conversely, in the propagation regime, larger firing frequency (f_{Pack}) or lower frequency variability (σ_{Pack}) increased $p(Evoked)$ but had no influence on $p(Spont.)$, increasing pack controllability (**Fig. 3.c**, middle and middle right). Finally, controllability displayed an optimum as a function of the threshold f_θ (as increasing f_θ first decreased p$(Spont.)$ then p$(Evoked)$, **Fig. 3.c**, far right).

Altogether, the model predicted that biophysical factors promoting a larger separation between spontaneous and propagation regimes (larger frequency distance or lower frequency variability) would increase the controllability of trajectory replays. On the other hand, the stability of replays increased with factors limiting downward transitions from the propagation to the spontaneous regime (i.e. larger f_{Pack} or lower σ_{Pack}, **Fig. 3.c**, middle and middle right).

Biophysical mechanisms promoting trajectory stability and controllability

These theoretical predictions led us investigating biophysical determinants of propagation behavior in the simulations. We searched, with large explorations of the parameter space, biophysical determinants that allowed a clear separation between spontaneous and propagation regimes, thus ensuring both pack stability and controllability. We found a very restricted set of specific architectural, synaptic and ionic determinants, distinct from simply strengthening the connective pathway underlying the replays.

Indeed, the straightforward solution of strengthening the connective pathway (i.e. increasing the STDP amplitude A_{STDP}) enhanced stability. However, a strong connective pathway also increased the probability of spontaneous pack emergence, thus having a limited impact upon controllability (**Fig. 4.a**, middle). The increased stability was due to a higher pack frequency (**Fig. 4a**, left) and the increased spontaneous pack probability arose from a decreased f_θ (**Fig. 4.a**, left), both caused by stronger synaptic connections along the pathway.

By contrast, we devised that decreasing the fluctuations of inhibitory currents onto excitatory neurons (while keeping their mean value constant) should reduce $f_{non-pack}$ and $p(Spont.)$ by rendering disinhibition scarce. As the spontaneous regime was mostly disinhibitory fluctuation-driven, while the evoked regime was excitatory mean-driven, our theory predicted that decreased $I \rightarrow E$ fluctuations should separate the two regimes. A larger number of proportionally weaker synapses from inhibitory to excitatory neurons could achieve this effect in the model (higher $p_{I\rightarrow E}$, see *Methods*), i.e. it decreased $GABA_A$ current fluctuations $\sigma(I_{GABA-A})$ (**Fig. S2.a**, top). As predicted, lower $\sigma(I_{GABA-A})$ decreased $f_{non-pack}$ (and thus $\sigma_{non-pack}$) (**Fig. 4.b**, left) and $p(Spont.)$ (**Fig. 4.b**, middle), leading to more controllable trajectories (surprisingly, f_{pack} increased because decreased $f_{non-pack}$ lowered the excitatory drive to inhibitory neurons and, as a consequence, the inhibitory drive on Pack neurons). Alternatively, slower but proportionally weaker GABA-A currents similarly increased controllability (by decreasing $f_{non-pack}$ and spontaneous pack emergence; **Fig. S2.a**, bottom and **Fig. S2.b**).

Combining tonic feedforward inhibition with stronger recurrent excitatory connectivity also led to more controllability and stability. Indeed, strong recurrent excitatory connectivity (e.g. strengthened STDP; $A_{STDP} = 75$) increased f_{Pack} and decreased f_θ without modifying $f_{non-Pack}$ (**Fig. 4c**, left), as previously shown. This resulted in greater separation between f_{Pack} and $f_{non-Pack}$, i.e. between regimes, although $f_{non-pack}$ was now much closer to f_θ, inducing high $p(Spont.)$ at low $\nu_{FF(Inh)}$ (**Fig. 4c**, left and middle). Therefore, at the same time, we also increased tonic inhibition (i.e. increased feedforward excitation onto inhibitory neurons, $\nu_{FF(Inh)}$), which decreased $f_{non-pack}$ and f_{pack} by the same amount (while keeping f_θ relatively constant; **Fig. 4.c**, left), and thus decreased both $p(Spont.)$ and $p(Evoked)$. The net result of combining both effects was a higher f_{pack} and lower $f_{non-pack}$, resulting in higher controllability and stability within an intermediate $\nu_{FF(Inh)}$ range ($p(Evoked)$ and thus controllability eventually decreasing at very high $\nu_{FF(Inh)}$). Intuitively, this could be

understood as favoring inhibitory hyperpolarizing currents independent of network frequency (i.e. stronger tonic inhibition), which decreased spontaneous frequency and replays, while keeping excitatory depolarizing currents dependent upon network frequency (through stronger excitatory recurrent connectivity-mediated amplification), increasing evoked frequency and replays.

Favoring hyperpolarizing frequency-independent currents could be achieved in many other different ways, reinforcing its validity as a general principle in real recurrent neural networks. Indeed, decreasing the hyperpolarizing leak current of inhibitory neurons yielded the same effect ($g_{L(Inh)}$, **Fig. S2.c**). Also, decreasing recurrent currents impinging upon inhibitory neurons led to comparatively stronger feedforward & leak currents in the spontaneous regime, with similar effects ($g_{X\to I}$, **Fig. S2.d**).

Besides synaptic and architectural parameters, we unraveled calcium-gated ionic currents (CAN and AHP) as major determinants of controllability and stability. Both types of conductances depend upon spike-driven calcium influx (through voltage-dependent calcium channels) and, thus, spiking frequency. The saturation and time constant properties of these currents define their frequency response profile. A slow rapidly-saturating AHP and a fast slowly-saturating CAN induced hyperpolarization at low firing frequencies (AHP) and depolarization at high frequencies (CAN). In individual neurons, CAN and AHP together entailed a loosely defined unstable fixed point at f'_θ~12.7Hz (**Fig. 4.e**, left), inducing hyperpolarization (favoring activity extinction) below f'_θ and depolarization (favoring self-amplifying activity) above. This cellular effect added to that related to the separation between spontaneous activity and pack propagation at the network level. As a consequence, $f_{non-pack}$ was decreased and f_{pack} was increased (**Fig. 4.d**, left), increasing controllability and stability (**Fig. 4.d**, middle). Interestingly, these results did not require strong conductances promoting absolute intrinsic bistability (i.e. persistent activity following transient input, Haj-Dahmane and Andrade, 1997). Rather, the weak CAN conductance, yielding transient bistability, sufficed to promote controllability and stability of sparse transient activity sequences (**Fig. 4.e**, middle and right; black vertical line, denoting the current conductance parameter value, is within the blue transient bistability range; bistability determined as in Rodriguez et al., 2018).

Independence of trajectory replay and outside network activity

Generally, increasing controllability and stability required decreased spontaneous network activity. In such networks, trajectory replay increased frequency of excitatory (& inhibitory) neurons not part of the trajectory, creating a sharp contrast between network dynamics outside the trajectory neurons before and during replay (**Fig. 4.b-d**, right). Such strong modulation of network activity outside the trajectory neurons might impede upon parallel concurrent computations, e.g. the replay of several trajectories simultaneously. We assessed, amongst the aforementioned mechanisms, those which allowed the best replay *independence*, i.e. less neural dynamics perturbation outside the trajectory. To do so, we measured the frequency of excitatory neurons outside the trajectory during evoked pack propagation $f_{nT}(Ev.)$ and during spontaneous pack absence $f_{nT}(\neg Sp.)$, with independence being calculated as $I = 1 - \left|\frac{f_{nT(Ev.)} - f_{nT(\neg Sp.)}}{f_{nT(Ev.)} + f_{nT(\neg Sp.)}}\right|$ (**Fig. 4.a-d**, middle). $I = 1$ corresponded to perfectly equal frequency during evoked pack propagation and spontaneous pack absence and thus unchanged network dynamics, decreasing I corresponded to increasingly different frequencies, and $I = 0$ to either frequency being null. Increasing controllability and stability generally decreased independence (~90% to ~50%). However, independence decreased less

for CAN & AHP (~70%), being the only mechanism with an excitatory component increasing spontaneous excitatory frequency (g_{CAN}). These results further support the merits of interacting synaptic (STDP-based trajectory replay) and intrinsic (CAN & AHP) properties (Rodriguez et al., 2018), as CAN and AHP components together led to transient bistability within neurons (**Fig. 4.e**, middle and right), lessening the burden on synaptic properties regarding the propagation of pack activity.

Robustness of controllable, stable and independent neural replays within the AI regime

While we deciphered a restricted set of biophysical determinants of controllable and stable replays (low inhibitory fluctuations, frequency-independent inhibition, and frequency-dependent intrinsic properties), we assessed the sensitivity of replays to parameter variations with these biophysical determinants. For each mechanism, preservation of network behavior to naturally occurring biophysical variability within and across cerebral structures (i.e. parameter variation) would make the given class of model more biologically plausible.

To do so, we studied the parametric width of regions allowing controllable, stable and independent replays and preserving asynchronous irregular network dynamics, by systematically varying important parameters of the model, for each of the aforementioned mechanisms (**Fig. 4.f**). To do so, we defined a set of criteria which were required to all be met, indicating whether the network was plausible in terms of ionic current balance (via conductance ratios), activity regime (via spiking activity measures), and trajectory quality (via controllability, stability and independence measures) (see *Methods* and **Fig. S3.a-c**).

In the standard model (i.e. without the aforementioned synaptic and intrinsic current mechanisms improving replay quality, see the two previous sections; Model ∅), controllable and stable trajectories emerged for moderately large parametric regions (overall robustness score of ~10%). They emerged for much larger regions with the additional mechanisms (~25-45%), peaking with the g_{CAN} & g_{AHP} mechanism (**Fig. 4.f**, left). Although the $\nu_{FF(Inh)}$ mechanism demonstrated the largest parametric regions allowing controllable and stable replays, the contribution of the independence criteria to overall robustness decreased with $\sigma(I_{GABA-A})$ and $\nu_{FF(Inh)}$ (~60%), compared to Model ∅. However, it remained at ~100% with g_{CAN} & g_{AHP}, further supporting intrinsic currents as important candidates for alleviating constraints on synaptic-based propagation (**Fig. 4.f**, right).

A common framework for generalized static and dynamical neural attractors

Another form of robustness lies in the functional versatility of the mechanisms supporting controllable, stable and independent replays, i.e. whether they generalize to other forms of neural representations. We found that, by applying one or several of the aforementioned mechanisms, the network could learn and reliably replay attractors spanning a larger class of models present in the theoretical literature, from discrete static (Hebbian assemblies) to dynamic (synfire chain and Hebbian phase assemblies) attractors, as well as continuous static (ring-like attractor) and dynamic (bidirectional ring) attractors (**Fig. 5.a**). Learning such attractors required modulation of the STDP window asymmetry and shift (**Fig. 5.b**) – as is observed across cerebral structures (Abbott & Nelson, 2000) and plausible under neuromodulation (e.g. dopamine, Zhang et al., 2009) –, as well as differently timed trajectory stimuli.

Symmetric STDP rules, combined with exposure to discrete stimuli, allowed for the emergence of discrete static attractors. Exposure to a single discrete stimulus (**Fig. 5.c1**, far left) with a symmetric STDP window (**Fig. 5.c1-2**, middle left) led to the formation of a Hebbian assembly (**Fig. 5.c1**, middle right). Combined with the g_{CAN} & g_{AHP} mechanism,

stimulating neurons resulted in the maintained activation ("replay") of the Hebbian assembly, with increased reliability (compared to the standard model; **Fig. 5.c1**, far right). Similarly, exposure to a stimulus jumping between multiple successive discrete positions (**Fig. 5.c2**, far left) led to the formation of multiple Hebbian assemblies (**Fig. 5.c2**, middle right), which could be independently selected and replayed, with increased reliability (compared to the standard model; g_{CAN} & g_{AHP} mechanism, **Fig. 5.c2**, far right).

By contrast, asymmetric STDP rules, combined with exposure to discrete stimuli, led to discrete dynamical attractors. A discretely moving stimulus (**Fig. 5.d1**, far left), with a strongly asymmetric and shifted STDP temporal window (**Fig. 5.d1**, middle left), led to the learning (**Fig. 5.d1**, middle right) and reliable replay (**Fig. 5.d1**, far right) of a synfire chain, with fast travelling of the spiking activity between successive neuron groups ($\sigma(I_{GABA-A})$ and $\nu_{FF(Inh)}$ mechanisms). This stimulus (**Fig. 5.d2**, far left), learned through a weakly asymmetric STDP temporal window (**Fig. 5.d2**, middle left) led to assemblies connected through feedforward connections (**Fig. 5.d2**, middle right) and replay of a so-called Hebbian phase sequence, i.e. with successive slow (few hundred ms) recalls of Hebbian assemblies ($\sigma(I_{GABA-A})$ mechanism, **Fig. 5.d2**, far right).

Besides, exposure to a stimulus moving in a continuous fashion (**Fig. 5.e1**, far left) with a symmetric STDP temporal window (**Fig. 5.e1**, middle left) led to a ring-like attractor (**Fig. 5.e1**, middle right) supporting multiple simultaneous replays and extremely slow drift across time (g_{CAN} & g_{AHP} mechanism, **Fig. 5.e1**, far right). Finally, a similar stimulus (**Fig. 5.e2**, far left) with a larger STDP window (**Fig. 5.e2**, middle left) resulted in a large ring attractor (i.e. large band in the synaptic matrix, **Fig. 5.e2**, middle right) allowing bidirectional trajectory replay when combined with slowly-saturating g_{AHP}, which activated at high frequency and induced pack propagation in the direction of initial stimuli (see *Methods*, $\sigma(I_{GABA-A})$ mechanism, **Fig. 5.e2**, far right).

Hence, we suggest the aforementioned mechanisms (low inhibitory fluctuations, frequency-independent inhibition, and frequency-dependent intrinsic properties), controlling transitions between fluctuation-driven to mean current-driven spiking, as generic properties allowing controllable and stable replays of a wide array of dynamical representations (static or dynamic, discrete or continuous). Together with the modulation of STDP windows and of the discrete or continuous nature of stimuli, they appear as key determinants of the functional expressivity of replays.

Discussion

Using simulations and theoretical analyses of realistic biophysically constrained network models, we show how interactions between intrinsic and synaptic properties of recurrent neural networks grant a large set of functionally reliable, robust and generic attractor dynamics including neural trajectories, despite the permanent disorganizing effects of chaotic asynchronous irregular (AI) dynamics in which they occur during the awake state.

STDP learning of neural trajectories in the AI regime

Although neural trajectories display generic prevalence and functional significance in many higher order behaviors and cognitive operations across numerous cerebral structures (Batuev, 1994; Yang et al., 2014; Jadhav et al., 2016; Schmitt et al., 2017; Lundqvist et al., 2018; Kaefer et al., 2020), current theoretical models have not explored the mechanisms underlying their functional emergence and propagation under the jeopardizing conditions encountered during awake cognition. Specifically, while Spike-Timing Dependent Plasticity (STDP)-based learning is considered a natural candidate for the emergence of neural trajectories, STDP-based models have not assessed how reliable and robust trajectories could be achieved in real noisy physiological conditions. Indeed, certain studies simply do not study trajectory replay in the AI state after learning (Hayashi and Igarashi, 2009; Clopath et al., 2010). In others, trajectories cannot be replayed from an initial trigger (Klampfl and Maass, 2013) or trajectory learning is either absent (Chenkov et al., 2017), based on artificial learning rules (Sussillo and Abbott, 2009; Laje and Buonomano, 2013; Xue et al., 2021) or biologically unrealistic neuronal activity and synaptic plasticity rules (Liu and Buonomano, 2009; Fiete et al., 2010; Klampfl and Maass, 2013), or even unrelated to external stimuli (Fiete et al., 2010). Furthermore, certain models simply lack the AI regime of neuronal activity (Liu and Buonomano, 2009; Fiete et al., 2010), removing the possibility to address sequence reliability. Compared to existing models, here we operationalized the problematic of replays in terms of stability and controllability of evoked replays, as well as the independence of network dynamics outside the sequence. This allowed us to dissect biophysical mechanisms that act as determinants of replays functionalities.

We found that the biophysical mechanisms considered (decreased disinhibitory fluctuations, tonic inhibition or intrinsic CAN/AHP conductances) were essential for the expression of reliable replays, allowing synaptic plasticity rules to yield functional neural trajectories. When varying the STDP temporal window and trajectory stimulus in the presence of these mechanisms, STDP allowed controllable and stable replays of the spectrum of principal known types of attractors, be they discrete static (Hebbian assemblies) or dynamic (synfire chain, Hebbian phase sequence), as well as continuous static (ring-like attractor) and dynamic (bidirectional ring attractor) attractors. Thus, the present model offers a unified common framework for the learning and generation of reliable attractor dynamics in realistic, biophysical and physiological conditions, by contrast to previous studies (e.g. Hayashi and Igarashi, 2009; Liu and Buonomano, 2009; Sussillo and Abbott, 2009; Clopath et al., 2010; Fiete et al., 2010; Laje and Buonomano, 2013; Chenkov et al., 2017; Xue et al., 2021). Hence, thanks to the interaction between STDP and the complementary synaptic and intrinsic mechanisms unraveled here, stability and independence of discrete static (Hebbian assemblies) attractors was increased. Dynamic attractors (synfire chain, Hebbian phase sequence) could be reliably replayed, escaping the classical issue of propagation failure or uncontrolled sequential propagation (Mehring et al., 2003; Chenkov et al., 2017). Continuous static (ring-like attractor) presented virtually null levels of drift, a

standard issue encountered in current models (Seeholzer et al., 2019). Finally continuous dynamic attractors allowed bidirectional propagation of neural trajectories, which is novel without a complex setup and hand-written synaptic matrices (Chenkov et al., 2017).

Here, we addressed the effect of chaotic AI network activity on trajectory replay with an offline STDP learning procedure emulating a trajectory being learned before network operation. In doing so, we did not assess the interactions between chaotic dynamics and online STDP learning of the trajectory. Indeed, the possibility exists, e.g., of unstable activity-connectivity runaway inducing over-strengthened connective pathway and incessant replays, or of degraded AI dynamics. We have attempted to address these questions in a similar model but with STDP operating online (Sarazin et al., 2021), although they remain to be evaluated with all biophysical mechanisms and attractor types mentioned here (the aforementioned article using the $\sigma(I_{GABA-A})$ mechanism with continuous uni-directional neural trajectories only), and furthermore raises new questions (e.g. the biophysical implementation of instantaneous or very fast synaptic scaling, Zenke et al., 2017).

Physiological consistency of the dual regime setting neural trajectory propagation

When investigating the underpinnings of network activity with and without activity packs replaying the trajectory, we observed that spontaneous activity outside of packs was driven by inhibitory current fluctuations (currents being balanced on average), while pack activity was driven by strongly imbalanced excitatory NMDA currents. The GABA-A disinhibitory fluctuation-driven spiking is consistent with cortical synaptic physiology. Indeed, inhibitory neurons are ~4x less numerous than excitatory ones, thus the arrival of IPSPs is globally sparser (i.e. at equivalent/slightly higher inhibitory firing frequency). Theoretical analyses suggest that inhibitory currents need to be at least 4x stronger to compensate for the difference in numbers to guarantee network stability (Brunel, 2000), so that individual spikes lead to strong inhibitory currents. Lastly, GABA-A channel's opening time constant is fast, leading to high temporal variability, as evidenced in our results. Our study also unraveled the crucial role of slow NMDA dynamics in increasing the reliability of trajectory propagation (dynamic attractor), consistent with what is observed for object working memory subserved by Hebbian assemblies (static attractor; Wang, 1999). Indeed, even though synaptic reverberation plays a less important role in trajectory propagation compared to its role in static neuronal assemblies, the slow and hetero-associative nature of NMDA dynamics temporally helps bridging excitatory pack activity across potentially destabilizing inhibitory current fluctuations as well as against weaknesses in transmission due to random sparsity-inducing partial "holes" in the potentiated synaptic pathway.

Interactions of synaptic/intrinsic processes with plasticity for reliable trajectory replays

A theoretical analysis of network activity and pack propagation in a reduced (*propagation threshold theory*) model allowed to predict that an excitatory frequency threshold existed separating both inhibitory fluctuation (non pack) / excitatory deterministic (pack) regimes. Modeling transitions between non-pack and pack activity as bistable excitatory frequency dynamics with additive noise (*regime transition* theory) then permitted to estimate threshold crossing probabilities and the way parameters affected the controllability and stability of replays. Altogether, we found that factors promoting a larger separation between spontaneous and propagation regimes (larger non-pack/pack frequency distance or lower frequency variability) increases replay controllability. Also, replay stability increased with factors limiting downward transitions from propagation to spontaneous activity (i.e. larger mean and lower variability of pack frequency).

Based on this knowledge , we have identified biophysical mechanisms increasing pack controllability and stability in actual simulations of the whole network: 1) decreasing GABA-A fluctuations (which decreased non-pack frequency and spontaneous replay probability), 2) combining tonic frequency-independent inhibition with stronger recurrent excitatory connectivity (which decreased non-pack frequency and increased pack frequency, increasing controllability and stability), and 3) frequency-dependent CAN/AHP ionic currents (which strengthened replays through transient bistability of individual neurons).

As a general rule, we found that a tradeoff dominated replay quality in that increased controllability and stability generally decreased trajectory independence. This was a concern, since independence represents the ability of a replayed trajectory to leave unchanged network dynamics (outside the replay) and thus, in turn, the possibility for multiple simultaneous independent trajectory replays. However, this question was partially alleviated when neurons where endowed with CAN/AHP currents, hinting at the importance of the interactions between synaptic and intrinsic properties in trajectory replay. Moreover, these properties were robust to variations of model's parameters up to 40% with the CAN/AHP mechanism, reinforcing the biophysical plausibility and potential genericity of replays across cerebral structures, since these currents are ubiquitous (Rodriguez et al., 2018).

Functionality of trajectory replays

An important aspect of our work concerned the reduction of the spontaneous occurrence of trajectory replays. Indeed, obtaining spontaneous replays is trivial (requiring only strong STDP), and does not explain the finer-tuned behavior of trajectories being reliably replayed *only when triggered*. Furthermore, spontaneous replay can be detrimental when incessant or overwhelming. However, spontaneous replays under certain contexts are observed experimentally, such as in the cortex and hippocampus, when animals consolidate learnt behaviors, evaluate past and future choices or switch to new behavioral rules (Jadhav et al., 2012; Pfeiffer and Foster, 2013; Kaefer et al., 2020). Indeed, scarce spontaneous replay may be functionally relevant, potentially anticipating future behavior (Diba and Buzsáki, 2007) and consolidating memory during slow-wave sleep (Lee and Wilson, 2002; Euston et al., 2007) and sharp-wave ripples (Girardeau et al., 2009), or potentially linking different sequences (Buzsáki and Moser, 2013).

Similarly, very stable replays are not systematically required physiologically, as in the case of transient dynamics, which have been theoretically described (Bondanelli and Ostojic, 2020) and experimentally observed (e.g. locust olfaction, Mazor and Laurent, 2005). However, they clearly represent a strategic advantage for cognitive operations or temporally complex behaviors, such as navigational trajectories and working memory delay period sequences, which need to be reliably executed over several seconds or tens of seconds, as when animals recall a navigation path, a movement or actively maintain a short-term memory (Sreenivasan et al., 2014; Yang et al., 2014; Mello et al., 2015; Bolkan et al., 2017; Schmitt et al., 2017; Spaak et al., 2017). It is to be noted that the longer the sequence, the higher the probability of local excitation to gradually amplify along the connective pathway, with a looped circular trajectory (**Fig. 1**) actually being of infinite-length, thus inducing higher spontaneous replay probability than non-looped trajectories.

Besides, experimental data regarding the independence of trajectories is scarce, with certain articles suggesting approximate independence of trajectory replay and network activity in hippocampus and posterior parietal cortex (Pastalkova et al., 2008; Harvey et al., 2012; Ito et al., 2015; Jadhav et al., 2016), whereas network activity is decreased in the PFC (Jadhav et al., 2016) during trajectory replay. This independence, which is essential for the

co-existence of parallel or distributed cognitive operations and alternative evaluations of behavioral choice, deserves further experimental and theoretical investigation.

Biophysical plausibility of identified biophysical mechanisms

While we have characterized general biophysical mechanisms increasing controllability and stability of trajectory replays through theoretical analysis, such mechanisms in the recurrent networks of animals may vary among cortical and sub-cortical structures.

Amplified feedforward inputs onto inhibitory neurons combined with stronger excitatory recurrent connections is reminiscent of mediodorsal thalamic activation, which increases FS sustained frequency and amplifies local RS functional connectivity in rodent mPFC, increasing the stability of sparse transient neural sequences and working memory performance (Rikhye et al., 2018). The CAN and AHP mechanism appears prominent in layer 5 PFC pyramidal neurons (Haj-Dahmane and Andrade, 1997; Villalobos et al., 2004) and ubiquitous among cortical and sub-cortical structures (Rodriguez et al., 2018).

Other mechanisms susceptible to improve quality of replays should be investigated. For example, computations via dendritic compartments could allow non-linear integration of synaptic inputs (Cazé et al., 2013; Tran-Van-Minh et al., 2015), e.g. by further amplifying synchronous EPSPs or inducing backward-propagating dendritic spikes (such as in the hippocampus, Jarsky et al., 2005), which could increase separation between spontaneous and pack activity regimes. Similarly, short-term plasticity could help amplify EPSPs resulting from coincident spikes through synaptic facilitation, as hinted to during PFC neural sequences of rodents (Fujisawa et al., 2008) and monkeys (Barak et al., 2010; Stokes et al., 2013).

Non-stationary or noisy input from feedforward currents

Feedforward currents were considered constant in the present model, in order to isolate the influence of network-generated synaptic-driven irregularity and chaotic dynamics onto trajectory replay. However, temporally structured input from other areas, such as rhythmic theta inputs from the hippocampus (Siapas et al., 2005; Benchenane et al., 2011) or delta rhythms from the olfactory pathways (Moberly et al., 2018) onto the PFC, would strongly affect trajectory replay. Indeed, oscillatory input induced spontaneous replays at each peak of the oscillatory signal (not shown). We thus favored slow excitation and fast inhibition (as the opposite fosters oscillations in any recurrent dynamical system) by increasing NMDA vs AMPA and GABA-A vs GABA-B currents. Similarly, Poisson spike trains of neurons projecting feedforward inputs onto the network introducing random noise into the feedforward currents, or even more directly random noise onto synaptic currents, would destabilize pack propagation and decrease trajectory controllability. Also, the role of inter-areal interactions has not been explored here. The observation of coordinated trajectory replay between structures (e.g. PFC – thalamus nucleus reuniens – hippocampus, Ito et al., 2015) deserves further investigation, as it could arise from different distributed synaptic structures, i.e. a connective pathway in only one structure which projects onto others, redundant connective pathways learned in all structures, or distributed connective pathways spread across structures.

Genericity of attractors

The biophysical mechanisms unraveled here allow controllable and stable replays of many different types of attractors, critically depending on the modulation of the STDP temporal window. Different STDP functions have been observed experimentally (Abbott and Nelson, 2000), and the LTP and LTD portions have been shown to respond to dopaminergic

neuromodulation (Zhang et al., 2009). We also found non-trivial interactions between the static or dynamic structure of the stimuli and the temporal asymmetry or shift of the STDP window, which constitute strong predictions to be verified experimentally in physiological conditions. Another interesting avenue of future research would require evaluating whether the identified mechanisms here allow independent replay of multiple trajectories in the same network, depending on the degree of overlap between learned trajectories.

The present model accounts for neural activity underlying temporally complex trajectories in explicit spaces (e.g. navigation), or in more implicit spaces (e.g. task space for working memory). Such external or internal trajectories subserved by neural sequences correspond to trajectories in the space of population activity (such as observed through principal component analysis of network activity, Churchland et al., 2007; Cunningham and Yu, 2014; Rubin et al., 2019). Population activity trajectories are prominently observed in many cerebral structures and contexts, e.g. in primate motor cortex during reaching (Churchland et al., 2012) and mammalian olfactory bulb or locust antennal lobe during olfaction (Mazor and Laurent, 2005; Bathellier et al., 2008). However, the present model cannot confidently account for all types of population trajectories. Indeed, while all neural activity sequences result in population activity trajectories, all population activity trajectories are not necessarily reflected by neural activity sequences. In other words, while we have studied neural activity sequences where each neuron has clear separate sparse transient activity bumps, it is less clear how synaptic learning rules could allow for the emergence of more complex temporal signatures at the neuronal level, such as mixtures of neurons ramping-up and down, or simply multiple activity bumps, which would also result in population activity trajectories.

References

Abbott, L. F., and Nelson, S. B. (2000). Synaptic plasticity: taming the beast. *Nat. Neurosci.* 3, 1178–1183. doi:10.1038/81453.

Akhlaghpour, H., Wiskerke, J., Choi, J. Y., Taliaferro, J. P., Au, J., and Witten, I. B. (2016). Dissociated sequential activity and stimulus encoding in the dorsomedial striatum during spatial working memory. *eLife* 5, e19507. doi:10.7554/eLife.19507.

Angulo-Garcia, D., Ferraris, M., Ghestem, A., Bernard, C., and Quilichini, P. P. (2018). Spatio-temporal organization of cell assemblies in Nucleus Reuniens during slow oscillations. *bioRxiv*, 474973. doi:10.1101/474973.

Bakhurin, K. I., Goudar, V., Shobe, J. L., Claar, L. D., Buonomano, D. V., and Masmanidis, S. C. (2017). Differential Encoding of Time by Prefrontal and Striatal Network Dynamics. *J. Neurosci.* 37, 854–870. doi:10.1523/JNEUROSCI.1789-16.2016.

Bakhurin, K. I., Mac, V., Golshani, P., and Masmanidis, S. C. (2016). Temporal correlations among functionally specialized striatal neural ensembles in reward-conditioned mice. *J. Neurophysiol.* 115, 1521–1532. doi:10.1152/jn.01037.2015.

Barak, O., Tsodyks, M., and Romo, R. (2010). Neuronal Population Coding of Parametric Working Memory. *J. Neurosci.* 30, 9424–9430. doi:10.1523/JNEUROSCI.1875-10.2010.

Bathellier, B., Buhl, D. L., Accolla, R., and Carleton, A. (2008). Dynamic Ensemble Odor Coding in the Mammalian Olfactory Bulb: Sensory Information at Different Timescales. *Neuron* 57, 586–598. doi:10.1016/j.neuron.2008.02.011.

Batuev, A. S. (1994). Two neuronal systems involved in short-term spatial memory in monkeys. *Acta Neurobiol. Exp. (Warsz.)* 54, 335–344.

Benchenane, K., Tiesinga, P. H., and Battaglia, F. P. (2011). Oscillations in the prefrontal cortex: a gateway to memory and attention. *Curr. Opin. Neurobiol.* 21, 475–485. doi:10.1016/j.conb.2011.01.004.

Bi, G. Q., and Poo, M. M. (1998). Synaptic modifications in cultured hippocampal neurons: dependence on spike timing, synaptic strength, and postsynaptic cell type. *J. Neurosci. Off. J. Soc. Neurosci.* 18, 10464–10472. doi:10.1038/25665.

Bolkan, S. S., Stujenske, J. M., Parnaudeau, S., Spellman, T. J., Rauffenbart, C., Abbas, A. I., et al. (2017). Thalamic projections sustain prefrontal activity during working memory maintenance. *Nat. Neurosci.* 20, 987–996. doi:10.1038/nn.4568.

Bondanelli, G., and Ostojic, S. (2020). Coding with transient trajectories in recurrent neural networks. *PLOS Comput. Biol.* 16, e1007655. doi:10.1371/journal.pcbi.1007655.

Boudewijns, Z. S. R. M., Groen, M., Lodder, B., McMaster, M., Kalogreades, L., de Haan, R., et al. (2013). Layer-specific high-frequency action potential spiking in the prefrontal cortex of awake rats. *Front. Cell. Neurosci.* 7. doi:10.3389/fncel.2013.00099.

Brunel, N. (2000). Dynamics of Sparsely Connected Networks of Excitatory and Inhibitory Spiking Neurons. *J. Comput. Neurosci.* 8, 183–208. doi:10.1023/A:1008925309027.

Brunel, N., and Wang, X. J. (2001). Effects of neuromodulation in a cortical network model of object working memory dominated by recurrent inhibition. *J. Comput. Neurosci.* 11, 63–85. doi:10.1023/A:1011204814320.

Buzsáki, G., and Moser, E. I. (2013). Memory, navigation and theta rhythm in the hippocampal-entorhinal system. *Nat. Neurosci.* 16, 130–138. doi:10.1038/nn.3304.

Camperi, M., and Wang, X.-J. (1998). A Model of Visuospatial Working Memory in Prefrontal Cortex: Recurrent Network and Cellular Bistability. *J. Comput. Neurosci.* 5, 383–405. doi:10.1023/A:1008837311948.

Carrillo-Reid, L., Han, S., Yang, W., Akrouh, A., and Yuste, R. (2019). Controlling Visually Guided Behavior by Holographic Recalling of Cortical Ensembles. *Cell* 178, 447-457.e5. doi:10.1016/j.cell.2019.05.045.

Cazé, R. D., Humphries, M., and Gutkin, B. (2013). Passive Dendrites Enable Single Neurons to Compute Linearly Non-separable Functions. *PLOS Comput. Biol.* 9, e1002867. doi:10.1371/journal.pcbi.1002867.

Chenkov, N., Sprekeler, H., and Kempter, R. (2017). Memory replay in balanced recurrent networks. *PLoS Comput. Biol.* 13. doi:10.1371/journal.pcbi.1005359.

Churchland, M. M., Cunningham, J. P., Kaufman, M. T., Foster, J. D., Nuyujukian, P., Ryu, S. I., et al. (2012). Neural population dynamics during reaching. *Nature* 487, 51–56. doi:10.1038/nature11129.

Churchland, M. M., Yu, B. M., Sahani, M., and Shenoy, K. V. (2007). Techniques for extracting single-trial activity patterns from large-scale neural recordings. *Curr. Opin. Neurobiol.* 17, 609–618. doi:10.1016/j.conb.2007.11.001.

Clopath, C., Büsing, L., Vasilaki, E., and Gerstner, W. (2010). Connectivity reflects coding: a model of voltage-based STDP with homeostasis. *Nat. Neurosci.* 13, 344–352. doi:10.1038/nn.2479.

Compte, A. (2003). Temporally Irregular Mnemonic Persistent Activity in Prefrontal Neurons of Monkeys During a Delayed Response Task. *J. Neurophysiol.* 90, 3441–3454. doi:10.1152/jn.00949.2002.

Compte, A. (2006). Computational and in vitro studies of persistent activity: Edging towards cellular and synaptic mechanisms of working memory. *Neuroscience* 139, 135–151. doi:10.1016/j.neuroscience.2005.06.011.

Cromer, J. A., Roy, J. E., and Miller, E. K. (2010). Representation of Multiple, Independent Categories in the Primate Prefrontal Cortex. *Neuron* 66, 796–807. doi:10.1016/j.neuron.2010.05.005.

Crowe, D. A., Averbeck, B. B., and Chafee, M. V. (2010). Rapid Sequences of Population

Activity Patterns Dynamically Encode Task-Critical Spatial Information in Parietal Cortex. *J. Neurosci.* 30, 11640–11653. doi:10.1523/JNEUROSCI.0954-10.2010.

Cunningham, J. P., and Yu, B. M. (2014). Dimensionality reduction for large-scale neural recordings. *Nat. Neurosci.* 17, 1500–1509. doi:10.1038/nn.3776.

Davidson, T. J., Kloosterman, F., and Wilson, M. A. (2009). Hippocampal Replay of Extended Experience. *Neuron* 63, 497–507. doi:10.1016/j.neuron.2009.07.027.

Destexhe, A., Rudolph, M., and Paré, D. (2003). The high-conductance state of neocortical neurons *in vivo*. *Nat. Rev. Neurosci.* 4, 739–751. doi:10.1038/nrn1198.

Diba, K., and Buzsáki, G. (2007). Forward and reverse hippocampal place-cell sequences during ripples. *Nat. Neurosci.* 10, 1241–1242. doi:10.1038/nn1961.

Euston, D. R., Tatsuno, M., and McNaughton, B. L. (2007). Fast-Forward Playback of Recent Memory Sequences in Prefrontal Cortex During Sleep. *Science* 318, 1147–1150. doi:10.1126/science.1148979.

Fiete, I. R., Senn, W., Wang, C. Z. H., and Hahnloser, R. H. R. (2010). Spike-Time-Dependent Plasticity and Heterosynaptic Competition Organize Networks to Produce Long Scale-Free Sequences of Neural Activity. *Neuron* 65, 563–576. doi:10.1016/j.neuron.2010.02.003.

Fujisawa, S., Amarasingham, A., Harrison, M. T., and Buzsáki, G. (2008). Behavior-dependent short-term assembly dynamics in the medial prefrontal cortex. *Nat. Neurosci.* 11, 823–833. doi:10.1038/nn.2134.

Girardeau, G., Benchenane, K., Wiener, S. I., Buzsáki, G., and Zugaro, M. B. (2009). Selective suppression of hippocampal ripples impairs spatial memory. *Nat. Neurosci.* 12, 1222–1223. doi:10.1038/nn.2384.

Goldman, M. S., Levine, J. H., Major, G., Tank, D. W., and Seung, H. S. (2003). Robust Persistent Neural Activity in a Model Integrator with Multiple Hysteretic Dendrites per Neuron. *Cereb. Cortex* 13, 1185–1195. doi:10.1093/cercor/bhg095.

Haj-Dahmane, S., and Andrade, R. (1997). Calcium-Activated Cation Nonselective Current Contributes to the Fast Afterdepolarization in Rat Prefrontal Cortex Neurons. *J. Neurophysiol.* 78, 1983–1989. doi:10.1152/jn.1997.78.4.1983.

Harvey, C. D., Coen, P., and Tank, D. W. (2012). Choice-specific sequences in parietal cortex during a virtual-navigation decision task. *Nature* 484, 62–68. doi:10.1038/nature10918.

Hayashi, H., and Igarashi, J. (2009). LTD windows of the STDP learning rule and synaptic connections having a large transmission delay enable robust sequence learning amid background noise. *Cogn. Neurodyn.* 3, 119–130. doi:10.1007/s11571-009-9076-2.

Hebb, D. O. (1949). *The organization of behavior; a neuropsycholocigal theory.* New York: John Wiley & Sons, Inc.

Hoffman, K. L., and McNaughton, B. L. (2002). Coordinated Reactivation of Distributed Memory Traces in Primate Neocortex. *Science* 297, 2070–2073. doi:10.1126/science.1073538.

Hussar, C. R., and Pasternak, T. (2012). Memory-Guided Sensory Comparisons in the Prefrontal Cortex: Contribution of Putative Pyramidal Cells and Interneurons. *J. Neurosci.* 32, 2747–2761. doi:10.1523/JNEUROSCI.5135-11.2012.

Ito, H. T., Zhang, S.-J., Witter, M. P., Moser, E. I., and Moser, M.-B. (2015). A prefrontal–thalamo–hippocampal circuit for goal-directed spatial navigation. *Nature* 522, 50–55. doi:10.1038/nature14396.

Itskov, V., Curto, C., Pastalkova, E., and Buzsaki, G. (2011). Cell Assembly Sequences Arising from Spike Threshold Adaptation Keep Track of Time in the Hippocampus. *J. Neurosci.* 31, 2828–2834. doi:10.1523/JNEUROSCI.3773-10.2011.

Jadhav, S. P., Kemere, C., German, P. W., and Frank, L. M. (2012). Awake Hippocampal Sharp-Wave Ripples Support Spatial Memory. *Science* 336, 1454–1458. doi:10.1126/science.1217230.

Jadhav, S. P., Rothschild, G., Roumis, D. K., and Frank, L. M. (2016). Coordinated Excitation and Inhibition of Prefrontal Ensembles during Awake Hippocampal Sharp-Wave Ripple Events. *Neuron* 90, 113–127. doi:10.1016/j.neuron.2016.02.010.

Jarsky, T., Roxin, A., Kath, W. L., and Spruston, N. (2005). Conditional dendritic spike propagation following distal synaptic activation of hippocampal CA1 pyramidal neurons. *Nat. Neurosci.* 8, 1667–1676. doi:10.1038/nn1599.

Ji, D., and Wilson, M. A. (2007). Coordinated memory replay in the visual cortex and hippocampus during sleep. *Nat. Neurosci.* 10, 100–107. doi:10.1038/nn1825.

Johnson, L. A., Euston, D. R., Tatsuno, M., and McNaughton, B. L. (2010). Stored-Trace Reactivation in Rat Prefrontal Cortex Is Correlated with Down-to-Up State Fluctuation Density. *J. Neurosci.* 30, 2650–2661. doi:10.1523/JNEUROSCI.1617-09.2010.

Kaefer, K., Nardin, M., Blahna, K., and Csicsvari, J. (2020). Replay of Behavioral Sequences in the Medial Prefrontal Cortex during Rule Switching. *Neuron*. doi:10.1016/j.neuron.2020.01.015.

Klampfl, S., and Maass, W. (2013). Emergence of Dynamic Memory Traces in Cortical Microcircuit Models through STDP. *J. Neurosci.* 33, 11515–11529. doi:10.1523/JNEUROSCI.5044-12.2013.

Koulakov, A. A., Raghavachari, S., Kepecs, A., and Lisman, J. E. (2002). Model for a robust neural integrator. *Nat. Neurosci.* 5, 775–782. doi:10.1038/nn893.

Kudrimoti, H. S., Barnes, C. A., and McNaughton, B. L. (1999). Reactivation of Hippocampal Cell Assemblies: Effects of Behavioral State, Experience, and EEG Dynamics. *J. Neurosci.* 19, 4090–4101. doi:10.1523/JNEUROSCI.19-10-04090.1999.

Laje, R., and Buonomano, D. V. (2013). Robust timing and motor patterns by taming chaos in recurrent neural networks. *Nat. Neurosci.* 16, 925–933. doi:10.1038/nn.3405.

Lara, A. H., and Wallis, J. D. (2014). Executive control processes underlying multi-item working memory. *Nat. Neurosci.* 17, 876–883. doi:10.1038/nn.3702.

Lee, A. K., and Wilson, M. A. (2002). Memory of Sequential Experience in the Hippocampus during Slow Wave Sleep. *Neuron* 36, 1183–1194. doi:10.1016/S0896-6273(02)01096-6.

Liu, J. K., and Buonomano, D. V. (2009). Embedding Multiple Trajectories in Simulated Recurrent Neural Networks in a Self-Organizing Manner. *J. Neurosci.* 29, 13172–13181. doi:10.1523/JNEUROSCI.2358-09.2009.

London, M., Roth, A., Beeren, L., Häusser, M., and Latham, P. E. (2010). Sensitivity to perturbations in vivo implies high noise and suggests rate coding in cortex. *Nature* 466, 123–127. doi:10.1038/nature09086.

Louie, K., and Wilson, M. A. (2001). Temporally structured replay of awake hippocampal ensemble activity during rapid eye movement sleep. *Neuron* 29, 145–156. doi:10.1016/S0896-6273(01)00186-6.

Lundqvist, M., Herman, P., Warden, M. R., Brincat, S. L., and Miller, E. K. (2018). Gamma and beta bursts during working memory readout suggest roles in its volitional control. *Nat. Commun.* 9, 394. doi:10.1038/s41467-017-02791-8.

Mazor, O., and Laurent, G. (2005). Transient dynamics versus fixed points in odor representations by locust antennal lobe projection neurons. *Neuron* 48, 661–673. doi:10.1016/j.neuron.2005.09.032.

Mehring, C., Hehl, U., Kubo, M., Diesmann, M., and Aertsen, A. (2003). Activity dynamics and propagation of synchronous spiking in locally connected random networks. *Biol. Cybern.* 88, 395–408. doi:10.1007/s00422-002-0384-4.

Mello, G. B. M., Soares, S., and Paton, J. J. (2015). A Scalable Population Code for Time in the Striatum. *Curr. Biol.* 25, 1113–1122. doi:10.1016/j.cub.2015.02.036.

Mizuseki, K., Royer, S., Diba, K., and Buzsáki, G. (2012). Activity dynamics and behavioral correlates of CA3 and CA1 hippocampal pyramidal neurons. *Hippocampus* 22, 1659–1680. doi:10.1002/hipo.22002.

Moberly, A. H., Schreck, M., Bhattarai, J. P., Zweifel, L. S., Luo, W., and Ma, M. (2018). Olfactory inputs modulate respiration-related rhythmic activity in the prefrontal cortex and freezing behavior. *Nat. Commun.* 9, 1528. doi:10.1038/s41467-018-03988-1.

Nádasdy, Z., Hirase, H., Czurkó, A., Csicsvari, J., and Buzsáki, G. (1999). Replay and Time Compression of Recurring Spike Sequences in the Hippocampus. *J. Neurosci.* 19, 9497–9507. doi:10.1126/science.1182395.

O'Keefe, J., and Dostrovsky, J. (1971). The hippocampus as a spatial map: Preliminary

evidence from unit activity in the freely-moving rat. *Brain Res.* 34, 171–175. doi:10.1016/0006-8993(71)90358-1.

O'Neill, J., Boccara, C. N., Stella, F., Schoenenberger, P., and Csicsvari, J. (2017). Superficial layers of the medial entorhinal cortex replay independently of the hippocampus. *Science* 355, 184–188. doi:10.1126/science.aag2787.

Pastalkova, E., Itskov, V., Amarasingham, A., and Buzsaki, G. (2008). Internally Generated Cell Assembly Sequences in the Rat Hippocampus. *Science* 321, 1322–1327. doi:10.1126/science.1159775.

Peyrache, A., Khamassi, M., Benchenane, K., Wiener, S. I., and Battaglia, F. P. (2009). Replay of rule-learning related neural patterns in the prefrontal cortex during sleep. *Nat. Neurosci.* 12, 919–926. doi:10.1038/nn.2337.

Pfeiffer, B. E., and Foster, D. J. (2013). Hippocampal place-cell sequences depict future paths to remembered goals. *Nature* 497, 74–79. doi:10.1038/nature12112.

Poulet, J. F. A., and Petersen, C. C. H. (2008). Internal brain state regulates membrane potential synchrony in barrel cortex of behaving mice. *Nature* 454, 881–885. doi:10.1038/nature07150.

Ratté, S., Karnup, S., and Prescott, S. A. (2018). Nonlinear Relationship Between Spike-Dependent Calcium Influx and TRPC Channel Activation Enables Robust Persistent Spiking in Neurons of the Anterior Cingulate Cortex. *J. Neurosci.* 38, 1788–1801. doi:10.1523/JNEUROSCI.0538-17.2018.

Renart, A., Rocha, J. de la, Bartho, P., Hollender, L., Parga, N., Reyes, A., et al. (2010). The Asynchronous State in Cortical Circuits. *Science* 327, 587–590. doi:10.1126/science.1179850.

Riehle, A., Grün, S., Diesmann, M., and Aertsen, A. (1997). Spike Synchronization and Rate Modulation Differentially Involved in Motor Cortical Function. *Science*. Available at: https://www.science.org/doi/abs/10.1126/science.278.5345.1950 [Accessed September 7, 2021].

Rikhye, R. V., Gilra, A., and Halassa, M. M. (2018). Thalamic regulation of switching between cortical representations enables cognitive flexibility. *Nat. Neurosci.* 21, 1753–1763. doi:10.1038/s41593-018-0269-z.

Rodriguez, G., Sarazin, M., Clemente, A., Holden, S., Paz, J. T., and Delord, B. (2018). Conditional bistability, a generic cellular mnemonic mechanism for robust and flexible working memory computations. *J. Neurosci.*, 1992–17. doi:10.1523/JNEUROSCI.1992-17.2017.

Rubin, A., Sheintuch, L., Brande-Eilat, N., Pinchasof, O., Rechavi, Y., Geva, N., et al. (2019). Revealing neural correlates of behavior without behavioral measurements. *Nat. Commun.* 10, 4745. doi:10.1038/s41467-019-12724-2.

Runyan, C. A., Piasini, E., Panzeri, S., and Harvey, C. D. (2017). Distinct timescales of

population coding across cortex. *Nature* 548, 92–96. doi:10.1038/nature23020.

Sarazin, M. X. B., Victor, J., Medernach, D., Naudé, J., and Delord, B. (2021). Online Learning and Memory of Neural Trajectory Replays for Prefrontal Persistent and Dynamic Representations in the Irregular Asynchronous State. *Front. Neural Circuits* 0. doi:10.3389/fncir.2021.648538.

Schmitt, L. I., Wimmer, R. D., Nakajima, M., Happ, M., Mofakham, S., and Halassa, M. M. (2017). Thalamic amplification of cortical connectivity sustains attentional control. *Nature* 545, 219–223. doi:10.1038/nature22073.

Seeholzer, A., Deger, M., and Gerstner, W. (2019). Stability of working memory in continuous attractor networks under the control of short-term plasticity. *PLOS Comput. Biol.* 15, e1006928. doi:10.1371/journal.pcbi.1006928.

Shafi, M., Zhou, Y., Quintana, J., Chow, C., Fuster, J., and Bodner, M. (2007). Variability in neuronal activity in primate cortex during working memory tasks. *Neuroscience* 146, 1082–1108. doi:10.1016/j.neuroscience.2006.12.072.

Shinomoto, S., Miyazaki, Y., Tamura, H., and Fujita, I. (2005). Regional and Laminar Differences in In Vivo Firing Patterns of Primate Cortical Neurons. *J. Neurophysiol.* 94, 567–575. doi:10.1152/jn.00896.2004.

Siapas, A. G., Lubenov, E. V., and Wilson, M. A. (2005). Prefrontal Phase Locking to Hippocampal Theta Oscillations. *Neuron* 46, 141–151. doi:10.1016/j.neuron.2005.02.028.

Skaggs, W. E., and McNaughton, B. L. (1996). Replay of Neuronal Firing Sequences in Rat Hippocampus During Sleep Following Spatial Experience. *Science* 271, 1870–1873. doi:10.1126/science.271.5257.1870.

Skaggs, W. E., McNaughton, B. L., Wilson, M. A., and Barnes, C. A. (1996). Theta phase precession in hippocampal neuronal populations and the compression of temporal sequences. *Hippocampus* 6, 149–172. doi:10.1002/(SICI)1098-1063(1996)6:2<149::AID-HIPO6>3.0.CO;2-K.

Spaak, E., Watanabe, K., Funahashi, S., and Stokes, M. G. (2017). Stable and Dynamic Coding for Working Memory in Primate Prefrontal Cortex. *J. Neurosci.* 37, 6503–6516. doi:10.1523/JNEUROSCI.3364-16.2017.

Sreenivasan, K. K., Curtis, C. E., and D'Esposito, M. (2014). Revisiting the role of persistent neural activity during working memory. *Trends Cogn. Sci.* 18, 82–89. doi:10.1016/j.tics.2013.12.001.

Stokes, M. G., Kusunoki, M., Sigala, N., Nili, H., Gaffan, D., and Duncan, J. (2013). Dynamic Coding for Cognitive Control in Prefrontal Cortex. *Neuron* 78, 364–375. doi:10.1016/j.neuron.2013.01.039.

Sussillo, D., and Abbott, L. F. (2009). Generating Coherent Patterns of Activity from Chaotic Neural Networks. *Neuron* 63, 544–557. doi:10.1016/j.neuron.2009.07.018.

Tchumatchenko, T., Geisel, T., Volgushev, M., and Wolf, F. (2010). Signatures of synchrony in pairwise count correlations. *Front. Comput. Neurosci.* 4. doi:10.3389/neuro.10.001.2010.

Tran-Van-Minh, A., Cazé, R. D., Abrahamsson, T., Cathala, L., Gutkin, B. S., and DiGregorio, D. A. (2015). Contribution of sublinear and supralinear dendritic integration to neuronal computations. *Front. Cell. Neurosci.* 9. doi:10.3389/fncel.2015.00067.

Turrigiano, G. G., Leslie, K. R., Desai, N. S., Rutherford, L. C., and Nelson, S. B. (1998). Activity-dependent scaling of quantal amplitude in neocortical neurons. *Nature* 391, 892–896. doi:10.1038/36103.

Villalobos, C., Shakkottai, V. G., Chandy, K. G., Michelhaugh, S. K., and Andrade, R. (2004). SKCa Channels Mediate the Medium But Not the Slow Calcium-Activated Afterhyperpolarization in Cortical Neurons. *J. Neurosci.* 24, 3537–3542. doi:10.1523/JNEUROSCI.0380-04.2004.

Wang, X.-J. (1999). Synaptic Basis of Cortical Persistent Activity: the Importance of NMDA Receptors to Working Memory. *J. Neurosci.* 19, 9587–9603.

Xue, M., Atallah, B. V., and Scanziani, M. (2014). Equalizing excitation–inhibition ratios across visual cortical neurons. *Nature* 511, 596–600. doi:10.1038/nature13321.

Xue, X., Halassa, M. M., and Chen, Z. S. (2021). Spiking recurrent neural networks represent task-relevant neural sequences in rule-dependent computation. *bioRxiv*, 2021.01.21.427464. doi:10.1101/2021.01.21.427464.

Yang, S.-T., Shi, Y., Wang, Q., Peng, J.-Y., and Li, B.-M. (2014). Neuronal representation of working memory in the medial prefrontal cortex of rats. *Mol. Brain* 7, 61. doi:10.1186/s13041-014-0061-2.

Zenke, F., Gerstner, W., and Ganguli, S. (2017). The temporal paradox of Hebbian learning and homeostatic plasticity. *Curr. Opin. Neurobiol.* 43, 166–176. doi:10.1016/j.conb.2017.03.015.

Zhang, J.-C., Lau, P.-M., and Bi, G.-Q. (2009). Gain in sensitivity and loss in temporal contrast of STDP by dopaminergic modulation at hippocampal synapses. *Proc. Natl. Acad. Sci.* 106, 13028–13033. doi:10.1073/pnas.0900546106.

Zielinski, M. C., Shin, J. D., and Jadhav, S. P. (2019). Coherent Coding of Spatial Position Mediated by Theta Oscillations in the Hippocampus and Prefrontal Cortex. *J. Neurosci.* 39, 4550–4565. doi:10.1523/JNEUROSCI.0106-19.2019.

Author contributions

MS JN BD designed the model and research project. MS DM BD simulated the model and analyzed its behavior. MS JN BD wrote the article.

Figure legends

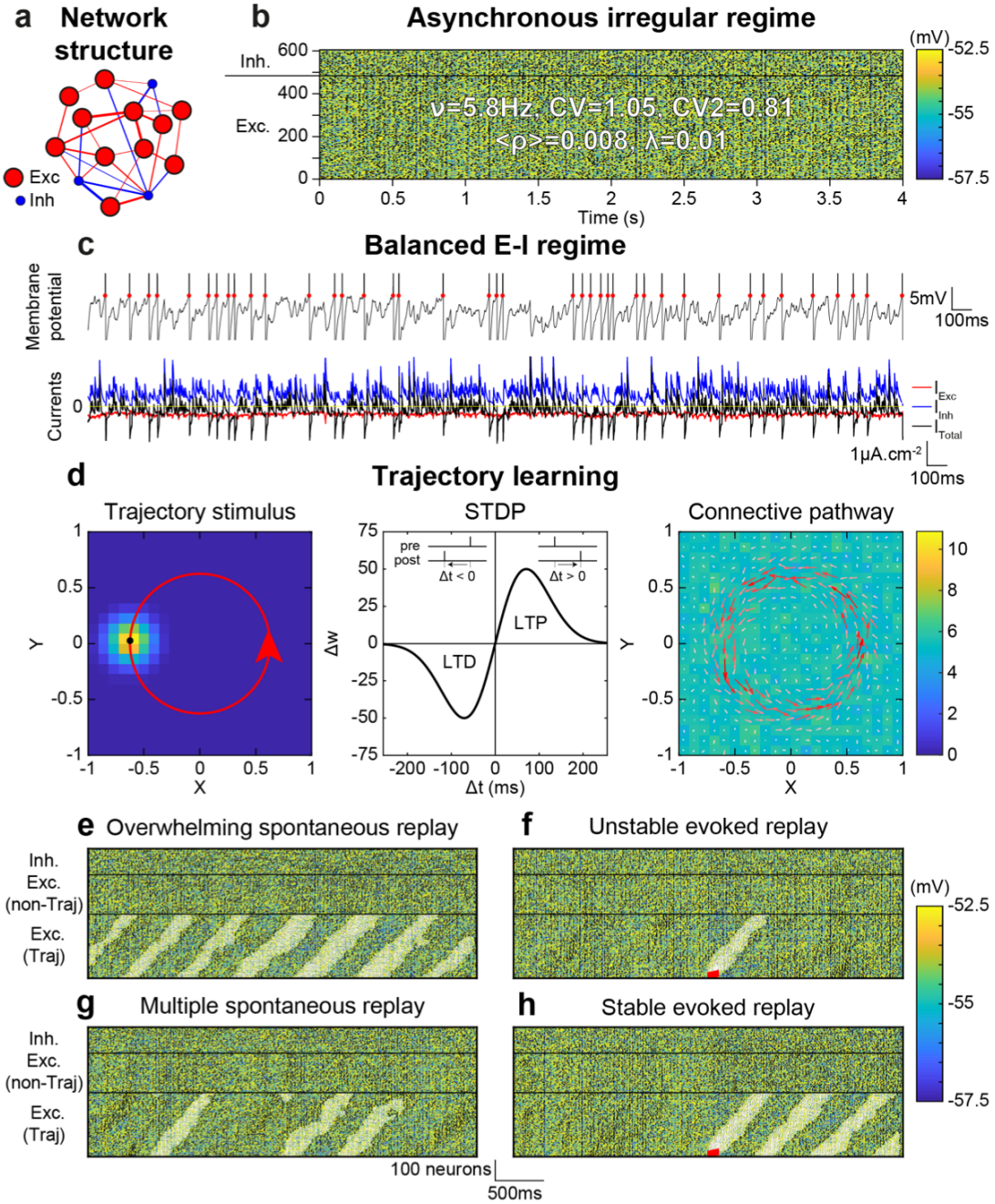

Figure 1. STDP-induced trajectory replay diversity within the balanced AI regime. (**a**) Randomly connected recurrent neural network of 80% excitatory and 20% inhibitory neurons (14 neurons are shown, whereas the model is composed of 605 neurons, i.e. 484 excitatory, 121 inhibitory). (**b**) Asynchronous irregular network activity, with spikes (black dots) and membrane potential of neurons across 4 seconds of simulation. (**c**) Subthreshold membrane potential and irregular spikes (top) driven by current fluctuations, since excitatory and inhibitory currents are balanced on average (bottom). (**d**) (Left) External circular trajectory stimulus (red circle), activating neurons through putative spatially-organized receptive fields. Example activity of neurons (background colors) induced by the trajectory stimulus at a given time point (black dot). (Middle) Temporal window of the STDP learning rule, inducing LTP for positive time differences (pre- then post-synaptic spikes) and LTD for negative time

differences (post- then pre-synaptic spikes). (Right) Resulting connective pathway, with normalized arrows showing the direction in which outgoing weights are most potentiated (white to red arrow color scheme with increasing arrow magnitude), and homogeneous background colors showing similar sums of total incoming weights onto neurons (due to synaptic scaling) (**e-h**) Resulting connective pathways induce a variety of different trajectory replays, which emerge spontaneously (**e** & **g**) or can be evoked via a strong stimulus onto the first 25 neurons of the trajectory (red rectangle, **f** & **h**).

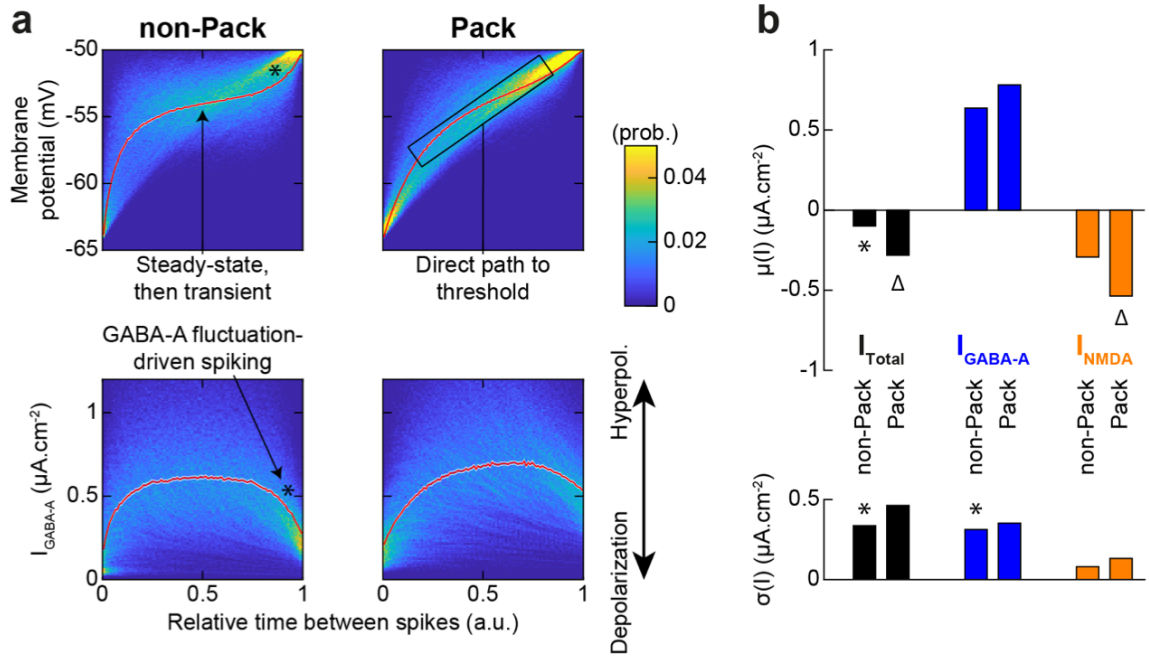

Figure 2. Pack propagation relies on a transition from GABA-A fluctuation- to NMDA mean current-driven deterministic spiking. (**a**) Membrane potential (top) and GABA-A current (bottom) of neurons when outside (left) and within (right) the trajectory activity pack, considered at the time scale of an ISI or between two spikes. Data is aggregated by normalizing time between two spikes (no matter the ISI duration). Background color shows the probability of individual membrane potentials or GABA-A currents curves (sum normalized to 1 in each time bin) across many ISI during one network simulation of 4 seconds, with red curves showing the average (weighted according to the underlying probabilities at each time bin). (**b**) Temporal average (top) and fluctuations (bottom) of total (left, black), GABA-A (middle, blue) and NMDA (right, orange) currents onto neurons when outside (non-Pack) or within (Pack) the trajectory activity pack, averaged across neurons.

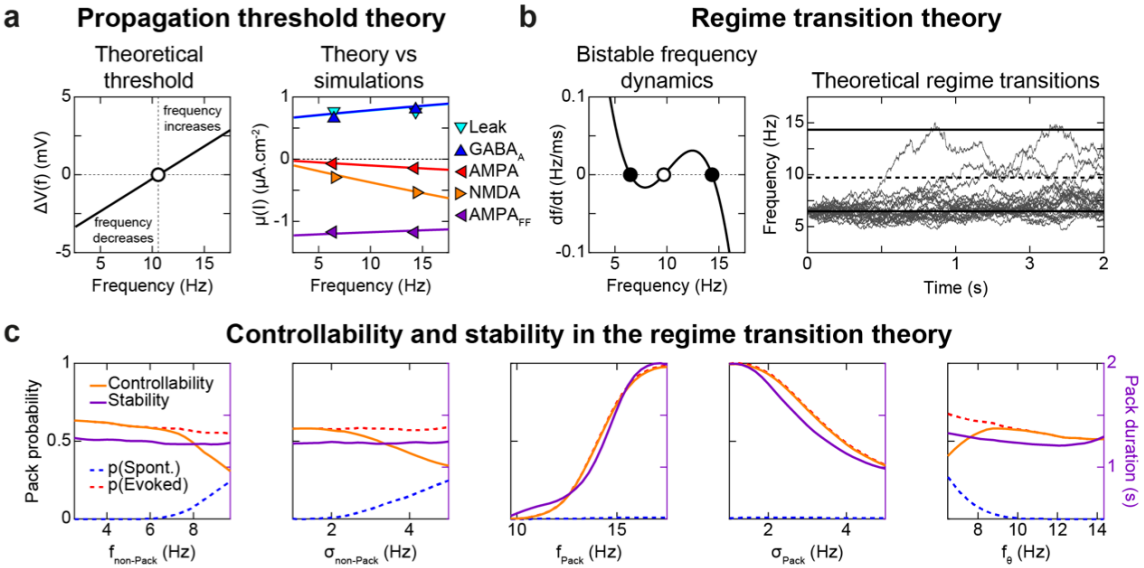

Figure 3. Theoretical account of the threshold separating, and transitions between, spontaneous and propagation regimes (**a**) Propagation threshold theory. (Left) In a 1D reduced analytical model (see Methods), frequency self-amplifies above f_θ and is extinguished below, i.e. as the membrane potential reaches ($\Delta V > 0$) or not ($\Delta V < 0$) a fluctuation-based spiking threshold at time $T = 1/f$ in a post-synaptic neuron, given pre-synaptic spiking at frequency f. (Right) The theoretical model is quantitatively consistent with network simulations at the fine-grain of ionic and synaptic currents in both the low frequency spontaneous and the higher frequency pack regimes. (**b**) Regime transition theory. (left) In a 1D reduced model of both regimes, frequency dynamics follows bistable dynamics with added Gaussian noise. (Right) Example simulations of the regime transition theory. (**c**) Probability of spontaneous and evoked transitions to the regime of pack propagation (dotted lines), and of controllability and stability of the pack regime (solid lines) in the regime transition theory, as a function of parameters (non-Pack and Pack mean frequencies and standard deviations, and the threshold frequency).

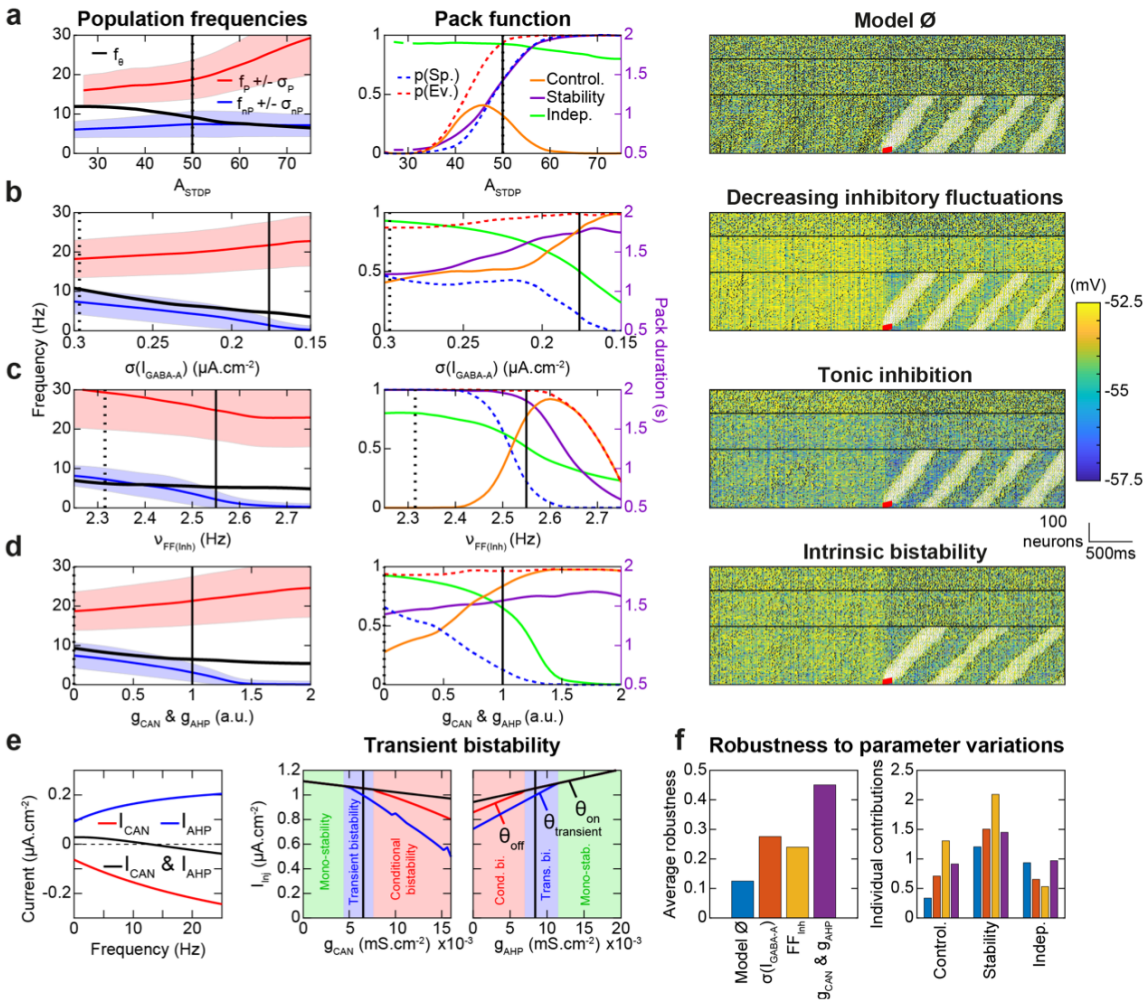

Figure 4. Modulation of controllability and stability by architectural, synaptic, and ionic determinants. (**a-d**) Mechanisms for increasing trajectory replay controllability and stability, as seen when varying different parameters, such as the GABA-A current fluctuations $\sigma(I_{GABA-A})$ (via a higher number of inh. → exc. synapses, see *Methods*) (**b**), the frequency of external neurons sending AMPA feedforward currents onto inhibitory neurons FF_{Inh} (**c**), and a multiplicative factor modulating CAN and AHP conductances together g_{CAN} & g_{AHP} (**d**). STDP amplitude A_{STDP} was varied across the different mechanisms (A_{STDP} = 47.5 for $\sigma(I_{GABA-A})$, 75 for FF_{Inh} and 50 for g_{CAN} & g_{AHP}), and is shown as a control for comparison's sake in (**a**). (Left) Non-pack and pack average frequency (+/- fluctuations) and threshold frequency, when varying the aforementioned parameters (X-axis). Normal parameter value (dotted vertical black line), and that chosen to illustrate the mechanism's effects (solid vertical black line), are indicated. (Middle) Probability of spontaneous and evoked packs (dotted lines), and pack controllability, propagation stability and independence (solid lines). (Right) Example of trajectory replay with illustrative mechanism parameters. The (A_{STDP}, mechanism parameter) value couple of each mechanism was systematically determined as that maximizing the product of controllability, stability and independence (all three being normalized between 0 and 1). (**e**) (Left) Equilibrium values of CAN (red), AHP (blue) and total (CAN & AHP, black) currents of excitatory neurons, when considering the time-averaged calcium concentration at different frequencies. (Right) CAN and AHP conductances induced transient spiking bistability (rather than mono-stability, conditional bistability or absolute bistability), as defined by the protocol in (Rodriguez et al., 2018, see *Methods*). Solid vertical black lines indicate the chosen mechanism parameters. (**f**) (Left) Average robustness of the physiological low-frequency asynchronous irregular network activity with controllable, stable and independent trajectory replays, to the variation of 22 of the model's

parameters (see *Methods* and **Fig. S3**). The different mechanisms, and the standard Model (Ø), are compared. (Right) Contribution of the trajectory replay controllability, stability and independence criteria to the overall robustness score.

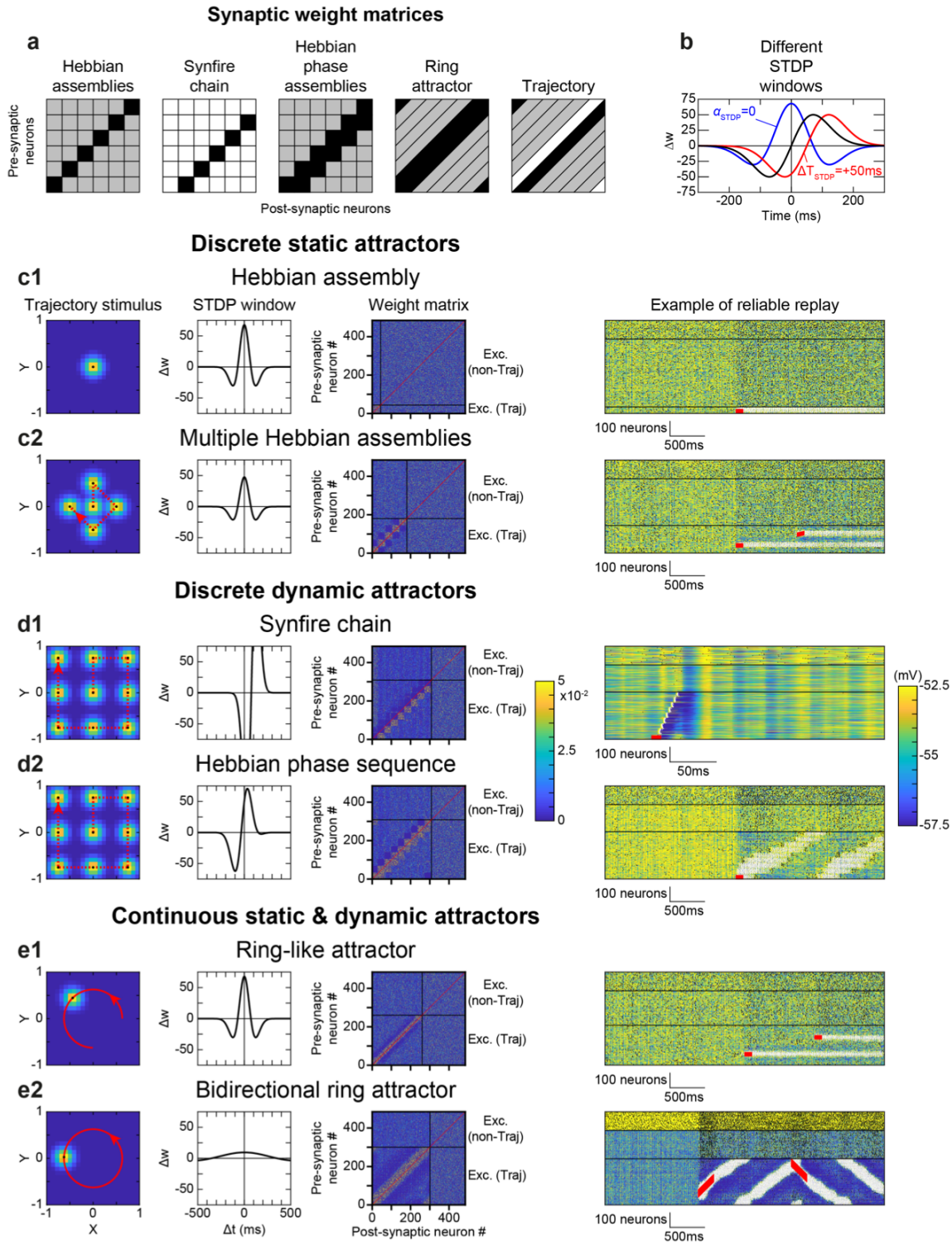

Figure 5. A common framework for attractor models. (**a**) Weight matrices underlying different types of network attractors. White, grey and black colors indicate the strength of synaptic weights (white = absence of synapses, grey = moderate weights, black = strong weights). (**b**) Modulation of the asymmetric STDP window (black) when varying its symmetry ($\alpha_{STDP} = 0$, symmetric STDP window, blue curve) and temporal shift ($\Delta t = +50ms$, red curve). (**c-e**) Altering the trajectory stimulus and STDP learning rule, when combined with the aforementioned mechanisms allowing controllable and stable trajectory replays, enabled the emergence of reliable attractors of different types, e.g. discrete

vs. continuous and static vs. dynamic attractors, as in (a). (Left) External trajectory stimulus (as in **Fig. 1.d** left). Dotted red lines indicate a discontinuous trajectory, jumping from one black dot to the next in a discrete manner (rather than continuously, as in (e)). (Middle left) STDP temporal window (as in **Fig. 1.d** middle). (Middle right) Resulting synaptic weight matrices between pre-synaptic and post-synaptic excitatory neurons on the Y- and X-axes respectively. Neurons affected by the trajectory are regrouped and ordered according to their activation time within the trajectory. (Right) Examples of resulting trajectory replay. The g_{CAN} & g_{AHP} mechanism was used for the Hebbian assembly, multiple Hebbian assemblies and ring-like attractors; the $\sigma(I_{GABA-A})$ mechanism was used for the synfire chain, Hebbian phase sequence and bidirectional ring attractors; the $\nu_{FF(Inh)}$ mechanism was used for the synfire chain. Additional modifications were necessary for the synfire chain ($g_{AMPA} = 0.5\ mS.cm^{-2}$, $g_{NMDA} = 0\ mS.cm^{-2}$ instead of $0.2\ mS.cm^{-2}$, $g_{NMDA} = 0.3\ mS.cm^{-2}$ for rapid pack propagation) and bidirectional ring attractors (see *Methods*).

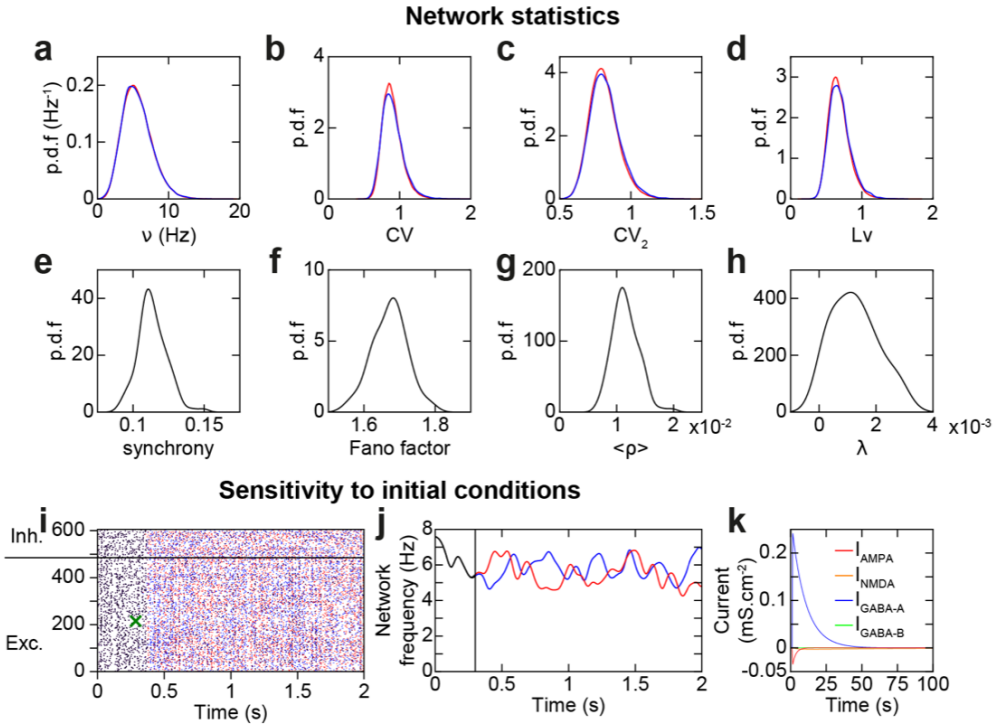

Figure S1. Distributions of network statistics over many network simulations. (**a-h**) Probability density functions of network spiking statistics, calculated on 100 network simulations of 10s. Frequency (**a**), CV (**b**), CV2 (**c**), and Lv (**d**) of individual excitatory (red) and inhibitory (blue) neuronal spiking activity. Synchrony measure (**e**), Fano factor (**f**), average pairwise correlation coefficient (**g**), and Lyapunov exponent (**h**) of network spiking activity. (**i**) Chaotic network activity seen through sensitivity to initial conditions. A network was simulated in identical initial conditions, until a single randomly chosen spike at ~300ms (green cross) was either kept (red spikes) or removed (blue spikes). Overlap in spikes between in both simulations are colored in black (notice that all spikes are identical and thus black before the green cross). (**j**) Same as (i), but average network frequency of both simulations (red & blue, overlap in black). (**k**) Stronger IPSC than EPSC, allowing balanced total currents and thus fluctuation-based spiking. IPSC and EPSC are subdivided into their individual (AMPA, NMDA, GABA-A, GABA-B) components.

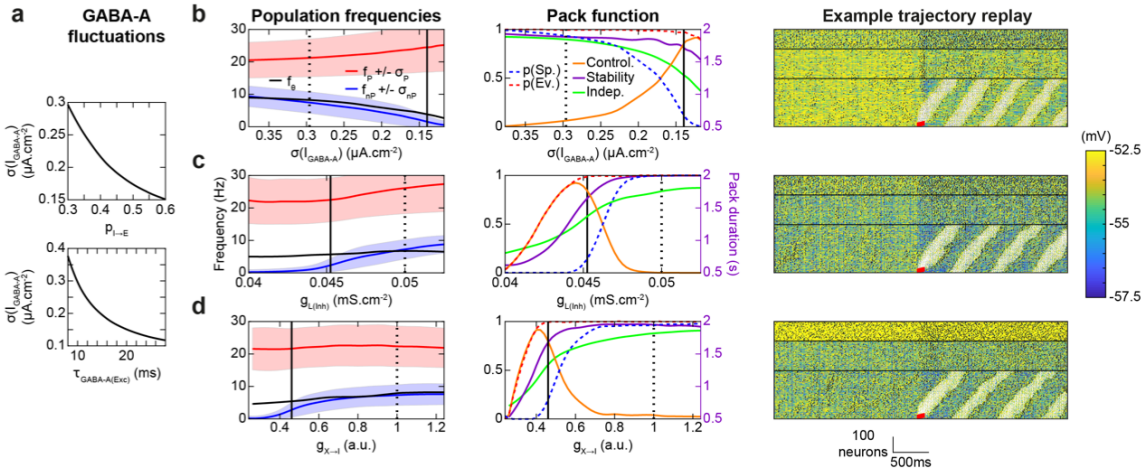

Figure S2. GABA-A fluctuations and alternative effects of lowering disinhibition on replay quality. (**a**) $\sigma(I_{GABA-A})$ as a function of $f_{I\to E}$ or $\tau_{GABA-A(Exc)}$ (for each value of these parameters, $g_{GABA-A(Exc)}$ was compensated so as to get a constant mean GABA-A conductance). (**b-d**) Same as **Fig. 4a-d**, but when varying the GABA-A current time constant of excitatory neurons $\tau_{GABA-A(Exc)}$ ($A_{STDP} = 57.5$) (**b**), Leak conductance of inhibitory neurons $g_{L,(Inh)}$ ($A_{STDP} = 67.5$) (**c**), and multiplicative factor of recurrent current conductances impinging upon inhibitory neurons $\rho_{X\to I}$ ($A_{STDP} = 60$) (**d**). For $\tau_{GABA-A(Exc)}$, Δp of inhibitory to excitatory neuron synapses were modulated in order for average p_{GABA-A} to be kept approximately constant at $\nu = 5.5\ Hz$, i.e. weakened for longer $\tau_{GABA-A(Exc)}$. To do so, Δp was multiplied by the estimated average p_{GABA-A} value at $\nu = 5.5\ Hz$ for $\tau_{GABA-A(Exc)} = 10\ ms$ (calculated as $p_{AMPA_{FF}}$) and divided by the same estimate but for the chosen value of $\tau_{GABA-A(Exc)}$.

Robustness to each individual parameter

a

Categories	Parameters
Synaptic matrix	μ_w, σ_w, A_{STDP}, τ_{STDP}, α_{STDP}
Recurrent synaptic currents	g_{AMPA}, g_{NMDA}, g_{GABA-A}, g_{GABA-B}, τ^{Decay}_{AMPA}, τ^{Decay}_{NMDA}, τ^{Decay}_{GABA-A}, τ^{Decay}_{GABA-B}, k_{NMDA}, α_{NMDA}, τ^{Rise}_{NMDA}, α_{GABA-B}, τ^{Rise}_{GABA-B}
Stimulus & intrinsic properties	σ_{RF}, υ_{Traj}, g_{Leak}, $g_{AMPA.FF}$

b

Criteria	Accepted range	References
Physiological peak IPSC/EPSC ratio	$5 \leq x \leq 10$	(Xue et al., 2014)
Physiological peak NMDA/AMPA ratio	$1 \leq x \leq 2$	(Myme et al., 2003; Wang et al., 2008)
Sustained network activity	$x \leq 100$ms	
Physiological neuronal activity	$x \leq 250$ms	
Physiological Exc. frequency	$0.1 \leq x \leq 15$Hz	(Boudewijns et al., 2013; Shafi et al., 2007)
Physiological Inh. frequency	$0.1 \leq x \leq 30$Hz	(Boudewijns et al., 2013; Shafi et al., 2007)
Physiological Exc. spontaneous CV	$0.5 \leq x \leq 1.5$	(Compte et al., 2003)
Physiological Exc. spontaneous CV2	$0.25 \leq x \leq 1.25$	(Compte et al., 2003)
Low pack frequency	$15 \leq x \leq 100$Hz	(Xue et al., 2014)
Controllability	$x = 1$	(Harvey et al., 2012; Jadhav et al., 2016)
Stability	$x \geq 1$s	(Harvey et al., 2012; Jadhav et al., 2016)
Independence	$0.5 \leq x \leq 1$	(Harvey et al., 2012)

c

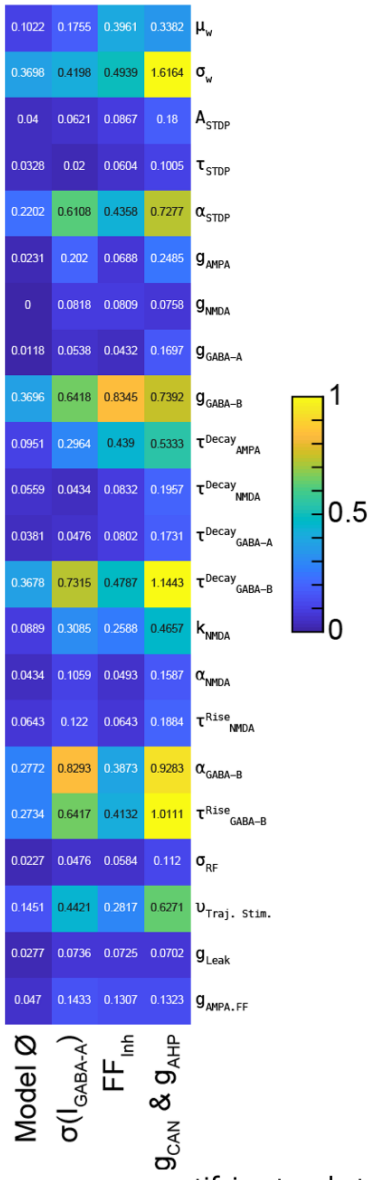

Figure S3. Robustness to parameters. Computation of the robustness score, quantifying to what extent the physiological low-frequency asynchronous irregular network activity with controllable, stable and independent trajectory replays is robust to the variation of the model's parameters. (**a**) Parameters varied (see *Methods*). (**b**) List of criteria that need to be simultaneously met within a model network simulation for it to be considered "correct". (**c**) Detail of the robustness score for each individual model parameter, for the different mechanisms and standard model (Ø).

Methods

Model of biophysical local recurrent neural network

We built a biophysical model of a generic local recurrent neural network, endowed with detailed biological properties of its neurons and connections, as in (Sarazin et al., 2021). The network model contained N neurons that were either excitatory (E) or inhibitory (I) (neurons projecting only glutamate or GABA, respectively; Dale, 1935), with probabilities p_E and $p_I = 1 - p_E$ respectively, and $p_E/p_I = 4$ (Beaulieu et al., 1992). Connectivity was sparse (i.e. only a fraction of all possible connections exists, see $p_{E\to E}, p_{E\to I}, p_{I\to E}, p_{I\to I}$ parameter values; Thomson 2002) with no autapses (self-connections) and EE connections (from E to E neurons) drawn to ensure the over-representation of bidirectional connections in cortical networks (four times more than randomly drawn according to a Bernoulli scheme; Song et al., 2005). The synaptic weights $w_{(i,j)}$ of existent connections were drawn identically and independently from a log-normal distribution of parameters μ_w and σ_w (Song et al., 2005). To cope with simulation times required for the massive explorations ran in the parameter space, neurons were modeled as leaky integrate-and-fire (LIF) neurons.

The membrane potential followed

$$\begin{cases} C\dfrac{dV_{(j)}}{dt} = -(I_{Ionic(j)} + I_{Syn.Rec(j)} + I_{Syn.FF(j)}) \\ V_{(j)} > \theta \rightarrow V_{(j)} = V_{rest} \end{cases}$$

where neurons spike when the membrane potential reached the threshold θ, and repolarization to V_{rest} occurred after a refractory period Δt_{AP}. Initial membrane potential of neurons were randomly drawn from a uniform distribution between θ and V_{rest}.

The ionic current followed

$$I_{Ionic(j)} = I_{L(j)} + I_{CAN(j)} + I_{AHP(j)}$$

in which the leak current was

$$I_L = \bar{g}_L \left(V_{(j)} - V_L\right)$$

where $\bar{g}_L$ was the maximal conductance and V_L the equilibrium potential of the leak current.

The cationic non-selective (I_{CAN}) current and the medium after-hyperpolarization (I_{AHP}) currents, responsible for frequency adaptation and bistable discharge in pyramidal neurons, were taken as

$$I_x = \bar{g}_x \, p_x^{\gamma_x}\left(V_{(j)} - V_x\right)$$

where p_x ($x \in \{CAN,\ AHP\}$) corresponded to the opening probability of both currents and γ_x the gating factor of opening probabilities. Denoting the intra-somatic calcium concentration as Ca, p_x followed

$$\frac{dp_x}{dt} = (p_x^{\infty}(Ca) - p_x)/\tau_x(Ca)$$

with

$$\tau_x(Ca) = 1/(\alpha_x Ca + \beta_x)$$

and

$$p_x^{\infty}(Ca) = \alpha_x Ca/(\alpha_x Ca + \beta_x)$$

where α_x and β_x respectively denoted activation and deactivation kinetic constants, consistent with experimental data in layer 5 PFC pyramidal neurons (Haj-Dahmane and Andrade, 1997; Villalobos et al., 2004; Faber and Sah, 2007).

The intra-somatic calcium concentration evolved according to discrete spike-induced increments and first-order exponential decay

$$\frac{dCa_{(j)}}{dt} = \frac{Ca_0 - Ca_{(j)}}{\tau_{Ca}} + \Delta Ca\ \delta\left(t - t_{(j)}^k\right)$$

where $t_{(j)}^k$ was the time of the k_{th} spike in the spike train of neuron j, δ the Dirac delta function, τ_{Ca} the time constant of calcium extrusion, Ca_0 the basal calcium and ΔCa a spike-induced increment of calcium concentration.

The recurrent synaptic current on post-synaptic neuron j, from – either excitatory or inhibitory – pre-synaptic neurons (indexed by i), was

$$I_{Syn.Rec(j)} = \sum_i \left(I_{AMPA(i,j)} + I_{NMDA(i,j)} + I_{GABA_A(i,j)} + I_{GABA_B(i,j)}\right)$$

The delay for synaptic conduction and transmission, Δt_{syn}, was considered uniform across the network (Brunel and Wang, 2001). Synaptic recurrent currents followed

$$I_{x(i,j)} = \bar{g}_x\ w_{(i,j)}\ p_{x(i)}\left(V_{(j)} - V_x\right)$$

where $w_{(i,j)}$ is the synaptic weight, $p_{x(i)}$ the opening probability of channel-receptors and V_x the reversal potential of the current. The NMDA current followed

$$I_{NMDA(i,j)} = \bar{g}_{NMDA}\ w_{(i,j)}\ p_{NMDA(i)}\ x_{NMDA}\left(V_{(j)}\right)\left(V_{(j)} - V_{NMDA}\right)$$

incorporating the magnesium block voltage-dependence modeled (Jahr and Stevens, 1990) as

$$x_{NMDA}(V) = (1 + [Mg^{2+}]e^{-0.062\,V}/3.57)^{-1}$$

AMPA and $GABA_A$ rise times were approximated as instantaneous (Brunel and Wang, 2001) and bounded, with first-order decay

$$\frac{dp_{x(i)}}{dt} = -\frac{p_{x(i)}}{\tau_x^{decay}} + \Delta p_x \left(1 - p_{x(i)}\right) \delta\left(t - t_{(i)}^k\right)$$

To take into account the longer NMDA (Wang et al., 2008) and GABA-B (Destexhe et al., 1998) rise times, opening probabilities followed second-order dynamics (Brunel and Wang, 2001)

$$\begin{cases} \frac{dq_{x(i)}}{dt} = -\frac{q_{x(i)}}{\tau_x^{rise}} + \Delta q_x \left(1 - q_{x(i)}\right) \delta\left(t - t_{(i)}^k\right) \\ \frac{dp_{x(i)}}{dt} = -\frac{p_{x(i)}}{\tau_x^{decay}} + \alpha_x \, q_{x(i)} \left(1 - p_{x(i)}\right) \end{cases}$$

Recurrent excitatory and inhibitory currents were balanced in each post-synaptic neuron (Xue et al., 2014), according to driving forces and the excitation/inhibition weight ratio, through

$$\begin{cases} \bar{g}_{GABA_A} = g_{GABA_A} \frac{-(V_{mean} - V_{Exc})}{\left(V_{mean} - V_{GABA_A}\right)} \frac{\sum_{i \in Exc} w_{(i,j)}}{\sum_{i \in Inh} w_{(i,j)}} \\ \bar{g}_{GABA_B} = g_{GABA_B} \frac{-(V_{mean} - V_{Exc})}{\left(V_{mean} - V_{GABA_B}\right)} \frac{\sum_{i \in Exc} w_{(i,j)}}{\sum_{i \in Inh} w_{(i,j)}} \end{cases}$$

with $V_{mean} = (\theta + V_{rest})/2$ being an approximation of the average membrane potential. The excitation/inhibition weight ratio notably balanced the currents coming from inhibitory neurons with the 4x more numerous excitatory neurons (rendering inhibitory currents 4x stronger on average). When specified (**.e2** and **Fig. S2.d**), both excitatory and inhibitory conductances onto excitatory neurons were multiplied by $g_{X \to E}$, and onto inhibitory neurons by $g_{X \to I}$.

The feed-forward synaptic current $I_{Syn.FF(j)}$ (putatively arising from sub-cortical and cortical inputs) consisted of an AMPA component

$$I_{Syn.FF(j)} = \bar{g}_{AMPA} \, p_{AMPA_{FF}} \left(V_{(j)} - V_{AMPA}\right)$$

with a constant opening probability $p_{AMPA_{FF}}$, determined as the temporal average of AMPA channel opening coming from n_{FF} neurons of putatively sub-cortical and cortico-cortical feedforward spiking at a given frequency ν_{FF}, thus following

$$p_{AMPA_{FF}} = \tau_{AMPA} \, n_{FF} \, \nu_{FF} \frac{\Delta p_{AMPA} \left(1 - e^{-\frac{1}{\tau_{AMPA} \, n_{FF} \, \nu_{FF}}}\right)}{1 + (\Delta p_{AMPA} - 1) \, e^{-\frac{1}{\tau_{AMPA} \, n_{FF} \, \nu_{FF}}}}$$

via integration (considering regular ISI for simplification during the integration). $p_{AMPA_{FF}}$ was considered constant so as to isolate the influence of deterministic chaos and spike irregularity on trajectory replay. However, to guarantee an initial stimulation sufficiently strong to start network activity, feedforward AMPA inputs were stronger at first ($n_{FF} = 200$ neurons, $\nu_{FF} = 3\ Hz$) and progressively decreased during $250\ ms$ to their constant value ($\nu_{FF} = 2.315\ Hz$; these initial $250\ ms$ were cut from all figures and analyses). Trajectory replay was evoked at 2s (**Fig. 1e-h**, red square) when the first 25 neurons of the trajectory received a strong feedforward AMPA stimulation ($n_{FF} = 20$ neurons, $\nu_{FF} = \nu_{\text{Traj. Stim.}} = 50\ Hz$, emulating a strong signal coming from few neurons). The epoch before this trajectory-evoking stimulus was considered "Spontaneous" and the epoch after "Evoked".

Learning protocol

The neural network was subjected to "offline" learning, i.e. before the network simulation, during which the receptive fields of excitatory neurons were sequentially stimulated. The resulting neural frequency conditioned learning of synaptic weights via STDP between excitatory neurons. This "offline" learning procedure would correspond to the trajectory stimulus being learned and memorized long before the time of simulation.

Neuronal receptor fields existed in a 2D spatial area (**Fig. 1d** left) following non-normalized bivariate Gaussian functions around their center points (x_j, y_j) organized along a square grid. For a stimulation point $s\ (x_s(t_s), y_s(t_s))$ of intensity I_s at moment t_s, the resulting neural frequency of the stimulation of the receptive field was

$$\nu_j(t_s) = I_s\ e^{-\left(\frac{\left(x_j - x_s(t_s)\right)^2 + \left(y_j - y_s(t_s)\right)^2}{\sigma_{RF}^2}\right)}$$

This stimulation was part of a dynamic spatiotemporal trajectory moving as time went by. The synaptic weights between neurons were then altered in proportion to their frequencies according to a phenomenological STDP rule (see below). A circular trajectory was chosen in order to study the sequence replay stability across multiple circle loops. The trajectory stimulus advanced by 0.05 (in the spatial area reference) every $dt_{Traj} = 20\ ms$ time step, with a small overlap between the trajectory start and end to ensure looping. For discrete stimuli (**Fig. 5**), the trajectory cycled 10x through the shown sequence of black dots (with the same trajectory time step). Neurons were considered as belonging to the trajectory when any of their stimulation-induced $\nu_j(t_s) > 5\%$ of the maximum neuron frequency the trajectory produced.

Spike-timing dependent plasticity

We assessed various STDP temporal windows, from entirely asymmetric ($\alpha_{STDP} = 1$) to symmetric ($\alpha_{STDP} = 0$) and time-shifted (ΔT_{STDP}) functions. To modulate STDP symmetry, we identified two STDP functions, an asymmetric and a symmetric one (whose integrals equal 0, so that LTP and LTD contributions are balanced), and then performed a linear combination of both to obtain various degrees of STDP temporal asymmetry. However, even though the integral stayed null, the integral of the positive part changed, which we corrected by normalizing according to the asymmetric function's integral's positive part. As such, the STDP function followed

$$f_{asym}(\Delta t) = A_{STDP}\sqrt{2e}\,\frac{\Delta t - \Delta T_{STDP}}{\tau_{STDP}}\,e^{-\left(\frac{\Delta t-\Delta T_{STDP}}{\tau_{STDP}}\right)^2}$$

$$f_{sym}(\Delta t) = A_{STDP}\left(1 - 2\left(\frac{\Delta t - \Delta T_{STDP}}{\tau_{STDP}}\right)^2\right)e^{-\left(\frac{\Delta t-\Delta T_{STDP}}{\tau_{STDP}}\right)^2}$$

$$f_{mixed}(\Delta t) = \alpha_{STDP} f_{asym}(\Delta t) + (1 - \alpha_{STDP}) f_{sym}(\Delta t)$$

$$f_{STDP}(\Delta t) = f_{mixed}(\Delta t)\,\frac{\int_{f_{asym}(\Delta t)>0} f_{asym}(\Delta t)}{\int_{f_{mixed}(\Delta t)>0} f_{mixed}(\Delta t)}$$

where $\Delta t = t_{post} - t_{pre}$ was the temporal difference between pre- and post-synaptic spikes, A_{STDP} the STDP amplitude and τ_{STDP} the STDP time constant. As such, taking into account the frequencies of pre- and post-synaptic neurons and the time difference between stimulation times, the weights were changed according to

$$\Delta w_{ij}(t_{s_1}, t_{s_2}) = \sum_{t_{s_1}}\sum_{t_{s_2}} \nu_i(t_{s_1})\nu_j(t_{s_2})\, f_{STDP}(\Delta t)$$

with $\Delta t = t_{s_2} - t_{s_1}$. A lower hardbound limit ($w \geq 0$) was imposed after STDP learning, whereas no upper hardbound limit was imposed.

Synaptic scaling

In order to keep neuronal activity within certain putative homeostatic bounds (Turrigiano et al., 1998), synaptic weights entering a postsynaptic neuron are subjected after STDP learning to a simple multiplicative phenomenological form of synaptic scaling, potentially representing hetero-synaptic LTD, where the sum of weights impinging upon a pyramidal neuron is kept constant before and after STDP. This is written

$$w_{Scaled(i,j)} = w_{After\ STDP(i,j)}\,\frac{\sum_i w_{Before\ STDP(i,j)}}{\sum_i w_{After\ STDP(i,j)}}$$

Detection of packs

In order to detect propagating activity pulse packets along the synaptic pathway, we first convolved neural spiking activity with a centered normalized Gaussian function where $\sigma = 30ms$, to then spatially convolute it with the bivariate Gaussian receptive field function (see above) centered on the discrete points of the spatiotemporal trajectory. Such smoothing procedures allowed us to reliably choose a frequency threshold ($12.5Hz$) above which trajectory point were considered "active". Conversely, from these "active" trajectory points, we considered trajectory neurons "active" when at least 40% of the trajectory points having stimulated that neuron's receptive field (weighted by the neural frequency resulting from trajectory stimulation) were "active". This allowed us to define pack emergence as when at least 20 dynamically changing but consecutive trajectory neurons were "active" at any time during 500 successive milliseconds (ensuring activity packets were strong enough, e.g. **Fig. 1e-h** white spikes).

Determining pack and non-pack frequency average, fluctuations or threshold

f_{nP} and σ_{nP} were determined as the frequency average and fluctuations of the aforementioned spatially-convoluted trajectory points of neurons outside the pack during

158

periods without packs, while f_P and σ_P were similarly determined but for neurons within the pack during packs. By manipulating the frequency of neurons along the trajectory f_T through different levels of feedforward AMPA currents, the frequency threshold f_θ was determined as the minimal f_{nP} for which packs propagate constantly ($\geq 1900\ ms$ out of $2\ s$ total, and $p_{Spont} \geq 0.95$). This understanding derived from the predictions of the bistable and noisy regime transition model, mimicking the process where the non-pack frequency f_{nP} stable fixed point increases until it annihilates with the threshold f_θ unstable fixed point (as in a saddle-node bifurcation), in which case only the pack frequency f_P stable fixed point remains and packs thus propagate constantly.

Maximum Lyapunov Estimate

To quantify the chaotic nature of the network's activity, we estimated the maximum Lyapunov exponent λ on the one-dimensional time series of the estimated instantaneous spiking frequency ($\sigma = 30\ ms$) averaged across excitatory neurons, based on the MATLAB program developed by Wolf and colleagues (Wolf et al., 1985). To do so, we reconstructed the phase space through time-delay embedding with heuristics agreed upon in the literature (Huffaker, 2010; Kliková and Raidl, 2011). The lag length was estimated as the first lag length for which the autocorrelation coefficient $AC < e^1$ (Kantz and Schreiber, 2004). The embedding dimension was estimated via a MATLAB program developed by "Mirwais" Kizilkaya (Kennel et al., 1992) according to the false nearest neighbor method (Kennel et al., 1992; Hegger and Kantz, 1999) as the minimal dimension with 0% false nearest neighbors as determined by tolerance factors ($R_{tol} = 10$, $A_{tol} = 2$, Kennel et al., 1992).

Spiking variability and synchrony

Spiking variability and synchrony measures are calculated as in (Sarazin et al., 2021). In an effort to compare spike variability between our model and experimental data, we quantified the coefficient of variation (CV) of the inter-spike interval (ISI) distribution of the spiking trains of neurons in the network (Compte, 2003) according to

$$CV = \frac{\sigma_{ISI}}{\mu_{ISI}}$$

However, the CV measure assumes stationarity of the data. Since this assumption isn't necessarily verified, we also computed the CV2 and Lv of the spike trains to evaluate the variability of ISIs at a local level, according to

$$CV_2 =< 2\frac{|ISI_{k+1} - ISI_k|}{ISI_{k+1} + ISI_k} >_k$$
$$Lv =< 3\frac{(ISI_k - ISI_{k+1})^2}{(ISI_k + ISI_{k+1})^2} >_k$$

$CV = CV_2 = Lv = 1$ for an ISI distribution drawn from homogeneous Poisson spike trains and $= 0$ for perfectly regular spike trains (all ISI are equal). CV typically stand around 1 to 1.5 *in vivo*, while CV2 and Lv stand around 0.25 to 1.25 and 0 to 2 respectively *in vivo* (Compte, 2003; Shinomoto et al., 2005). CV was calculated on all ISI, while CV2 and Lv are calculated for each neuron then averaged across neurons.

Multiple synchrony measures were calculated, a synchrony measure S (Golomb et al., 2001), pairwise correlation coefficient averaged over all pairs of neurons $<\rho>$ (Tchumatchenko et al., 2010), and Fano factor F, following

$$S = \sqrt{\frac{Var(<f>_n)}{<Var(f_{(n)})>_n}}$$

$$<\rho> = \frac{1}{N(N-1)/2}\sum_i \sum_{j>i} \frac{cov(f_{(i)}, f_{(j)})}{\sqrt{Var(f_{(i)})Var(f_{(j)})}}$$

$$F = \frac{Var(\sum_n s_n)}{<\sum_n s_n>_t}$$

where f was the estimated instantaneous neural spiking frequency via Gaussian convolution ($\sigma = 30ms$), n the neuron index, and s the population sum of spike counts, where $S = \frac{1}{\sqrt{N}} \sim 0.041$, $<\rho> = 0$ and $F = 1$ for perfectly asynchronous network activity, and $S = <\rho> = 1$ while F increased for perfectly synchronous network activity.

Protocol for assessing the nature of intrinsic bistability

The protocol for evaluating the nature of neural intrinsic bistability, taken from (Rodriguez et al., 2018), consisted of a strong phasic input (of amplitude $2\theta_{on}$ during $200\ ms$) followed by a weaker delay-period tonic input (of amplitude I_{Inj} during $10s$), in order to reveal conditional bistability activated by the phasic input but conditional on (i.e. requiring the) weaker delay-period tonic input. θ_{on} corresponded to the minimal delay-period tonic input current required to induce sustained firing during the delay without the strong initial phasic input, and θ_{off} the same but with the strong initial phasic input. $\theta_{transient}$ was the same as θ_{off} but corresponded to the minimal delay-period tonic input required to induce unstable (rather than sustained) firing. Firing was considered sustained when there were three or more spikes during the last $2\ s$ of the tonic input with stable ISIs (determined when $<\frac{ISI_{k+1}-ISI_k}{ISI_k}>_k$ was inferior to 0.05). Otherwise, firing was considered unstable for a single spike beyond 25ms after the initial phasic input, or for two spikes or more during non-sustained firing.

When $\theta_{on} = \theta_{off} = \theta_{transient}$, the neuron was considered monostable, i.e. the strong initial input current did not activate any intrinsic mechanisms generating sustained firing. When $\theta_{on} = \theta_{off} > \theta_{transient}$, the neuron was considered transiently bistable, the strong initial input inducing weak mechanisms generating unstable (but not sustained) firing. When $\theta_{on} > \theta_{off}$, the neuron was considered conditionally bistable, since the delay-period input, weaker than the initial phasic input but non-zero, could induce sustained firing, bistability being thus conditional upon the delay-period input. Finally, if $\theta_{on} > 0 > \theta_{off}$, the neuron's bistability was considered absolute, i.e. sustained neuronal firing after an initial input lasts until a hyperpolarizing current stops it.

Calculating robustness to variability of the model's parameters

We studied how sensitive the phenomenon of interest (namely controlled, stable and independent trajectory replay with asynchronous irregular network dynamics) was to the variability of model parameters, since biological systems present strong variability. To do so, we systematically varied important parameters, and defined a list of criteria which all need

to be met (**Fig. S3**), encompassing physiological peak conductance ratios (top row), spiking activity regime (middle row) and controllable stable independent trajectory replays (bottom row). Sustained network activity (middle row) was determined when the maximal duration without network spikes was 100ms, to exclude strongly oscillating networks prohibiting controllable trajectory replay. Physiological neuronal activity was determined when neuronal activity was 100Hz at most for 250ms (to exclude trivial cases where trajectory replay was detected as a single neuron firing at 100Hz during 500ms). CV and CV2 were determined during the spontaneous epoch (before the trajectory replay evoking stimulus at 2s, **Fig. 1e-h**).

Parameters were varied over a range of 40 equally-spaced values, generally spanning $\left(\frac{1}{3}, 3\right)$x the standard parameter value. Network simulations were repeated 5 times for each value (due to the potential variability of trajectory replays), with each repetition being evaluated independently concerning the criteria. The robustness score was calculated as

$$R = \frac{\Delta p}{< p >}$$

where $< p >$ represented the average correct parameter value (weighted by the proportion of correct repetitions), and Δp the sum of correct parameter steps (once again weighted by the proportion of correct repetitions) where a step was the difference between the next and previous parameter value divided by 2, or $\frac{|p_{k+1} - p_{k-1}|}{2}$ (values being equally spaced).

This robustness score was conservative no matter the arbitrarily chosen range, to the extent that all robustness scores are biased underestimations approaching their true maximal limit value. Indeed, robustness was only limited by 1) how large the parameter range considered was (for the maximal value) and 2) how close parameter steps were (for the minimal value). The robustness score decreased from its true maximal value with ranges too small and step values too large. Contributions of individual criteria (**Fig. 4f**, right) were calculated as the Δp when considering only that one criteria (with the same $< p >$ value calculated over all criteria, for better comparison of individual contributions).

Numerical integration and parameters of the biophysical network model

Models were simulated and explored using custom developed code under MATLAB and were numerically integrated using the forward Euler method with time-step $\Delta t = 0.5ms$ in network models.

Unless indicated in figure legends, standard parameter values were as following. Concerning the network architecture, $N = n_{Exc} + n_{Inh} = 605$ neurons, $p_{Exc} = 0.8$, so that $n_{Exc} = Np_{Exc} = 484$ neurons and $n_{Inh} = Np_{Inh} = 121$ neurons. Concerning Integrate-and-Fire neuron properties, $C = 1\ \mu F.cm^{-2}$, $V_{rest} = -65\ mV$, $\theta = -50\ mV$, $V_{mean} = \frac{V_{rest}+\theta}{2} = -57.5\ mV$, $\Delta t_{AP} = 3\ ms$. Concerning ionic currents, $\bar{g}_L = 0.05\ mS.cm^{-2}$, $V_L = -70\ mV$, $\bar{g}_{CAN} = 0\ mS.cm^{-2}$, $V_{CAN} = 30\ mV$, $\alpha_{CAN} = 0.03125\ \mu M^{-1}.ms^{-1}$, $\beta_{CAN} = 0.025\ ms^{-1}$, $\gamma_{CAN} = 1$, $\bar{g}_{AHP} = 0\ mS.cm^{-2}$, $V_{AHP} = -90\ mV$, $\alpha_{AHP} = 0.125\ \mu M^{-1}.ms^{-1}$, $\beta_{AHP} = 0.025\ ms^{-1}$, $\gamma_{AHP} = 1$, $\Delta Ca = 0.2\ \mu M$, $Ca_0 = 0.1\ \mu M$, $\tau_{Ca} = 100\ ms$. Concerning the weight matrix, $\mu_w = 0.03$, $\sigma_w = 0.015$, $p_{E\to E} = p_{E\to I} = p_{I\to I} = p_{I\to E} = 0.3$. Concerning synaptic currents, $\Delta t_{syn} = 0.5\ ms$, $\bar{g}_{AMPA} = 0.2\ mS.cm^{-2}$, $\tau_{AMPA}^{decay} = 2.5\ ms$, $\bar{g}_{NMDA} = 0.3\ mS.cm^{-2}$, $\alpha_{NMDA} = 0.275\ ms^{-1}$, $\tau_{NMDA}^{rise} = 4.65\ ms$, $\tau_{NMDA}^{decay} = 75\ ms$, $[Mg^{2+}] = 1.5\ mM$, $V_{AMPA} = V_{NMDA} = 0\ mV$, $g_{GABA_A} = 0.35\ mS.cm^{-2}$, $\tau_{GABA_A}^{decay} = 10\ ms$, $V_{GABA_A} =$

$-70\ mV$, $g_{GABA_B} = 5.10^{-4}\ mS.cm^{-2}$, $\alpha_{GABA_B} = 0.015\ ms^{-1}$, $\tau_{GABA_B}^{rise} = 90\ ms$, $\tau_{GABA_B}^{decay} = 160\ ms$, $V_{GABA_B} = -90\ mV$, $\Delta p_{AMPA} = \Delta q_{NMDA} = \Delta p_{GABA_A} = \Delta q_{GABA_B} = 0.1$. Concerning the learning procedure and STDP, $\sigma_{RF} = 0.13$, $I_s = 0.02925$, $\tau_{STDP} = 100\ ms$, $A_{STDP} = 50$, $\alpha_{STDP} = 1$, $\Delta T_{STDP} = 0\ ms$.

Parameters for the biophysical mechanisms (**Fig. 4**) were systematically determined as the (A_{STDP}, mechanism parameter) value couple maximizing the product of controllability, stability and independence (all three being normalized between 0 and 1).

For the bidirectional ring attractor (**Fig. 5.e2**), model parameters were as followed: $p_{I\to E} = 0.4$, $g_{X\to E} = 1.5$, $g_{X\to I} = 0.5$, $\bar{g}_{AHP} = 0.2\ mS.cm^{-2}$, $\alpha_{AHP} = 0.001\ \mu M^{-1}.ms^{-1}$, $\beta_{AHP} = 0.002\ ms^{-1}$, $\gamma_{AHP} = 2$, $I_s = 0.03$.

Propagation condition model

We evaluated conditions for propagation of a pack of activity between neurons along the trajectory. Basically, propagation requires that, on average, spiking at frequency f in (upstream) pre-synaptic neurons must induce spiking at a frequency superior or equal to f in (down-stream) post-synaptic neurons. Therefore, we wrote a set of equations where pre-synaptic AMPA and NMDA input currents to a post-synaptic neuron are scaled by the firing frequency f of the pre-synaptic neuron and searched for frequency conditions where post-synaptic neurons fire at a frequency at least f. This *propagation condition model* is an extremely simplified one-dimensional reduced representation of pack propagation within the local cortical recurrent network. This model is space-free and shall be considered as a representation of internal dynamics within the pack during its propagation, i.e. in a referential moving at the speed of pack propagation. Noticeably, the propagation condition model only considers a pre-/post-synaptic feedforward interaction, but does not take into account possible recurrent effects of the post-synaptic neuron on the pre-synaptic neurons or on the network. The propagation condition model nevertheless considers incoming excitatory and inhibitory inputs from the entire network onto the post-synaptic neuron. These inputs are lumped together into common AMPA, NMDA and GABA-A terms that are quantitatively fitted on average synaptic currents impinging pack neurons in network simulations. The additional assumption is made that excitatory currents are essentially provided by upstream neurons within the pack (vs from neurons outside the pack, whether inside or outside the trajectory), so that AMPA and NMDA currents are scaled by f.

To tract the problem in a deterministic way, we leveraged from the observation that, regardless of whether neurons spike in the spontaneous regime or within the pack, 1) ISIs generally terminate through rapid final depolarizing fluctuations, due to chaotic dynamics, and that 2) these fluctuations start Δt_{fluct}~$15ms$ before spiking. We numerically determined, from all ISIs during pack activity in network simulations, the mean time-to-spiking $\Delta t_{spiking}(V, f)$, as a function of the membrane potential and the firing frequency of the current ISI. We found that $\Delta t_{spiking}(V, f) = \Delta t_{fluct}$ was largely independent of firing frequency, which allowed numerically estimating V_S' (around -53 mV).

We also considered, based on neuronal dynamics in the network model, that the membrane potential was essentially deterministically driven – before reaching V_S' and the final fluctuation to spiking – by average input and leak currents. Thus the membrane potential converged exponentially to its steady state V^* :

$$V(t) = V^*(f) + (V_R - V^*(f))\exp(-t/\tau_m(f)),$$

where $V^*(f)$ was obtained from the equilibrium of ionic currents at steady-state:

$$\overline{g_{AMPA}}\alpha_{fg}f(V^* - V_{AMPA}) + \overline{g_{NMDA}}\alpha_{fg}fm(V')(V^* - V_{NMDA}) + \overline{g_{GABA-A}}(V^* - V_{GABA-A}) + g_L(V^* - V_L) + \overline{g_{AMPA,FF}}(V^* - V_{AMPA,FF})) = 0,$$

with α_{fg} a conversion factor for dimensional compatibility and the non-linearity of the NMDA approximated to its value V', so that one can solve explicitly in terms of V^*:

$$V^*(f) = \frac{I}{g}(1 + \frac{g_{AN}}{g}f)^{-1},$$

with

$$I = g_L V_L + \overline{g_{GABA-A}}V_{GABA-A},$$

$$g = g_L + \overline{g_{GABA-A}} + \overline{g_{AMPA,FF}},$$

and

$$g_{AN} = \alpha_{fg}(\overline{g_{AMPA}} + \overline{g_{NMDA}})$$

which could be linearized ($\frac{g_{AN}}{g}f \ll 1$) to

$$V^*(f) = \frac{I}{g}(1 - \frac{g_{AN}}{g}f),$$

the membrane time-constant writing

$$\tau_m(f) = \frac{C}{\overline{g_{AMPA}}\alpha_{fg}f + \overline{g_{NMDA}}\alpha_{fg}fm(V') + \overline{g_{GABA-A}} + g_L + \overline{g_{AMPA,FF}}},$$

and

$$\overline{g_{AMPA}} = \frac{I_{AMPA}^{Pack}}{\alpha_{fg}f_{pack}(\langle V^{Pack}\rangle - V_{AMPA})},$$

$$\overline{g_{NMDA}} = \frac{I_{NMDA}^{Pack}}{\alpha_{fg}f_{pack}(\langle V^{Pack}\rangle - V_{NMDA})},$$

$$\overline{g_{GABA-A}} = \frac{I_{GABA-A}^{Pack}}{(\langle V^{Pack}\rangle - V_{GABA-A})},$$

$$\overline{g_L} = \frac{I_L^{Pack}}{(\langle V^{Pack}\rangle - V_L)},$$

$$\overline{g_{AMPA-FF}} = \frac{I_{AMPA-FF}^{Pack}}{(\langle V^{Pack}\rangle - V_{AMPA-FF})},$$

being estimated from pack mean membrane potential $\langle V^{Pack} \rangle$, mean currents (see below) and mean firing frequency f_{pack} obtained from network simulations.

As a final step of the propagation condition model, we then computed:

$$\Delta V(f) = V\left(t = \frac{1}{f}\right) - V_S' = V^*(f) + (V_R - V^*(f))\exp\left(-f^{-1}\tau_m(f)^{-1}\right) - V_S'.$$

A negative $\Delta V(f)$ indicates that the potential has not yet reached, at time $T = \frac{1}{f}$, the threshold V_S' yielding rapid fluctuation-driven spiking so that post-synaptic frequency is lower than f, the pre-synaptic firing frequency. Therefore, propagation will fail. Conversely, a positive $\Delta V(f)$ indicates that the post-synaptic frequency exceeded the pre-synaptic one, so that propagation continues downstream. Finding a critical frequency f_θ such that $\Delta V(f_\theta) = 0$ indicates that pre- and post-synaptic frequencies are equal and propagation of spiking occurs a frequency f_θ. Moreover, the slope of $\Delta V(f)$ at f_θ determines the stability of the propagation. A negative slope indicates a stable propagation at frequency f_θ as fluctuations (due to chaotic network dynamics) will be quenched out by restoring forces driving back frequency to f_θ (frequency increases below f_θ ($\Delta V(f) > 0$) and decreases above it ($\Delta V(f) < 0$)). A positive slope, to the contrary, indicates an unstable propagation with firing frequency ineluctably diverging from f_θ.

Computing the model indicated that, under our simplifying hypotheses, a single critical frequency f_θ was found at which the slope of the $\Delta V(f)$ was positive (see Results). Therefore, the propagation condition model suggested that f_θ corresponded to an unstable fixed-point in the frequency dimension, acting as a threshold that separated, for trajectory neurons, the spontaneous regime (no pack propagation) from the regime of pack propagation. Actually, the propagation condition model predicted the value of f_θ quite well (see *Results*), with a value very close to that directly estimated from network simulations (see below). The quality of the propagation condition model was also evaluated by computing mean currents and comparing them to those found in network simulations (see *Results*). Currents were computed as:

$$I_{AMPA}(f) = \overline{g_{AMPA}}\alpha_{fg} f(\langle V \rangle(f) - V_{AMPA}),$$

$$I_{NMDA(f)} = \overline{g_{NMDA}}\alpha_{fg} f(\langle V \rangle(f) - V_{NMDA}),$$

$$I_{GABA-A}(f) = \overline{g_{GABA-A}}(\langle V \rangle(f) - V_{GABA-A}),$$

$$I_L(f) = \overline{g_L}(\langle V \rangle(f) - V_L),$$

$$I_{AMPA-FF(f)} = \overline{g_{AMPA-FF}}(\langle V \rangle(f) - V_{AMPA-FF}),$$

where

$$\langle V \rangle(f) = V^*(f) - f\tau_m(f)(V_R - V^*(f))(\exp(-f^{-1}\tau_m(f)^{-1}) - 1),$$

Regime transition model

Although well estimating f_θ and average currents (see *Results*) propagation condition, the model was however unable to identify the two stable frequency fixed-points $f_{non-pack}$ and f_{pack} setting the average spiking frequency in the spontaneous regime and during pack propagation in network simulations. This was because the simplifications regarding recurrent interactions within the network between excitatory neurons within the pack and neurons outside the pack (i.e. excitatory neurons inside and outside the trajectory and inhibitory neurons) were too strong to account for the non-linearity ensuring negative feedbacks in the vicinity of $f_{non-pack}$ and f_{pack} stable fixed-point.

However, to better understand propagation of the pack within the network, we considered the co-existence of the unstable f_θ fixed-point and of the two stable $f_{non-pack}$ and f_{pack} stable fixed-points to build a phenomenological one-dimensional reduced *regime transition* model. Moreover, to evaluate the ability of this simplified model in explaining complex propagation behavior in the whole network by a simple model based on an unstable fixed-point separating two spontaneous and pack propagation regimes, we included a stochastic component and determined to which extent the simplified propagation model was able to evaluate transition rates between the spontaneous and propagation mode in trajectory neurons. Specifically, the probability of the emergence of propagating packs from the spontaneous regime, $p(SpP)$), the probability of propagating evoked packs $p(EvP)$) and their duration ($d(SpP)$)) were computed from the model.

In the model, the firing frequency of neurons within the trajectory followed:

$$\frac{df}{dt} = -\alpha_f(f - f_{non-pack})(f - f_\theta)\big(f - f_{pack}\big)/\tau_f + \sigma_f\sqrt{dt}x(t)$$

were α_f is a scaling factor, τ_f=$\tau_m(f_\theta)$, $x(t)$ is a Gaussian stochastic variable with mean 0 and standard deviation 1 and $\sigma_f = \sigma_{non-pack}$ for $f < f_{criterion}$ and $\sigma_f = \sigma_{pack}$ for $f \geq f_{criterion}$ with $\sigma_{non-pack}$ and σ_{pack} estimated from network simulations. The empirical estimation of f_θ in the network model was obtained by finding the frequency best separating pack and non-pack frequency distributions (see above).

Parameters

$\alpha_{fg} = 1mS.cm^{-2}.Hz^{-1}$, $V_S' = -53.05$ mV, $\langle V^{pack}\rangle = -53.23mV$, $f_{non-pack} = 6.48\ Hz$, $f_{pack} = 14.34\ Hz$, $f_\theta = 9.7\ Hz$, $\alpha_f = 1e-3s^2$, $\sigma_{non-pack} = 1.96\ Hz$, $\sigma_{pack} = 3.55\ Hz$.

Methods references

Beaulieu, C., Kisvarday, Z., Somogyi, P., Cynader, M., and Cowey, A. (1992). Quantitative distribution of gaba-immunopositive and -immunonegative neurons and synapses in the monkey striate cortex (area 17). *Cereb. Cortex* 2, 295–309. doi:10.1093/cercor/2.4.295.

Brunel, N., and Wang, X. J. (2001). Effects of neuromodulation in a cortical network model of object working memory dominated by recurrent inhibition. *J. Comput. Neurosci.* 11, 63–85. doi:10.1023/A:1011204814320.

Compte, A. (2003). Temporally Irregular Mnemonic Persistent Activity in Prefrontal Neurons of Monkeys During a Delayed Response Task. *J. Neurophysiol.* 90, 3441–3454. doi:10.1152/jn.00949.2002.

Dale, H. (1935). Pharmacology and Nerve-endings (Walter Ernest Dixon Memorial Lecture): (Section of Therapeutics and Pharmacology). *Proc. R. Soc. Med.* 28, 319–332.

Destexhe, A., Mainen, Z. F., and Sejnowski, T. J. (1998). Kinetic models of synaptic transmission. *Methods Neuronal Model.* 2, 1–25.

Faber, E. S. L., and Sah, P. (2007). Functions of SK channels in central neurons. *Clin. Exp. Pharmacol. Physiol.* 34, 1077–1083. doi:10.1111/j.1440-1681.2007.04725.x.

Golomb, D., Hansel, D., and Mato, G. (2001). "Chapter 21 Mechanisms of synchrony of neural activity in large networks," in *Handbook of Biological Physics* Neuro-Informatics and Neural Modelling., eds. F. Moss and S. Gielen (North-Holland), 887–968. doi:10.1016/S1383-8121(01)80024-5.

Haj-Dahmane, S., and Andrade, R. (1997). Calcium-Activated Cation Nonselective Current Contributes to the Fast Afterdepolarization in Rat Prefrontal Cortex Neurons. *J. Neurophysiol.* 78, 1983–1989. doi:10.1152/jn.1997.78.4.1983.

Hegger, R., and Kantz, H. (1999). Improved false nearest neighbor method to detect determinism in time series data. *Phys. Rev. E Stat. Phys. Plasmas Fluids Relat. Interdiscip. Top.* 60, 4970–4973. doi:10.1103/PhysRevE.60.4970.

Huffaker, R. (2010). Phase Space Reconstruction from Econommic Time Series Data: Improving Models of Complex Real-World Dynamic Systems. *Int. J. Food Syst. Dyn.* 1, 184–193.

Jahr, C. E., and Stevens, C. F. (1990). Voltage dependence of NMDA-activated macroscopic conductances predicted by single-channel kinetics. *J. Neurosci. Off. J. Soc. Neurosci.* 10, 3178–3182.

Kantz, H., and Schreiber, T. (2004). *Nonlinear Time Series Analysis*. Cambridge University Press.

Kennel, M. B., Brown, R., and Abarbanel, H. D. I. (1992). Determining embedding dimension for phase-space reconstruction using a geometrical construction. *Phys. Rev. A* 45,

3403–3411. doi:10.1103/PhysRevA.45.3403.

Kliková, B., and Raidl, A. (2011). Reconstruction of Phase Space of Dynamical Systems Using Method of Time Delay. *Proc. 20th Annu. Conf. Dr. Stud. - WDS 2011*, 83–87.

Rodriguez, G., Sarazin, M., Clemente, A., Holden, S., Paz, J. T., and Delord, B. (2018). Conditional bistability, a generic cellular mnemonic mechanism for robust and flexible working memory computations. *J. Neurosci.*, 1992–17. doi:10.1523/JNEUROSCI.1992-17.2017.

Sarazin, M. X. B., Victor, J., Medernach, D., Naudé, J., and Delord, B. (2021). Online Learning and Memory of Neural Trajectory Replays for Prefrontal Persistent and Dynamic Representations in the Irregular Asynchronous State. *Front. Neural Circuits* 0. doi:10.3389/fncir.2021.648538.

Shinomoto, S., Miyazaki, Y., Tamura, H., and Fujita, I. (2005). Regional and Laminar Differences in In Vivo Firing Patterns of Primate Cortical Neurons. *J. Neurophysiol.* 94, 567–575. doi:10.1152/jn.00896.2004.

Song, S., Sjöström, P. J., Reigl, M., Nelson, S., and Chklovskii, D. B. (2005). Highly Nonrandom Features of Synaptic Connectivity in Local Cortical Circuits. *PLOS Biol.* 3, e68. doi:10.1371/journal.pbio.0030068.

Tchumatchenko, T., Geisel, T., Volgushev, M., and Wolf, F. (2010). Signatures of synchrony in pairwise count correlations. *Front. Comput. Neurosci.* 4. doi:10.3389/neuro.10.001.2010.

Thomson, A. M. (2002). Synaptic Connections and Small Circuits Involving Excitatory and Inhibitory Neurons in Layers 2-5 of Adult Rat and Cat Neocortex: Triple Intracellular Recordings and Biocytin Labelling In Vitro. *Cereb. Cortex* 12, 936–953. doi:10.1093/cercor/12.9.936.

Turrigiano, G. G., Leslie, K. R., Desai, N. S., Rutherford, L. C., and Nelson, S. B. (1998). Activity-dependent scaling of quantal amplitude in neocortical neurons. *Nature* 391, 892–896. doi:10.1038/36103.

Villalobos, C., Shakkottai, V. G., Chandy, K. G., Michelhaugh, S. K., and Andrade, R. (2004). SKCa channels mediate the medium but not the slow calcium-activated afterhyperpolarization in cortical neurons. *J. Neurosci. Off. J. Soc. Neurosci.* 24, 3537–3542. doi:10.1523/JNEUROSCI.0380-04.2004.

Wang, H., Stradtman, G. G., Wang, X.-J., and Gao, W.-J. (2008). A specialized NMDA receptor function in layer 5 recurrent microcircuitry of the adult rat prefrontal cortex. *Proc. Natl. Acad. Sci.* doi:10.1073/pnas.0804318105.

Wolf, A., Swift, J., Swinney, H., and Vastano, J. (1985). Determining Lyapunov exponents from a time series. *Phys. Nonlinear Phenom.*, 285–317.

Xue, M., Atallah, B. V., and Scanziani, M. (2014). Equalizing excitation–inhibition ratios across visual cortical neurons. *Nature* 511, 596–600. doi:10.1038/nature13321.

Chapter 6. "Online" STDP learning and replay of neural trajectories in synaptic noise

6.1. Summary

The previous chapter evaluated the conditions under which controllable, stable and independent trajectory replay can emerge within AI chaotic awake cortical activity. However, trajectory learning and replay phases were separated, with learning occurring "offline" beforehand via phenomenological STDP and network simulations of trajectory replay studied afterwards without synaptic plasticity, even though noisy activity affects both trajectory replay and learning. Indeed, activity-dependent synaptic plasticity with noisy activity can add erratic synaptic modifications within and outside the synaptic engram during trajectory presentation, as well as gradually erase the learned synaptic engram through non-specific plasticity. Conversely, trajectory stimuli and replay activity can disrupt the stationary AI regime via runaway activity-plasticity interactions. Even without synaptic engrams, the complexity of AI dynamics undergoing STDP might drastically decrease from chaos to limit cycle (e.g. saturation) or even fixed points (e.g. silence).

We addressed these issues in a PFC neural network model capable of stable and controllable replays (building upon the previous chapter), and studied trajectory learning, replay, and memory maintenance, with calcium-based "online" STDP learning and instantaneous scaling of excitatory synapses occurring within the AI regime of awake cortex. We found that calcium-based STDP preserved AI dynamics due to the faint activation of kinase/phosphatase cycles at near-basal synaptic calcium during rest stationary activity. Massive calcium inputs during trajectory learning stimulus led to rapid learning of the synaptic chain (pathway). The existence of a dynamic engram didn't affect AI dynamics during rest activity, and stimulating the starting neurons allowed successful trajectory replay.

Weak non-specific plasticity induced by low-frequency noisy activity led to slow forgetting of the dynamic engram (~2h) and faster forgetting of trajectory replay (~15min). To compensate engram erasure, repeating trajectory replays led to positive activity-plasticity feedback loops, resulting in paroxysmal activity and catastrophic forgetting. Slowing down plasticity in response, combined with multiple learning stimuli, led to proportionally slower engram erasure and less likely paroxysmal activity. Trajectory replay was consequently maintained ~3x longer than expected, since repeating learning stimuli simultaneously replayed the trajectory, recruiting more neurons and further stabilizing the engram. As such, slower plasticity allowed a greater (~3x) physiological range between stable and paroxysmal replay.

Furthermore, the model offered answers concerning the underpinnings of regular vs. fast timescale navigational trajectory replays, modeled as putative rapid reversible dopaminergic neuromodulation of NMDA opening dynamics. Similarly, it offered a framework for simultaneous dynamic and stable coding, where individual neurons displayed relay race dynamic coding (~200ms) while average population frequency displayed decaying persistent coding (~1s). Finally, the model accounted for part-based learning in PFC and chunking of HP navigational trajectories, as trajectories could be successfully replayed even when presented as disjointed (slightly overlapping) fragments in any arbitrary order.

6.1.1. Contributions

I developed the biophysical neural network model and STDP rule, supervised Julie Victor's master thesis work, converting certain figures to article format, and produced other results and figures (figure 1, AI nature of activity across time, chunking, regular/fast replay, dynamic / persistent coding, multiple replays with slower plasticity, time constant analysis), and entirely reviewed and finalized all texts.

6.2. Article

frontiers in Neural Circuits

ORIGINAL RESEARCH
published: 08 July 2021
doi: 10.3389/fncir.2021.648538

Online Learning and Memory of Neural Trajectory Replays for Prefrontal Persistent and Dynamic Representations in the Irregular Asynchronous State

Matthieu X. B. Sarazin[1*†], *Julie Victor*[2†], *David Medernach*[1], *Jérémie Naudé*[3†] *and Bruno Delord*[1*†]

[1] *Institut des Systèmes Intelligents et de Robotique, CNRS, Inserm, Sorbonne Université, Paris, France,* [2] *CEA Paris-Saclay, CNRS, NeuroSpin, Saclay, France,* [3] *Neuroscience Paris Seine - Institut de biologie Paris Seine, CNRS, Inserm, Sorbonne Université, Paris, France*

In the prefrontal cortex (PFC), higher-order cognitive functions and adaptive flexible behaviors rely on continuous dynamical sequences of spiking activity that constitute neural trajectories in the state space of activity. Neural trajectories subserve diverse representations, from explicit mappings in physical spaces to generalized mappings in the task space, and up to complex abstract transformations such as working memory, decision-making and behavioral planning. Computational models have separately assessed learning and replay of neural trajectories, often using unrealistic learning rules or decoupling simulations for learning from replay. Hence, the question remains open of how neural trajectories are learned, memorized and replayed online, with permanently acting biological plasticity rules. The asynchronous irregular regime characterizing cortical dynamics in awake conditions exerts a major source of disorder that may jeopardize plasticity and replay of locally ordered activity. Here, we show that a recurrent model of local PFC circuitry endowed with realistic synaptic spike timing-dependent plasticity and scaling processes can learn, memorize and replay large-size neural trajectories online under asynchronous irregular dynamics, at regular or fast (sped-up) timescale. Presented trajectories are quickly learned (within seconds) as synaptic engrams in the network, and the model is able to chunk overlapping trajectories presented separately. These trajectory engrams last long-term (dozen hours) and trajectory replays can be triggered over an hour. In turn, we show the conditions under which trajectory engrams and replays preserve asynchronous irregular dynamics in the network. Functionally, spiking activity during trajectory replays at regular timescale accounts for both dynamical coding with temporal tuning in individual neurons, persistent activity at the population level, and large levels of variability consistent with observed cognitive-related PFC dynamics. Together, these results offer a consistent theoretical framework accounting for how neural trajectories can be learned, memorized and replayed in PFC networks circuits to subserve flexible dynamic representations and adaptive behaviors.

Keywords: prefrontal cortex, neural trajectory, attractor, persistent and dynamical coding, working memory, learning, replay, asynchronous irregular state

OPEN ACCESS

Edited by:
Shintaro Funahashi, Kyoto University, Japan

Reviewed by:
Shantanu P. Jadhav, Brandeis University, United States
Lukas Ian Schmitt, RIKEN Center for Brain Science (CBS), Japan

***Correspondence:**
Matthieu X. B. Sarazin
matthieu.sarazin@live.fr
Bruno Delord
bruno.delord@sorbonne-universite.fr

[†] *These authors have contributed equally to this work*

Received: *31 December 2020*
Accepted: *31 May 2021*
Published: *08 July 2021*

Citation:
Sarazin MXB, Victor J, Medernach D, Naudé J and Delord B (2021) Online Learning and Memory of Neural Trajectory Replays for Prefrontal Persistent and Dynamic Representations in the Irregular Asynchronous State. Front. Neural Circuits 15:648538. doi: 10.3389/fncir.2021.648538

INTRODUCTION

As when a few introductory notes recall a melody, in the immense space of known melodies, cerebral networks are able to memorize and replay complex temporal patterns in a flexible way. Such temporal patterns rely on continuous dynamical sequences of spiking activity, i.e., neural trajectories, that occur in recurrent neural networks of the prefrontal cortex (PFC) (Bakhurin et al., 2017; Paton and Buonomano, 2018; Wang et al., 2018). These neural trajectories emerge with learning, relying on dynamical engrams, which distinguish them from classical static engrams underlying Hebbian neuronal assemblies. In turn, these engrams likely arise through activity-dependent synaptic plasticity (Goto et al., 2010; Bittner et al., 2017). Hence, a robust understanding of the interplay between prefrontal dynamics and biological plastic processes is necessary to understand the emergence of functional neural trajectories and engrams. In the PFC of behaving animals, neural trajectories are embedded in an asynchronous and irregular background state activity that is markedly disordered (Destexhe et al., 2003; London et al., 2010). However, how synaptic plasticity builds engrams that are not erased by spontaneous activity and yet are not strong enough to alter irregular PFC dynamics remains an open question.

Neural trajectories correspond to organized spatio-temporal representations that peregrinate within the neural space (Shenoy et al., 2013). They are prominent in prefrontal cortices (Mante et al., 2013), where they subserve higher-order cognitive functions at diverse levels of abstraction (Wutz et al., 2018). In prefrontal areas, at the lowest levels of abstraction, neural trajectories can map the actual animal's position during effective trajectories within explicit spaces during visual perception (Mante et al., 2013) or navigation (Fujisawa et al., 2008; Zielinski et al., 2019). Beyond spatial mapping, neural trajectories can also depict generalized topological locations that are isomorphic to the task space, by multiplexing position, representation of goal locations and choice-related information (Fujisawa et al., 2008; Mashhoori et al., 2018; Yu et al., 2018; Kaefer et al., 2020). Neural trajectories have also been shown to subserve dynamical coding and manipulation of information during delay activities in working memory tasks involving the PFC (Lundqvist et al., 2018). In this context, neural trajectories do not represent explicit trajectories in external spaces, but implicit representations—of ongoing information and cognitive operations—that may prove useful for the task.

Rather than static maintenance of persistent activity in a group of cells, many working-memory representations unfold in the space of neural activity under the form of continuous trajectories, as neurons successively activate in "relay races" sequences of transient activity (Batuev, 1994; Brody et al., 2003; Cromer et al., 2010; Yang et al., 2014; Schmitt et al., 2017; Enel et al., 2020). In the PFC, neural trajectories can form the substrate for dynamic (Sreenivasan et al., 2014) but also, counterintuitively, for stable representations (Druckmann and Chklovskii, 2012). Neural trajectory-mediated dynamical representations can subserve the retrospective working memory of spatial (Batuev, 1994; Yang et al., 2014) or quantitative (Brody et al., 2003) cues, symbolic categories (Cromer et al., 2010), values (Enel et al., 2020), or behavioral rules (Schmitt et al., 2017). They can also serve prospective working memory in computational processes transforming previously encoded information, such as, for e.g., in visuo-motor transformations (Spaak et al., 2017), in the representation of elapsed time (Tiganj et al., 2017) or in the encoding of forthcoming behaviors (Fujisawa et al., 2008; Ito et al., 2015; Nakajima et al., 2019; Passecker et al., 2019). Neural trajectories in the neural space can also appear as sequences of states that involve combinations of active neurons (Batuev, 1994; Abeles et al., 1995; Seidemann et al., 1996; La Camera et al., 2019). Thus, neural trajectories appear in diverse forms and in different functional contexts where they can map actual trajectories in external spaces, remember previously encountered trajectories, or predict forthcoming trajectories during active computational processes requiring dynamical representations.

Neural trajectories in the PFC are adaptive (Euston et al., 2012; Mante et al., 2013): they are learned and memorized, to be "replayed" later. The timescale of the replay depends on the behavioral context. Regular timescale replays operate at the behavioral timescale, lasting seconds (Batuev, 1994; Fujisawa et al., 2008; Cromer et al., 2010; Mante et al., 2013; Yang et al., 2014; Ito et al., 2015; Schmitt et al., 2017; Tiganj et al., 2017; Nakajima et al., 2019; Passecker et al., 2019; Enel et al., 2020). Thus, such replays unfold online as current behavior is executed in interaction with the external world, to subserve retrospective working memory of past information, ongoing dynamical computations, or prospective representation of forthcoming behaviors. Typically, regular replays are triggered by behaviorally–relevant external events (e.g., cues or go signals in working memory tasks, or the current position in navigational tasks). Some replays that may appear as spontaneous can be presumably triggered by internal self-paced decision signals within the PFC (e.g., choices). In all cases, such triggered regular replays rely on internal mechanisms within PFC circuits allowing for the autonomous propagation of proper sequences of activity, once initial neurons of the neural trajectory have been triggered. A major goal of the present study is to decipher how plastic processes allow PFC circuits to learn and replay trajectories, i.e., autonomously generate neural trajectory completion, based on an initial trigger.

Besides, fast timescale replays exist that last a few hundred milliseconds during awake (Jadhav et al., 2016; Mashhoori et al., 2018; Yu et al., 2018; Shin et al., 2019; Kaefer et al., 2020) and sleeping (Euston et al., 2007; Peyrache et al., 2009) states. Beyond their much shorter duration, PFC fast replays are distinct from regular ones, in that they typically operate offline and often co-occur with fast replays in the hippocampal CA1 field (Jadhav et al., 2016). Replay activity in PFC and CA1 presents high degrees of task-dependent spatial and temporal correlations (Jadhav et al., 2016; Yu et al., 2018; Shin et al., 2019), subserving functional coordination combining metric (hippocampus) and task-related (PFC) spatial representations (Pfeiffer and Foster, 2013; Zielinski et al., 2019). These fast replays occur during sharp-wave ripples (SWR) episodes (Jadhav et al., 2016; Yu et al., 2018; Shin et al., 2019), which represent critical events for behavioral learning (Jadhav et al., 2012) and during which animals forge forthcoming decisions (choices,

trajectories, for e.g., Jadhav et al., 2016; Mashhoori et al., 2018; Kaefer et al., 2020), based on the recall of past experiences (actions, trajectories, outcomes, for e.g., Jadhav et al., 2012; Mashhoori et al., 2018). Such coordination across both structures presumably emerges through their reciprocal, direct and indirect, synaptic interactions (Witter and Amaral, 2004). Different studies have pointed out information flow biases from CA1 to PFC (Jadhav et al., 2016) or from PFC to CA1 (Ito et al., 2015) directions, depending on behavioral contexts. However, SWR-related replays in the hippocampus correlate with fast replays in reduced subsets of PFC neurons (Jadhav et al., 2016; Yu et al., 2018) that carry generalized spatial representations but not specific trajectories (Yu et al., 2018). Moreover, fast timescale PFC replays are independent of hippocampal replays during computational processes inherent to the PFC, such as rule switching tasks (Kaefer et al., 2020). Therefore, as for regular replays, we examined how plastic processes allow for the emergence of fast timescale replays autonomously within local recurrent PFC circuits.

Neuronal trajectories consist of robust forms of ordered local activity occurring within a disordered global activity, i.e., the chaotic, asynchronous irregular (AI) state characteristic of the prefrontal cortex in the waking state (Destexhe et al., 2003; London et al., 2010). This coexistence poses a problem at the plasticity level, because the noisy AI regime constitutes a potential source of perturbation for synaptic engrams (Boustani et al., 2012; Litwin-Kumar and Doiron, 2014), whereas strengthened connectivity pathways may exert a synchronizing influence on the network, dramatically altering the chaotic nature of background activity. However, there is currently no biophysically-grounded theoretical framework accounting for the way neural trajectories are learned, memorized and replayed within recurrent cortical networks. In principle, synaptic plasticity, a major substrate of learning, may sculpt oriented connective pathways promoting the propagation of neuronal trajectories, because modifications of synaptic connections are activity-dependent. Specifically, the sequential activation of differentially tuned neurons during successively crossed spatial positions (during navigational trajectories) or representational states (during dynamical cognitive processes) could strengthen connections between neurons, creating oriented pathways (referred to as trajectory engrams hereafter) within recurrent cortical networks. If sufficiently strengthened, engrams could allow the propagation of packets of neuronal activity along them. From an initial stimulation of neurons located at the beginning of the engram, due to the strong connections linking them in the direction of the trajectory, neurons could reactivate sequentially, i.e., perform trajectory replay.

Recurrent neural network models have shown that activity-dependent synaptic plasticity rules can enable the formation of trajectory engrams due to long-term potentiation (LTP) and depression (LTD) together with homeostatic scaling (Liu and Buonomano, 2009; Clopath et al., 2010; Fiete et al., 2010; Klampfl and Maass, 2013). Moreover, trajectory engrams can propagate neuronal trajectories through sequential activation of neurons in recurrent model networks (Liu and Buonomano, 2009; Fiete et al., 2010; Klampfl and Maass, 2013; Laje and Buonomano, 2013; Chenkov et al., 2017). However, the above models of neural trajectories do not elucidate the biological basis of learning and replay in neurophysiological situations encountered by PFC networks for several reasons. First, in these models, trajectory learning is either ignored (hard-written trajectory engram; Chenkov et al., 2017), unrelated to behavior (random formation of arbitrary trajectory; Liu and Buonomano, 2009; Fiete et al., 2010), based on artificial learning rules (Laje and Buonomano, 2013) or on biophysically unrealistic rules in terms of neuronal activity and synaptic plasticity constraints (Liu and Buonomano, 2009; Fiete et al., 2010; Klampfl and Maass, 2013). Moreover, trajectory replay is absent (Clopath et al., 2010) or unable to operate from an initial trigger (Klampfl and Maass, 2013), or the ability to memorize and replay trajectory engrams and replays long-term is not tested (Liu and Buonomano, 2009; Clopath et al., 2010; Fiete et al., 2010; Klampfl and Maass, 2013; Laje and Buonomano, 2013; Chenkov et al., 2017). Finally, none of these models evaluate the capacity for trajectory learning and replay in the realistic context where network activity undergoes AI dynamics, whereas it is characteristic of the awake state in the cortex (Destexhe et al., 2003; London et al., 2010). The interactions between synaptic plasticity and AI dynamics has so far only been assessed for static Hebbian engrams (Morrison et al., 2007; Boustani et al., 2012; Litwin-Kumar and Doiron, 2014) but not for dynamic trajectories.

The disordered activity of AI cortical dynamics represents a potentially important source of disturbance at many stages. Indeed, AI regime activity may spontaneously engage plastic processes (before any trajectory presentation), affecting the synaptic network matrix, and leading to altered network dynamics with divergence toward silence or saturation (Siri et al., 2007). Noisy activity may also interfere with the learning of the trajectory engram, by adding erratic entries of calcium to trajectory presentation-induced calcium, leading to jeopardized downstream decoding of calcium as well as erratic switches between long-term potentiation (LTP) and long-term depression (LTD) of synaptic weights. After learning, the continuous effects of AI regime activity-induced plastic processes (LTD or scaling) might erase the trajectory engram during memorization and jeopardize trajectory replay through the destabilizing influence of activity noise. On the other side of the interaction, trajectory learning through Hebbian synaptic plasticity may potentially, in turn, seriously disrupt AI regime activity (Morrison et al., 2007; Siri et al., 2007). Therefore, it remains uncertain whether realistic biological synaptic plasticity rules are well-suited for proper learning and memorizing of trajectory engrams as well as replay of learned trajectories in PFC physiological conditions.

Here, we assessed how learning, memorization and replay of trajectories can arise from biologically realistic synaptic learning rules in physiological PFC networks displaying disordered AI regime activity. To do so, we built a local recurrent biophysical network model designed to capture replay events like those observed in the PFC. Although designed to fit PFC collective spontaneous and triggered neural dynamics, its intrinsic, synaptic and architectural properties are shared across other cortices, allowing for generalization of the results to other non-PFC cortical areas displaying replays. The model displayed AI

dynamics and was endowed with realistic Hebbian (Hebb, 1949) spike timing-dependent plasticity (STDP) of excitatory synapses (Bi and Poo, 1998). Synaptic modifications operate through calcium-signaling dynamics capturing NMDA-dependent non-linear pre- to post-synaptic associativity (Graupner and Brunel, 2012) and calcium-dependent phosphorylation of synaptic weights with realistic activity-dependent kinase/phosphatase (aKP) dynamics, conferring a rapid, graded and bidirectional induction together with slow maintenance, consistent with learning and memory timescales observed in animal and human (Delord et al., 2007). Moreover, the model incorporates synaptic scaling, which ensures normalization of pre-synaptic weights, as found in the cortex (Turrigiano et al., 1998; Wang and Gao, 2012; Sweatt, 2016). We show, that, in this realistic model, presenting a stimulus trajectory allowed for rapid learning of a trajectory engram as well as long-term memorization of the trajectory engram despite the disturbing influence of the AI regime. In turn, the STDP learning rule and trajectory engram did not affect the spontaneous AI regime despite their influence on all excitatory neurons from the network. Moreover, we show that trajectory replay accounted for essential aspects of information coding in the PFC, including robustness of replays at the timescale of seconds, fast and regular replays, chunking, large inter-trial variability, and the ability to account for the dual dynamical and persistent aspects of working memory representations.

MATERIALS AND METHODS

Model of Biophysical Local Recurrent Neural Network

We built a biophysical model of a prefrontal local recurrent neural network, endowed with detailed biological properties of its neurons and connections. While the model is presented as PFC, its synaptic and neural properties are generally preserved across cortical areas, allowing for generalization of the results to non-PFC cortical areas. The network model contained N neurons that were either excitatory (E) or inhibitory (I) (neurons projecting only glutamate or GABA, respectively; Dale, 1935), with probabilities p_E and $p_I = 1 - p_E$, respectively, and $\frac{p_E}{p_I} = 4$ (Beaulieu et al., 1992). Connectivity was sparse (i.e., only a fraction of all possible connections exists, see $p_{E\to E}$, $p_{E\to I}$, $p_{I\to E}$, $p_{I\to I}$ parameter values; Thomson, 2002) with no autapses (self-connections) and EE connections (from E to E neurons) drawn to insure the over-representation of bidirectional connections in cortical networks (four times more than randomly drawn according to a Bernoulli scheme; Song et al., 2005; Wang et al., 2006). The synaptic weights $w_{(i,j)}$ of existing connections were drawn identically and independently from a log-normal distribution of parameters μ_w and σ_w (Song et al., 2005).

To cope with simulation times required for the massive explorations ran in the parameter space, neurons were modeled as leaky integrate-and-fire (LIF) neurons. The membrane potential of neuron j followed

$$\begin{cases} C\frac{dV_{(j)}}{dt} = -(I_{L(j)} + I_{Syn.Rec(j)} + I_{Syn.FF(j)}) \\ V_{(j)} > \theta \rightarrow V_{(j)} = V_{rest} \end{cases}$$

where neurons spike when the membrane potential reaches the threshold θ, and repolarization to V_{rest} occurred after a refractory period $\Delta\, t_{AP}$.

The leak current followed

$$I_{L(j)} = \bar{g}_L \left(V_{(j)} - V_L\right)$$

where $\bar{g}_L$ is the maximal conductance and V_L the equilibrium potential of the leak current.

The recurrent synaptic current on post-synaptic neuron j, from—either excitatory or inhibitory—pre-synaptic neurons (indexed by i), was

$$I_{Syn.Rec(j)} = \sum_i \Big(I_{AMPA(i,j)} + I_{NMDA(i,j)} + I_{GABA_A(i,j)} + I_{GABA_B(i,j)} \Big)$$

The delay for synaptic conduction and transmission, Δt_{syn}, was considered uniform across the network (Brunel and Wang, 2001). Synaptic recurrent currents followed

$$I_{x(i,j)} = \bar{g}_x\, w_{(i,j)}\, p_{x(i)} \left(V_{(j)} - V_x\right)$$

where $w_{(i,j)}$ is the synaptic weight, $p_{x(i)}$ the opening probability of channel-receptors and V_x the reversal potential of the current. The NMDA current followed

$$I_{NMDA(i,j)} = \bar{g}_{NMDA}\, w_{(i,j)}\, p_{NMDA(i)}\, x_{NMDA}\left(V_{(j)}\right)\left(V_{(j)} - V_{NMDA}\right)$$

incorporating the magnesium block voltage-dependence modeled (Jahr and Stevens, 1990) as

$$x_{NMDA}(V) = \left(1 + \left[Mg^{2+}\right] e^{-0.062\ V}/3.57\right)^{-1}$$

The channel rise times were approximated as instantaneous (Brunel and Wang, 2001) and bounded, with first-order decay

$$\frac{dp_{x(i)}}{dt} = -\frac{p_{x(i)}}{\tau_x} + p_x \left(1 - p_{x(i)}\right) \delta\left(t - t_{(i)}\right)$$

where δ is the dirac function and $t_{(i)}$ the times of the pre-synaptic action potentials (APs).

Recurrent excitatory and inhibitory currents were balanced in each post-synaptic neuron (Shu et al., 2003; Haider et al., 2006; Xue et al., 2014), according to driving forces and excitation/inhibition weight ratio, through

$$\begin{cases} \bar{g}_{GABA_A} = g_{GABA_A} \frac{-(V_{mean} - V_{AMPA})}{(V_{mean} - V_{GABA_A})} \frac{\sum_{i\in Exc} w_{(i,j)}}{\sum_{i\in Inh} w_{(i,j)}} \\ \bar{g}_{GABA_B} = g_{GABA_B} \frac{-(V_{mean} - V_{AMPA})}{(V_{mean} - V_{GABA_B})} \frac{\sum_{i\in Exc} w_{(i,j)}}{\sum_{i\in Inh} w_{(i,j)}} \end{cases}$$

with $V_{mean} = \frac{(\theta + V_{rest})}{2}$ being an approximation of the average membrane potential.

Furthermore, all recurrent maximal conductances were multiplied by g_{Rec}, and by $g_{E\to E}$, $g_{E\to I}$, $g_{I\to E}$ or $g_{I\to I}$ according to the excitatory or inhibitory nature of pre- and post-synaptic populations.

The feed-forward synaptic current $I_{Syn.FF(j)}$ (putatively arising from sub-cortical and cortical inputs) consisted of an AMPA component.

$$I_{Syn.FF(j)} = \bar{g}_{AMPA}\, p_{AMPA.FF}\, \left(V_{(j)} - V_{AMPA}\right)$$

with a constant opening probability $p_{AMPA.FF}$.

Synaptic Spike Timing-Dependent Plasticity (STDP)

We used a biophysical model of spike timing-dependent plasticity of excitatory synapses of the network. This rule operated constantly on the weights of the excitatory synapses during simulations. Synaptic weights evolved according to a first-order dynamic (Shouval et al., 2002; Delord et al., 2007) under the control of intra-synaptic calcium (Graupner and Brunel, 2012) through

$$\dot{w}_{(i,j)}(t) = K_{\max}\frac{Ca\,(t)^{nH}}{{K_{Ca}}^{nH} + Ca\,(t)^{nH}} - P_{\max}\frac{Ca\,(t)^{nH}}{{P_{Ca}}^{nH} + Ca\,(t)^{nH}}\, w_{ij}$$

where the plastic modifications of the synapses, i.e., the phosphorylation and dephosphorylation processes of the synaptic receptor channels, depended on a kinase (e.g., PKC type) and a phosphatase (e.g., calcineurin type) whose allosteric activation was dependent on calcium. Here, $K_{\max}$ represents the maximum reaction rate of the kinase, $P_{\max}$ that of the phosphatase, K_{Ca} and P_{Ca} the calcium half-activation concentration, Ca the synaptic calcium concentration and nH is the Hill's coefficient. The term t-LTP, kinase-related, was independent of synaptic weight ("additive" t-LTP) while t-LTD, phosphatase-related, was weight-proportional ("multiplicative" t-LTD), consistent with the literature (Bi and Poo, 1998; van Rossum et al., 2000). This model of STDP is extremely simple, but a detailed implementation would be prohibitive in an RNN of the order of a thousand neurons. There was no term related to the auto-phosphorylation of CaMKII present in many models to implement a form of molecular memory, because on one hand it is not actually involved in the maintenance of memory of synaptic modifications (Chen et al., 2001), and on the other hand memory is ensured here by the dynamics of kinase and phosphatase at low calcium concentration (Delord et al., 2007).

The time dependence of the APs (Bi and Poo, 1998; He et al., 2015) came from calcium dynamics, according to the model of Graupner and Brunel (2012). In this model, synaptic calcium followed

$$Ca\,(t) = Ca_0 + Ca_{pre}(t) + Ca_{post}\,(t)$$

where the total calcium concentration takes into account pre- and post-synaptic calcium contributions.

Pre-synaptic spiking mediated calcium dynamics followed

$$\dot{Ca}_{pre}(t) = -\frac{Ca_{pre}(t)}{\tau_{Ca}} + \Delta Ca_{pre}\sum_i \delta\left(t - t_{(i)} - D\right)$$

where the first term corresponds to calcium extrusion/buffering with time constant τ_{Ca} and the second term to voltage-dependent calcium channels (VDCC)-mediated calcium entry due to pre-synaptic spiking, with Ca_{pre} the amplitude of calcium entering at each AP of the presynaptic neuron, $t_{(i)}$ the times of the pre-synaptic APs, and D a delay modeling the time required for the activation of AMPA channels, the depolarizing rise of the associated excitatory post-synaptic potential (EPSP) and the subsequent opening of VDCC that induces this calcium entry.

Post-synaptic spiking-mediated calcium dynamics evolved according to

$$\dot{Ca}_{post}(t) = -\frac{Ca_{post}(t)}{\tau_{Ca}} + \Delta Ca_{post}\sum_j \delta\left(t - t_{(j)}\right) + \xi_{PrePost}\sum_j \delta\left(t - t_{(j)}\right) Ca_{pre}(t)$$

and modeled extrusion/buffering (first-term) as well as calcium entries due to post-synaptic, back-propagated spiking from the post-synaptic soma along the dendritic tree to the synapse, opening VDCC (central term) and NMDA channels (right term). $\xi_{PrePost}$ is an interaction coefficient and $t_{(j)}$ corresponds to the AP time of the post-synaptic neuron. NMDA activation is non-linear and depends on the product of a pre- and a post-synaptic term, representing the dependence of NMDA channel openings on the associative conjunction of pre-synaptic glutamate and post-synaptic depolarization, which releases the magnesium blockade of NMDA channels.

Synaptic Scaling

Synaptic weights were subjected to a homeostatic form of synaptic normalization, present in the cortex (Turrigiano et al., 1998; Wang and Gao, 2012; Sweatt, 2016), which was modeled in a simplified, multiplicative and instantaneous form (Zenke et al., 2013), following at each time step

$$w_{(ij)}(t + dt) = w_{(ij)}(t)\frac{\sum_i w_{ij}(t = 0)}{\sum_i w_{ij}(t)}$$

This procedure ensured that the sum of the incoming weights on a post-synaptic neuron remained constant despite the plastic modifications due to STDP.

Estimation of the Time Constant of STDP With Synaptic Scaling

Without synaptic scaling, $\dot{w}_{ij} = \dot{w}_{STDP} = K\,(Ca) - P\,(Ca)\,w$. However, synaptic scaling plays an important role in the slow decay of weights, so to study the time constant of this decay we needed to incorporate the effect of synaptic scaling. Considering n weights of average value μ_w incoming upon a post-synaptic neuron, where a proportion p of weights undergo STDP of value

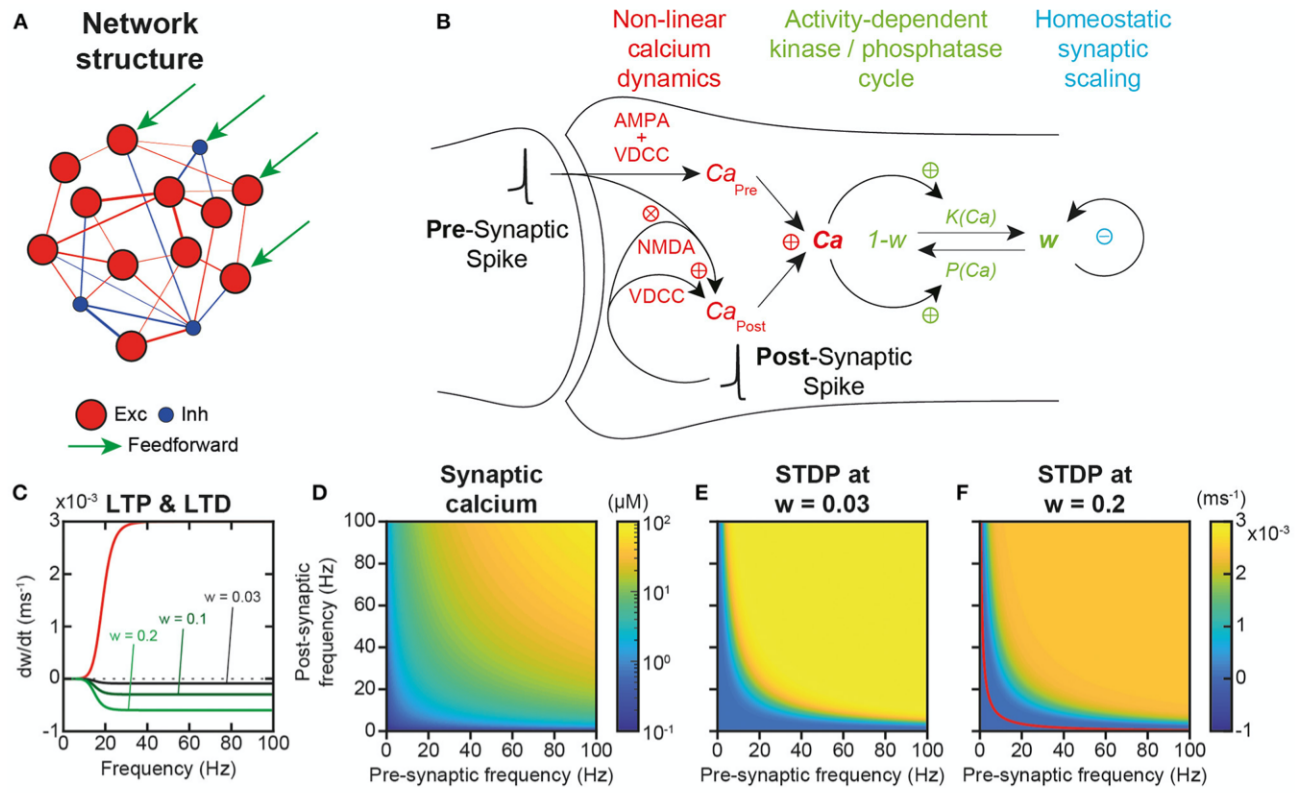

FIGURE 1 | Network structure and plastic properties. **(A)** Scheme of the recurrent network model of the local prefrontal cortex circuit with 484 excitatory (red) and 121 inhibitory (blue) integrate and fire (IAF) neurons. **(B)** Scheme of excitatory synaptic plastic processes. In the post-synaptic compartment, calcium dynamics originates from two distinct sources (Ca_{Pre} and Ca_{Post}), as well as from extrusion/buffering (Graupner and Brunel, 2012). Ca_{Pre} arises from pre-synaptic spiking mediated through α-amino-3-hydroxy-5-methyl-4-isoxazolepropionic acid (AMPA) depolarization and the subsequent activation of voltage-dependent calcium (VDCC) channels. Ca_{Post} models calcium entries due to post-synaptic spiking back-propagated from the post-synaptic soma to the synapse, opening VDCC and N-methyl-D-aspartate (NMDA) channels. NMDA activation is non-linear and depends on the interaction of pre- and post-synaptic spiking to account for the associative dependence of NMDA channel openings on the conjunction of pre-synaptic glutamate and post-synaptic depolarization that releases magnesium blockade. Plastic modifications operate through calcium-dependent phosphorylation and dephosphorylation of channel AMPA receptors that determine the synaptic weight (aKP model; Delord et al., 2007). Synaptic scaling continuously normalizes weights so as to insure the homeostatic regulation of the sum of incoming (pre-synaptic) weights for each individual neuron (Turrigiano et al., 1998). **(C)** Both long-term spike timing-dependent potentiation (t-LTP) and long-term spike timing-dependent depression (t-LTD) increase non-linearly with pre- and post-synaptic spiking frequency ($\nu_{Pre} = \nu_{Post} = \nu$), due to the allosteric calcium-activation of both enzymes. Kinase-mediated t-LTP is additive, i.e., independent of synaptic weight, while phosphatase-mediated t-LTD is multiplicative, i.e., weight-proportional (Bi and Poo, 1998; van Rossum et al., 2000). **(D)** Because of the associative dependance of NMDA-mediated calcium entry to pre- and post-spiking, synaptic calcium depends multiplicatively on pre- and post-synaptic spiking frequencies. **(E)** In the spontaneous AI regime, plastic modifications are virtually null because STDP plasticity occurs similarly at all synapses, with synaptic scaling compensating STDP (see Results). **(F)**. In synapses connecting neurons in the engram of a learned trajectory, where plasticity has occurred in a subset of synapses, Hebbian t-LTP dominates at large multiplicative pre-/post- frequencies and Hebbian t-LTD at lower frequencies (separated by the red curve for which plasticity is null, see Results).

$\dot{w}_{STDP}$ at time step t followed by scaling, then for a given weight w within the proportion p,

$$w(t+\Delta t) = (w(t) + \dot{w}_{STDP}\Delta t)\left(\frac{n\mu_w}{n\mu_w + np\dot{w}_{STDP}\Delta t}\right)$$

so that after algebra, one obtains

$$\frac{w(t+\Delta t) - w(t)}{\Delta t} = \left(1 - p\frac{w(t) + \dot{w}_{STDP}\Delta t}{\mu_w + p\dot{w}_{STDP}\Delta t}\right)\dot{w}_{STDP}$$

Passing to the limit $\Delta t \to 0$, one finds:

$$\dot{w} = \left(1 - p\frac{w}{\mu_w}\right)\dot{w}_{STDP}$$

i.e.

$$\dot{w} = \left(1 - p\frac{w}{\mu_w}\right)\left(K(Ca) - P(Ca)w\right)$$

To find an estimate of the time constant of plasticity, linearization aroundμ_w gives

$$\dot{w} \sim \left(P(Ca)\left(2p-1\right) - \frac{K(Ca)p}{\mu_w}\right)w + K(Ca) - pP(Ca)\mu_w$$

so that

$$\tau \sim \frac{\mu_w}{\left|pK(Ca) - \left(2p-1\right)P(Ca)\,\mu_w\right|}$$

Theoretical Dependences Under Asynchronous Irregular Dynamics

The steady-state theoretical concentration of calcium in individual synapses was obtained from fixed-points of Ca_{Pre} and Ca_{Post}, which yielded

$$Ca^*(\nu_{Pre}, \nu_{Post}) \sim Ca_0 + \tau_{Ca}(\Delta Ca_{Pre}\nu_{Pre} + \Delta Ca_{Post}\nu_{Post} + \xi_{PrePost}\Delta Ca_{Pre}\nu_{Pre}\nu_{Post})$$

which was used to determine STDP modification rates

$$\dot{w} = K(Ca^*) - P(Ca^*)w$$

and to determine the time constant for plasticity, in the case of the network asynchronous irregular regime at low frequency, where $p = 1$, i.e.

$$\tau \sim \frac{\mu_w}{\left|K\left(Ca^*\right) - P\left(Ca^*\right)\mu_w\right|}$$

Weights Within and Outside the Engram

Initial excitatory weights (before the 1 h simulation) were convolved with a centered normalized Gaussian function ($\sigma = 5$ *neurons*). Convolved weights with values above 0.1 (times $p_{E\to E} = 0.35$ to take into account inexistent weights) were considered within the engram, the other weights were considered outside the engram. Both weight populations were kept constant and their evolution was studied across time (see **Figures 6**, **7**).

Trajectory Replay Detection

In order to detect coherent propagating activity pulse packets along the synaptic pathway, we convolved spiking activity across time and neurons with centered normalized Gaussian functions ($\sigma = 30$ *ms* and $\sigma \sim 10$ *neurons*). Neurons were considered "active" when at least 40% of the convolved frequencies which include them (>5% of normalized Gaussian function maximum) are above 12.5*Hz*. We considered the emergence of an activity packet when it contained more than 20 neurons.

Spiking Irregularity

To capture spiking irregularity, we quantified the CV (coefficient of variation), CV2 and Lv (time-local variation) of the inter-spike interval (ISI) distribution of the spiking trains of neurons in the network (Compte, 2003; Shinomoto et al., 2005) according to

$$CV = \frac{\sigma_{ISI}}{< ISI >}$$

$$CV_2 = < 2\frac{\left|ISI_{k+1} - ISI_k\right|}{ISI_{k+1} + ISI_k} >_k$$

$$Lv = < 3\frac{\left(ISI_k - ISI_{k+1}\right)^2}{\left(ISI_k + ISI_{k+1}\right)^2} >_k$$

where $CV = CV_2 = Lv = 1$ for a homogeneous Poisson spike train and $= 0$ for a perfectly regular spike train where all *ISI* are equal. CV stands around 1 to 2 *in vivo* (Compte, 2003; Shinomoto et al., 2005), representing the global variability of an entire ISI sequence, but is sensitive to firing rate fluctuations. CV2 and Lv stand around 0.25 to 1.25 and 0 to 2, respectively *in vivo* (Compte, 2003; Shinomoto et al., 2005), evaluating the ISI variability locally in order to be less sensitive to firing rate fluctuations. The CV was calculated on every ISI across neurons, while the CV2 and Lv were calculated for each excitatory neuron and averaged across the whole population.

Spiking Synchrony

Three measures of synchrony were adopted, a synchrony measure S (Golomb et al., 2001), pairwise correlation coefficient averaged over all pairs of excitatory neurons $< \rho >$ (Tchumatchenko et al., 2010), and Fano factor F. The first two were calculated on the estimated instantaneous neural frequency f (Gaussian convolution of spikes, $\sigma = 30ms$), while the last was calculated on the population sum of spike counts s, following

$$S = \sqrt{\frac{Var\left(< f >_n\right)}{< Var\left(f_{(n)}\right) >_n}}$$

$$< \rho >= \frac{1}{N(N-1)/2}\sum_i\sum_{j>i}\frac{cov\left(f_{(i)}, f_{(j)}\right)}{\sqrt{Var\left(f_{(i)}\right)Var\left(f_{(j)}\right)}}$$

$$F = \frac{Var\left(\sum_n s_n\right)}{< \sum_n s_n >_t}$$

These measures equal $S = \frac{1}{\sqrt{n_E}} \sim 0.0455$, $< \rho >= 0$ and $F = 1$ for perfectly asynchronous network activity, and $S =< \rho >= 1$ while F increases for perfectly synchronous network activity.

Procedures and Parameters

Models were simulated and explored using custom developed code (MATLAB) and were numerically integrated using the forward Euler method with time-step $\Delta t = 0.5ms$ in network models. Unless indicated in the text, standard parameter values were as following. Concerning the network architecture, $N = 605$ *neurons*, $n_E = 484$ *neurons*, $n_I = 121$ *neurons*, $p_{E\to E} = 0.35$, $p_{E\to I} = 0.2056$, $p_{I\to E} = 0.22$, $p_{I\to I} = 0.25$, $\mu_w = 0.03$, $\sigma_w = 0.02$. Concerning the Integrate-and-Fire neural properties, $C = 1\ \mu F.cm^{-2}$, $\theta = -52\ mV$, $V_{rest} = -67\ mV$, $\Delta t_{AP} = 3\ ms$. Concerning currents, $\bar{g}_L = 0.05\ mS.cm^{-2}$, $V_L = -70\ mV$, $\Delta t_{syn} = 0.5\ ms$, $\bar{g}_{AMPA} = 0.23\ mS.cm^{-2}$, $\bar{g}_{NMDA} = 0.9\ mS.cm^{-2}$, $g_{GABA_A} = 0.3\ mS.cm^{-2}$, $g_{GABA_B} = 0.017\ mS.cm^{-2}$, $V_{AMPA} = V_{NMDA} = 0\ mV$, $V_{GABA_A} = -70\ mV$, $V_{GABA_B} = -90\ mV$, $\left[Mg^{2+}\right] = 1.5\ mM$, $\tau_{AMPA} = 2.5\ ms$, $\tau_{NMDA} = 62\ ms$, $\tau_{GABA_A} = 10\ ms$, $\tau_{GABA_B} = 25\ ms$, $p_{AMPA} = p_{NMDA} = p_{GABA_A} = p_{GABA_B} = 0.1$, $g_{Rec} = 0.65$, $g_{E\to E} = g_{E\to I} = g_{I\to E} = 1$, $g_{I\to I} = 0.7$, $p_{AMPA.FF} \sim 0.0951$. Concerning synaptic properties, $K_{\max} = 3.10^{-3}\ ms^{-1}$, $K_{Ca} = 3\ \mu M$, $P_{\max} = 3.10^{-3}\ ms^{-1}$, $P_{Ca} = 2\ \mu M$, $nH = 4$, $Ca_0 = 0.1\ \mu M$, $\tau_{Ca} = 100\ ms$, $\Delta Ca_{pre} = 0.02\ \mu M$, $D = 10\ ms$, $\Delta Ca_{post} = 0.02\ \mu M$, $\xi_{PrePost} = 4\ ms^{-1}$.

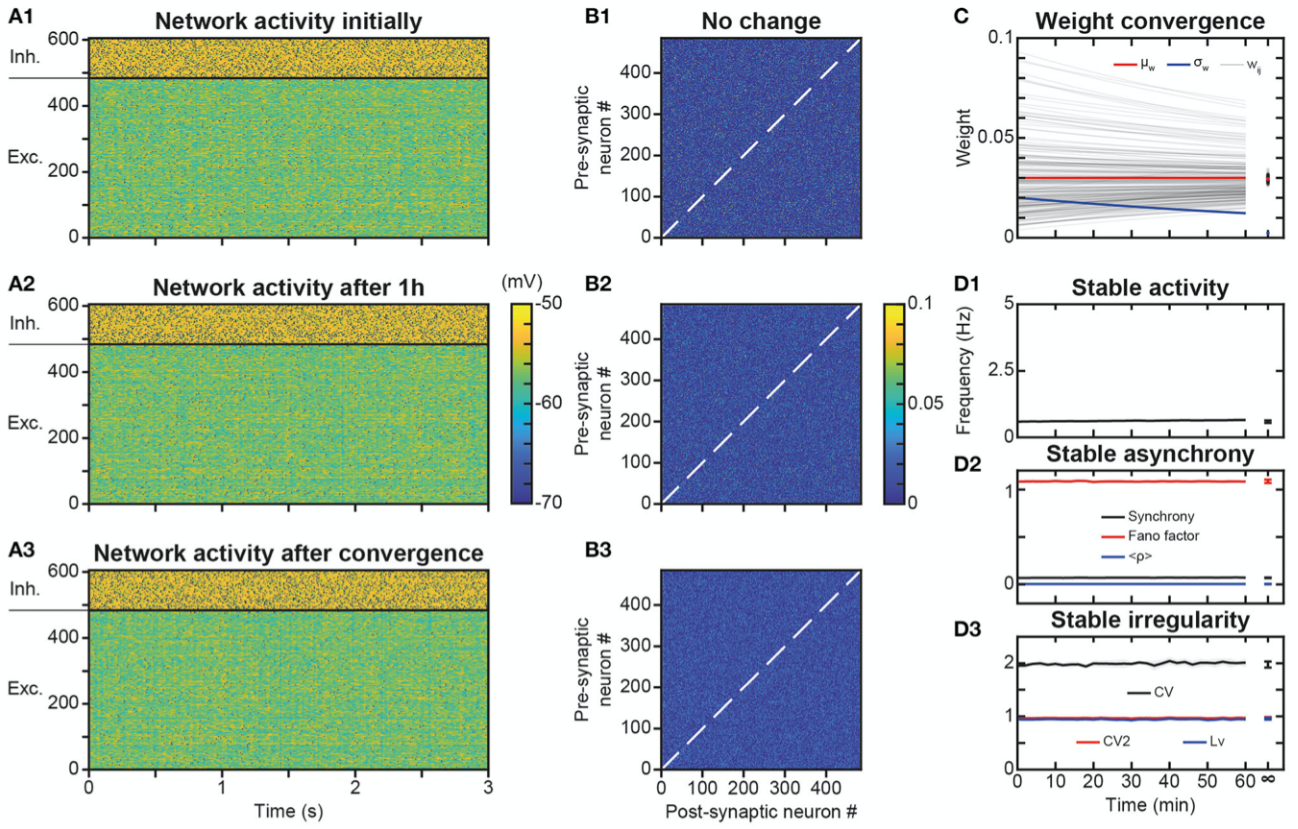

FIGURE 2 | Stability of spontaneous irregular asynchronous (AI) network dynamics under synaptic plasticity. **(A1–A3)** Membrane potential of network neurons during 3 s of spontaneous AI regime in the absence of plasticity **(A1)**, after 1 h of plasticity **(A2)** and after full convergence of synaptic weights due to plasticity **(A3)**. The same initial random connectivity matrix is used for simulations in **(A1–A3)**. Spikes indicated by black dots. Full convergence of the synaptic matrix was obtained by simulating the networks with very fast kinetic constants. **(B1–B3)** Synaptic weights between excitatory neurons of the network at the end of each of simulations presented in **A1–A3**. **(C)** Convergence of synaptic weights toward the mean weight of their post-synaptic neuron as a function of time, due to synaptic scaling normalization (black curves, see Results). Time evolution of the mean (red curve) and standard deviation (blue curve) of synaptic weights. For sake of clarity, only a random selection of synapses is shown. The mean is constant and the standard deviation decreases with time, due to scaling. **(D)**. Average excitatory neural spiking frequency **(D1)** and irregularity **(D3)** and excitatory population synchrony **(D2)** quantifiers, as a function of time, for five different simulations of the network with different realizations of the initial random synaptic matrix. Dots on the right indicate values obtained from network simulations after full convergence of synaptic weights. Shaded areas represent 95% confidence intervals of the mean.

RESULTS

Predicting Fundamental Plastic Properties of PFC Recurrent Networks

To evaluate neural trajectory learning, memorization and replay, we studied a local prefrontal cortex (PFC) recurrent network model, with 484 excitatory and 121 inhibitory integrate and fire (IAF) neurons with topographically tuned feed-forward inputs. Synaptic connections were constrained by cortical connectivity data, following Dale's law, sparseness and log-normal weight distributions, and α-amino-3-hydroxy-5-methyl-4-isoxazolepropionic acid (AMPA) and N-methyl-D-aspartate (NMDA) excitatory and γ-aminobutyric acid (GABA-A and GABA-B) inhibitory synaptic currents (**Figure 1A;** see *Materials and Methods*). Most synaptic and neural properties, while present in PFC, are generic across cortex, such that the following results can be generalized to non-PFC cortical areas.

Excitatory synapses were plastic, i.e., endowed with realistic calcium dynamics (Graupner and Brunel, 2012) accounting for linear voltage-dependent calcium channels (VDCC)-dependent and non-linear NMDA calcium entries, as well as for linear extrusion and buffering (**Figure 1B**). These calcium dynamics are responsible for the temporal asymmetry of pre- and post-synaptic spike-timing dependent (STDP) plastic modifications (Bi and Poo, 1998; He et al., 2015). Note, however, that with these realistic calcium dynamics, plasticity essentially depends on firing frequency rather than on the precise timing of spikes, because of the frequency and variability of *in vivo*-like spiking (Graupner et al., 2016).

Plastic modifications operated through calcium-dependent kinase-phosphatase kinetics (Delord et al., 2007), which accounts for their fast induction and slower maintenance dynamics (**Figure 1B**). No Ca^{2+}/calmodulin-dependent protein kinase II (CaMKII) auto-phosphorylation was present because it

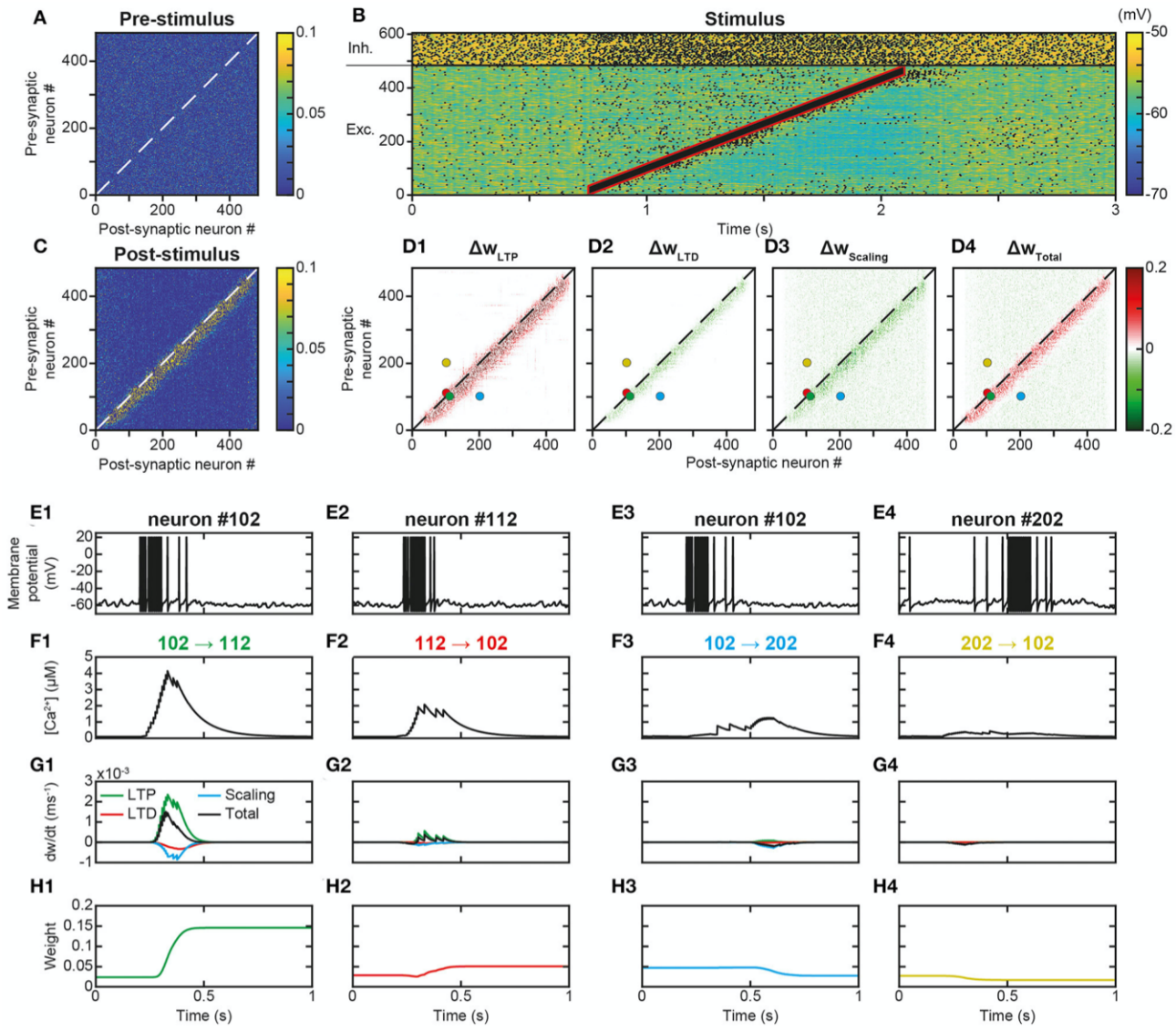

FIGURE 3 | Learning a trajectory stimulus into a trajectory engram. **(A)**. Synaptic matrix between excitatory neurons prior to stimulus presentation. **(B)**. Membrane potential of network neurons in response to the presentation of a trajectory stimulus (stimulus in red) that successively activates all excitatory neurons over a duration of 1,350 ms. Spikes indicated by black dots. **(C)**. Synaptic matrix between excitatory neurons after stimulus presentation. **(D1–D4)**. Weight modifications resulting, after trajectory presentation, from t-LTP **(D1)**, t-LTD **(D2)**, scaling **(D3)**, and their sum **(D4)**. **(E–H)** Membrane potential **(E)**, calcium **(F)**, plastic rates **(G)** and synaptic weight dynamics **(H)** during the passage of the trajectory stimulus in a pair of neurons with nearby topographical tuning #102 **(E1)** and #112 **(E2)** and their reciprocal connections 102→112 **(F1-H1)** and 112→102 **(F2-H2)**, and in a pair of neurons with more distant topographical tuning #102 **(E3)** and #202 **(E4)** and their reciprocal connections 102→202 **(F3-H3)** and 202→102 **(F4-H4)**.

is actually not involved in the maintenance of synaptic modifications (Chen et al., 2001; Lengyel et al., 2004). Rather, the long-term maintenance of plastic modifications emerges from kinase and phosphatase dynamics at low calcium concentrations (see below; Delord et al., 2007). Besides, synapses underwent synaptic scaling (**Figure 1B**), which ensures total weight normalization at the neuron level, as observed in the cortex (Turrigiano et al., 1998; Wang and Gao, 2012; Sweatt, 2016) and, as a consequence, introduces competition between synaptic weights within each neuron (intra-neuronal inter-synaptic competition).

Most importantly, plasticity operated online—i.e., permanently, without offline learning periods—on excitatory synaptic weights, as a function of neuronal activity in the network, whether it corresponds to the spontaneous, asynchronous and irregular (AI) activity of the network, the activity evoked by the feed-forward currents during the input presentation of an example trajectory, or the replay activity

after learning (see below). Both kinase-mediated long-term spike timing-dependent potentiation (t-LTP) and phosphatase-mediated long-term spike timing-dependent depression (t-LTD) increased non-linearly with pre- and post-synaptic spiking frequency, due to the allosteric activation of enzymes by calcium (**Figure 1C**). However, they differed in that kinase-mediated t-LTP was independent of synaptic weight (additive or hard-bounded) while phosphatase-mediated t-LTD was weight-proportional (multiplicative or soft-bounded), consistent with the literature (Bi and Poo, 1998; van Rossum et al., 2000; **Figure 1C**). In the model, the steady-state theoretical concentration of calcium in individual synapses depended multiplicatively upon pre-synaptic and post-synaptic spiking activity (**Figure 1D**), from which one could compute the rate of STDP as a function of pre- and post-synaptic spiking frequency (**Figures 1E,F**) see Materials and Methods). In conditions with weak synaptic weights, such as prior to learning, t-LTP dominated at all frequencies because t-LTD is multiplicative and thus scaled by, here, very low synaptic weights. Thus, STDP effects were always positive and depended multiplicatively on pre- and post-synaptic frequencies (**Figure 1E**). By contrast, when plasticity had previously occurred ($w = 0.2$), such as in the engram of a learned trajectory (see below), t-LTD was stronger due to the stronger weights, and the model predicted Hebbian t-LTP at large multiplicative pre-/post-frequencies and t-LTD at lower frequencies (**Figure 1F**). In the following, we explore the extent to which these predictions are correct in simulations of the whole network model under spontaneous AI dynamics with synaptic scaling, and when assessing learning and memorization upon trajectory presentation.

Stability of Network AI Dynamics Under Synaptic Plasticity

A potential issue of synaptic plasticity in network models remains its sensitivity to spontaneous activity. Hence, before testing the possible role of STDP in trajectory learning and replay, we first studied the effect of STDP on the spontaneous regime, with the aim of verifying that network activity remained stable over the long term and that neurons always discharged in the AI regime. Indeed, Hebbian or post-Hebbian rules of the STDP type, by modifying the matrix of synaptic weights, may lead to saturation of neuronal activity and a collapse of the complexity of the dynamics, from initially AI chaotic activity characteristic of the waking state (Destexhe et al., 2003; London et al., 2010), to activity of the limit-cycle or fixed point type (Siri et al., 2007). We considered here as long term the 1 h time scale, which is the scale classically used experimentally to test the memory of synaptic plasticity modifications (Bi and Poo, 1998). Moreover, a duration of 1 h extends way beyond the classical time scales used in models (Morrison et al., 2007; Boustani et al., 2012; Litwin-Kumar and Doiron, 2014). For this purpose, we have observed the activity (**Figure 2A**) and connectivity (**Figure 2B**) of the network at different time scales, in order to reveal possible modifications in the network behavior.

Simulations showed that the spontaneous activity of the network was identical without plasticity (**Figure 2A1**), after 1 h in the presence of plasticity (**Figure 2A2**) and after full convergence (**Figure 2A3**) of weight matrix dynamics. This observation is consistent with the absence of changes in the connectivity matrix in the presence of STDP, even after 1 h of simulation (**Figures 2B2,B3**), compared to the condition without STDP (**Figure 2B1**). Mechanistically, the low spiking frequency of neurons resulted in moderate average elevations of calcium above its basal concentration in synapses, so that kinase and phosphatase were only very weakly activated. Therefore, weights underwent extremely slow plastic modifications where additive t-LTP (which dominated the multiplicative t-LTD at weak weights) was compensated by synaptic scaling. Due to these effects, weights converged toward the mean initial weight of their post-synaptic neuron (**Figure 2C**) with an apparent time constant of 2 h, close to the theoretical estimation of the time constant of plasticity (see *Materials and Methods* and *Discussion*), which predicts a time constant of 1.95 h during learning at low spiking frequencies and calcium concentrations ($Ca \sim Ca_0$) in the AI regime. These steady-state values were normally distributed, with a constant mean value (due to the synaptic scaling) and a decreasing standard deviation, due to the homogenization of weights within each post-synaptic neuron (**Figure 2C**). Even with this more homogeneous synaptic matrix (**Figure 2B3**), AI dynamics were preserved (**Figure 2A3**). Indeed, excitatory frequency was stable (**Figure 2D1**), as well as markers of synchrony (**Figure 2D2**) and irregularity (**Figure 2D3**). Thus, overall, the activity regime of the network was not altered by the presence of plastic processes. Note that in PFC circuits experiencing dynamically changing feed-forward inputs, convergence of the synaptic matrix may be attenuated or even non-existent.

Learning Trajectory Engrams Under AI Dynamics

Trajectory learning during network activity has already been investigated in the theoretical literature, but either without chaotic dynamics or using biologically unrealistic learning rules (see *Introduction*). To test for the possibility of learning trajectories within physiologically irregular activity, we presented to the network a moving stimulus (**Figure 1A**, feedforward connections) that successively activated all the excitatory neurons over 1,350 ms (**Figure 3B**). Such a stimulation corresponds to a displacement speed of ∼0.3 neurons/ms, where each excitatory neuron was stimulated for ∼100 ms and discharged at ∼100 Hz. This single stimulus presentation triggered neural activity much stronger than the spontaneous activity, sufficient to modify the matrix of synaptic weights. Indeed, whereas the synaptic matrix was initially formed of low random weights (**Figure 3A**), after presentation, the weights of synapses connecting neurons activated by the stimulus at close successive times were increased (**Figure 3C**). This diagonal band of increased weights formed an oriented connectivity path along stimulus-activated neurons and is referred to as the trajectory engram hereafter. Weight modifications inside and outside this trajectory engram resulted from increases due to t-LTP (**Figure 3D1**, Δw_{LTP}) and decreases due to t-LTD (**Figure 3D2**, Δw_{LTD}). Moreover, the homeostatic

process of synaptic scaling, which ensures the constancy of the sum of the incoming weights of the cortical neurons, decreased the total incoming synaptic weights on post-synaptic neurons, in order to compensate for weight modifications due to STDP (**Figure 3D3**, $\Delta w_{Scaling}$). In fine, STDP and scaling led together to an increase in engram weights and a slight decrease in off-engram weights (**Figure 3D4**, Δw_{Total}; also observe the darker area in **Figure 3C**, compared to **Figure 3A**).

The observation, on a local scale, of the details of the processes at work for the synapses linking the neurons of the engram allowed for a better understanding of these network effects. For illustration, neurons #102 and #112, with close spatial topographical tuning, discharged one following the other with partial overlap during the stimulus (**Figure 3E**). At the level of the synapse between neurons #102 and #112 (102→112), whose orientation was that of the trajectory, the arrival of pre-synaptic action potentials (APs) was followed by that of postsynaptic APs (pre #102 then post #112 neuron, **Figures 3E1,E2**), which triggered a massive input of calcium via the VDCC channels and the NMDA receptor channels (**Figure 3F1**). Conversely, in the synapse 112→102, for which the sequence of arrival of the APs was reversed (pre #112 then post #102 neuron), NMDA channels did not open (see above), such that the calcium input resulted only from the VDCC channels and was thus moderate (**Figure 3F2**). These calcium elevations activated the kinases and phosphatases, which, respectively, phosphorylated and dephosphorylated AMPA channels, increasing (t-LTP) and decreasing (t-LTD) synaptic weights (only phosphorylated AMPA channels are functional and ensure synaptic transmission). These kinase and phosphatase activations were important for synapse 102→112 (**Figure 3G1**), but less so for the synapse 112→102 (**Figure 3G2**). For both synapses (**Figures 3G1,G2**), the phosphatase was more strongly activated (lower half-activation; Delord et al., 2007), but the resulting t-LTD modification rate was low, because it is multiplicative, i.e., it scales with synaptic weight, which was low. Conversely, the rate of modification due to t-LTP was higher because it is additive and depends only on kinase activation (van Rossum et al., 2000). These STDP effects, cumulated with those of scaling, resulted in a positive speed (increase in weight), which was strong for synapse 102→112 (**Figure 3G1**) and very weak for synapse 112→102 (**Figure 3G2**). Together, these plastic processes increased the weight of the synapse oriented in the same direction as the stimulus (**Figure 3H1**) leaving the weight of the synapse of opposite orientation almost unchanged (**Figure 3H2**).

For neurons whose receptive fields were more spatially distant, activation by the stimulus occurred at more temporally distant times (for example, neurons #102 and #202, **Figures 3E3,E4**). In this case, regardless of the sequence of arrival of the APs in both neurons, their succession was too distant in time to open NMDA channels, so that incoming calcium came only from the VDCC channels and was therefore low (**Figures 3F3,F4**). Consequently, kinase and phosphatase were weakly activated, resulting in virtually null STDP velocity (**Figures 3G3,G4**). Synaptic scaling (**Figures 3G3,G4**), induced by the increase of weights in the engram (**Figures 3H1,H2**), ultimately decreased synaptic weights (**Figures 3H3,H4**). As such, there was no learning of any trajectory between distant neurons, contrary to what happened between closer neurons.

Trajectory Replays From Learned Trajectory Engrams

In behaving animals, learnt trajectories are replayed later in appropriate behavioral conditions. In the model, we assessed whether trajectories could be replayed, the dynamics of trajectory replays and the way they affect the network connectivity compared to before they occur (**Figure 4A**). Trajectory replay was defined as the reactivation of neurons of the entire trajectory engram, after temporarily stimulating only initial neurons at the beginning of the engram. To assess trajectory replay in the network, we applied a stimulus of 100 ms to the first 50 neurons of the engram, 500 ms after trajectory learning was completed (**Figure 4B**). We found that the network was able to replay the trajectory entirely after learning (**Figure 4B1**). Fundamentally, the replay emerged because neurons were linked by strong synapses so that preceding neurons activated subsequent neurons in the engram, forming an oriented propagating wave (**Figure 4B2**).

Because it activated neurons at several tens of Hz, the replay could have brought into play plastic processes at the synapses forming the engram, and, in doing so, either reinforce or diminish their weights, possibly disturbing or even destroying the engram. To evaluate these possibilities, we observed the variation of synaptic weights before and after the replay. We found that after replay, the engram was still present (**Figure 4C**) and its structure identical to that before replay (**Figure 4A**). However, when dissecting the effects at work, we found that the engram had slightly thickened during the trajectory replay, due to the combined effect of t-LTP (**Figure 4D1** Δw_{LTP}), t-LTD (**Figure 4D2** Δw_{LTD}) and scaling (**Figure 4D3** $\Delta w_{Scaling}$). Weights above and below the engram increased, whereas weights slightly decreased within the engram (**Figure 4D4**, Δw_{Total}, red fringes).

Up to this point, the neural trajectory was presented as a whole. However, whole trajectories are generally not accessible directly to the PFC. Rather, PFC circuits generally encounter elementary trajectory fragments at separate points in time to produce prospective planning of future behaviors (Ito et al., 2015; Mashhoori et al., 2018; Kaefer et al., 2020), as well as learn transitions between them and chunk fragments together as whole trajectories independently of their presentation order (ordinal knowledge) (Ostlund et al., 2009; Dehaene et al., 2015). We trained the network with four fragments of the whole trajectory, noted A-D, that overlapped at their extremities and which were presented sequentially every 2 s, so as to learn separately different parts of the trajectory (**Figure 4E**). We found that, once fragments were presented in forward order (ABCD), stimulating neurons at the beginning of the A fragment induced propagation of activity that recapitulated the whole trajectory, by subsequently recalling ABCD fragments in the forward order

(**Figure 4E1**). Therefore, the network was able to learn trajectory fragments themselves and the transitions between fragments so as to chunk them into a whole trajectory. Moreover, we found that chunking was possible even when fragments had been learned in reverse order (DCBA; **Figure 4E2**). Hence, the network was able to replay a chunked trajectory based on the presentation of overlapping stimuli, independently of their order of presentation.

Functional Diversity of Trajectory Replays

Neural activity during the replay was less focused than the stimulus trajectory (**Figure 4B**), i.e., it involved more (∼90 vs. 35) neurons, spiking at a lower (∼65 vs. 100 Hz) discharge frequency. The replay also unfolded at a faster speed, lasting ∼750 ms—for a stimulus of 1,350 ms—so that it exhibited a temporal compression factor (tCF) of ∼1.8, which is situated between fast and regular timescale replays observed in animals. Regular timescale replays operate at the timescale of behaviors they were learnt from, i.e., a few seconds (in navigation or working memory tasks, e.g.), hence typically displaying tCF∼1. By contrast, fast timescale replays last several hundred ms in the awake PFC (200–1,500 ms; Jadhav et al., 2016; Mashhoori et al., 2018; Kaefer et al., 2020), yielding several-fold compression factors (tCF∼2–15). We assessed whether varying biophysical parameters of the network could account for durations and tCF ranges characterizing regular and fast replays. As regular and fast timescale replays frequently alternate within trials in behavioral tasks, we discarded trivial replay speed control that can be readily obtained by scaling structural parameters that vary at extremely slow timescales (e.g., number of neurons in the trajectory, synaptic delay, etc., not shown). Rather, we focused on synaptic and intrinsic neuronal properties likely to be rapidly regulated by ongoing neuromodulation in the PFC, as attentional demands or reward outcomes vary at the trial timescale. Among passive and synaptic neuronal parameters tested, the NMDA conductance decay time constant (τ_{NMDA}) emerged as a critical factor controlling the duration and tCF of replays. Hence, the same network, taught with the same trajectory and stimulated with the same initiation stimulus, could generate a large range of replay timescales spanning from regular (duration 1,680 ms, tCF = 0.8; **Figure 5A1**) to fast (duration 375 ms, CF∼3.6; **Figure 5A2**) replays, when the decay time constant of NMDA, τ_{NMDA}, was varied. Consistently, dopaminergic neuromodulation, the major determinant of reward signaling, rapidly slows the decaying dynamics of NMDA currents in PFC circuits (Chen et al., 2004; Onn and Wang, 2005; Onn et al., 2006). Such neuromodulatory effects, as well as others forms of neuromodulation of NMDA dynamics (Lutzu and Castillo, 2021) may control the duration and compression factor of trajectory replays, as well as the relative rate of occurrence of regular vs. fast timescale replays. Inspecting neuronal activity during replays in terms of firing frequency, we found that in single replays individual neurons displayed a sequence of overlapping transient bumps of activity of a few hundred milliseconds (**Figure 5B1**) resembling "relay race" of PFC individual activities during regular replays in working memory tasks (Batuev, 1994; Brody et al., 2003; Cromer et al., 2010; Yang et al., 2014; Schmitt et al., 2017). By contrast, the averaged frequency over the population of excitatory neurons displayed a persistent decaying activity pattern that lasted at the second time scale (**Figure 5B2**) and mimicked population-level working memory maintenance in the PFC (Murray et al., 2017; Cavanagh et al., 2018; Enel et al., 2020). This dichotomy recalls that found in the PFC, whereby individual neurons encode information at short timescale while the population holds stabilized persistent representations on longer timescales (Meyers et al., 2008; Murray et al., 2017; Cavanagh et al., 2018). Moreover, we found that inter-trial variability for each neuron was important, due to disordered network AI dynamics, and that it increased as activity traveled later in the trajectory in individual neurons (**Figure 5B3**) and at the population level (**Figure 5B4**), as found experimentally (Compte, 2003; Shafi et al., 2007; Tiganj et al., 2017).

Globally, the model thus not only indicated that it was possible to learn trajectories online by creating synaptic engrams, thanks to the STDP-type plasticity rule. It also showed that learned trajectories were functional as a memory process, in the sense that their replay was possible and globally preserved the synaptic structure of the learned engram. Finally, the model accounted for the large functional diversity of replays observed in behaving animals, both with regard to the timescale (fast vs. regular) they exhibit, as well as to the type of coding (dynamical vs. stable) they may subserve in navigational or working memory tasks.

Stability of Network AI Dynamics in the Presence of Trajectory Engrams

After evaluating the stability of the learned trajectory in the presence of AI network activity, we asked the symmetrical question, i.e., whether the engram of a previously learned trajectory could alter the irregular features of spontaneous network dynamics. Indeed, the altered synaptic structure (which implies large weights in all neurons of the recurrent network) may induce correlated activations of neurons (e.g., partial replays) resulting in runaway activity-plasticity interactions and drifts in network activity and synaptic structure. We monitored network connectivity (**Figure 6A**) and activity dynamics (**Figures 6B1–B3**) for 1 h to assess the stability of the spontaneous AI regime in the presence of the engram. We observed that following learning of the engram, synaptic weights outside the engram (i.e., responsible for the AI dynamics) increased exponentially toward their new steady-state in a very slow manner (**Figure 6A**) with an apparent time constant of 1.91 h, consistent with the theoretical estimation of 1.95 h (see above). This increase resulted from the decrease of within-engram large synaptic weights via synaptic scaling (**Figure 6E1**, see above). Despite this slow and moderate structural reorganization, AI dynamics were preserved with stable frequency (**Figure 6B1**), synchrony (**Figure 6B2**), and irregularity (**Figure 6B3**). Thus, overall, both the synaptic structure outside the engram as well as the spontaneous AI regime remained stable in the presence of the engram.

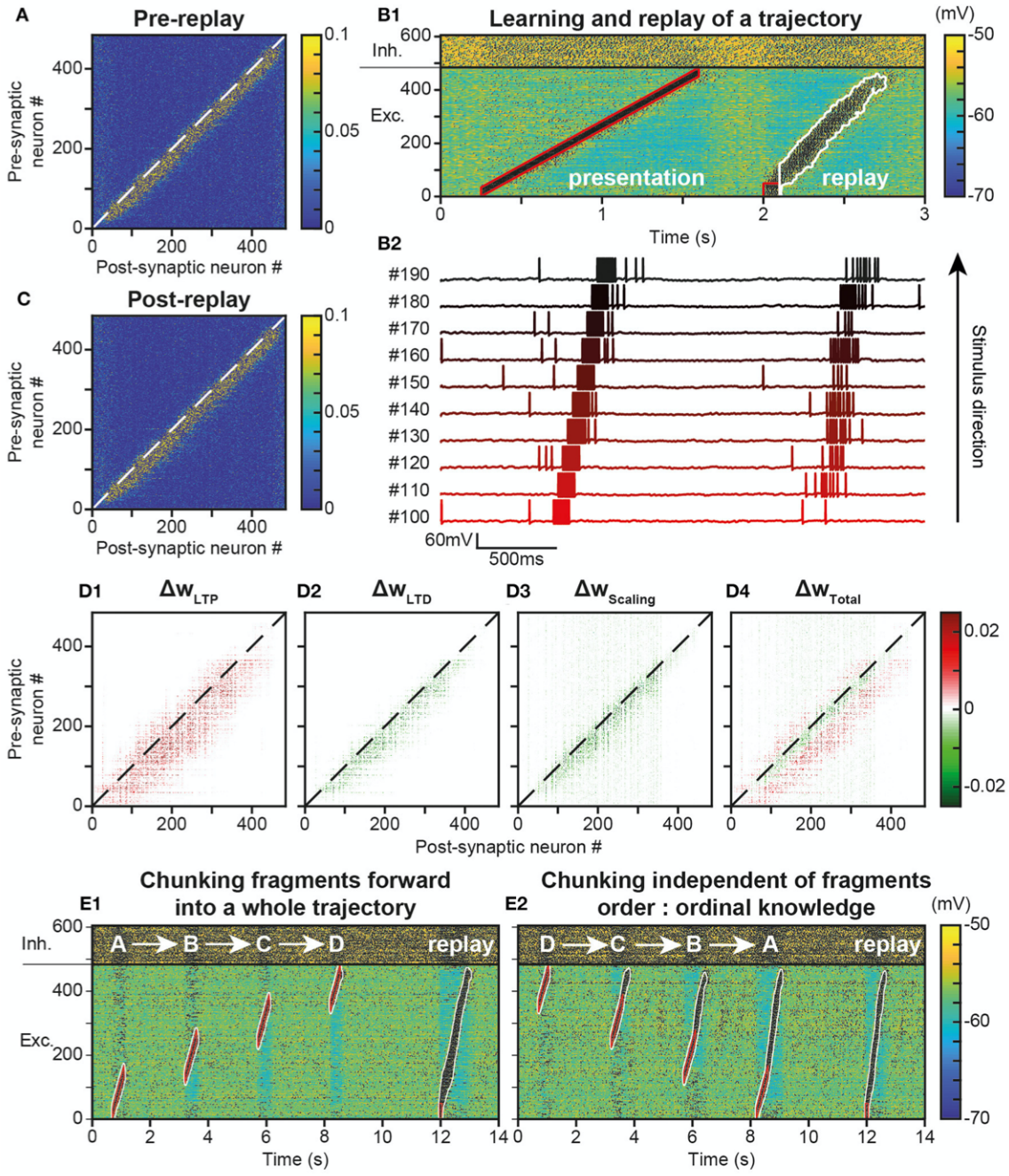

FIGURE 4 | Replay of learned trajectories. **(A)**. Synaptic matrix between excitatory neurons after stimulus presentation but prior to trajectory replay. **(B)**. Membrane potential of network neurons (**B1**, spikes indicated by black dots) in response to the trajectory stimulus, followed by a transient trajectory replay triggered by stimulating the start of the trajectory (neurons #1–50, stimulus in red). Membrane potential of a selected subset of neurons along the trajectory (**B2**, arbitrary colors). **(C)**. Synaptic matrix between excitatory neurons after stimulus and replay. **(D)**. Weight modifications resulting, after compared to before trajectory replay, from t-LTP **(D1)**, t-LTD **(D2)**, scaling **(D3)**, and their sum **(D4)**. **(E)** Recapitulation of the whole trajectory after separately learning four individual trajectory fragments (ABCD) in the forward order (**E1**; chunking) or backward order (**E2**; ordinal knowledge). Each fragment corresponds to 180 neurons. Fragments overlap over 65 neurons.

Memory of Trajectory Engrams in the Presence of Network AI Dynamics

We then studied whether the spontaneous AI activity could disrupt the engram of the learned trajectory and the possibility for trajectory replay. Indeed, the trajectory engram may be gradually erased, due to AI activity at low frequency favoring t-LTD, or even amplified, due to the activity in the trajectory engram caused by plasticity (resulting in further plasticity

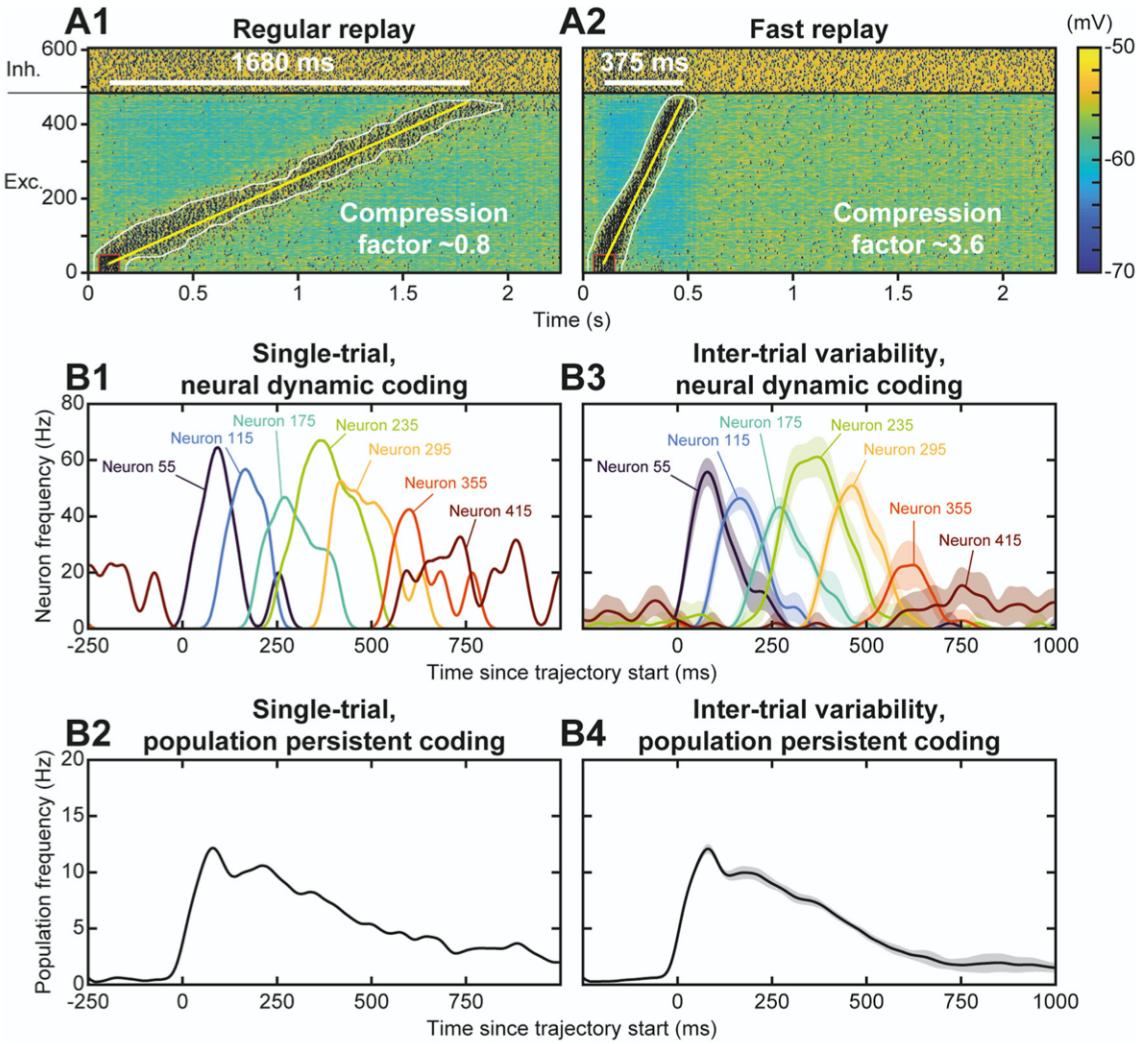

FIGURE 5 | Functional diversity of trajectory replays. **(A)** Trajectory replay duration (upper left white bar) and compression factor (tCF; lower right) depend on the NMDA conductance decay time constant (τ_{NMDA}, range 30–150 ms). NMDA maximal conductance was scaled (range 0.475–1.8) so as to insure similar levels of firing frequency drive during trajectory replays. Regular **(A1)** and fast **(A2)** timescale replay are due to slower and faster NMDA dynamics. **(B)**. Single-trial **(B1, B2)** and inter-trial variability **(B3,B4)** of firing frequency of individual neurons **(B1,B3)** and of the population **(B2,B4)** for 10 different simulations similar to the replay shown **Figure 4B**. Lines represent mean values, shaded regions represent 95% confidence intervals of the mean.

runaway). To do so, we assessed the timescale of potential drifts in engram connectivity and activity following learning, and of the network ability to replay the engram. Intuitively, engram erasure, runaway or stability probably depended on network dynamics after learning: spontaneous AI regime, spontaneous replays, or other forms of activity.

To address these questions, we simulated the network for 1 h after trajectory learning and recorded "snapshots" of the continuous evolution of the synaptic matrix every minute. Using these successive recorded matrices as initial conditions for independent simulations of replays, we were able to quantify network ability for trajectory replay, at different times of the evolution of the network. We found that while trajectory replay occurred in full after 1 s, activating all neurons of the trajectory (**Figure 6C1**), it was slightly attenuated after 1 min (last neurons spiking at lower frequency; **Figure 6C2**) and failed after 1 h (**Figure 6C3**). Observing the synaptic matrix at these three moments allowed us to understand the origin of this degradation in replay ability. Indeed, whereas after 1 min (**Figure 6D2**), the synaptic weights of the engram changed only a little compared to 1 s (**Figure 6D1**), the engram was narrowed and weights attenuated after 1 h (**Figure 6D3**). Such degradation of the engram was probably the cause of the failure to replay the trajectory 1 h after learning.

To more precisely monitor degradation of the trajectory engram and replay, we measured averaged engram weights as well as replay frequency and duration across time. We found that the engram weights declined exponentially with a fitted time constant of 1.91 h (**Figure 6E1**), very close to that predicted by the theory (1.95 h). The measures of trajectory replay decreased

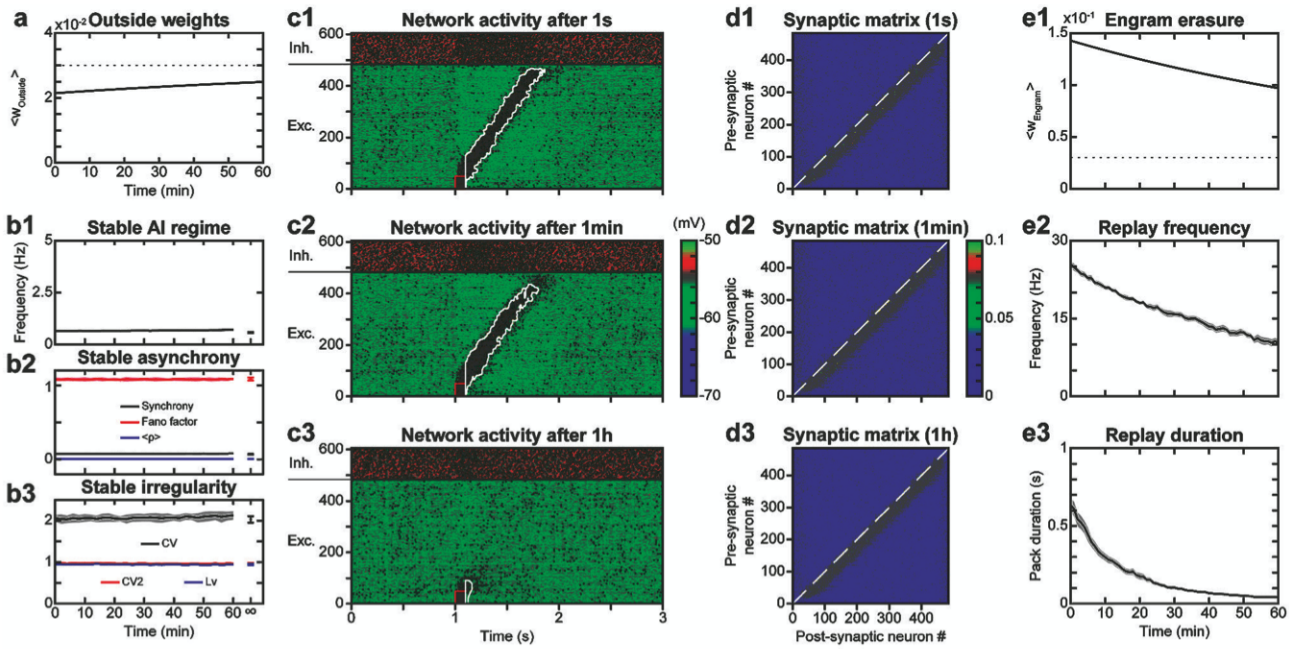

FIGURE 6 | Stability of the spontaneous AI regime in the presence of the engram. **(A)**. Average synaptic weights outside the engram after learning for 1 h. Shaded areas represent 95% confidence intervals of the mean for 5 network simulations. **(B)**. Networks dynamics after learning for 1 h: frequency **(B1)**, synchrony **(B2)**, and irregularity **(B3)** of excitatory neurons. Shaded areas as in **(A)**. **(C)**. Membrane potential of neurons in the neural network for 3 s following a replay stimulation of the 50 first neurons at 1 s **(C1)**, 1 min **(C2)** or 1 h **(C3)** after trajectory learning. **(D)** Synaptic matrices between excitatory neurons of the network, at the end of the simulations presented in **(C)**. **(E)** Network engram synaptic weight average **(E1)** as well as frequency **(E2)** and duration **(E3)** of trajectory replays during 1 h after trajectory learning. Shaded areas as in **(A)**.

faster than the engram weights, with time constants of ∼54 min for mean frequency during the replay (**Figure 6E2**) and ∼13 min for replay duration (**Figure 6E3**). Specifically, replay of the full trajectory lasted 4 min. The degradation of trajectory replay was mainly due to progressive replay failure in the neurons located later in the trajectory engram. The faster decrease in trajectory activity, compared to the average engram weights, was probably a consequence of a cooperative mechanism of propagation in the engram: the non-linearity in NMDA current activation, requiring synergistic activation of pre- and post-synaptic neurons in the engram, rendered the propagation of activity non-linearly sensitive to decreases in engram weights.

Repeated Trajectory Replays Can Destabilize Trajectory Engrams and Replays

We have observed that a single replay of the trajectory only marginally modified the engram (**Figure 4C** vs. **Figure 4A**). However, we assessed whether replay repetitions could strengthen the engram significantly further. Such strengthening through repetition could compensate for the engram erasure due to spontaneous activity after the learning (**Figure 6E1**) and its functional consequence, the relatively rapid loss of replay capacity (**Figures 6E2,E3**). Intuitively, the partial increase in weight at the border of the trajectory engram after one replay (**Figure 4D4** Δw_{Total}, red fringes) could, after repeated replays, be strong enough to counteract the decrease observed outside replays during memorization (**Figure 6D3**, light blue fringe). To test this possibility, we repeated the replay stimulus every 3 s for 30 s after the presentation of the initial trajectory stimulus (**Figure 7A**). We observed, from the very first seconds, and even before we could test the effect of the protocol at larger timescales, that these successive stimuli, initially triggering correct trajectory replays, rapidly led to hyperactivity involving most of the neurons in the network (**Figure 7A1**). Such paroxysmal activity typically appeared via avalanche dynamics activating neurons at the end of the trajectory (a fraction of the network, therefore), which propagated to the whole network at increasingly higher discharge frequencies (up to tens of Hz). Moreover, this activity had an oscillatory component, visible on the time course of the frequency of the excitatory and inhibitory neurons (**Figure 7A2**). This paroxysmal activity partially erased the engram of the learned trajectory via synaptic scaling (**Figure 7B**), making it impossible to replay the trajectory following this seizure (see last stimulus, **Figure 7A1**), consistent with similar effects found in empirical observation during epileptic seizures (Hu et al., 2005; Meador, 2007; Truccolo et al., 2011).

Slow Learning Stabilizes Trajectory Engram and Replays

As the repetition of replay learning led to over-activation of the trajectory with plasticity speed parameters sufficiently fast for a single stimulus presentation to be learned and replayed, we investigated how slower STDP kinetic coefficients could prevent

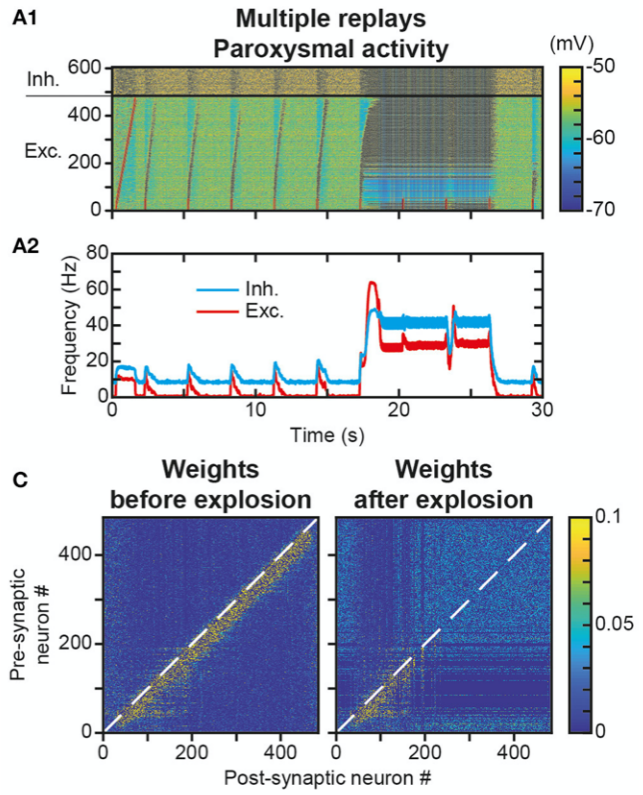

FIGURE 7 | Unstable engram and network dynamics after repeated trajectory replays. **(A)**. Membrane potential of neurons in the neural network **(A1)** for 30 s during which a replay stimulus is performed on the first 50 neurons every 3 s. Mean activity of excitatory (red) and inhibitory (blue) neurons **(A2)**. **(B)**. Matrix of synaptic weights between excitatory neurons before (left) and after (right) paroxysmal network activity.

paroxysmal activity during stimulus presentations and replays. For this, we used smaller values of K_{max} and P_{max}, i.e., here, divided by a factor of 6. With these values, 4 presentations of the trajectory stimulus were necessary for increasing the engram weights enough to sustain trajectory replays (**Figure 8A**). After such a learning protocol, the replay of the full trajectory was possible even beyond 1 h after learning (**Figure 8B**), whereas replay ability lasted only a few minutes with previous parameters (**Figures 6E2,E3**). This increase in replay memory timescale is consistent with that of the engram time constant, which was 11.5 h (**Figure 8C**), of the order of its theoretical estimation ∼11.7 h, i.e., it was increased by a factor 6 compared to that obtained with previous parameters (1.91 and 1.95 h, respectively **Figure 6E1**). Remarkably, the memory of trajectory replay was increased by a factor >20 (trajectory completely replayed at >1.4 h vs. 4 min with previous parameters), so that, relatively to the timescale of the trajectory engram, the timescale for trajectory replay was further increased by a factor 3.5. Indeed, the presentation of several stimuli recruited a thicker-tailed weight distribution, with higher probability of large weights (blue curve above the red one in ∼0.05–0.125; **Figure 8D**) but lowered probabilities of highly-weighted synapses (blue curve with negligible probabilities above 0.15; **Figure 8D**), because successive trajectory stimuli simultaneously evoked progressively stronger trajectory replays, recruiting more neurons at lower frequencies (**Figure 8A**), therefore imprinting larger engrams. Thus, slower plasticity kinetics required a larger number of successive presentations to learn the trajectory, but ensured a more robust engram involving more synapses, resulting in a better resilience to forgetting, i.e., a better quality of learning.

Finally, we assessed whether slow plasticity with multiple stimulus presentations also preserved network dynamics. AI dynamics were preserved with stable frequency (**Figure 8E1**), synchrony (**Figure 8E2**), and irregularity (**Figure 8E3**). We then repeated the replay stimulus every 3 s for 30 s after the presentation of the initial trajectory stimulus, a protocol which led to paroxysmal activity when considering fast plasticity. With slower kinetics, multiple replay stimuli triggered correct trajectory replays for the whole duration of the simulation (**Figure 8F**). We then asked whether a threshold of plasticity speed exists above which paroxysmal activity is triggered, or, conversely, the risk of paroxysmal activity linearly scales with the ability to learn fast. To do so, we parametrically explored simulations with plasticity rate divided by a slowdown factor in the range 1–10. The minimal number of stimulus presentations required to form a strong enough engram (i.e., allowing a replay) increased slowly with slower plasticity kinetics (**Figure 8G**, red). In parallel, the increase in the maximal number of replays before turning network dynamics into paroxysmal activity was much larger (**Figure 8G**, black), so that slowing plasticity kinetics increased the physiological range allowing learning while preserving network dynamics from paroxysmal activity. Hence, plasticity slow enough to preserve healthy dynamics may constitute a key constraint on the ability to learn rapidly. Furthermore, if the product of plasticity speed with the number of stimulus presentation was constant, it would indicate a linear summation of plastic effects arising from each presentation. By contrast, the number of stimulus presentations necessary for replay was lower than the factor of plasticity slowdown (5 stimuli for 10x plasticity slowdown instead of 10 stimuli, **Figure 8G**). This is due to successive stimulations overlapping with replays (i.e., stimulus presentations after the first one induce replays, **Figure 8A**), suggesting progressive facilitation of learning at slow plasticity speeds.

DISCUSSION

Here, we show that it is possible to learn neural trajectories (dynamical representations) using a spike timing-dependent plasticity (STDP) learning rule in local PFC circuits displaying spontaneous activity in the asynchronous irregular (AI) regime. We used a physiological model of plasticity (Delord et al., 2007; Graupner and Brunel, 2012; He et al., 2015) continuously occurring online, i.e., without decoupling simulations of learning and activity. Presentation of a dynamic stimulus, the trajectory, resulted in the writing of a synaptic engram of the trajectory on a rapid timescale (seconds), as well as its long-term storage at

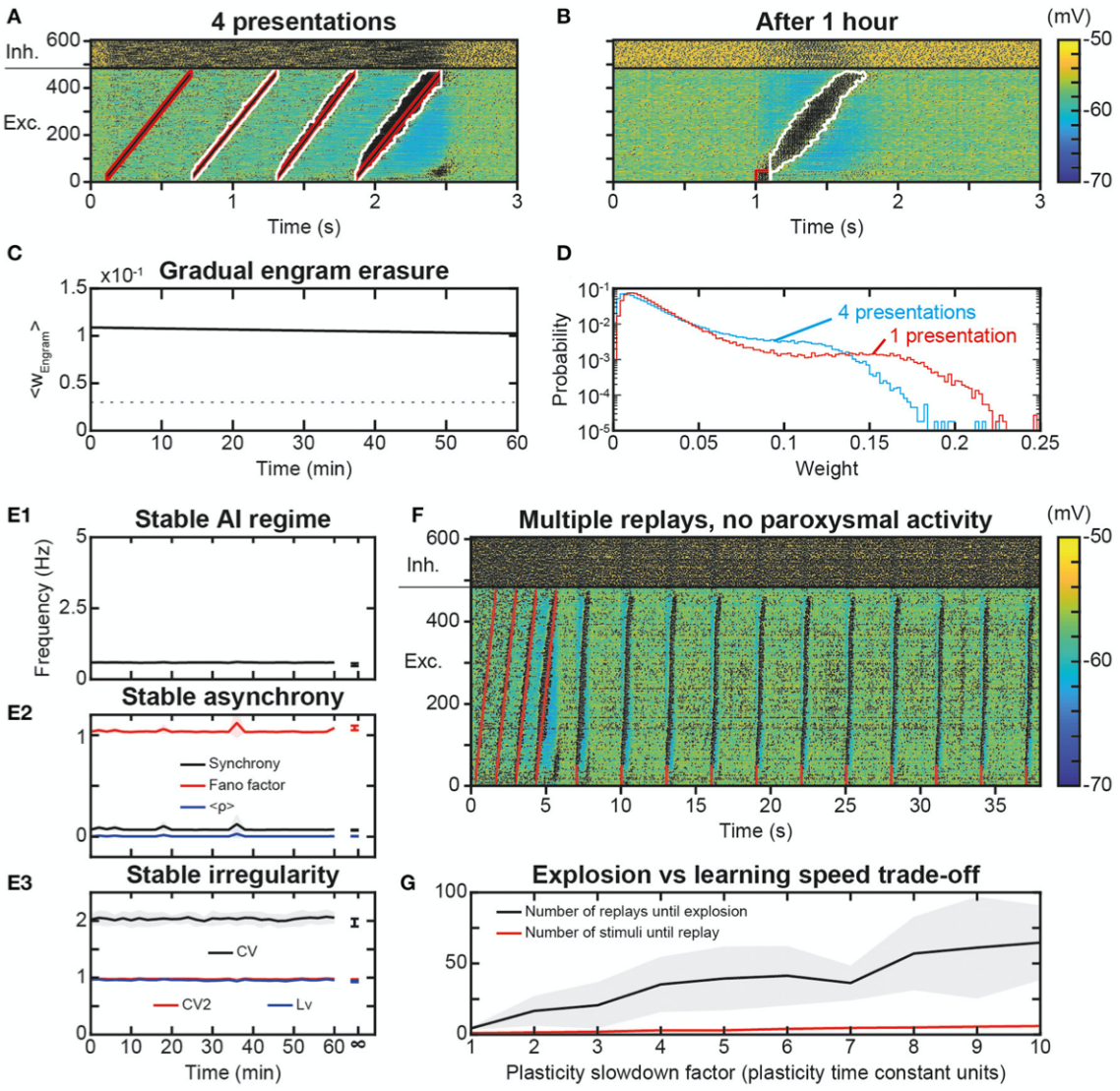

FIGURE 8 | Slower learning stabilization of the engram and network dynamics. **(A)**. Membrane potential of the neural network in response to the presentation of 4 trajectory stimuli in the presence of slower STDP learning kinetics. **(B)**. Membrane voltage of the neural network for 3 s following a replay stimulation on the first 50 neurons at 1 s, 1 h after trajectory learning. **(C)**. Average weight of all engram synapses after learning for 1 h. **(D)**. Probability distribution of the synaptic weights of the excitatory synapses after 4 presentations of the trajectory stimulus during slow learning (blue), and after one presentation of the trajectory stimulus during learning with faster (standard) parameters (red). **(E)** Networks dynamics after learning with slow plasticity: frequency **(E1)**, synchrony **(E2)**, and irregularity **(E3)** of excitatory neurons. Shaded areas represent 95% confidence intervals of the mean for five network simulations. **(F)** Membrane potential of the neural network for 38 s during which a replay stimulus is performed on 50 neurons every 3 s for 10 total repetitions (as in **Figure 7A**) after 4 trajectory stimuli in the presence of slower STDP learning kinetics (as in **Figure 8A**). **(G)** Minimal number of stimulus presentations required to learn a replay (red) and maximal number of replays before paroxysmal activity (black), as a function of the plasticity slowdown factor expressed in units of plasticity standard time constant (i.e., by which slowdown factor plasticity rates are divided). The number of replays until explosion is evaluated with the same weight matrix (learned at standard plasticity speed or x1 slowdown) across different plasticity speeds, for better comparison of the effect of plasticity speeds on replay. Shaded areas represent 95% confidence intervals of the mean for 10 network simulations.

the timescale of the order of several hours. The network replayed the trajectory upon stimulation of a subset of the engram at the timescale of the order of dozens of minutes. These results indicate that disordered AI activity does not necessarily jeopardize the encoding and replay of neural trajectories. Conversely, the weak but continuous plastic processes that noisy AI produces did not erase the synaptic engram of neural trajectories, at least before several hours. In turn, the learning of a trajectory engram within network synapses was not found to alter the AI characteristics of PFC activity. From a functional perspective, we show that trajectory activity accounted for both types of dynamics subserving working-memory in the PFC, i.e., persistent activity (Constantinidis et al., 2018) and dynamical coding (Lundqvist et al., 2018), and help understanding how they can be reconciled (Murray et al., 2017; Cavanagh et al., 2018; Enel et al., 2020). Together, these results offer a consistent theoretical

framework accounting for how dynamical representations can be learned, memorized and replayed in PFC circuits in physiological conditions.

This model was built to reproduce functional phenomenology of the PFC (learning, replays at different timescales, dynamic or persistent coding, see below), based on biophysical constraints from the experimental literature at the molecular, cellular and network levels, rather than by artificial training. If overall architectural properties of the model are observed in the PFC, such properties are also compatible with other non-prefrontal cortices with trajectory replays, lending strength to the genericity of the current study's results. For example, the excitatory/inhibitory network balance, observed in the PFC (Shu et al., 2003; Haider et al., 2006), is also observed and essential to computations across non-PFC structures (Isaacson and Scanziani, 2011). Similarly, the over-representation of bidirectional connections in the PFC (Wang et al., 2006) is a general property in cortical networks (Song et al., 2005). While the PFC has been less subject to the investigation of synaptic scaling compared to other structures, its presence across many non-PFC cortical structures (for e.g., sensory cortices, hippocampus, motor cortex) and crucial role for synaptic learning stabilization (Keck et al., 2017) makes it a plausible mechanism in PFC. Certain lines of evidence suggest its presence in PFC (Wang and Gao, 2012; Sweatt, 2016), although further confirmation is needed.

In the model, external feedforward inputs are constant, as in previous models of characteristic PFC activity (for e.g., Brunel, 2000). Therefore, the variability of neuronal discharge observed in the network entirely arises from internal dynamics among recurrent connections, as the network is in the asynchronous irregular regime (Destexhe et al., 2003; London et al., 2010). It would be interesting to study versions of the model with feedforward inputs variability, as occurring in real PFC circuits. However, this option was out of scope as we focused on the internal interactions between the spontaneous AI regime, learning processes affecting the synaptic matrix and trajectory replays. As another potential extension to our study, one could explore the influence of rhythmic inputs from the hippocampus (theta rhythms, Siapas et al., 2005; Benchenane et al., 2011) or from the olfactory pathways (delta rhythms, Moberly et al., 2018), which are known to be important for behaviorally-relevant neural activity and memory replays.

Molecular Plasticity and Memory in the PFC

In the PFC, e-STDP necessitates more than the pre-post synaptic pairings used in spike-timing protocols, as long-term potentiation (t-LTP) emerges in the presence of dopaminergic or cholinergic tonic neuromodulation, or when inhibitory synaptic transmission is decreased (Couey et al., 2007; Xu and Yao, 2010; Ruan et al., 2014). Moreover, Hebbian STDP (i.e., t-LTP for pre-then-post and t-LTD for post-then-pre spiking) is observed when followed by phasic noradrenergic, dopaminergic or serotoninergic neuromodulation (He et al., 2015). Hence, we assumed that t-LTP and t-LTD co-exist, and STDP is thus Hebbian, in the PFC of behaving animals, where both phasic and tonic neuromodulation are encountered during behaviorally relevant learning (Dembrow and Johnston, 2014). The present study did not incorporate noradrenergic, serotoninergic and dopaminergic transformation of eligibility traces into effective plastic modifications found at PFC excitatory synapses (He et al., 2015), a possible substrate of context- and reward-modulated learning in PFC circuits (Ellwood et al., 2017). The present work also did not consider alternative biophysical processes that may participate to sculpt dynamical and flexible neural representations in the PFC (Buonomano and Maass, 2009; Stokes, 2015). For instance, short-term synaptic plasticity (Mongillo et al., 2008) may affect network dynamics through slow hidden (e.g., biochemical) variables. Such a silent-based coding of past activity could possibly account for the near-complete disappearance of activity observed sometimes during working memory (Stokes, 2015) and its interaction with activity-based working-memory in the PFC (Barbosa et al., 2020) remains to be elucidated. Similarly, inward current-mediated bistability such as with persistent sodium, or calcium-activated non-specific currents (Delord et al., 1997; Rodriguez et al., 2018), can produce cellular forms of memory that may take part in dynamic representations in the PFC, either through retrospective memory of past information or in prospective computations of forthcoming decisions and actions. Finally, the present study did not consider anti-homeostatic forms of intrinsic plasticity (i.e., the plasticity of intrinsic properties) which may represent an essential mean to learn and regulate dynamic representations (Zhang and Linden, 2003).

Stable Spontaneous AI Dynamics in the PFC in the Presence of Plasticity and Learning

Hebbian forms of plasticity (Abbott and Nelson, 2000), such as the STDP of excitatory synapses (Markram et al., 2012) modeled here, increase weights between neurons that are frequently co-activated. Stronger synapses potentiated by STDP, in turn, statistically increase the frequency of future co-activations. These rules thus constitute positive feedback loops (anti-homeostatic) between activity and connectivity. As a consequence, synaptic runaway (Keck et al., 2017; Zenke et al., 2017) produces network instability toward saturated or quiescent activity and connectivity. In recurrent network models, synaptic plasticity typically decreases the dynamics complexity toward regular activity such as limit-cycle or quasi-periodic attractors (Morrison et al., 2007; Siri et al., 2007; Litwin-Kumar and Doiron, 2014) that resembles neural dynamics encountered during sleep or paroxysmal crises. However, activity in the PFC and other cortices during wakefulness is characterized by asynchronous irregular spiking at low frequency (Ecker et al., 2010; Renart et al., 2010), due to the balance between strong excitatory and inhibitory synaptic currents (Destexhe et al., 2003). AI spiking is compatible with critical or even chaotic dynamics (Beggs and Plenz, 2003; Hahn et al., 2010; London et al., 2010), which may benefit temporally complex computations (Bertschinger and Natschläger, 2004) believed to be performed by the PFC (Compte, 2003).

Many studies show that e-STDP rules are deleterious to AI dynamics such that compensating homeostatic mechanisms are

required to control neuronal activity, for e.g., a metaplastic e-STDP rule with sliding-threshold (Boustani et al., 2012), synaptic scaling (which keeps the sum of pre-synaptic excitatory weights constant, Zenke et al., 2013), STDP of inhibitory synapses (i-STDP; ensuring excitation-inhibition balance, Vogels et al., 2011) or intrinsic plasticity of ionic conductances (regulating action potential threshold, Naudé et al., 2013). In the present detailed biophysical model, we found that a combination of e-STDP where all pre-/post- pairings were taken into account (all-to-all STDP), together with synaptic scaling, preserves AI dynamics. All-to-all e-STDP without scaling can also preserve AI dynamics, but at the price of unstable fluctuating synaptic weights (Morrison et al., 2007), while weight distributions were stable here. Moreover, the present study shows that network stability held not only with random recurrent connections, but also in the presence of an engram involving a significant fraction of strong, potentiated synapses in all excitatory neurons. In the absence of synaptic scaling, learning static patterns into synaptic engrams with e-STDP disrupts AI dynamics toward pathological high-frequency oscillations (Morrison et al., 2007; Litwin-Kumar and Doiron, 2014), or with i-STDP leads to AI activity with unrealistic high firing frequency states and sharp state transitions (Litwin-Kumar and Doiron, 2014), at odds with PFC dynamics in awake animals (Compte, 2003). A metaplastic form of e-STDP conserves AI dynamics on a short-timescale (one second) but AI stability remains unchecked at longer timescales (Boustani et al., 2012). This is only the case with static stimulus, as learning receptive fields using dynamical stimulus leads to a catastrophic decrease in the complexity of the AI regime (Boustani et al., 2012). Altogether, our study thus suggests that synaptic scaling represents a more efficient form of homeostatic compensation (rather than metaplastic e-STDP, or i-STDP) for learning trajectory engrams without the deleterious effects of STDP disrupting AI dynamics. We used here an instantaneous synaptic scaling, because our model, like most models, requires synaptic scaling at faster or equal timescales than synaptic plasticity for stable learning, far from the experimentally observed homeostatic or metaplastic timescales of hours to weeks (Zenke et al., 2017). This constraint suggests the existence of as yet unidentified rapid compensatory processes, potential candidates being heterosynaptic plasticity (Fiete et al., 2010), intrinsic plasticity (Zhang and Linden, 2003; Naudé et al., 2013), input normalization by feed-forward inhibition (Pouille et al., 2009; Keck et al., 2012), and the implication of astrocytes (Papouin et al., 2017). Additionally, at slower timescales, sleep-dependent consolidation mechanisms may provide global compensatory synaptic down-scaling offline (Tononi and Cirelli, 2003).

Learning Dynamical Representations in the PFC Under AI Dynamics

Phenomenological e-STDP models fail to learn engrams in noisy AI states because of their sensitivity to spontaneous activity. The absence of STDP weight-dependence forbids learning and induces the direct loss of engrams (Boustani et al., 2012), while without synaptic scaling, learning fails with catastrophic consequences in terms of network dynamics (see above; Morrison et al., 2007). A weight-dependent e-STDP rule endowed with homeostatic metaplasticity (instead of synaptic scaling, as here) allowed learning the engram of a presented stimulus while preserving AI dynamics, although it unrealistically left neurons of the engram in a state of permanent activity (Boustani et al., 2012). Likewise, i-STDP enables learning of engrams, but with unrealistic AI activity (see above; Litwin-Kumar and Doiron, 2014). Here, we find that the combination of a weight-dependent Hebbian e-STDP rule and synaptic scaling allows for the learning of engrams in local PFC recurrent networks under conditions of AI dynamics, as found in behaving mammals.

Phenomenological STDP models based on neighboring spike-doublet or spike-triplet schemes often produce side effects (either sensitivity to noisy activity, or runaway plasticity) due to the temporal bounds of the pre- and post-couplings they consider (Boustani et al., 2012). The present STDP model describes continuous post-synaptic biophysical dynamics that account for all pre-/post-pairings (all-to-all STDP) and is thus more realistic than phenomenological STDP models. Here, the temporal asymmetry of the spike-timing dependence of the e-STDP rule arises from a detailed description of calcium dynamics. Calcium arises from two different sources of calcium that originate from the influence of AMPA, NMDA and VDCC channel activations (see *Materials and Methods*; Graupner and Brunel, 2012), which accounts for the relative influence of pre-synaptic evoked excitatory post-synaptic potentials and of backpropagating post-synaptic activity. However, this rule remains simple compared to models describing more complete signaling scenarios (Manninen et al., 2010), allowing simulation at the network scale.

In feed-forward networks endowed with this STDP rule, and for conditions of spiking frequency and irregularity similar to AI activity, plastic modifications essentially depend on firing frequency rather than on the precise timing of spikes, because equivalent probabilities of encountering pre-then-post and post-then-pre spike pairs in conditions of stationary spiking essentially blurs net spike-timing effects (Graupner et al., 2016). Moreover, t-LTP dominates t-LTD, because t-LTD is multiplicative (Bi and Poo, 1998; van Rossum et al., 2000), i.e., scaled by weak weight values (Graupner et al., 2016). Consistent with these observations, in the present PFC recurrent network model, plasticity was essentially frequency-dependent under conditions of stationary spiking, and t-LTP dominated t-LTD under spontaneous AI dynamics, being principally compensated by synaptic scaling. However, during trajectory presentation or trajectory replay, i.e., when pre-post spiking was enforced to be temporally asymmetric, t-LTD nevertheless contributed to compensate t-LTP and determined overall resulting modifications on the same order than scaling.

The previous studies that have addressed the possibility of engram learning in recurrent networks with AI dynamics focused on static stimuli (Morrison et al., 2007; Boustani et al., 2012; Litwin-Kumar and Doiron, 2014). By contrast, our study demonstrates engram learning and activity replay of dynamical stimuli, such as the sequences or trajectories of activity that

occur during cortical AI dynamics in behaving animals (Kaefer et al., 2020). Standard static Hebbian assemblies, which learn static stimuli through strong bidirectional connections between neurons of the assembly and replay the static activity through pattern completion, induce avalanche-like convergent dynamics toward a static attractor, which are too low-dimensional to account for physiological data. Remarkably, the present study demonstrates the possibility for engrams of dynamic stimuli in the disordered AI state, despite the fact that they relied on mono-directional strengthening of synaptic connections, which favors propagation of activity, but does not allow for the convergent effect of static patterns and the positive feedback inherent to it.

Long-Term Memory of Dynamical Representations in the PFC Under AI Dynamics

The present study underlines the importance of slow plasticity kinetics together with repeated presentations for learning dynamic representations in PFC networks. Faster kinetics allowed one-shot learning of trajectory engrams, but extensive training could then induce paroxysmal activity during the trajectory replays that partly erased the engram, which was ultimately detrimental to the learning and replay process. This synchronous increase in neuronal activity in the model is reminiscent of epileptic seizures (Truccolo et al., 2011), which have been found to cancel out the plasticity effects of synaptic weights (Hu et al., 2005), and affect memory (Meador, 2007), as we found here. By contrast, slower kinetics resulted in more stable engrams, while highlighting the importance of repeated presentations of the dynamic stimulus, similarly to observations with static patterns (Boustani et al., 2012). Parametric exploration of plasticity kinetics showed a tradeoff between the number of stimulus repetitions required to form an engram and the risk of paroxysmal activity. However, slowing down plasticity decreased the risk of over-activation while preserving the ability to learn fast (even though not through one-shot learning). Consistent with our results, learning occurs gradually in the PFC, and at a slower pace than in the hippocampus and basal ganglia (Pasupathy and Miller, 2005; Buschman and Miller, 2014). The tradeoff between fast learning and paroxysmal risk may constitute a constraint for the PFC, with the preservation of asynchronous irregular dynamics preventing one-shot learning based on synaptic plasticity alone. One-shot learning, which occurs in well-trained animals, may thus require additional mechanisms for structural learning (Gallistel and Matzel, 2013).

Fast learning together with stable memory is considered in many synaptic plasticity models to rely on auto-phosphorylation of the calmodulin-dependent protein kinase II (CaMKII). CaMKII auto-phosphorylation is appealing because it constitutes a positive-feedback loop (inducing fast plasticity) underlying bistable dynamics (providing infinite memory of a single potentiated synaptic state). However, we did not consider CaMKII in the present model, because CamKII is not necessary to the maintenance of synaptic modifications (Chen et al., 2001; Lengyel et al., 2004). Moreover, activity-dependent synaptic modifications are not systematically bistable (i.e., they can be graded; Montgomery and Madison, 2002; Tanaka et al., 2008; Enoki et al., 2009) and they can fade with time scales from seconds to minutes (Hempel et al., 2000).

Here, the stability of molecular memory originated from extremely slow synaptic weight dynamics, resulting in slow exponential forgetting of the engram. Slow weight dynamics arose from activity-dependent kinase and phosphatase (aKP, Delord et al., 2007), which are weakly activated at near-basal calcium concentrations associated with low spiking frequency during AI dynamics. Such aKP signaling processes are ubiquitous (e.g., PKA, PKC, calcineurin) and confer an activity-dependent control over the rate of plasticity and memory (Delord et al., 2007), which is essential for flexible learning in the PFC (Fusi et al., 2005). Alternatively, when implemented with low copy molecule numbers at individual synapses, bistable models faced with noise also exhibit exponential forgetting of memory when averaged over synapses and trials (Fusi et al., 2005). Here, the memory of the trajectory engram admitted an effective time constant of the order of 2 h in network simulations, consistent with its theoretical prediction (see *Materials and Methods*), but longer memories could be expected for lower values of $P_{\max}$ and $K_{\max}$, the maximum phosphatase and kinase activations. However, the time constant for plasticity would also increase, slowing learning too, while its current value is compatible with induction times of synaptic plasticity (Malenka et al., 1992). Alternatively, a higher calcium phosphatase half-activation (P_{Ca}), which is physiologically possible (Delord et al., 2007), would allow for a longer memory timescale while preserving rapid learning (at large calcium, the time constant of plasticity is independent of P_{Ca}). Hence, specifying biophysical models with precise kinetic parameters is essential because they have huge consequences on the stability of network dynamics, learning and the time scale of memory (Zenke et al., 2013). Specifically, homeostatic scaling appeared important here as for learning, since its absence was reported to forbid the memory of static patterns in recurrent network models because of catastrophic forgetting due to fluctuating synaptic weights (Morrison et al., 2007).

The timescale of trajectory replay scaled with that of the engram. This is because replay requires a sufficiently preserved engram to emerge from synaptic interactions between neurons. However, the lifetime of trajectory replay was an order of magnitude smaller than that of the trajectory engram, because replay requires neuronal interactions that are non-linear and therefore sensitive to decreases in synaptic weights. Interestingly, the long-term degradation of trajectory replay was due to incomplete replay at the end of the trajectories learned, in a manner consistent with the primacy effect of medium-term learned sequences (Greene et al., 2000). Besides, the memory of trajectory replay did not only rely on biophysical parameters but also on the learning protocol. Indeed, slower learning with repetitions increased the quality of engram by better anchoring the learned trajectory, through a larger number of synapses. Slow plasticity of a large number of synapses from a recurrent network, through repetition, may thus underlie the robustness of PFC-dependent memories (Buschman and

Miller, 2014). In addition to extensive training, the maintenance of trajectory engrams over longer timescales may be reached by regular replays, as observed in PFC-dependent active executive processes such as trajectory reactivations (Stokes, 2015), spontaneous replays (Kaefer et al., 2020), rehearsal and refreshing (Raye et al., 2007), or consolidations (Dudai, 2012). At the molecular scale, the possibility of synaptic tagging could be incorporated in the model (Clopath et al., 2008) in order to stabilize the engram and account for longer memory timescales.

Humans or animals generally learn complex navigational paths such as sensory, motor or behavioral sequences in a progressive manner. Thus, PFC circuits are often challenged with the necessity to process several parts of whole neural trajectories that are discovered as sequences of elementary parts encountered at separate points in time. Moreover, prospective processes in the PFC require recombining elementary neural trajectories into new trajectory representations serving the planning of future actions, choices or navigational paths, for e.g., during rule switching and behavioral adaptation (Ito et al., 2015; Mashhoori et al., 2018; Kaefer et al., 2020). Besides, sequences of non-spatial items have been shown to be processed in a spatial frame in primates (Jensen et al., 2013), likely involving neural trajectories. We found that STDP-based trajectory learning and replay in the network was able to learn trajectory fragments, transitions between fragments, and to chunk them into a whole trajectory, as found in the PFC (Ostlund et al., 2009; Dehaene et al., 2015). Moreover, the network displayed the ability to reconstitute a whole trajectory (i.e., a macroscopic sequence) based on trajectory fragments (i.e., overlapping microscopic sequences), independently of their order of presentation, i.e., to acquire ordinal knowledge about sequences of trajectory fragments (Jensen et al., 2013; Dehaene et al., 2015). However, STDP-based trajectory learning in our PFC network model was unable to learn higher-order representations of algebraic patterns or more complex nested structures (Dehaene et al., 2015), or to categorize sequences into specific classes (Shima et al., 2007). Assessing such possibilities using more elaborated, reward-dependent, forms of STDP learning rules might deserve future explorations.

Multiple Functional Relevance of STDP-Based Neural Trajectories in the PFC

We found in our model that the same network, taught with the same stimulus, could generate a large range of replay duration and compression factors, including those characterizing regular (Batuev, 1994; Fujisawa et al., 2008; Cromer et al., 2010; Mante et al., 2013; Yang et al., 2014; Ito et al., 2015; Markowitz et al., 2015; Schmitt et al., 2017; Tiganj et al., 2017; Nakajima et al., 2019; Passecker et al., 2019; Enel et al., 2020) and fast (Jadhav et al., 2016; Tiganj et al., 2017; Mashhoori et al., 2018; Yu et al., 2018; Shin et al., 2019; Kaefer et al., 2020) timescale replays in behaving animal. We found that the time constant of NMDA decay dynamics was essential in controlling the duration and compression factor of trajectory replays. In PFC circuits, dopamine slows decaying dynamics of NMDA-mediated EPSPs through D1-receptors (Chen et al., 2004; Onn et al., 2006) in an almost instantaneous manner (Onn and Wang, 2005). In addition to dopaminergic regulation, other forms of neuromodulation affect NMDA dynamics (Lutzu and Castillo, 2021). Our results suggest that rapid and bidirectional regulation of biophysical parameters in PFC networks by ongoing neuromodulation—as attentional demands and reward outcomes vary at the trial timescale—may control replay duration, compression factors, and the relative rate of regular vs. fast timescale replays.

Besides, individual neuronal activity displayed lower firing frequency during replay compared to the activity induced by the stimulus, consistent with sparse coding of representations after learning. Firing rates of individual neurons during stimuli or delays in working memory tasks, as well as in navigation tasks, vary considerably across species and behavioral contexts, spanning two orders of magnitude from ∼1 to ∼100 Hz (Fuster and Alexander, 1971; Batuev, 1994; Romo et al., 1999; Baeg et al., 2003; Yang et al., 2014; Markowitz et al., 2015; Tiganj et al., 2017). Frequencies of dozens Hz are common in individual PFC neurons (Funahashi et al., 1989; Romo et al., 1999; Brody et al., 2003; Fujii and Graybiel, 2003; Shinomoto et al., 2003; Jun et al., 2010; Tiganj et al., 2017; Enel et al., 2020). In the present model, frequencies of individual neurons were actually ∼100 Hz during stimuli and presentations, and 20–60 Hz during replays (**Figures 5B1,B3**). Thus, although larger than those observed during stimuli, individual frequencies were globally of the order of magnitude of those empirically observed. Mean frequencies in our network ranged below 10 Hz (**Figures 5B1,B3**), (**7A2**), in accord with experimental literature (Funahashi et al., 1989; Romo et al., 1999; Brody et al., 2003; Fujii and Graybiel, 2003; Shinomoto et al., 2003; Jun et al., 2010; Tiganj et al., 2017; Enel et al., 2020).

In the PFC, representations for executive functions and cognition can present less explicit dynamic coding schemes than regular timescale neural trajectories presented here. For instance, working memory can display intricate patterns of complex (heterogeneous but non-random) dynamic activities that can hardly be disentangled into simpler well-separate transient patterns of activity (Jun et al., 2010). However, during working memory tasks, PFC persistent delay activity is selective and maintains online content-specific representations. Working memory does often, but not systematically, require underlying persistent activities, often in a stable activity state (Goldman-Rakic, 1995; Compte et al., 2000; Durstewitz et al., 2000; Wang, 2001; Constantinidis et al., 2018). It can also rely on dynamical sequences of activities disappearing and reappearing, depending on instantaneous computational task-relevant requirements (Sreenivasan et al., 2014; Stokes, 2015; Lundqvist et al., 2018). The coexistence of stable population coding together with heterogeneous neural dynamics has been observed in the PFC during working memory tasks (Murray et al., 2017).

Here, trajectory replays offer a possible unified framework that can participate to reconcile opposite views regarding the nature of information persistent vs. dynamic coding in the PFC (Constantinidis et al., 2018; Lundqvist et al., 2018). Indeed, we find that while individual neurons displayed transient (hundreds

of milliseconds) overlapping bumps of activity, implementing a "relay race" form of explicit dynamic coding (Batuev, 1994; Brody et al., 2003; Cromer et al., 2010; Yang et al., 2014; Schmitt et al., 2017), their population activity persisted at the second timescale, ensuring the maintenance of the representation across time (Murray et al., 2017; Cavanagh et al., 2018; Enel et al., 2020). Depending on the functional context, neural trajectories learned here could be interpreted as the actual explicit representation of a trajectory unfolding online, granted that the decoding downstream neural structure can resolve individual activities of the network. Alternatively, if the downstream decoding neural structure only globally decodes the population average of network dynamics, activity would then be interpreted as an integrated and stable persistent representation of the trajectory as a whole (i.e., as a symbolic entity). This dichotomy is congruent with that found in the PFC, whereby individual neurons encode information at short timescales while the population as a whole persistently maintains information at longer time scales (Meyers et al., 2008). In this scheme, working memory representations would rely on individual neurons collectively stabilizing a dynamic population-level process (Murray et al., 2017; Cavanagh et al., 2018; Enel et al., 2020).

Interestingly, we found that the population activity of trajectory replays accounted for the decreasing pattern of activity that can be observed in the PFC (Cavanagh et al., 2018; Enel et al., 2020). Trajectory replays also displayed strong variability, as observed in the PFC during delay activities (Compte, 2003; Shafi et al., 2007). While within-trial variability across neurons essentially came from the fact that neurons spiked at distinct periods along the trajectory, inter-trial variability for each neuron originated from the noisy AI dynamics. Inter-trial variability accumulated over time for neurons situated later in the trajectory, henceforth the temporal tuning of neurons widened with their position in the sequence (Tiganj et al., 2017).

DATA AVAILABILITY STATEMENT

The raw data supporting the conclusions of this article will be made available by the authors, without undue reservation.

AUTHOR CONTRIBUTIONS

MS, JV, JN, and BD developed the model. MS, JV, DM, and BD contributed to numerical simulations and their analysis. MS, JV, DM, JN, and BD wrote the article. All authors contributed to the article and approved the submitted version.

REFERENCES

Abbott, L. F., and Nelson, S. B. (2000). Synaptic plasticity: taming the beast. *Nat. Neurosci.* 3, 1178–1183. doi: 10.1038/81453

Abeles, M., Bergman, H., Gat, I., Meilijson, I., Seidemann, E., Tishby, N., et al. (1995). Cortical activity flips among quasi-stationary states. *Proc. Natl. Acad. Sci. U.S.A.* 92, 8616–8620. doi: 10.1073/pnas.92.19.8616

Baeg, E. H., Kim, Y. B., Huh, K., Mook-Jung, I., Kim, H. T., and Jung, M. W. (2003). Dynamics of population code for working memory in PFC. *Neuron* 40, 177–188. doi: 10.1016/S0896-6273(03)00597-X

Bakhurin, K. I., Goudar, V., Shobe, J. L., Claar, L. D., Buonomano, D. V., and Masmanidis, S. C. (2017). Differential encoding of time by prefrontal and striatal network dynamics. *J. Neurosci.* 37, 854–870. doi: 10.1523/JNEUROSCI.1789-16.2016

Barbosa, J., Stein, H., Martinez, R. L., Galan-Gadea, A., Li, S., Dalmau, J., et al. (2020). Interplay between persistent activity and activity-silent dynamics in the prefrontal cortex underlies serial biases in working memory. *Nat. Neurosci.* 23, 1016–1024. doi: 10.1038/s41593-020-0644-4

Batuev, A. S. (1994). Two neuronal systems involved in short-term spatial memory in monkeys. *Acta Neurobiol. Exp.* 54, 335–344.

Beaulieu, C., Kisvarday, Z., Somogyi, P., Cynader, M., and Cowey, A. (1992). Quantitative distribution of gaba-immunopositive and -immunonegative neurons and synapses in the monkey striate cortex (area 17). *Cerebral Cortex* 2, 295–309. doi: 10.1093/cercor/2.4.295

Beggs, J. M., and Plenz, D. (2003). Neuronal avalanches in neocortical circuits. *J. Neurosci.* 23, 11167–11177. doi: 10.1523/JNEUROSCI.23-35-11167.2003

Benchenane, K., Tiesinga, P. H., and Battaglia, F. P. (2011). Oscillations in the prefrontal cortex: a gateway to memory and attention. *Curr. Opin. Neurobiol.* 21, 475–485. doi: 10.1016/j.conb.2011.01.004

Bertschinger, N., and Natschläger, T. (2004). Real-time computation at the edge of chaos in recurrent neural networks. *Neural Comput.* 16, 1413–1436. doi: 10.1162/089976604323057443

Bi, G. Q., and Poo, M. M. (1998). Synaptic modifications in cultured hippocampal neurons: dependence on spike timing, synaptic strength, and postsynaptic cell type. *J. Neurosci.* 18, 10464–10472. doi: 10.1523/JNEUROSCI.18-24-10464.1998

Bittner, K. C., Milstein, A. D., Grienberger, C., Romani, S., and Magee, J. C. (2017). Behavioral time scale synaptic plasticity underlies CA1 place fields. *Science* 357, 1033–1036. doi: 10.1126/science.aan3846

Boustani, S. E., Yger, P., Frégnac, Y., and Destexhe, A. (2012). Stable learning in stochastic network states. *J. Neurosci.* 32, 194–214. doi: 10.1523/JNEUROSCI.2496-11.2012

Brody, C. D., Hernández, A., Zainos, A., and Romo, R. (2003). Timing and neural encoding of somatosensory parametric working memory in macaque prefrontal cortex. *Cereb Cortex* 13, 1196–1207. doi: 10.1093/cercor/bhg100

Brunel, N. (2000). Dynamics of Sparsely Connected Networks of Excitatory and Inhibitory Spiking Neurons. *J Comput Neurosci* 8, 183–208. doi: 10.1023/A:1008925309027

Brunel, N., and Wang, X. J. (2001). Effects of neuromodulation in a cortical network model of object working memory dominated by recurrent inhibition. *J. Comput. Neurosci.* 11, 63–85. doi: 10.1023/A:1011204814320

Buonomano, D. V., and Maass, W. (2009). State-dependent computations: spatiotemporal processing in cortical networks. *Nat. Rev. Neurosci.* 10, 113–125. doi: 10.1038/nrn2558

Buschman, T. J., and Miller, E. K. (2014). Goal-direction and top-down control. *Philos. Transac. R. Soc. B Biol. Sci.* 369:20130471. doi: 10.1098/rstb.2013.0471

Cavanagh, S. E., Towers, J. P., Wallis, J. D., Hunt, L. T., and Kennerley, S. W. (2018). Reconciling persistent and dynamic hypotheses of working memory coding in prefrontal cortex. *Nat. Commun.* 9:3498. doi: 10.1038/s41467-018-05873-3

Chen, G., Greengard, P., and Yan, Z. (2004). Potentiation of NMDA receptor currents by dopamine D1 receptors in prefrontal cortex. *PNAS* 101, 2596–2600. doi: 10.1073/pnas.0308618100

Chen, H.-X., Otmakhov, N., Strack, S., Colbran, R. J., and Lisman, J. E. (2001). Is persistent activity of calcium/calmodulin-dependent kinase

required for the maintenance of LTP? *J. Neurophysiol.* 85, 1368–1376. doi: 10.1152/jn.2001.85.4.1368

Chenkov, N., Sprekeler, H., and Kempter, R. (2017). Memory replay in balanced recurrent networks. *PLoS Comput. Biol.* 13:e1005359. doi: 10.1371/journal.pcbi.1005359

Clopath, C., Büsing, L., Vasilaki, E., and Gerstner, W. (2010). Connectivity reflects coding: a model of voltage-based STDP with homeostasis. *Nat. Neurosci.* 13, 344–352. doi: 10.1038/nn.2479

Clopath, C., Ziegler, L., Vasilaki, E., Büsing, L., and Gerstner, W. (2008). Tag-trigger-consolidation: a model of early and late long-term-potentiation and depression. *PLoS Comput. Biol.* 4:e1000248. doi: 10.1371/journal.pcbi.1000248

Compte, A. (2003). Temporally irregular mnemonic persistent activity in prefrontal neurons of monkeys during a delayed response task. *J. Neurophysiol.* 90, 3441–3454. doi: 10.1152/jn.00949.2002

Compte, A., Brunel, N., Goldman-Rakic, P. S., and Wang, X.-J. (2000). Synaptic mechanisms and network dynamics underlying spatial working memory in a cortical network model. *Cereb Cortex* 10, 910–923. doi: 10.1093/cercor/10.9.910

Constantinidis, C., Funahashi, S., Lee, D., Murray, J. D., Qi, X.-L., Wang, M., et al. (2018). Persistent spiking activity underlies working memory. *J. Neurosci.* 38, 7020–7028. doi: 10.1523/JNEUROSCI.2486-17.2018

Couey, J. J., Meredith, R. M., Spijker, S., Poorthuis, R. B., Smit, A. B., Brussaard, A. B., et al. (2007). Distributed network actions by nicotine increase the threshold for spike-timing-dependent plasticity in prefrontal cortex. *Neuron* 54, 73–87. doi: 10.1016/j.neuron.2007.03.006

Cromer, J. A., Roy, J. E., and Miller, E. K. (2010). Representation of multiple, independent categories in the primate prefrontal cortex. *Neuron* 66, 796–807. doi: 10.1016/j.neuron.2010.05.005

Dale, H. (1935). Pharmacology and nerve-endings (Walter Ernest Dixon memorial lecture): (Section of Therapeutics and Pharmacology). *Proc. R. Soc. Med.* 28, 319–332. doi: 10.1177/003591573502800330

Dehaene, S., Meyniel, F., Wacongne, C., Wang, L., and Pallier, C. (2015). The neural representation of sequences: from transition probabilities to algebraic patterns and linguistic trees. *Neuron* 88, 2–19. doi: 10.1016/j.neuron.2015.09.019

Delord, B., Berry, H., Guigon, E., and Genet, S. (2007). A new principle for information storage in an enzymatic pathway model. *PLoS Comput. Biol.* 3:e124. doi: 10.1371/journal.pcbi.0030124

Delord, B., Klaassen, A. J., Burnod, Y., Costalat, R., and Guigon, E. (1997). Bistable behaviour in a neocortical neurone model. *Neuroreport* 8, 1019–1023. doi: 10.1097/00001756-199703030-00040

Dembrow, N., and Johnston, D. (2014). Subcircuit-specific neuromodulation in the prefrontal cortex. *Front. Neural Circuits* 8:54. doi: 10.3389/fncir.2014.00054

Destexhe, A., Rudolph, M., and Paré, D. (2003). The high-conductance state of neocortical neurons *in vivo*. *Nat. Rev. Neurosci.* 4, 739–751. doi: 10.1038/nrn1198

Druckmann, S., and Chklovskii, D. B. (2012). Neuronal circuits underlying persistent representations despite time varying activity. *Curr. Biol.* 22, 2095–2103. doi: 10.1016/j.cub.2012.08.058

Dudai, Y. (2012). The restless engram: consolidations never end. *Annu. Rev. Neurosci.* 35, 227–247. doi: 10.1146/annurev-neuro-062111-150500

Durstewitz, D., Seamans, J. K., and Sejnowski, T. J. (2000). Neurocomputational models of working memory. *Nat. Neurosci.* 3, 1184–1191. doi: 10.1038/81460

Ecker, A. S., Berens, P., Keliris, G. A., Bethge, M., Logothetis, N. K., and Tolias, A. S. (2010). Decorrelated neuronal firing in cortical microcircuits. *Science* 327, 584–587. doi: 10.1126/science.1179867

Ellwood, I. T., Patel, T., Wadia, V., Lee, A. T., Liptak, A. T., Bender, K. J., et al. (2017). Tonic or phasic stimulation of dopaminergic projections to prefrontal cortex causes mice to maintain or deviate from previously learned behavioral strategies. *J. Neurosci.* 37, 8315–8329. doi: 10.1523/JNEUROSCI.1221-17.2017

Enel, P., Wallis, J. D., and Rich, E. L. (2020). Stable and dynamic representations of value in the prefrontal cortex. *Elife* 9:e54313. doi: 10.7554/eLife.54313.sa2

Enoki, R., Hu, Y., Hamilton, D., and Fine, A. (2009). Expression of long-term plasticity at individual synapses in hippocampus is graded, bidirectional, and mainly presynaptic: optical quantal analysis. *Neuron* 62, 242–253. doi: 10.1016/j.neuron.2009.02.026

Euston, D. R., Gruber, A. J., and McNaughton, B. L. (2012). The role of medial prefrontal cortex in memory and decision making. *Neuron* 76, 1057–1070. doi: 10.1016/j.neuron.2012.12.002

Euston, D. R., Tatsuno, M., and McNaughton, B. L. (2007). Fast-forward playback of recent memory sequences in prefrontal cortex during sleep. *Science* 318, 1147–1150. doi: 10.1126/science.1148979

Fiete, I. R., Senn, W., Wang, C. Z. H., and Hahnloser, R. H. R. (2010). Spike-time-dependent plasticity and heterosynaptic competition organize networks to produce long scale-free sequences of neural activity. *Neuron* 65, 563–576. doi: 10.1016/j.neuron.2010.02.003

Fujii, N., and Graybiel, A. M. (2003). Representation of action sequence boundaries by macaque prefrontal cortical neurons. *Science* 301, 1246–1249. doi: 10.1126/science.1086872

Fujisawa, S., Amarasingham, A., Harrison, M. T., and Buzsáki, G. (2008). Behavior-dependent short-term assembly dynamics in the medial prefrontal cortex. *Nat. Neurosci.* 11, 823–833. doi: 10.1038/nn.2134

Funahashi, S., Bruce, C. J., and Goldman-Rakic, P. S. (1989). Mnemonic coding of visual space in the monkey's dorsolateral prefrontal cortex. *J. Neurophysiol.* 61, 331–349. doi: 10.1152/jn.1989.61.2.331

Fusi, S., Drew, P. J., and Abbott, L. F. (2005). Cascade models of synaptically stored memories. *Neuron* 45, 599–611. doi: 10.1016/j.neuron.2005.02.001

Fuster, J. M., and Alexander, G. E. (1971). Neuron activity related to short-term memory. *Science* 173, 652–654. doi: 10.1126/science.173.3997.652

Gallistel, C. R., and Matzel, L. D. (2013). The neuroscience of learning: beyond the Hebbian synapse. *Annu. Rev. Psychol.* 64, 169–200. doi: 10.1146/annurev-psych-113011-143807

Goldman-Rakic, P. S. (1995). Cellular basis of working memory. *Neuron* 14, 477–485. doi: 10.1016/0896-6273(95)90304-6

Golomb, D., Hansel, D., and Mato, G. (2001). "Mechanisms of synchrony of neural activity in large networks," in Handbook of Biological Physics, *Volume 4: Neuro-Informatics and Neural Modelling*, eds F. Moss, and S. Gielen (Amsterdam: Elsevier Science), 887–968.

Goto, Y., Yang, C. R., and Otani, S. (2010). Functional and dysfunctional synaptic plasticity in prefrontal cortex: roles in psychiatric disorders. *Biol. Psychiatry* 67, 199–207. doi: 10.1016/j.biopsych.2009.08.026

Graupner, M., and Brunel, N. (2012). Calcium-based plasticity model explains sensitivity of synaptic changes to spike pattern, rate, and dendritic location. *PNAS* 109, 3991–3996. doi: 10.1073/pnas.1109359109

Graupner, M., Wallisch, P., and Ostojic, S. (2016). Natural firing patterns imply low sensitivity of synaptic plasticity to spike timing compared with firing rate. *J. Neurosci.* 36, 11238–11258. doi: 10.1523/JNEUROSCI.0104-16.2016

Greene, A. J., Prepscius, C., and Levy, W. B. (2000). Primacy versus recency in a quantitative model: activity is the critical distinction. *Learn. Mem.* 7, 48–57. doi: 10.1101/lm.7.1.48

Hahn, G., Petermann, T., Havenith, M. N., Yu, S., Singer, W., Plenz, D., et al. (2010). Neuronal avalanches in spontaneous activity *in vivo*. *J. Neurophysiol.* 104, 3312–3322. doi: 10.1152/jn.00953.2009

Haider, B., Duque, A., Hasenstaub, A. R., and McCormick, D. A. (2006). Neocortical network activity *in vivo* is generated through a dynamic balance of excitation and inhibition. *J. Neurosci.* 26, 4535–4545. doi: 10.1523/JNEUROSCI.5297-05.2006

He, K., Huertas, M., Hong, S. Z., Tie, X., Hell, J. W., Shouval, H., et al. (2015). Distinct eligibility traces for LTP and LTD in cortical synapses. *Neuron* 88, 528–538. doi: 10.1016/j.neuron.2015.09.037

Hebb, D. O. (1949). *The Organization of Behavior: A Neuropsychologicgal Theory*. New York, NY: John Wiley & Sons, Inc.

Hempel, C. M., Hartman, K. H., Wang, X.-J., Turrigiano, G. G., and Nelson, S. B. (2000). Multiple forms of short-term plasticity at excitatory synapses in rat medial prefrontal cortex. *J. Neurophysiol.* 83, 3031–3041. doi: 10.1152/jn.2000.83.5.3031

Hu, B., Sergei, K., Lei, Z., and Armin, S. (2005). Reversal of hippocampal LTP by spontaneous seizure-like activity: role of group i mGlur and cell depolarization. *J. Neurophysiol.* 93, 316–336. doi: 10.1152/jn.00172.2004

Isaacson, J. S., and Scanziani, M. (2011). How inhibition shapes cortical activity. *Neuron* 72, 231–243. doi: 10.1016/j.neuron.2011.09.027

Ito, H. T., Zhang, S.-J., Witter, M. P., Moser, E. I., and Moser, M.-B. (2015). A prefrontal–thalamo–hippocampal circuit for goal-directed spatial navigation. *Nature* 522, 50–55. doi: 10.1038/nature14396

Jadhav, S. P., Kemere, C., German, P. W., and Frank, L. M. (2012). Awake hippocampal sharp-wave ripples support spatial memory. *Science* 336, 1454–1458. doi: 10.1126/science.1217230

Jadhav, S. P., Rothschild, G., Roumis, D. K., and Frank, L. M. (2016). Coordinated excitation and inhibition of prefrontal ensembles during awake hippocampal sharp-wave ripple events. *Neuron* 90, 113–127. doi: 10.1016/j.neuron.2016.02.010

Jahr, C. E., and Stevens, C. F. (1990). Voltage dependence of NMDA-activated macroscopic conductances predicted by single-channel kinetics. *J. Neurosci.* 10, 3178–3182. doi: 10.1523/JNEUROSCI.10-09-03178.1990

Jensen, G., Altschul, D., Danly, E., and Terrace, H. (2013). Transfer of a serial representation between two distinct tasks by rhesus macaques. *PLoS ONE* 8:e70285. doi: 10.1371/journal.pone.0070285

Jun, J. K., Miller, P., Hernández, A., Zainos, A., Lemus, L., Brody, C. D., et al. (2010). Heterogenous population coding of a short-term memory and decision task. *J. Neurosci.* 30, 916–929. doi: 10.1523/JNEUROSCI.2062-09.2010

Kaefer, K., Nardin, M., Blahna, K., and Csicsvari, J. (2020). Replay of behavioral sequences in the medial prefrontal cortex during rule switching. *Neuron* 106, 154–165.e6. doi: 10.1016/j.neuron.2020.01.015

Keck, C., Savin, C., and Lücke, J. (2012). Feedforward inhibition and synaptic scaling – two sides of the same coin? *PLoS Comput. Biol.* 8:e1002432. doi: 10.1371/journal.pcbi.1002432

Keck, T., Toyoizumi, T., Chen, L., Doiron, B., Feldman, D. E., Fox, K., et al. (2017). Integrating Hebbian and homeostatic plasticity: the current state of the field and future research directions. *Philos. Transac. R. Soc. B Biol. Sci.* 372:20160158. doi: 10.1098/rstb.2016.0158

Klampfl, S., and Maass, W. (2013). Emergence of dynamic memory traces in cortical microcircuit models through STDP. *J. Neurosci.* 33, 11515–11529. doi: 10.1523/JNEUROSCI.5044-12.2013

La Camera, G., Fontanini, A., and Mazzucato, L. (2019). Cortical computations via metastable activity. *Curr. Opin. Neurobiol.* 58, 37–45. doi: 10.1016/j.conb.2019.06.007

Laje, R., and Buonomano, D. V. (2013). Robust timing and motor patterns by taming chaos in recurrent neural networks. *Nat. Neurosci.* 16, 925–933. doi: 10.1038/nn.3405

Lengyel, I., Voss, K., Cammarota, M., Bradshaw, K., Brent, V., Murphy, K. P. S. J., et al. (2004). Autonomous activity of CaMKII is only transiently increased following the induction of long-term potentiation in the rat hippocampus. *Eur. J. Neurosci.* 20, 3063–3072. doi: 10.1111/j.1460-9568.2004.03748.x

Litwin-Kumar, A., and Doiron, B. (2014). Formation and maintenance of neuronal assemblies through synaptic plasticity. *Nat. Commun.* 5:5319. doi: 10.1038/ncomms6319

Liu, J. K., and Buonomano, D. V. (2009). Embedding multiple trajectories in simulated recurrent neural networks in a self-organizing manner. *J. Neurosci.* 29, 13172–13181. doi: 10.1523/JNEUROSCI.2358-09.2009

London, M., Roth, A., Beeren, L., Häusser, M., and Latham, P. E. (2010). Sensitivity to perturbations *in vivo* implies high noise and suggests rate coding in cortex. *Nature* 466, 123–127. doi: 10.1038/nature09086

Lundqvist, M., Herman, P., and Miller, E. K. (2018). Working Memory: delay activity, yes! Persistent activity? Maybe not. *J. Neurosci.* 38, 7013–7019. doi: 10.1523/JNEUROSCI.2485-17.2018

Lutzu, S., and Castillo, P. E. (2021). Modulation of NMDA receptors by g-protein-coupled receptors: role in synaptic transmission, plasticity and beyond. *Neuroscience* 456, 27–42. doi: 10.1016/j.neuroscience.2020.02.019

Malenka, R. C., Lancaster, B., and Zucker, R. S. (1992). Temporal limits on the rise in postsynaptic calcium required for the induction of long-term potentiation. *Neuron* 9, 121–128. doi: 10.1016/0896-6273(92)90227-5

Manninen, T., Hituri, K., Hellgren Kotaleski, J., Blackwell, K. T., and Linne, M.-L. (2010). Postsynaptic signal transduction models for long-term potentiation and depression. *Front. Comput. Neurosci.* 4:152. doi: 10.3389/fncom.2010.00152

Mante, V., Sussillo, D., Shenoy, K. V., and Newsome, W. T. (2013). Context-dependent computation by recurrent dynamics in prefrontal cortex. *Nature* 503, 78–84. doi: 10.1038/nature12742

Markowitz, D. A., Curtis, C. E., and Pesaran, B. (2015). Multiple component networks support working memory in prefrontal cortex. *PNAS* 112, 11084–11089. doi: 10.1073/pnas.1504172112

Markram, H., Gerstner, W., and Sjöström, P. J. (2012). Spike-timing-dependent plasticity: a comprehensive overview. *Front. Synaptic Neurosci.* 4:2. doi: 10.3389/fnsyn.2012.00002

Mashhoori, A., Hashemnia, S., McNaughton, B. L., Euston, D. R., and Gruber, A. J. (2018). Rat anterior cingulate cortex recalls features of remote reward locations after disfavoured reinforcements. *Elife* 7:e29793. doi: 10.7554/eLife.29793

Meador, K. J. (2007). The basic science of memory as it applies to epilepsy. *Epilepsia* 48, 23–25. doi: 10.1111/j.1528-1167.2007.01396.x

Meyers, E. M., Freedman, D. J., Kreiman, G., Miller, E. K., and Poggio, T. (2008). Dynamic population coding of category information in inferior temporal and prefrontal cortex. *J. Neurophysiol.* 100, 1407–1419. doi: 10.1152/jn.90248.2008

Moberly, A. H., Schreck, M., Bhattarai, J. P., Zweifel, L. S., Luo, W., and Ma, M. (2018). Olfactory inputs modulate respiration-related rhythmic activity in the prefrontal cortex and freezing behavior. *Nat. Commun.* 9:1528. doi: 10.1038/s41467-018-03988-1

Mongillo, G., Barak, O., and Tsodyks, M. (2008). Synaptic theory of working memory. *Science* 319, 1543–1546. doi: 10.1126/science.1150769

Montgomery, J. M., and Madison, D. V. (2002). State-dependent heterogeneity in synaptic depression between pyramidal cell pairs. *Neuron* 33, 765–777. doi: 10.1016/S0896-6273(02)00606-2

Morrison, A., Aertsen, A., and Diesmann, M. (2007). Spike-timing-dependent plasticity in balanced random networks. *Neural Comput.* 19, 1437–1467. doi: 10.1162/neco.2007.19.6.1437

Murray, J. D., Bernacchia, A., Roy, N. A., Constantinidis, C., Romo, R., and Wang, X.-J. (2017). Stable population coding for working memory coexists with heterogeneous neural dynamics in prefrontal cortex. *PNAS* 114, 394–399. doi: 10.1073/pnas.1619449114

Nakajima, M., Schmitt, L. I., and Halassa, M. M. (2019). Prefrontal cortex regulates sensory filtering through a basal ganglia-to-thalamus pathway. *Neuron* 103, 445–458.e10. doi: 10.1016/j.neuron.2019.05.026

Naudé, J., Cessac, B., Berry, H., and Delord, B. (2013). Effects of cellular homeostatic intrinsic plasticity on dynamical and computational properties of biological recurrent neural networks. *J. Neurosci.* 33, 15032–15043. doi: 10.1523/JNEUROSCI.0870-13.2013

Onn, S.-P., and Wang, X.-B. (2005). Differential modulation of anterior cingulate cortical activity by afferents from ventral tegmental area and mediodorsal thalamus. *Eur. J. Neurosci.* 21, 2975–2992. doi: 10.1111/j.1460-9568.2005.04122.x

Onn, S.-P., Wang, X.-B., Lin, M., and Grace, A. A. (2006). Dopamine D1 and D4 receptor subtypes differentially modulate recurrent excitatory synapses in prefrontal cortical pyramidal neurons. *Neuropsychopharmacology* 31, 318–338. doi: 10.1038/sj.npp.1300829

Ostlund, S. B., Winterbauer, N. E., and Balleine, B. W. (2009). Evidence of action sequence chunking in goal-directed instrumental conditioning and its dependence on the dorsomedial prefrontal cortex. *J. Neurosci.* 29, 8280–8287. doi: 10.1523/JNEUROSCI.1176-09.2009

Papouin, T., Dunphy, J., Tolman, M., Foley, J. C., and Haydon, P. G. (2017). Astrocytic control of synaptic function. *Philos. Transac. R. Soc. B Biol. Sci.* 372:20160154. doi: 10.1098/rstb.2016.0154

Passecker, J., Mikus, N., Malagon-Vina, H., Anner, P., Dimidschstein, J., Fishell, G., et al. (2019). Activity of prefrontal neurons predict future choices during gambling. *Neuron* 101, 152–164.e7. doi: 10.1016/j.neuron.2018.10.050

Pasupathy, A., and Miller, E. K. (2005). Different time courses of learning-related activity in the prefrontal cortex and striatum. *Nature* 433, 873–876. doi: 10.1038/nature03287

Paton, J. J., and Buonomano, D. V. (2018). The neural basis of timing: distributed mechanisms for diverse functions. *Neuron* 98, 687–705. doi: 10.1016/j.neuron.2018.03.045

Peyrache, A., Khamassi, M., Benchenane, K., Wiener, S. I., and Battaglia, F. P. (2009). Replay of rule-learning related neural patterns in the prefrontal cortex during sleep. *Nat. Neurosci.* 12, 919–926. doi: 10.1038/nn.2337

Pfeiffer, B. E., and Foster, D. J. (2013). Hippocampal place-cell sequences depict future paths to remembered goals. *Nature* 497, 74–79. doi: 10.1038/nature12112

Pouille, F., Marin-Burgin, A., Adesnik, H., Atallah, B. V., and Scanziani, M. (2009). Input normalization by global feedforward inhibition expands cortical dynamic range. *Nat. Neurosci.* 12, 1577–1585. doi: 10.1038/nn.2441

Raye, C. L., Johnson, M. K., Mitchell, K. J., Greene, E. J., and Johnson, M. R. (2007). Refreshing: a minimal executive function. *Cortex* 43, 135–145. doi: 10.1016/S0010-9452(08)70451-9

Renart, A., Rocha, J., de la, Bartho, P., Hollender, L., Parga, N., Reyes, A., et al. (2010). The asynchronous state in cortical circuits. *Science* 327, 587–590. doi: 10.1126/science.1179850

Rodriguez, G., Sarazin, M., Clemente, A., Holden, S., Paz, J. T., and Delord, B. (2018). Conditional bistability, a generic cellular mnemonic mechanism for robust and flexible working memory computations. *J. Neurosci.* 38, 5209–5219. doi: 10.1523/JNEUROSCI.1992-17.2017

Romo, R., Brody, C. D., Hernández, A., and Lemus, L. (1999). Neuronal correlates of parametric working memory in the prefrontal cortex. *Nature* 399, 470–473. doi: 10.1038/20939

Ruan, H., Saur, T., and Yao, W.-D. (2014). Dopamine-enabled anti-Hebbian timing-dependent plasticity in prefrontal circuitry. *Front. Neural Circuits* 8:38. doi: 10.3389/fncir.2014.00038

Schmitt, L. I., Wimmer, R. D., Nakajima, M., Happ, M., Mofakham, S., and Halassa, M. M. (2017). Thalamic amplification of cortical connectivity sustains attentional control. *Nature* 545, 219–223. doi: 10.1038/nature22073

Seidemann, E., Meilijson, I., Abeles, M., Bergman, H., and Vaadia, E. (1996). Simultaneously recorded single units in the frontal cortex go through sequences of discrete and stable states in monkeys performing a delayed localization task. *J. Neurosci.* 16, 752–768. doi: 10.1523/JNEUROSCI.16-02-00752.1996

Shafi, M., Zhou, Y., Quintana, J., Chow, C., Fuster, J., and Bodner, M. (2007). Variability in neuronal activity in primate cortex during working memory tasks. *Neuroscience* 146, 1082–1108. doi: 10.1016/j.neuroscience.2006.12.072

Shenoy, K. V., Sahani, M., and Churchland, M. M. (2013). Cortical control of arm movements: a dynamical systems perspective. *Annu. Rev. Neurosci.* 36, 337–359. doi: 10.1146/annurev-neuro-062111-150509

Shima, K., Isoda, M., Mushiake, H., and Tanji, J. (2007). Categorization of behavioural sequences in the prefrontal cortex. *Nature* 445, 315–318. doi: 10.1038/nature05470

Shin, J. D., Tang, W., and Jadhav, S. P. (2019). Dynamics of awake hippocampal-prefrontal replay for spatial learning and memory-guided decision making. *Neuron* 104, 1110–1125.e7. doi: 10.1016/j.neuron.2019.09.012

Shinomoto, S., Miyazaki, Y., Tamura, H., and Fujita, I. (2005). Regional and laminar differences in *in vivo* firing patterns of primate cortical neurons. *J. Neurophysiol.* 94, 567–575. doi: 10.1152/jn.00896.2004

Shinomoto, S., Shima, K., and Tanji, J. (2003). Differences in spiking patterns among cortical neurons. *Neural Comput.* 15, 2823–2842. doi: 10.1162/089976603322518759

Shouval, H. Z., Bear, M. F., and Cooper, L. N. (2002). A unified model of NMDA receptor-dependent bidirectional synaptic plasticity. *PNAS* 99, 10831–10836. doi: 10.1073/pnas.152343099

Shu, Y., Hasenstaub, A., and McCormick, D. A. (2003). Turning on and off recurrent balanced cortical activity. *Nature* 423, 288–293. doi: 10.1038/nature01616

Siapas, A. G., Lubenov, E. V., and Wilson, M. A. (2005). Prefrontal phase locking to hippocampal theta oscillations. *Neuron* 46, 141–151. doi: 10.1016/j.neuron.2005.02.028

Siri, B. B., Quoy, M., Delord, B., Cessac, B., and Berry, H. (2007). Effects of Hebbian learning on the dynamics and structure of random networks with inhibitory and excitatory neurons. *J. Physiol. Paris* 101, 136–148. doi: 10.1016/j.jphysparis.2007.10.003

Song, S., Sjöström, P. J., Reigl, M., Nelson, S., and Chklovskii, D. B. (2005). Highly nonrandom features of synaptic connectivity in local cortical circuits. *PLoS Biol.* 3:e68. doi: 10.1371/journal.pbio.0030068

Spaak, E., Watanabe, K., Funahashi, S., and Stokes, M. G. (2017). Stable and dynamic coding for working memory in primate prefrontal cortex. *J. Neurosci.* 37, 6503–6516. doi: 10.1523/JNEUROSCI.3364-16.2017

Sreenivasan, K. K., Curtis, C. E., and D'Esposito, M. (2014). Revisiting the role of persistent neural activity during working memory. *Trends Cogn. Sci.* 18, 82–89. doi: 10.1016/j.tics.2013.12.001

Stokes, M. G. (2015). 'Activity-silent' working memory in prefrontal cortex: a dynamic coding framework. *Trends Cogn. Sci.* 19, 394–405. doi: 10.1016/j.tics.2015.05.004

Sweatt, J. D. (2016). Dynamic DNA methylation controls glutamate receptor trafficking and synaptic scaling. *J. Neurochem.* 137, 312–330. doi: 10.1111/jnc.13564

Tanaka, J., Horiike, Y., Matsuzaki, M., Miyazaki, T., Ellis-Davies, G. C. R., and Kasai, H. (2008). Protein synthesis and neurotrophin-dependent structural plasticity of single dendritic spines. *Science* 319, 1683–1687. doi: 10.1126/science.1152864

Tchumatchenko, T., Geisel, T., Volgushev, M., and Wolf, F. (2010). Signatures of synchrony in pairwise count correlations. *Front. Comput. Neurosci.* 4:1. doi: 10.3389/neuro.10.001.2010

Thomson, A. M. (2002). Synaptic connections and small circuits involving excitatory and inhibitory neurons in layers 2-5 of adult rat and cat neocortex: triple intracellular recordings and biocytin labelling *in vitro*. *Cerebral Cortex* 12, 936–953. doi: 10.1093/cercor/12.9.936

Tiganj, Z., Jung, M. W., Kim, J., and Howard, M. W. (2017). Sequential firing codes for time in rodent medial prefrontal cortex. *Cerebral Cortex* 27, 5663–5671. doi: 10.1093/cercor/bhw336

Tononi, G., and Cirelli, C. (2003). Sleep and synaptic homeostasis: a hypothesis. *Brain Res. Bull.* 62, 143–150. doi: 10.1016/j.brainresbull.2003.09.004

Truccolo, W., Donoghue, J. A., Hochberg, L. R., Eskandar, E. N., Madsen, J. R., Anderson, W. S., et al. (2011). Single-neuron dynamics in human focal epilepsy. *Nat. Neurosci.* 14, 635–641. doi: 10.1038/nn.2782

Turrigiano, G. G., Leslie, K. R., Desai, N. S., Rutherford, L. C., and Nelson, S. B. (1998). Activity-dependent scaling of quantal amplitude in neocortical neurons. *Nature* 391, 892–896. doi: 10.1038/36103

van Rossum, M. C., Bi, G. Q., and Turrigiano, G. G. (2000). Stable Hebbian learning from spike timing-dependent plasticity. *J. Neurosci.* 20, 8812–8821. doi: 10.1523/JNEUROSCI.20-23-08812.2000

Vogels, T. P., Sprekeler, H., Zenke, F., Clopath, C., and Gerstner, W. (2011). Inhibitory plasticity balances excitation and inhibition in sensory pathways and memory networks. *Science* 334, 1569–1573. doi: 10.1126/science.1211095

Wang, H.-X., and Gao, W.-J. (2012). Prolonged exposure to NMDAR antagonist induces cell-type specific changes of glutamatergic receptors in rat prefrontal cortex. *Neuropharmacology* 62, 1808–1822. doi: 10.1016/j.neuropharm.2011.11.024

Wang, J., Narain, D., Hosseini, E. A., and Jazayeri, M. (2018). Flexible timing by temporal scaling of cortical responses. *Nat. Neurosci.* 21, 102–110. doi: 10.1038/s41593-017-0028-6

Wang, X.-J. (2001). Synaptic reverberation underlying mnemonic persistent activity. *Trends Neurosci.* 24, 455–463. doi: 10.1016/S0166-2236(00)01868-3

Wang, Y., Markram, H., Goodman, P. H., Berger, T. K., Ma, J., and Goldman-Rakic, P. S. (2006). Heterogeneity in the pyramidal network of the medial prefrontal cortex. *Nat. Neurosci.* 9, 534–542. doi: 10.1038/nn1670

Witter, M. P., and Amaral, D. G. (2004). "CHAPTER 21 - Hippocampal Formation," in *The Rat Nervous System (Third Edition)*, ed G. Paxinos (Burlington, NJ: Academic Press), 635–704. doi: 10.1016/B978-012547638-6/50022-5

Wutz, A., Loonis, R., Roy, J. E., Donoghue, J. A., and Miller, E. K. (2018). Different levels of category abstraction by different dynamics in different prefrontal areas. *Neuron* 97, 716–726.e8. doi: 10.1016/j.neuron.2018.01.009

Xu, T.-X., and Yao, W.-D. (2010). D1 and D2 dopamine receptors in separate circuits cooperate to drive associative long-term potentiation in the prefrontal cortex. *PNAS* 107, 16366–16371. doi: 10.1073/pnas.1004108107

Xue, M., Atallah, B. V., and Scanziani, M. (2014). Equalizing excitation–inhibition ratios across visual cortical neurons. *Nature* 511, 596–600. doi: 10.1038/nature13321

Yang, S.-T., Shi, Y., Wang, Q., Peng, J.-Y., and Li, B.-M. (2014). Neuronal representation of working memory in the medial prefrontal cortex of rats. *Mol. Brain* 7:61. doi: 10.1186/s13041-014-0061-2

Yu, J. Y., Liu, D. F., Loback, A., Grossrubatscher, I., and Frank, L. M. (2018). Specific hippocampal representations are linked to generalized cortical representations in memory. *Nat. Commun.* 9:2209. doi: 10.1038/s41467-018-04498-w

Zenke, F., Gerstner, W., and Ganguli, S. (2017). The temporal paradox of Hebbian learning and homeostatic plasticity. *Curr. Opin. Neurobiol.* 43, 166–176. doi: 10.1016/j.conb.2017.03.015

Zenke, F., Hennequin, G., and Gerstner, W. (2013). Synaptic plasticity in neural networks needs homeostasis with a fast rate detector. *PLoS Comput. Biol.* 9:e1003330. doi: 10.1371/journal.pcbi.1003330

Zhang, W., and Linden, D. J. (2003). The other side of the engram: experience-driven changes in neuronal intrinsic excitability. *Nat. Rev. Neurosci.* 4:885. doi: 10.1038/nrn1248

Zielinski, M. C., Shin, J. D., and Jadhav, S. P. (2019). Coherent coding of spatial position mediated by theta oscillations in the hippocampus and prefrontal cortex. *J. Neurosci.* 39, 4550–4565. doi: 10.1523/JNEUROSCI.0106-19.2019

Conflict of Interest: The authors declare that the research was conducted in the absence of any commercial or financial relationships that could be construed as a potential conflict of interest.

Chapter 7. Dopamine builds and reveals reward-associated attractors

7.1. Summary

The previous chapter described the learning of presented stimulus sequences within synaptic noise and subsequent replay by an external triggering cue. However, it does not account for sequence learning toward a rewarding goal, rather solely replicating presented external stimulus sequences, even though sequences are commonly observed within the context of reward-assigning tasks. Furthermore, they do not consider how motivated intrinsically-generated decisions are taken, in the absence of external triggering cues. Dopamine (DA) neuromodulation is key to both answers, and no theory currently accounts for both of its effects on learning and motivation. The machine learning theory of reinforcement learning interprets phasic DA as a reward teaching signal for learning the values of reward-inducing actions, but doesn't explain DA's online motivational effect during behavior, with phasic release at the initiation of self-paced movements. The neuroscientific literature suggests for motivation either a directional effect, where stimulus-driven DA increases the salience and directs behavior toward the currently processed cue, or an activational effect, where DA increases the probability or vigor of all motor actions. While the directional account doesn't explain external cue-independent internally-generated behaviors, the activational account doesn't explain why DA specifically impacts non-stereotyped effortful behavior toward a goal far away in physical or task space.

As such, we proposed a double effect for DA, tested both within a recurrent neural network emulating frontal decision-making and through DA electrode stimulation and optogenetics in behaving mice. In the model, DA modulated online synaptic STDP, inducing the emergence of Hebbian assemblies oriented toward the goal within neurons encoding a repeatedly rewarded spatial location. This STDP learning rule (based on the previous chapter's) was supplemented with decaying early LTP/LTD synaptic eligibility traces, which were transformed into synaptic changes through DA impulse at rewarded locations. This assembly attracted network dynamics within its basin of attraction, whereas convergence of network activity from outside the basin was solely driven by noise or an external cue stimulus. Hence, internally-generated motivational DA impulse also multiplicatively gated synaptic NMDA excitability, inducing stronger synaptic reverberation and neural activity within the attractor. This attracted far-away resting-state network activity within behavioral timescales by effectively widening the basin of attraction of the goal-encoding assembly.

This double effect was tested experimentally, with DA-induced learning through medial forebrain bundle (MFB) electrode rewarding stimulations at the goal location, and DA-induced motivation through VTA photostimulation at random times in far-away locations. After mice learned the rewarding goal through uncued MFB electrode stimulation (discarding directional accounts), VTA photostimulation decreased the delay to reward and increased animal speed, as predicted. The mice also converged straight to the goal, showcasing the specific (vs. activational) effect of DA on behavior. This was confirmed through VTA photostimulation without MFB learning, which showed the delay to center or global speed didn't change, discrediting the global energizing of undirected actions predicted by the activational account.

Our experimentally-tested theory thus proposes motivational effects of DA as the revealing of an (otherwise covert) attractor previously learned by the reinforcing effects of DA.

7.1.1. Contributions

I developed the biophysical neural network model and calcium-based kinase-phosphatase couples-mediated eligibility traces and dopamine-based STDP rule, produced all model-related results as well as main and supplementary figures, and reviewed all text.

7.2. Article

DOPAMINE BUILDS AND REVEALS/UNVEILS REWARD-ASSOCIATED ATTRACTORS

Naudé J.*[1], Sarazin MXB.[2], Mondoloni S.[1], Hanesse B.[1], Vicq E.[1], Amegandjin F.[1], Tricoire L.[1], Mourot A.[1], Faure P.[1] ‡, Delord B[2]. ‡

Authors affiliations:

1. Sorbonne Université, Inserm, CNRS, Neuroscience Paris Seine - Institut de biologie Paris Seine (NPS - IBPS), 75005 Paris, France.

2. Institut des Systèmes Intelligents et de Robotique, CNRS, Inserm, Sorbonne Université, Paris, France.

‡ co-last authors

* correspondence to jeremie.naude@igf.cnrs.fr

ABSTRACT

Transient increase in ventral tegmental area (VTA) dopamine is interpreted as a valuation-updating signal, increasing the frequency of rewarded behaviors. However, performance also depends on the online, neuromodulatory effect of phasic dopamine. Here we develop and test a new computational characterization of dopamine's dual role. We considered mice navigating between places reinforced by VTA optogenetics, modeled by a recurrent network model of decision. Dopamine-modulated synaptic plasticity transformed neural assemblies representing the rewarded places into stable states, but only attracting the network dynamics locally. The online effect of phasic dopamine on synaptic excitability made the goal-encoding assembly accessible from remote initial conditions. We verified the model predictions that VTA photostimulation directs and energizes movements specifically toward a rewarded place, without exerting any motor effects out of context. We thus propose that the motivational role of VTA dopamine is to express a potential goal, by widening the basin of a dopamine-built attractor.

INTRODUCTION

Transient dopamine (DA) neuron activity contributes to both future decisions (learning) and ongoing behavior (motivation), but reconciling these two roles remains challenging (Schultz, 2007; Westbrook and Braver, 2016; Berke, 2018). The popular reinforcement learning theory, inspired by computer science, interprets fast, phasic dopamine activity as a reward-related teaching signal (Sutton and Barto, 1998; Schultz, 2007). At the neuronal level, the role of dopamine in learning is thought to rely on the modulation of long-term synaptic plasticity (Tritsch and Sabatini, 2012; He et al., 2015; Shindou et al., 2019), effectively building neural representations of the value of actions leading to reward (Izhikevich, 2007; Brzosko et al., 2015). Dopamine's role in value learning was further demonstrated by optogenetic stimulations of DA cells from the ventral tegmental area (VTA), inducing a place preference (Steinberg et al., 2013; Hamid et al., 2016). By contrast, it was presumed that slow, tonic variations in dopamine levels are needed for the generation of movements (Niv et al., 2007). However, a body of evidence now suggest a role for phasic dopamine in motivation (Berke, 2018; Coddington and Dudman, 2019; Klaus et al., 2019). Phasic DA has been observed at the initiation of self-paced movements (Howe and Dombeck, 2016; Syed et al., 2016; Coddington and Dudman, 2018; da Silva et al., 2018), while optogenetic DA manipulation to induce movements has given mixed results depending on the DA nuclei and the intensity of photostimulation (Coddington and Dudman, 2018; da Silva et al., 2018). Dopamine roles on ongoing behavior have thus proven hard to reconcile with learning accounts of dopamine (Berke, 2018; Klaus et al., 2019). Reinforcement learning theories does not assign any effect to dopamine in ongoing behavior, once the value of actions has been learned through dopamine modulation of plasticity (Sutton and Barto, 1998; Schultz, 2007).

Accounts on the immediate effect of dopamine suggest either a "directional" role with dopamine cells specifying the decision (Barter & Yin 2015) or an "activational" role with dopamine determining the level of motor resources to engage in actions (Salamone and Correa, 2012; Berke, 2018; Klaus et al., 2019). The limited encoding capacity of dopamine cells (Engelhard 2019) and the larger impact of dopamine antagonists on action probability and vigor than on preferences have argued in favor of an activational role (Salamone and

Correa, 2012). In the activational framework, dopamine would gate decisions by lowering a decision threshold, effectively increasing the probability, and reducing the latency, of all actions. It is however unclear how decision-threshold models of dopamine explain its effects of movement vigor. Most importantly, and contrary to decision-threshold models, dopamine does not impact every actions equally. Dopamine is mostly associated with, and necessary for, non-stereotyped, anticipatory, distal, or effortful behaviors, i.e. when some physical or cognitive distance separate the animal from a reward (Nicola, 2010; Westbrook and Braver, 2016; Walton and Bouret, 2019). Such dopamine role, neither purely activational nor directional, does thus not fit in simple, phenomenological models of decisions.

We instead considered the biophysical effects of DA and used dynamical system theory to characterize the motivational role of DA. Dopamine modulation of synaptic plasticity is believed to carve "Hebbian" (Hebb, 1949) assemblies of strongly interconnected neurons, representing a decision that was repeatedly rewarded. Such a neural assembly can constitute an attractor of the network dynamics (Hopfield, 1982), i.e. a particular state of activity (e.g. sustained, reverberating activity among the neuronal assembly, Brunel and Wang, 2001; Wang, 2002; Durstewitz and Seamans, 2008; Neiman and Loewenstein, 2013) toward which the network activity converges. In standard models, convergence from a rest state toward the decision-related attractor either requires a cue stimulus (Wang, 2002), or is driven by noise (Neiman and Loewenstein, 2013), despite behaviors being also driven by internally-generated motivated intentions (Balleine, 2019). Here we hypothesized that the motivational role of phasic dopamine consists in favoring the switch from a rest state to a decision-related attractor. To test this hypothesis, we achieved a specific control of VTA DA with optogenetics, to test predictions derived from a dynamical model based on the biophysical actions of DA on recurrent decision networks. We considered two DA effects, on synaptic plasticity (long term) and synaptic excitability (short term) (Seamans and Yang, 2004; Durstewitz and Seamans, 2008; Tritsch and Sabatini, 2012). When phasic DA release was systematically contingent with a particular decision, plasticity effects prevailed and built a neural assembly representing the rewarded decision (Izhikevich, 2007; Brzosko et al., 2015). Spontaneous-like phasic DA release (Patriarchi et al., 2018) at random times, by modulating ongoing synaptic excitability, increased the convergence toward existing neural assemblies. Our model thus predicted that motivational DA, rather than promoting every

action, would energize specifically actions aimed at goals previously paired with DA. Experimental test showed that phasic VTA photostimulation decreased the latency to travel from random places toward a learned goal, by increasing the speed and reorienting the animal, as predicted by the model. Furthermore, this effect of DA on movement was specific to convergence toward a goal, as the same photostimulation did not promote movements in a context without DA-associated goals. We thus propose that rather than increasing the probability of every action (Berke, 2018; da Silva et al., 2018), phasic DA specifically gates learned goals, by revealing attractors previously built by DA.

RESULTS

We sought a computational characterization of the dual role of dopamine in learning and motivation based on dynamical systems, rather than on the reinforcement learning field of computer science. In reinforcement learning (Figure 1a), reward (signaled by phasic dopamine, Sutton and Barto, 1998; Schultz, 2007) modulates the (synaptic) weights that link sensory states to rewarded actions, i.e. it teaches stimulus-action value, with decisions stochastically following highest-valued actions. Hence, in the original theory, dopamine only affects decisions indirectly through learning. How phasic dopamine also affects actions at the time of decision-making is however unclear in the reinforcement learning framework (Berke, 2018; Klaus et al., 2019). In the dynamical system framework, decisions correspond to an attractor, i.e. an activity state of the network that is stable. Possible states of the network map to an energy landscape, in which a decision may be seen as a ball rolling downhill to the nearest minimum, if initial activity lies within its basin of attraction (Figure 1b). Reinforcement can be seen as the carving of such a minimum (Wang, 2002; Neiman and Loewenstein, 2013). However, if the rest state is stable and outside the attractor's basin of attraction, an event (in most models, a stimulus, Wang, 2002; or a strong noise, Neiman and Loewenstein, 2013) is required to push the dynamics toward the basin. Here we propose and test the hypothesis that the online motivational effect of phasic dopamine participates in making goal-related attractors (previously learned by reward DA) accessible.

To test this hypothesis, we achieved selective manipulation of dopamine neurons, by expressing ChR2 in the ventral tegmental area (VTA) from dopamine transporter (DAT)-Cre mice (Figure 1c) and assessed that 500 ms photostimulation at 20 Hz drove bursting in dopamine cells (see Methods, Figure 1d). To test for the role of phasic dopamine neuron activity in place–reward association, we used an optogenetic conditioning procedure (see Methods, Figure 1e). Similar to a classical place preference conditioning, this task requires the animals to learn internal representations of the task space (i.e. an explicit memory of the reward location) rather than the association of a discrete sensory stimulus with reward, as in pavlovian conditioning. We paired three locations of a circular open-field with 500 ms, 20hz VTA photostimulation (Figure 1e). As mice freely explored the open field, DA cells were activated when the animals were detected on one of the locations. Following consecutive visits of the same location were not paired with photostimulation. Mice learned

to alternate between the rewarded locations (Figure 1e) and increased the number of photostimulations earned with learning sessions (Figure 1f, two-way ANOVA, condition: $F_{(1,9)}$=135.6, p=0, learning sessions: $F_{(1,9)}$=4.7, p=0, condition x sessions: $F_{(1,9)}$=4.0, p=0.0001), which validated that phasic bursting in VTA DA neurons constitutes a teaching signal for place–reward association (Tsai et al., 2009).

We modeled the decision process in this setup as a recurrent network coding for the desired position of the animal in task space, and in which the rewarded goal is represented by a neural "Hebbian" assembly of interconnected neurons (see Methods, Figure 1g). We modeled how dopamine may build the representation of a reward-associated place in the task space (Frémaux and Gerstner, 2016). In this task, there is no discrete sensory stimulus that would trigger the action as in stimulus-action models, but an internal representation that a particular location of the environment is rewarding (Balleine, 2019; Coddington and Dudman, 2019; Klaus et al., 2019). We thus modeled a topological decision network, in which each neuron biases the animal's decision toward a point in space (see Methods, Figure 1g). We considered a recurrent network of integrate-and-fire neurons with connectivity derived from frontal cortical areas. The prefrontal cortex is implicated in value-based and space-based decision-making, learning and memory of reward-associated actions and stimuli (Cisek, 2007; Euston et al., 2012). PFC cells present mixed selectivity for space and reward, i.e. cells are activated by both the representation of the outcome and its location (Euston et al., 2012; Rigotti et al., 2013). We thus validated that DA terminals were infected in mice that underwent the place conditioning procedure (Figure 1c). Nevertheless, this model does not imply a reductionist view that place-reward association solely occurs in the PFC, but aims instead at capturing the core computation realized by a more distributed network of value- and space-based decisions (Penner and Mizumori, 2012; Hunt and Hayden, 2017), encompassing the basal ganglia (Supplementary Figure 1), thalamus, hippocampus and amygdala. In the model, neurons receive an input representing the current position of the animal (putatively by the hippocampus). The bump of neuronal activity resulting from network recurrent dynamics is read out as the desired position of the animal (Figure 1g), toward which its actual position converges (through motor cortex and basal ganglia processes, lumped here as simple first order dynamics), and so on. Recurrent dynamics ensures that the network has spontaneous activity which is only biased by the input activity, differing from passive, feedforward stimulus-action mapping. Recurrent

dynamics are also ideally suited to perform decisions based on internal representations, with recurrent connections hypothesized to form interconnected neuronal assemblies (Hebbian assemblies) memorizing a goal (Hopfield, 1982). In this model, we observed that considering the effects of DA on both synaptic plasticity and excitability (see Methods) (Seamans and Yang, 2004; Tritsch and Sabatini, 2012) resulted in a high rate of visits of rewarded locations after learning, similar to experiments, in opposition to considering dopamine-modulated plasticity alone (Figure 1h). We analyze the requirements for implementing the two effects of dopamine in the next section, in order to extract from the model the dynamical interpretation of the learning and decision processes in the experimental setup (Figure 1i). Dopamine modulation of long-term synaptic plasticity results in carving energy minima, i.e. transforming network states corresponding to an action into attractors (Figure 1i). Attractors, while being stable states, only constitute potential goals. If initial conditions are far from the basin of attraction, or in near-stable states (e.g. rest states) in which the speed of evolution is significantly slow, decisions cannot be made on behavioral timescales (as in Figure 1h). In this framework, the online effect of dopamine consists in widening the basins of attraction, so that the rest state disappears and neural dynamics converge toward the attractor representing the goal, corresponding to the motivational role of dopamine (Figure 1i).

We next present the biophysical and biochemical conditions upon which such a dual effect of dopamine is possible. Standard Hebbian synaptic plasticity alone, in which the coincidence of presynaptic and postsynaptic plasticity results in synaptic potentiation, would strengthen any behavioral trajectory associated with a chain of neuronal activation that occurred by chance. By contrast, synapses from the decision network should only be modified (e.g. potentiated) if they participated in a rewarded trajectory. However, each neuron is myopic: it only fires at a particular point of space, and the reward arrives long after the synapse was activated. How local synaptic plasticity learns global trajectories, from distant points of the open-field to the reward-associated locations, constitutes a "distal credit assignment" problem. Here we propose a constrained, biochemical model of the intracellular pathways implicated in synaptic plasticity that performs distal credit assignment through eligibility traces (Figure 2a, Supplementary Figure 2, see Methods). In the model, DA both regulates long-term plasticity, and also directly increases the effective level of NMDA conductance online (Seamans and Yang, 2004; Tritsch and Sabatini, 2012)

(Figure 2b). Coincident presynaptic and postsynaptic activities (Figure 2c) are detected by NMDA receptors (NMDA-R), which are activated by concomitant presynaptic glutamate release and postsynaptic depolarization. Calcium flow from opened NMDAR (and voltage-dependent calcium channels, Graupner and Brunel, 2012) activates activity-dependent kinases and phosphatases (putatively, CaMKII and Calcineurin) that compete to form early long-term potentiation (eLTP) or depression (eLTD) (Figure 2c) (He et al., 2015; Shindou et al., 2019; Magee and Grienberger, 2020). eLTP and eLTD constitute synaptic tags called eligibility traces (Izhikevich, 2007; Frémaux and Gerstner, 2016; Magee and Grienberger, 2020). These synaptic tags (e.g. phospho-ERK, Zhang et al., 2018; Okuda et al., 2020) decay to a non-phosphorylated state (Figure 2c) if not consolidated by neuromodulators into effective changes in glutamate receptors (e.g. through CREB-induced protein synthesis, Zhang et al., 2018; Okuda et al., 2020). In the model, dopamine, through D1 receptors (D1R), increases cAMP levels and consequently protein kinase A (PKA) activity (Tritsch and Sabatini, 2012; Zhang et al., 2018; Magee and Grienberger, 2020), resulting in the transformation of eligibility traces into synaptic changes (Figure 2c, Supplementary Figure 2) (Izhikevich, 2007; Brzosko et al., 2015).

In a recurrent network equipped with this plasticity pathway, a neuronal sequence of activity corresponding to a trajectory from a random initial point to a dopamine-paired location results in potentiation of the synapses between the neurons coding along the trajectory, i.e. the model correctly solves the distal credit assignment problem (Figure 2d). After repetition of such learning procedure from different initial points, dopamine-modulated synaptic plasticity has built a neuronal assembly of strongly connected neurons coding for the dopamine-paired location (Figure 2d). As a consequence of the learning mechanism based on eligibility, synapses onto neurons which represent points of space nearest to the rewarded location were the strongest, and incoming synaptic weights slowly decreased along neurons representing locations further and further from the rewarded location (Figure 2e). Standard Hebbian assemblies are composed of strongly interconnected neurons with often symmetrical connections, resulting in stable, reverberating activity, but not necessarily more connections with the rest of the network than the average. Here, the rest of the network also "points" toward the goal-encoding assembly, with both strong symmetrical weights between the neurons of the assembly and medium asymmetrical weights from outside neurons toward assembly neurons (Supplementary Figure 2). These

features suggest that the assembly was both stable and also attracting trajectories from outside.

We thus assessed which parts of the space trajectories were indeed attracted toward the goal assembly. We observed that the attractor corresponding to the neuronal assembly built by dopamine-modulated synaptic plasticity had a very restricted basin of attraction: starting from an initial condition of the network activity outside the neuronal assembly, we did not observe any convergence at the behavioral timescale (Figure 2f). We thus considered the second effect of dopamine: besides its modulation of synaptic plasticity, dopamine is a neuromodulator, affecting synaptic excitability online (Seamans and Yang, 2004; Tritsch and Sabatini, 2012). We simulated a phasic release of dopamine, with temporal dynamics compatible with existing PFC and striatum data (Patriarchi et al., 2018), exerting an immediate, rather than plastic, effect on NMDA currents. With the dopamine effect on synaptic excitability, the network dynamics converged toward the assembly from every point in the space, corresponding to a large widening of the basin of attraction (Figure 2f). In summary, the Hebbian assembly learned with dopamine (i.e. reinforcement signal, Figure 2d) defined a restricted attractor basin. The assembly was then revealed with dopamine (i.e. motivational signal) as high spike frequency in assembly neurons (Figure 2G). This widened the attractor basin (Figure 2f), resulting in mouse convergence toward the previously rewarded location (Figure 2g).

We thus derived behavioral predictions from this dynamical model rooted in actual biophysical and biochemical mechanisms. Considering the presence or the absence of an assembly coding for the goal, a pulse of dopamine did not exert the same effect in the model. First, stimulating VTA DA neurons when the animal is outside of a previously rewarded location, should favor the convergence of the animal toward this location (Figure 2g), compared to situations with low or infrequent spontaneous DA pulses (Figure 2g). This would translate into an immediate effect of DA on movement and direction toward the goal. Second, in the absence of a goal-encoding assembly, the immediate effect of DA on synaptic excitability did not change much the network dynamics (Figure 2g). This corresponds to a context unpaired to reward, in which no goal-encoding assembly has been formed, and stimulating VTA DA neurons would not trigger any movement or reorientations.

To test this prediction, we implanted animals with two distinct sources of dopamine reward: an electrode in the medial forebrain bundle (MFB) and an optic fiber (after a Chr2-expressing viral injection) in the VTA (Figure 3a). Electrical stimulation of the MFB has long been considered as a potent substrate for brain stimulation reward (Gallistel et al., 1981). As it is not purely dopaminergic, we used MFB stimulation to build the reward-place association in a round open-field context, as was performed with VTA DA specific stimulation in Figure 1. Once the association was learned, we used VTA photostimulation (which the animals never encountered before, controlling that the LED light was not being used as a cue) to test for the motivational effect of phasic dopamine, by providing random stimulations when the animal was outside the location in the same, round open-field context, and in another context unpaired with MFB reward (square open-field, Figure 3a).

We expressed ChR2 in the VTA from DAT-Cre mice (Supplementary Figure 3) and trained the mice in a simplified version of the task from Figure 1. We paired one central location of a circular open-field with 20, 0.5ms electrical pulses at 100Hz in the MFB, requiring mice to leave the location before being stimulated again upon reentry. This led to strong reinforcement of the central place preference, so that current intensity was adjusted in order to achieve a moderate rate of visits (Supplementary Figure 3). After this electrical conditioning, VTA photostimulation (which mice never received in the first step) was delivered to animals when they were at the periphery of the open-field (see Methods, Figure 3b). VTA photostimulation decreased the delay to the reward location compared to control times (paired t-test: $T_{(10)}$= -3.75, p=0.0038, KS test on all trials from all mice: $p=1.10^{-7}$), an effect not observed in YFP expressing animals (Figure 3c-d, paired t-test: $T_{(7)}$= 0.96, p=0.37, KS test on all trials from all mice: p=0.97), comparable to a faster convergence of decision dynamics toward the goal assembly (Figure 2g). We investigated whether the reduced delay following peripheral VTA stimulation reflected an increase in speed, i.e. an energizing effect rather than an increase in the overall pace of behavior (Niv et al., 2007). VTA stimulation resulted in a fast increase of animal speed (paired t-test on acceleration after stimulation vs control: $T_{(10)}$=3.64, p=0.0046, see Methods), not observed in YFP controls (paired t-test on acceleration after stimulation vs control: $T_{(7)}$=-0.11, p=0.92, unpaired t-test on acceleration: $T_{(17)}$=-2.83,p=0.012, Figure 3e), excluding a global effect on the pace of the behavior.

We next investigated other alternative interpretations such as increased probability of performing any action (i.e. a decreased decision threshold) or an energizing effect induced by dopamine (Berke, 2018; Klaus et al., 2019), which would result in undirected increases in speed (da Silva et al., 2018). We thus computed the sum of successive angles between the animal and the goal, which is low if the animal goes straight to the location, but high if the animal simply goes faster in any direction before visiting the location. This angle error decreased following stimulation in Chr2 expressing animals (paired t-test stimulation vs control: $T_{(10)}=5.0$, $p = 5.10^{-4}$), but not in YFP expressing animals (paired t-test stimulation vs control: $T_{(10)}=-0.24$, $p = 0.82$; unpaired t-test Chr2 vs YFP: $T_{(17)}=-3.16$, $p=0.0058$, Figure 3f). Hence, the increase in animal speed following VTA stimulation was directed toward the central location, suggesting that the action induced by DA stimulation had a specific content: retrieving the goal learned under DA. This pattern of results is also consistent with the model, which predicted that DA photostimulation would exert a directed energizing effect in the context of a goal.

We thus challenged the same animals, conditioned in a circular open-field, by photostimulating the VTA in the different context of a square open-field in which animals never received any MFB rewards (Figure 3g). In this context, the animals did not express any tendency to visit the center of the open-field (Figure 3g) and VTA photostimulation did not affect the delay to visit the center (KS test on all trials from all mice: $p=0.82$, Figure 3h). Hence, VTA stimulation did not affect the animals speed outside the context of a rewarding goal (Figure 3i), contrary to SNc stimulation with the same parameters (da Silva et al., 2018). This result is consistent with the model prediction in the absence of dopamine-induced movements when no neural assembly representing a potential goal is present (Figure 2g). Overall, these results indicate that motivational effects of the VTA stimulation consist in the expression of a content-specific and context-dependent goal, rather than an aimless action.

DISCUSSION

Our biophysical theory interprets goal-directed actions as a two-step process: neural assemblies representing a potential goal are learned through DA-regulated synaptic plasticity, but not automatically expressed, i.e. they are "covert" in terms of behavior (Spence and Lippitt, 1946; Balleine, 2019). Then, phasic DA signaling has the ability to reveal these hidden attractors by widening its basin of attraction. We propose that short-term biophysical effects of DA, by affecting the NMDA receptors already upregulated by previous DA-dependent plasticity, implement a multiplicative logic able to support the DA-dependent expression of DA-built memory. We tested this theory using optogenetics, showing that short-term DA directs the animal and energize specifically actions previously learned by long-term DA, preferentially to other actions, and in a context-dependent manner.

Biophysical network modeling of behavior

Contrary to reinforcement learning models that focus on the phenomenology of behavior rather than on biological implementation, our model constitutes an attempt to root a dynamical theory on biophysical and biochemical properties, relying on three key features. First, we considered a recurrent network, because it links attractor dynamics to elemental computations of decisions (Wang, 2002). Even if inspired by the cortical stage of decision-making (Cisek, 2007; Euston et al., 2012), our model does not exclude other parts of the mesocorticolimbic loop from the decision process (Penner and Mizumori, 2012; Hunt and Hayden, 2017). In particular, striatal dopamine is needed for approaching rewards (Nicola, 2010; Salamone and Correa, 2012), and our theoretical proposal that online dopamine affects the energy levels of decision networks encompasses the striatal neurons in the definition of network states. Deciphering the respective effects of dopamine on corticostriatal NMDAR and on the intrinsic excitability of medium spiny neurons compared to NMDAR from recurrent connections would refine the link between the model predictions and the neurobiology literature. However, DA is likely to also affect online the amygdala, thalamus and hippocampus, as well as the connections between these structures and the cortex and basal ganglia (Penner and Mizumori, 2012; Tritsch and Sabatini, 2012), and such full-scale modeling was out of scope. We thus lumped some of the decisions processes, e.g.

space coding and motor convergence, as simple equations (feed-forward excitation and first-order convergence, respectively). We considered a coding of space in prefrontal neurons, which present mixed selectivity (Euston et al., 2012; Rigotti et al., 2013) that include space together with other task features. Even if the experimental test considered the physical space of the open-field as the task space, the conceptual consequences of our model extends to non-physical spaces. Indeed, dopamine is needed for approaching rewards when the animal is far both in terms of physical space or task state (Nicola, 2010; Westbrook and Braver, 2016). Our model, while predicting prefrontal sequences of activity during choice and navigation (Figure 2), would thus benefit from further testing and refining, by recording in the PFC in the present task as well as in tasks with more abstract states.

The second important feature of our model is the plasticity pathways implementing eligibility traces with synaptic tags. We followed the recent literature describing two distinct eligibility traces for LTP and LTD (He et al., 2015), but this separation leaves holes in the implementation by intracellular pathways. Indeed, early LTP and LTD are believed to depend on CaMKII and calcineurin, respectively, while in our model a different couple of kinase and a phosphatase is needed for LTP and LTP. This may be implemented by compartmentalization via synaptic scaffolds linking different forms of CaMKII with different phosphatases (Cai et al., 2021). Likewise, downstream decoding of early LTP/D may be realized by ERK and CREB (Zhang et al., 2018; Okuda et al., 2020), although they may not be specific to increases in the number of glutamate receptors and a refined model would need to include other DA regulations (Tritsch and Sabatini, 2012; Magee and Grienberger, 2020) such as intrinsic and structural plasticity. In the model, dopamine is key to transform eligibility traces into effective plasticity, but other neuromodulators such as noradrenaline (NE), serotonine (5HT) and acetycholine (ACh) seem to exert differential effects on the read-out of LTP and LTD (He et al., 2015). Linking these neuromodulators, i.e. the behavioral events they are triggered by, with the precise form of eligibility mechanism they implement, would enrich our comprehension of reward (or other outcomes) -gated plasticity. The third key feature is the online modulation exerted by DA. Here we focused on NMDA effects for DA, whereas it can affect a vast diversity of receptors and ionic channels depending on the structure and the subtype of DA receptors (Seamans and Yang, 2004; Tritsch and Sabatini, 2012). Here we mainly modeled D1R effects, but D2R may not be as

antagonistic as previously believed. D1R and D2R are actually synergistic when considering the cAMP-PKA pathway that we modeled (Tritsch and Sabatini, 2012). Even the regulation of intrinsic excitability of medium spiny neurons is more complex than D1R-mediated increases in excitability and D2R-mediated decreases: D2R may exert destabilizing influences (rather than inhibitory) that promote or oppose D1R effects depending on down or up-states, respectively (Tritsch and Sabatini, 2012). These interactions hint at complementary roles in our dynamical framework, that we discuss below.

Relations to other theories of dopamine function

Reinforcement learning theories do not assign any effect to dopamine during ongoing behavior, once the value of actions has been learned through DA modulation of plasticity (Sutton and Barto, 1998; Schultz, 2007). In alternative views to RL, dopamine has been suggested to exert either directional effects, i.e. stimulus-driven dopamine release directs the behavior toward the cue (Berridge and Robinson, 1998; Steinberg et al., 2013) or activational effects, i.e. dopamine increases the probability and vigor of any motor behavior (Berke, 2018; Klaus et al., 2019). Both views explain subparts of the vast literature on phasic dopamine. DA nuclei do not have enough encoding capacity and DA projections are not selective enough (Berke, 2018; Klaus et al., 2019) to precisely represent the goal toward which the animal should be directed. As such, in the directional account of dopamine, DA is proposed to add incentive motivation or salience to the cue being currently processed, promoting approach through yet-unknown mechanisms. The DA-associated cue is described in incentive-salience accounts as becoming "magnetic" (Berridge and Robinson, 1998; Steinberg et al., 2013), which is exactly what is expected in our model for a state suddenly attracting the decision network's dynamics. However, actions that are not cue-driven but self-generated rely on internal representations, in which case the role of DA in incentive-salience is less specified. Our proposal is based on contextual decisions, in which animals rely on learned internal representations to approach reward. It reinterprets incentive motivation as making attractors representing potential goals, either sensory or internal, accessible for the network dynamics.

Activational accounts assign a general role to phasic dopamine in gating decisions (increasing DA makes all decisions more probable) and energizing actions. Incentive

motivation models, in which decisions are sequentially evaluated, i.e. accepted or not based on the intensity of phasic DA (McClure et al., 2003), would predict undirected increase in the probability of every action following VTA photostimulation, in opposition to our experimental data showing a reduced angle to reward, and with the absence of DA effects outside the reward context. Furthermore, we show that speed profiles, not just latency or average speed, are affected by phasic DA, which go beyond the scope of discrete-time models (McClure et al., 2003). Phasic DA has also been suggested to move the threshold for decisions in drift-diffusion models (Berke, 2018; Klaus et al., 2019) predicting context-independent increase in undirected actions, which is also inconsistent with our observations on context-dependent directed energization of actions. Widening the basin of attraction in our model naturally increases both the likelihood, directness and speed of actions in a reward context-dependent fashion. Finally, in time-processing accounts, dopamine affects the sense of time: under high DA time goes fast, while under low DA time is felt as slower (Soares et al., 2016). We would interpret this as the speeding up of neuronal dynamics upon attractor unveiling. In the context of working memory, prefrontal DA has been related to the gating and maintenance of persistent activity encoding a goal (Seamans and Yang, 2004; Durstewitz and Seamans, 2008). This account, in which D2R-mediated gating allows for stimulus-driven transition toward a goal stabilized by D1R-mediated deepening of its basin of attraction, however differs from ours, in which D1R activation widens the basins of attraction of underlying goals. These roles are not necessarily opposite, and DA may do a "double duty" in cognitive motivation (Westbrook and Braver, 2016). The theory closest to ours is the "flexible approach" hypothesis: online DA is needed to approach reward in non-habitual situations, when the animal is disengaged from its goal, or when there is a motor cost and that DA is needed to travel some distance (in either physical or task space) specifically to retrieve DA-associated goals.

In the experimental literature, exogenous stimulation of phasic DA has provided conflicting results, with context-independent (da Silva et al., 2018) and context-dependent (Howe and Dombeck, 2016) movement following SNc/dorsal striatum stimulation (Howe and Dombeck, 2016; da Silva et al., 2018), but only when the animal is preparing to move (Coddington and Dudman, 2019). Stimulation of VTA DA (Hamid et al., 2016) exerts either context-dependent effects, or fails to affect online behavior (Coddington and Dudman, 2018). Our theory reconciles these conflicting results: when the animal is head fixed, already

close to a rewarded state (Coddington and Dudman, 2018), DA is unneeded and its stimulation does not change behavior, while for situations in which animals have to perform some displacement in a physical space or in task space, DA increases the likelihood and speed of convergence toward the goal (Hamid et al., 2016; Howe and Dombeck, 2016; da Silva et al., 2018). Our model also explains why no dopamine is needed for no-go conditioning, as the rest state is the goal state, while it is associated with go conditioning (Syed et al., 2016). Alternatively, the dichotomy between SNc and VTA may be based on the type of attractor these nuclei affect. VTA would build and express high level goals (deep, well separated wells in the energy landscape), and SNc low level, context-independent goals (i.e. locomotor actions) corresponding to multiple nearby attractors, explaining context-independent locomotion upon SNc stimulation. In either case, the motivational effect of DA has been described as gating or energizing decisions taken elsewhere (Berke, 2018; Coddington and Dudman, 2019; Klaus et al., 2019), while pharmacological manipulations can affect decision-making and the reward features being favored (e.g. high-effort high-gain). By hypothesizing and testing that the neuromodulatory effect of DA is to alter the network energy landscape on a fast timescale, we suggest the opposite view that DA would bias how ongoing decisions are being made.

REFERENCES

Balleine, B. W. (2019). The Meaning of Behavior: Discriminating Reflex and Volition in the Brain. *Neuron* 104, 47–62. doi:10.1016/j.neuron.2019.09.024.

Berke, J. (2018). What does dopamine mean? *Nat. Neurosci.* 21, 787–793. doi:10.1038/s41593-018-0152-y.

Berridge, K. C., and Robinson, T. E. (1998). What is the role of dopamine in reward: hedonic impact, reward learning, or incentive salience? *Brain Res. Rev.* 28, 309–369. doi:10.1016/S0165-0173(98)00019-8.

Brunel, N., and Wang, X. J. (2001). Effects of neuromodulation in a cortical network model of object working memory dominated by recurrent inhibition. *J. Comput. Neurosci.* 11, 63–85. doi:10.1023/A:1011204814320.

Brzosko, Z., Schultz, W., and Paulsen, O. (2015). Retroactive modulation of spike timing-dependent plasticity by dopamine. *eLife* 4, e09685. doi:10.7554/eLife.09685.

Cai, Q., Zeng, M., Wu, X., Wu, H., Zhan, Y., Tian, R., et al. (2021). CaMKIIα-driven, phosphatase-checked postsynaptic plasticity via phase separation. *Cell Res.* 31, 37–51. doi:10.1038/s41422-020-00439-9.

Cisek, P. (2007). Cortical mechanisms of action selection: the affordance competition hypothesis. *Philos. Trans. R. Soc. B Biol. Sci.* 362, 1585–1599. doi:10.1098/rstb.2007.2054.

Coddington, L. T., and Dudman, J. T. (2018). The timing of action determines reward prediction signals in identified midbrain dopamine neurons. *Nat. Neurosci.* 21, 1563–1573. doi:10.1038/s41593-018-0245-7.

Coddington, L. T., and Dudman, J. T. (2019). Learning from Action: Reconsidering Movement Signaling in Midbrain Dopamine Neuron Activity. *Neuron* 104, 63–77. doi:10.1016/j.neuron.2019.08.036.

da Silva, J. A., Tecuapetla, F., Paixão, V., and Costa, R. M. (2018). Dopamine neuron activity before action initiation gates and invigorates future movements. *Nature* 554, 244–248. doi:10.1038/nature25457.

Durstewitz, D., and Seamans, J. K. (2008). The Dual-State Theory of Prefrontal Cortex Dopamine Function with Relevance to Catechol-O-Methyltransferase Genotypes and Schizophrenia. *Biol. Psychiatry* 64, 739–749. doi:10.1016/j.biopsych.2008.05.015.

Euston, D. R., Gruber, A. J., and McNaughton, B. L. (2012). The Role of Medial Prefrontal Cortex in Memory and Decision Making. *Neuron* 76, 1057–1070. doi:10.1016/j.neuron.2012.12.002.

Frémaux, N., and Gerstner, W. (2016). Neuromodulated Spike-Timing-Dependent Plasticity, and Theory of Three-Factor Learning Rules. *Front. Neural Circuits* 9. doi:10.3389/fncir.2015.00085.

Gallistel, C. R., Shizgal, P., and Yeomans, J. S. (1981). A portrait of the substrate for self-stimulation. *Psychol. Rev.* 88, 228–273. doi:10.1037/0033-295X.88.3.228.

Graupner, M., and Brunel, N. (2012). Calcium-based plasticity model explains sensitivity of synaptic changes to spike pattern, rate, and dendritic location. *Proc. Natl. Acad. Sci.*, 201109359. doi:10.1073/pnas.1109359109.

Hamid, A. A., Pettibone, J. R., Mabrouk, O. S., Hetrick, V. L., Schmidt, R., Vander Weele, C. M., et al. (2016). Mesolimbic dopamine signals the value of work. *Nat. Neurosci.* 19, 117–126. doi:10.1038/nn.4173.

He, K., Huertas, M., Hong, S. Z., Tie, X., Hell, J. W., Shouval, H., et al. (2015). Distinct Eligibility Traces for LTP and LTD in Cortical Synapses. *Neuron* 88, 528–538. doi:10.1016/j.neuron.2015.09.037.

Hebb, D. O. (1949). *The organization of behavior; a neuropsycholocigal theory.* New York: John Wiley & Sons, Inc.

Hopfield, J. J. (1982). Neural networks and physical systems with emergent collective computational abilities. *Proc. Natl. Acad. Sci.* 79, 2554–2558. doi:10.1073/pnas.79.8.2554.

Howe, M. W., and Dombeck, D. A. (2016). Rapid signalling in distinct dopaminergic axons during locomotion and reward. *Nature* 535, 505–510. doi:10.1038/nature18942.

Hunt, L. T., and Hayden, B. Y. (2017). A distributed, hierarchical and recurrent framework for reward-based choice. *Nat. Rev. Neurosci.* 18, 172–182. doi:10.1038/nrn.2017.7.

Izhikevich, E. M. (2007). Solving the distal reward problem through linkage of STDP and dopamine signaling. *Cereb. Cortex* 17, 2443–2452. doi:10.1093/cercor/bhl152.

Klaus, A., Alves da Silva, J., and Costa, R. M. (2019). What, If, and When to Move: Basal Ganglia Circuits and Self-Paced Action Initiation. *Annu. Rev. Neurosci.* 42, 459–483. doi:10.1146/annurev-neuro-072116-031033.

Magee, J. C., and Grienberger, C. (2020). Synaptic Plasticity Forms and Functions. *Annu. Rev. Neurosci.* 43, 95–117. doi:10.1146/annurev-neuro-090919-022842.

McClure, S. M., Daw, N. D., and Read Montague, P. (2003). A computational substrate for incentive salience. *Trends Neurosci.* 26, 423–428. doi:10.1016/S0166-2236(03)00177-2.

Neiman, T., and Loewenstein, Y. (2013). Covariance-Based Synaptic Plasticity in an

Attractor Network Model Accounts for Fast Adaptation in Free Operant Learning. *J. Neurosci.* 33, 1521–1534. doi:10.1523/JNEUROSCI.2068-12.2013.

Nicola, S. M. (2010). The Flexible Approach Hypothesis: Unification of Effort and Cue-Responding Hypotheses for the Role of Nucleus Accumbens Dopamine in the Activation of Reward-Seeking Behavior. *J. Neurosci.* 30, 16585–16600. doi:10.1523/JNEUROSCI.3958-10.2010.

Niv, Y., Daw, N. D., Joel, D., and Dayan, P. (2007). Tonic dopamine: opportunity costs and the control of response vigor. *Psychopharmacology (Berl.)* 191, 507–520. doi:10.1007/s00213-006-0502-4.

Okuda, K., Højgaard, K., Privitera, L., Bayraktar, G., and Takeuchi, T. (2020). Initial memory consolidation and the synaptic tagging and capture hypothesis. *Eur. J. Neurosci.* doi:10.1111/ejn.14902.

Patriarchi, T., Cho, J. R., Merten, K., Howe, M. W., Marley, A., Xiong, W.-H., et al. (2018). Ultrafast neuronal imaging of dopamine dynamics with designed genetically encoded sensors. *Science* 360. doi:10.1126/science.aat4422.

Penner, M. R., and Mizumori, S. J. Y. (2012). Neural systems analysis of decision making during goal-directed navigation. *Prog. Neurobiol.* 96, 96–135. doi:10.1016/j.pneurobio.2011.08.010.

Rigotti, M., Barak, O., Warden, M. R., Wang, X.-J., Daw, N. D., Miller, E. K., et al. (2013). The importance of mixed selectivity in complex cognitive tasks. *Nature* 497, 585–590. doi:10.1038/nature12160.

Salamone, J. D., and Correa, M. (2012). The Mysterious Motivational Functions of Mesolimbic Dopamine. *Neuron* 76, 470–485. doi:10.1016/j.neuron.2012.10.021.

Schultz, W. (2007). Behavioral dopamine signals. *Trends Neurosci.* 30, 203–210. doi:10.1016/j.tins.2007.03.007.

Seamans, J. K., and Yang, C. R. (2004). The principal features and mechanisms of dopamine modulation in the prefrontal cortex. *Prog. Neurobiol.* 74, 1–58. doi:10.1016/j.pneurobio.2004.05.006.

Shindou, T., Shindou, M., Watanabe, S., and Wickens, J. (2019). A silent eligibility trace enables dopamine-dependent synaptic plasticity for reinforcement learning in the mouse striatum. *Eur. J. Neurosci.* 49, 726–736. doi:10.1111/ejn.13921.

Soares, S., Atallah, B. V., and Paton, J. J. (2016). Midbrain dopamine neurons control judgment of time. Science 354, 1273–1277. doi:10.1126/science.aah5234.

Spence, K. W., and Lippitt, R. (1946). An experimental test of the sign-gestalt theory of trial and error learning. *J. Exp. Psychol.* 36, 491–502. doi:10.1037/h0062419.

Steinberg, E. E., Keiflin, R., Boivin, J. R., Witten, I. B., Deisseroth, K., and Janak, P. H. (2013). A causal link between prediction errors, dopamine neurons and learning. *Nat. Neurosci.* 16, 966–973. doi:10.1038/nn.3413.

Sutton, R. S., and Barto, A. G. (1998). *Reinforcement Learning: An Introduction*. doi:10.1109/TNN.1998.712192.

Syed, E. C. J., Grima, L. L., Magill, P. J., Bogacz, R., Brown, P., and Walton, M. E. (2016). Action initiation shapes mesolimbic dopamine encoding of future rewards. *Nat. Neurosci.* 19, 34–36. doi:10.1038/nn.4187.

Tritsch, N. X., and Sabatini, B. L. (2012). Dopaminergic Modulation of Synaptic Transmission in Cortex and Striatum. *Neuron* 76, 33–50. doi:10.1016/j.neuron.2012.09.023.

Tsai, H.-C., Zhang, F., Adamantidis, A., Stuber, G. D., Bonci, A., de Lecea, L., et al. (2009). Phasic Firing in Dopaminergic Neurons Is Sufficient for Behavioral Conditioning. *Science* 324, 1080–1084. doi:10.1126/science.1168878.

Walton, M. E., and Bouret, S. (2019). What Is the Relationship between Dopamine and Effort? *Trends Neurosci.* 42, 79–91. doi:10.1016/j.tins.2018.10.001.

Wang, X.-J. (2002). Probabilistic Decision Making by Slow Reverberation in Cortical Circuits. *Neuron* 36, 955–968. doi:10.1016/S0896-6273(02)01092-9.

Westbrook, A., and Braver, T. S. (2016). Dopamine Does Double Duty in Motivating Cognitive Effort. *Neuron* 89, 695–710. doi:10.1016/j.neuron.2015.12.029.

Zhang, J., Ko, S.-Y., Liao, Y., Kwon, Y., Jeon, S. J., Sohn, A., et al. (2018). Activation of the dopamine D1 receptor can extend long-term spatial memory persistence via PKA signaling in mice. *Neurobiol. Learn. Mem.* 155, 568–577. doi:10.1016/j.nlm.2018.05.016.

AUTHORS CONTRIBUTIONS

JN BD PF designed the study. BD JN MS designed the model, and performed the simulations with FA. JN BH performed the behavioral experiments. SM EV JN performed viral injections and histology. JN PF analyzed the behavioral data. AM LT contributed tools/reagents. JN MS PF BD wrote the article.

FIGURE LEGENDS

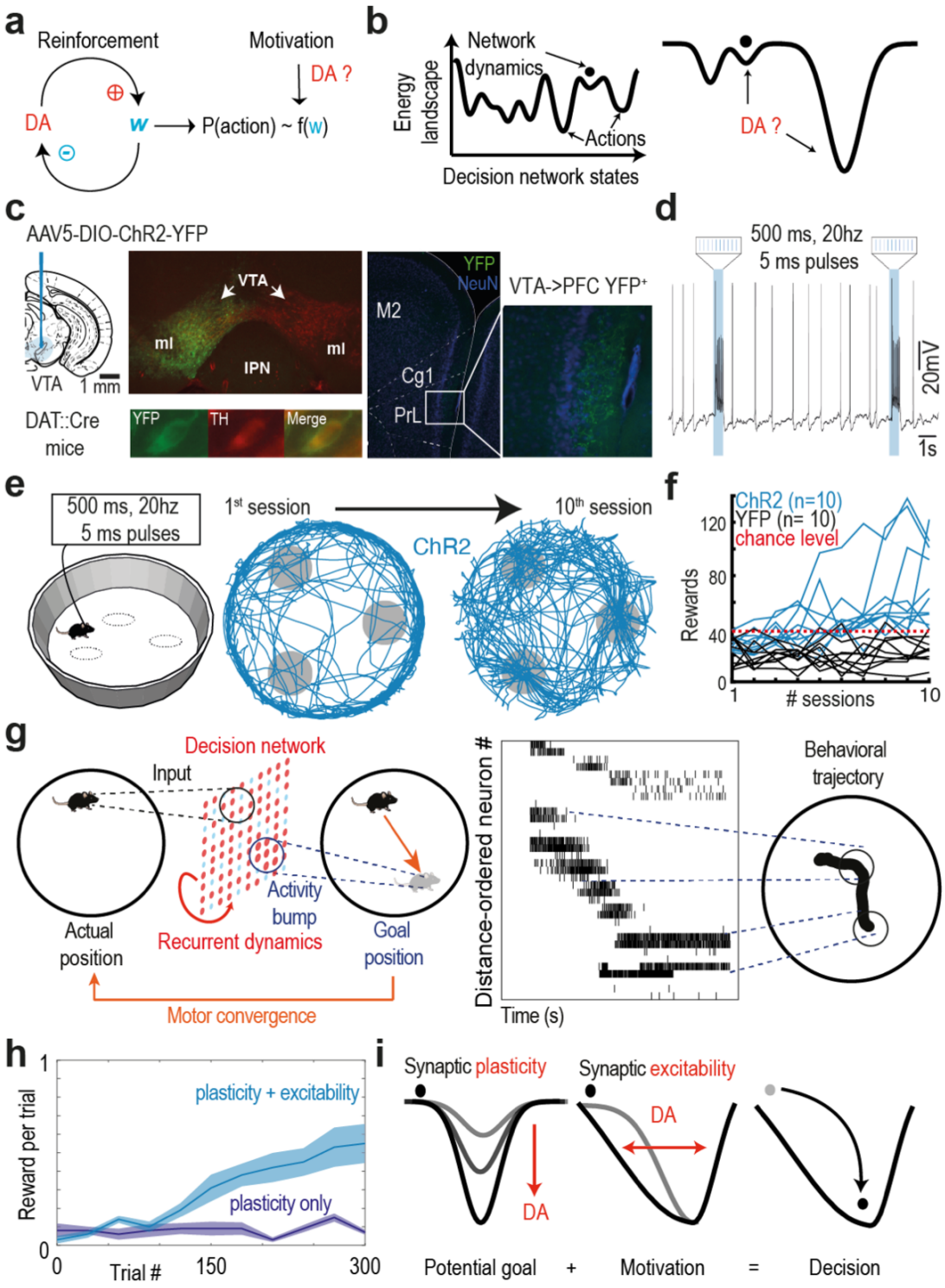

Figure 1. A new paradigm to study the dual role of dopamine in reinforcement and motivation.

a. In reinforcement learning models, dopamine reinforces synaptic weights used for decision-making, but the motivational role of dopamine is unclear.
b. Decision-making can also be seen as the convergence of neural dynamics to stable energy states. We ask how dopamine affects energy landscapes in reinforcement and motivation.
c. Left, schematics of virus injection in the ventral tegmental area (VTA). Right, ChR2 was expressed in VTA DAT+ (dopamine) neurons in DAT-Cre mice.
d. Example voltage trace from slice recordings, showing dopamine neuron bursting upon photostimulation in DAT-Cre mice.
e. Left, schematic of the task design. Three explicit circle locations were placed in the open field, forming an equilateral triangle. VTA photostimulation was delivered when mice were detected within one of the location circles, but mice could not receive two consecutive photostimulations at the same location. Middle to right: trajectories (10 min) of one mouse expressing ChR2 in the VTA (blue) and on expressing YFP (black), at the beginning (middle) and at the end (right) of the learning sessions.
f. Number of photostimulations against session number for Chr2-expressing (blue) and YFP-expressing (black) animals.
g. Left: schematics of the biophysical network model. A recurrent network of integrate-and-fire neurons receives the current position of the animals as an excitatory input, transformed by recurrent dynamics into a bump of neuronal activity (right) that encodes the goal position of the animal.
h. In the model (see Methods), dopamine modulation of both synaptic plasticity and synaptic excitability produced greater performance, similar to experiments, than dopamine modulation of synaptic plasticity alone. Animal learning was divided into 300 learning trials of 2 seconds each, where the mouse converged towards the dopamine-releasing reward and learned a neuronal assembly through dopaminergic neuromodulation of STDP. 20 test trials of 3 seconds each were conducted every 15 learning trials, either with (plasticity + excitability) or without (plasticity only) an initial release of dopamine inducing online neuromodulation of NMDAR.

i. The model interprets dopamine reinforcement as building neuronal assemblies forming attractors that are attained by the network dynamics ("unveiled") through the online motivational effect of dopamine.

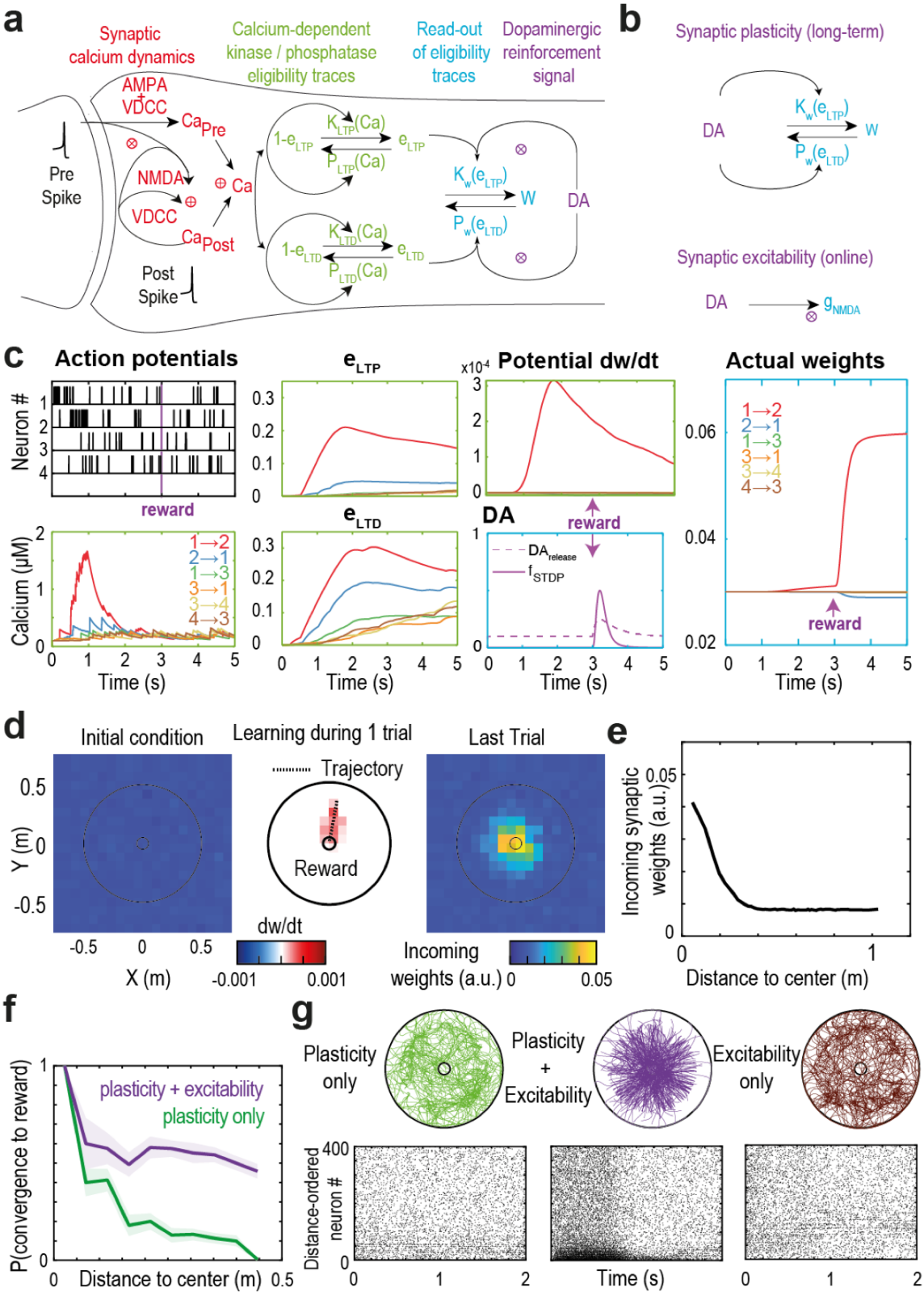

Figure 2. Phasic dopamine builds and unveils goal-encoding attractors.

a. Detailed schematics of the plasticity model. Synaptic calcium (red), depending on pre- and post-synaptic activity, activated kinases and phosphatases (green) forming eligibility traces (synaptic tags). At the time of dopamine (DA, purple) release (e.g. during reward), eligibility traces were translated into actual synaptic modification (blue).
b. DA acted on NMDA receptors at two timescales: at a learning timescale, through DA-modulated synaptic plasticity increasing the total number of glutamate receptors, but also in the ongoing behavior via the online modulation of NMDAR. These two roles acted in synergy: neurons previously interconnected through DA-modulated plasticity will be reactivated by the online modulation of NMDAR.
c. During navigation, the neural sequence leading to reward may be separated by several seconds from the DA signal. In a toy neural network model of 4 neurons with simulated spike trains (~4Hz) testing STDP dynamics, strong coincident neural activity (putatively arising from mouse locomotion toward the reward, neuron 1 (0-0.5s) -> neuron 2 (0.5s-1s) at 40Hz) induced a calcium entry resulting in eLTP/eLTD (green panels), whose respective levels maintain a trace of potential weight change, finally translating into actual weight change at the time of DA release (blue panels) and modifying only synapses activated during the sequence to reward.
d. Mean of synaptic connections received by the neurons, ordered by their topologic encoding (the position in space they bias for, equivalent to spatial receptive fields). Before learning, the mean synaptic weights received by neurons of the network followed a gaussian distribution. Middle panel shows the synaptic plasticity induced by a single learning trial. After learning, the sum of plastic changes, induced by repeated dopamine paired with a location in task space over 300 learning trials, formed a Hebbian assembly of strongly interconnected neurons coding for the reward location.
e. Mean synaptic weights as a function of the distance of locations encoded by the neurons from the reward center.
f. Probability to converge toward the goal (in less than 3s, averaged over 200 trials) after neural assembly learning, as a function of the distance to the goal, with and without DA's effect on ongoing synaptic excitability. DA increased the distance for

which there is a significant probability to converge toward the goal, i.e. DA widened the basin of attraction of goal-encoding attractor.

g. Raster plots with one example of network activity (bottom) and all the behavioral trajectories in the open-field (top). Left: without ongoing dopamine, activity in the neuronal assembly encoding for the goal does not differ from background. Middle: upon dopamine release outside the location, the neuronal assembly is strongly activated and the trajectories converge toward the reward location. Right: before learning, without any neural assembly, dopamine does not affect the network activity nor the behavioral trajectory.

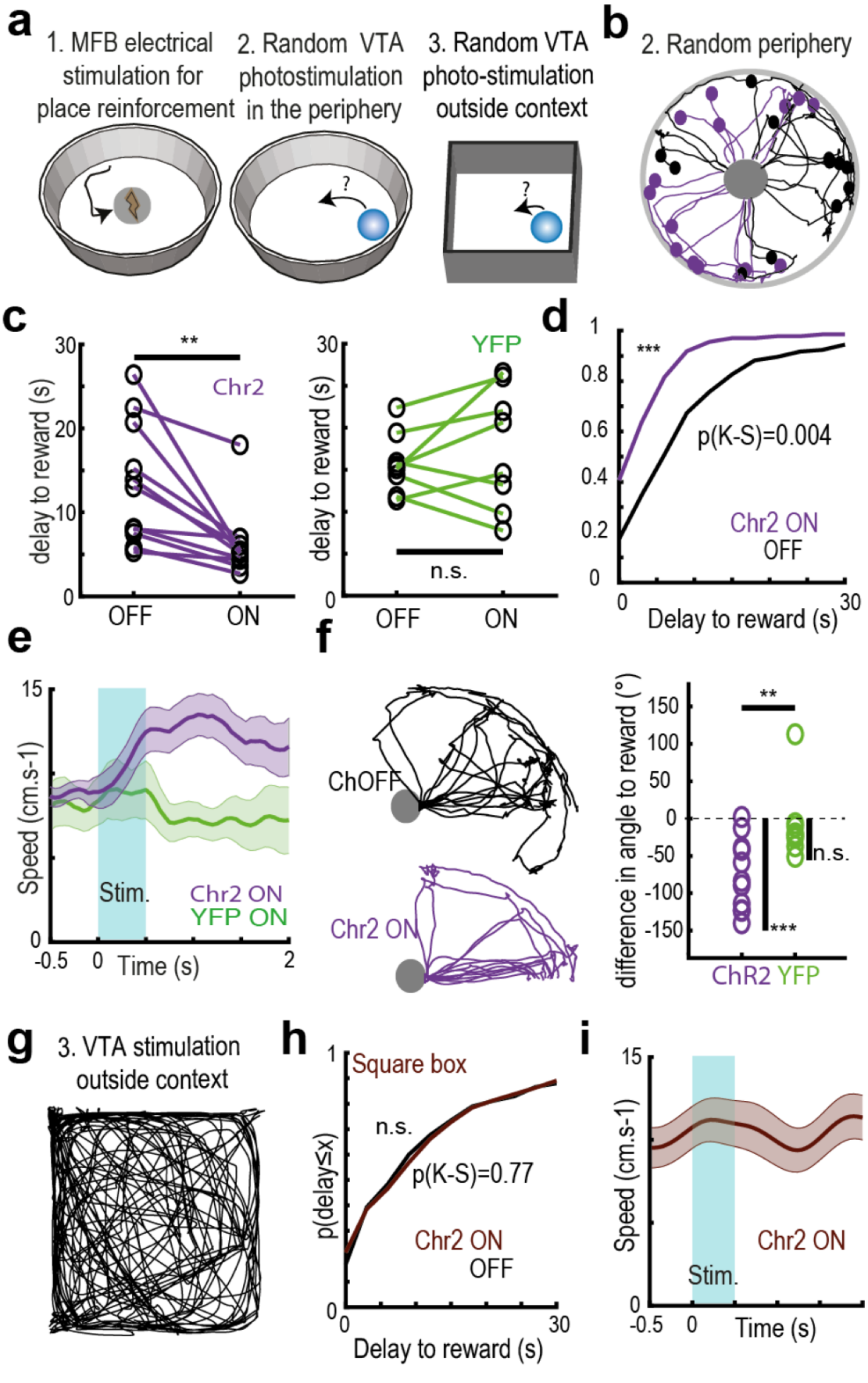
a
1. MFB electrical stimulation for place reinforcement
2. Random VTA photostimulation in the periphery
3. Random VTA photo-stimulation outside context
b
2. Random periphery
c
delay to reward (s)
Chr2
YFP
**
n.s.
OFF
ON
d
***
p(K-S)=0.004
Chr2 ON
OFF
Delay to reward (s)
e
Speed (cm.s-1)
Stim.
Chr2 ON
YFP ON
Time (s)
f
ChOFF
Chr2 ON
difference in angle to reward (°)
**
n.s.
***
ChR2 YFP
g
3. VTA stimulation outside context
h
Square box
n.s.
p(K-S)=0.77
Chr2 ON
OFF
p(delay≤x)
Delay to reward (s)
i
Speed (cm.s-1)
Chr2 ON
Stim.
Time (s)

Figure 3. Testing the prediction that VTA photostimulation-induced movements are goal-specific and context-dependent.

a. Schematics of the experimental test of the model predictions.
b. Left: all the trajectories from one example session, after VTA photostimulations in the periphery (purple) and after control (surrogate) times (black).
c. Individual differences between stimulation-location delays (ON) and surrogate time-location delays (OFF), for ChR2-expressing (left, purple) and YFP (right, green) animals.
d. Cumulative distribution of the duration between VTA DA stimulation (purple) and surrogate time points (black) and visit of the rewarded location, for ChR2-expressing animals.
e. Speed around the time of random VTA photostimulation in the periphery for ChR2-expressing (purple) and YFP (green) animals.
f. Left: same trajectories as in a, realigned to the same line relative to the rewarded location, showing straight trajectories stimulation times (purple) and more indirect trajectories with pauses for surrogate times (black). Right: difference in angle error (sum of angles from stimulation to reward) for ChR2-expressing (left, purple) and YFP (right, green) animals.
g. Experimental test of context-dependance: after learning, photostimulation of VTA DA neurons at random times in a different, square open-field.
h. Cumulative distribution of the duration between VTA DA stimulation (brown) and surrogate time points (black) and visit of the rewarded location, for ChR2-expressing animals.
i. Speed around the time of random VTA photostimulation in the periphery (brown), for Chr2 expressing animals.

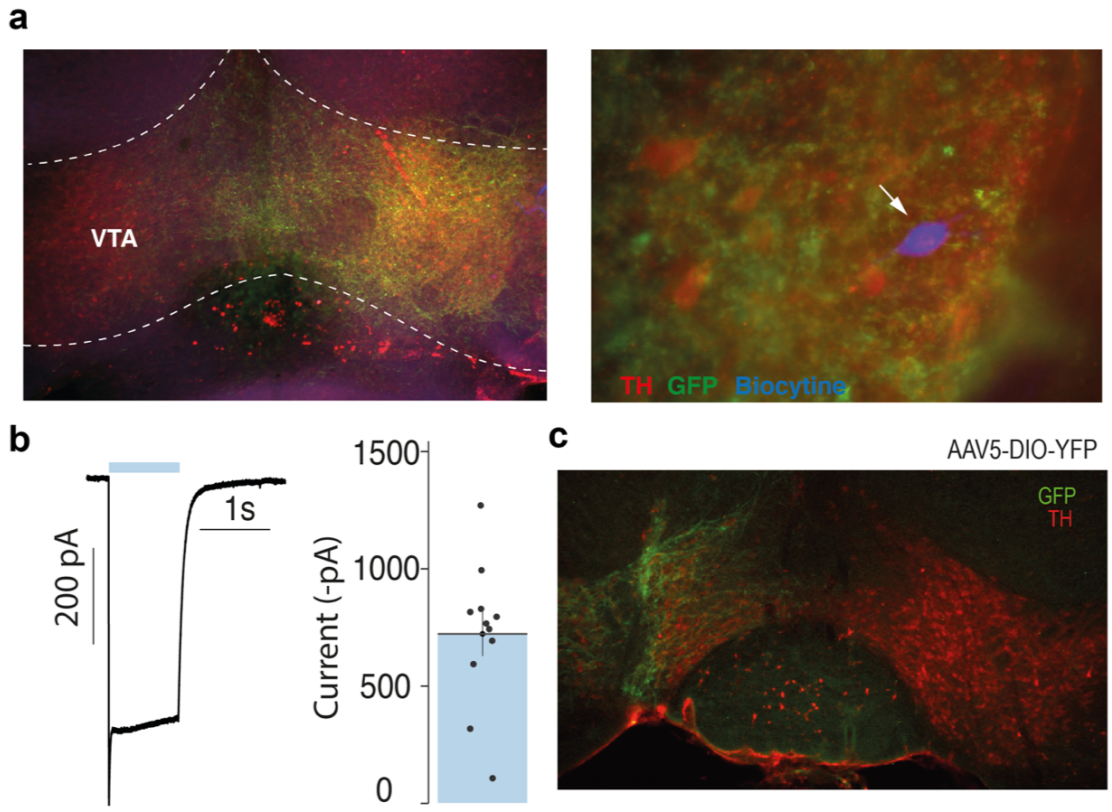

Supplementary Figure 1: Specificity of dopamine control by optogenetics

a. ChR2 was expressed in VTA DAT+ (dopamine) neurons in slices from DAT-Cre mice used for ex-vivo recording.
b. Zoom in the example neuron recorded, expressing TH, YFP and filled with biocytin (blue).
c. Example of current induced by a one second-pulse (left) and average currents from n cells (right), induced by the 10 5ms pulses at 20Hz from n cells.
d. YFP was also expressed in VTA DAT+ (dopamine) neurons in slices from DAT-Cre mice used as controls.

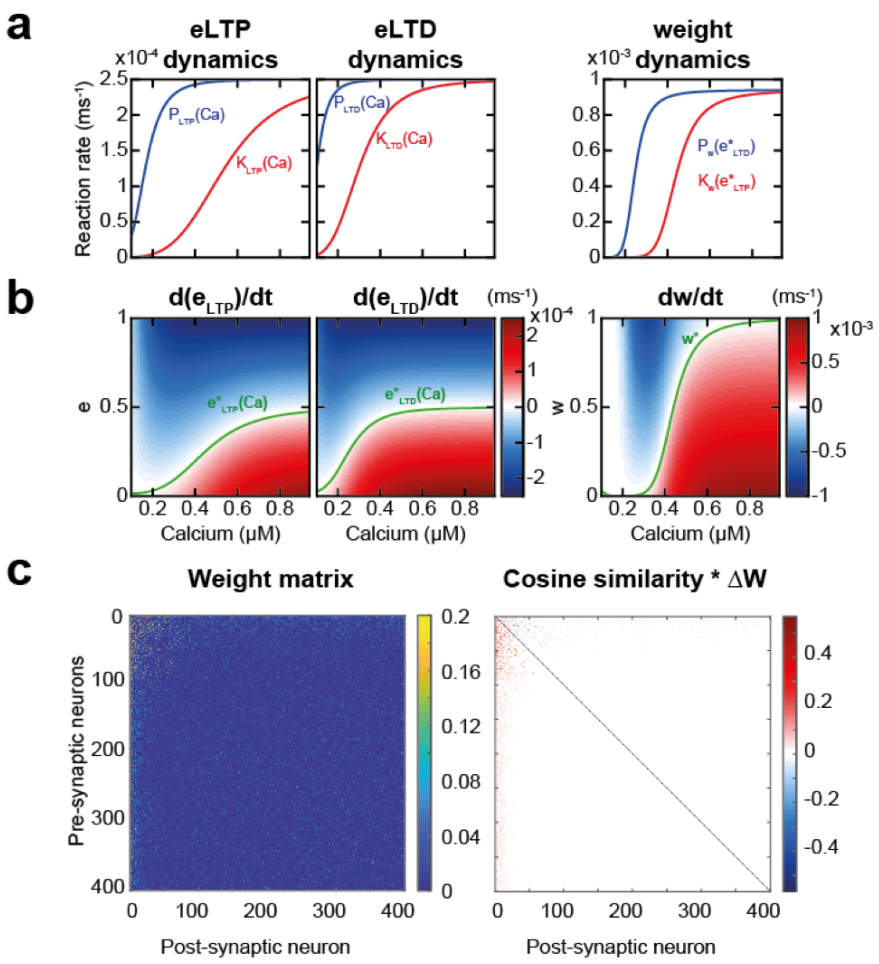

Supplementary Figure 2: Plasticity dynamics in the model.

a. Kinase and phosphatase rates for early LTP (left), LTD (middle) and weight (right) as a function of synaptic calcium concentration. Eligibility traces were considered at their equilibrium value at any given calcium concentration for the right subpanel (same for b).
b. Eligibility trace dynamics as a function of the current level of the trace (e, left) or weight (w, right) and of synaptic calcium concentration.
c. Left : synaptic weights between pre- and post-synaptic neurons after learning. Neurons are ordered from top to bottom according to their proximity with the arena center (top = close, bottom = far). Right : synaptic weight differences after vs. before learning, multiplied by how much the synaptic weight is oriented toward the reward (defined as the cosine similarity between the pre-post vector, a.k.a. the vector from the pre- to post-synaptic receptive field center, and the pre-reward vector, a.k.a. the vector from the pre-synaptic receptive field center and the reward location). Neurons are ordered as in the left subpanel.

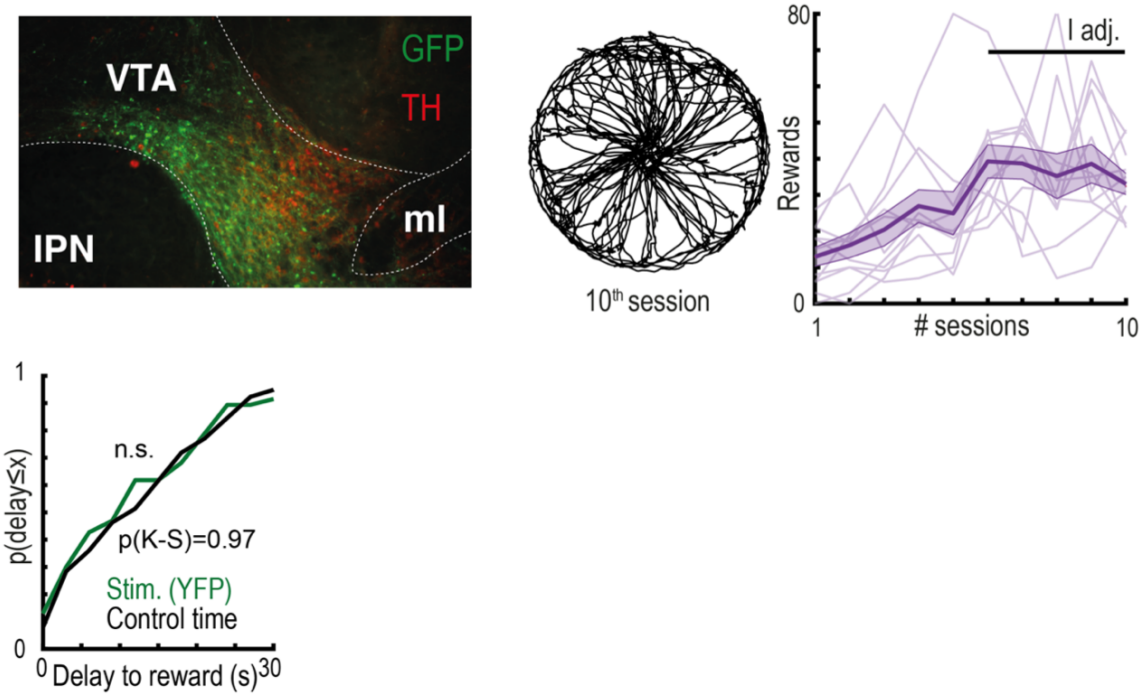

Supplementary Figure 3: control experiments for Figure 3

a. ChR2 was expressed in VTA DAT+ (dopamine) neurons in animals used in Figure 3 experiments.
b. Example trajectories at the end of MFB reward learning.
c. Number of location visits across sessions of MFB reward learning.
d. Distribution of stimulation-reward delays in YFP animals.

METHODS

Animals

Experiments were performed on DAT^{iCRE} female (N) and male (N) mice, from 8 to 16 weeks old, weighing 25-35 grams. Mice were housed in cages in an animal facility where the temperature (21+/- 1°C) and a 12h light/dark cycle were automatically monitored with food and water available ad libitum. DAT^{iCRE} mice were provided by Ludovic Tricoire (local breeding). All experiments were performed in accordance with the recommendations for animal experiments issued by the European Commission directives 219/1990, 220/1990 and 2010/63, approved by Sorbonne University, and n° 014378.01 supervised by the CEEA - 005.

Viruses production

AAV vectors were produced as previously described (Khabou et al., 2018) using the co-transfection method, and purified by iodixanol gradient ultracentrifugation (Choi et al., 2007). AAV vector stocks were titrated by quantitative PCR (qPCR) (Aurnhammer et al., 2012) using SYBR Green (Thermo Fischer Scientific).

Virus injections

Mice were anaesthetized with a gas mixture of oxygen (1 L/min) and 1-3 % of isoflurane (Piramal Healthcare, UK), then placed into a stereotaxic frame (Kopf Instruments, CA, USA). After the administration of an analgesic (Buprecare 0,1 mL at 0,015 mg/L) and of a local anesthetic (Lurocain, 0.1 mL at 0.67 mg/kg), a median incision revealed the skull which was drilled at the level of the VTA. Mice were then injected unilaterally in the VTA (1 µL, coordinates from bregma: AP -3.1 mm; ML ±0.5 mm; DV -4.5 mm from the skull) with an adeno-associated virus (AAV5.EF1-a.DIO.Chr2.YFP 6.89e13 ng/µL or AAV5.EF1a.DIO.YFP or 9.10e13 ng/µL). A double-floxed inverse open reading frame (DIO) allowed to restrain the expression of ChR2 opsins to VTA dopaminergic neurons. After stitching and administration of a dermal antiseptic, mice were then placed back in their home-cage and had 14 days to recover from surgery.

Fibers and electrodes implantations

Two weeks after the virus injection, mice were anaesthetized similar as above. After the administration of the analgesic and local anesthetic, skin was incised, the skull was drilled at the level of the VTA. An optical fiber (200 µm core, NA=0.39, Thor Labs) coupled to a ferule (1.25 mm) was implanted just above the VTA ipsilateral to the viral injection (coordinates from bregma: AP -3.1 mm, ML ±0.5 mm, DV 4.4 mm), and fixed to the skull with dental cement (SuperBond, Sun Medical).

For dual implantation experiments, the skull was also drilled at the level of the Median Forebrain Bundle (MFB). A bipolar stimulating electrode for ICSS was then implanted unilaterally (ipsilateral to the optic fiber in the VTA) in the brain (stereotaxic coordinates from bregma according to Paxinos atlas: AP -1.4 mm, ML ±1.2 mm, DV -4.8 mm from the brain).

After stitching and administration of a dermal antiseptic, mice were then placed back in their home-cage and had 14 days to recover from surgery. The behavioral task thus began 4 weeks after virus injection to allow the transgene to be expressed in the target dopamine cells.

Ex vivo patch-clamp recordings of VTA DA neurons

To verify the functional expression of the excitatory opsin ChR2, 8-12 week-old male and female DATiCRE mice were injected with the ChR2-expressing virus as described above. 4 weeks after infection, mice were deeply anesthetized with an intraperitoneal (IP) injection of a mix of ketamine/xylazine. Coronal midbrain sections (250 µm) were sliced using a Compresstome (VF-200; Precisionary Instruments) after intracardial perfusion of cold (4°C) sucrose-based artificial cerebrospinal fluid (SB-aCSF) containing (in mM): 125 NaCl, 2.5 KCl, 1.25 NaH_2PO_4, 5.9 $MgCl_2$, 26 $NaHCO_3$, 25 Sucrose, 2.5 Glucose, 1 Kynurenate (pH 7.2, 325 mOsm). After 10-60 min at 35°C for recovery, slices were transferred into oxygenated aCSF containing (in mM): 125 NaCl, 2.5 KCl, 1.25 NaH_2PO_4, 2 $CaCl_2$, 1 $MgCl_2$, 26 $NaHCO_3$, 15 Sucrose, 10 Glucose (pH 7.2, 325 mOsm) at room temperature for the rest of the day and individually transferred to a recording chamber continuously perfused at 2 ml/min with

oxygenated aCSF. Patch pipettes (4–8 MΩ) were pulled from thin wall borosilicate glass (G150TF-3, Warner Instruments) using a micropipette puller (P-87, Sutter Instruments, Novato, CA) and filled with a KGlu based intra-pipette solution containing (in mM): 116 K-gluconate, 10-20 HEPES, 0.5 EGTA, 6 KCl, 2 NaCl, 4 ATP, 0.3 GTP and 2 mg/mL biocytin (pH adjusted to 7.2). Transfected VTA DA cells were visualized using an upright microscope coupled with a Dodt contrast lens and illuminated with a white light source (Scientifica). A 460 nm LED (Cooled) was used both for visualizing YFP positive cells (using a bandpass filter cube) and for optical stimulation through the microscope (with same parameters used for behavioral experiments: ten 5 ms pulses at 20Hz). Whole-cell recordings were performed using a patch-clamp amplifier (Axoclamp 200B, Molecular Devices) connected to a Digidata (1550 LowNoise acquisition system, Molecular Devices). Signals were low pass filtered (Bessel, 2 kHz) and collected at 10 kHz using the data acquisition software pClamp 10.5 (Molecular Devices). All the electrophysiological recordings were extracted using Clampfit (Molecular Devices) and analyzed with R.

Behavior acquisition and conditioning procedures

Experiments were performed using a video camera connected to a video-track system, out of sight of the experimenter. A home-made software (Labview National instrument) tracked the animal, recorded its trajectory (20 frames per s) for 10 min and sent TTL pulses to the electrical stimulator or LED device when appropriate.

Conditioning procedure with VTA DA photostimulation: three explicit square locations, marked on the floor, were placed in a circular open-field (67 cm diameter), forming an equilateral triangle (side = 35 cm). Each time a mouse was detected (by its centroid) in the area of one of the rewarding locations (area radius = 3 cm), a 500ms train of ten 5ms pulses at 20Hz was delivered to the LED device. An ultra-high-power LED (470 nm, Prizmatix) coupled to a patch cord (500 µm core, NA=0.5, Prizmatix) plugged onto the ferrule was used for optical stimulation (output intensity of 10 mW). Animals could not receive two consecutive stimulations on a same location.

Conditioning procedure with MFB electrical stimulation: only one explicit location was marked on the floor, at the center of the open-field. Each time a mouse centroid was detected

in the area (radius=5cm) of the location, a 200-ms train of twenty 0.5-ms biphasic square waves pulsed at 100 Hz was delivered to the electrical stimulator. Mice were required to leave the location (i.e. to be detected at least 10cm from the central point) so that stimulation was made available again. The training consisted of a block of 5 daily sessions of 10 min at 80 µA, followed by 5 daily sessions of 10 min in which ICSS intensity was adjusted (in a range of 20-200 µA) so that mice visited the central location between 20 and 50 times at the end of the training.

Test sessions with VTA DA photostimulation: after the end of the MFB electrical conditioning procedure, the optical stimulation patch cord was plugged onto the ferrule during at least one OFF day (maximum=5) to habituate the animals, until the criterion (between 20 and 50 locations visits in 10 min) was reached again. On ON test day, photostimulation was delivered by the experimenter when the animal was outside of the reinforced location (at least 10cm from the central point). When the experimenter clicked to stimulate, it had a 50% probability to deliver an actual TTL pulse leading to photostimulation, otherwise this control time point was recorded as a control. In the square open-field test, occurring after the test session in the circular open-field, the procedure was exactly similar, except that it took place in square open-field (side = 70 cm) without any mark on the center.

Behavioral analyses

Stimulation-reward duration was computed as the time between the start of the photostimulation (or of the control time) and the first detection of the animal in the central location. Durations greater than 60s were excluded from the analysis for the sake of representations, but did not affect the statistical significance of the tests. Cumulative distributions of durations were computed by pooling stimulation-reward and control time-reward from all animals in one condition (e.g. ChR2 or YFP), with a 3s time bin. Average delays to rewards were also computed for each animal. For all groups of mice, the trajectory was smoothed using a triangular filter before computing the instantaneous speed, which corresponds to the distance traveled by the animal between two video frames (every 50ms) as a function of time. Mean acceleration following stimulation was taken as the time derivative of speed during the first second after stimulation. Angles to reward were computed as the angles between each successive positions of the animal relative to the initial

angle (at photostimulation of control time). Angle error was taken as the mean of $\| \sum e^{i\theta} \|$ where θ are the successive angles to reward.

Immunochemistry

After euthanasia, brains were rapidly removed and fixed in 4% paraformaldehyde (PFA). After a period of at least three days of fixation at 4°C, serial 60-µm sections were cut with a vibratome (Leica). Immunostaining experiments were performed as follows: VTA brain sections were incubated for 1 hour at 4°C in a blocking solution of phosphate-buffered saline (PBS) containing 3% bovine serum albumin (BSA, Sigma; A4503) (vol/vol) and 0.2% Triton X-100 (vol/vol), and then incubated overnight at 4 °C with a mouse anti-tyrosine hydroxylase antibody (anti-TH, Sigma, T1299) at 1:500 dilution, in PBS containing 1.5% BSA and 0.2% Triton X-100. The following day, sections were rinsed with PBS, and then incubated for 3 hours at 22-25 °C with Cy3-conjugated anti-mouse and secondary antibodies (Jackson ImmunoResearch, 715-165-150) at 1:500 in a solution of 1.5% BSA in PBS, respectively. After three rinses in PBS, slices were wet-mounted using Prolong Gold Antifade Reagent (Invitrogen, P36930). Microscopy was carried out with a fluorescent microscope, and images captured using a camera and analyzed with ImageJ.

Identification of the transfected neurons on DAT^{iCRE} mice by immunohistofluorescence was performed as described above, with the addition of 1:500 Chicken-anti-GFP primary IgG (ab13970, Abcam) in the solution. A Goat-anti-chicken AlexaFluor 488 (1:500, Life Technologies) was then used as secondary IgG. Neurons labelled for TH in the VTA allowed to confirm their neurochemical phenotype, and those labelled for GFP to confirm the transfection success.

Model of mouse locomotion

In the present model, mouse navigation was modeled as a process where orientation and speed were governed by a convergence toward either a default objective that consisted in approaching and aligning with the arena wall (answering to a need for security), or a goal-directed objective (answering to a need for exploration and reward retrieval). While the

default behavior was set according to ballistic laws in the model, goals were driven by population dynamics of the recurrent neural network.

In the model, the mouse position was denoted $P = \{X_P, Y_P\}$, with X_P and Y_P its cartesian coordinates. The position vector was

$$\vec{P} = \begin{pmatrix} X_P \\ Y_P \end{pmatrix} = d_P \begin{pmatrix} cos(\theta_P) \\ sin(\theta_P) \end{pmatrix}$$

with $d_P = \left\|\vec{P}\right\|$ the distance to the center of the arena and $\theta_P = \widehat{(\vec{P}, \vec{\imath})}$ the directional angle of the position vector (where $\vec{\imath}$ represents the unit vector $(1, 0)$). The mouse navigated in the environment according to

$$\vec{V} = \frac{d\vec{P}}{dt} = \begin{pmatrix} \frac{dX_P}{dt} \\ \frac{dY_P}{dt} \end{pmatrix} = V_P \begin{pmatrix} cos(\theta_V \\ sin(\theta_V) \end{pmatrix}$$

where V_P was the linear speed and $\theta_V = \widehat{(\vec{V}, \vec{\imath})}$ the direction of movement, i.e. the directional angle of the mouse speed vector, termed hereafter the speed angle.

Mouse speed evolution

The mouse linear speed evolved according to

$$\tau_V \frac{dV_P}{dt} = \mathrm{F}_{V_D} + \mathrm{F}_{V_G}$$

where the terms $\mathrm{F}_{V_D} = V_D - V_P$ and $\mathrm{F}_{V_G} = V_G - V_P$ modeled the contributions of default and goal behaviors to the linear speed. Briefly, F_{V_D} described the mouse's propensity to converge toward the nearest point on the wall and then run alongside it, whereas F_{V_G} defined the mouse's drive to converge towards an internally-generated goal when far from it and then escape recently visited rewards.

On the one hand, the contribution of the default behavior, governed by F_{V_D}, drove the mouse linear speed toward the default speed V_D, which was expressed as

$$V_D = V_{max} L(d_D, \sigma_D) A(\Delta\theta_D)$$

where V_{max} was the mouse's maximal speed, $L(d,\sigma) = \exp\left(-\frac{d^2}{2\sigma^2}\right)$ and $A(\theta) = \frac{1+\cos(\theta)}{2}$ respectively denoted exponential colinear and cosine angular tuning functions for motor command (Todorov, 2002), d_D was the distance between the mouse center and the default objective point D, and $\Delta\theta_D = \theta_V - \theta_D$ the angular difference between the speed and default objective angles. At each time, the default objective point D was defined as the projection of the animal's position onto the nearest point of the circular arena wall at a radius

$$r_d = r_{arena} - r_{mouse}$$

from the center, with r_{arena} the arena radius and r_{mouse} the mouse body's half width, i.e. at the nearest possible distance from the wall, considering the physical dimension of the mouse body (the mouse was not allowed to exceed that distance from the arena center). The default objective angle was computed as

$$\theta_D = (1 - L(d_D, \sigma_D))\theta_P + L(d_D, \sigma_D)\theta_T$$

where θ_P was the directional angle of the animal position P and its projection onto the wall D, and θ_T was the directional angle tangential to the arena circular wall at point D and in the direction of mouse movement.

Overall, the term F_{V_D} modeled the propensity of the mouse to be driven by the default command speed when 1) approaching the arena wall, due to both $L(d_D, \sigma_D)$ which was stronger when approaching the wall, and $(1 - L(d_D, \sigma_D))\theta_P$ which set a default direction toward the nearest position on the wall (i.e. D) when at distance from it, and 2) aligning parallel to the arena wall, due to $A(\Delta\theta_D)$ and $L(d_D, \sigma_D)\theta_T$ which induced convergence of the speed angle θ_V toward θ_T when approaching the wall. Conversely, the contribution of the default behavior to the mouse overall speed vanished when the mouse was far from, or not aligned with, the arena wall.

On the other hand, the contribution of the goal behavior to the linear speed, governed by F_{V_G}, drove the mouse linear speed toward the goal command speed V_G, which was expressed as

$$V_G = V_{min} + (V_{max} - V_{min})[(1 - L(d_G, \sigma_{TG}))A(\Delta\theta_G) + L(d_G, \sigma_{FG})A(\Delta\theta_G + \pi)]$$

where V_{min} was the mouse's minimal speed, d_G was the distance between the mouse's center and the goal objective point G,

$$\Delta\theta_G = \theta_V - \theta_G$$

the angular difference between the speed angle and $\theta_G = (\widehat{\overrightarrow{PG}, \vec{\imath}})$ the directional angle from the mouse to the goal objective.

Altogether, the term F_{V_G} modeled the propensity of the mouse to be driven by the goal command speed when 1) far from the goal objective position and facing it due to the $(1 - L(d_G, \sigma_{TG}))A(\Delta\theta_G)$ term, or 2) near to and moving from it due to the $L(d_G, \sigma_{FG})A(\Delta\theta_G + \pi)$ term. The scaling of linear tuning functions, when moving toward or away from the goal objective point, were determined by the σ_{TG} and σ_{FG} parameters, with $\sigma_{TG} < \sigma_{FG}$ so that navigation was faster when escaping a recently visited rewarded point. This hypothesis was necessary to escape repeating navigational loops of the mouse around (to and from) rewarded points in the arena.

The goal objective position G was determined through first-order dynamics of an instantaneous goal objective position G_i, the latter resulting from population coding of topographically-tuned excitatory neurons activity. Excitatory neurons each had a spatial receptive field (putatively arising from hippocampal place-cell inputs), the centers of the receptive fields being arranged along a 2D square grid (as in Figure 2d). G_i was then determined by each excitatory neuron voting for the distance from the center and the angle coordinates (within the unit circle) of its own spatial receptive field, their contributions being summed in proportion to a softmax function (with inverse temperature β) of the neurons' spiking frequencies (estimated through an exponential function with $\tau_F = 100ms$). The goal objective vector $\vec{G}$ thus followed

$$\frac{d\vec{G}}{dt} = \frac{\overrightarrow{G_\iota} - \vec{G}}{\tau_G}$$

with τ_G the time constant of goal objective position convergence to its instantaneous counterpart.

Evolution of mouse angular direction

The angular direction of the mouse evolved according to

$$\tau_{\theta_V} \frac{d\theta_V}{dt} = (1 - \frac{V}{V_{max}})(\mathrm{F}_{\theta_D} + \mathrm{F}_{\theta_G})$$

where $(1 - \frac{V}{V_{max}})$ expressed the fact that animals rotate slower when moving faster, and F_{θ_D} and F_{θ_G} represented the contributions of default and goal behaviors to the orientation of the mouse.

Rotation toward the default objective was governed by

$$\mathrm{F}_{\theta_D} = L(d_D, \sigma_D)\Delta\theta_D$$

so that rotational speed toward the default objective was larger when approaching the arena walls. This term ensured a progressive rotation of the mouse angle toward θ_T, i.e. the mouse aligned with the arena wall when it approached it (as $L(d_D, \sigma_D)$ increased to 1). Rotation of the mouse was essentially independent of the default behavior far from the wall, being instead mostly goal-directed with rotation toward the goal objective governed by

$$\mathrm{F}_{\theta_G} = A(\Delta\theta_G)\Delta\theta_G$$

so that rotational speed toward the goal objective vanished for a speed angle far away from (i.e. typically on the opposite direction of) θ_G, i.e. the mouse was essentially influenced by goals situated in its visual foreground landscape. This hypothesis, which expressed a visual gating of internally-guided behaviors, reduced the noise of goal-directed navigation but was not essential to the results.

Pause and redirection behaviors

The mouse had pause and redirection behaviors, occurring spontaneously (mostly at arena borders) and upon reward delivery, as observed empirically (Naudé et al., 2016). The time at which the mouse started a spontaneous pause was drawn at each time step dt with probability with $p_{Pause} = \frac{dt}{\tau_{Pause}} \frac{d_P}{r_{arena}}$, the latter term inducing higher pause probabilities when closer to the arena borders. Redirections of the mouse occurred at the end of pause episodes, by setting the new direction at an angle drawn from a von Mises distribution with mean θ_V and concentration $\kappa_{Pause\ Redir} = 0.83$ (i.e. with a circular standard deviation of $\frac{\pi}{4}$). In order to bias redirections towards the center of the arena when at the edges, directions were redrawn if they were not included within the half-circle centered on the arena center with random probability $p_{redraw} = L(d_D, \sigma_D)$ (closer to 1 as the mouse is closer to the edges). Reward delivery similarly induced a pause and redirection, but with a new direction at an

angle drawn from a von Mises distribution with mean $\theta_V + \pi$ (i.e. turning around) and concentration $\kappa_{Pause\ Reward} = 3.6$ (i.e. with a circular standard deviation of $\frac{\pi}{8}$). Mouse linear speed V_P was set at $\frac{V_{max}}{2}$ at the moment of redirection, simulating a strong starting speed impulse.

Spontaneous pauses and redirections, as well as reward redirections, occurred only during test trials (in order to allow a linear approach of the reward during learning trials, see below). Pauses were considered instantaneous in test trials (since they didn't meaningfully affect the results and allowed to save computational resources). However, reward pauses lasted 500ms during learning trials as observed experimentally (Naudé et al., 2016) since they did affect the results, allowing synaptic plasticity to affect mostly synapses in the vicinity of the reward in order for a local neuronal assembly to emerge.

Model of biophysical local recurrent neural network

We built a biophysical model of a prefrontal local recurrent neural network, endowed with detailed biological properties of its neurons and connections, based on (Sarazin et al., 2021).

The network model contained N neurons that were either excitatory (E) or inhibitory (I) (neurons projecting only glutamate or GABA, respectively; Dale, 1935), with probabilities p_E and $p_I = 1 - p_E$ respectively, and $p_E/p_I = 4$ (Beaulieu et al., 1992). Connectivity was sparse (i.e. only a random fraction of all possible connections exists, see $p_{E\to E}$, $p_{E\to I}$, $p_{I\to E}$, $p_{I\to I}$ parameter values; Thomson 2002) with no autapses (self-connections). The synaptic weights $w_{(i,j)}$ of existing connections were drawn identically and independently from a log-normal distribution of parameters μ_w and σ_w (Song et al., 2005).

To cope with simulation times required for the massive explorations ran in the parameter space, neurons were modeled as leaky integrate-and-fire (LIF) neurons. The membrane potential of neuron j followed

$$\begin{cases} C\dfrac{dV_{(j)}}{dt} = -(I_{L(j)} + I_{Syn.Rec(j)} + I_{Syn.FF(j)}) \\ V_{(j)} > \theta_{(j)} \rightarrow V_{(j)} = V_{rest} \end{cases}$$

where neurons spike when the membrane potential reaches the threshold θ_j, and repolarization to V_{rest} occurred after a refractory period Δt_{AP}.

The membrane potential threshold leading to action potential was adaptive in excitatory neurons, with a spike-induced instantaneous increase and exponential decrease between spikes, following

$$\frac{d\theta_{(j)}}{dt} = \frac{\theta_0 - \theta_{(j)}}{\tau_\theta} + \Delta\theta\ \delta\left(t - t_{(j)}\right)$$

where δ was the Dirac function and $t_{(j)}$ the times of APs (action potentials).

The leak current followed

$$I_{L(j)} = \bar{g}_L\left(V_{(j)} - V_L\right)$$

where $\bar{g}_L$ was the maximal conductance and V_L the equilibrium potential of the leak current.

The recurrent synaptic current on post-synaptic neuron j, from either excitatory or inhibitory pre-synaptic neurons (indexed by i), was

$$I_{Syn.Rec(j)} = \sum_i \left(I_{AMPA(i,j)} + I_{NMDA(i,j)} + I_{GABA_A(i,j)} + I_{GABA_B(i,j)}\right)$$

The delay for synaptic conduction and transmission, Δt_{syn}, was considered uniform across the network (Brunel and Wang, 2001). Synaptic recurrent currents followed

$$I_{x(i,j)} = \bar{g}_x\ w_{(i,j)}\ p_{x(i)}\left(V_{(j)} - V_x\right)$$

where $w_{(i,j)}$ was the synaptic weight, $p_{x(i)}$ the opening probability of channel-receptors and V_x the reversal potential of the current. The NMDA current followed

$$I_{NMDA(i,j)} = \bar{g}_{NMDA}\ w_{(i,j)}\ p_{NMDA(i)}\ x_{NMDA}\left(V_{(j)}\right)\left(V_{(j)} - V_{NMDA}\right)f_{DA}^{NMDA}$$

incorporating the magnesium block voltage-dependence modeled (Jahr and Stevens, 1990) as

$$x_{NMDA}(V) = \left(1 + [Mg^{2+}]e^{-0.062\,V}/3.57\right)^{-1}$$

while f_{DA}^{NMDA} represented the dopamine-dependent gating of NMDA conductance (see below).

AMPA and GABAA channel rise times were approximated as instantaneous (Brunel and Wang, 2001) and bounded, with first-order decay

$$\frac{dp_{x(i)}}{dt} = -\frac{p_{x(i)}}{\tau_x^{decay}} + \Delta p_x \left(1 - p_{x(i)}\right) \delta\left(t - t_{(i)}\right)$$

where $t_{(i)}$ represented the times of the pre-synaptic APs.

To take into account the longer NMDA (Wang et al., 2008) and GABAB (Destexhe et al., 1998) channel rise times, opening probabilities followed second-order dynamics (Brunel and Wang, 2001)

$$\begin{cases} \frac{dq_{x(i)}}{dt} = -\frac{q_{x(i)}}{\tau_x^{rise}} + \Delta q_x \left(1 - q_{x(i)}\right) \delta\left(t - t_{(i)}^k\right) \\ \frac{dp_{x(i)}}{dt} = -\frac{p_{x(i)}}{\tau_x^{decay}} + \alpha_x \, q_{x(i)} \left(1 - p_{x(i)}\right) \end{cases}$$

Recurrent excitatory and inhibitory currents were balanced on average in post-synaptic neurons (Xue et al., 2014) according to driving forces and excitation/inhibition weight ratio, through

$$\begin{cases} \bar{g}_{GABA_A} = g_{GABA_A} \dfrac{-(V_{mean} - V_{AMPA})}{(V_{mean} - V_{GABA_A})} \dfrac{p_{E\to X} \, N \, p_E}{p_{I\to X} \, N \, p_I} \\ \bar{g}_{GABA_B} = g_{GABA_B} \dfrac{-(V_{mean} - V_{AMPA})}{(V_{mean} - V_{GABA_B})} \dfrac{p_{E\to X} \, N \, p_E}{p_{I\to X} \, N \, p_I} \end{cases}$$

with $V_{mean} = (\theta_0 + V_{rest})/2$ being an approximation of the average membrane potential, and X the excitatory or inhibitory identity of the post-synaptic neuron receiving the inhibitory current.

The feed-forward synaptic current $I_{Syn.FF(j)}$ (putatively arising from sub-cortical and cortical inputs) consisted of an AMPA component

$$I_{Syn.FF(j)} = \bar{g}_{AMPA.FF} \, p_{AMPA.FF} \left(V_{(j)} - V_{AMPA}\right)$$

where $p_{AMPA.FF}$ was the sum of two components,

$$p_{AMPA.FF} = p_{Ext} + p_{FB}$$

The first, p_{Ext}, corresponded to network-wide AMPA input from external sources, and was described by the convolution of a normalized exponential kernel k_{Ext} with random variables drawn from the normal distribution $\sim\mathcal{N}(m_{Ext}, \sigma_{Ext})$ for every neuron and time bin, following

$$m_{Ext} = \Delta p_{AMPA.FF} \, n_{Ext} \, x_{Ext}$$

$$\sigma_{Ext} = \Delta p_{AMPA.FF} \sqrt{n_{Ext}\, x_{Ext}(1 - x_{Ext})}$$

$$k_{Ext} = \frac{e^{-\frac{t}{\tau_{AMPA}}}}{\int_0^{+\infty} e^{-\frac{t}{\tau_{AMPA}}}}$$

$$p_{Ext} = \mathcal{N}(m_{Ext},\, \sigma_{Ext}) * k_{Ext}$$

where n_{Ext} corresponded to the number of external neurons projecting onto the decision network and x_{Ext} the probability of them spiking within a given time bin.

The second, p_{FB}, corresponded to the (putatively hippocampal) position feedback (Fig.2a), with each neuron *j* receiving AMPA input proportional to the activation $k_{FB}\ (j)$ of their spatial receptive field equivalent. Receptive fields' activation function are modeled as bivariate normal distributions centered on the receptive field center $(X_{RF\ (j)}, Y_{RF\ (j)})$. As such, p_{FB} followed

$$k_{FB\ (j)} = \frac{1}{\sqrt{2\pi}\,\sigma_{RF}} e^{-\frac{1}{2}\left(\frac{\left(X_P - X_{RF\ (j)}\right)^2 + \left(Y_P - Y_{RF\ (j)}\right)^2}{\sigma_{RF}^2}\right)}$$

$$p_{FB} = k_{FB}\, x_{FB}$$

where σ_{FB} represents the spatial width of receptive fields, (X_P, Y_P) the spatial position of the mouse in the arena at time t, and x_{FB} a constant factor.

Spike Timing-Dependent Plasticity (STDP) plasticity

In this model, the excitatory synapses were subjected to a dopamine-modulated spike timing-dependent (STDP) plasticity rule, where potentiation and depression depends upon the relative timing of pre- and post-synaptic activity, with pre-then-post (post-then-pre) activity leading to potentiation (depression). Coincident spiking activity did not not immediately translate into synaptic changes, but rather into synaptic tags, called eligibility traces (Sutton and Barto, 1998), which were read out at the time of dopamine release (Izhikevich, 2007). Eligibility traces are known to perform distal-credit assignment: only connections between neurons that were activated when the animal aimed for reward are modified, and coincident activity outside the reward aiming behavior left corresponding weights unchanged.

More precisely, coincident presynaptic and postsynaptic activities were detected by NMDA receptors (NMDA-R), which were activated by concomitant glutamate release and postsynaptic depolarization (see above). Calcium-dependent kinases and phosphatases competed for the phosphorylation of early LTP (eLTP) and early LTD (eLTD) synaptic tags (Figure 2a). Experimental data suggest the existence of distinct eLTP and eLTD traces (He et al., 2015), which are furthermore needed for the overall potential synaptic changes to become positive or negative. eLTP and eLTD tags formed traces that were short-lived: they decayed to a non-phosphorylated state if not stabilized by a second event that consolidated the early plasticity. This second event may be the release of a neuromodulator (He et al., 2015), dopamine in the present model. Dopamine, through activation of D1 receptors (D1R), activated another kinase-phosphatase couple that gated the eligibility traces into an increase or decrease in the number of NMDAR at the synapse (Fig. 2a). In terms of biochemical implementation, calcium-dependent CAMKinase II and calcineurin phosphatase have been suggested to participate in early LTP/LTD traces, putatively competing for the phosphorylation of an ERK tag (Frémaux and Gerstner, 2016; Okuda et al., 2020), which would decay if not reinforced by neuromodulators. D1R, through an increase of cAMP, would activate the protein kinase A, translating pERK into changes in glutamate receptors (e.g. through CREB-induced protein synthesis).

As such, the weight $w_{(i,j)}$ evolved according to the dopaminergic gating of kinase/phosphatase cycles under the control of distinct e_{LTP} and e_{LTD} eligibility traces (He et al., 2015), following

$$\frac{dw_{(i,j)}}{dt} = f_{DA}^{STDP}\left(K_w^{max}\frac{e_{LTP}(Ca)^{nH}}{{K_w}^{nH} + e_{LTP}(Ca)^{nH}} - P_w^{max}\frac{e_{LTD}(Ca)^{nH}}{{P_w}^{nH} + e_{LTD}(Ca)^{nH}}w_{(i,j)}\right)$$

Here, K_w^{max} represented the maximum reaction rate of the kinase, P_w^{max} that of the phosphatase, K_w and P_w the half-activation values, Ca the synaptic calcium concentration and nH is the Hill's coefficient. The kinase-related t-LTP term was independent of synaptic weight ("additive" t-LTP) while the phosphatase-related t-LTD term was weight-proportional ("multiplicative" t-LTD), consistent with the literature (Bi and Poo, 1998; van Rossum et al., 2000). Weight dynamics were gated by f_{DA}^{STDP}, representing the level of dopamine-dependent PKA activation (see below).

The distinct e_{LTP} and e_{LTD} eligibility traces themselves followed first-order dynamics with intra-synaptic calcium-dependent kinase/phosphatase cycles, where

$$\frac{de_{LTP}}{dt} = K_{LTP}^{max} \frac{Ca^{nH}}{{K_{LTP}}^{nH} + Ca^{nH}} (1 - e_{LTP}) - P_{LTP}^{max} \frac{Ca^{nH}}{{P_{LTP}}^{nH} + Ca^{nH}} e_{LTP}$$

$$\frac{de_{LTD}}{dt} = K_{LTD}^{max} \frac{Ca^{nH}}{{K_{LTD}}^{nH} + Ca^{nH}} (1 - e_{LTD}) - P_{LTD}^{max} \frac{Ca^{nH}}{{P_{LTD}}^{nH} + Ca^{nH}} e_{LTD}$$

The eligibility traces were considered distinct since LTP and LTD traces have different dynamics and can be activated by different monoamines (e.g. NE for LTP and 5-HT for LTD, He et al., 2015).

The dependence of the synaptic plasticity rule upon AP times (Bi and Poo, 1998; He et al., 2015) came from calcium dynamics, according to the models of (Graupner and Brunel, 2012; Sarazin et al., 2021). In this model, synaptic calcium followed

$$Ca = Ca_0 + Ca_{pre} + Ca_{post}$$

where the total calcium concentration took into account pre- and post-synaptic calcium contributions.

Pre-synaptic spiking mediated calcium dynamics followed

$$\frac{dCa_{pre}}{dt} = -\frac{Ca_{pre}}{\tau_{Ca}} + \Delta Ca_{pre} \sum_i \delta\left(t - t_{(i)} - t_D\right)$$

where the first term corresponded to calcium extrusion/buffering with time constant τ_{Ca} and the second term to VDCC-mediated calcium entry due to pre-synaptic spiking, with ΔCa_{pre} the amplitude of calcium entering at each AP of the presynaptic neuron, $t_{(i)}$ the times of the pre-synaptic APs, and t_D a delay modeling the time required for the activation of AMPA channels, the depolarizing rise of the associated excitation post-synaptic potential (EPSP) and the subsequent opening of voltage-dependent calcium channels (VDCC) that induces this calcium entry.

Post-synaptic spiking-mediated calcium dynamics evolved according to

$$\frac{dCa_{post}}{dt} = -\frac{Ca_{post}}{\tau_{Ca}} + \Delta Ca_{post} \sum_j \delta\left(t - t_{(j)}\right) + \xi_{PrePost} \sum_j \delta\left(t - t_{(j)}\right) Ca_{pre}$$

and modeled extrusion/buffering (first-term) as well as calcium entries due to post-synaptic, back-propagated spiking from the post-synaptic soma along the dendritic tree to the

synapse, opening VDCC (central term) and NMDA channels (right term). $\xi_{PrePost}$ was an interaction coefficient and $t_{(j)}$ corresponded to AP times of the post-synaptic neuron. NMDA activation was non-linear and depended on the product of a pre- and a post-synaptic term, representing the dependence of NMDA channel openings on the associative conjunction of pre-synaptic glutamate and post-synaptic depolarization, which releases the magnesium blockade of NMDA channels.

Dopamine dynamics

Dopamine concentration followed second-order dynamics

$$\frac{dq_{DA}}{dt} = -\frac{q_{DA}}{\tau_{DA}^{rise}} + \delta(t - t_{DA})$$
$$\frac{dp_{DA}}{dt} = \frac{-p_{DA} + p_{DA}^{max} q_{DA}}{\tau_{DA}^{decay}}$$
$$x_{DA} = x_{DA}^{min} + p_{DA}$$

where τ_{DA}^{rise} and τ_{DA}^{decay} capture the slow rise and decay time constants of dopamine released at time t_{DA} in the network following reward, x_{DA}^{min} the minimum dopamine concentration, and p_{DA}^{max} chosen such that dopamine concentration peaks at x_{DA}^{peak} after a single reward-induced dopamine release.

Dopaminergic neuromodulation gated NMDA conductance (Chen et al., 2004) and synaptic plasticity through D1R, and equally affected all synapses of the network, corresponding to diffuse VTA dopamine input. NMDA conductance gating followed

$$f_{DA}^{NMDA} = f_{DA}^{NMDA}{}_{min} + (f_{DA}^{NMDA}{}_{min} - f_{DA}^{NMDA}{}_{max}) \frac{1}{1 + e^{-(x_{DA} - x_{DA}^{NMDA})/k_{DA}^{NMDA}}}$$

where $f_{DA}^{NMDA}{}_{min}$ and $f_{DA}^{NMDA}{}_{max}$ corresponded to the function's minimum and maximal values, and x_{DA}^{NMDA} and k_{DA}^{NMDA} the half-activation and inverse slope of the sigmoid function.

Similarly, synaptic plasticity gating followed

$$f_{DA}^{STDP} = \frac{1}{1 + e^{-(x_{DA} - x_{DA}^{STDP})/k_{DA}^{STDP}}}$$

where x_{DA}^{STDP} and k_{DA}^{STDP} represented the half-activation and inverse slope of the sigmoid function.

For simplicity purposes, dopamine gating of NMDA conductance and synaptic plasticity were separated into learning (synaptic plasticity gating only) and test (NMDA conductance gating only) trials (see below).

Learning and test trials

Animal learning was cut into 300 learning trials of 2 seconds each, where the mouse started at a fixed distance (0.75 times the arena size) and random angle from the center while facing the center, and converged in a straight line towards the center of the reward circle (of radius r_{reward}). Dopamine was released in the network when the mouse obtained the reward, i.e. entered the reward circle, leading to translation of synaptic eligibility traces into effective long-term consolidation. 20 test trials of 3 seconds each were conducted every 15 learning trials to evaluate the effect of synaptic plasticity on animal convergence towards the reward, with the mouse's position being similarly initialized. Networks were initialized with randomized membrane potentials (uniformly distributed between θ_0 and $\theta_0 - 5$) and synaptic channel openings mimicking average channel openings (p_{AMPA}~0.0025, p_{NMDA}~0.2, p_{GABA_A}~0.0025, p_{GABA_B}~0.15).

Procedures and parameters

Models were simulated and explored using custom developed code under MATLAB and were numerically integrated using the forward Euler method with time-step $\Delta t = 1ms$ in network models. Unless indicated in the text, standard parameter values were as following. Concerning mouse locomotion, $\tau_V = 500\ ms, \tau_{\theta_V} = 50\ ms, V_{max} = 1\ m/s, V_{min} = 0.1\ m/s$, $r_{arena} = 0.5\ m$, $r_{mouse} = 0.03\ m$, $\sigma_D = 0.025\ m$, $\sigma_{TG} = 0.1\ m$, $\sigma_{FG} = 0.2\ m$, $\tau_G = 20\ ms$, $\beta = 1$, $\tau_{pause} = 1\ s$, $r_{reward} = 0.05\ m$. Concerning the network architecture, $N = 500\ neurons$, $p_E = 0.8$, $p_I = 0.2$, $p_{E\to E} = p_{E\to I} = p_{I\to E} = p_{I\to I} = 0.25$, $\mu_w = 0.03$, $\sigma_w = 0.02$. Concerning the Integrate-and-Fire neural properties, $C = 1\ \mu F.cm^{-2}$, $\theta_0 = -50\ mV$, $\Delta\theta = 5\ mV$, $\tau_\theta = 5\ ms$, $V_{rest} = -60\ mV$, $\Delta t_{AP} = 1\ ms$. Concerning currents, $\bar{g}_L = 0.05\ mS.cm^{-2}$, $V_L = -70\ mV$, $\Delta t_{syn} = 1\ ms$, $\bar{g}_{AMPA} = 0.02\ mS.cm^{-2}$, $\bar{g}_{NMDA} = 0.155\ mS.cm^{-2}$, $g_{GABA_A} = 0.02\ mS.cm^{-2}$, $g_{GABA_B} = 0.001\ mS.cm^{-2}$, $V_{AMPA} = V_{NMDA} = 0\ mV$, $V_{GABA_A} = -70\ mV$, $V_{GABA_B} = -90\ mV$, $[Mg^{2+}] = 1.5\ mM$, $\tau_{AMPA}^{decay} = 2.5\ ms$, $\tau_{NMDA}^{decay} = 75\ ms$, $\tau_{GABA_A}^{decay} = 10\ ms$, $\tau_{GABA_B}^{decay} = 160\ ms$, $\alpha_{NMDA} = 0.275\ ms^{-1}$, $\tau_{NMDA}^{rise} = 4.65\ ms$, $\alpha_{GABA_B} = 0.015\ ms^{-1}$, $\tau_{GABA_B}^{rise} = 90\ ms$, $\bar{g}_{AMPA.FF} = 0.2\ mS.cm^{-2}$, $n_{Ext} = 30\ neurons$, $x_{Ext} = 0.025$, $\Delta p_{AMPA} = \Delta q_{NMDA} = \Delta p_{GABA_A} = \Delta q_{GABA_B} = \Delta p_{AMPA.FF} = 0.1$,

$\sigma_{RF} = 0.1\,m$, $x_{FB} = 0.01$. Concerning synaptic properties, $K_w^{max} = P_w^{max} = 10^{-3}\,ms^{-1}$, $K_w = P_w = 0.25$, $K_{LTP}^{max} = P_{LTP}^{max} = K_{LTD}^{max} = P_{LTD}^{max} = 2.5 \cdot 10^{-4}\,ms^{-1}$, $K_{LTP} = 0.5379\,\mu M$, $P_{LTP} = 0.165\,\mu M$, $K_{LTD} = 0.3\,\mu M$, $P_{LTD} = 0.1\,\mu M$, $nH = 4$, $Ca_0 = 0.1\,\mu M$, $\tau_{Ca} = 400\,ms$, $\Delta Ca_{pre} = \Delta Ca_{post} = 0.005\,\mu M$, $t_D = 10\,ms$, $\xi_{PrePost} = 4$. Concerning reward and dopamine properties, $x_{DA}^{min} = 0.1$, $x_{DA}^{peak} = 0.25$, $\tau_{DA}^{rise} = 100\,ms$, $\tau_{DA}^{decay} = 500\,ms$, ${f_{DA}^{NMDA}}_{min} = 0.1$, ${f_{DA}^{NMDA}}_{min} = 0.5$, $x_{DA}^{NMDA} = 0.15$, $k_{DA}^{NMDA} = 0.01$, $x_{DA}^{STDP} = 0.25$, $k_{DA}^{STDP} = 0.025$.

Statistical analysis

All statistical analyses were computed using Matlab (the Mathworks). Results were plotted as a mean ± s.e.m. The total number (n) of observations in each group and the statistics used are indicated in figure legends. Classical comparisons between means were performed using parametric tests (Student's T-test, or ANOVA for comparing more than two groups) when parameters followed a normal distribution (Shapiro test P > 0.05), and non-parametric tests (here, Wilcoxon or Mann-Whitney) when the distribution was skewed. Multiple comparisons were Bonferroni corrected. Probability distributions were compared using the Kolmogorov–Smirnov (KS) test.

REFERENCES FOR THE METHODS

Aurnhammer, C., Haase, M., Muether, N., Hausl, M., Rauschhuber, C., Huber, I., et al. (2012). Universal Real-Time PCR for the Detection and Quantification of Adeno-Associated Virus Serotype 2-Derived Inverted Terminal Repeat Sequences. *Hum. Gene Ther. Methods* 23, 18–28. doi:10.1089/hgtb.2011.034.

Beaulieu, C., Kisvarday, Z., Somogyi, P., Cynader, M., and Cowey, A. (1992). Quantitative distribution of gaba-immunopositive and -immunonegative neurons and synapses in the monkey striate cortex (area 17). *Cereb. Cortex* 2, 295–309. doi:10.1093/cercor/2.4.295.

Bi, G. Q., and Poo, M. M. (1998). Synaptic modifications in cultured hippocampal neurons: dependence on spike timing, synaptic strength, and postsynaptic cell type. *J. Neurosci. Off. J. Soc. Neurosci.* 18, 10464–10472. doi:10.1038/25665.

Brunel, N., and Wang, X. J. (2001). Effects of neuromodulation in a cortical network model of object working memory dominated by recurrent inhibition. *J. Comput. Neurosci.* 11, 63–85. doi:10.1023/A:1011204814320.

Chen, G., Greengard, P., and Yan, Z. (2004). Potentiation of NMDA receptor currents by

dopamine D1 receptors in prefrontal cortex. *Proc. Natl. Acad. Sci.* 101, 2596–2600. doi:10.1073/pnas.0308618100.

Choi, V. W., Asokan, A., Haberman, R. A., and Samulski, R. J. (2007). Production of Recombinant Adeno-Associated Viral Vectors for In Vitro and In Vivo Use. *Curr. Protoc. Mol. Biol.* 78, 16.25.1-16.25.24. doi:10.1002/0471142727.mb1625s78.

Dale, H. (1935). Pharmacology and Nerve-endings (Walter Ernest Dixon Memorial Lecture): (Section of Therapeutics and Pharmacology). *Proc. R. Soc. Med.* 28, 319–332.

Destexhe, A., Mainen, Z. F., and Sejnowski, T. J. (1998). Kinetic models of synaptic transmission. *Methods Neuronal Model.* 2, 1–25.

Frémaux, N., and Gerstner, W. (2016). Neuromodulated Spike-Timing-Dependent Plasticity, and Theory of Three-Factor Learning Rules. *Front. Neural Circuits* 9. doi:10.3389/fncir.2015.00085.

Graupner, M., and Brunel, N. (2012). Calcium-based plasticity model explains sensitivity of synaptic changes to spike pattern, rate, and dendritic location. *Proc. Natl. Acad. Sci.*, 201109359. doi:10.1073/pnas.1109359109.

He, K., Huertas, M., Hong, S. Z., Tie, X., Hell, J. W., Shouval, H., et al. (2015). Distinct Eligibility Traces for LTP and LTD in Cortical Synapses. *Neuron* 88, 528–538. doi:10.1016/j.neuron.2015.09.037.

Izhikevich, E. M. (2007). Solving the distal reward problem through linkage of STDP and dopamine signaling. *Cereb. Cortex* 17, 2443–2452. doi:10.1093/cercor/bhl152.

Jahr, C. E., and Stevens, C. F. (1990). Voltage dependence of NMDA-activated macroscopic conductances predicted by single-channel kinetics. *J. Neurosci. Off. J. Soc. Neurosci.* 10, 3178–3182.

Khabou, H., Garita-Hernandez, M., Chaffiol, A., Reichman, S., Jaillard, C., Brazhnikova, E., et al. (2018). Noninvasive gene delivery to foveal cones for vision restoration. *JCI Insight* 3, 96029. doi:10.1172/jci.insight.96029.

Naudé, J., Tolu, S., Dongelmans, M., Torquet, N., Valverde, S., Rodriguez, G., et al. (2016). Nicotinic receptors in the ventral tegmental area promote uncertainty-seeking. Nat Neurosci 19, 471–478. doi:10.1038/nn.4223.

Okuda, K., Højgaard, K., Privitera, L., Bayraktar, G., and Takeuchi, T. (2020). Initial memory consolidation and the synaptic tagging and capture hypothesis. *Eur. J. Neurosci.* doi:10.1111/ejn.14902.

Sarazin, M. X. B., Victor, J., Medernach, D., Naudé, J., and Delord, B. (2021). Online Learning and Memory of Neural Trajectory Replays for Prefrontal Persistent and Dynamic Representations in the Irregular Asynchronous State. *Front. Neural Circuits* 0. doi:10.3389/fncir.2021.648538.

Song, S., Sjöström, P. J., Reigl, M., Nelson, S., and Chklovskii, D. B. (2005). Highly

Nonrandom Features of Synaptic Connectivity in Local Cortical Circuits. *PLOS Biol.* 3, e68. doi:10.1371/journal.pbio.0030068.

Sutton, R. S., and Barto, A. G. (1998). *Reinforcement Learning: An Introduction*. doi:10.1109/TNN.1998.712192.

Thomson, A. M. (2002). Synaptic Connections and Small Circuits Involving Excitatory and Inhibitory Neurons in Layers 2-5 of Adult Rat and Cat Neocortex: Triple Intracellular Recordings and Biocytin Labelling In Vitro. *Cereb. Cortex* 12, 936–953. doi:10.1093/cercor/12.9.936.

Todorov, E. (2002). Cosine Tuning Minimizes Motor Errors. Neural Computation 14, 1233–1260. doi:10.1162/089976602753712918.

van Rossum, M. C., Bi, G. Q., and Turrigiano, G. G. (2000). Stable Hebbian learning from spike timing-dependent plasticity. *J. Neurosci. Off. J. Soc. Neurosci.* 20, 8812–8821. doi:20/23/8812 [pii].

Wang, H., Stradtman, G. G., Wang, X.-J., and Gao, W.-J. (2008). A specialized NMDA receptor function in layer 5 recurrent microcircuitry of the adult rat prefrontal cortex. *Proc. Natl. Acad. Sci.* doi:10.1073/pnas.0804318105.

Xue, M., Atallah, B. V., and Scanziani, M. (2014). Equalizing excitation–inhibition ratios across visual cortical neurons. *Nature* 511, 596–600. doi:10.1038/nature13321.

Chapter 8. Discussion

This thesis has demonstrated how conditionally bistable intrinsic currents, slow or tonic inhibition and slow excitation increase the reliability of stable and dynamic attractors (or mixtures of both) at the neuronal and network level in frontal circuits, in the context of chaotic noise that characterizes awake cortical dynamics. These attractors emerge from non-learned random synaptic connectivity matrices, inhibitory anti-Hebbian assemblies and anti-synaptic chains (pathways), or excitatory Hebbian assemblies and synaptic chains learned through detailed biophysical models of calcium-mediated and dopaminergic-gated STDP.

8.1. Mechanisms promoting the emergence of reliable attractors

8.1.1. Macroscopic gradients of interneuron proportions

Based upon experimental observations of an increasing gradient of dendritic spines numbers on pyramidal neurons (Elston, 2007; Wang, 2020) and slower NMDA currents (Wang, 2020), previous research has modeled longer neuronal timescales within the cortical hierarchy as stronger and slower excitation (Chaudhuri et al., 2015), even though proportionally stronger inhibitory currents are required to balance the effects of excitation positive feedback loops (i.e. extinction or saturation of activity) and reinforce physiological bistability (Joglekar et al., 2018). Accordingly, they do not account for the macroscopic gradient of interneuron proportions (i.e. more SST+/CB+ and VIP+/CR+ interneurons in frontal areas; Torres-Gomez et al., 2020; Wang, 2020), nor the stronger and slower inhibitory currents in MCC (vs. LPFC lower in the cortical hierarchy, Medalla et al., 2017). Chapter 3 and 4 give meaning to these observations, by proposing that long neuronal timescales or bursting neural activity, peregrination between stable discrete states, and even neural sequences – which are all essential for the operation of executive functions in frontal circuits – emerge through inhibitory intrinsic (AHP) and strong slow synaptic (GABA-B) currents, the latter amplifying the effect of synaptic heterogeneity on global network activity. Such amplification could notably implement the temporal integration of reward-action outcome history at multiple timescales, as well as evaluation of and switches between behavioral strategies, both functions associated with the MCC.

Excitatory- or inhibitory-based gradient alternatives are not exclusive, as they concern distinct synapses ($Exc. \rightarrow Exc.$ vs. $Inh. \rightarrow Exc./Inh.$), the combination of both allowing maximum expression of network dynamics and storage capacity (Mongillo et al., 2018). These hypotheses seem actually rather complementary, as strong inhibition may gate multimodal integration of diverse information provided through excitatory inputs (proposed in Chapter 4). Indeed, VIP+/CR+ interneurons are known to inhibit specific SST+/CB+ neurons, which themselves selectively inhibit pyramidal dendrites, allowing flexible pathway gating of excitatory inputs through disinhibitory motifs (Wang and Yang, 2018). Furthermore, activation of VIP cells in dorsomedial frontal cortex has been shown to enhance working memory retention

and selectivity of pyramidal cell activity to specific stimuli (Kamigaki and Dan, 2017). This tells us that disinhibition is crucial in separating pyramidal sustained delay activity to different stimuli, and more generally that inhibitory to inhibitory connectivity contributes to disentangling activity of assemblies.

Nonetheless, the aforementioned macroscopic gradients do not specify the proportions of neurogliaform (NGF) cells (5HT3aR+ but VIP-, Rudy et al., 2011), which connect to different types of interneurons and are an important locus of GABA-Bergic synaptic transmission in mouse primary somatosensory cortex (S1) (Rudy et al., 2011). Furthermore, the MCC model in Chapter 3 assumes all interneurons have strong GABA-B synaptic transmission, whereas NGF cells represent 15% of neurons in mouse S1 (Rudy et al., 2011). As such, further modeling work is required to confirm whether small proportions of neurons projecting strong GABA-B currents can similarly result in long timescales, network states and neuronal sequences. Injecting a GABA-B antagonist during tasks requiring temporal integration of reward outcomes over long periods of time while recording MCC neural activity would also help confirm the role of GABA-B currents in generating long neuronal autocorrelogram timescales.

8.1.2. Inhibitory currents, assemblies and sequences

We were surprised to discover in Chapter 4's additional results indicating that slow GABA-B inhibition amplified the effect of synaptic heterogeneity on network activity such that we could backtrack unprecedented synaptic architectures in the cortex (inhibitory anti-assemblies and synaptic chains; but see Ponzi and Wickens, 2010, in a very different anatomical (striatum) and functional context), from their resulting network dynamics (persistent activity and sequence propagation, respectively) in randomly organized synaptic matrices. To our knowledge, such a level of organizational complexity of network dynamics is without equivalent, with network collective activity peregrinating according to three nested levels of dynamical organization : 1) meta-states combining states, 2) elementary states themselves, and 3) persistent or sequential spatiotemporal spiking patterns within states. Remarkably, this highly structured dynamics emerged without any form of artificial or realistic plasticity rule, whether at the intrinsic or synaptic level.

Retrospectively, such a powerful role of GABA-B makes sense, since the lower number of inhibitory neurons and projecting synapses result in more pronounced effects of interneuron activity on network dynamics (comparatively to 4x more numerous and thus diffuse effect of excitatory neurons and synapses on network activity). This hints at the idea that the less investigated and theoretically described inhibitory synaptic plasticity, beyond simply a balancing role (Vogels et al., 2013; Froemke, 2015; Hennequin et al., 2017), might underpin network attractor behavior.

Inhibitory currents can also promote reliable attractors emerging through excitatory synaptic engrams. Indeed, Chapter 5 demonstrates that tonic increase of inhibitory frequency or slower inhibitory currents onto excitatory neurons (when paired with stronger excitatory connectivity) increases the stability and controllability (i.e. the capacity to replay sequences only after an initial trigger) of learned excitatory sequences, thus representing biophysical mechanisms that increase reliable attractor emergence. The identification of these mechanisms comes from a theoretical understanding of the two activity regimes defining pack propagation

and resting-state activity, namely strong excitatory NMDA average-driven spiking and disinhibitory GABA-A current fluctuations-driven spiking respectively. Theoretically, this can be simply understood as bistable frequency dynamics, where excitatory frequency amplifies into pack propagation above a frequency threshold and decreases until it reaches resting-state activity below the threshold. In conjunction with STDP modulation and discrete or static presentation stimuli, these mechanisms allow reliable emergence of many different types of attractors, be they static/dynamic, discrete/continuous and uni-bidirectional (e.g. Hebbian assembly, synfire chain, Hebbian phase sequence, ring attractors). As such, inhibitory currents represent a generic mechanism promoting reliable emergence of a wide spectrum of attractor types, potentially present across cognitive structures and functions.

While it is tempting to conclude that the generic inhibition-based mechanisms of Chapter 5 and slow GABA-B inhibition of Chapter 3-4 bear the same consequences, the tonic increase of inhibition acts to stabilize and decrease excitatory activity outside of pack propagation, whereas slow GABA-B inhibition precisely induces temporally-heterogeneous high frequency activity such as inhibitory sequences. In other words, while assembly activation or sequence propagation is supported by slow NMDA currents in excitatory assemblies or synaptic chains and dampened by tonic inhibition, assembly activation or sequence propagation results from slow GABA-B current disinhibition in inhibitory anti-assemblies or -synaptic chains. Both thus have similar effects *in fine* but by different means, the control of excitatory synaptic structures vs inhibitory-based synaptic structures. As such, strong GABA-B-induced currents precisely leads to spontaneous sequence replay, drastically decreasing controllability of trajectory replay without biophysical mechanisms to dampen such uncontrolled replay.

Accordingly, transitions between stable network states in monkey frontal areas (putatively GABA-B-mediated, as suggested in Chapter 3), and dynamic network states containing RS activity sequences in mouse mPFC (putatively NMDA-mediated) during working memory might be similarly inhibition-induced. Indeed, interneuron spike bursts (LFP beta-band) occur briefly before those of pyramidal neurons in LPFC and ACC when macaques shift from non-selective to selective attentional stable states during a working memory task (~10ms before, Womelsdorf et al., 2014). This is reminiscent of context switching between different RS neuronal sequences (possibly each contained within a network state) during working memory in mouse mPFC, promoted by mediodorsal thalamic activation of cortical inhibition (Rikhye et al., 2018). This suggests a common role for inhibition as inducing transitions between network states, potentially via GABA-B also in mouse mPFC.

8.1.3. Generic role of intrinsic bistability in prefrontal dynamics

Chapter 2 shows that in a layer 5 PFC pyramidal neuron model, spike-mediated CAN and CaL intrinsic currents promote conditional bistability (CB), i.e. where persistent activity after an initial cue event is conditional upon depolarizing current (or, more directly, depolarized membrane potential) during the delay period. This is in contrast to absolute bistability (AB), in which persistent activity only requires the initial cue and is strongly stereotyped (highly regular spiking). CB, representing a weaker form of bistability compared to AB, paradoxically allows a

richer dynamical repertoire, with persistent activity being stable yet sufficiently labile to support PFC network states transitions for elaborating adaptive working memory-related cognitive processes (Abeles et al., 1995; Seidemann et al., 1996; Cossart et al., 2003).

This same weak bistability could also help temporarily stabilize sequences of neural activity, with stable firing being conditional on subliminal input from vanishing activities of previous neurons in the sequence. Indeed, Chapter 5 shows that, in addition to slow synaptic current dynamics (NMDA, GABA-B) and tonic inhibition, sequence propagation is stabilized through intrinsic currents promoting intrinsic transient bistability (i.e. intrinsic bistability induced transiently, during the hundreds of milliseconds in which the previous excitatory neurons of the sequence fire many action potentials at the next neurons). Furthermore, amongst the other mechanisms, CAN and AHP currents was the only mechanism allowing excitatory network activity to be unaffected by trajectory replay (*independence*), allowing parallel computations (e.g. multiple simultaneous trajectory replay).

Finally, the LPFC and MCC models of Chapter 3-4 also required AHP currents, supporting GABA-B currents by decreasing short states (and thus increasing the duration of network states), and CAN currents, counterbalancing the strong GABA-B- and AHP-mediated frequency decrease. Such versatile functionality hints at the importance of assessing the interaction between intrinsic and synaptic properties for reliable emergence of attractors, alleviating the constraints ensuring attractor stability from depending solely on synaptic currents and engrams (Compte, 2006), ultimately enriching the computational capacities of neurons and networks.

8.1.4. Alternative mechanisms and improvements

Beyond inhibitory and intrinsic currents, what other mechanisms promote reliability and stability of static or dynamic attractors within synaptic noise? One of the shortcomings of the current model is the lack of description of dendritic compartments. Computations using dendritic compartments have been shown to allow supra-linear integration of synaptic inputs (Cazé et al., 2013; Tran-Van-Minh et al., 2015), amplifying EPSPs evoked by action potential coincidence, thus further separating the low frequency asynchronous irregular regime and high frequency synchronous activity induced by sequence stimulus and replay. Furthermore, dendritic membrane potential inflections due to backward-propagating dendritic spikes (such as in HP, Jarsky et al., 2005) represent a more direct biophysical substrate for STDP (instead of calcium, Graupner and Brunel, 2012), removing the magnesium block in NMDA receptors via strong depolarization and thus inducing LTP. The thesis neuronal model is iso-potential, potentially cutting short dendritic membrane potential and NMDA depolarization. Finally, recruitment of distinct dendrites performing spatial summation of synaptic inputs may allow further discrimination between multiple sequences or more complex population trajectories, potentially solving the question raised above.

Additionally, short-term plasticity, in which synapses connecting bursting neurons undergo facilitation, can promote more reliable network states and sequences. Similar to before, short-term facilitation potentiates synapses on a short timescale (hundreds of milliseconds), allowing supra-linear EPSP temporal summation during high frequency pre-synaptic activity. In line with this idea, reliable reactivation of stable representations stored within short-term plasticity hidden variables during dynamic neural activity has been proposed (Barak et al., 2010; Stokes et

al., 2013; Stokes, 2015), and observed for rat mPFC neural activity sequences (Fujisawa et al., 2008).

8.2. Learning reliable attractors

8.2.1. Learning working memory and navigational sequences

While the aforementioned mechanisms explain how attractors can be replayed in the absence of learning or once learned, they do not describe the conditions underlying reliable learning of such attractors during noisy synaptic activity. Chapter 6 describes how neural activity sequences are learned through STDP and replay during network AI activity, whose disordering influence potentially jeopardizes learning, replay and memory maintenance of trajectories (in contrast to Chapter 5, which used a phenomenological STDP rule "offline", i.e. not during network AI activity). STDP results from non-linear spike-mediated calcium-based activation of kinase-phosphatase couples, the non-linear activation dynamics inducing rapid learning of the sequence through a single stimulus presentation while guaranteeing slow synaptic chain forgetting (~2h) during network resting-state activity (preserving AI dynamics). Furthermore, the stimulus could be iteratively learned through overlapping fragmented chunks (as for navigational HP trajectories, Buzsáki and Moser, 2013).

However, while the current thesis focuses on learned neuronal sequences, several lines of evidence point to navigational sequences pre-existing and being repurposed by behavior (Buhry et al., 2011), with sequential activity during SWS or awake rest occurring before animals are exposed to novel environments or representing trajectories never experienced by the animal. It is possible that the former sequences subserve other representations than navigational trajectories but co-occur with them, while the latter sequences might correspond to trajectories learned outside of the experimental setup, questioning the exact nature of navigational trajectory learning. Interestingly, the sequences arising within states (additional results of Chapter 4) could form the neural basis of such pre-existing trajectories (as a form of "dynamical whiteboard") that can be repurposed by learning. Furthermore, while navigational sequences are characterized by straightforward sequential stimuli during behavioral runs, i.e. presentation-based learning which we extensively model in Chapter 5 and 6, working memory and cortical slice sequences might arise simply from repetition of the initial trigger, where the synaptic chain beyond the initial neurons is iteratively built through repeated stimulation of initial neurons, i.e. trigger-based learning, questioning the exact nature of working memory sequence learning.

It is less clear how STDP rules during AI network activity could induce synaptic chains based upon multiple repetitions of an initial trigger stimulus. Models that have achieved trigger-based learning lack AI activity (Liu and Buonomano, 2009). In contrast, within the calcium-based STDP concomitant to AI activity of Chapter 6, such repetition of high frequency stimuli can simply lead to paroxysmal activity. However, even with slower plasticity, the unidirectional plasticity rule would need to associate pre-synaptic high-frequency with post-synaptic low-frequency neurons (instead of high-frequency neurons together only). Each trigger repetition of the initial neurons would induce potentiation in a large proportion of outgoing synapses, affecting different

proportions of synapses according to which post-synaptic neurons happen to fire. Competition of outgoing synapses, e.g. via synaptic scaling of outgoing synapses, would allow progressive selection of specific neurons as the next steps of the synaptic chain (Liu and Buonomano, 2009; Fiete et al., 2010), although the biological realism of such meta-plasticity remains to be determined. The chosen parameters for the calcium-based learning rule of Chapter 6 do not allow such learning, due to its strongly non-linear hetero-associative nature, guaranteeing strong potentiation of synapses only between neurons strongly co-active. Going further, such a learning rule should instead solely potentiate synapses between a neuron with high and another with low frequency – which is non-sensical since NMDA-mediated LTP detects coincident strong firing –, or include stronger multiplicative LTD, in order to avoid paroxysmal activity. Finally, the resulting synaptic chain might be much more complex than a sequence, potentially leading to tree-like synaptic structures, i.e. multiple progressively diverging synaptic chains, each activated in turn due to inhibitory retroaction-based competition between sequences.

8.2.2. Dopaminergic neuromodulation of sequences

While it is unclear how STDP could promote sequence learning based on a repeated trigger, Chapter 6 does not describe how sequence are learned toward a rewarding goal, even though these navigational and working memory sequences are precisely observed within the context of rewarding tasks. Furthermore, they cannot explain how internally-generated decisions are taken in the absence of external triggering cues, even though animals can freely navigate. Chapter 7 proposes an answer to these questions by assessing the interaction between two biophysical effects of DA, 1) gating STDP eligibility traces such that a Hebbian assembly oriented toward the repeatedly-rewarded goal emerges, and 2) gating synaptic NMDA excitability (conductance strength), inducing strong synaptic reverberation and neural activity within the assembly of neurons encoding the rewarded goal location, the mouse thus converging toward the reward.

The current thesis further unravels a third biophysical role to dopaminergic neuromodulation, that of modulating synaptic excitability by slowing NMDA channel closing dynamics (Chen et al., 2004; Onn and Wang, 2005; Onn et al., 2006). Since excitatory sequences are mostly mediated by NMDA currents, such neuromodulation has been shown in Chapter 6 to underpin the fast and regular timescale navigational trajectory replays (Skaggs and McNaughton, 1996).

8.2.3. States and sequences in the larger context of complex temporal computations

It has been proposed that working memory delay activity translates into transient sequential activity in rodent mPFC, whereas it translates into predominantly persistent activity in monkey LPFC, due to the expansion of prefrontal microcircuits and their interconnectedness in primates (Constantinidis et al., 2018). While the present thesis separately models these two as dynamic and stable attractors respectively, both are in reality simultaneously observed in animal cortices. Indeed, observations of dynamic coding subserved by transient or sequential neuronal activity

profiles are becoming more common in monkey prefrontal cortex, as previously mentioned (Rainer and Miller, 2002; Brody et al., 2003; Shafi et al., 2007; Meyers et al., 2008, 2008; Barak et al., 2010; Machens et al., 2010; Stokes et al., 2013; Sreenivasan et al., 2014; Stokes and Spaak, 2016; Murray et al., 2017; Parthasarathy et al., 2017; Spaak et al., 2017; Cavanagh et al., 2018; Lundqvist et al., 2018a; Wasmuht et al., 2018). Conversely, persistent RS activity profiles are observed alongside transient RS activity profiles in equal proportions in rodent mPFC (Rikhye et al., 2018), blurring the distinction between persistent and dynamic activity. This further reinforces the plausibility of mechanisms promoting reliability of both types of attractors (e.g. aforementioned CAN and AHP intrinsic bistability).

More generally, the recent advent of massive multi-unit recording techniques coupled with the development of dimensionality reduction techniques (Churchland et al., 2007; Cunningham and Yu, 2014) allows the reinterpretation of complex single neuron coding schemes within population activity repeatable trajectory single-trial coding schemes, such as for motor cortex during reaching (Churchland et al., 2012), olfactory cortex during olfaction (Mazor and Laurent, 2005; Bathellier et al., 2008), and prefrontal cortex during working memory (Lundqvist et al., 2018a). One might be tempted to interpret these as sequences of neural activity. However, although repeated neural activity sequences do lead to repeated trajectories in the population activity space, the inverse is not necessarily true, i.e. that repeated trajectories of population activity necessarily translate to sequences of neural activity. Indeed, population trajectories in motor and olfactory cortex can potentially emerge from any temporally heterogeneous neural activity profiles repeated across trials, not just transient sequential activity. In summary, all neuronal sequences describe population trajectories, but not all population trajectories correspond to neuronal sequences. Only the observation of raster plots of many simultaneously recorded neurons may validate such conclusions, as is the case for rodent navigational and working memory neural activity sequences.

In this context, it remains an open question whether the thesis model, or STDP-based learning within asynchronous irregular (AI) activity in general, can generalize to population activity trajectories with more complex neuronal temporal activity profiles. Indeed, models have shown learning of multiple population trajectories within temporally complex activity (Laje and Buonomano, 2013), but via non-STDP based learning rules, or have shown learning of multiple sequences (Liu and Buonomano, 2009) but without AI network activity. A starting point for learning multiple sequences through STDP within AI activity would be learning several (e.g. two) transient bumps of neuronal activity (instead of only one) at different times within a sequence replay. In such a case, synapses from two different sets of neurons (each representing a different time in the sequence) will strongly project onto a given neuron. If both sets of neurons do not strongly overlap, the given neuron will be able to differentiate between both sequence contexts, leading to sequential replay where neurons strongly fire twice. This question is closely linked to that of the maximum number of separate sequences a given network can learn and successfully replay, in which some models have shown learning of such double sequences, although they lack AI network activity (Liu and Buonomano, 2009).

For increasing heterogeneity of neural frequency temporal profiles (beyond simply two or even N bumps), phenomenological frequency-based or biophysical calcium-based STDP might not suffice. Indeed, temporal relationships between neurons would change across time, leading to learning and unlearning of specific temporal relationships. Artificial learning rules, with

synapses updated according to the distance between stimulus-induced and replay-induced frequency temporal profiles, have been shown to allow robust learning of population trajectories (Laje and Buonomano, 2013).

Theoretically, sequences of transient neuronal activity have the disadvantage of requiring many more neurons to encode elapsed time (Goldman, 2009) compared to orthogonal subspaces of stable and dynamic coding (Machens et al., 2010; Murray et al., 2017). Indeed, sequences require more neurons to encode greater elapsed times, whereas no additional neurons are required within dynamic subspaces as it would be encoded through time-varying activity (i.e. changing neural frequency). However, recent evidence suggests that representation of time elapsed in neural sequences is scalable in rat dorsal striatum, adapting to the required time duration (Mello et al., 2015), the mechanisms of which are yet to be determined (as well as resolved with contradicting evidence of non-scalable rat dorsal striatum sequences, Akhlaghpour et al., 2016).

8.3. Multi-areal collaboration

The model explored in the thesis is a local recurrent neural network without distance-dependent connectivity between pyramidal cells and interneurons, potentially corresponding to a cortical column. Indeed, it has been shown that temporal sequences of neuronal activity are anatomically intermixed at the ~200μm scale in mouse PPC (Harvey et al., 2012), i.e. an order of distance compatible with within columnar organization. Furthermore, subnetworks in V1 layer 2/3 share interneurons (Yoshimura et al., 2005; Itskov et al., 2011), such that mechanisms for reliable attractor replay based on local inhibition (although effective) may not be appropriate (e.g. Hebbian phase sequence with multiple distinct excitatory and inhibitory neuronal assemblies, Chenkov et al., 2017). However, it is not always clear at what spatial scale sequences and assemblies are defined, and whether they truly do spatially extend beyond the confines of the recording technique (e.g. ~1-2mm of multi-electrode array).

Such local networks are inscribed within larger interconnected brain areas, as can be observed during navigational PFC-thalamic nucleus reuniens (NR)-HP and working memory PFC-mediodorsal thalamus (MD) sequences, and proposed in the cortical hierarchy distributed working memory theory (Mejias and Wang, 2020). It is not always clear whether synaptic chains reflecting the same dynamic stimulus exist within each area, whether the synaptic chain is distributed across areas, or whether the synaptic chain exists in only one area and neuronal activity sequences are projected onto other areas. The trace-reactivation theory of memory consolidation stipulates that hippocampal one-shot learned episodic memories are replayed during SWR and gradually consolidated within PFC (Peyrache et al., 2009). The coordination of sequence replays in HP and PFC generally linked to SWR events suggests synaptic chain formation in both structures, whereas the proposed relay-function of NR thalamus could signify an absence of synaptic chains within NR thalamus (Ito et al., 2015), although NR sequences preceding PFC sequences could signify the opposite (Angulo-Garcia et al., 2018).

Furthermore, proposed models of multi-areal emergence of timescales within the cortical hierarchy show how time-varying external inputs due to long-range projections originating from other cortical areas are necessary to correctly capture local area timescales (Chaudhuri et al., 2015). In the present model, external feedforward input does not vary across time. This

assumption arises from its historical use guaranteeing AI dynamics (Brunel, 2000), as well as the desire to capture how local (and not external) network synaptic mechanisms allow robust states and sequences within chaotic dynamics and synaptic noise (itself arising from local synapses). However, future work could investigate how time-varying or rhythmic external feedforward input, e.g. originating from hippocampal theta (Siapas et al., 2005; Benchenane et al., 2011; Zielinski et al., 2019) and olfactory delta (Moberly et al., 2018) rhythmic activity, modulates state transitions and sequence propagation. Probably, strong rhythmic feedforward input would disrupt stable sequence propagation at timescales above the rhythm's duration (as previously mentioned), as well as induce repeated sequences of state transitions, in a similar vein to cortical oscillation gating working memory persistent activity (Dipoppa and Gutkin, 2013). The effect of time-varying inputs would depend on their neuronal targets and specific temporal profile, where ramping-up and -down inputs onto pyramidal cells would lead to more and less frequent sequence replay respectively, as well as erasure of network states driven by inhibition.

8.4. Biophysical models

Throughout the thesis, biophysically detailed models, with excitatory and inhibitory populations within recurrent synaptic matrices, synaptic and intrinsic current dynamics, and biophysical learning rules are prioritized instead of artificial or phenomenological models. Indeed, most of the answers found require comprehensive descriptions of intrinsic and synaptic current dynamics, particularly the slow NMDA and GABA-B current dynamics inducing bursts of neuronal activity and long-lasting collective dynamics. Furthermore, the origin of synaptic noise itself, i.e. the high conductance state (Destexhe et al., 2003), is best described by detailed biophysical descriptions of membrane potential, tight average balance of excitatory and inhibitory currents, and current fluctuations. Simulating Poisson spike trains or noisy injected currents to emulate synaptic noise does not allow to fully analyze interactions between reliable attractors and synaptic noise. Indeed, both arise from similar mechanisms in the brain, i.e. synaptic currents, resulting in complex interactions that cannot be modeled by separate formalisms. In a similar fashion, assessing the physiological basis of plastic processes allowing functional dynamics and representations in frontal cortices obviously requires to consider biologically validated intrinsic and synaptic rules, rather than engineer-based artificial rules targeted at efficiency rather than plausibility.

While most of the model's biophysical properties are derived from previous experimental literature, some aspects have been informed by active dialogue with experimentalists, notably Jérémie Naudé's team in Paris and Emmanuel Procyk's team in Lyon. These exchanges have been extremely productive, the former collaboration contributing, e.g. to correctly describing GABA-B dynamics, which in turn allowed for the discovery of GABA-B currents being relevant in capturing autocorrelogram timescales in the latter collaboration.

In this context, most of the conclusions are backed up by systematic parametric explorations, checking whether articles' conclusions hold when strongly varying model parameters. This is important because biological systems present large variability at different levels, and phenomena are observed across cortical structures with varying properties, such that parametric analyses reinforce the plausibility of the models' results. Nonetheless, testing whether the results hold when removing different elemental model bricks would strengthen

their plausibility across structures and contexts, and allow further identification of its minimal set of necessary and sufficient constituents. Moreover, the currents described and which are required in accounting for the studied network behaviors are ubiquitous across neurons (NMDA, calcium-activated potassium channels inducing AHP and non-specific cationic channels or CAN) and neocortices (GABA-B, Tamás et al., 2003; Oláh et al., 2007), thus representing parsimonious model choices which reinforce the genericity of the resulting network behaviors across cortical structures.

In conclusion, we have studied the mechanistic underpinnings of reliable and emerging static and dynamic attractorial collective forms of activity within noisy frontal networks in the awaken state, be it at the levels of 1) individual neurons (intrinsic CAN/AHP conditional bistability), 2) inhibitory networks (GABA-B-mediated sequential peregrination between discrete states, composed of anti-assembly-based persistent activity and anti-synaptic chain-based neural activity sequences) or 3) excitatory networks (NMDA-mediated sequences, controlled and stabilized through slow or tonic inhibition and intrinsic CAN/AHP transient bistability). We have also described how these attractors are learned (through phenomenological and calcium-mediated STDP, or dopaminergic-gated eligibility-trace-based STDP toward a reward) or not (GABA-B amplification of synaptic random heterogeneity). Finally, we have described their successful recall (spontaneous or cue-based sequences and states, as well as intrinsic dopamine-induced motivated recall).

As shown in this thesis, a description of neuronal and network dynamics through the attractorial grammar of dynamical systems allows us to more easily understand the role of low-level biophysical determinants, e.g. opening dynamics of specific channels, in the context of functional properties of cortical networks, and by extension, of entire cortical areal networks determining animal behaviors. This offers the neuroscientific community a better constrained methodological paradigm in order to test hypotheses for the effect of local biophysical determinants on behavior through biologically realistic models (e.g. GABA-A and autism, Coghlan et al., 2012).

Bibliography

The present bibliography concerns only articles referenced in the Introduction and Discussion. For the bibliography of individual chapters, see the accompanying bibliography within the articles.

Abbott, L. F., and Nelson, S. B. (2000). Synaptic plasticity: taming the beast. *Nature Neuroscience* 3, 1178–1183. doi:10.1038/81453.

Abeles, M., Bergman, H., Gat, I., Meilijson, I., Seidemann, E., Tishby, N., et al. (1995). Cortical activity flips among quasi-stationary states. *Proceedings of the National Academy of Sciences* 92, 8616–8620. doi:10.1073/pnas.92.19.8616.

Abeles, M., Bergman, H., Margalit, E., and Vaadia, E. (1993). Spatiotemporal firing patterns in the frontal cortex of behaving monkeys. *Journal of*, 1629–1638.

Akhlaghpour, H., Wiskerke, J., Choi, J. Y., Taliaferro, J. P., Au, J., and Witten, I. B. (2016). Dissociated sequential activity and stimulus encoding in the dorsomedial striatum during spatial working memory. *eLife* 5, e19507. doi:10.7554/eLife.19507.

Almeida-Filho, D. G., Lopes-dos-Santos, V., Vasconcelos, N. A. P., Miranda, J. G. V., Tort, A. B. L., and Ribeiro, S. (2014). An investigation of Hebbian phase sequences as assembly graphs. *Front. Neural Circuits* 8. doi:10.3389/fncir.2014.00034.

Angulo-Garcia, D., Ferraris, M., Ghestem, A., Bernard, C., and Quilichini, P. P. (2018). Spatio-temporal organization of cell assemblies in Nucleus Reuniens during slow oscillations. *bioRxiv*, 474973. doi:10.1101/474973.

Asaad, W. F., Rainer, G., and Miller, E. K. (1998). Neural Activity in the Primate Prefrontal Cortex during Associative Learning. *Neuron* 21, 1399–1407. doi:10.1016/S0896-6273(00)80658-3.

Baker, S. N., and Lemon, R. N. (2000). Precise spatiotemporal repeating patterns in monkey primary and supplementary motor areas occur at chance levels. *Journal of neurophysiology* 84, 1770–1780.

Bakhurin, K. I., Goudar, V., Shobe, J. L., Claar, L. D., Buonomano, D. V., and Masmanidis, S. C. (2017). Differential Encoding of Time by Prefrontal and Striatal Network Dynamics. *J. Neurosci.* 37, 854–870. doi:10.1523/JNEUROSCI.1789-16.2016.

Bakhurin, K. I., Mac, V., Golshani, P., and Masmanidis, S. C. (2016). Temporal correlations among functionally specialized striatal neural ensembles in reward-conditioned mice. *Journal of Neurophysiology* 115, 1521–1532. doi:10.1152/jn.01037.2015.

Barak, O., Tsodyks, M., and Romo, R. (2010). Neuronal Population Coding of Parametric Working Memory. *J. Neurosci.* 30, 9424–9430. doi:10.1523/JNEUROSCI.1875-10.2010.

Bathellier, B., Buhl, D. L., Accolla, R., and Carleton, A. (2008). Dynamic Ensemble Odor Coding in the Mammalian Olfactory Bulb: Sensory Information at Different Timescales. *Neuron* 57, 586–598. doi:10.1016/j.neuron.2008.02.011.

Batuev, A. S. (1994). Two neuronal systems involved in short-term spatial memory in monkeys. *Acta Neurobiologiae Experimentalis* 54, 335–344.

Beggs, J. M., and Plenz, D. (2003). Neuronal Avalanches in Neocortical Circuits. *The Journal of Neuroscience* 23, 11167–11177. doi:23/35/11167 [pii].

Benchenane, K., Tiesinga, P. H., and Battaglia, F. P. (2011). Oscillations in the prefrontal cortex: a gateway to memory and attention. *Current Opinion in Neurobiology* 21, 475–485. doi:10.1016/j.conb.2011.01.004.

Bernacchia, A., Seo, H., Lee, D., and Wang, X.-J. (2011). A reservoir of time constants for memory traces in cortical neurons. *Nat Neurosci* 14, 366–372. doi:10.1038/nn.2752.

Bi, G. Q., and Poo, M. M. (1998). Synaptic modifications in cultured hippocampal neurons: dependence on spike timing, synaptic strength, and postsynaptic cell type. *The Journal of neuroscience : the official journal of the Society for Neuroscience* 18, 10464–10472. doi:10.1038/25665.

Bienenstock, E. L., Cooper, L. N., and Munro, P. W. (1982). Theory for the development of neuron selectivity: orientation specificity and binocular interaction in visual cortex. *J. Neurosci.* 2, 32–48. doi:10.1523/JNEUROSCI.02-01-00032.1982.

Bolkan, S. S., Stujenske, J. M., Parnaudeau, S., Spellman, T. J., Rauffenbart, C., Abbas, A. I., et al. (2017). Thalamic projections sustain prefrontal activity during working memory maintenance. *Nat. Neurosci.* 20, 987–996. doi:10.1038/nn.4568.

Booth, V., and Rinzel, J. (1995). A minimal, compartmental model for a dendritic origin of bistability of motoneuron firing patterns. *J Comput Neurosci* 2, 299–312. doi:10.1007/BF00961442.

Brody, C. D., Hernández, A., Zainos, A., and Romo, R. (2003). Timing and Neural Encoding of Somatosensory Parametric Working Memory in Macaque Prefrontal Cortex. *Cereb Cortex* 13, 1196–1207. doi:10.1093/cercor/bhg100.

Brunel, N. (2000). Dynamics of Sparsely Connected Networks of Excitatory and Inhibitory Spiking Neurons. *J Comput Neurosci* 8, 183–208. doi:10.1023/A:1008925309027.

Brunel, N., and Wang, X. J. (2001). Effects of neuromodulation in a cortical network model of object working memory dominated by recurrent inhibition. *Journal of Computational*

Neuroscience 11, 63–85. doi:10.1023/A:1011204814320.

Buhry, L., Azizi, A. H., and Cheng, S. (2011). Reactivation, Replay, and Preplay: How It Might All Fit Together. *Neural Plast* 2011. doi:10.1155/2011/203462.

Buonomano, D. V. (2003). Timing of neural responses in cortical organotypic slices. *Proc Natl Acad Sci U S A* 100, 4897–4902. doi:10.1073/pnas.0736909100.

Buzsáki, G., and Moser, E. I. (2013). Memory, navigation and theta rhythm in the hippocampal-entorhinal system. *Nature Neuroscience* 16, 130–138. doi:10.1038/nn.3304.

Camperi, M., and Wang, X.-J. (1998). A Model of Visuospatial Working Memory in Prefrontal Cortex: Recurrent Network and Cellular Bistability. *J Comput Neurosci* 5, 383–405. doi:10.1023/A:1008837311948.

Cavanagh, S. E., Towers, J. P., Wallis, J. D., Hunt, L. T., and Kennerley, S. W. (2018). Reconciling persistent and dynamic hypotheses of working memory coding in prefrontal cortex. *Nature Communications* 9, 3498. doi:10.1038/s41467-018-05873-3.

Cazé, R. D., Humphries, M., and Gutkin, B. (2013). Passive Dendrites Enable Single Neurons to Compute Linearly Non-separable Functions. *PLOS Computational Biology* 9, e1002867. doi:10.1371/journal.pcbi.1002867.

Chaudhuri, R., Knoblauch, K., Gariel, M.-A., Kennedy, H., and Wang, X.-J. (2015). A Large-Scale Circuit Mechanism for Hierarchical Dynamical Processing in the Primate Cortex. *Neuron* 88, 419–431. doi:10.1016/j.neuron.2015.09.008.

Chen, G., Greengard, P., and Yan, Z. (2004). Potentiation of NMDA receptor currents by dopamine D1 receptors in prefrontal cortex. *PNAS* 101, 2596–2600. doi:10.1073/pnas.0308618100.

Chenkov, N., Sprekeler, H., and Kempter, R. (2017). Memory replay in balanced recurrent networks. *PLoS Computational Biology* 13. doi:10.1371/journal.pcbi.1005359.

Churchland, M. M., Cunningham, J. P., Kaufman, M. T., Foster, J. D., Nuyujukian, P., Ryu, S. I., et al. (2012). Neural population dynamics during reaching. *Nature* 487, 51–56. doi:10.1038/nature11129.

Churchland, M. M., Yu, B. M., Sahani, M., and Shenoy, K. V. (2007). Techniques for extracting single-trial activity patterns from large-scale neural recordings. *Current Opinion in Neurobiology* 17, 609–618. doi:10.1016/j.conb.2007.11.001.

Clopath, C., Büsing, L., Vasilaki, E., and Gerstner, W. (2010). Connectivity reflects coding: a model of voltage-based STDP with homeostasis. *Nature Neuroscience* 13, 344–352. doi:10.1038/nn.2479.

Coghlan, S., Horder, J., Inkster, B., Mendez, M. A., Murphy, D. G., and Nutt, D. J. (2012). GABA system dysfunction in autism and related disorders: From synapse to symptoms. *Neuroscience & Biobehavioral Reviews* 36, 2044–2055. doi:10.1016/j.neubiorev.2012.07.005.

Compte, A. (2003). Temporally Irregular Mnemonic Persistent Activity in Prefrontal Neurons of Monkeys During a Delayed Response Task. *Journal of Neurophysiology* 90, 3441–3454. doi:10.1152/jn.00949.2002.

Compte, A. (2006). Computational and in vitro studies of persistent activity: Edging towards cellular and synaptic mechanisms of working memory. *Neuroscience* 139, 135–151. doi:10.1016/j.neuroscience.2005.06.011.

Compte, A., Brunel, N., Goldman-Rakic, P. S., and Wang, X.-J. (2000). Synaptic Mechanisms and Network Dynamics Underlying Spatial Working Memory in a Cortical Network Model. *Cereb Cortex* 10, 910–923. doi:10.1093/cercor/10.9.910.

Constantinidis, C., Funahashi, S., Lee, D., Murray, J. D., Qi, X.-L., Wang, M., et al. (2018). Persistent Spiking Activity Underlies Working Memory. *J. Neurosci.* 38, 7020–7028. doi:10.1523/JNEUROSCI.2486-17.2018.

Cossart, R., Aronov, D., and Yuste, R. (2003). Attractor dynamics of network UP states in the neocortex. *Nature* 423, 283–288. doi:10.1038/nature01614.

Cromer, J. A., Roy, J. E., and Miller, E. K. (2010). Representation of Multiple, Independent Categories in the Primate Prefrontal Cortex. *Neuron* 66, 796–807. doi:10.1016/j.neuron.2010.05.005.

Crowe, D. A., Averbeck, B. B., and Chafee, M. V. (2010). Rapid Sequences of Population Activity Patterns Dynamically Encode Task-Critical Spatial Information in Parietal Cortex. *J. Neurosci.* 30, 11640–11653. doi:10.1523/JNEUROSCI.0954-10.2010.

Cunningham, J. P., and Yu, B. M. (2014). Dimensionality reduction for large-scale neural recordings. *Nature Neuroscience* 17, 1500–1509. doi:10.1038/nn.3776.

Davidson, T. J., Kloosterman, F., and Wilson, M. A. (2009). Hippocampal Replay of Extended Experience. *Neuron* 63, 497–507. doi:10.1016/j.neuron.2009.07.027.

Delord, B. (1996). An intrinsic bistable mechanism in neocortical pyramidal neurons might be involved in the generation of sustained discharge patterns related to working memory. *Neural Network World* 4, 525–533.

Delord, B., Klaassen, A. J., Burnod, Y., Costalat, R., and Guigon, E. (1997). Bistable behaviour in a neocortical neurone model. *NeuroReport* 8, 1019–1023.

Dembrow, N. C., Chitwood, R. A., and Johnston, D. (2010). Projection-Specific Neuromodulation

of Medial Prefrontal Cortex Neurons. *J. Neurosci.* 30, 16922–16937. doi:10.1523/JNEUROSCI.3644-10.2010.

Denève, S., and Machens, C. K. (2016). Efficient codes and balanced networks. *Nature Neuroscience* 19, 375–382. doi:10.1038/nn.4243.

Destexhe, A., Rudolph, M., and Paré, D. (2003). The high-conductance state of neocortical neurons *in vivo*. *Nature Reviews Neuroscience* 4, 739–751. doi:10.1038/nrn1198.

Diba, K., and Buzsáki, G. (2007). Forward and reverse hippocampal place-cell sequences during ripples. *Nature Neuroscience* 10, 1241–1242. doi:10.1038/nn1961.

Diba, K., and Buzsáki, G. (2008). Hippocampal Network Dynamics Constrain the Time Lag between Pyramidal Cells across Modified Environments. *J. Neurosci.* 28, 13448–13456. doi:10.1523/JNEUROSCI.3824-08.2008.

Dipoppa, M., and Gutkin, B. S. (2013). Flexible frequency control of cortical oscillations enables computations required for working memory. *PNAS* 110, 12828–12833. doi:10.1073/pnas.1303270110.

Duarte, R. C. F., and Morrison, A. (2014). Dynamic stability of sequential stimulus representations in adapting neuronal networks. *Front. Comput. Neurosci.* 8. doi:10.3389/fncom.2014.00124.

Durstewitz, D., Vittoz, N. M., Floresco, S. B., and Seamans, J. K. (2010). Abrupt Transitions between Prefrontal Neural Ensemble States Accompany Behavioral Transitions during Rule Learning. *Neuron* 66, 438–448. doi:10.1016/j.neuron.2010.03.029.

Egorov, A. V., Hamam, B. N., Fransén, E., Hasselmo, M. E., and Alonso, A. A. (2002). Graded persistent activity in entorhinal cortex neurons. *Nature* 420, 173–178. doi:10.1038/nature01171.

Elston, G. N. (2007). "4.13 - Specialization of the Neocortical Pyramidal Cell during Primate Evolution," in *Evolution of Nervous Systems*, ed. J. H. Kaas (Oxford: Academic Press), 191–242. doi:10.1016/B0-12-370878-8/00164-6.

Enel, P., Procyk, E., Quilodran, R., and Dominey, P. F. (2016). Reservoir Computing Properties of Neural Dynamics in Prefrontal Cortex. *PLOS Computational Biology* 12, e1004967. doi:10.1371/journal.pcbi.1004967.

Engel, T. A., Steinmetz, N. A., Gieselmann, M. A., Thiele, A., Moore, T., and Boahen, K. (2016). Selective modulation of cortical state during spatial attention. *Science* 354, 1140–1144. doi:10.1126/science.aag1420.

Ermentrout, B. (2003). Dynamical Consequences of Fast-Rising, Slow-Decaying Synapses in Neuronal Networks. *Neural Computation* 15, 2483–2522.

doi:10.1162/089976603322385054.

Euston, D. R., Tatsuno, M., and McNaughton, B. L. (2007). Fast-Forward Playback of Recent Memory Sequences in Prefrontal Cortex During Sleep. *Science* 318, 1147–1150. doi:10.1126/science.1148979.

Felleman, D. J., and Van Essen, D. C. (1991). Distributed hierarchical processing in the primate cerebral cortex. *Cereb Cortex* 1, 1–47. doi:10.1093/cercor/1.1.1-a.

Ferbinteanu, J., and Shapiro, M. L. (2003). Prospective and Retrospective Memory Coding in the Hippocampus. *Neuron* 40, 1227–1239. doi:10.1016/S0896-6273(03)00752-9.

Fiete, I. R., Senn, W., Wang, C. Z. H., and Hahnloser, R. H. R. (2010). Spike-Time-Dependent Plasticity and Heterosynaptic Competition Organize Networks to Produce Long Scale-Free Sequences of Neural Activity. *Neuron* 65, 563–576. doi:10.1016/j.neuron.2010.02.003.

Frank, L. M., Brown, E. N., and Wilson, M. (2000). Trajectory Encoding in the Hippocampus and Entorhinal Cortex. *Neuron* 27, 169–178. doi:10.1016/S0896-6273(00)00018-0.

Froemke, R. C. (2015). Plasticity of Cortical Excitatory-Inhibitory Balance. *Annual Review of Neuroscience* 38, 195–219. doi:10.1146/annurev-neuro-071714-034002.

Fujisawa, S., Amarasingham, A., Harrison, M. T., and Buzsáki, G. (2008). Behavior-dependent short-term assembly dynamics in the medial prefrontal cortex. *Nature Neuroscience* 11, 823–833. doi:10.1038/nn.2134.

Funahashi, S., Bruce, C. J., and Goldman-Rakic, P. S. (1989). Mnemonic coding of visual space in the monkey's dorsolateral prefrontal cortex. *Journal of Neurophysiology* 61, 331–349. doi:10.1152/jn.1989.61.2.331.

Gat, I., and Tishby, N. (1992). Statistical Modeling of Cell Assemblies Activities in Associative Cortex of Behaving Monkeys. in *Proceedings of the 5th International Conference on Neural Information Processing Systems* NIPS'92. (San Francisco, CA, USA: Morgan Kaufmann Publishers Inc.), 945–952. Available at: http://dl.acm.org/citation.cfm?id=2987061.2987177 [Accessed December 19, 2019].

Gee, S., Ellwood, I., Patel, T., Luongo, F., Deisseroth, K., and Sohal, V. S. (2012). Synaptic Activity Unmasks Dopamine D2 Receptor Modulation of a Specific Class of Layer V Pyramidal Neurons in Prefrontal Cortex. *J. Neurosci.* 32, 4959–4971. doi:10.1523/JNEUROSCI.5835-11.2012.

Gerstein, G. L. (2004). Searching for significance in spatio-temporal firing patterns. *Acta Neurobiologiae Experimentalis* 64, 203–207.

Girardeau, G., Benchenane, K., Wiener, S. I., Buzsáki, G., and Zugaro, M. B. (2009). Selective

suppression of hippocampal ripples impairs spatial memory. *Nat Neurosci* 12, 1222–1223. doi:10.1038/nn.2384.

Goldman, M. S. (2009). Memory without Feedback in a Neural Network. *Neuron* 61, 621–634. doi:10.1016/j.neuron.2008.12.012.

Goldman, M. S., Levine, J. H., Major, G., Tank, D. W., and Seung, H. S. (2003). Robust Persistent Neural Activity in a Model Integrator with Multiple Hysteretic Dendrites per Neuron. *Cerebral Cortex* 13, 1185–1195. doi:10.1093/cercor/bhg095.

Goldman-Rakic, P. S. (1995). Cellular basis of working memory. *Neuron* 14, 477–485. doi:10.1016/0896-6273(95)90304-6.

Graupner, M., and Brunel, N. (2012). Calcium-based plasticity model explains sensitivity of synaptic changes to spike pattern, rate, and dendritic location. *PNAS*, 201109359. doi:10.1073/pnas.1109359109.

Haj-Dahmane, S., and Andrade, R. (1997). Calcium-Activated Cation Nonselective Current Contributes to the Fast Afterdepolarization in Rat Prefrontal Cortex Neurons. *Journal of Neurophysiology* 78, 1983–1989. doi:10.1152/jn.1997.78.4.1983.

Harvey, C. D., Coen, P., and Tank, D. W. (2012). Choice-specific sequences in parietal cortex during a virtual-navigation decision task. *Nature* 484, 62–68. doi:10.1038/nature10918.

He, K., Huertas, M., Hong, S. Z., Tie, X., Hell, J. W., Shouval, H., et al. (2015). Distinct Eligibility Traces for LTP and LTD in Cortical Synapses. *Neuron* 88, 528–538. doi:10.1016/j.neuron.2015.09.037.

Hebb, D. O. (1949). *The organization of behavior; a neuropsycholocigal theory.* New York: John Wiley & Sons, Inc.

Hennequin, G., Agnes, E. J., and Vogels, T. P. (2017). Inhibitory Plasticity: Balance, Control, and Codependence. *Annual Review of Neuroscience* 40, 557–579. doi:10.1146/annurev-neuro-072116-031005.

Hoffman, K. L., and McNaughton, B. L. (2002). Coordinated Reactivation of Distributed Memory Traces in Primate Neocortex. *Science* 297, 2070–2073. doi:10.1126/science.1073538.

Hussar, C. R., and Pasternak, T. (2012). Memory-Guided Sensory Comparisons in the Prefrontal Cortex: Contribution of Putative Pyramidal Cells and Interneurons. *J. Neurosci.* 32, 2747–2761. doi:10.1523/JNEUROSCI.5135-11.2012.

Ikegaya, Y., Aaron, G., Cossart, R., Aronov, D., Lampl, I., Ferster, D., et al. (2004). Synfire Chains and Cortical Songs: Temporal Modules of Cortical Activity. *Science* 304, 559–564. doi:10.1126/science.1093173.

Ito, H. T., Zhang, S.-J., Witter, M. P., Moser, E. I., and Moser, M.-B. (2015). A prefrontal–thalamo–hippocampal circuit for goal-directed spatial navigation. *Nature* 522, 50–55. doi:10.1038/nature14396.

Itskov, V., Curto, C., Pastalkova, E., and Buzsaki, G. (2011). Cell Assembly Sequences Arising from Spike Threshold Adaptation Keep Track of Time in the Hippocampus. *Journal of Neuroscience* 31, 2828–2834. doi:10.1523/JNEUROSCI.3773-10.2011.

Izhikevich, E. M. (2006). Polychronization: Computation with Spikes. *Neural Computation* 18, 245–282. doi:10.1162/089976606775093882.

Izhikevich, E. M. (2007). Solving the distal reward problem through linkage of STDP and dopamine signaling. *Cerebral Cortex* 17, 2443–2452. doi:10.1093/cercor/bhl152.

Izhikevich, E. M., Gally, J. A., and Edelman, G. M. (2004). Spike-timing dynamics of neuronal groups. *Cerebral Cortex* 14, 933–944. doi:10.1093/cercor/bhh053.

Jadhav, S. P., Rothschild, G., Roumis, D. K., and Frank, L. M. (2016). Coordinated Excitation and Inhibition of Prefrontal Ensembles during Awake Hippocampal Sharp-Wave Ripple Events. *Neuron* 90, 113–127. doi:10.1016/j.neuron.2016.02.010.

Jarsky, T., Roxin, A., Kath, W. L., and Spruston, N. (2005). Conditional dendritic spike propagation following distal synaptic activation of hippocampal CA1 pyramidal neurons. *Nat Neurosci* 8, 1667–1676. doi:10.1038/nn1599.

Ji, D., and Wilson, M. A. (2007). Coordinated memory replay in the visual cortex and hippocampus during sleep. *Nature Neuroscience* 10, 100–107. doi:10.1038/nn1825.

Joglekar, M. R., Mejias, J. F., Yang, G. R., and Wang, X.-J. (2018). Inter-areal Balanced Amplification Enhances Signal Propagation in a Large-Scale Circuit Model of the Primate Cortex. *Neuron* 98, 222-234.e8. doi:10.1016/j.neuron.2018.02.031.

Johnson, H. A., Goel, A., and Buonomano, D. V. (2010a). Neural dynamics of in vitro cortical networks reflects experienced temporal patterns. *Nature Neuroscience* 13, 917–919. doi:10.1038/nn.2579.

Johnson, L. A., Euston, D. R., Tatsuno, M., and McNaughton, B. L. (2010b). Stored-Trace Reactivation in Rat Prefrontal Cortex Is Correlated with Down-to-Up State Fluctuation Density. *J. Neurosci.* 30, 2650–2661. doi:10.1523/JNEUROSCI.1617-09.2010.

Kaefer, K., Nardin, M., Blahna, K., and Csicsvari, J. (2020). Replay of Behavioral Sequences in the Medial Prefrontal Cortex during Rule Switching. *Neuron*. doi:10.1016/j.neuron.2020.01.015.

Kamigaki, T., and Dan, Y. (2017). Delay activity of specific prefrontal interneuron subtypes modulates memory-guided behavior. *Nature Neuroscience* 20, 854–863.

doi:10.1038/nn.4554.

Keck, T., Toyoizumi, T., Chen, L., Doiron, B., Feldman, D. E., Fox, K., et al. (2017). Integrating Hebbian and homeostatic plasticity: the current state of the field and future research directions. *Philosophical Transactions of the Royal Society B: Biological Sciences* 372, 20160158. doi:10.1098/rstb.2016.0158.

Kenet, T., Bibitchkov, D., Tsodyks, M., Grinvald, A., and Arieli, A. (2003). Spontaneously emerging cortical representations of visual attributes. *Nature* 425, 954–956. doi:10.1038/nature02078.

Klampfl, S., and Maass, W. (2013). Emergence of Dynamic Memory Traces in Cortical Microcircuit Models through STDP. *J. Neurosci.* 33, 11515–11529. doi:10.1523/JNEUROSCI.5044-12.2013.

Koulakov, A. A., Raghavachari, S., Kepecs, A., and Lisman, J. E. (2002). Model for a robust neural integrator. *Nature Neuroscience* 5, 775–782. doi:10.1038/nn893.

Krnjević, K., Pumain, R., and Renaud, L. (1971). The mechanism of excitation by acetylcholine in the cerebral cortex. *The Journal of Physiology* 215, 247–268. doi:10.1113/jphysiol.1971.sp009467.

Kruskal, P. B., Li, L., and MacLean, J. N. (2013). Circuit reactivation dynamically regulates synaptic plasticity in neocortex. *Nature Communications* 4, 2574. doi:10.1038/ncomms3574.

Kudrimoti, H. S., Barnes, C. A., and McNaughton, B. L. (1999). Reactivation of Hippocampal Cell Assemblies: Effects of Behavioral State, Experience, and EEG Dynamics. *J. Neurosci.* 19, 4090–4101. doi:10.1523/JNEUROSCI.19-10-04090.1999.

Kumar, A., Rotter, S., and Aertsen, A. (2008). Conditions for Propagating Synchronous Spiking and Asynchronous Firing Rates in a Cortical Network Model. *J. Neurosci.* 28, 5268–5280. doi:10.1523/JNEUROSCI.2542-07.2008.

La Camera, G., Fontanini, A., and Mazzucato, L. (2019). Cortical computations via metastable activity. *Current Opinion in Neurobiology* 58, 37–45. doi:10.1016/j.conb.2019.06.007.

Laje, R., and Buonomano, D. V. (2013). Robust timing and motor patterns by taming chaos in recurrent neural networks. *Nature Neuroscience* 16, 925–933. doi:10.1038/nn.3405.

Lara, A. H., and Wallis, J. D. (2014). Executive control processes underlying multi-item working memory. *Nat Neurosci* 17, 876–883. doi:10.1038/nn.3702.

Leavitt, M. L., Pieper, F., Sachs, A. J., and Martinez-Trujillo, J. C. (2018). A Quadrantic Bias in Prefrontal Representation of Visual-Mnemonic Space. *Cerebral Cortex* 28, 2405–2421. doi:10.1093/cercor/bhx142.

Lee, A. K., and Wilson, M. A. (2002). Memory of Sequential Experience in the Hippocampus during Slow Wave Sleep. *Neuron* 36, 1183–1194. doi:10.1016/S0896-6273(02)01096-6.

Liu, J. K., and Buonomano, D. V. (2009). Embedding Multiple Trajectories in Simulated Recurrent Neural Networks in a Self-Organizing Manner. *Journal of Neuroscience* 29, 13172–13181. doi:10.1523/JNEUROSCI.2358-09.2009.

London, M., Roth, A., Beeren, L., Häusser, M., and Latham, P. E. (2010). Sensitivity to perturbations in vivo implies high noise and suggests rate coding in cortex. *Nature* 466, 123–127. doi:10.1038/nature09086.

Louie, K., and Wilson, M. A. (2001). Temporally structured replay of awake hippocampal ensemble activity during rapid eye movement sleep. *Neuron* 29, 145–156. doi:10.1016/S0896-6273(01)00186-6.

Luczak, A., Barthó, P., and Harris, K. D. (2009). Spontaneous Events Outline the Realm of Possible Sensory Responses in Neocortical Populations. *Neuron* 62, 413–425. doi:10.1016/j.neuron.2009.03.014.

Luczak, A., Bartho, P., Marguet, S. L., Buzsaki, G., and Harris, K. D. (2007). Sequential structure of neocortical spontaneous activity in vivo. *Proceedings of the National Academy of Sciences* 104, 347–352. doi:10.1073/pnas.0605643104.

Lundqvist, M., Herman, P., and Miller, E. K. (2018a). Working Memory: Delay Activity, Yes! Persistent Activity? Maybe Not. *J. Neurosci.* 38, 7013–7019. doi:10.1523/JNEUROSCI.2485-17.2018.

Lundqvist, M., Herman, P., Warden, M. R., Brincat, S. L., and Miller, E. K. (2018b). Gamma and beta bursts during working memory readout suggest roles in its volitional control. *Nat Commun* 9, 394. doi:10.1038/s41467-017-02791-8.

Maboudi, K., Ackermann, E., de Jong, L. W., Pfeiffer, B. E., Foster, D., Diba, K., et al. (2018). Uncovering temporal structure in hippocampal output patterns. *eLife* 7, e34467. doi:10.7554/eLife.34467.

Machens, C. K., Romo, R., and Brody, C. D. (2010). Functional, But Not Anatomical, Separation of "What" and "When" in Prefrontal Cortex. *J. Neurosci.* 30, 350–360. doi:10.1523/JNEUROSCI.3276-09.2010.

MacLean, J. N., Watson, B. O., Aaron, G. B., and Yuste, R. (2005). Internal dynamics determine the cortical response to thalamic stimulation. *Neuron* 48, 811–823. doi:10.1016/j.neuron.2005.09.035.

Mao, B. Q., Hamzei-Sichani, F., Aronov, D., Froemke, R. C., and Yuste, R. (2001). Dynamics of spontaneous activity in neocortical slices. *Neuron* 32, 883–898. doi:10.1016/S0896-6273(01)00518-9.

Marder, E., and Calabrese, R. L. (1996). Principles of rhythmic motor pattern generation. *Physiological Reviews* 76, 687–717. doi:10.1152/physrev.1996.76.3.687.

Markov, N. T., Ercsey-Ravasz, M., Van Essen, D. C., Knoblauch, K., Toroczkai, Z., and Kennedy, H. (2013). Cortical High-Density Counterstream Architectures. *Science* 342, 1238406. doi:10.1126/science.1238406.

Mazor, O., and Laurent, G. (2005). Transient dynamics versus fixed points in odor representations by locust antennal lobe projection neurons. *Neuron* 48, 661–673. doi:10.1016/j.neuron.2005.09.032.

Mazzucato, L., Fontanini, A., and Camera, G. L. (2015). Dynamics of Multistable States during Ongoing and Evoked Cortical Activity. *J. Neurosci.* 35, 8214–8231. doi:10.1523/JNEUROSCI.4819-14.2015.

McLelland, D., and Paulsen, O. (2007). Cortical Songs Revisited: A Lesson in Statistics. *Neuron* 53, 319–321. doi:10.1016/j.neuron.2007.01.020.

Medalla, M., Gilman, J. P., Wang, J.-Y., and Luebke, J. I. (2017). Strength and Diversity of Inhibitory Signaling Differentiates Primate Anterior Cingulate from Lateral Prefrontal Cortex. *J. Neurosci.* 37, 4717–4734. doi:10.1523/JNEUROSCI.3757-16.2017.

Mehring, C., Hehl, U., Kubo, M., Diesmann, M., and Aertsen, A. (2003). Activity dynamics and propagation of synchronous spiking in locally connected random networks. *Biol. Cybern.* 88, 395–408. doi:10.1007/s00422-002-0384-4.

Mejias, J. F., and Wang, X.-J. (2020). Mechanisms of distributed working memory in a large-scale model of macaque neocortex. *bioRxiv*, 760231. doi:10.1101/760231.

Mello, G. B. M., Soares, S., and Paton, J. J. (2015). A Scalable Population Code for Time in the Striatum. *Current Biology* 25, 1113–1122. doi:10.1016/j.cub.2015.02.036.

Meyers, E. M., Freedman, D. J., Kreiman, G., Miller, E. K., and Poggio, T. (2008). Dynamic Population Coding of Category Information in Inferior Temporal and Prefrontal Cortex. *Journal of Neurophysiology* 100, 1407–1419. doi:10.1152/jn.90248.2008.

Mizuseki, K., Royer, S., Diba, K., and Buzsáki, G. (2012). Activity dynamics and behavioral correlates of CA3 and CA1 hippocampal pyramidal neurons. *Hippocampus* 22, 1659–1680. doi:10.1002/hipo.22002.

Moberly, A. H., Schreck, M., Bhattarai, J. P., Zweifel, L. S., Luo, W., and Ma, M. (2018). Olfactory inputs modulate respiration-related rhythmic activity in the prefrontal cortex and freezing behavior. *Nature Communications* 9, 1528. doi:10.1038/s41467-018-03988-1.

Mokeichev, A., Okun, M., Barak, O., Katz, Y., Ben-Shahar, O., and Lampl, I. (2007). Stochastic Emergence of Repeating Cortical Motifs in Spontaneous Membrane Potential

Fluctuations In Vivo. *Neuron* 53, 413–425. doi:10.1016/j.neuron.2007.01.017.

Mongillo, G., Rumpel, S., and Loewenstein, Y. (2018). Inhibitory connectivity defines the realm of excitatory plasticity. *Nature Neuroscience* 21, 1463–1470. doi:10.1038/s41593-018-0226-x.

Murray, J. D., Bernacchia, A., Freedman, D. J., Romo, R., Wallis, J. D., Cai, X., et al. (2014). A hierarchy of intrinsic timescales across primate cortex. *Nature Neuroscience* 17, 1661–1663. doi:10.1038/nn.3862.

Murray, J. D., Bernacchia, A., Roy, N. A., Constantinidis, C., Romo, R., and Wang, X.-J. (2017). Stable population coding for working memory coexists with heterogeneous neural dynamics in prefrontal cortex. *PNAS* 114, 394–399. doi:10.1073/pnas.1619449114.

Nádasdy, Z., Hirase, H., Czurkó, A., Csicsvari, J., and Buzsáki, G. (1999). Replay and Time Compression of Recurring Spike Sequences in the Hippocampus. *The Journal of Neuroscience* 19, 9497–9507. doi:10.1126/science.1182395.

Nakajima, M., Schmitt, L. I., and Halassa, M. M. (2019). Prefrontal Cortex Regulates Sensory Filtering through a Basal Ganglia-to-Thalamus Pathway. *Neuron* 103, 445-458.e10. doi:10.1016/j.neuron.2019.05.026.

O'Keefe, J., and Dostrovsky, J. (1971). The hippocampus as a spatial map: Preliminary evidence from unit activity in the freely-moving rat. *Brain Research* 34, 171–175. doi:10.1016/0006-8993(71)90358-1.

Oláh, S., Komlósi, G., Szabadics, J., Varga, C., Tóth, É., Barzó, P., et al. (2007). Output of neurogliaform cells to various neuron types in the human and rat cerebral cortex. *Front. Neural Circuits* 1. doi:10.3389/neuro.04.004.2007.

O'Neill, J., Boccara, C. N., Stella, F., Schoenenberger, P., and Csicsvari, J. (2017). Superficial layers of the medial entorhinal cortex replay independently of the hippocampus. *Science* 355, 184–188. doi:10.1126/science.aag2787.

Onn, S.-P., and Wang, X.-B. (2005). Differential modulation of anterior cingulate cortical activity by afferents from ventral tegmental area and mediodorsal thalamus. *European Journal of Neuroscience* 21, 2975–2992. doi:https://doi.org/10.1111/j.1460-9568.2005.04122.x.

Onn, S.-P., Wang, X.-B., Lin, M., and Grace, A. A. (2006). Dopamine D1 and D4 Receptor Subtypes Differentially Modulate Recurrent Excitatory Synapses in Prefrontal Cortical Pyramidal Neurons. *Neuropsychopharmacology* 31, 318–338. doi:10.1038/sj.npp.1300829.

Oram, M. W., Wiener, M. C., Lestienne, R., and Richmond, B. J. (1999). Stochastic nature of precisely timed spike patterns in visual system neuronal responses. *Journal of neurophysiology* 81, 3021–3033.

Parthasarathy, A., Herikstad, R., Bong, J. H., Medina, F. S., Libedinsky, C., and Yen, S.-C. (2017). Mixed selectivity morphs population codes in prefrontal cortex. *Nat Neurosci* 20, 1770–1779. doi:10.1038/s41593-017-0003-2.

Pasquale, V., Martinoia, S., and Chiappalone, M. (2017). Stimulation triggers endogenous activity patterns in cultured cortical networks. *Scientific Reports* 7, 9080. doi:10.1038/s41598-017-08369-0.

Pasquale, V., Massobrio, P., Bologna, L. L., Chiappalone, M., and Martinoia, S. (2008). Self-organization and neuronal avalanches in networks of dissociated cortical neurons. *Neuroscience* 153, 1354–1369. doi:10.1016/j.neuroscience.2008.03.050.

Passecker, J., Mikus, N., Malagon-Vina, H., Anner, P., Dimidschstein, J., Fishell, G., et al. (2019). Activity of Prefrontal Neurons Predict Future Choices during Gambling. *Neuron* 101, 152-164.e7. doi:10.1016/j.neuron.2018.10.050.

Pastalkova, E., Itskov, V., Amarasingham, A., and Buzsaki, G. (2008). Internally Generated Cell Assembly Sequences in the Rat Hippocampus. *Science* 321, 1322–1327. doi:10.1126/science.1159775.

Peyrache, A., Khamassi, M., Benchenane, K., Wiener, S. I., and Battaglia, F. P. (2009). Replay of rule-learning related neural patterns in the prefrontal cortex during sleep. *Nature Neuroscience* 12, 919–926. doi:10.1038/nn.2337.

Pfeiffer, B. E., and Foster, D. J. (2013). Hippocampal place-cell sequences depict future paths to remembered goals. *Nature* 497, 74–79. doi:10.1038/nature12112.

Ponzi, A., and Wickens, J. (2010). Sequentially Switching Cell Assemblies in Random Inhibitory Networks of Spiking Neurons in the Striatum. *J. Neurosci.* 30, 5894–5911. doi:10.1523/JNEUROSCI.5540-09.2010.

Poulet, J. F. A., and Petersen, C. C. H. (2008). Internal brain state regulates membrane potential synchrony in barrel cortex of behaving mice. *Nature* 454, 881–885. doi:10.1038/nature07150.

Prut, Y., Vaadia, E., Bergman, H., Haalman, I., Slovin, H., and Abeles, M. (1998). Spatiotemporal Structure of Cortical Activity: Properties and Behavioral Relevance. *Journal of Neurophysiology* 79, 2857–2874. doi:10.1152/jn.1998.79.6.2857.

Rainer, G., and Miller, E. K. (2000). Neural Ensemble States in Perfrontal Cortex Identified Using a Hidden Markov Model with a Modified Em Algorithm. *Neurocomputing* 32, 961.

Rainer, G., and Miller, E. K. (2002). Timecourse of object-related neural activity in the primate prefrontal cortex during a short-term memory task. *European Journal of Neuroscience* 15, 1244–1254. doi:10.1046/j.1460-9568.2002.01958.x.

Rich, E. L., and Wallis, J. D. (2016). Decoding subjective decisions from orbitofrontal cortex. *Nature Neuroscience* 19, 973–980. doi:10.1038/nn.4320.

Riehle, A., Grün, S., Diesmann, M., and Aertsen, A. (1997). Spike Synchronization and Rate Modulation Differentially Involved in Motor Cortical Function. *Science*. Available at: https://www.science.org/doi/abs/10.1126/science.278.5345.1950 [Accessed September 7, 2021].

Rikhye, R. V., Gilra, A., and Halassa, M. M. (2018). Thalamic regulation of switching between cortical representations enables cognitive flexibility. *Nat Neurosci* 21, 1753–1763. doi:10.1038/s41593-018-0269-z.

Rolston, J. D., Wagenaar, D. A., and Potter, S. M. (2007). Precisely timed spatiotemporal patterns of neural activity in dissociated cortical cultures. *Neuroscience* 148, 294–303. doi:10.1016/j.neuroscience.2007.05.025.

Roxin, A., Hakim, V., and Brunel, N. (2008). The Statistics of Repeating Patterns of Cortical Activity Can Be Reproduced by a Model Network of Stochastic Binary Neurons. *Journal of Neuroscience* 28, 10734–10745. doi:10.1523/JNEUROSCI.1016-08.2008.

Rudy, B., Fishell, G., Lee, S., and Hjerling-Leffler, J. (2011). Three groups of interneurons account for nearly 100% of neocortical GABAergic neurons. *Developmental Neurobiology* 71, 45–61. doi:10.1002/dneu.20853.

Runyan, C. A., Piasini, E., Panzeri, S., and Harvey, C. D. (2017). Distinct timescales of population coding across cortex. *Nature* 548, 92–96. doi:10.1038/nature23020.

Schmitt, L. I., Wimmer, R. D., Nakajima, M., Happ, M., Mofakham, S., and Halassa, M. M. (2017). Thalamic amplification of cortical connectivity sustains attentional control. *Nature* 545, 219–223. doi:10.1038/nature22073.

Schwindt, P. C., Spain, W. J., Foehring, R. C., Chubb, M. C., and Crill, W. E. (1988). Slow conductances in neurons from cat sensorimotor cortex in vitro and their role in slow excitability changes. *Journal of Neurophysiology* 59, 450–467. doi:10.1152/jn.1988.59.2.450.

Seidemann, E., Meilijson, I., Abeles, M., Bergman, H., and Vaadia, E. (1996). Simultaneously recorded single units in the frontal cortex go through sequences of discrete and stable states in monkeys performing a delayed localization task. *The Journal of neuroscience : the official journal of the Society for Neuroscience* 16, 752–768.

Shafi, M., Zhou, Y., Quintana, J., Chow, C., Fuster, J., and Bodner, M. (2007). Variability in neuronal activity in primate cortex during working memory tasks. *Neuroscience* 146, 1082–1108. doi:10.1016/j.neuroscience.2006.12.072.

Shinomoto, S., Miyazaki, Y., Tamura, H., and Fujita, I. (2005). Regional and Laminar Differences

in In Vivo Firing Patterns of Primate Cortical Neurons. *Journal of Neurophysiology* 94, 567–575. doi:10.1152/jn.00896.2004.

Shmiel, T., Drori, R., Shmiel, O., Ben-Shaul, Y., Nadasdy, Z., Shemesh, M., et al. (2006). Temporally Precise Cortical Firing Patterns Are Associated With Distinct Action Segments. *Journal of Neurophysiology* 96, 2645–2652. doi:10.1152/jn.00798.2005.

Shouval, H. Z., and Gavornik, J. P. (2011). A single spiking neuron that can represent interval timing: analysis, plasticity and multi-stability. *J Comput Neurosci* 30, 489–499. doi:10.1007/s10827-010-0273-0.

Siapas, A. G., Lubenov, E. V., and Wilson, M. A. (2005). Prefrontal Phase Locking to Hippocampal Theta Oscillations. *Neuron* 46, 141–151. doi:10.1016/j.neuron.2005.02.028.

Silva, L. R., Amitai, Y., and Connors, B. W. (1991). Intrinsic Oscillations of Neocortex Generated by Layer 5 Pyramidal Neurons. *Science* 251, 432–435. doi:10.1126/science.1824881.

Sjöström, P. J., Turrigiano, G. G., and Nelson, S. B. (2003). Neocortical LTD via Coincident Activation of Presynaptic NMDA and Cannabinoid Receptors. *Neuron* 39, 641–654. doi:10.1016/S0896-6273(03)00476-8.

Skaggs, W. E., and McNaughton, B. L. (1996). Replay of Neuronal Firing Sequences in Rat Hippocampus During Sleep Following Spatial Experience. *Science* 271, 1870–1873. doi:10.1126/science.271.5257.1870.

Skaggs, W. E., McNaughton, B. L., Wilson, M. A., and Barnes, C. A. (1996). Theta phase precession in hippocampal neuronal populations and the compression of temporal sequences. *Hippocampus* 6, 149–172. doi:10.1002/(SICI)1098-1063(1996)6:2<149::AID-HIPO6>3.0.CO;2-K.

Spaak, E., Watanabe, K., Funahashi, S., and Stokes, M. G. (2017). Stable and Dynamic Coding for Working Memory in Primate Prefrontal Cortex. *J. Neurosci.* 37, 6503–6516. doi:10.1523/JNEUROSCI.3364-16.2017.

Sreenivasan, K. K., Curtis, C. E., and D'Esposito, M. (2014). Revisiting the role of persistent neural activity during working memory. *Trends in Cognitive Sciences* 18, 82–89. doi:10.1016/j.tics.2013.12.001.

Stokes, M. G. (2015). 'Activity-silent' working memory in prefrontal cortex: a dynamic coding framework. *Trends in Cognitive Sciences* 19, 394–405. doi:10.1016/j.tics.2015.05.004.

Stokes, M. G., Kusunoki, M., Sigala, N., Nili, H., Gaffan, D., and Duncan, J. (2013). Dynamic Coding for Cognitive Control in Prefrontal Cortex. *Neuron* 78, 364–375. doi:10.1016/j.neuron.2013.01.039.

Stokes, M., and Spaak, E. (2016). The Importance of Single-Trial Analyses in Cognitive

Neuroscience. *Trends in Cognitive Sciences* 20, 483–486. doi:10.1016/j.tics.2016.05.008.

Stoll, F. M., Fontanier, V., and Procyk, E. (2016). Specific frontal neural dynamics contribute to decisions to check. *Nat Commun* 7, 1–14. doi:10.1038/ncomms11990.

Sussillo, D., and Abbott, L. F. (2009). Generating Coherent Patterns of Activity from Chaotic Neural Networks. *Neuron* 63, 544–557. doi:10.1016/j.neuron.2009.07.018.

Taghia, J., Cai, W., Ryali, S., Kochalka, J., Nicholas, J., Chen, T., et al. (2018). Uncovering hidden brain state dynamics that regulate performance and decision-making during cognition. *Nat Commun* 9, 2505. doi:10.1038/s41467-018-04723-6.

Tahvildari, B., Fransén, E., Alonso, A. A., and Hasselmo, M. E. (2007). Switching between "On" and "Off" states of persistent activity in lateral entorhinal layer III neurons. *Hippocampus* 17, 257–263. doi:10.1002/hipo.20270.

Tamás, G., Andrea Lőrincz, A. S., and Szabadics, J. (2003). Identified Sources and Targets of Slow Inhibition in the Neocortex. *Science* 299, 1902–1905. doi:10.1126/science.1082053.

Tang, A., Jackson, D., Hobbs, J., Chen, W., Smith, J. L., Patel, H., et al. (2008). A Maximum Entropy Model Applied to Spatial and Temporal Correlations from Cortical Networks In Vitro. *Journal of Neuroscience* 28, 505–518. doi:10.1523/JNEUROSCI.3359-07.2008.

Tang, W., Shin, J. D., and Jadhav, S. P. (2021). Multiple time-scales of decision-making in the hippocampus and prefrontal cortex. *eLife* 10, e66227. doi:10.7554/eLife.66227.

Tegnér, J., Compte, A., and Wang, X.-J. (2002). The dynamical stability of reverberatory neural circuits. *Biol Cybern* 87, 471–481. doi:10.1007/s00422-002-0363-9.

Thuault, S. J., Malleret, G., Constantinople, C. M., Nicholls, R., Chen, I., Zhu, J., et al. (2013). Prefrontal Cortex HCN1 Channels Enable Intrinsic Persistent Neural Firing and Executive Memory Function. *J. Neurosci.* 33, 13583–13599. doi:10.1523/JNEUROSCI.2427-12.2013.

Tiganj, Z., Jung, M. W., Kim, J., and Howard, M. W. (2017). Sequential Firing Codes for Time in Rodent Medial Prefrontal Cortex. *Cerebral Cortex* 27, 5663–5671. doi:10.1093/cercor/bhw336.

Torres-Gomez, S., Blonde, J. D., Mendoza-Halliday, D., Kuebler, E., Everest, M., Wang, X. J., et al. (2020). Changes in the Proportion of Inhibitory Interneuron Types from Sensory to Executive Areas of the Primate Neocortex: Implications for the Origins of Working Memory Representations. *Cereb Cortex* 30, 4544–4562. doi:10.1093/cercor/bhaa056.

Tran-Van-Minh, A., Cazé, R. D., Abrahamsson, T., Cathala, L., Gutkin, B. S., and DiGregorio, D. A. (2015). Contribution of sublinear and supralinear dendritic integration to neuronal computations. *Front. Cell. Neurosci.* 9. doi:10.3389/fncel.2015.00067.

Turrigiano, G. G., Leslie, K. R., Desai, N. S., Rutherford, L. C., and Nelson, S. B. (1998). Activity-dependent scaling of quantal amplitude in neocortical neurons. *Nature* 391, 892–896. doi:10.1038/36103.

Vogels, T. P., Froemke, R. C., Doyon, N., Gilson, M., Haas, J. S., Liu, R., et al. (2013). Inhibitory synaptic plasticity: spike timing-dependence and putative network function. *Front. Neural Circuits* 7. doi:10.3389/fncir.2013.00119.

Wang, M., Yang, Y., Wang, C.-J., Gamo, N. J., Jin, L. E., Mazer, J. A., et al. (2013). NMDA Receptors Subserve Persistent Neuronal Firing during Working Memory in Dorsolateral Prefrontal Cortex. *Neuron* 77, 736–749. doi:10.1016/j.neuron.2012.12.032.

Wang, X.-J. (1999). Synaptic Basis of Cortical Persistent Activity: the Importance of NMDA Receptors to Working Memory. *J. Neurosci.* 19, 9587–9603.

Wang, X.-J. (2001). Synaptic reverberation underlying mnemonic persistent activity. *Trends in Neurosciences* 24, 455–463. doi:10.1016/S0166-2236(00)01868-3.

Wang, X.-J. (2020). Macroscopic gradients of synaptic excitation and inhibition in the neocortex. *Nature Reviews Neuroscience* 21, 169–178. doi:10.1038/s41583-020-0262-x.

Wang, X.-J., and Yang, G. R. (2018). A disinhibitory circuit motif and flexible information routing in the brain. *Current Opinion in Neurobiology* 49, 75–83. doi:10.1016/j.conb.2018.01.002.

Wasmuht, D. F., Spaak, E., Buschman, T. J., Miller, E. K., and Stokes, M. G. (2018). Intrinsic neuronal dynamics predict distinct functional roles during working memory. *Nat Commun* 9, 3499. doi:10.1038/s41467-018-05961-4.

Womelsdorf, T., Ardid, S., Everling, S., and Valiante, T. A. (2014). Burst Firing Synchronizes Prefrontal and Anterior Cingulate Cortex during Attentional Control. *Current Biology* 24, 2613–2621. doi:10.1016/j.cub.2014.09.046.

Xue, X., Halassa, M. M., and Chen, Z. S. (2021). Spiking recurrent neural networks represent task-relevant neural sequences in rule-dependent computation. *bioRxiv*, 2021.01.21.427464. doi:10.1101/2021.01.21.427464.

Yada, Y., Kanzaki, R., and Takahashi, H. (2016). State-Dependent Propagation of Neuronal Sub-Population in Spontaneous Synchronized Bursts. *Front. Syst. Neurosci.* 10. doi:10.3389/fnsys.2016.00028.

Yang, S.-T., Shi, Y., Wang, Q., Peng, J.-Y., and Li, B.-M. (2014). Neuronal representation of working memory in the medial prefrontal cortex of rats. *Molecular Brain* 7, 61. doi:10.1186/s13041-014-0061-2.

Yoshimura, Y., Dantzker, J. L. M., and Callaway, E. M. (2005). Excitatory cortical neurons form fine-scale functional networks. *Nature* 433, 868–873. doi:10.1038/nature03252.

Yu, J. Y., Liu, D. F., Loback, A., Grossrubatscher, I., and Frank, L. M. (2018). Specific hippocampal representations are linked to generalized cortical representations in memory. *Nature Communications* 9, 2209. doi:10.1038/s41467-018-04498-w.

Zaksas, D., and Pasternak, T. (2006). Directional Signals in the Prefrontal Cortex and in Area MT during a Working Memory for Visual Motion Task. *J. Neurosci.* 26, 11726–11742. doi:10.1523/JNEUROSCI.3420-06.2006.

Zenke, F., Gerstner, W., and Ganguli, S. (2017). The temporal paradox of Hebbian learning and homeostatic plasticity. *Current Opinion in Neurobiology* 43, 166–176. doi:10.1016/j.conb.2017.03.015.

Zenke, F., Hennequin, G., and Gerstner, W. (2013). Synaptic Plasticity in Neural Networks Needs Homeostasis with a Fast Rate Detector. *PLOS Computational Biology* 9, e1003330. doi:10.1371/journal.pcbi.1003330.

Zhang, Z., and Séguéla, P. (2010). Metabotropic Induction of Persistent Activity in Layers II/III of Anterior Cingulate Cortex. *Cerebral Cortex* 20, 2948–2957. doi:10.1093/cercor/bhq043.

Zielinski, M. C., Shin, J. D., and Jadhav, S. P. (2019). Coherent Coding of Spatial Position Mediated by Theta Oscillations in the Hippocampus and Prefrontal Cortex. *J. Neurosci.* 39, 4550–4565. doi:10.1523/JNEUROSCI.0106-19.2019.